



UNIVERSIDADE D
COIMBRA

Cristian Vasile Miculaș,

**INNOVATIVE PLUG-AND-PLAY
JOINTS FOR HYBRID TUBULAR
CONSTRUCTIONS**

**Ph.D. thesis in Steel and Composite Construction supervised by
Professor Ricardo Joel Teixeira Costa and Professor Luís Alberto
Proença Simões da Silva and presented to the Department of Civil
Engineering of the Faculty of Sciences and Technology of the
University of Coimbra**

March 2023



FACULDADE DE
CIÊNCIAS E TECNOLOGIA
UNIVERSIDADE D
COIMBRA

Cristian Vasile Miculaș

INNOVATIVE PLUG-AND-PLAY JOINTS FOR HYBRID TUBULAR CONSTRUCTIONS

Ph.D. thesis in Steel and Composite Construction supervised by Professor Ricardo Joel Teixeira Costa and Professor Luís Alberto Proença Simões da Silva and presented to the Department of Civil Engineering of the Faculty of Sciences and Technology.

March 2023

fct Fundação
para a Ciência
e a Tecnologia

isise Institute for Sustainability and
Innovation in Structural Engineering

Acknowledgment

Firstly, I would like to express my profound appreciation to Professor Ricardo Joel Teixeira Costa, my co-supervisor, for his mentorship, kindness, and unyielding forbearance during my Ph.D. journey. He possesses a unique talent for conveying complex concepts in an easily comprehensible fashion, which has been a source of inspiration and encouragement to me. It is through his invaluable guidance that this thesis has come to fruition.

Next, I extend my sincere appreciation to Professor Luís Alberto Proença Simões da Silva for his support and guidance throughout my doctoral journey. Under his tutelage, I acquired crucial knowledge and skills that I will always treasure. Although I wish he could have honored me with more of his valuable time, it was an honor to have had such an outstanding supervisor.

I would like to acknowledge the financial support provided by the Portuguese Foundation for Science and Technology (Fundação para a Ciência e a Tecnologia) under the grant SFRH/BD/138151/2018.

Furthermore, I express my heartfelt thanks to esteemed Professor Cosmin G. Chiorean of the Technical University of Cluj-Napoca, whose guidance and support paved the way for my entry into the world of academia. His impeccable principles of ethical conduct and moral decorum serve as a beacon of aspiration that I fervently aspire to emulate. His incisive and rational counsel played an indispensable role in the successful culmination of my academic pursuits. I would also like to sincerely thank Ovidiu Prodan and Marius Buru.

I would like to extend my utmost gratitude to Dr. Silva Mazzoni and Professor Michael H. Scott for their invaluable support in rendering OpenSees comprehensible. Furthermore, I wish to express my profound appreciation to all members of the OpenSees Café.

I wish to acknowledge Professor Aldina Maria da Cruz Santiago, whose exceptional kindness and support have been priceless to me throughout my academic journey.

Additionally, I extend my gratitude to all esteemed members of the DEC, ISISE, and INNO3DJOINTS project, whose invaluable contributions played a pivotal role in the successful realization of this endeavor.

Moreover, I express my sincere gratitude to the administrative staff members of DEC, namely Dulce Marques, Sandra Borges, Cristina Carolino, Nuno Almeida, Ricardo Oliveira, and Néilson Fernandes. Their tireless dedication and unwavering commitment to ensuring the seamless functioning of the department have been critical in facilitating the smooth execution of my academic pursuits.

Lastly, I would like to express my deep gratitude to my family and M for their unconditional love and support, particularly during the demanding last months of this project.

Abstract

Modular construction has become increasingly popular in recent years due to its various benefits, including faster construction time, reduced on-site work, automated production, and enhanced design capabilities. Despite these advantages, there are also several challenges that must be addressed, such as limited design flexibility, transportation and logistics difficulties, and building code restrictions. One effective approach to overcome these challenges is to shift the focus from on-site joint execution to off-site joint production using industrialized or automated methodologies. A potential solution that has gained traction is the development of plug-and-play joints, which enable modularity, facilitate steel structure erection, promote reusability, and reduce construction time.

In today's engineering landscape, the use of computational tools is critical to achieve efficiency in any field. Therefore, the possibility of modeling these new types of plug-and-play joints in calculation software is of utmost importance. This enables the incorporation of the joint's actual behavior into the structural analysis, as required by practitioners in design offices. Only by providing the necessary calculation tools to designers can these types of modular constructions and plug-and-play joints be successful.

This work presents a macro-element formulation for the modeling of the innovative 3D plug-and-play joints for the structural system developed within the European project INNO3DJOINTS. This system enables modularity, faster construction, and deconstruction. The modular construction system is hybrid, combining tubular columns with cold-formed lightweight steel profiles using plug-and-play connections and cross-laminated timber slabs to provide an efficient structural system.

The macro-element is based on the component method, accounts for the 3D interaction between the faces of the tubular column, and its components have a clear physical meaning. The conceptual design of this element is validated through parametric studies against models developed in a higher-order finite element commercial software, Abaqus. Moreover, the macro-element's architecture is implemented in the framework of OpenSees, as a standalone beam-to-column joint finite element.

Simplified procedures, using the Equivalent Frame Models technique, are developed for the closed-form computation of the stiffness matrix of the macro-element from the geometric and mechanical

properties of the joint region, thus making the macro-element practical for everyday design purposes.

An analytical definition of the strength criterion is also proposed based on the Equivalent Frame Models technique. This strength criterion is global as it does not rely on evaluating internal forces in a specific component. Although it presents a conservative threshold, it guarantees safety across all considered scenarios.

Additionally, the conceptual framework of nonlinear behavior attributed to the components of the beam-to-column joint finite element is established. The findings against higher-order finite element models indicate that while the evaluation of the onset of the nonlinear regime of joints can be conducted conservatively, further research is necessary with regard to the modeling of the post-yielding behavior in this context.

In conclusion, the proposed beam-to-column joint finite element can be utilized by design practitioners to design, analyze, and optimize the outputs of structures under various loading conditions, especially within the elastic regime.

Keywords: plug-and-play joints, macro-element, joint finite element, OpenSees, modular construction

Resumo

Presentemente a popularidade da construção modular tem vindo a crescer significativamente devido às suas vantagens, tais como reduzido tempo de produção, redução do trabalho em obra, produção automatizável e procedimentos expeditos para análise e dimensionamento. Contudo, apesar destas vantagens existem ainda vários desafios como a reduzida flexibilidade que oferece aos projectistas, dificuldades inerentes à logística de construção e transporte e restrições nos códigos de construção que geralmente não abordam este tipo de solução. Uma abordagem que permite potenciar as vantagens da construção modular passa por alterar o foco da execução das ligações em obra para a execução das juntas em ambiente controlado utilizando métodos industriais e automatizados. Uma possível solução que tem vindo a ganhar popularidade crescente é o desenvolvimento de juntas plug-and-play, que permitem modularidade, facilidade na montagem de estruturas em aço, promovem a reutilização da estrutura e reduzem o tempo de construção.

Hoje em dia, no ramo da engenharia, a utilização de ferramentas computacionais é fundamental para se alcançar elevada produtividade e eficiência. Assim sendo, a possibilidade de modelar este novo tipo de junta plug-and-play através de programas computacionais é crucial. Tal análise permitiria a incorporação do comportamento real da junta na análise estrutural, tal como requerido pelos gabinetes de projeto. Esta nova tipologia de junta apenas será bem-sucedida, caso sejam fornecidas as ferramentas de cálculo necessárias aos projetistas de construção modular.

O presente trabalho apresenta uma formulação de macroelementos para a modelação do sistema estrutural das juntas 3D plug-and-play, desenvolvida no âmbito do projeto europeu INNO3DJOINTS. Este sistema permite modularidade, construção e desconstrução mais rápidas. O sistema de construção modular é híbrido, combinando colunas tubulares com perfis em aço leve enformado a frio com a utilização de conexões plug-and-play e lajes em madeira por forma a formar um sistema estrutural leve e eficiente.

O macroelemento é baseado no método das componentes e considera a interação tridimensional entre as faces da coluna tubular e os seus componentes. Este elemento é validado através de análises paramétricas em que os resultados da análise das juntas modeladas desta forma é confrontado com

resultados de modelos de elementos finitos de ordem superior desenvolvidos em um software comercial Abaqus. Além disso, a arquitetura do macroelemento é implementada na estrutura do OpenSees, como um elemento finito de junta autónomo e independente do elementos viga e coluna.

Foram desenvolvidos procedimentos simplificados, utilizando modelos de estruturas porticadas equivalentes (EFMs), para o cálculo de forma fechada da matriz de rigidez do macroelemento a partir das propriedades geométricas e mecânicas da zona nodal, tornando o macroelemento prático e de fácil utilização.

Uma definição analítica de critérios de resistência também é proposta com base na técnica EFMs. Estes critérios de resistência são globais, não dependendo da avaliação de esforços internos de componentes específicos. Embora apresente um limiar conservador, garante a segurança para todos os cenários considerados.

Adicionalmente, estabeleceu-se o quadro conceptual para a análise e modelação não linear de estruturas definindo relações constitutivas não lineares para as componentes do elemento finito junta viga-pilar – a capacidade de análise não linear do elemento junta viga-pilar foi definida na fase de desenvolvimento e implementação em regime linear. A partir da confrontação com resultados de modelos de elementos finitos de ordem superior também em regime não linear conclui-se que embora a avaliação do início do regime não linear das juntas possa ser realizada de forma conservadora com o elemento junta viga-pilar, são necessários desenvolvimentos adicionais no campo da modelação do regime pós-cedência das componentes.

Em suma, o elemento finito proposto para a junta viga-coluna pode ser utilizado por projetistas profissionais para analisar e otimizar a estrutura sob várias condições de carregamento, especialmente dentro do regime elástico.

Palavras-chave: juntas plug-and-play, macroelemento, elemento finito de junta, OpenSees, construção modular

DISCLAIMER

This document presents the results of the research conducted within the framework of the grant SFRH/BD/138151/2018 funded by the Portuguese Foundation for Science and Technology (Fundação para a Ciência e a Tecnologia). This study is a component of a more extensive investigation on the connection between open cold-formed lightweight truss-girders and tubular columns, supported by the Research Fund for Coal and Steel under grant agreement No. 749959 (INNO3DJOINTS): “Innovative 3D joints for robust and economical hybrid tubular construction”.

It is important to note that the views, findings, and conclusions or recommendations presented in this publication are exclusively those of the author and do not necessarily reflect the views of the funding entities, the Portuguese Foundation for Science and Technology (Fundação para a Ciência e a Tecnologia) and the European Commission Research Programme of the Research Fund for Coal and Steel.

Contents

- Acknowledgment** **i**

- Abstract** **iii**

- Resumo** **v**

- DISCLAIMER** **vii**

- List of Figures** **xix**

- List of Tables** **xxix**

- 1 Introduction** **1**
 - 1.1 Scope and motivation of the research 1
 - 1.2 Objective of the research 2
 - 1.3 Organization of the document 3

- 2 Literature review** **5**
 - 2.1 Introduction to steel structures 5
 - 2.2 Modular construction 5
 - 2.2.1 Tubular steel structures 6
 - 2.2.2 Lightweight steel structures 6
 - 2.3 Steel joints 7
 - 2.3.1 Hybrid joints 8
 - 2.3.2 CFS joints 9
 - 2.3.3 Plug-and-play joints 9
 - 2.3.3.1 Desirable features in plug-and-play joints 11
 - 2.3.3.2 Design codes specification 11
 - 2.4 Modeling of joints 12

ix

2.4.1	Introduction	12
2.4.2	0D models	12
2.4.3	Component method	15
2.4.4	3D FEM models	16
2.4.5	Macro-element models	17
2.4.6	Code limitations	21
2.5	OpenSees	22
2.5.1	Software framework	22
2.5.2	OpenSees joint element library	25
2.5.2.1	BeamColumnJoint2D and BeamColumnJoint3D	25
2.5.2.2	Joint2D and Joint3D	26
2.5.2.3	ElasticTubularJoint	28
2.5.2.4	LehighJoint2D	29
2.5.3	Conclusion	29
2.6	An innovative hybrid modular structural system	29
2.6.1	Introduction	29
2.6.2	Conceptual design	31
2.6.3	Main advantages	31
2.6.4	P&PJ system	32
2.6.4.1	Overall configuration	32
2.6.4.2	Assembly process	36
2.6.4.3	Main geometric constraints	36
2.6.5	Macro-modeling of the P&PJ with a single CFS truss-girder	36
2.6.5.1	Components under tension and compression internal forces	37
2.6.5.2	Components under vertical shear force	40
2.6.5.3	Strength interaction models	43
2.6.6	Formulation of the P&PJ macro-element	43
2.6.6.1	Introduction	43
2.6.6.2	General overview	43
2.6.6.3	Drawbacks and limitations	46
3	Development of the macro-element formulation	55
3.1	Introduction	55
3.2	P&PJ systematic approach for development	55

3.3	Proof of concept	57
3.3.1	Formulation	57
3.3.2	Validation	63
3.4	Extension to beam-to-column joint finite element	68
3.4.1	Sign convention	70
3.4.2	Linear formulation	84
3.4.3	Compatibility matrix's elements computation	87
4	Implementation of the macro-element in OpenSees	91
4.1	Inno3DPnPJoint Class	91
4.2	Transformation matrix	94
4.3	Nonlinear formulation	96
4.4	Inno3DPnPJoint user manual	98
4.4.1	Element info	98
4.4.2	Element source code	98
4.4.3	Command line and input arguments	98
4.4.4	Node definition requirements	99
4.4.4.1	Input Order	100
4.4.4.2	Coplanarity	100
4.4.4.2.1	Verification overview	100
4.4.4.2.2	Mathematical description	100
4.4.4.3	Perpendicularity	101
4.4.4.3.1	Verification overview	101
4.4.4.3.2	Mathematical description	102
4.4.4.4	Collinearity	102
4.4.4.4.1	Verification overview	102
4.4.4.4.2	Mathematical description	102
4.4.4.5	Centrality and dimensionality	103
4.4.5	Common error messages	103
4.4.6	Output recorders	104
4.4.6.1	Element level	104
4.4.6.2	Component level	104

5	Computation of mechanical properties of the macro-element for linear regime	109
5.1	Introduction	109
5.2	Analytical definition of stiffness of the components	109
5.2.1	Introduction	109
5.2.2	General procedure to compute the stiffness of the components	111
5.2.3	Application of the procedure to the EFMs	114
5.2.4	Description of the EFMs	116
5.2.4.1	HS-EFM	116
5.2.4.2	HR-EFM-IF	116
5.2.4.3	HR-EFM-IEq	117
5.2.4.4	PS-EFM	117
5.2.4.5	PR-EFM-IF	118
5.2.4.6	PR-EFM-IEq	120
5.2.5	Stiffness of the tube components of the EFMs	120
5.2.5.1	HS-EFM	120
5.2.5.2	HR-EFM-IF	120
5.2.5.3	HR-EFM-IEq	122
5.2.5.4	PS-EFM	122
5.2.5.5	PR-EFM-IF	122
5.2.5.6	PR-EFM-IEq	123
5.3	EFM's effective bending stiffness	123
5.3.1	Neves-Gomes Model	123
5.3.1.1	Linear elastic regime	123
5.3.1.1.1	Extension to rectangular cross-sections	125
5.3.1.2	Post-elastic regime	126
5.3.2	Effective bending stiffness	127
5.4	Validation and calibration of EFM's effective bending stiffness	129
5.4.1	Load patterns and socket configurations	130
5.4.1.1	Load patterns	130
5.4.1.2	Socket configurations	134
5.4.1.3	Naming convention of the analyzed models	134
5.4.2	OpenSees models	134
5.4.3	Refined Finite Element Models	139
5.4.3.1	Description	139

5.4.3.2	Mesh sensitivity analysis	142
5.4.3.3	Geometry and boundary condition	145
5.4.4	Comparison of results	151
5.4.5	Calibration of the effective stiffness	156
5.4.5.1	Method 1: ideal correction factor based correction	156
5.4.5.1.1	Ideal correction factor	156
5.4.5.1.2	Global correction factor	159
5.4.5.1.3	Geometry-related correction factors	161
5.4.5.2	Method 2: matching displacements based correction	165
5.4.5.3	Conclusion	169
5.5	Analytical definition of the strength criterion	169
5.5.1	Introduction	169
5.5.2	General procedure to compute the strength of the components	169
5.5.3	Critical sections on SEFMs	171
5.5.4	Equivalent bending strength	174
5.5.5	Nonlinear behavior of the beam-to-column joints	175
5.5.6	Bending moments in SEFM	177
5.5.7	Application of the procedure to the EFMs	179
5.5.8	Adjustment factor	180
5.5.8.1	Cases considered	180
5.5.8.2	Results unadjusted	181
5.5.8.3	Results adjusted	182
5.5.9	Conclusion	183
6	Conceptual framework for nonlinear analysis	185
6.1	Introduction	185
6.2	Conceptual framework	186
6.3	Predictive capability of NGM nonlinear formulation for P&PJ setup	192
6.4	Strength reduction factor of the NGM yield force	196
6.5	Validation of the framework for nonlinearity	202
6.5.1	OpenSees models	202
6.5.2	RFEMs build with Abaqus	203
6.5.3	Load Patterns	203
6.5.4	Results	203

Contents

6.6	Conclusions	205
7	Conclusions and future lines of investigations	215
7.1	Summary of the work	215
7.2	Conclusions	218
7.3	Future lines of investigation	218
	Appendices	221
A	P&PJ's components under tension and/or compression	223
A.1	Column side wall	223
A.1.1	Strength	223
A.1.2	Stiffness	225
A.2	Column face	225
A.2.1	Strength	225
A.2.2	Stiffness	227
A.3	Welds between column and socket	235
A.3.1	Strength	235
A.3.2	Stiffness	236
A.4	Socket	236
A.4.1	Strength	236
A.4.2	Stiffness	238
A.5	Bearing in the socket	239
A.5.1	Strength	239
A.5.2	Stiffness	240
A.6	Bolt between the socket and the T-plug in shear	240
A.6.1	Strength	240
A.6.2	Stiffness	241
A.7	Bearing in the T-plug	241
A.8	T-plug	242
A.8.1	Strength	242
A.8.2	Stiffness	243
A.9	Welds between T-plug and clipping part	244
A.10	Y-part (clip on the CFS)	244
A.10.1	Strength	244

A.10.2 Stiffness	246
A.11 Bearing of the Y-part	247
A.12 Bolt between the clipping part and the cold-formed member in shear	248
A.13 Bearing of cold-formed member (chord)	248
A.14 Gross and net section of cold-formed member (chord)	249
B P&PJ’s components under vertical shear load	251
B.1 Column side wall	251
B.2 Column face	251
B.3 Welds between column and socket	252
B.4 Socket	252
B.5 Bearing in the socket	252
B.6 Bolt between the socket and the T-plug in shear	253
B.7 Bearing in the T-plug	254
B.8 T-plug	254
B.9 Welds between T-plug and Y-part	255
B.10 Y-part	255
B.11 Bearing in the Y-part	255
B.12 Bolt between the Y-part and the cold-formed member in shear	256
B.13 Bearing of cold-formed member (truss)	256
B.14 Gross and net section of the CFS end post	256
C Macro-element developed within the INNO3DJOINTS project	259
C.1 The element formulation	259
C.1.1 Sign convention	259
C.1.2 Linear formulation	259
C.1.3 Compatibility matrix	260
C.2 Implementation in OpenSees	260
C.2.1 Inno3DJointND Class	260
C.2.2 Nonlinear formulation	260
C.2.3 Inno3DJointND user manual	263
C.2.3.1 Element info	263
C.2.3.2 Element source code	263
C.2.3.3 Command line and input arguments	263

C.2.3.4	Input requirements	264
C.2.3.5	Common errors messages	265
C.2.4	Output recorders	267
D	Values of the parameters used in the calculation for the Euler-Bernoulli elements	269
E	Detailed analytical computation of the condensed stiffness matrix of the EFMs	271
E.1	HS-EFM	271
E.1.1	LP-EFM.1	271
E.1.2	LP-EFM.2	273
E.1.3	LP-EFM.3	275
E.1.4	LP-EFM.4	277
E.1.5	Condensed stiffness matrix of HS-EFM	279
E.2	HR-EFM-IF	280
E.2.1	LP-EFM.1	280
E.2.2	LP-EFM.2	282
E.2.3	LP-EFM.3	284
E.2.4	LP-EFM.4	286
E.2.5	Condensed stiffness matrix of HR-EFM-IF	288
E.3	HR-EFM-IEq	290
E.3.1	Condensed stiffness matrix of HR-EFM-IEq	290
E.4	PS-EFM	290
E.4.1	LP-EFM.1	291
E.4.2	LP-EFM.2	291
E.4.3	LP-EFM.3	294
E.4.4	LP-EFM.4	296
E.4.5	Condensed stiffness matrix of PS-EFM	298
E.5	PR-EFM-IF	299
E.5.1	LP-EFM.1	299
E.5.2	LP-EFM.2	301
E.5.3	LP-EFM.3	303
E.5.4	LP-EFM.4	305
E.5.5	Condensed stiffness matrix of PR-EFM-IF	307
E.6	PR-EFM-IEq	309

E.6.1	Condensed stiffness matrix of PR-EFM-IEq	309
F	OpenSees model file example for Tcl	311
F.1	Main file	311
F.2	Beam-to-column joint element definition file for the elastic case	315
F.3	Beam-to-column joint element definition file for the elastic-plastic case	319
G	Results RFEMs - material elastic	325
H	Results stiffness	331
I	Results RFEMs - material elastic-plastic	353
J	Attainment of $F_{el} - \delta_{el}$	359
K	Detailed analytical computation of the strength criterion of the EFMs	363
K.1	HS-EFM	363
K.2	HR-EFM-IF	366
K.3	HR-EFM-IEq	369
K.4	PS-EFM	370
K.5	PR-EFM-IF	373
K.6	PR-EFM-IEq	376
L	Quadrant Calculation	379
M	Results strength - unadjusted	381
N	Results strength - adjusted	385
O	Force-displacement curves for a column plate	389
P	Results nonlinearity	395

List of Figures

2.1	Typical joint types in a building frame [3].	8
2.2	Joints and Connections [3].	8
2.3	Hybrid construction systems.	8
2.4	Macro-element of an interior composite connection [7].	18
2.5	Macro-element for beam-to-column steel joints in 2D with beams of equal depth (single shear panel) [148].	19
2.6	Macro-element for beam-to-column steel joints in 2D with beams of unequal depth (double shear panel) [148].	19
2.7	Macro-element for beam-to-column steel joints in 3D: X-Z plane [149].	20
2.8	Macro-element for beam-to-column steel joints in 3D: Y-Z plane [149].	20
2.9	Macro-element for beam-to-column steel joints in 3D: Y-X plane [149].	21
2.10	OpenSees – software framework (console).	22
2.11	OpenSees Joint Element Library: BeamColumnJoint [181].	26
2.12	OpenSees Joint Element Library: Joint2D - 5 SPR [161].	27
2.13	OpenSees Joint Element Library: Joint2D - 1 SPR [161].	27
2.14	OpenSees Joint Element Library: Joint3D [161].	28
2.15	OpenSees Joint Element Library: ElasticTubularJoint [183].	28
2.16	OpenSees Joint Element Library: LehighJoint2D [185].	29
2.17	INNO3DJOINTS structural system.	30
2.18	Detail of the INNO3DJOINTS structural system’s main components.	32
2.19	Innovative 3D plug-and-play joint (P&PJ) system.	33
2.20	INNO3DJOINTS plug-and-play joint system: load direction.	34
2.21	INNO3DJOINTS plug-and-play joint system: axis.	35
2.22	Experimental test at various structure levels [192].	35
2.23	Geometric parameters of the plug and socket [196].	37

2.24 Plug-and-play connection decomposition into components for the case of tension or compression internal forces [197].	38
2.25 Tension and compression connections in the joint under bending moment [197]. . . .	41
2.26 Plug-and-play connection decomposition into components for the case of vertical shear force.	41
2.27 Schematic representation of a P&PJ within the INNO3DJOINTS project [5].	44
2.28 Proposed beam-to-column joint finite element within the INNO3DJOINTS project [5]: 3D overview.	44
2.29 Proposed beam-to-column joint finite element within the INNO3DJOINTS project [5]: external DOFs.	45
2.30 Components of the beam-to-column joint finite element developed within the INNO3DJOINTS project [5]: linear deformation in the X direction.	47
2.31 Components of the beam-to-column joint finite element developed within the INNO3DJOINTS project [5]: linear deformation in the Y direction.	47
2.32 Components of the beam-to-column joint finite element developed within the INNO3DJOINTS project [5]: linear deformation in the Z direction.	48
2.33 Components of the beam-to-column joint finite element developed within the INNO3DJOINTS project [5]: linear deformation diagonally (in Y-Z and Y-X planes).	48
2.34 Components of the beam-to-column joint finite element developed within the INNO3DJOINTS project [5]: rotational deformation in the X direction.	49
2.35 Components of the beam-to-column joint finite element developed within the INNO3DJOINTS project [5]: rotational deformation in the Y direction.	49
2.36 Components of the beam-to-column joint finite element developed within the INNO3DJOINTS project [5]: rotational deformation in the Z direction.	50
2.37 Components of the beam-to-column joint finite element developed within the INNO3DJOINTS project [5]: X-Y plane.	50
2.38 Components of the beam-to-column joint finite element developed within the INNO3DJOINTS project [5]: Y-Z plane.	51
2.39 Components of the beam-to-column joint finite element developed within the INNO3DJOINTS project [5]: Z-X plane.	52
2.40 Proposed beam-to-column joint finite element within the INNO3DJOINTS project [5]: schematic representation in 3D view.	52
2.41 Proposed beam-to-column joint finite element within the INNO3DJOINTS project [5]: schematic representation in 2D view.	53

3.1	INNO3DJOINTS plug-and-play joint system.	57
3.2	Schematic representation of a full P&PJ.	57
3.3	Component-based macro-element of a tubular profile at cross-section level (2D view).	59
3.4	Modeling strategy of P&PJ with a sectional macro-element.	61
3.5	Deformation modes disregarded in the macro-element design (top view).	62
3.6	Definition of the stiffness of the tube components.	62
3.7	Component-based macro-element of a tubular profile in the joint's region (top view).	63
3.8	Tube components for the short face (width).	65
3.9	Tube components for the long face (length).	66
3.10	Cross-section's deformed shape for tube components on U1 and U2 for SC02.	68
3.11	Load patterns (LP) used to validate the CME proof of concept.	68
3.12	Positive sign convention of components.	71
3.13	Proposed beam-to-column joint finite element: 3D overview.	72
3.14	Proposed beam-to-column joint finite element: internal and external DOFs.	73
3.15	Components of the beam-to-column joint finite element: linear deformation in the X direction.	74
3.16	Components of the beam-to-column joint finite element: linear deformation in the Y direction.	75
3.17	Components of the beam-to-column joint finite element: linear deformation in the Z direction.	76
3.18	Components of the beam-to-column joint finite element: rotational deformation in the X direction.	77
3.19	Components of the beam-to-column joint finite element: rotational deformation in the Y direction.	78
3.20	Components of the beam-to-column joint finite element: rotational deformation in the Z direction.	79
3.21	Components of the beam-to-column joint finite element: tube components for face 1.	80
3.22	Components of the beam-to-column joint finite element: tube components for face 2.	81
3.23	Components of the beam-to-column joint finite element: tube components for face 3.	82
3.24	Components of the beam-to-column joint finite element: tube components for face 4.	83
3.25	Compatibility matrix elements color-coded by values.	86
3.26	Compatibility matrix: element $a_{(2,2)}$ after load application $U_2 = 1$	88
4.1	Class diagram of the beam-to-column joint finite elements library of OpenSees.	94

4.2	Code execution sequence for linear elastic analysis.	95
5.1	Degrees of Freedom in the Displacement Method Application.	111
5.2	Load Patterns for the Equivalent Frame-Models.	113
5.3	General procedure for calculating stiffness of components in all EFMs.	115
5.4	HS-EFM: a general overview.	117
5.5	HR-EFM-IF: general overview.	118
5.6	PS-EFM: a general overview.	119
5.7	Frame-elements divided into points of interest.	119
5.8	PR-EFM-IF: general overview.	121
5.9	Frame-elements divided into points of interest.	121
5.10	Gomes-Neves Model (adapted from [207]).	125
5.11	Gomes-Neves Model: Out-of-plane force-deformation relation model (adapted from [207]).	127
5.12	Gomes-Neves Model adapted to innovative 3D plug-and-play joint system (schematic representation).	128
5.13	OpenSees FEM network for stiffness calculation: SHS (<i>160 cases</i>).	138
5.14	OpenSees FEM network for stiffness calculation: RHS (<i>544 cases</i>).	138
5.15	Influence of rounded corners on column face dimensions.	138
5.16	Schematic representation of the RFEMs build in Abaqus.	139
5.17	Abaqus FEM network for stiffness calculation: SHS (<i>40 cases</i>).	140
5.18	Abaqus FEM network for stiffness calculation: RHS (<i>68 cases</i>).	140
5.19	Tubular columns (SHS and RHS): height and cross-section dimension.	141
5.20	Finite Element types used in Abaqus [113]	141
5.21	Load application: CF on RP.	142
5.22	BC for mesh sensitivity analysis.	143
5.23	Out-of-plane displacement extraction locations for the tubular column face.	143
5.24	Out-of-plane displacements of tube face in section H1 for different mesh sizes.	144
5.25	Out-of-plane displacements of tube faces in section W0.	144
5.26	Out-of-plane displacements of tube face in section H1 for different meshing techniques.	144
5.27	Final mesh configuration for tubular columns.	145
5.28	Points and regions for BC application.	146
5.29	Applied BC.	146
5.30	Overall deformation of the cross-section of tubes: U Magnitude.	147

5.31	Out-of-plane displacement of tube faces in section W0 for different BC.	147
5.32	Out-of-plane displacements from section W0.	148
5.33	Applied BC.	149
5.34	Deformed tube in 3D using different BC: U magnitude.	149
5.35	Deformed tube in 2D in section W0 using different BC.	150
5.36	Final BC applied to the tubular column.	150
5.37	PS-EFM-R1.	154
5.38	PR-EFM-IF-R1.	155
5.39	Schematic representation of the iterative process for SHS.	156
5.40	Schematic representation of the iterative process for RHS.	157
5.41	PS-EFM-R1 - Method 1.	163
5.42	PR-EFM-IF-R1 - Method 1.	164
5.43	PS-EFM-R1 - Method 2.	167
5.44	PR-EFM-IF-R1 - Method 2.	168
5.45	General procedure for computing the strength criterion.	172
5.46	Analyzed Equivalent Frame-Models (EFM).	173
5.47	Critical sections on a generic Simplified Equivalent Frame-Model (SEFM).	174
5.48	Element with fixed-fixed end supports subjected to a concentrated load at mid-span.	174
5.49	Schematic representation of the computation of F_{el} and δ_{el}	176
5.50	Stiffness coefficients associated with the DOFs.	178
5.51	Bending moments in critical sections caused by unit load on the DOFs.	179
5.52	Displacements association for quadrant calculations for a generic SEFM.	180
5.53	Network for strength calculation: SHS (<i>1280 cases</i>).	181
5.54	Network for strength calculation: RHS (<i>2176 cases</i>).	181
6.1	Stress and plasticity related results at the joint region gathered from RFEMs: actively yielding (AC yield), equivalent plastic strain (PEEQ), and Mises equivalent stress (von Mises).	187
6.2	Stiffness of the tube components (generic).	189
6.3	Constitutive relations for components.	190
6.4	Reference case to set the nonlinear modeling approach.	191
6.5	Curves for the reference case: $F^A - d^A$ and $R^{BD} - d^A$	191
6.6	Network for F_{pl} calculation from the NGM (<i>40 cases</i>) [mm].	193
6.7	RFEM of a column plate: assembly and discretization.	193

List of Figures

6.8	RFEM of a column plate: deformation in the loaded region.	193
6.9	Schematic representation of the yielding force (adapted from [207]).	195
6.10	$F - \delta$ comparison between RFEM and NGM for $L_1 = 200$ and $u = 120$ and all SCs.	197
6.11	$F - \delta$ comparison between RFEM and NGM for $L_2 = 300$ and $u = 120$ and all SCs.	197
6.12	Analogy between a 1D element and 1/2 EFM for the strength reduction factor.	198
6.13	Strength reduction factor for the shorter column face (w_1).	199
6.14	Strength reduction factor for the longer column face (w_2).	200
6.15	Force-deformation curves used as input in OpenSees for the PR-EFM-IF-R0-SC01 case.	204
6.16	Load Patterns for the nonlinear calculation.	204
6.17	Force-displacement under LP01-L1.	206
6.18	Force-deformation curves in the tube components under LP01-L1.	207
6.19	Force-displacement under LP02-L1.	208
6.20	Force-deformation curves in the tube components under LP02-L1.	209
6.21	Force-displacement under LP03-L1.	210
6.22	Force-deformation curves in the tube components under LP03-L1.	211
6.23	Force-displacement under LP04-L1.	212
6.24	Force-deformation curves in the tube components under LP04-L1.	213
A.1	Column side wall under tensile or compressive force.	224
A.2	Column face under tensile or compressive force.	226
A.3	Calculation model for tubular section [197].	227
A.4	Face of the tubular column [197].	228
A.5	Springs model [197].	234
A.6	Symbols for the socket's strength and stiffness [197].	237
A.7	Edge distance e_1 for the socket under tensile force [197].	240
A.8	Symbols for the T-plug strength and stiffness [197].	243
A.9	Symbols for the Y-part strength and stiffness [197].	245
A.10	Edge distance, e_1 , and pitch distance, p_1 , for the Y-part [197].	248
A.11	Edge distance, e_1 , and pitch distance, p_1 , for the CFS chord [197].	248
B.1	Pitch distance, p_1 , and edge distance, e_1 , for the socket under shear load [197].	253
B.2	Pitch distance, p_1 , and edge distance, e_1 , for the T-plug under shear load [197].	254
B.3	Pitch distance, p_1 , and edge distance, e_1 , for the Y-part [197].	256
B.4	Pitch distance, p_1 , and edge distance, e_1 , for the Y-part [197].	257

C.1	Compatibility matrix elements color-coded by values.	262
C.2	Proposed beam-to-column joint finite element within the INNO3DJOINTS project [5]: Inno3DJointND element’s schematic representation.	263
C.3	Proposed beam-to-column joint finite element within the INNO3DJOINTS project [5]: Inno3DJointND element’s node input order.	264
C.4	Proposed beam-to-column joint finite element within the INNO3DJOINTS project [5]: Inno3DJointND element’s dimensions.	265
C.5	Proposed beam-to-column joint finite element within the INNO3DJOINTS project [5]: Inno3DJointND element’s dimensions.	265
D.1	1D element with fixed-roller end supports.	269
D.2	1D element with fixed-fixed end supports.	270
E.1	HS-EFM under LP-EFM.1.	272
E.2	HS-EFM under LP-EFM.2.	274
E.3	HS-EFM under LP-EFM.3.	276
E.4	HS-EFM under LP-EFM.4.	278
E.5	HR-EFM under LP-EFM.1.	281
E.6	HR-EFM under LP-EFM.2.	283
E.7	HR-EFM under LP-EFM.3.	285
E.8	HR-EFM under LP-EFM.4.	287
E.9	PS-EFM under LP-EFM.1.	292
E.10	PS-EFM under LP-EFM.2.	293
E.11	PS-EFM under LP-EFM.3.	295
E.12	PS-EFM under LP-EFM.4.	297
E.13	PR-EFM under LP-EFM.1.	300
E.14	PR-EFM under LP-EFM.2.	302
E.15	PR-EFM under LP-EFM.3.	304
E.16	PR-EFM under LP-EFM.4.	306
H.1	HS-EFM-R0.	342
H.2	HS-EFM-R1.	343
H.3	PS-EFM-R0.	344
H.4	HR-EFM-IF-R0.	345
H.5	HR-EFM-IEq-R0.	346

List of Figures

H.6	HR-EFM-IF-R1.	347
H.7	HR-EFM-IEq-R1.	348
H.8	PR-EFM-IF-R0.	349
H.9	PR-EFM-IEq-R0.	350
H.10	PR-EFM-IEq-R1.	351
J.1	$F_{el} - \delta_{el}$ (absolute value) curve: for RHS-m03-H01-SC02.	361
K.1	HS-EFM and its SEFM with the critical sections.	364
K.2	Stiffness coefficients associated to d_3 for the HS-EFM.	364
K.3	Bending moments in critical sections under unit load in DOFs for the HS-EFM.	365
K.4	Bending moments in critical sections under unit load in DOFs for the HS-EFM.	366
K.5	HR-EFM and its SEFM with the critical sections.	367
K.6	Stiffness coefficients associated to d_3 for the HR-EFM-IF.	367
K.7	Bending moments in critical sections under unit load in DOFs for the HR-EFM-IF.	368
K.8	Bending moments in critical sections under unit load in DOFs for the HR-EFM-IF.	369
K.9	PS-EFM and its SEFM with the critical sections.	371
K.10	Stiffness coefficients associated to d_3 for the PS-EFM.	371
K.11	Bending moments in critical sections under unit load in DOFs for the PS-EFM.	372
K.12	Bending moments in critical sections under unit load in DOFs for the PS-EFM.	373
K.13	PR-EFM and its SEFM with the critical sections.	374
K.14	Stiffness coefficients associated to d_3 for the PR-EFM-IF.	374
K.15	Bending moments in critical sections under unit load in DOFs for the PR-EFM-IF.	375
K.16	Bending moments in critical sections under unit load in DOFs for the PR-EFM-IF.	376
O.1	$F - \delta$ comparison between RFEM and NGM for $L_1 = 200$ and $u = 20$ and all SCs.	389
O.2	$F - \delta$ comparison between RFEM and NGM for $L_2 = 300$ and $u = 20$ and all SCs.	390
O.3	$F - \delta$ comparison between RFEM and NGM for $L_1 = 200$ and $u = 40$ and all SCs.	390
O.4	$F - \delta$ comparison between RFEM and NGM for $L_2 = 300$ and $u = 40$ and all SCs.	391
O.5	$F - \delta$ comparison between RFEM and NGM for $L_1 = 200$ and $u = 80$ and all SCs.	391
O.6	$F - \delta$ comparison between RFEM and NGM for $L_2 = 300$ and $u = 80$ and all SCs.	392
O.7	$F - \delta$ comparison between RFEM and NGM for $L_1 = 200$ and $u = 190$ and all SCs.	392
O.8	$F - \delta$ comparison between RFEM and NGM for $L_2 = 300$ and $u = 160$ and all SCs.	393
P.1	Force-displacement under LP01-L2.	395
P.2	Force-deformation curves in the tube components under LP01-L2.	396

P.3	Force-displacement under LP02-L2.	397
P.4	Force-deformation curves in the tube components under LP02-L2.	398
P.5	Force-displacement under LP03-L2.	399
P.6	Force-deformation curves in the tube components under LP03-L2.	400
P.7	Force-displacement under LP04-L2.	401
P.8	Force-deformation curves in the tube components under LP04-L2.	402

List of Tables

2.1	Components under tension/compression internal forces [197].	38
2.2	Components under vertical shear force [197].	42
2.3	Internal DOFs deformation direction.	44
2.4	Components deformation direction.	45
2.5	Summary of the 0D elements.	46
3.1	Tube components stiffness raw values [kN/m].	67
3.2	Tube components stiffness: final values [kN/m].	67
3.3	Results validation: RFEM vs. CME [mm]	69
3.4	Internal DOFs.	70
3.5	Components deformation direction.	71
3.6	The non-zero elements of the compatibility matrix \mathbf{A}	85
3.7	Steps to calculate elements $a_{i,j}$ of \mathbf{A}	87
3.8	Worked example for DOF 2.	89
4.1	Methods Comprising the Inno3DPnPJoint Class.	92
4.2	Input arguments for Inno3DPnPJoint joint finite element.	99
4.3	Common errors.	104
4.4	Valid \$arg – at element level.	105
4.5	Valid \$arg – at component level.	106
5.1	Index of tables for stiffness calculation.	115
5.2	LPs considered for the SHS.	131
5.3	LPs considered for the RHS.	132
5.4	LPs and SCs naming examples.	135
5.5	SCs considered for the SHS.	135
5.6	SCs considered for the RHS.	136
5.7	Linear elastic material characteristics of the tubular column.	141

List of Tables

5.8	Number of finite elements for each mesh configuration.	145
5.9	Method for results comparison: case examples.	151
5.10	Results: PS-EFM-R1.	152
5.11	R^2 for each column face: RHS.	152
5.12	Results: PR-EFM-IF-R1.	153
5.13	R^2 for each column face: SHS.	153
5.14	PS-EFM-R1: cf_i and $\varepsilon_{2,i}$	157
5.15	PR-EFM-IF-R1: $cf_{i,1}$, $cf_{i,2}$ and $\varepsilon_{2,i}$	158
5.16	Average ideal correction factor, cf_a , for SHS.	160
5.17	Average ideal correction factors, $cf_{a,1}$ and $cf_{a,2}$, for RHS.	160
5.18	Global correction factor, cf_p : SHS.	160
5.19	Global correction factor, $cf_{p,1}$ and $cf_{p,2}$: RHS.	160
5.20	Geometry-related correction factors: ideal values for var_1 and var_2 in SHS.	162
5.21	Geometry-related correction factors: ideal values for var_1 and var_2 in RHS.	162
5.22	R^2 for each column face: SHS-R0.	165
5.23	R^2 for each column face: RHS-R0.	166
5.24	R^2 for each column face: SHS-R1.	166
5.25	R^2 for each column face: RHS-R1.	166
5.26	Bilinear elastic-plastic material characteristics of the tubular column.	175
5.27	Index of tables for strength calculation.	180
5.28	Results: PS-EFM-R1 [kNm] (unadjusted).	182
5.29	Results: PR-EFM-IF-R1 [kNm] (unadjusted).	182
5.30	Results: PS-EFM-R1 [kNm] (adjusted).	183
5.31	Results: PR-EFM-IF-R1 [kNm] (adjusted).	183
6.1	Comparing yield strengths obtained by different methods.	195
6.2	Values of F_{NGM} for RHS [kN].	201
6.3	Values of SRF for RHS-R0.	201
6.4	Values of SRF for RHS-R1.	201
C.1	The non-zero elements of the compatibility matrix A	261
C.2	Input arguments for Inno3DJointND joint finite element.	264
C.3	Conditions for node coordinates.	266
C.4	Common errors.	266
C.5	Valid \$arg – at element level.	267

C.6	Valid $\$arg$ – at component level.	268
G.1	Values of displacements δ_i for SHS.	325
G.2	Values of displacements δ_i for RHS.	326
G.3	Deformed shape for SHS for all LPs with SC02.	329
G.4	Deformed shape for RHS for all LP with SC02.	330
H.1	Index of tables for stiffness results.	331
H.2	Results: HS-EFM-R0.	332
H.3	Results: HS-EFM-R1.	333
H.4	Results: PS-EFM-R0.	334
H.5	Results: HR-EFM-IF-R0.	335
H.6	Results: HR-EFM-IEq-R0.	336
H.7	Results: HR-EFM-IF-R1.	337
H.8	Results: HR-EFM-IEq-R1.	338
H.9	Results: PR-EFM-IF-R0.	339
H.10	Results: PR-EFM-IEq-R0.	340
H.11	Results: PR-EFM-IEq-R1.	341
I.1	Values of displacements δ_{el}^i and $\delta_{el.min}^i$ for SHS.	353
I.2	Values of displacements δ_{el}^i and $\delta_{el.min}^i$ for RHS.	354
L.1	Values of d_1^{EFM} and d_2^{EFM} for RHS-m01-V01-SC01.	379
M.1	Index of tables for unadjusted strength results.	381
M.2	Results: HS-EFM-R0 [kNm] (unadjusted).	381
M.3	Results: HS-EFM-R1 [kNm] (unadjusted).	382
M.4	Results: PS-EFM-R0 [kNm] (unadjusted).	382
M.5	Results: HR-EFM-IF-R0 [kNm] (unadjusted).	382
M.6	Results: HR-EFM-IEq-R0 [kNm] (unadjusted).	382
M.7	Results: HR-EFM-IF-R1 [kNm] (unadjusted).	383
M.8	Results: HR-EFM-IEq-R1 [kNm] (unadjusted).	383
M.9	Results: PR-EFM-IF-R0 [kNm] (unadjusted).	383
M.10	Results: PR-EFM-IEq-R0 [kNm] (unadjusted).	383
M.11	Results: PR-EFM-IEq-R1 [kNm] (unadjusted).	384
N.1	Index of tables for adjusted strength results.	385

N.2	Results: HS-EFM-R0 [kNm] (adjusted).	385
N.3	Results: HS-EFM-R1 [kNm] (adjusted).	386
N.4	Results: PS-EFM-R0 [kNm] (adjusted).	386
N.5	Results: HR-EFM-IF-R0 [kNm] (adjusted).	386
N.6	Results: HR-EFM-IEq-R0 [kNm] (adjusted).	386
N.7	Results: HR-EFM-IF-R1 [kNm] (adjusted).	387
N.8	Results: HR-EFM-IEq-R1 [kNm] (adjusted).	387
N.9	Results: PR-EFM-IF-R0 [kNm] (adjusted).	387
N.10	Results: PR-EFM-IEq-R0 [kNm] (adjusted).	387
N.11	Results: PR-EFM-IEq-R1 [kNm] (adjusted).	388

Chapter 1

Introduction

1.1 Scope and motivation of the research

Modular construction has gained widespread popularity recently due to its numerous benefits, including faster construction time, automated production and design capabilities, reduced resource usage and waste, and cost-effectiveness [1], [2]. Despite these advantages, several challenges need to be addressed, such as limited design flexibility, transportation and logistics difficulties, and building code restrictions.

To remain competitive in the steel construction industry, new solutions are needed to overcome new challenges, such as decreasing execution times, costs, and the possibility of reusing structures. The joint is critical in achieving these goals, as it is vital in determining the costs and ease of (dis)assembling the structure [3]. To tackle these challenges, joints with improved fabrication and erection characteristics can be developed based on innovative structural engineering solutions.

One effective approach to overcome these challenges is to shift the focus from on-site joint execution to off-site joint production utilizing industrialized or automated methods. A solution that has gained traction is the development of plug-and-play joints, which appeal to modularity, facilitate the erection of steel structures, and reduce construction time. In addition, a surge has been seen in the use of plug-and-play joints because they simplify the construction process and make it more efficient, [4]. However, there are still challenges to be addressed, such as structural integrity and analysis of these structures, costs, compatibility, and maintenance.

These considerations prompted the scope of research within the European project INNO3DJOINTS [5], where an innovative plug-and-play joint system for hybrid tubular construction connects tubular columns with cold-formed lightweight steel truss-girders and cross-laminated timber slabs to create a

highly efficient structural system.

Accurate knowledge of connection behavior is crucial for effective design and construction, ensuring the overall performance, safety, durability, and sustainability of structures. The motivation for this research is to understand the behavior of the innovative 3D plug-and-play joint system developed within the INNO3DJOINTS project through extensive analytical and numerical simulations.

1.2 Objective of the research

The primary objective of this research is to develop a 3D macro-element for the innovative plug-and-play steel joint system that has been proposed within the INNO3DJOINTS project [5]. This macro-element is aimed to be used in daily design practices and to simulate the real behavior of joints in a structural analysis.

In today's engineering landscape, the use of computational aids is crucial to achieving efficiency in any field. For this reason, the implementation of the macro-element in calculation software is of utmost importance. This will enable the incorporation of the joint's real behavior into the structural analysis and make the model versatile enough to accommodate different possible joint configurations, as required by practitioners.

To accomplish the main objective, the following specific objectives have been established:

1. conceptualization of a macro-element for the 3D innovative plug-and-play joint system, which is :
 - (a) based on the component method;
 - (b) accounts for the 3D interaction between the faces of the tubular column;
 - (c) has components that have a clear physical meaning;
 - (d) is versatile enough to support any joint configuration and load pattern;
2. extension of the macro-element into a beam-to-column joint finite element;
3. implementation of the beam-to-column joint finite element within a free, open-source, and powerful general finite element computational tool as a standalone element;
4. definition of appropriate stiffness parameters leading to realistic internal force distributions;
5. establishment of a strength criterion to evaluate the structural safety of the beam-column joint;
6. definition of a post-elastic behavior of the joints components.

The axiomatic idea behind the study is that by successfully achieving these objectives, the beam-to-column joint finite element can be utilized by design practitioners to design, analyze, and optimize the outputs of structures under various loading conditions.

1.3 Organization of the document

The present thesis is organized into 7 chapters, as follows:

Chapter 1: Introduction – describes the purpose and scope of this study, including the research motivation and objectives. The chapter concludes with a discussion of the organization of the document.

Chapter 2: Literature review – presents a concise overview of the relevant literature on beam-to-column connections, establishing the current state of knowledge on which the study is based. It then describes modular construction systems that utilize tubular steel and lightweight structures, emphasizing steel joints, particularly plug-and-play joint systems. The chapter also focuses on modeling beam-to-column joints, employing macro-modeling approaches, and describing the OpenSees framework and its joint element library. Finally, the chapter outlines the conceptual design of the innovative hybrid modular system developed within the INNO3DJOINTS project, highlighting its advantages, and it provides a detailed description of the project's 3D plug-and-play joint system, including geometry, layout, assembly, and design process as well as the macro-element developed within the project.

Chapter 3: Development of the macro-element formulation – introduces the conceptualization and validation of the proposed macro-element for modeling the innovative 3D plug-and-play joint system. The extension of this macro-element to a beam-to-column joint finite element is then outlined. The section also includes a discussion on the components of the joint, the adopted sign convention, and the formulation for linear elastic analysis.

Chapter 4: Implementation of the macro-element in OpenSees – explains the implementation of the proposed beam-to-column joint finite element within the OpenSees framework. The nonlinear formulation is also discussed. The chapter includes a manual for the Inno3DPnPJoint element, which contains the element information, command line, and necessary input arguments for creating the element. Additionally, the node definition requirements are explained in terms of input order, coplanarity, perpendicularity, collinearity, centrality, and dimensionality. The chapter concludes with a list of common error messages and an overview of valid output recorders at the element and component levels.

Chapter 5: Computation of mechanical properties of the macro-element for the linear regime

Chapter 1. Introduction

– outlines the analytical definition of the mechanical properties of the macro-element for the linear elastic regime. Specifically, this chapter presents the analytical definition of the stiffness of the macro-element components, which have been validated against higher-order finite element models developed in Abaqus. Additionally, the analytical definition of the strength criterion, which ensures the structural safety of the beam-to-column joint, is also presented and validated against refined finite element models through various parametric studies that involve varying several parameters. These parametric studies were conducted to obtain a comprehensive overview of the capabilities and limitations of the model and to make the definition of it as general as possible.

Chapter 6: Conceptual framework for nonlinear analysis – details the development of a conceptual framework to analyze the nonlinear behavior of beam-to-column joint finite element. The chapter emphasizes the need for further research to investigate the post-yielding behavior of the joint. The behavior of the tubular column within the joint region is analyzed and validated using higher-order finite element models developed in Abaqus by employing bilinear behavior curves for the tube components. Additionally, the study investigates the onset of post-yielding behavior.

Chapter 7: Conclusions and future lines of investigation — the final chapter of this study provides a comprehensive overview of the work done in this thesis. The analysis results are synthesized to draw meaningful conclusions regarding the model's behavior under various loading conditions. In addition, the chapter identifies areas for future research and development that will enhance the accuracy and robustness of the model.

Chapter 2

Literature review

2.1 Introduction to steel structures

Steel is one of the most flexible building materials for structural applications. Aside from its good load-bearing performance and variety of shapes and sizes, it allows for an off-site fabrication process that securely assesses the quality and reduces on-site erection time. Moreover, steel can be infinitely recycled and transformed into new elements without losing its quality or mechanical properties.

Steel structures have evolved in tandem with the rise of modular solutions, which can reduce construction times and costs by up to 50% compared to traditional methods, potentially saving up to \$22 billion annually, considering only Europe and the United States. Tubular structures and lightweight steel frames are ideal for modularity, but their increased number of joints presents a challenge for designers. Developing tools to solve this problem is critical to continued growth and innovation in the field [6], [7].

2.2 Modular construction

Modular construction involves manufacturing building units off-site, which are then assembled into large volumetric components or significant building features at the construction site [8], [9]. Modular construction has grown significantly in recent years for residential, commercial, educational, or office buildings, warehouses, mixed-use purposes, and healthcare facilities. However, the lack of solid structural systems and joining techniques and the absence of design guidelines limit the modular high-rise building sector's growth. Modular construction has two main concepts: (i) the use of previously manufactured elements of a frame system and (ii) the use of 3D blocks that include

all the internal facilities and finishings. Prefabrication is categorized into five types: components, panelized structures, modular structures, hybrid structures, and entire buildings, based on the degree of prefabrication, size, and complexity of parts, and the building's configuration [10], [11]. A summarized review of the current state of modular construction was carefully detailed by Lacey et al. [12] and Ferdous et al. [13].

2.2.1 Tubular steel structures

Tubular elements are becoming increasingly popular due to their aesthetic appeal, superior weight-to-strength ratio, and resistance to global buckling under compressive stresses. Circular and square shapes with doubly symmetrical cross-sections are the ideal choices for these elements. According to Packer [14], the smaller exposed areas of tubular elements reduce the costs of coating and maintenance and minimize the probability of corrosion.

Tubular steel structures are widespread in construction, for example, in large-span roofs, stadiums, walkways, bridges, offshore structures, and modular buildings. However, there were many limitations for tubular steel structures in the past, mainly due to difficulties associated with the design and execution of joints.

Most likely, welding is the preferred method for joining tubular elements due to their complex geometries, and knowledge in this field is more advanced than bolted joints [15]. However, the scenario is changing with the rise in modularity, quality fabrication, and the need to reduce construction times and offer the possibility to disassemble structures. Design recommendations for tubular joint configurations are available, and additional research is being conducted [16]. Section 2.3 will provide a summary of popular joint types for steel structures.

2.2.2 Lightweight steel structures

Lightweight steel (LWS) structures are an attractive option for low-rise buildings due to their low weight, excellent strength-to-weight ratio, and sustainability. LWS framing occupies 39% of commercial steel applications in construction [17], with a growing interest in the residential and industrial sectors. Modern industry and fabrication technologies allow for high levels of prefabrication, resulting in benefits such as modularity, ease of installation, economy in handling, quick construction times, high-quality control, and flexibility of sectional profiles and shapes [18]–[20].

LWS in cold-formed steel frames differ from traditional steel structures due to their modular nature, particularly in their connections. Investigations have focused on the robustness of this system, including the influence of screw connections on stiffness and resistance, as suggested by Henriques et

al. [21]. However, this work is a small part of the extensive research carried out in recent years, as shown by Sharafi et al.'s [22] comprehensive review.

LWS seismic design is often conservative and poorly understood, as shown by Schafer et al. [23]. More recently, the earthquake-resistant design of LWS was revised, and new provisions were developed for Eurocode 8 Part 1, [24], and guidelines for LWS in medium to high seismicity locations were suggested by Landolfo et al. [25].

2.3 Steel joints

Frame structures of hot-rolled steel (HRS) composed of columns, beams, and slabs are the most common steel structural system in modern construction. Beam-to-column moment-resisting joints in steel frame structures include welded connections, bolted end plate connections, and bolted connections with angle cleats. These processes require skilled labor and pose inherent risks. However, steel construction offers the advantage of prefabrication, which can be done either in the workshop or directly on-site [3], [26].

While forging was the most typical method of joining steel components in the past, welds and mechanical fasteners such as bolts, pins, or nails are now the most popular solutions. Welded joints are ubiquitous in steel structures due to their attractive appearance and effective performance at transferring bending forces. However, welding steel requires highly skilled labor and vigorous quality control due to its susceptibility to discontinuities and defects. Welds also have an imperfect behavior when subjected to fatigue actions [27].

Mechanical fasteners, on the other hand, offer excellent simplicity for installation and disassembly for reuse or repair, with bolts being the preferred solution for steel. Bolted connections can be categorized by the acting force as shear, tension, or a combination of both [28]. Preloading is frequently applied to improve fatigue behavior. However, complex node geometries may restrict the use of bolts.

A typical steel frame consisting of beams and columns is shown in Fig. 2.1. The joints are between a beam and a column, two beams, two columns, and a column and its foundation.

According to Jaspart and Weynand [3], a connection is a set of physical components that mechanically fasten connected elements, such as the beam-to-column joint where the connection is concentrated at the site of the fastening action. The joint is the corresponding zone of interaction between the connected members, which can be single- or double-sided depending on the number of in-plane elements connected. Fig. 2.2 provides an illustration of the defined joints and connections in a 2D frame.

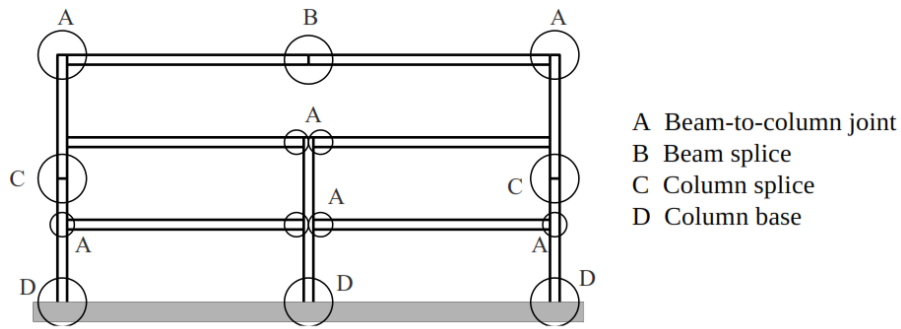


Figure 2.1: Typical joint types in a building frame [3].

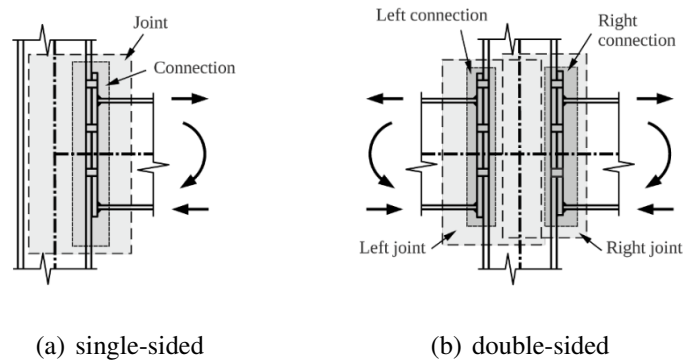


Figure 2.2: Joints and Connections [3].

2.3.1 Hybrid joints

Hybrid construction combines structural elements of different materials with varying mechanical properties instead of using structural elements of the same material. Unlike composite construction, where different materials act as one structural unit, hybrid materials can work together or independently, but they always provide advantages over using a single material [31]. In addition, hybrid construction allows for more efficient design as materials can have different deformations tailored to their capacity, unlike composite steel-concrete structures where the compatibility of deformations requires the two



(a) hybrid construction [29]



(b) hybrid joint: concrete-timber [30]

Figure 2.3: Hybrid construction systems.

materials to be in the same range [32]. However, designing hybrid solutions may not be effortless since each element inherently has a particular stiffness that may decrease the benefits of using hybrid solutions, and hybrid connections are not recommended by experts in the field [28]. Despite this, some hybrid constructions are being researched and used, including steel-timber hybrid construction [33]. Hybrid joints between steel and timber have great potential due to their high strength, stiffness, and ductility [33], [34]. For example, the joint between timber walls and floor components made of steel frames succeeded in transmitting lateral loads and enhancing the overall performance of the hybrid building [34]. Fig. 2.3 shows examples of hybrid construction in which concrete, steel, and timber are combined.

2.3.2 CFS joints

CFS members are typically connected using techniques such as zinc-coated self-drilling or self-tapping screws, while welding can be used for prefabricated elements to enhance their strength and rigidity [35]. Joints between beam-to-beam, beam-to-column, and truss connections using CFS members often experience local instability and elongation of bolt holes, with joint stiffness being strongly influenced by the thickness and shape of the profiles [36]. Experimental investigations have demonstrated the possibility of extending the component method to bolted gusset plate joints made of CFS members, indicating that cyclic loads could reduce joint strength and stiffness [37], [38]. The joints of cold-formed steel trusses have also shown significantly superior performance compared to well-known design standards [39]. The pattern of self-drilling screws used in the joints between CFS members significantly affects joint strength, and it can be captured by numerical modeling when including a fracture criterion for the steel sheets [40]. To mitigate non-ductile local buckling in CFS beams, friction-slip connections have been proposed and shown to increase energy dissipation, with bolt slip acting as a fuse mechanism [41].

2.3.3 Plug-and-play joints

Currently, the steel construction industry must tackle new challenges to remain competitive. One such challenge is the decrease in execution times, costs, and the possibility of reusing the same structure. The joint is central here, as it is an essential factor in determining the costs and the capability for (dis)assembling the same structure again [3]. Therefore, joints with enhanced fabrication and erection characteristics could be developed based on new innovative structural engineering solutions. Transcending the concept of joints from a local production technology to an industrialized or automated one is one suitable method to face the abovementioned challenges.

This leads to the development of plug-and-play joints, a solution that appeals to modularity, facilitating the erection of steel structures and reducing construction times. Likewise, one of the main incentives for developing these innovative joints is to improve fabrication procedures, i.e., to automate the process of structural assembly and to eliminate erroneous erection practices by reducing human assistance during construction.

First used in 1984, the term "plug-and-play" referred to a feature in which an operating system automatically detects and configures peripherals [42]. However, this term has since been utilized in various domains to indicate the readiness and immediate usability of interconnected parts. In this text, "plug-and-play" pertains to the joints linking distinct structural elements, for instance, beam-to-column connections that allow instant use of a structure without auxiliary structures such as scaffolding, props, or forms. Unlike reinforced concrete or composite structures, this method precludes the need to wait for material resistance.

A thorough review of the most recent developments concerning plug-and-play joints, sometimes called inter-module connections, was performed by Cofrar and Tsavdaridis [4]. Up to 60 different joints were collected from scientific literature and classified into three main groups according to their key features: (i) locking devices, (ii) post-tensioned joints, and (iii) bolted connections. Also, bolted connections were subdivided into three more subgroups depending on their application: column-to-column, beam-to-beam, and fitting-to-fitting. The research also proposed a multi-attribute ranking to facilitate the evaluation of each one of the 60 proposals.

The corner bracket inter-module connection has recently been studied in detail in Chinese and Australian universities at a numerical and experimental scale for tension, shear, and bending [43], [44] and under monotonic and cyclic lateral loads [45]–[47]. The results show that this joint allows easy installation and disassembly but has limited bending stiffness.

The post-tensioned vertical inter-module connection, featuring post-tensioned rods coupled through shear keys and accessed by an opening on connecting members, has been extensively studied for shear actions numerically and experimentally [45], [48], [49]. Additionally, guidelines have been proposed for its design and implementation [50], [51]. This inter-module connection has high shear stiffness but depends on the slip factor and bolt preload.

The use of interlocking pin and plate joints in modular construction has been researched Lacey et al. [52], [53], and satisfactory results were obtained through numerical and experimental analysis of these joints for shear. Nevertheless, precise bolt alignment during installation is crucial.

A seismic-resistant interlocking joint with intermediate resilient rubber layers was developed by Sendanayake et al. [54]–[56], which concentrates damage in end plates instead of column elements. Nevertheless, the ease of installation and repair is a drawback.

Plug-and-play applications have been widely studied, including the self-locking joint proposed by Nadeem et al. [57], which employs spring-activated pins to remove gaps between modules and ease installation and dismantling. Although numerical analysis indicates that the joint can exhibit semi-rigid behavior, no experimental tests have been carried out.

Energy dissipation devices have also been included in modular joints in the form of haunches, as shown by Zhang et al. [58], [59]. The joint is composed of an internal plug-like device and secured through hunched braces that provide superior seismic performance and promises significant damage reduction. Nonetheless, the configuration of this self-centering connection is complex, and it may be difficult to maintain and repair due to the permanent state of the components after installation.

A device more closely related to the plug-and-play concept was studied by Lee et al. [60]. The idea heavily appeals to pre-manufactured components and a short assembly process. In the study by Cofrar and Tsavdaridis [4], this joint had the highest ranking position, which considered manufacturing, construction, and structural aspects.

In conclusion, and in agreement with the findings of Cofrar and Tsavdaridis [4], it appears that most of the existing plug-and-play devices for modular buildings do not fully meet the requirements for such joints. This suggests that further research is necessary for this area. Furthermore, while experimental and numerical models have been used to investigate the behavior of these devices, there is a lack of robust, clear, and simple analytical models that can accurately predict and explain the behavior of these connections and that are suitable for use in design offices.

2.3.3.1 Desirable features in plug-and-play joints

Lytle et al. [61] and Cofrar and Tsavdaridis [4] identified key features for successful plug-and-play joints in modular constructions. These include self-alignment, tolerances for misalignment, easy adjustment, stiffness, strength, and stability for erection loads, resilience in seismic areas using structural fuse devices, modularity for mass production and flexibility, and disassembly for reuse and recycling, particularly in seismic areas with energy dissipation devices.

2.3.3.2 Design codes specification

Design codes for traditional joints (bolted or welded) can be applied to plug-and-play joints for designing similar components since steel joints can be analyzed as a composition of basic components to calculate their stiffness, strength, and rotation capacity. However, when using non-traditional components like clamps and hooks, experiments must be conducted, and the results should be statistically analyzed to obtain reliable design values for the plug-and-play joint's stiffness, strength,

and rotation capacity. This enables them to be used in the design of structures, as mentioned by Bijlaard and Brekelmans [62].

2.4 Modeling of joints

2.4.1 Introduction

In order to achieve efficiency in the design process of a steel structure, it is necessary to possess a comprehensive understanding of the behavior of its joints. Generally, a beam-to-column joint is subjected to axial force, shear force, and bending moment, considering only its in-plane behavior. However, the deformation caused by axial and shear forces may be insignificant compared to the bending moment. Therefore most of the in-plane behavior can be represented by a moment-rotation curve, $M - \Theta_r$.

Over the past several decades, extensive experimental campaigns have been conducted to study the behavior of beam-to-column joints. However, due to the complexity of testing every possible configuration of actual joints, researchers have sought to develop prediction equations that simulate the behavior of steel connections. According to Najafi [63], these techniques for predicting the behavior of beam-to-column joints can be classified into four distinct categories: empirical models, analytical models, mechanical models, and finite element models. These categories can take various forms, including linear, bilinear, multilinear, and nonlinear models, depending on the complexity of the joint and the level of accuracy desired.

The behavior of the above-mentioned categories describing the beam-to-column joints behavior can be assigned to spring elements (i.e., 0D elements); therefore, the most-relevant work undertaken on this topic will be summarized in the next sections. Furthermore, a succinct overview will be provided of the mechanical model (i.e., component method [64]), as well as 3D finite element models and macro-element models.

2.4.2 0D models

Traditionally, when modeling a structure of any type, the size of joints is often neglected or modeled through complementary techniques, such as rotational springs attached to the beam ends near the centerlines of the columns, i.e., 0D elements. This is also because most commercial packages do not offer a true solution for this issue, e.g., joint finite element. The most commonly used complementary technique is the calculation of a moment-rotation curve, represented as $M - \Theta_r$, which represents

the joint behavior under specified loads and the assignment of this behavior to a rotational spring positioned at the beam ends.

The loads acting on the beam-to-column joints are generally classified into static (i.e., monotonic) and dynamic (i.e., cyclic). Predicting the monotonic behavior of the joints is challenging due to the nonlinear nature of both the material and geometric properties. The complexity is further compounded when predicting their cyclic behavior due to additional phenomena, such as loading-unloading cycles and deterioration of mechanical properties.

Further on, a brief overview of the most renowned models to determine analytically the moment-rotation curves will be given.

The behavior of the joints under static loading can be defined using the following models [63], [65]:

- linear – represents the initial stiffness and was mainly used in early studies on semi-rigid connections to derive the mathematical representation of the moment-rotation curve [66]–[69]. Although it is easy to apply, it overestimates the connection stiffness at finite rotation because it does not account for the reduced stiffness of the joint at higher moments; therefore, it is acceptable at very low load levels. Nevertheless, it provides sufficient information for design purposes in the elastic range, i.e., serviceability limit state;
- bilinear – described by two lines: first, is the secant of the stiffness of a point on the actual moment-rotation, and second, is either horizontal or has a small slope. It was introduced by Lionberger and Weaver [70] and Romstad and Subramanian [71], recognizing the decrease in stiffness at higher loads. This model has seen various modifications and simplifications; for example, Tarpy and Cardinal [72], Melchers and Kaur [73], Lui and Chen [74], Zandonini and Zanon [75];
- piecewise multilinear – approximates the nonlinear behavior of the moment-rotation curve through a series of straight-line segments. The higher the number of segments used, the more accurate the approximation curve becomes. However, the presence of inaccuracies and jumps in stiffness at transition points make them less desirable. Several alternative models have been proposed in the literature, such as the trilinear model by Moncarz and Gerstle [76], the quadrilinear model by Melchers and Kaur [73], and the multilinear model by Razzaq [77] and Poggi and Zandonini [78];
- multilinear – obtained from curve fitting techniques, mechanical models, or finite element methods. The most common curves are itemized below:

- polynomial – first introduced by Kennedy [79] and Sommer [80], served as the foundation for the work of Frye and Morris, who were the pioneers in the development of a mathematical model based on an odd power polynomial factor to evaluate the moment-rotation curves of beam-to-column joints [81]. Subsequently, several studies have aimed to improve the Frye and Morris model. For example, Picard et al. [82] and Altman et al. [83] developed predictive models for strap-angle connections and top- and seat-angle connections with double web angles, respectively. Additionally, Goverdhan [84] re-evaluated the size parameters for flush end-plate connections, and Prabha et al. [85] included the air gap distance as an additional size parameter. Despite these advancements, the Frye and Morris model remains widely used and is incorporated into the Indian design code [86];
- exponential – proposed by Lui and Chen [74], presents an exponential moment-rotation curve that effectively represents the monotonic nonlinear behavior of connections. However, the model failed to capture sharp changes in the curve's slope [87]. Therefore, Kishi and Chen [88] proposed refinements, thus allowing for the incorporation of sharp changes in slope observed in experimental data. Additionally, other notable models were also proposed by Yee and Melchers [88];
- power – requires two or three parameters in its functions. The two-parameter model was first introduced by Batho and Lash [89] and later by Krishnamurthy et al. [90]. On the other hand, Colson and Louveau [91] proposed a three-parameter power model. Furthermore, Kishi and Chen [92], [93] proposed similar models, which aimed to address the strain-hardening stiffness issue in the Richard-Abott model [94]. Other noteworthy models were developed by Kukreti et al. [95] for a bolted steel end-plate connection and by Benterkia [96] for unstiffened flush end-plate connections, both of which were based on curve-fitting of available data;
- bounding line – first proposed by Al-bermani et al. [97] and later by Zhu et al. [98], requires four parameters. The central concept of this model is the division of the curve into three segments: the first and third segments represent linear elastic and plastic portions, respectively, while the second segment represents a smooth transition between the two.
- Ramberg-Osgood – originally proposed for nonlinear stress-strain relationships by Ramberg and Osgood [99] and then standardized by Ang and Morris [100]. This method examines experimental data on the moment-rotation behavior of a specific connection type to assess the influence of various size parameters. An iterative procedure is then

employed, where successive approximations are made to assumed stiffness characteristics of all connections in the structure to determine the appropriate connection stiffnesses. Subsequently, a single linear analysis is performed to determine the correct structural displacements and internal forces, thus effectively accounting for the nonlinear behavior of the connections;

- Richard-Abbott Model – represents a four-parameter power model, and it was proposed by Richard and Abbott [94] for modeling elastic-plastic stress-strain relation.

The behavior of the joints under dynamic loading can be defined using the following models [65]:

- independent hardening – developed by Chen and Saleeb [101] and assumes that material behavior characteristics remain unchanged after the initial loading and reloading conditions. The relation between moment and rotation in each loading cycle is independent; therefore, the hardening effect is not considered;
- kinematic hardening – a modification of the independent hardening taking into account the influence of hardening;
- bounding surface model with internal variables – developed to overcome the deficiency of the previous two models for repetitive loading cycles; representative work on this model has been done by Dafalias and Popov [102], Cook [103] and Goto et al. [104], [105].

2.4.3 Component method

Based on the work of Zoetemeijer [106] on bolted beam-to-column steel joints, which was further developed by many other researchers such as Huber and Tschemmerneegg [107], Jaspart [108], Tschemmerneegg et al. [109] and Weynand et al. [110]. the originality of the component method is to consider any joint as a set of individual basic components.

The component method is nowadays widely recognized, particularly by the Eurocode 3 Part 1-8 [28], as a general and convenient procedure to evaluate the mechanical properties of joints subjected to various loading situations, including static, dynamic, fire, and earthquake. A detailed review was done by Jaspart and Weynand [3], which concluded that the component method relies on the following steps:

- identification of the active basic components in the joint being considered (Table 6.1 from [28]);
- evaluation of each basic component's behavior, a simplified behavior can be considered based on the initial stiffness, strength, and ductility of the component;

- assembly of all constituent components and evaluation of the overall joint behavior or specific characteristics (i.e., initial stiffness, strength, or ductility); the mechanical properties of the joint are derived from those of all the individual constituent components, in a way that satisfies equilibrium between the external forces applied on the joint and the internal forces acting on the components.

2.4.4 3D FEM models

The Finite Element Method (FEM) is a numerical technique used to simulate for solving partial differential equations that describe physical systems, such as a structure or an element, under various loading conditions. The basic idea behind FEM is to divide the system into a collection of simpler, interconnected elements and approximate the system's behavior by solving equations for each element. The method then uses these local solutions to construct a global solution for the entire system. FEM is widely used in various fields, such as mechanical engineering, aerospace engineering, and civil engineering, to study and predict the behavior of structures and machines under various loading conditions. It is an efficient and powerful tool for design, optimization, and failure analysis [111].

According to Najafi [63], one of the first documented applications of the FEM in connections was carried out by Bose et al. [112] for a welded beam-to-column connection, in which the column web was at the center of the study. The concurrence between the simulated model and experimental data instigated other researchers to employ this method further. For instance, some of the nonlinear models previously mentioned by Krishnamurthy [90], Tarpay [72], and Kukreti [95] were derived from finite element analysis of end-plate connections.

The use of the FEM has seen a significant increase in recent times, particularly with the emergence of high-performance computing machines and the availability of various finite element software with intuitive graphical user interfaces. Notable examples include Abaqus [113], ANSYS [114], OpenSees [115], NASTRAN [116], NEFCAD 3D [117]–[119] and LS-DYNA [120].

Nowadays, the FEM acts as a link between experimental testing and mechanical and analytical modeling [121]. Many researchers have demonstrated the effectiveness of the FEM in the field of beam-to-column connections. For example, the efficacy of the FEM was demonstrated for beam-to-column end-plate bolted connections [122], welded beam-to-column joints with beams of unequal depth [123], bolted shear connectors and headed studs behavior [124], high-strength steel welded beam-to-column joints [125], bolted beam-column connections having thick extended end-plates and multiple bolts per row [126], T-stub joint component at ambient and elevated temperatures [127], the yield line patterns corresponding to the different collapse mechanisms in T-stubs with four bolts

per row [128], extended end-plate connection using the T-stub approach [129], stress concentration reduction at panel zone under cyclic loading using reduced beam section [130], characterization of web panel components in double-extended bolted end-plate steel joints [131], [132], semi-rigid joint for single-layer reticulated structures [133], novel pin-jointed connection for cold-formed steel trusses [134], preloaded bolts [135], innovative flush end-plate semi-rigid beam-to-column composite joint comprising deconstructable post-installed friction-grip bolted shear connectors [136], thermal loading on four types of beam-to-column joints: bolted end-plate, bolted cover-plate, bolted tee, and welded cover-plate [137], [138], response of friction joints under different velocity rates [139], different beam-to-column typologies, under accidental loading scenarios, namely, vehicle collision [140], [141], cyclic behavior of the collar connection [142], self-centering steel column bases [143], and plug-and-play joints between RHS columns and CFS trusses [144].

In conclusion, the use of FEM offers a highly advanced and accurate representation of joint behavior through numerical simulation. However, their implementation in design can be both time-consuming and challenging due to issues of convergence and calibration. Additionally, the cost of combining these models with physical testing can be cost-prohibitive [145]. Therefore, a simpler and more efficient solution is desirable, particularly for use in design offices, such as the utilization of macro-element modeling.

2.4.5 Macro-element models

Most elements typically available in FEM software used for design and research in structural engineering are geared toward modeling beams, columns, slabs, and shells. These structural design FEM packages typically do not include models specifically designed for joints and in the best cases, may only offer 0D elements.

However, there has been a growing need to model and design joints in recent years, particularly for use in structures such as buildings, bridges, and offshore structures. The use of macro-elements to model these joints has gained attention in recent years for two main reasons: (i) the relatively large size of beam-to-column joints and (ii) the ability to account for interaction using this approach.

Consequently, in the last few years, the macro-modeling approach of steel and steel-concrete composite joints has been known as a great development. A key aspect of using this technique is that the joint is treated independently of the rest of the members in a structure. In this way, the behavior of a connection is not added, as traditionally done by a rotational spring to the end of the beams, but rather by two connections (i.e., left and right side) and a web panel, which are all treated jointly and seamlessly in a single joint element. A series of new innovative models were proposed and some

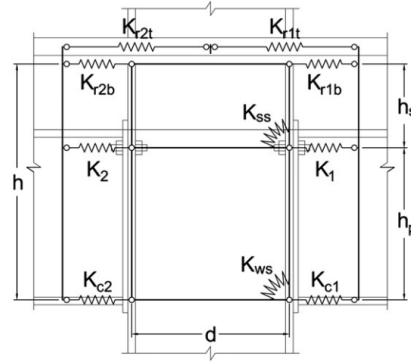


Figure 2.4: Macro-element of an interior composite connection [7].

which are most relevant to the current work are briefly described henceforth.

A component-based mechanical model for internal and external semi-rigid composite connections for the global analysis of frames is proposed by Bayo et al. [146], as depicted in Fig. 2.4. The method proposes a cruciform finite-sized elastic-plastic joint element that considers its deformation characteristics, including those of the panel zone and the left and right connections. This element is based on a previously developed model [147], but with a significantly improved component model for the composite that separates the contribution of the reinforcement and the bolt rows, the consideration of a double shear panel, and a displacement-based formulation that takes into consideration all the deformation modes.

For 2D connections of steel structures, Costa et al. [148] proposed a simplified model based on the component method [64]. This model allows for the characterization of a cruciform configuration where the left and right connections are modeled by two separate moment-rotation curves and the web panel by one supplementary moment-rotation curve. Moreover, the macro-element can be applied to both connections with equal and unequal beam depths, as shown in Fig. 2.5 and Fig. 2.6.

Following the same concept, a 3D model for steel joints is proposed by Gentili et al. [149], which considers the 3D behavior of the joints. The three plane views of the macro-element are presented in Figs. 2.7 to 2.9.

A more advanced macro-element for 2D steel joints is presented by Bayo et al. [150], [151]. This model is suitable for three different cases: (i) single rectangular panels suitable for internal joints with beams of equal depth at both sides; (ii) trapezoidal panels for joints with beams of different depths at both sides and inclined stiffeners; and (iii) double rectangular panels for the case of joints with beams of different depths at both sides and with or without horizontal stiffeners in the panel zone. Moreover, this joint model is suitable for both rigid and semi-rigid joints.

Extensive research has been carried out by Harada and Simões da Silva [152]–[154] on modeling beam-to-RHS column joints without diaphragm plates, an extension of the research done by

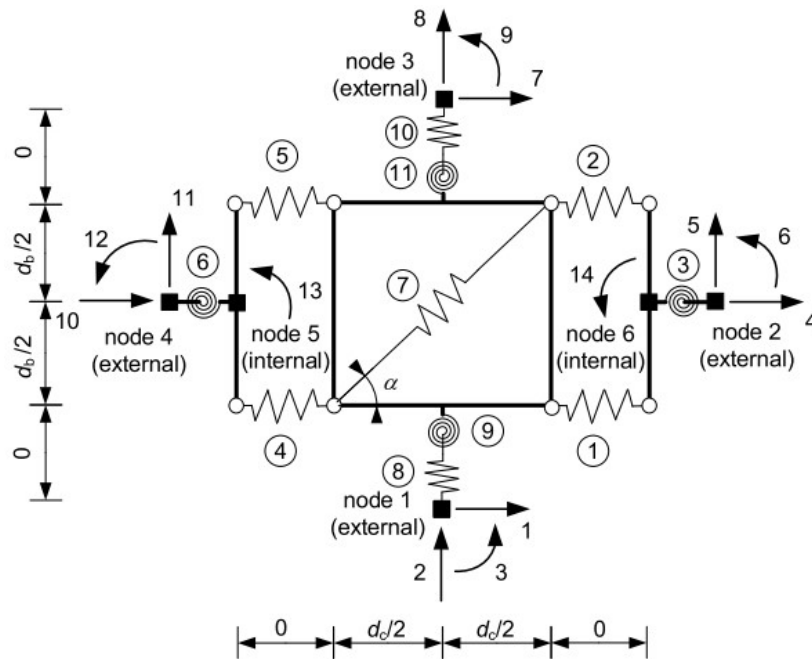


Figure 2.5: Macro-element for beam-to-column steel joints in 2D with beams of equal depth (single shear panel) [148].

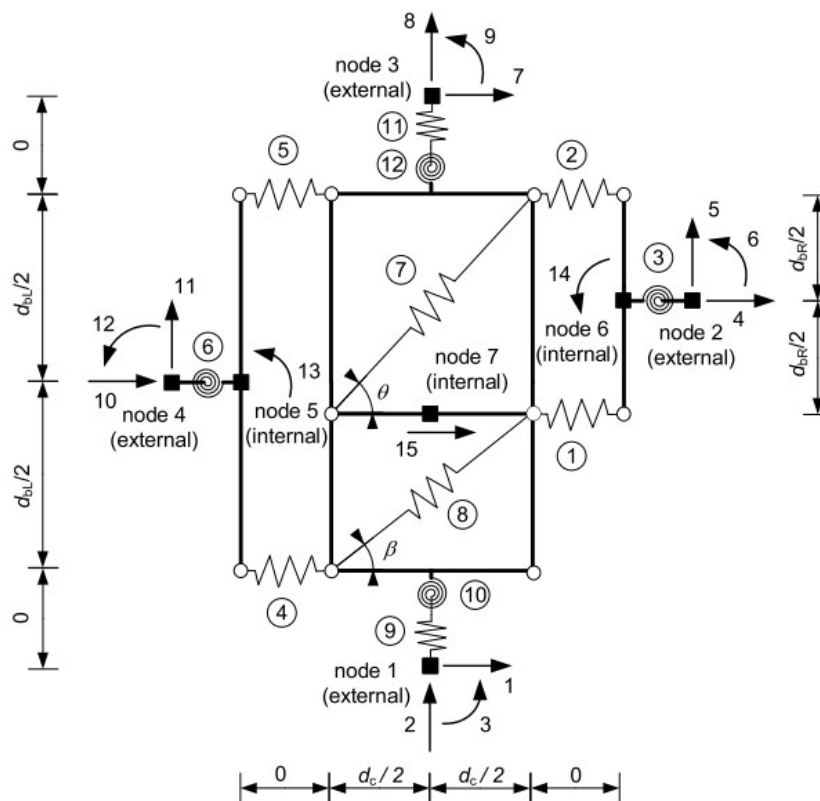


Figure 2.6: Macro-element for beam-to-column steel joints in 2D with beams of unequal depth (double shear panel) [148].

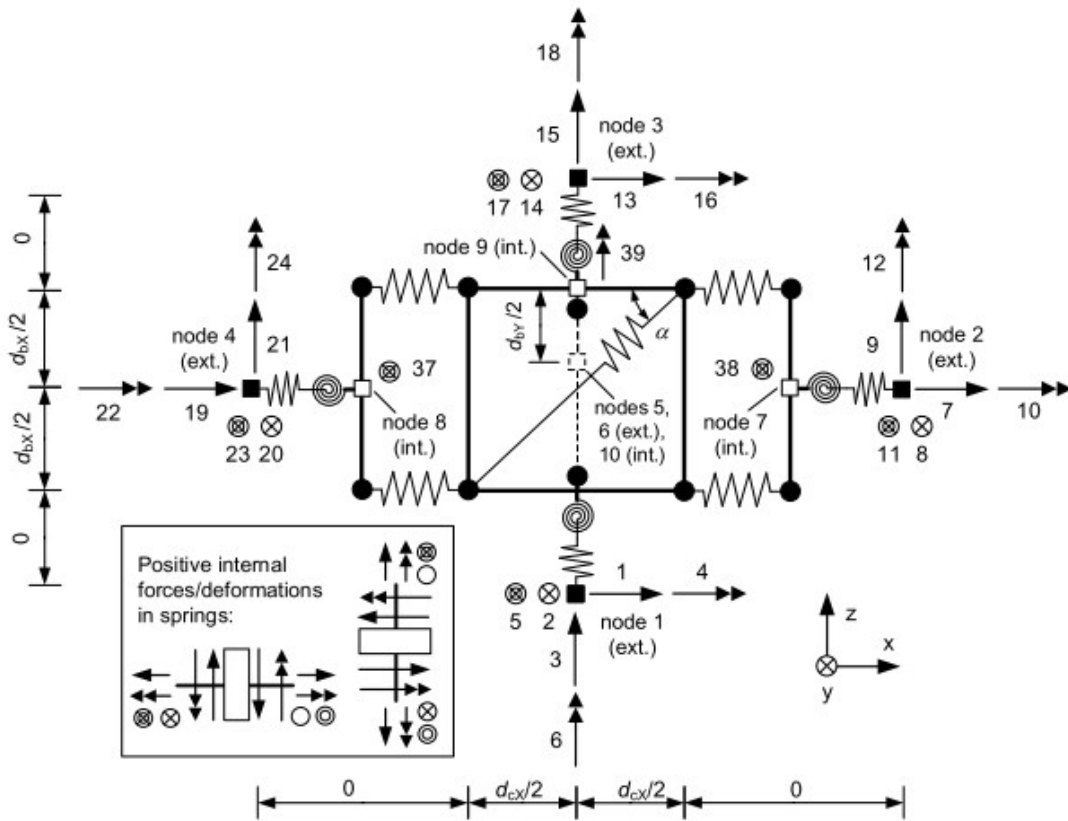


Figure 2.7: Macro-element for beam-to-column steel joints in 3D: X-Z plane [149].

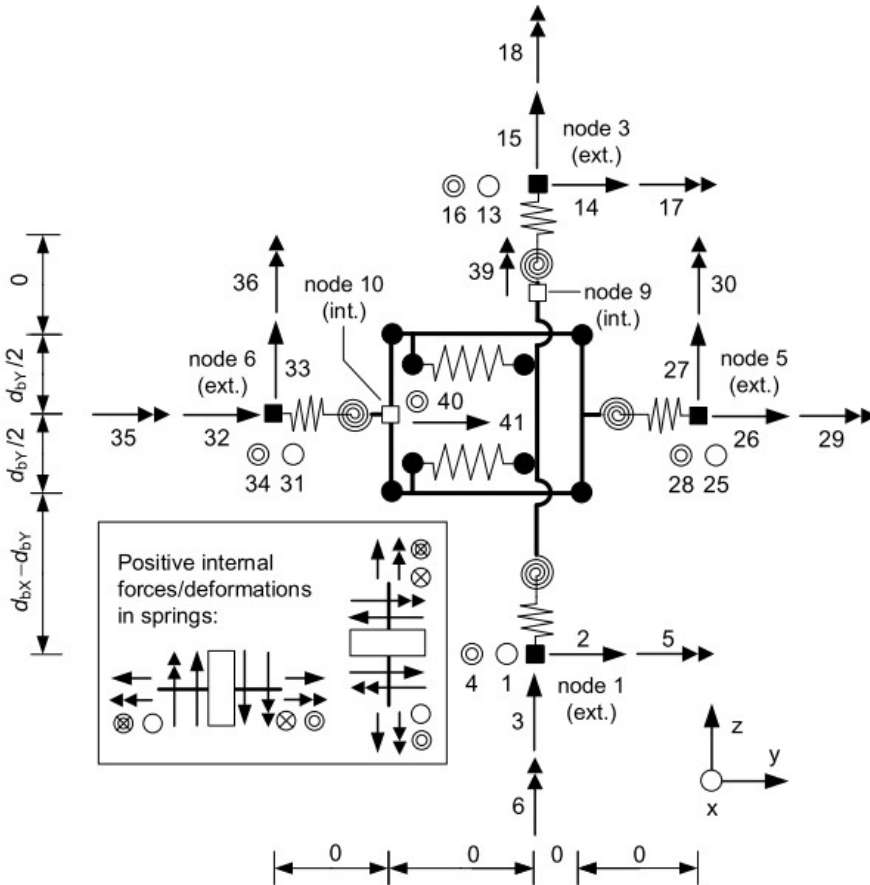


Figure 2.8: Macro-element for beam-to-column steel joints in 3D: Y-Z plane [149].

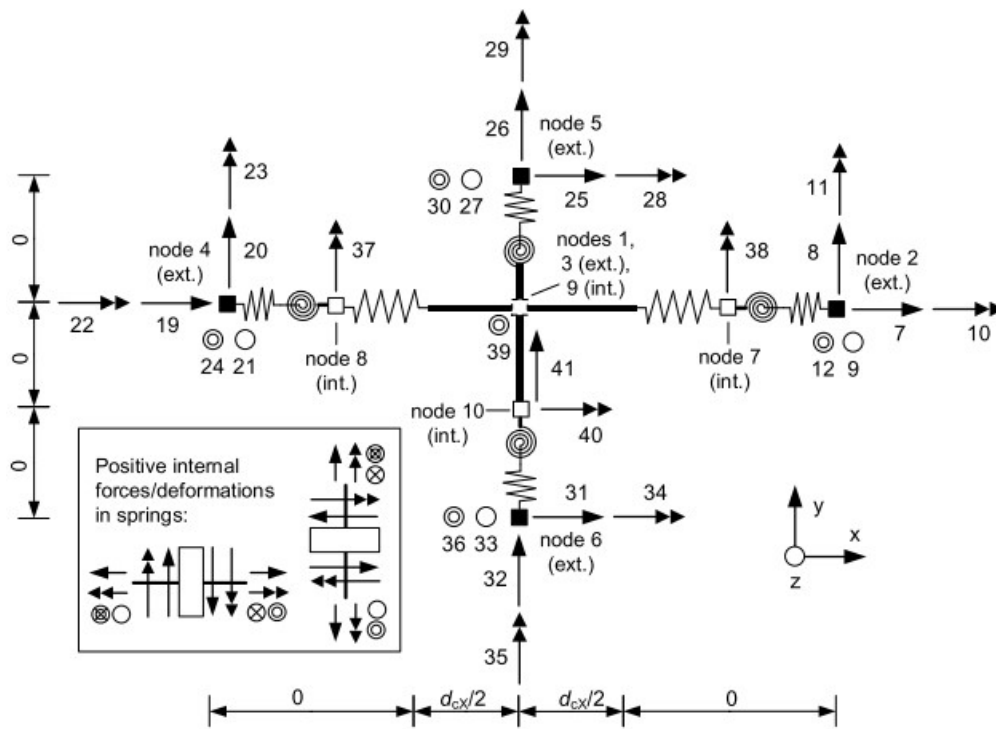


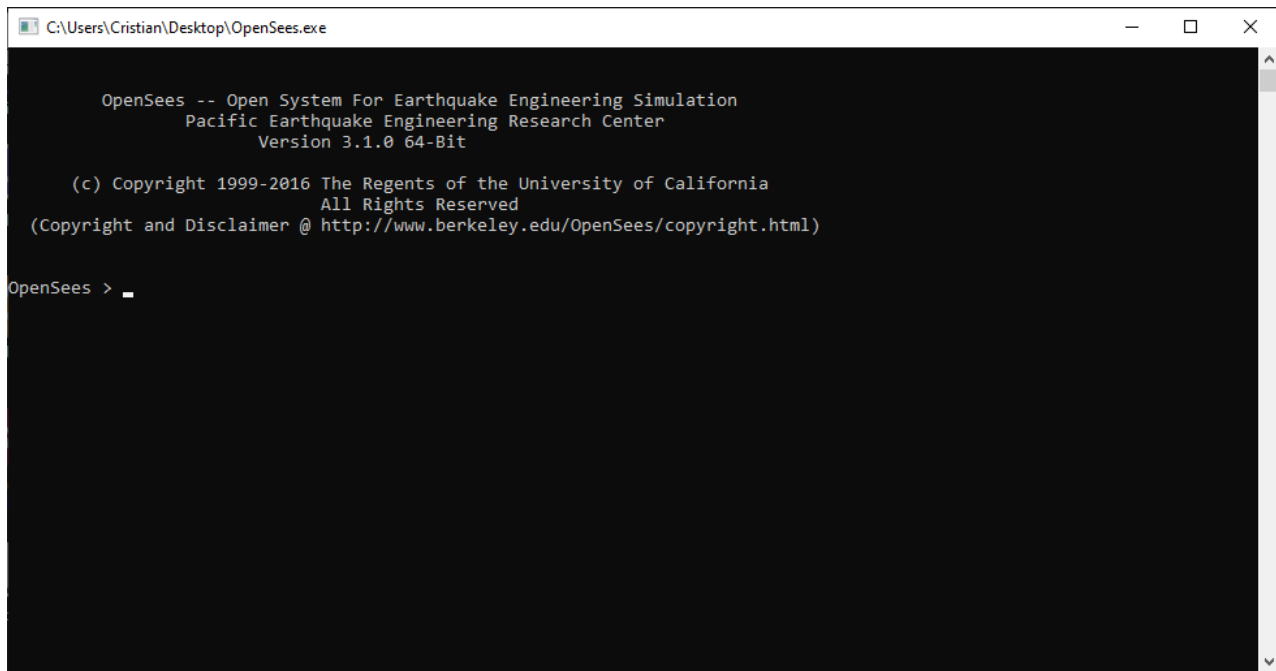
Figure 2.9: Macro-element for beam-to-column steel joints in 3D: Y-X plane [149].

Neves [155]. The research introduced a new joint component called the cross-section component, representing the local deformation of the RHS tube's cross-section in the beam-to-column joints. The joint's behavior is complex because the out-of-plane behaviors of the column's plates are interdependent, not independent, as previously assumed. The research consists of implementing and validating the 3D joint macro-element containing the new cross-section component. The macro-element approach successfully represents the correlation behavior of the four column plates in the beam-to-RHS column joint, especially in describing the nonlinear joint behavior under various loading configurations.

The studies discussed above demonstrate that macro-modeling of steel and steel-concrete joints yield results that are in good agreement with experimental results and complete finite element models. Based on these findings, it can be inferred that it is crucial to model the joint as an independent entity and that macro-modeling is a viable option due to its primary benefits of decreased computational expense and reduced modeling duration.

2.4.6 Code limitations

Presently, the European standards' design rules and component method are only applicable to basic joint configurations, predominantly in HRS. Although certain CFS-specific connections are addressed in Eurocode 3 Part 1-3 [156], the principal challenge remains the inability to implement the component method for CFS joints.



```
C:\Users\Cristian\Desktop\OpenSees.exe

OpenSees -- Open System For Earthquake Engineering Simulation
Pacific Earthquake Engineering Research Center
Version 3.1.0 64-Bit

(c) Copyright 1999-2016 The Regents of the University of California
All Rights Reserved
(Copyright and Disclaimer @ http://www.berkeley.edu/OpenSees/copyright.html)

OpenSees > _
```

Figure 2.10: OpenSees – software framework (console).

2.5 OpenSees

2.5.1 Software framework

OpenSees [115] (opensees.berkeley.edu) is an object-oriented open-source software framework, initially developed for simulation in earthquake engineering using finite element methods. The framework of the software is written in C++ [157], and it is based on the Ph.D. Thesis of McKenna [158]. Due to its open-source nature and object-oriented design, the OpenSees software framework is the most suitable platform for researchers and practicing engineers to implement, test, and develop their finite element ideas and use them for their purpose.

These ideas can be written using C++ [157], C [159], or Fortran [160] and make use of the OpenSees application programming interface (API) to, for example, find nodal coordinates and displacements.

Hitherto, many researchers have enriched this framework with valuable and diverse software components that enable researchers and practicing engineers to perform complex simulations of the structures, i.e., earthquake analysis, thermal analysis, multihazard type analysis, etc.

These components include model-building tools, model domain definitions, element formulations, material models, analysis procedures, numerical solvers, data management tools, and methods to support reliability analysis.

A summary of some of the key object-oriented concepts and features of OpenSees, as described in detail by Altoontash [161], are also presented below:

- *Class*: Classes are one of the building blocks of object-oriented programming, or in technical words, classes are basic units of abstraction in C++. A class is used to encapsulate the user-defined data as well as operators to access and manipulate that data. A class is a prototype that defines the variables and the methods common to all objects of a certain kind.
- *Object*: An object is a run-time value that belongs to a class, used to store the class state. The class defines all the operations for its instances. Since the objects know what class they belong to, so they automatically know what operations they are capable of. The word "instance" is another term for "object".
- *Message and Method*: Object-oriented programming uses "messages" instead of function calls. Sending a message to an object causes that object to perform an operation. The receiver knows what operations it can perform because it knows its class. The code corresponding to the message is known as the "method" for that message. A message is just a string, while the method is the code in the Stack class which is triggered by the message. The C++ specific term for method is "member function".
- *Constructors*: Methods that are automatically called on behalf of the client whenever a new instance, be it statically or dynamically allocated, comes into scope.
- *Model Builder*: The first step in generating a finite element analysis model is subdividing the body being studied into finite element components. A Model Builder object creates the finite element model in a running program. Each Model Builder object is associated with a single Domain object. The model builder is responsible for generating nodes, masses, materials, sections, elements, load patterns, time series, transformations, blocks, and constraints.
- *Domain*: The domain object is responsible for storing the objects created by the model builder object and for providing the analysis and recorder objects access to these objects. The domain holds the state of the model at time t and $t + \delta t$.
- *Domain Component*: The domain component class is an abstract class. Its subclasses include elements, nodes, single point constraints, multipoint constraints, nodal loads, elemental loads, etc. Each object of these types is a component of an enclosing Domain object. The domain component class provides methods to set and retrieve a pointer to the enclosing Domain object.
- *Analysis*: The Analysis object is responsible for performing the analysis. This may vary from a simple static linear analysis to a transient nonlinear analysis. In OpenSees, each Analysis object is composed of several component objects, which define how the analysis is performed.

The component classes consist of constraint handler, DOF number, analysis model, solution algorithm, integrator, linear system of equation, and the solver. The analysis performs the calculations and solves the state of the model from the state at time t and $t + \delta t$.

- *Recorders*: The recorder object monitors the state of a domain during an Analysis, writes this state to a file or to a database at selected intervals during the analysis, or plots and monitors user-defined parameters in the model during the analysis. The user-defined parameter could be the displacement history at a node in a transient analysis or the entire state of the model at each step of the solution procedure. Usually, several Recorder objects are created by the analyst to monitor the analysis.
- *Constraint handlers*: The constraint handler object is responsible for providing an initial mapping between the nodal DOFs and equation numbers of the analysis. The Constraint Handler object does not handle the constraints as its name would suggest, and the handling of the constraints is performed by the Analysis object, where the constraint equations are enforced as relationships between DOFs.
- *Material models*: A general object representing stress-strain relationships or force-deformation (moment-rotation) at integration points of continuum or element components. Material Models always belong to an element or a section.
- *Uniaxial Materials*: A material model object representing single DOF force-deformation (or stress-strain) relationships.

OpenSees does not have a built-in graphical user interface (GUI), as shown in Fig. 2.10. Instead, it is a command-line based program, which means that users interact with it by typing commands into a terminal or command prompt. To create and run finite element models using OpenSees, the user must first write a script using the Tool Command Language (Tcl) [162]. The Tcl interpreter then interacts with the OpenSees solver. Alternatively, models can be created using the recently developed OpenSeesPy [163] Python module [164].

There are also third-party software options that provide a GUI interface for pre- and post-processing. Examples of these include OpenSees Navigator [165], BuildingTcl/BuildingTclViewer [166], NextFEM Designer [167], GiD+OpenSees [168], STKO [169], Build-X [170], PileGroupTool [171], MDOF [172], MSBridge [173], DYANAS [174], FeView [175], eSEES [176], Hyperomet [177], gmsh2opensees [178], and OpenSeesPyView [179].

2.5.2 OpenSees joint element library

Unfortunately, the joint library of OpenSees currently has only a limited number of joint models available. To the author's best knowledge, there are currently only four joint finite elements available in the software library [180]. These include three developed in the United States [161], [181], [182] and one developed in Iran [183]. Each of the following four sections will feature the presentation of one of these joint models.

2.5.2.1 BeamColumnJoint2D and BeamColumnJoint3D

A joint element for reinforced concrete interior beam-to-column joints is introduced by Lowes et al. [181], as `BeamColumnJoint2D` and `BeamColumnJoint3D`.

The 2D element has four external nodes with 12 external and four internal DOFs, and is shown in Fig. 2.11. The joint consists of (i) a closed frame bordering the outer limits of the beam-to-column joint made out of four rigid bi-articulated elements; (ii) a panel inside the frame (a plane stress shear panel), and (iii) rigid interfaces at beam and column ends. The connection between the closed frame and the rigid interfaces is realized with three linear springs on each side of the four sides of the joint.

In all the cases, there are two parallel springs and one perpendicular to the beams/columns centerline. The former simulates the anchorage of the longitudinal rebars of the beams and columns inside the beam-to-column joint. In contrast, the latter simulates the loss of shear-transfer capacity at the joint-to-beam and joint-column perimeter under severe joint loading. Additionally, the panel in the frame's interior simulates the strength and stiffness loss associated with the shear failure of the joint core.

For this joint model, an update is proposed and implemented by Mitra and Lowes [184], consisting of three changes (i) a new element formulation that offers an improved simulation of joint response mechanism, (ii) a new method which assumes that the joint shear is transferred through a confined concrete strut and simulates strength loss due to load history and joint damage following yielding of beam longitudinal steel, and (iii) an improved behavior of the anchorage zone response. With all these changes, the joint's response prediction is increased, and its range of applicability is extended.

The inelastic action observed in a reinforced beam-to-column joint is simulated by the joint element using 13 uniaxial 1D material types taken as input.

The 3D version of the element has four nodes with 24 external DOFs and is a finite area super-element, a slight variation of the 2D one. Even though it has six DOFs per node, the out-of-plane nodal DOFs are constrained or fixed, and the in-plane nodal DOFs are activated. As in the 2D model, the inelastic action is simulated using 13 uniaxial material types.

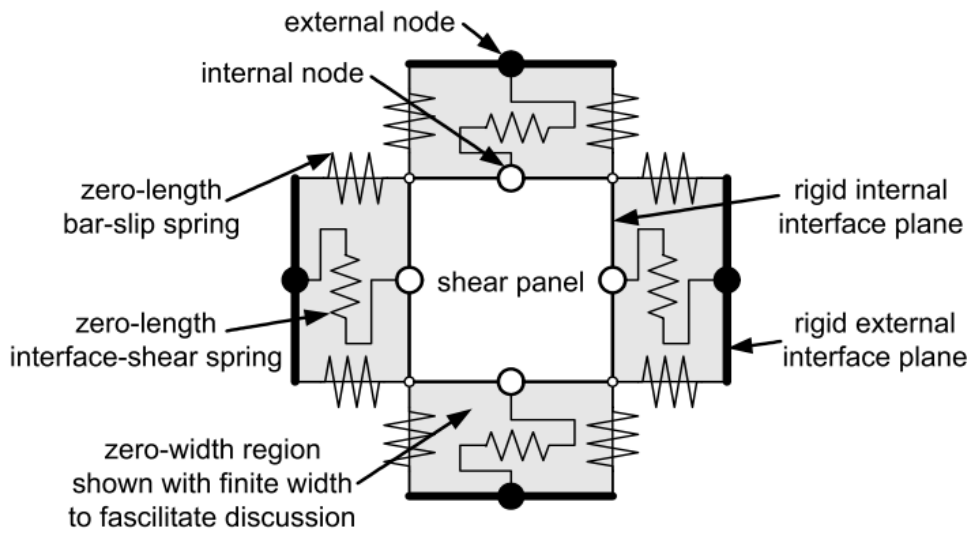


Figure 2.11: OpenSees Joint Element Library: BeamColumnJoint [181].

2.5.2.2 Joint2D and Joint3D

A joint element formulated to simulate the nonlinear response of beam-to-column joints in 2D and 3D models under cyclic loading, with the capability of integrating both geometric and material nonlinearities, is implemented by Altoontash [161], as Joint2D and Joint3D.

The 2D version of the joint element comes in two configurations (i) with member-end rotations and five springs (Joint2D-SPR5) and (ii) with rigid member-end connections and one shear spring (Joint2D-1SPR), as shown in Fig. 2.12 and Fig. 2.13, respectively. The element is connected to four external nodes with three DOFs per node and has one central node with four DOFs (i.e., two translations and two rotations). The outer limits of the joint element form a parallelogram with axially rigid sides, where an angle change between the sides allows the shear panel to deform in the shear mode. The five nodes of Joint2D have 16 DOFs: eight DOFs for Joint2D5-SPR and 12 DOFs for Joint2D-1SPR are constrained to the central node. The Joint2D-SPR5 has four rotational springs at the midpoints of the parallelogram's faces to which the beams and columns are connected. These springs aim to model the relative rotation between the joint faces and the end of the beams and columns. In the Joint2D model, the shear deformation at the interfaces of the joint-beam and joint-column is neglected.

The 3D version of the joint element (Joint3D) is constructed as an extension of the 2D with one central spring model (Joint2D – 1SPR) and is shown in Fig. 2.14. The joint is constructed over six external nodes with six DOFs each and one central node with nine DOFs (i.e., six for the rigid-body motion and three for shear deformation) to represent the shear deformation. The displacements of the external nodes are constrained to the central node by multi-point constraints and move attached to the shear block; therefore, the central node controls both rigid body motion and shear deformation of the

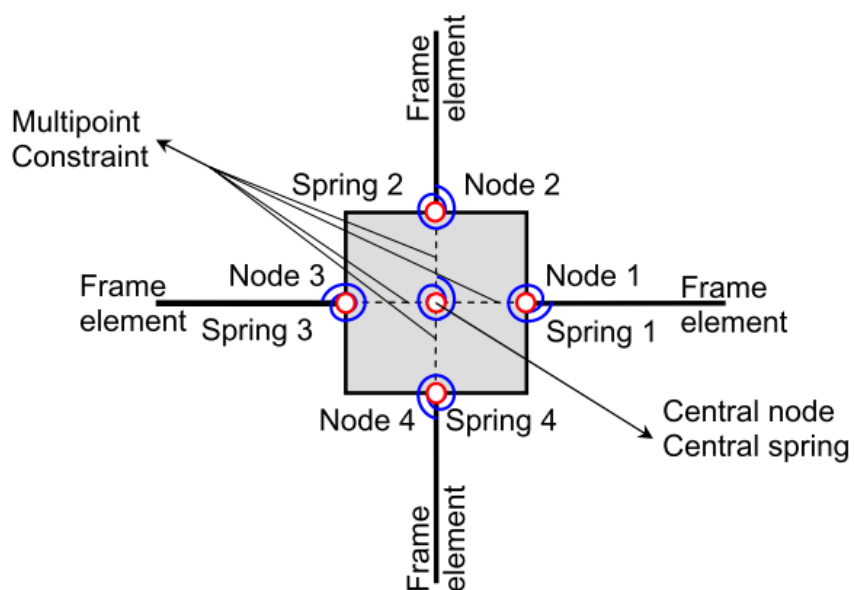


Figure 2.12: OpenSees Joint Element Library: Joint2D - 5 SPR [161].

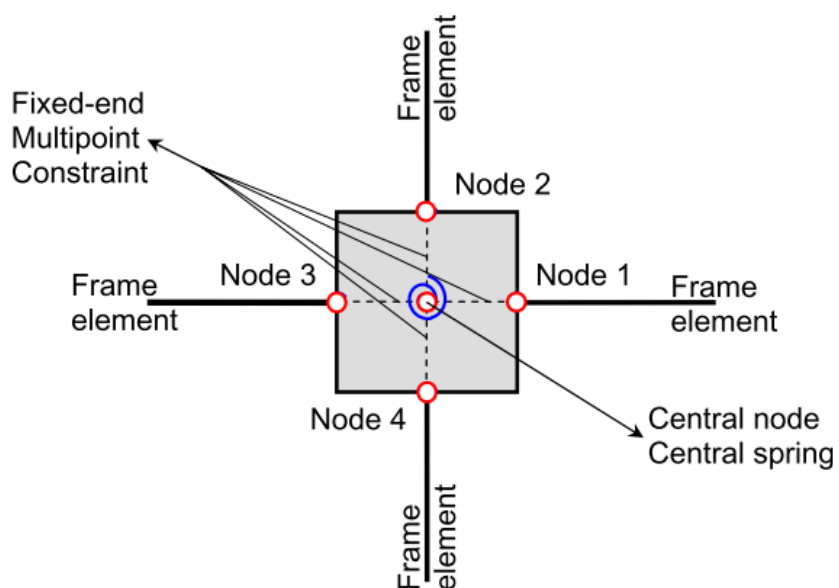


Figure 2.13: OpenSees Joint Element Library: Joint2D - 1 SPR [161].

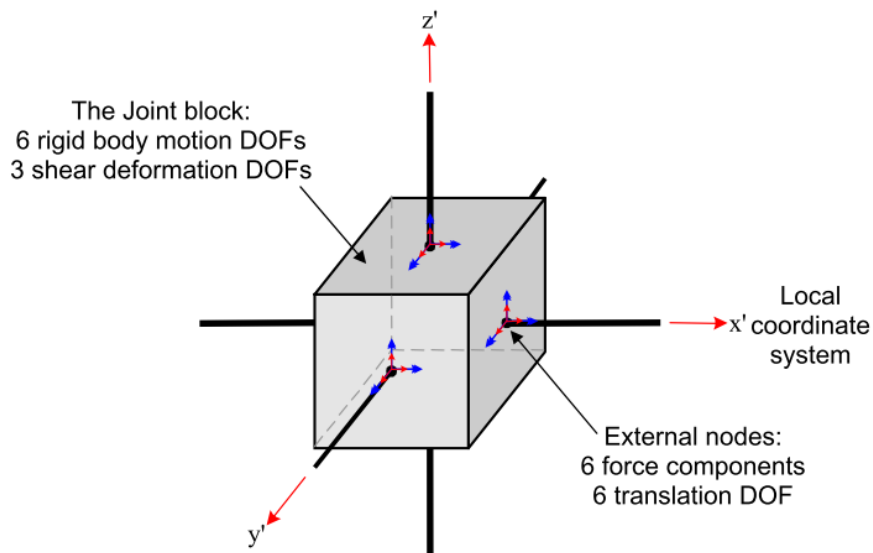


Figure 2.14: OpenSees Joint Element Library: Joint3D [161].

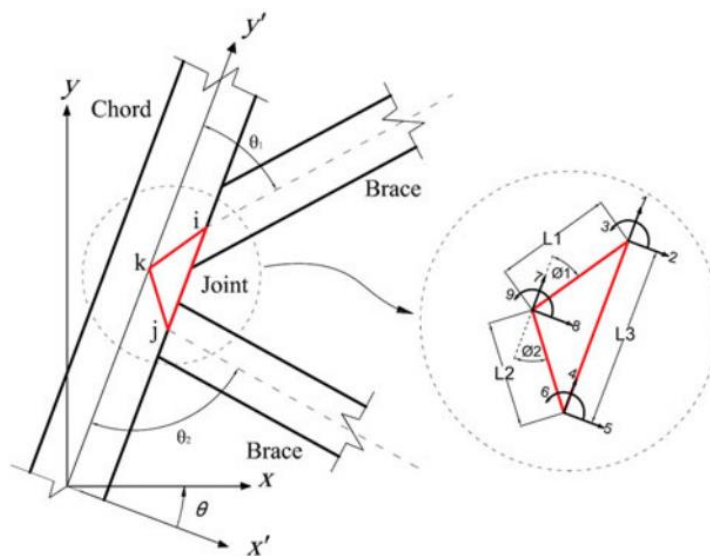


Figure 2.15: OpenSees Joint Element Library: ElasticTubularJoint [183].

element with its nine DOFs. The adjacent members are rigidly connected to the external nodes, so the displacement of the external nodes directly determines the global deformations of the connected beam-to-column members.

2.5.2.3 ElasticTubularJoint

An elastic tubular joint that incorporates the effects of joint flexibility to produce a more realistic response for offshore structures is developed by Alanjari et al. [183] as ElasticTubularJoint. The element considers the local flexibilities for TY- and K-type tubular joints (Fig. 2.15) and is suitable for modeling multi-brace, uni-planar tubular joints.

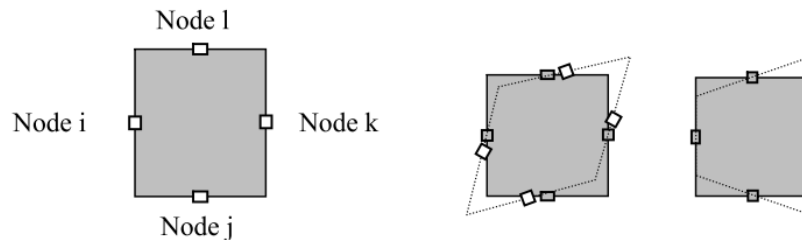


Figure 2.16: OpenSees Joint Element Library: LehighJoint2D [185].

2.5.2.4 LehighJoint2D

A 2D planar panel zone element is developed at Lehigh University [182] as LehighJoint2D. The element is a four-sided planar element with one node at the center point of each side, as shown in Fig. 2.16, with each node having three DOFs: two translations and one rotation. The element requires the four nodes to be defined in counter-clockwise order. The panel zone element presents nine deformation modes and three rigid body modes, each independent of the other. The panel zone deformations are ensured by defining nine material tags as input.

This element is also implemented in HybridFEM software that is used for dynamic time history analysis of 2D inelastic framed structures and real-time hybrid simulation [185].

2.5.3 Conclusion

In conclusion, by offering a few joint finite elements to model beam-to-column nodes, the joint library of OpenSees could be considered rich by comparison with other commercial finite element software [113], [117], [186], [187], which usually have no finite elements for joint modeling. Accordingly, there is a need to develop and implement joint macro-elements, especially for steel and steel-concrete composite joints and for 3D applications.

2.6 An innovative hybrid modular structural system

2.6.1 Introduction

To capitalize on the advantages of modular systems and plug-and-play joints, but mainly to tackle the existing challenges, an international consortium has initiated the European research project named INNO3DJOINTS [5], which aimed to develop an innovative structural system for hybrid tubular construction. The system combines tubular columns with cold-formed lightweight steel truss-girders and cross-laminated timber slabs to create a highly efficient structural system mainly intended for

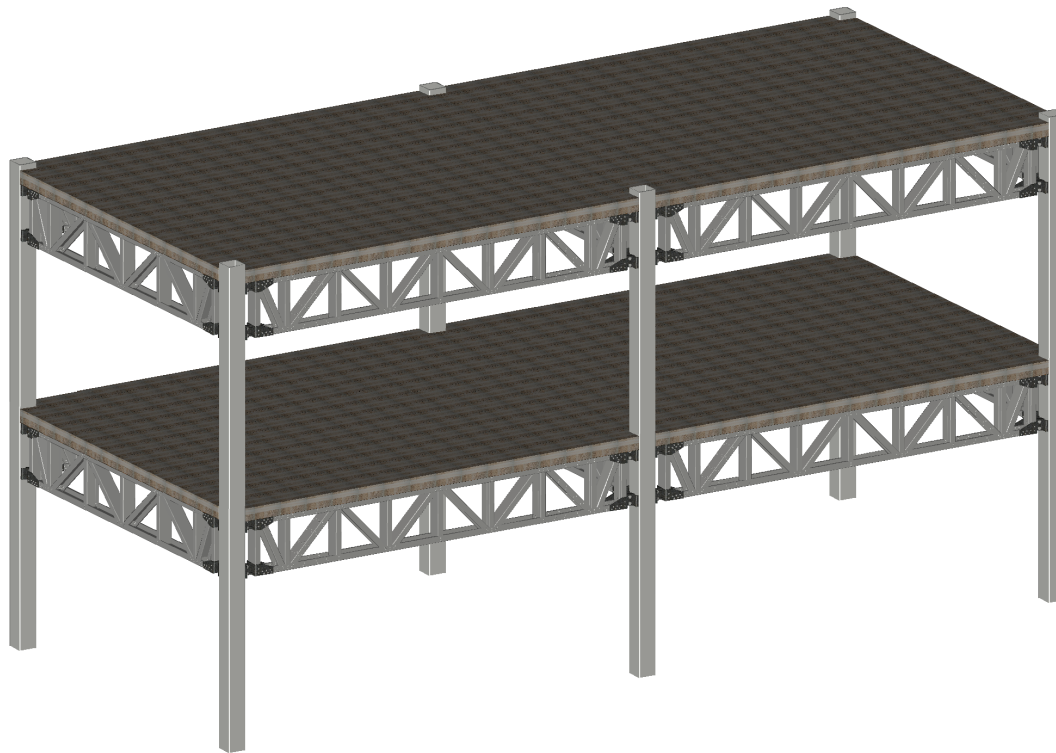


Figure 2.17: INNO3DJOINTS structural system.

residential and office buildings. Furthermore, the project has also developed an innovative 3D plug-and-play joint system that can be employed in other specific scenarios, such as retrofitting existing buildings. The performance of the INNO3DJOINTS structural system is detailed by Simões da Silva et al. [1], [188] and it is shown in Fig. 2.17.

The INNO3DJOINTS project team was composed of representatives from industry, including universities (University of Coimbra in Portugal, Technical University of Delft in the Netherlands, and University of Naples Federico II in Italy), a research institute (CTICM in France), tube producers (Ferpinta in Portugal and Condessa in Spain), and a steel structures producer (FAMETAL in Portugal).

The research presented in this doctoral thesis began as part of the INNO3DJOINTS project, in which the author was a member of the team from the University of Coimbra, focusing on the mathematical formulation, development, and implementation of a macro-element for the analysis and design of the innovative 3D plug-and-play joint system. However, the work developed for this thesis, which will be addressed in the upcoming parts of this document, focuses on the creation, development, implementation, and calibration of an alternative approach for modeling analysis and design of these joints, which differs from the one considered in the European project but still aims to achieve the same goal. Nevertheless, both approaches follow a research line that has been ongoing for several years at the University of Coimbra's ISISE department, which is focused on using 3D component-based macro-element modeling of beam-to-column steel joints. The current thesis's procedure aimed

to create a flexible, physically meaningful, and more comprehensible approach to designers. This approach results in a more transparent model that is more likely to be used by designers.

Consequently, this section will briefly overview the INNO3DJOINTS research project and its main outputs.

2.6.2 Conceptual design

The main components of the INNO3DJOINTS structural system are detailed in Fig. 2.18 and may be resumed as follows:

- cold-formed tubular columns: circular (CHS), square (SHS), or rectangular (RHS) profiles as the main vertical structural elements;
- cold-formed steel (CFS) truss-girders: trusses that span up to 6000 mm, formed with light-gauge cold-formed profiles as the main horizontal structural elements; depending on the span of the truss-girders additional bracing system may be considered to connect the bottom chord of the truss-girder to the slab (steel diagonal straps); additionally, for spans without openings, the LSF walls are stiffened by OSB panels, as structural elements;
- cross-laminated timber (CLT) slab: floor system providing the necessary gravity load-bearing capacity and in-plane diaphragm effect, provided the connections between adjacent slabs and slabs to truss-girders are adequately designed;
- innovative 3D plug-and-play joint (P&PJ) system: innovative 3D plug-and-play devices connecting the CFS truss-girders to the columns.

2.6.3 Main advantages

The INNO3DJOINTS plug-and-play joint system presents several advantages, for example:

- takes advantage of the bidirectional resistance of the tubular members to provide vertical load resistance and leverages the utilization of CFS truss-girders and CLT slab to provide horizontal load resistance, concurrently ensuring an efficient rigid diaphragm effect through the use of CLT slab;
- the "weak axis" problem, a common issue associated with I/H-shaped profiles, is mitigated when utilizing RHS profiles and eliminated when utilizing CHS or SHS profiles;

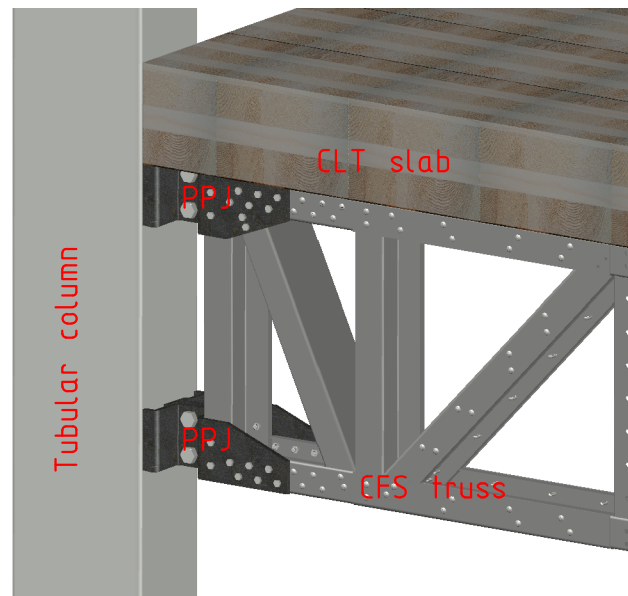


Figure 2.18: Detail of the INNO3DJOINTS structural system's main components.

- uses cold-formed lightweight steel truss-girders combined with steel diagonal straps and OSB panels, providing high lateral stiffness with great material economy;
- is a dry construction method that utilizes standardized profiles resulting in a simple and fast erection stage;
- presents a competitive advantage that is not yet present in the construction market;
- is light and thus very efficient in seismic conditions [189];
- has a plug-and-play joint system that provides an easy assembly and disassembly process on-site, reducing construction site hazards and increasing offsite prefabrication;
- allows the modular construction to evolve to the mid-rise building range (i.e., 2- to 6-story buildings);
- proposes simple calculation formulae for the analysis and design of joints based on the component method [28] for the everyday designer [190];
- develops a consistent design approach between the European design codes [28], [156].

2.6.4 P&PJ system

2.6.4.1 Overall configuration

The P&PJ system proposed within the INNO3DJOINTS project [5] is composed of two parts that help connect the CFS truss-girder to the tubular column, named *socket* and *plug*, as shown in Fig. 2.19.

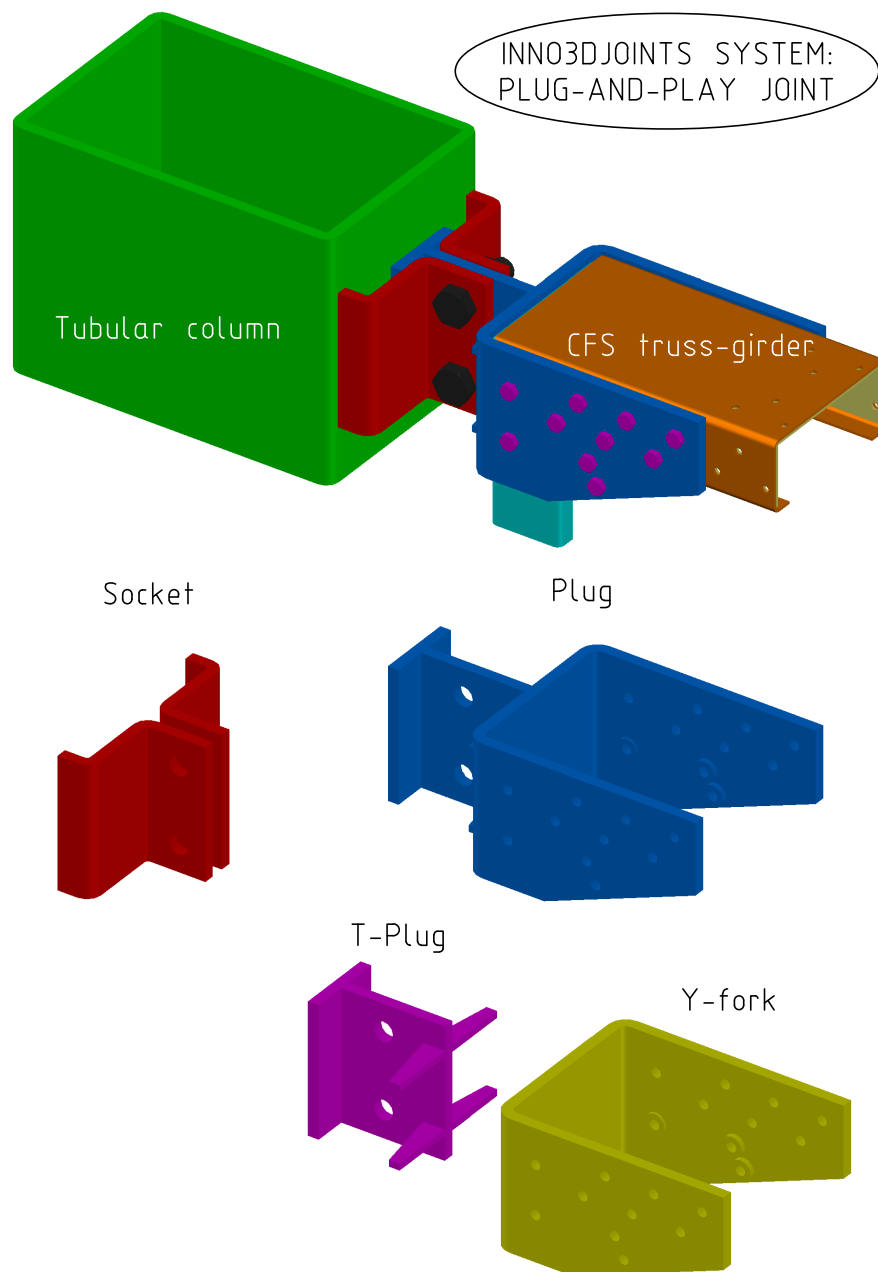


Figure 2.19: Innovative 3D plug-and-play joint (P&PJ) system.

These parts are connected through bolt assemblies.

The socket comprises two separate Z-shaped, cold-bent plates welded symmetrically to the column's face. It features predrilled holes that facilitate assembly with the plug, forming a whole unit. It also serves as a guide for the T-plug, which slides into position between the two parts.

The plug consists of two sub-parts: *Y-fork* and *T-plug*, which are welded together, as seen in Fig. 2.19. The Y-fork comes adjusted to the width of the CFS truss chords, and the T-plug has predrilled holes to facilitate the assembly with the socket. These are aligned with the top and bottom chords of the CFS truss.

During the fabrication process in the steel workshop, the T-plug and Y-fork are welded to each

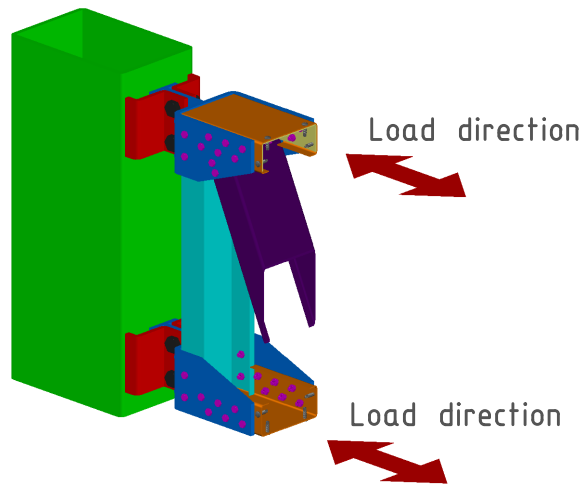


Figure 2.20: INNO3DJOINTS plug-and-play joint system: load direction.

other, the Y-fork is connected to the CFS truss-girder by a simple bolted lap joint, and the socket is welded to the column as shown in Fig. 2.19.

The bolt assemblies that connect the Y-fork and the CFS truss-girder are divided into two groups according to their size and role: the larger bolts distribute the loads into the connection, while the smaller bolts ensure the transmission of the forces between the truss-girder elements (chord, diagonal and vertical elements). This method provides a clear idea of the purpose of all parts of the joint and guarantees that the construction process is easy, fast, and safe.

Since the elements of the CFS truss-girder are subjected mainly to axial forces, the connection is subjected to large forces acting along the longitudinal axis of the chords, as represented in Fig. 2.20. The longitudinal axes of the connections and chords are shown in Fig. 2.21.

A comprehensive experimental campaign was carried out at the University of Coimbra to examine the behavior of P&PJ between RHS columns and CFS trusses. The study comprised of tests on components (Fig. 2.22(a)), full-scale joint (Fig. 2.22(b)) and full-scale structure (Fig. 2.22(c) and Fig. 2.22(d)). The results of the experiments were complemented by numerical simulations, which facilitated the development of guidelines [191] on the geometries for optimizing the performance of the P&PJ system.

Additionally, experimental tests and finite element simulations aimed to investigate the buckling response of the cold-formed square and rectangular hollow section columns have been carried out at the University of Naples Federico II [193]–[195].

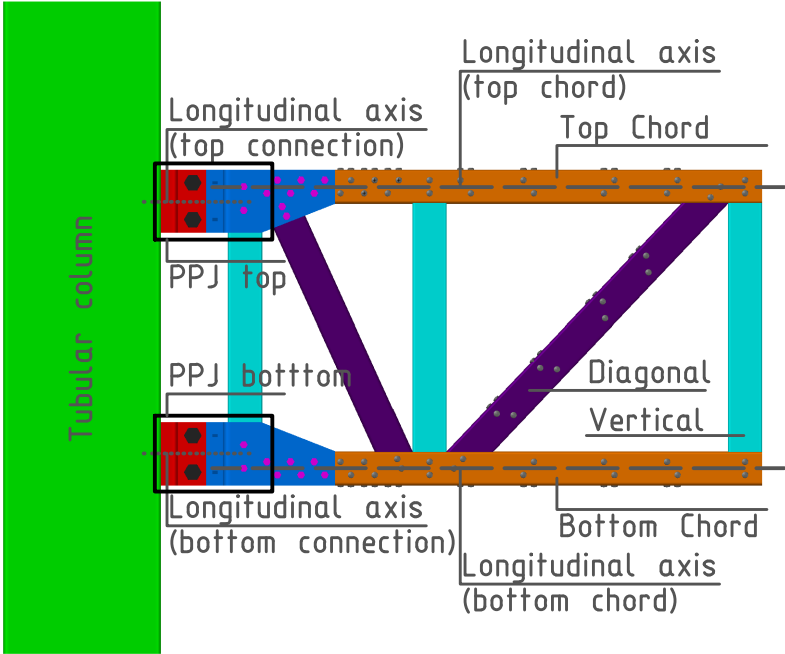


Figure 2.21: INNO3DJOINTS plug-and-play joint system: axis.

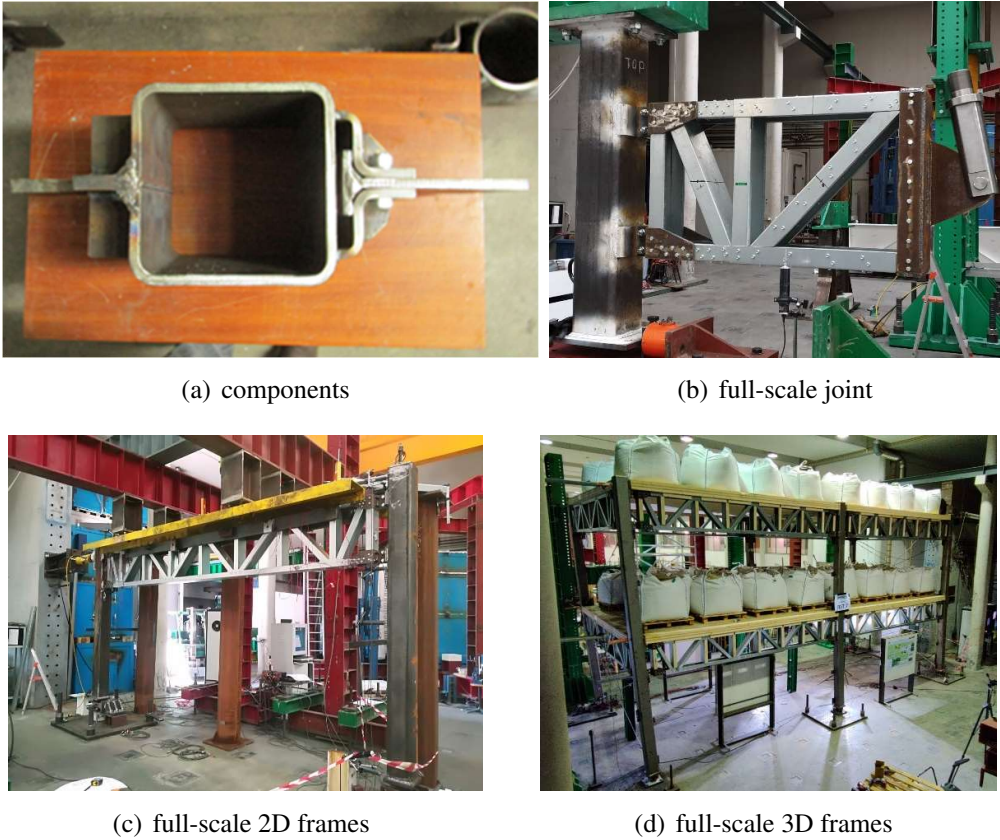


Figure 2.22: Experimental test at various structure levels [192].

2.6.4.2 Assembly process

The P&PJ's configuration allows for an easy (dis)assembly operation based on the following steps (Fig. 2.19):

1. the columns with the sockets previously welded to them are placed in position;
2. the T-plug with the CFS truss-girders attached to it is inserted vertically (i.e., descending movement) in the existing gap between the two pieces of the socket;
3. the T-plug and socket are bolted;
4. the CLT slab is positioned and fastened to the CFS truss-girders.

Since the two connections are aligned with the top and bottom chords (Fig. 2.21), they are mainly subjected to axial forces in the form of tension or compression in conjunction with vertical shear forces. Therefore, depending on the design specifications of the joint, the P&PJ system can behave as a partial moment-resisting joint or a pinned joint if the joint's design is flexible enough or if only the upper chord of the CFS truss-girder is bolted to the socket. However, it is recommended to avoid bolting only the lower chord, as doing so may result in an unstable configuration.

2.6.4.3 Main geometric constraints

The geometric parameters of the plug and socket are shown in Fig. 2.23. The P&PJ's geometry is mainly influenced by the width of the chord of the truss-girder, the width of the column face, the positioning and dimensions of the bolts, and the thickness of the plates. As the joint's formulation is based on the Eurocodes framework, the distance between the bolts and the thickness of the plates are in accordance with the specifications outlined in Table 3.3 of Eurocode 3 Part 1-8 [28].

The socket's and plug's thickness is the principal geometric parameter for the strength of the joint. An extensive parametric analysis undertaken with the FEM showed that the plates' bending significantly influences the strength and deformability of the plug-and-play connection [196]. For this reason, in some cases, stiffeners were added to the Y-fork and the socket in the bending regions, as depicted in Fig. 2.23.

2.6.5 Macro-modeling of the P&PJ with a single CFS truss-girder

Generally, the behavior of joints can be characterized by their strength, stiffness, and ductility. In the past, joints have been considered nominally pinned or rigid to simplify the analysis and design

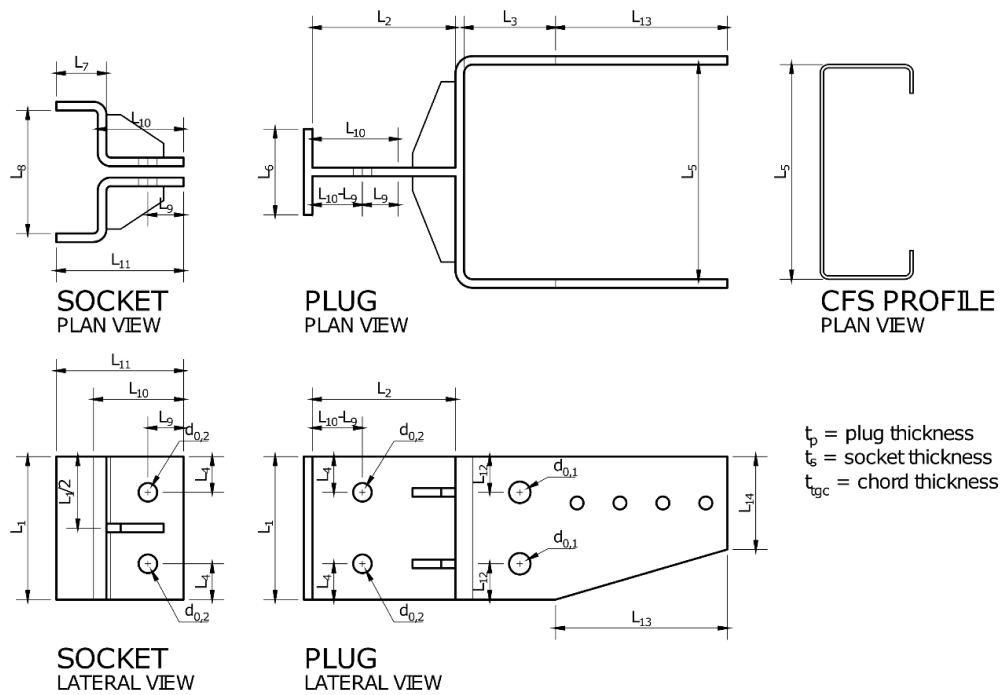


Figure 2.23: Geometric parameters of the plug and socket [196].

process. However, these assumptions usually do not correspond to reality, e.g., research on beam-to-beam, beam-to-column, and truss connections using CFS members revealed that most connections could be considered semi-rigid and hinged [36]. Therefore, by considering the actual behavior of beam-to-column joints, it is possible to achieve significant savings in time and cost while avoiding laborious work.

Recently, the applicability of the component method has been extended to CFS members [37] and to the P&PJ system in the scope of the INNO3DJOINTS project [197].

2.6.5.1 Components under tension and compression internal forces

The relevant components identified for the INNO3DJOINTS plug-and-play joint system, specifically for the simplest configuration of the P&PJ, in which a single CFS truss-girder is connected to the column and where only forces in the direction of the truss-girder chords are applied to the P&PJ (e.g., tension or compression internal forces) are depicted in Fig. 2.24.

Moreover, the components are enumerated in Tab. 2.1 which provides the full list of symbols for strength and stiffness [197] for all the components for tension and compression forces applied by the CFS truss-girder to the joint.

Components 2, 4, and 10 are split into two sub-components with a layout in series. The detailed presentation of the models developed for the computation of the strength and stiffness of each component is given in Appendix A.

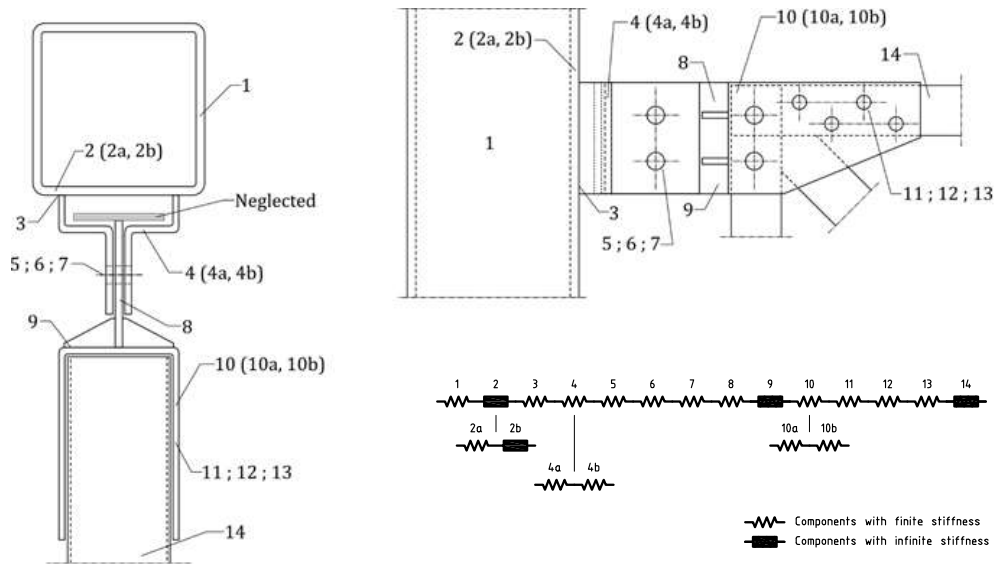


Figure 2.24: Plug-and-play connection decomposition into components for the case of tension or compression internal forces [197].

Table 2.1: Components under tension/compression internal forces [197].

No.	Component name	Strength	Stiffness
1	Column side wall:		
	- tension	$N_{t,csw}$	k_{csw}
	- compression	$N_{c,csw}$	k_{csw}
2	Tube components (column face):		
2a	- bending: tension	$N_{t,cb}$	k_{cb}
	- bending: compression	$N_{c,cb}$	k_{cb}
2b	- punching shear: tension	$N_{t,cps}$	$k_{cps} = \infty$
	- punching shear: compression	$N_{c,cps}$	$k_{cps} = \infty$
3	Welds (column and socket):		
	- tension	$N_{t,w}$	$k_w = \infty$
	- compression	$N_{c,w}$	$k_w = \infty$
4	Socket:		
4a	- bending: tension	$N_{t,sb}$	k_{sb}
	- bending: compression	$N_{c,sb}$	k_{sb}
4b	- elongation/contraction: tension	$N_{t,sg}, N_{t,su}$	k_{sg}
	- elongation/contraction: compression	$N_{c,sg}, N_{c,su}$	k_{sg}
5	Bolts, bearing in socket:		

Continued on next page

Table 2.1: Components under tension/compression internal forces [197] (*cont.*).

No.	Component name	Strength	Stiffness
	- tension	$N_{t,bb}$	k_{bb}
	- compression	$N_{c,bb}$	k_{bb}
6	Bolts, shear (T-plug and socket):		
	- tension	$N_{t,bs}$	k_{bs}
	- compression	$N_{c,bs}$	k_{bs}
7	Bolts, bearing in T-plug:		
	- tension	$N_{t,bb}$	k_{bb}
	- compression	$N_{c,bb}$	k_{bb}
8	T-plug:		
	- tension	$N_{t,Tg}, N_{t,Tu}$	k_{Tg}
	- compression	$N_{c,Tg}, N_{c,Tu}$	k_{Tg}
9	Weld (T-plug and Y-part):		
	- tension	$N_{t,w}$	$k_w = \infty$
	- compression	$N_{c,w}$	$k_w = \infty$
10	Y-part:		
10a	- bending: tension	$N_{t,Yb}$	k_{Yb}
	- bending: compression	$N_{c,Yb}$	k_{Yb}
10b	- elongation/contraction: tension	$N_{t,Yg}, N_{t,Yu}$	k_{Yg}
	- elongation/contraction: compression	$N_{c,Yg}, N_{c,Yu}$	k_{Yg}
11	Bolts, bearing in Y-part:		
	- tension	$N_{t,bb}$	k_{bb}
	- compression	$N_{c,bb}$	k_{bb}
12	Bolts, shear (Y-part and CFS):		
	- tension	$N_{t,bs}$	k_{bs}
	- compression	$N_{c,bs}$	k_{bs}
13	Bolts, bearing in CFS:		
	- tension	$N_{t,bb}$	k_{bb}
	- compression	$N_{c,bb}$	k_{bb}
14	CFS chord gross and net section:		
	- tension	$N_{t,cg}, N_{t,cu}$	-

Continued on next page

Table 2.1: Components under tension/compression internal forces [197] (*cont.*).

No.	Component name	Strength	Stiffness
	- compression	$N_{c,cg}, N_{c,cu}$	-

Fig. 2.24 shows the component model for a P&PJ under tension/compression internal forces whose mechanical properties can be found in Tab. 2.1 [197]. The components of this model can be easily lumped into a single 0D element (i.e., linear spring), giving:

$$\frac{1}{k_{\text{lumped}}} = \sum \frac{1}{k_i} \quad (2.1)$$

where k_i is the stiffness of each component listed in Tab. 2.1 [197].

The strength of the lumped 0D element, f_{lumped} , is the minimum strength of all the components, thus:

$$f_{\text{lumped}} = \min(f_i) \quad (2.2)$$

where f_i is the strength of each component listed in Tab. 2.1 [197].

Due to the T-plug and socket shapes, the P&PJ can transfer axial forces without bolts. This ability improves safety during the erection phase and provides additional robustness to the connections at the ultimate stage. However, for specific design purposes considered (i.e., SLS and ULS), the load transfer between the T-plug and socket relies solely on the bolts' shear and bearing behavior. Consequently, the behavior of a P&PJ subjected to tension/compression can be analyzed as an assembly of components in series. This aspect is illustrated in Fig. 2.24 and described in [197].

The global joint behavior of the CFS truss-girder under bending moment can be easily computed considering that the P&PJ model of one truss-girder is made of the two identical lumped assemblages represented in Fig. 2.25.

2.6.5.2 Components under vertical shear force

For moment-resisting plug-and-play joints, the global vertical shear load in the CFS truss-girder is equally distributed between the two connections. For pinned plug-and-play joints, the global vertical shear load in the CFS truss-girder is entirely carried by P&PJ system.

Taking into account that the CFS truss-girders transmit to the P&PJ internal forces in a direction orthogonal to the axis of their chords (i.e., vertical shear forces), the relevant components identified in the INNO3DJOINTS project are presented in Fig. 2.26.

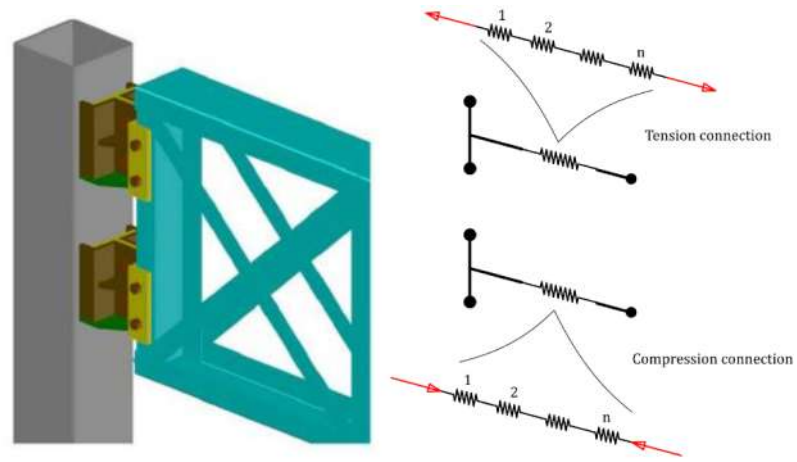


Figure 2.25: Tension and compression connections in the joint under bending moment [197].

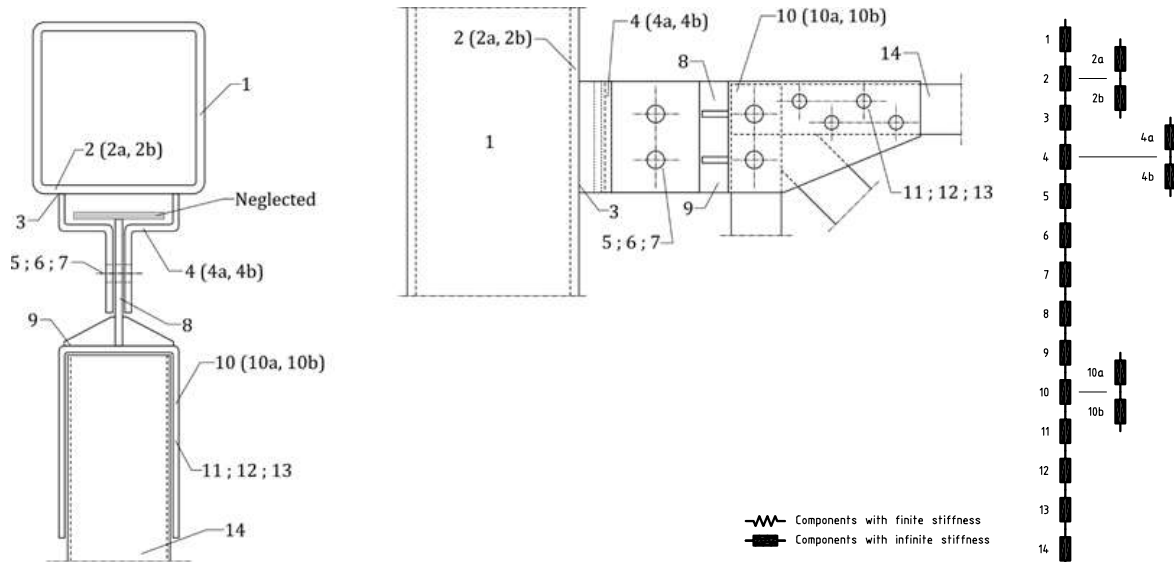


Figure 2.26: Plug-and-play connection decomposition into components for the case of vertical shear force.

The project also revealed that the flexibility of the components involved in the shear-resistant mechanism is insignificant. Therefore, all of the components identified in Fig. 2.26 can be assumed to be nominally rigid. As a result, only the strength of these components was considered in the analysis.

The complete list of components under shear load is shown in Tab. 2.2, with symbols for strength [197]. In addition, the detailed presentation of models developed for the computation of the strength of each component is given in Appendix B.

According to Fig. 2.26, the vertical shear strength of the joint is also provided by Eq. (2.2) where f_i is the strength of each component listed in Tab. 2.2.

Table 2.2: Components under vertical shear force [197].

No.	Component name	Strength
1	Column side wall:	V_{csw}
2	Tube components (column face):	
2a	- bending	V_{cb}
2b	- punching shear	V_{cps}
3	Welds (column and socket):	V_w
4	Socket:	
4a	- bending	V_{sb}
4b	- elongation/contraction	V_{sg}, V_{su}
5	Bolts, bearing in socket	V_{bb}
6	Bolts, shear (T-plug and socket)	V_{bs}
7	Bolts, bearing in T-plug	V_{bb}
8	T-plug	V_{Tg}, V_{Tu}
9	Weld (T-plug and Y-part)	V_w
10	Y-part:	
10a	- bending	V_{Yb}
10b	- elongation/contraction:	V_{Yg}, V_{Yu}
11	Bolts, bearing in Y-part	V_{bb}
12	Bolts, shear (Y-part and CFS)	V_{bs}
13	Bolts, bearing in CFS	V_{bb}
14	CFS chord gross and net section	V_{cg}, V_{cu}

2.6.5.3 Strength interaction models

The verification of the P&PJ under a combination of an axial force and a vertical shear load can be performed using component-by-component interpolations as follows [5]:

$$\begin{aligned}
 \text{components: } 5, 6, 7 &\Rightarrow \left(\frac{N_{Ed,i}}{N_{Rd,i}}\right)^2 + \left(\frac{V_{Ed,i}}{V_{Rd,i}}\right)^2 \leq 1.0 \\
 \text{components: } 14 &\Rightarrow \text{no interaction} \\
 \text{components: others} &\Rightarrow \frac{N_{Ed,i}}{N_{Rd,i}} + \frac{V_{Ed,i}}{V_{Rd,i}} \leq 1.0
 \end{aligned} \tag{2.3}$$

To simplify the analysis, a global linear interpolation method may be utilized as an alternative approach:

$$\frac{N_{Ed}}{N_{Rd}} + \frac{V_{Ed}}{V_{Rd}} \leq 1.0 \tag{2.4}$$

2.6.6 Formulation of the P&PJ macro-element

2.6.6.1 Introduction

In every joint configuration, the P&PJ can be regarded as two distinct joints: one that connects the upper chord and the other that connects the bottom chord of the truss-girder to the column. However, the conceptual model of the macro-element developed by CTICM [197], [198] for the P&PJ considers these two joints as a single entity, as illustrated in Fig. 2.27.

Consequently, the following section will provide a comprehensive presentation of the macro-element created by the author in the context of the INNO3DJOINTS project [5] based on this conceptual model.

2.6.6.2 General overview

The macro-element developed within the INNO3DJOINTS project [5] for the purpose of designing an P&PJ system is shown in Fig. 2.28. The element consists of six external nodes with thirty-six external DOFs, and eight internal DOFs, as shown in Fig. 2.29. The internal DOFs' deformation direction is detailed in Tab. 2.3. Notably, the joint model facilitates the creation of all three types of joint designs, namely central, edge, and corner, while certain nodes may or may not be connected to any beam-to-column 1D element, contingent upon the preferred configuration.

The proposed joint model consists of thirty-eight components, as shown in Figs. 2.30 to 2.36,

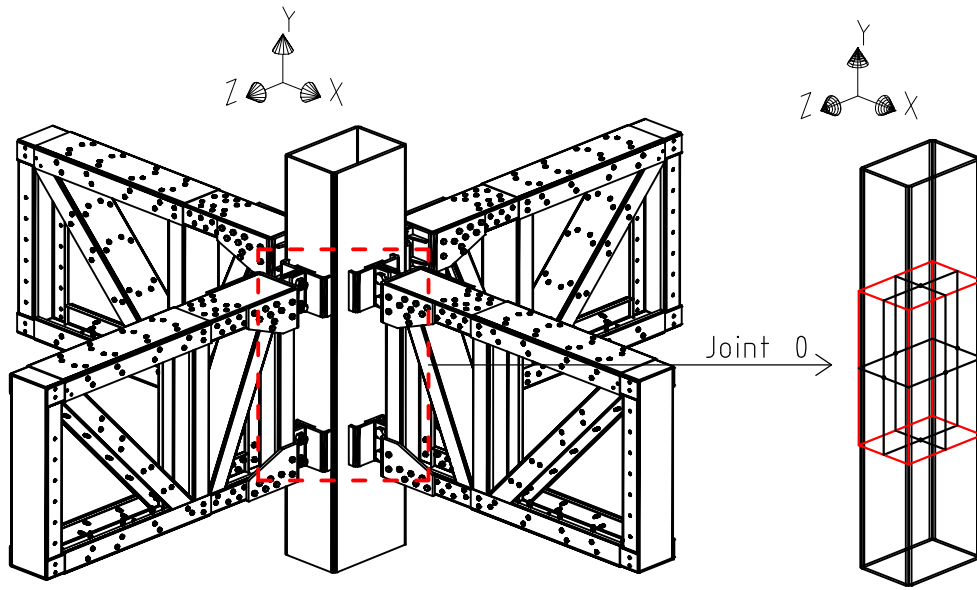


Figure 2.27: Schematic representation of a P&PJ within the INNO3DJOINTS project [5].

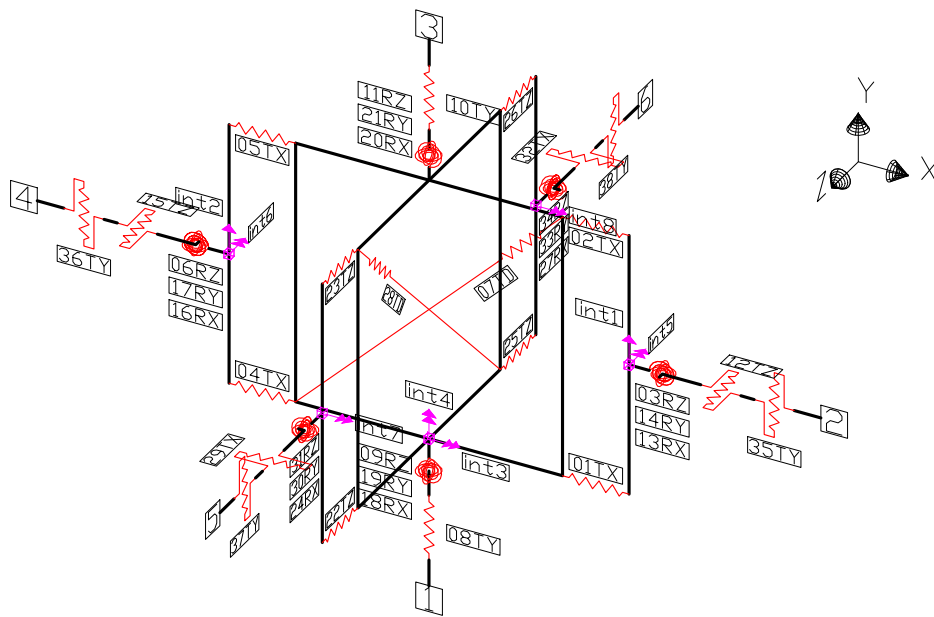


Figure 2.28: Proposed beam-to-column joint finite element within the INNO3DJOINTS project [5]: 3D overview.

Table 2.3: Internal DOFs deformation direction.

Internal DOFs	Description
1, 2	linear deformation in the Y direction
3, 7, 8	bending deformation after X axis (plane Y-Z)
4	bending deformation after Y axis (plane Z-X)
5, 6	bending deformation after Z axis (plane X-Y)

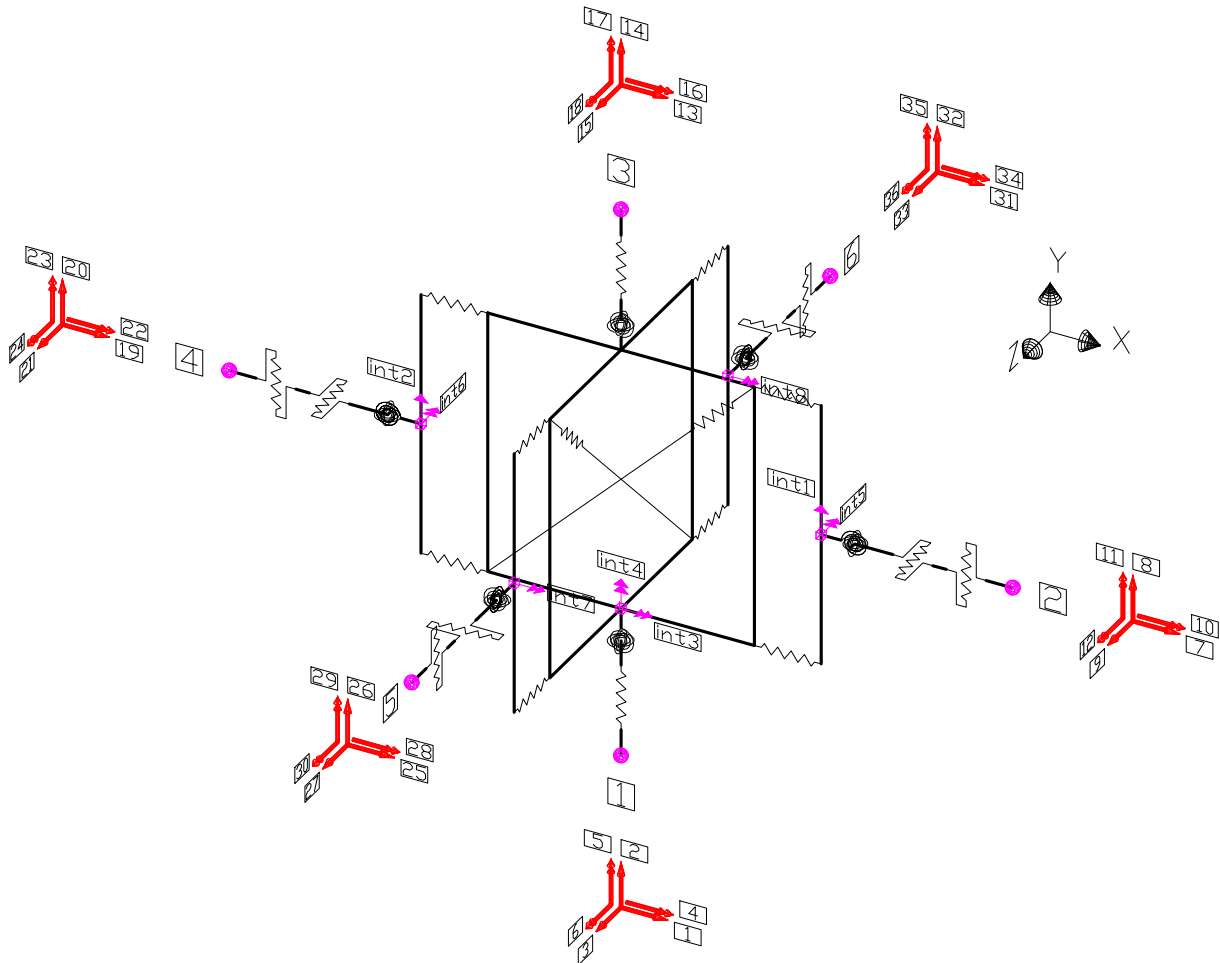


Figure 2.29: Proposed beam-to-column joint finite element within the INNO3DJOINTS project [5]: external DOFs.

Table 2.4: Components deformation direction.

Components	Description
1, 2, 4, 5, 29, 32	linear deformation in the X direction
8, 10, 35, 36, 37, 38	linear deformation in the Y direction
12, 15, 22, 23, 25, 26	linear deformation in the Z direction
7, 28	shear deformation in planes Y-X and Y-Z
13, 16, 18, 20, 24, 27	bending deformation after X axis (plane Y-Z)
14, 17, 19, 21, 30, 33	bending deformation after Y axis (plane Z-X)
3, 6, 9, 11, 31, 34	bending deformation after Z axis (plane X-Y)

Table 2.5: Summary of the 0D elements.

Components	Description
1, 2, 4, 5, 22, 23, 25, 26	load introduction components in the column web (tension or compression)
3, 6, 24, 27	connections [28]
7	column web in shear in plane Y-X
28	column web in shear in plane Y-Z
8, 10	column axial deformation, usually sleeping components
9, 11, 18, 20	column bending deformation, usually sleeping components
12 to 21, 29 to 38	sleeping components

and enumerated in Tab. 2.4. These components are characterized by 0D elements and are defined by uniaxial material objects (i.e., single DOF), with each component capable of exhibiting an independent load-deformation response history. Notably, the shear-panel components (i.e., 7 and 28 from Fig. 2.33) are assumed to undergo deformation solely in shear and, therefore, possess a 1D load-deformation response. Tab. 2.5 provides a comprehensive listing of the components and their interconnections in the 3D beam-to-column joint finite element.

A 2D representation of the proposed joint model is depicted in Figs. 2.37 to 2.39.

The components are assigned a finite length in all the figures illustrating the joint model to facilitate the discussion and representation of the model. However, in actual implementation, the interior and exterior planes are coincident, as demonstrated in Fig. 2.40 to Fig. 2.41.

More detailed information regarding the element formulation and its implementation in OpenSees can be found in Appendix C. While the proposed model is anticipated to be a useful tool in developing P&PJ systems for various structural engineering applications, it is important to acknowledge that certain limitations and drawbacks are associated with its use.

2.6.6.3 Drawbacks and limitations

Upon analyzing the macro-element that was developed as part of the INNO3DJOINTS project [5], several limitations were identified, for example:

- lumps several components (i.e., 1 to 11 shown in Section 2.6.5) of the P&PJ connection into a single spring, such as the T-plug, socket, and bolts;
- is incompatible with truss-girders of unequal depths. Specifically, in the current configuration,

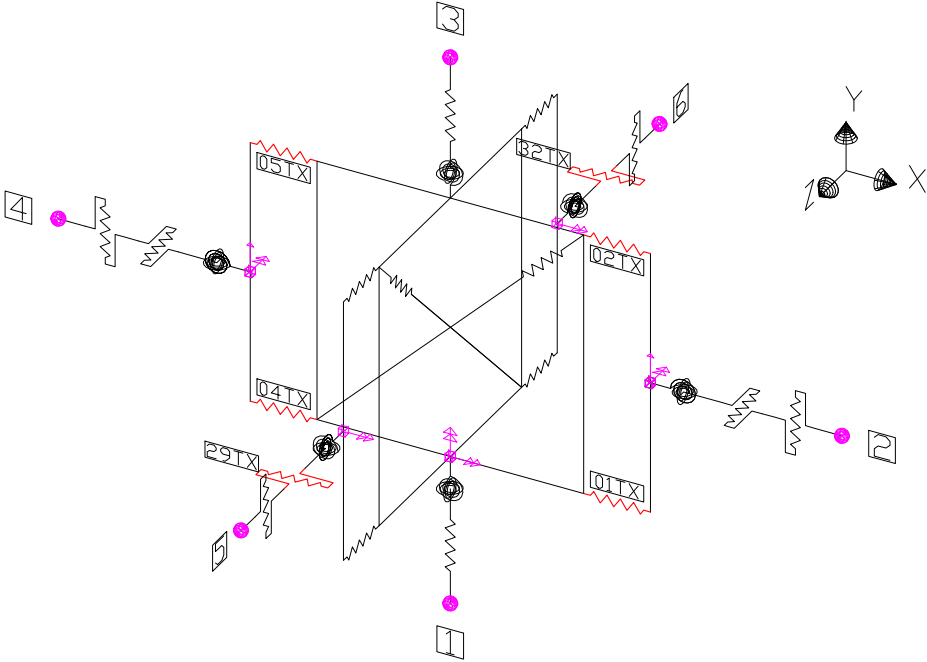


Figure 2.30: Components of the beam-to-column joint finite element developed within the INNO3DJOINTS project [5]: linear deformation in the X direction.

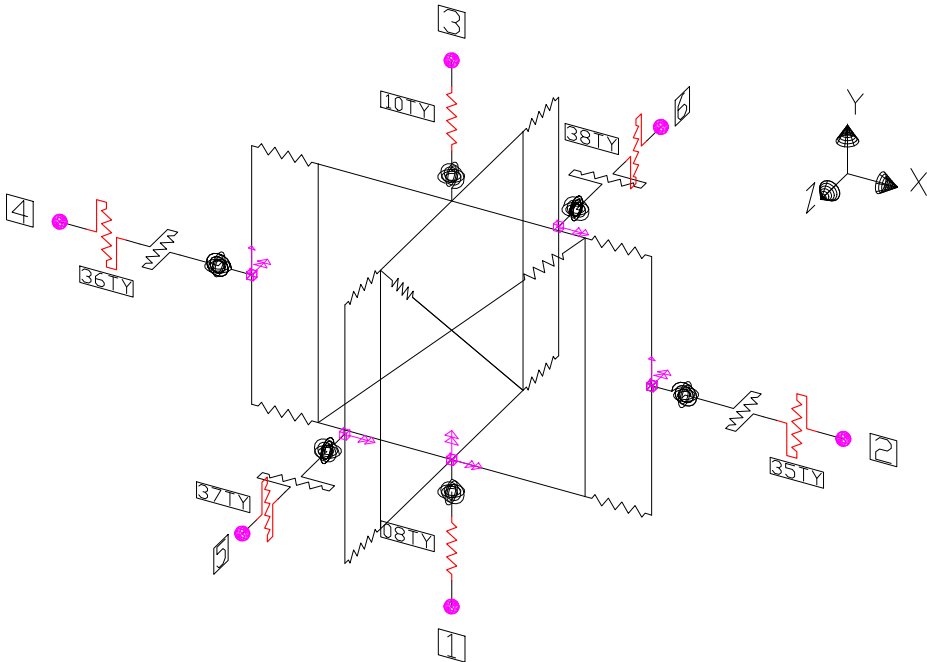


Figure 2.31: Components of the beam-to-column joint finite element developed within the INNO3DJOINTS project [5]: linear deformation in the Y direction.

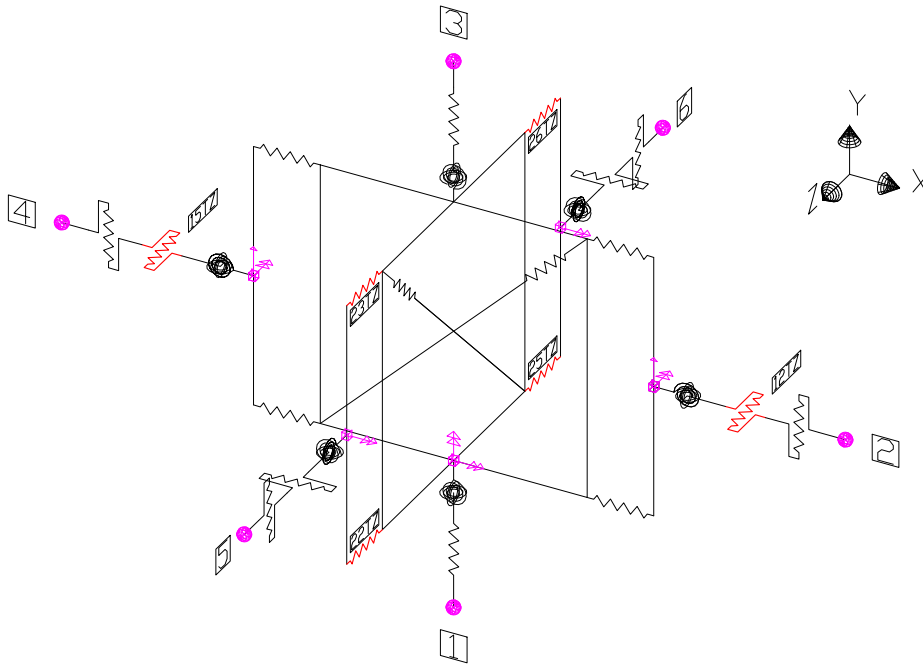


Figure 2.32: Components of the beam-to-column joint finite element developed within the INNO3DJOINTS project [5]: linear deformation in the Z direction.

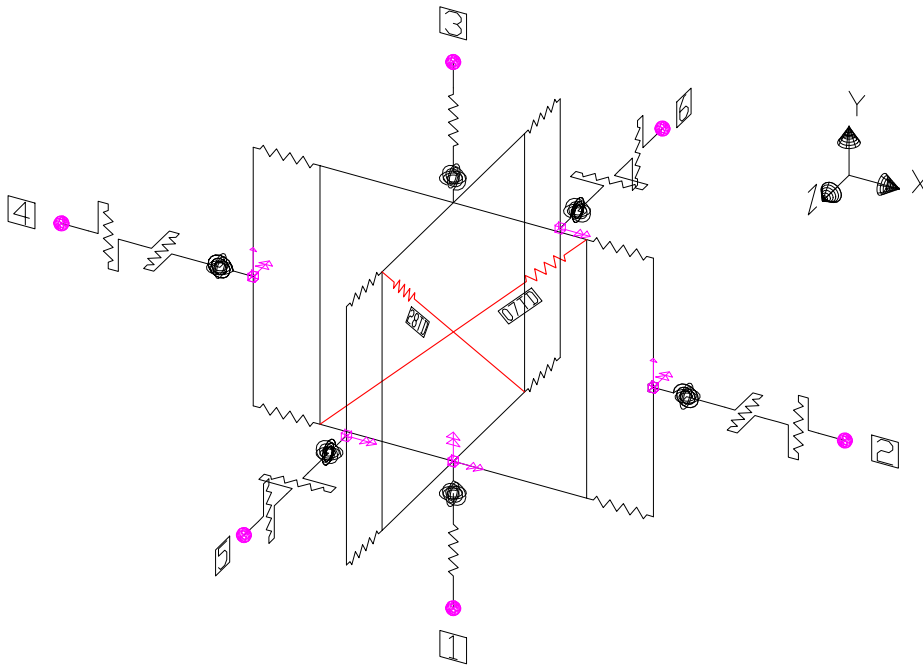


Figure 2.33: Components of the beam-to-column joint finite element developed within the INNO3DJOINTS project [5]: linear deformation diagonally (in Y-Z and Y-X planes).

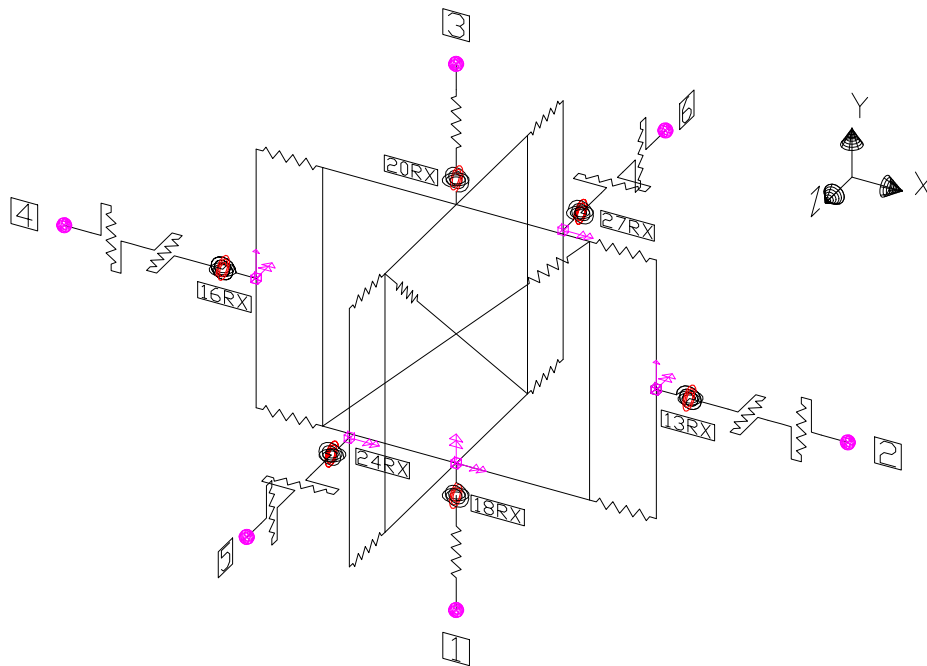


Figure 2.34: Components of the beam-to-column joint finite element developed within the INNO3DJOINTS project [5]: rotational deformation in the X direction.

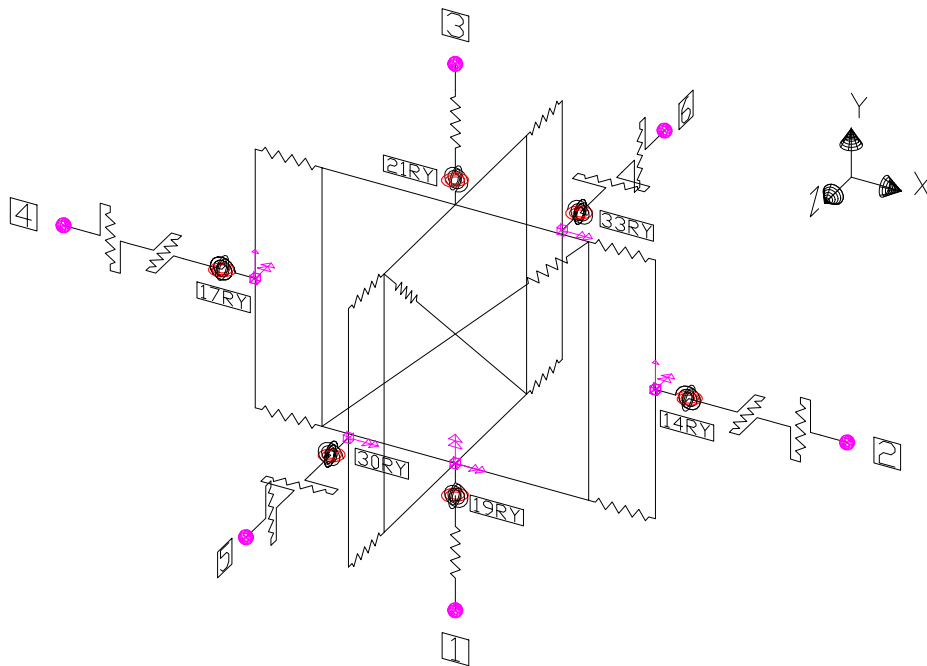


Figure 2.35: Components of the beam-to-column joint finite element developed within the INNO3DJOINTS project [5]: rotational deformation in the Y direction.

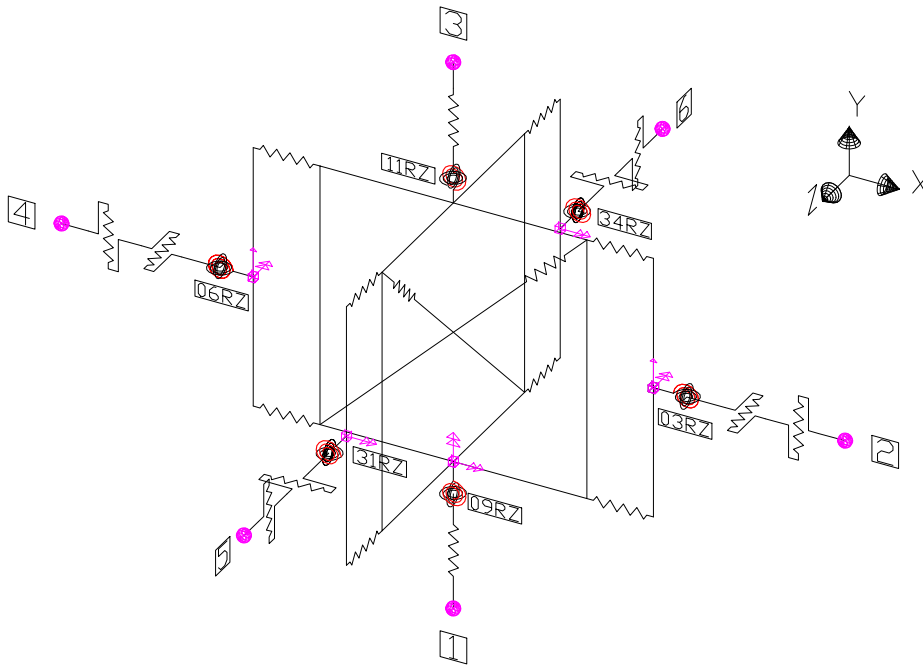


Figure 2.36: Components of the beam-to-column joint finite element developed within the INNO3DJOINTS project [5]: rotational deformation in the Z direction.

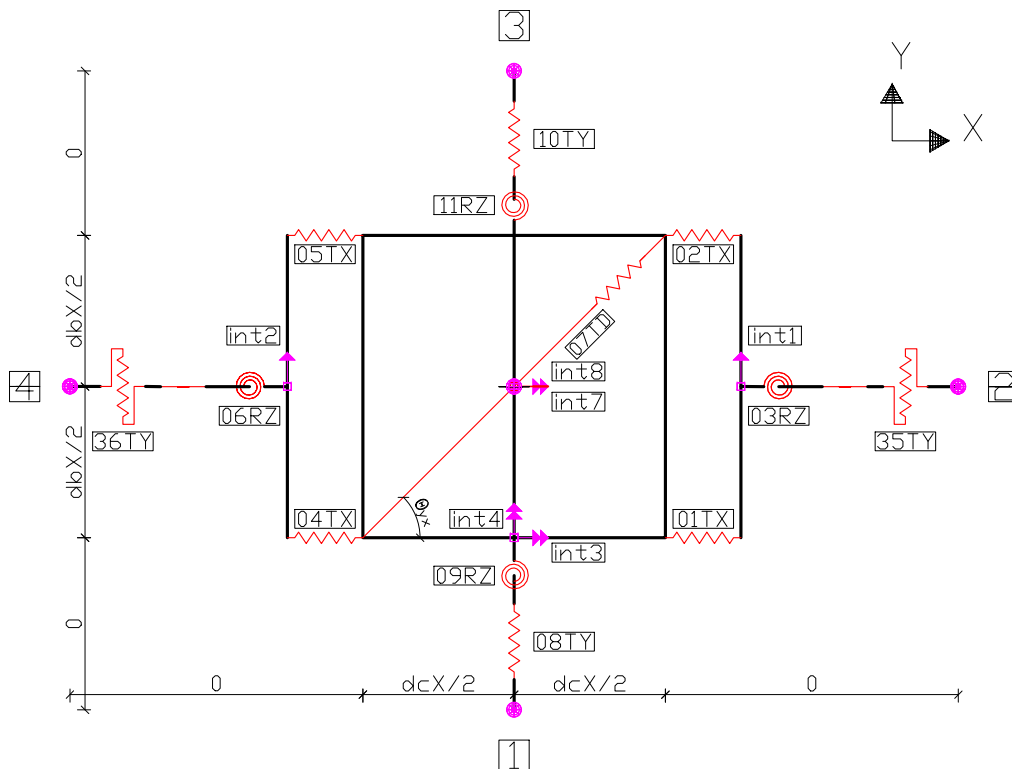


Figure 2.37: Components of the beam-to-column joint finite element developed within the INNO3DJOINTS project [5]: X-Y plane.

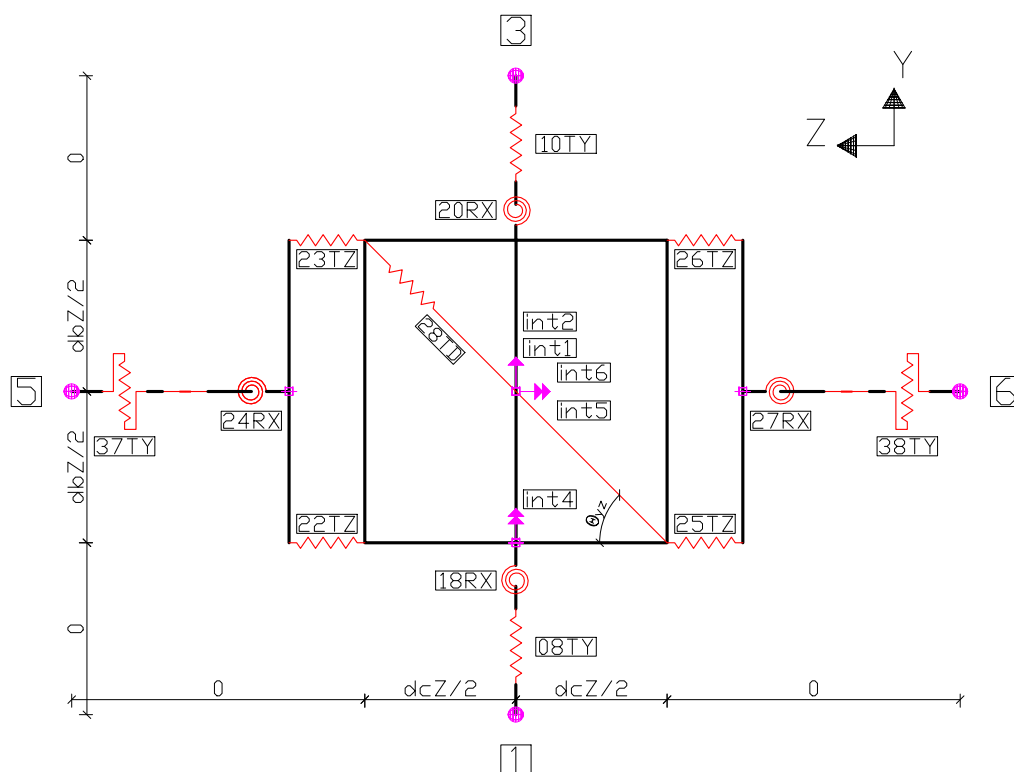


Figure 2.38: Components of the beam-to-column joint finite element developed within the INNO3DJOINTS project [5]: Y-Z plane.

all four beams entering the node must have equal heights;

- cannot support inclined members as it is incompatible with truss-girders that are not horizontally aligned;
- deals mathematically with the 3D interaction of the column face without a solid and intuitive mechanical model to support it. The out-of-diagonal elements of the constitutive matrix introduce this interaction in the joint's formulation;
- incorporates the part of the column between the two connections made by the truss-girders with the column (i.e., the top and bottom of the chords), making it challenging to compute the constitutive relations for the related components;
- cannot account for local bending or shear deformation in each connection (top and bottom chord);
- does not account for the parallel layout of the bolt in shear and the T-plug in tension in each connection.

These limitations and drawbacks required the development of an alternative method, presented in this document in the next sections. In the author's view, this method could enhance the design and modeling of the beam-to-column P&PJ system using the macro-element presented in Section 3.3.1.

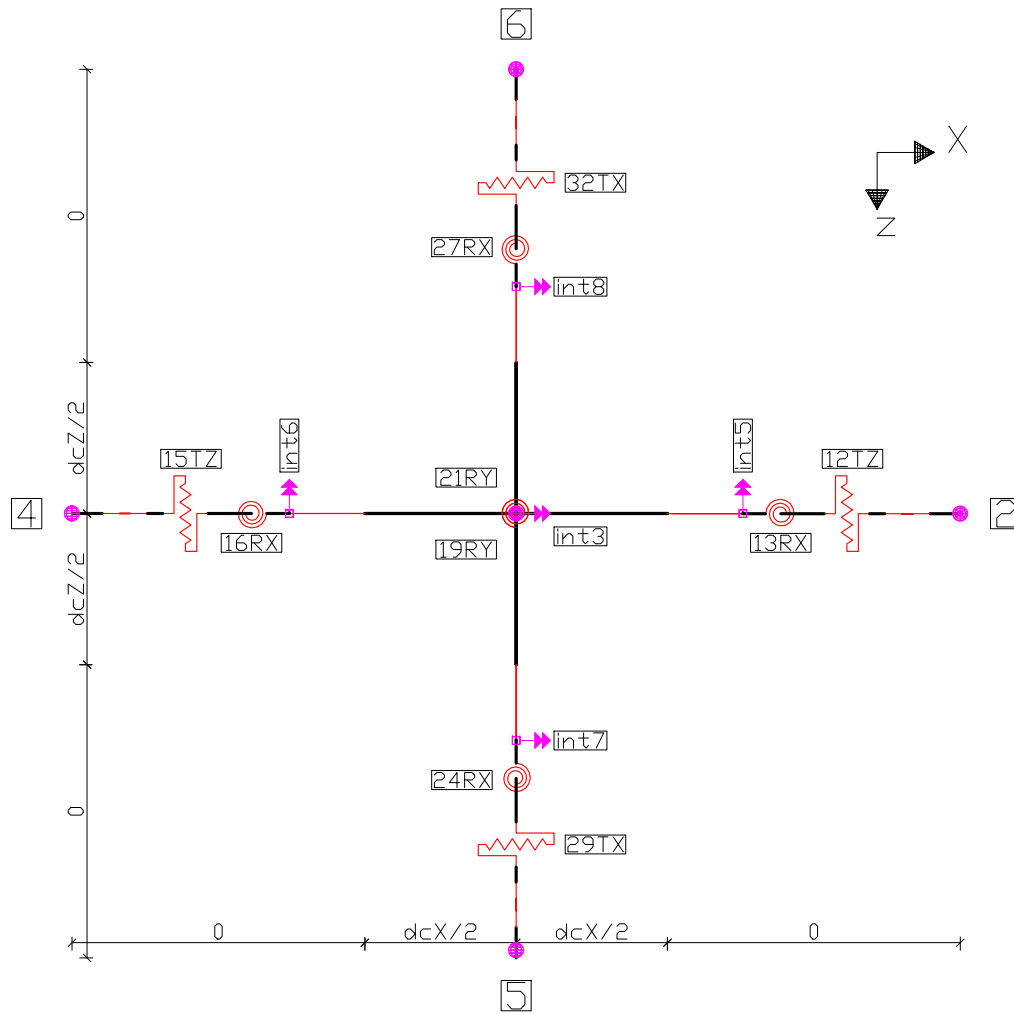


Figure 2.39: Components of the beam-to-column joint finite element developed within the INNO3DJOINTS project [5]: Z-X plane.

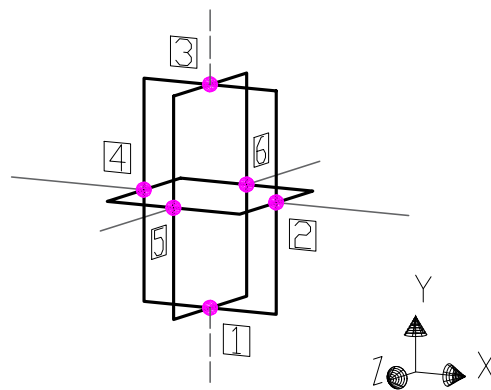


Figure 2.40: Proposed beam-to-column joint finite element within the INNO3DJOINTS project [5]: schematic representation in 3D view.

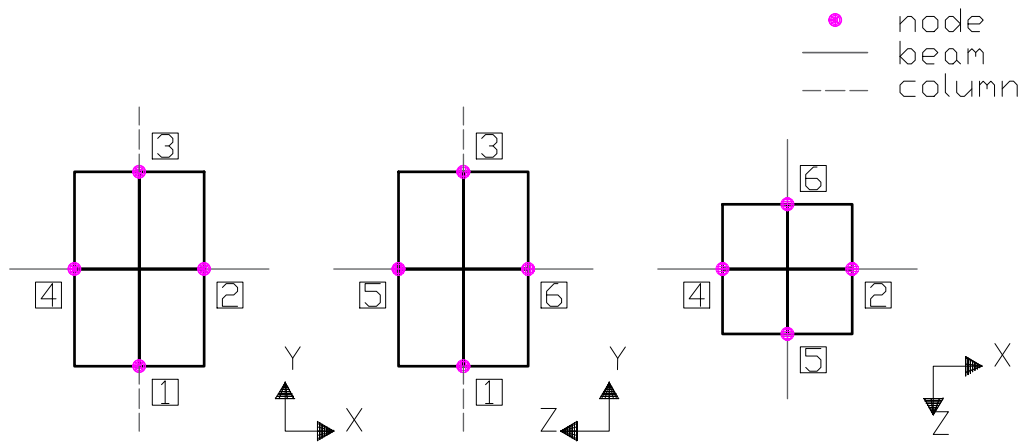


Figure 2.41: Proposed beam-to-column joint finite element within the INNO3DJOINTS project [5]: schematic representation in 2D view.

Chapter 3

Development of the macro-element formulation

3.1 Introduction

The present chapter aims to describe the development of the macro-element for the innovative 3D plug-and-play joint (P&PJ) system in the context of this thesis. This is because, as previously observed, the macro-element produced in the INNO3DJOINTS project [5] could be improved. A thorough presentation of the concept, validation, and mathematical formulation of the macro-element will be presented to achieve this goal.

3.2 P&PJ systematic approach for development

The installation process of the P&PJ, as outlined in Section 2.6.4.2, is straightforward. However, analyzing and designing it can be somewhat intricate. Therefore, the components method approach was utilized, following the guidelines of Eurocode 3 Part 1-8 [28]. In an intermediate stage, however, the joint had to be partitioned into four separate components with a higher level of complexity, as illustrated in Fig. 3.1 and enumerated below:

- column – socket interface: welded connection, where the main challenge was the behavior of the welds on the bend parts of the columns;
- socket – T-plug connection: bolted connection, ensuring the transfer of forces through the bolts in shear and bearing of the plates; the novelty in this part was not the connection itself, but the modeling of the bend plates;

- Y-fork – CFS truss-girder connection: bolted connection, ensuring the transfer of shear forces between the CFS plates of the chord profile and the HRS plates of the plug; as previously mentioned, these regions contain three bolt arrangements with different purposes:
 - vertical: transfer of vertical forces between the horizontal and the vertical element of the truss-girder;
 - horizontal: transfer of horizontal forces between the truss-girder and the joint;
 - diagonal: transfer of the diagonal forces between the diagonal and the node of the truss-girder;
- tubular column: the part of the column in the joint region; the novelty of this part is the need to account for the integration of multiple CFS truss-girders seamlessly.

The main focus of the INNO3DJOINTS experimental campaign was on the first three parts [1], [144], [188] (i.e., column – socket interface, socket – T-plug, and Y-fork – CFS truss-girder connections). Consequently, the behavior and analysis of the tubular column in the joint region were addressed numerically and analytically.

Accordingly, the present study concentrates on modeling the tubular regions in the beam-to-column joint area, considering the possibility of having multiple CFS truss-girders connected to the column in the same region.

Nonetheless, the model developed in this study also encompasses the other parts of the joint. Therefore, the components of the P&PJ, assuming no integration between CFS truss-girders (i.e., for a P&PJ with only a single truss-girder, as depicted in Section 2.6.5), are also taken into consideration in this study because these components are crucial and necessary inputs for this study as well. However, for a joint configuration with more than one truss-girder, the stiffness and strength of the tube components depend on the forces acting on each column face with truss-girders attached to it due to the 3D interaction between the column faces.

In any P&PJ configuration with CFS truss-girders connected to the column at the same level, the P&PJ can be analyzed as two separate joints: one connecting the upper chord and the other connecting the bottom chord of the truss-girder to the column, as seen in Fig. 3.2. Further on, these regions will be referred to as *joint(s)*. Accordingly, in the case of a joint configuration with truss-girders of different depths or positioned at different heights, the P&PJ will have more than two joints.

Hereinafter, the relevant components of the P&PJ system are classified into two categories, namely *connection components* and *tube components*. The connection components account for the mechanical behavior of the socket, T-plug, and CFS truss-girder's ends. In contrast, the tube component describes

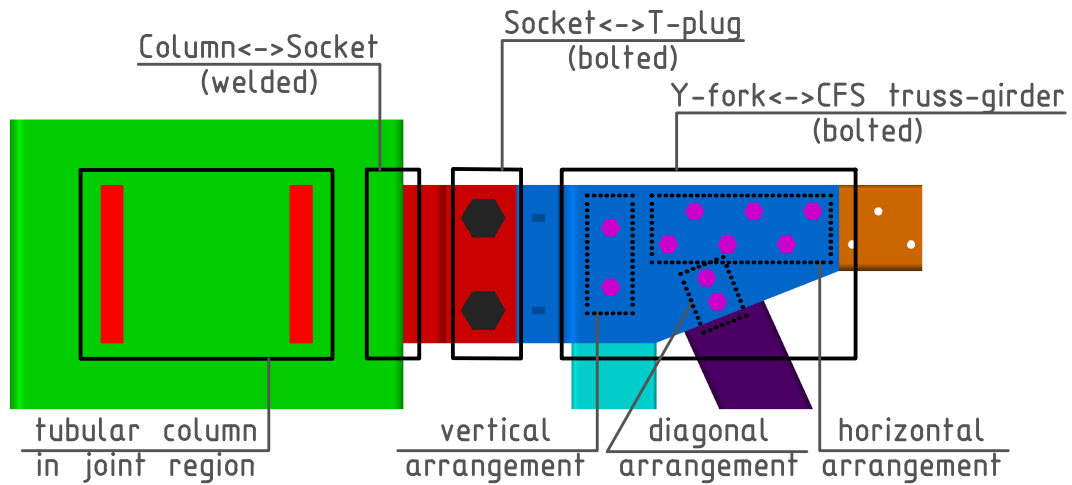


Figure 3.1: INNO3DJOINTS plug-and-play joint system.

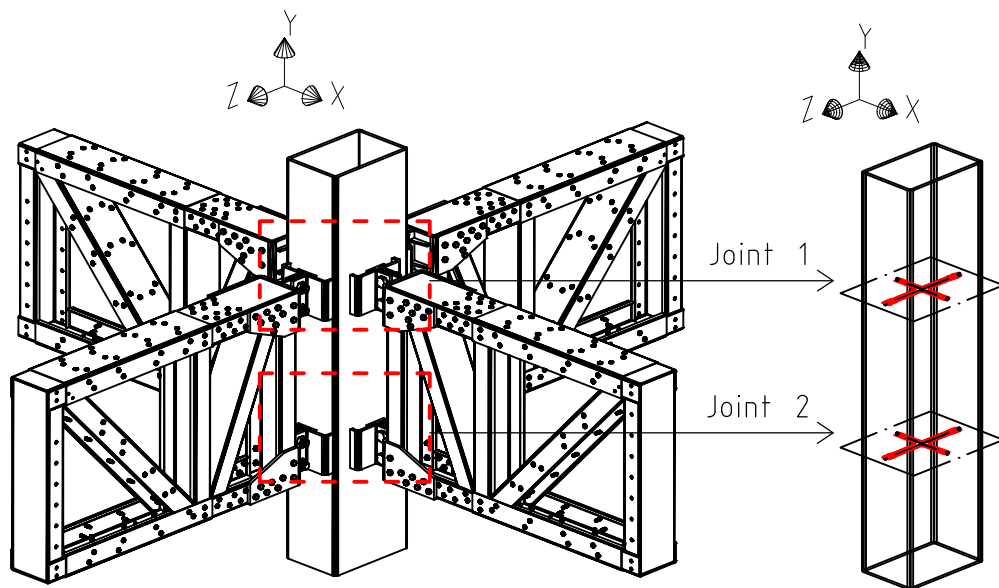


Figure 3.2: Schematic representation of a full P&PJ.

the mechanical behavior of the tube faces and their interaction.

3.3 Proof of concept

3.3.1 Formulation

According to experimental evidence and numerical results [153], [154], [199], when multiple loads are applied simultaneously to multiple tube faces, the out-of-plane deformations will be different than when each load is applied individually to each face. This difference in displacements suggests that there is an interaction between the different tube faces. In other words, instead of behaving independently, the faces interact with each other.

Accordingly, an appropriate model for the P&PJ must consider not only the components outlined in Section 2.6.5 (i.e., which are determined for a joint configuration with a single CFS truss-girder connected to the column in which there is no interaction between the faces of the tube) but also the interaction between the faces of the tube when multiple truss-girders are attached to it at the same level.

The approach taken in this study to consider the interaction between column faces uses the component method but focuses on the development of a straightforward mechanical model that is easily comprehended and whose components possess a clear physical meaning. These aspects represent the fundamental principles of the component method, which likely explains its efficacy. Conversely, the method described in Section 2.6.6 employs a more mathematically-based approach, resulting in a model that may prove more challenging for users to comprehend with regards to interpreting and validating the model's inputs and outputs.

Over the course of this study, following the former principle, it was found that the simplest model for handling the interaction of column faces is the cross-section level macro-element schematically represented in Fig. 3.3. The key characteristics of this macro-element are:

- has five nodes, with nodes 1 to 4 serving as edge or face nodes and node 5 functioning as the center node;
 - the edge nodes ensure the connection of the CFS truss-girder chords to the column;
 - the center node is utilized to connect with the centerline of the column.
- the edge nodes are allowed to exhibit translational movement in the direction of the centerline of the corresponding CFS truss-girder;
- the components outlined in Section 2.6.5, with the exception of those corresponding to the column face, are explicitly considered and are lumped into the single OD element that is located adjacent to the edge nodes, as depicted by the green OD elements in Fig. 3.3;
- it is assumed that only the interaction between adjacent tube faces is significant, e.g., if the displacements in faces B and D in Fig. 3.3 are blocked, then there will be no interaction between faces A and C;
- the interaction between the column faces is taken into account through a series of OD elements, the physical meaning of which will be explained below (as depicted by the blue and red OD elements in Fig. 3.3).

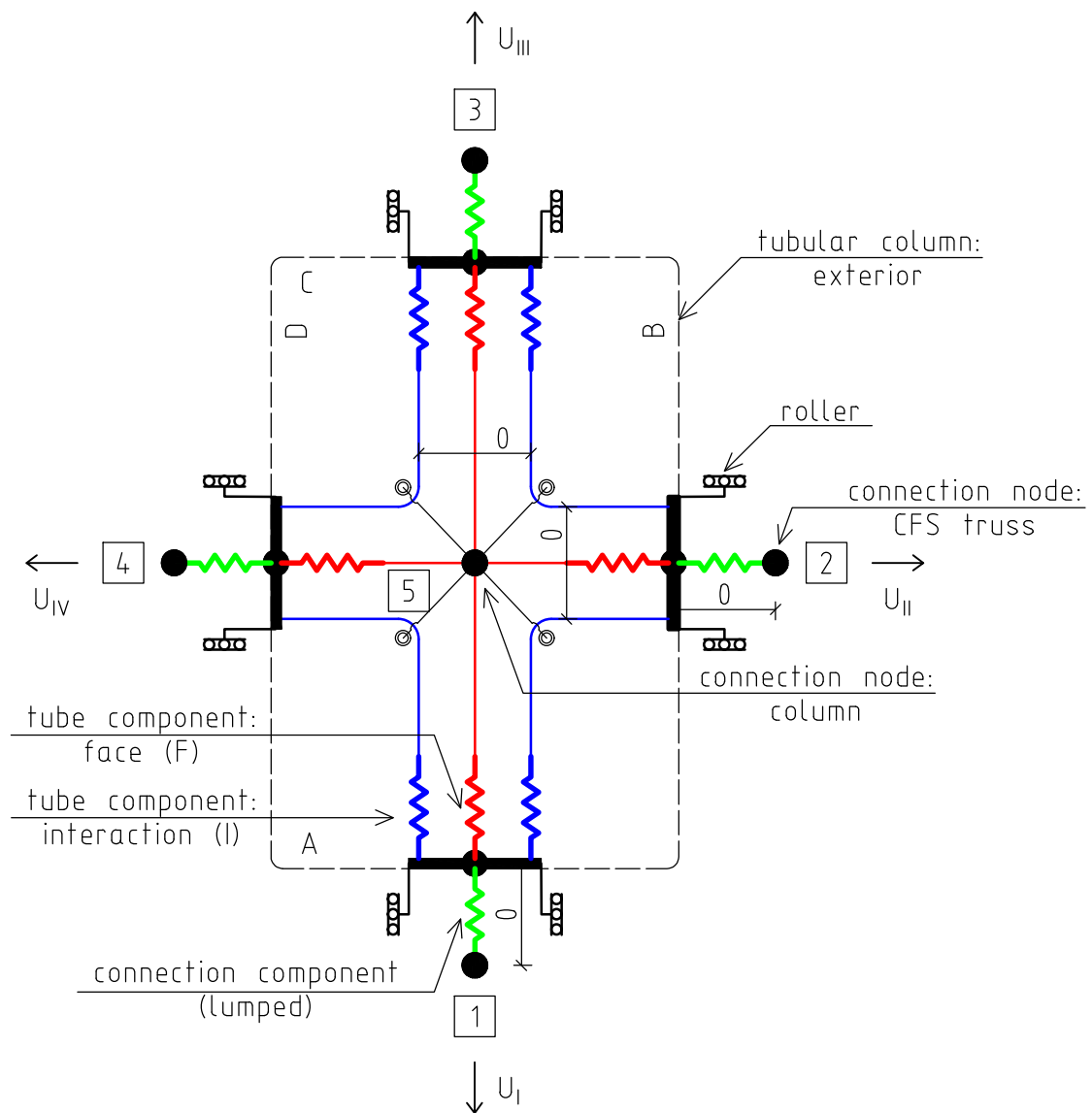


Figure 3.3: Component-based macro-element of a tubular profile at cross-section level (2D view).

This model follows the split of the P&PJ in two joints and accounts for the behavior of each joint separately. This means that the connection of a CFS truss-girder to a column will require the use of two macro-elements (i.e., one at the level of each chord, as shown in Fig. 3.4(a)) and that the bending and shear behavior of the tube between these two macro-elements is accounted for using a traditional 1D element. This approach also deals with cases where the truss-girders have different depths (Fig. 3.4(b)) or are placed at different heights (Fig. 3.4(c)).

It is important to note that the proposed macro-element disregards the deformation modes illustrated in Fig. 3.5 that occur from the application of shear force, bending moment, and axial load (i.e., tension or compression).

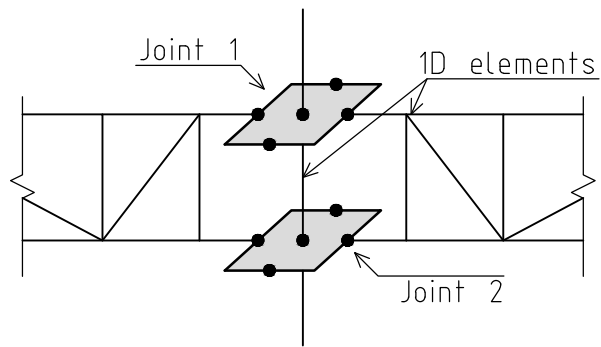
A mechanical model referred to as the *column macro-element* (CME) is considered to facilitate the validation of the proof of concept of the macro-element. In the CME, the connection components which are considered lumped are assumed to be rigid and are therefore not taken into account. As a result of this simplification, the CME comprises only two types of components:

- the *face component* (denoted as F and represented in red in Fig. 3.3): a 0D element that connects an edge node with the central node within the CME;
- *interaction component* (denoted as I and represented in blue in Fig. 3.3): a 0D element that connects two edge nodes located on adjacent sides of the CME.

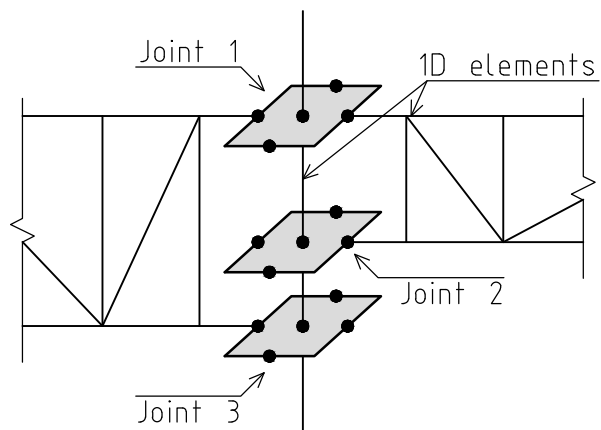
The physical meaning of each component type (i.e., F and I) can be comprehended through their stiffness definition for a generic column face. For instance, for face A in Fig. 3.6, these are:

- face component's stiffness (k_F) – the force that produces a unitary out-of-plane displacement on face A, when simultaneously unitary out-of-plane displacements are imposed on the adjacent faces B and D in Fig. 3.6(b);
- interaction component's stiffness (k_I) – the force that keeps null the out-of-plane displacements on faces B or C in Fig. 3.6(c), while a unitary out-of-plane displacement is imposed on face A in Fig. 3.6(c).

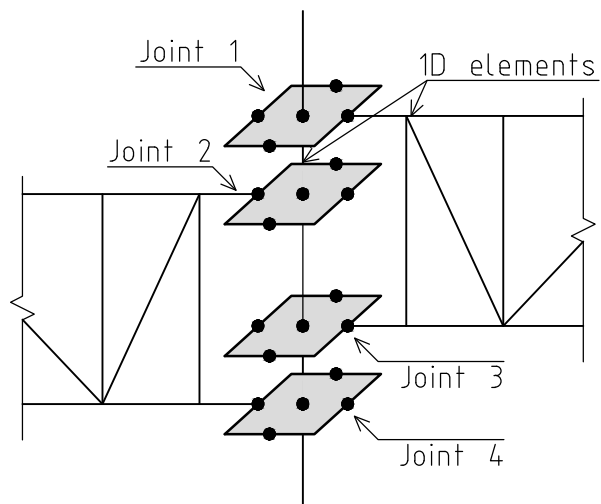
It is observed that, in accordance with this definition, all face components within a square cross-section have the same stiffness, k_F . However, due to the dissimilarity in dimensions between the faces of a rectangular cross-section, distinct values for the stiffness of face components, $k_{F,1}$ and $k_{F,2}$, are obtained for the shorter (i.e., width) and longer (i.e., length) side of the column cross-section, respectively. Nevertheless, only a single value for the stiffness of the interaction component, k_I , is obtained for both square and rectangular cross-sections.



(a) truss-girders with equal depth and with chords at the same height



(b) truss-girders with unequal depth and with top chords at the same height



(c) truss-girders with with chords at different heights

Figure 3.4: Modeling strategy of P&PJ with a sectional macro-element.

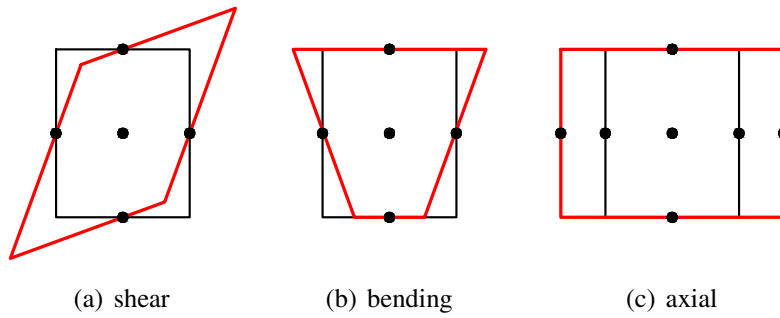
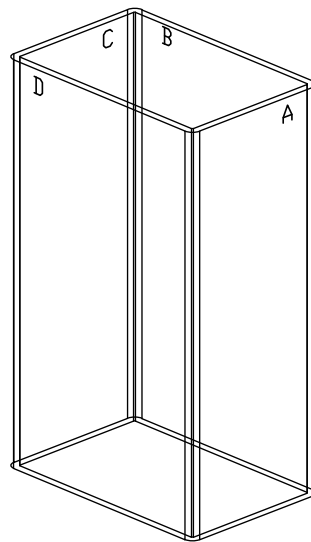
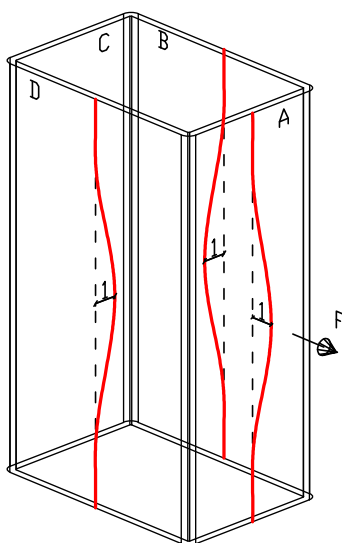


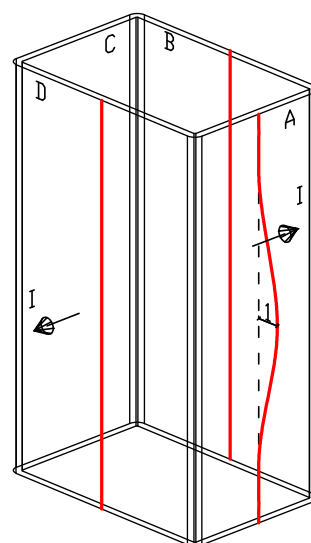
Figure 3.5: Deformation modes disregarded in the macro-element design (top view).



(a) undeformed tube



(b) face component



(c) interaction component

Figure 3.6: Definition of the stiffness of the tube components.

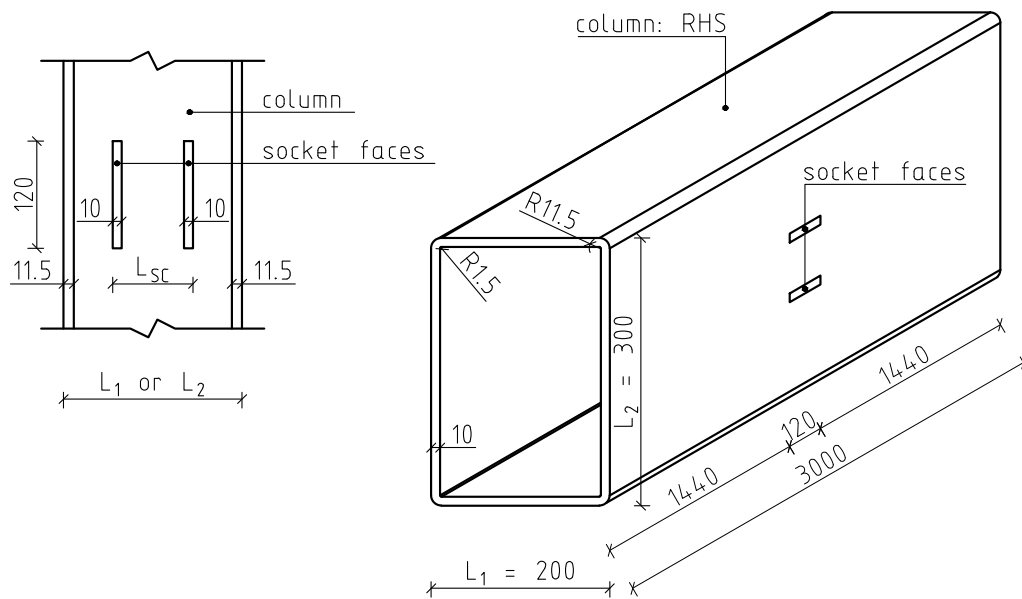


Figure 3.7: Component-based macro-element of a tubular profile in the joint's region (top view).

3.3.2 Validation

To demonstrate the validity of the macro-element outlined in the preceding section as a reliable representation of tube behavior, a proof of concept validation was conducted based on the following steps:

1. compute the stiffness of the tube components using a Refined Finite Element Model (RFEM) according to the physical meaning described previously;
2. assemble the stiffness matrix of the column macro-element (CME);
3. select a load pattern (LP);
4. compute the out-of-plane displacements of the column faces for the selected LP using the RFEM;
5. compute the out-of-plane displacements of the column faces for the selected LP using the CME;
6. compare the RFEM and CME results; ideally, they should match or be within an acceptable error range.

Subsequently, the validation procedure of the proof of concept is presented for a rectangular tubular column. The stiffness of the tube components is obtained from a finite element model, which was developed using Abaqus [113], with the geometry as illustrated in Fig. 3.7. The material characteristics, mesh, boundary conditions, and analysis type are described in more detail in Section 5.4.3.

The cross-sectional geometry requires the determination of the stiffness of two face components (k_{F1} and k_{F2}) and an interaction component (k_I). Depending on the case, the values for these

components are obtained by applying either a unitary or a null displacement-based load to the reference points (RPs) on the socket faces, as shown in Fig. 3.8 and in Fig. 3.9.

In accordance with the notations of the column faces in Fig. 3.6, the stiffness of the face components for faces A and C, and B and D are represented by k_{F1}^{AC} and k_{F2}^{BD} , respectively.

As mentioned, the interaction component's stiffness should be the same for all interaction components, regardless of the tube shape. However, this scenario cannot be achieved numerically due to small differences in the finite element model. Therefore, the interaction component's values k_{I1} (Fig. 3.8) and k_{I2} (Fig. 3.9) have small variations. Since a fundamental criterion of any stiffness matrix is symmetry, an average of these values is proposed through Eq. (3.1).

$$k_I = \frac{k_{I1} + k_{I2}}{2} \quad (3.1)$$

The stiffness of the tube components is assessed for three socket configuration(s) (SC(s)), which result from adjusting the distance between socket faces, L_{SC} from Fig. 3.7. However, the same SC is applied to all column faces. The designated SCs, namely SC01 to SC03, are presented in Tab. 3.1 and are utilized for various computational purposes throughout the document. Therefore, a detailed discussion on the SC is provided in Section 5.4.1.

The displacement vector of the CME, \mathbf{U}_{CME}^{SC0i} , with node 5 fixed to prevent rigid body movements, is defined as:

$$\mathbf{U}_{CME}^{SC0i} = \begin{bmatrix} U_I & U_{II} & U_{III} & U_{IV} \end{bmatrix}^T \quad (3.2)$$

Under the same conditions, the stiffness matrix of the CME will be represented as follows:

$$\mathbf{K}_{CME}^{SC0i} = \begin{bmatrix} k_{F1}^{AC} + 2 k_I & k_I & 0 & k_I \\ k_I & k_{F2}^{BD} + 2 k_I & k_I & 0 \\ 0 & k_I & k_{F1}^{AC} + 2 k_I & k_I \\ k_I & 0 & k_I & k_{F2}^{BD} + 2 k_I \end{bmatrix} \quad (3.3)$$

Under certain circumstances, the stiffness of tube components may exhibit a negative sign. Nevertheless, it is noteworthy that within the global stiffness matrix of the beam-to-column joint finite element, \mathbf{K}_j^{cond} , which will be elaborated upon in Section 3.4.2 via Eq. (3.20), all constituent elements are positive in value.

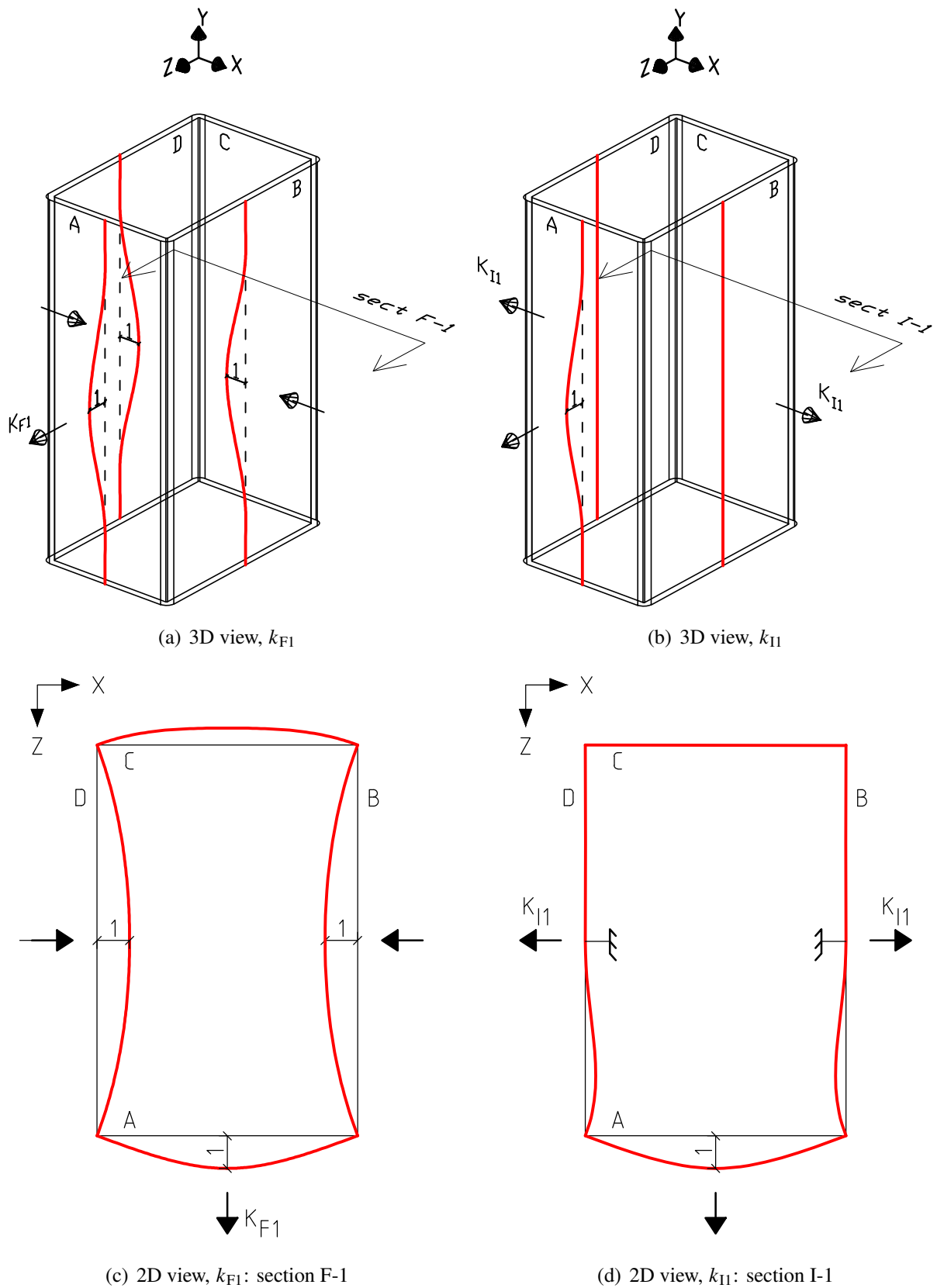


Figure 3.8: Tube components for the short face (width).

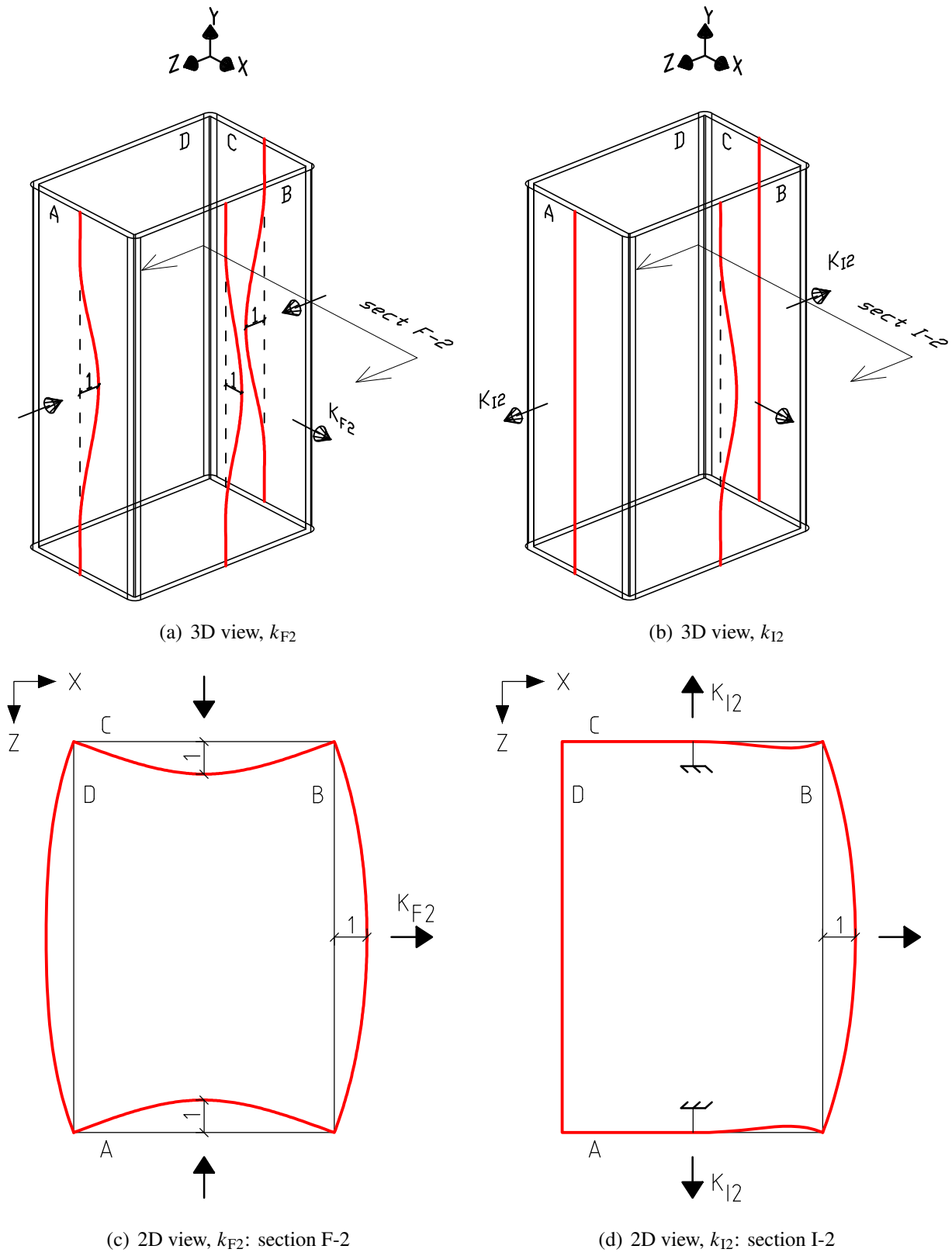


Figure 3.9: Tube components for the long face (length).

Table 3.1: Tube components stiffness raw values [kN/m].

SC	L_{SC} [mm]	k_{F1}	k_{F2}	k_{I1}	k_{I2}
01	20	62.33	10.87	12.52	12.65
02	40	78.74	9.97	15.87	16.04
03	90	187.32	0.75	34.08	34.46

Table 3.2: Tube components stiffness: final values [kN/m].

SC	k_{F1}	k_{F2}	k_I
01	62.33	10.87	12.58
02	78.74	9.97	15.96
03	187.32	0.75	34.27

Additionally, for an arbitrary LP, the applied forces vector, \mathbf{P}_{CME}^{SC0i} , will be expressed as:

$$\mathbf{P}_{CME}^{SC0i} = \begin{bmatrix} P_I & P_{II} & P_{III} & P_{IV} \end{bmatrix}^T \quad (3.4)$$

According to the classical displacement method [200], the out-of-plane displacements of the column faces, \mathbf{U}_{CME}^{SC0i} , are determined as:

$$\mathbf{U}_{CME}^{SC0i} = \left(\mathbf{K}_{CME}^{SC0i} \right)^{-1} \mathbf{P}_{CME}^{SC0i} \quad (3.5)$$

The raw values of the stiffness of the tube components for each SC, calculated using the RFEMs, are presented in Tab. 3.1. The final values (i.e., the mathematical average of k_{I1} and k_{I2}) of the stiffness of the tube components, utilized to construct the stiffness matrix of the mechanical model, are presented in Tab. 3.2.

The deformed shapes of the tube cross-section at a mid-height of the column (i.e., section cut W0 from Fig. 5.23) in directions 1 and 2 (i.e., U1 and U2) obtained from Abaqus are shown in Fig. 3.10.

A set of three LPs is defined to validate the proof of concept of the CME. They are schematically represented in Fig. 3.11, with a dummy load $P = 1000$ kN.

The out-of-plane displacement values for the RFEM and CME, as well as the relative error, ε_1 , defined by Eq. (3.6), are shown in Tab. 3.3. The relative error values fall within a range of plus or minus 3%, which is considered acceptable, thereby demonstrating the ability of the CME to accurately account for the 3D interaction between the faces of the tube. However, it should be noted that the

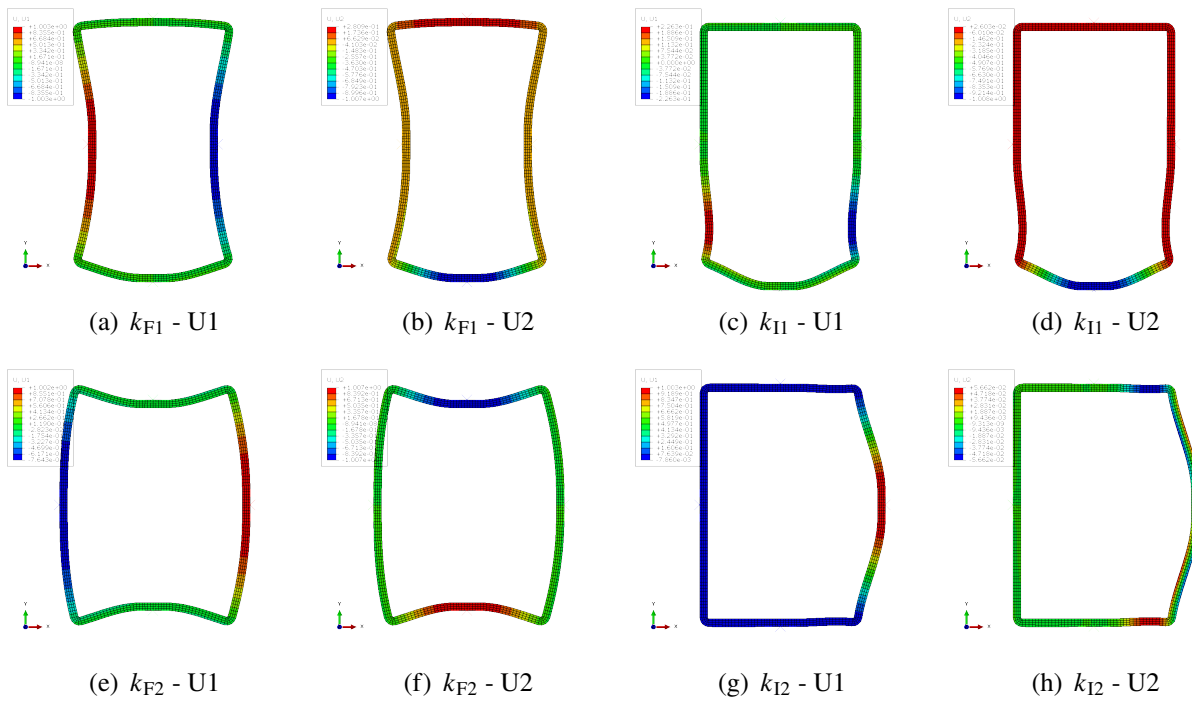


Figure 3.10: Cross-section's deformed shape for tube components on U1 and U2 for SC02.

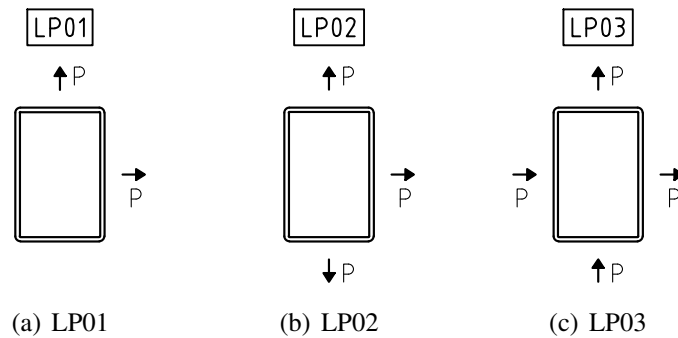


Figure 3.11: Load patterns (LP) used to validate the CME proof of concept.

error may be high in cases with very small displacement values, as exemplified by LP01 with SC03 in direction IV (or on face D).

$$\varepsilon_1 = \frac{U_{RFEM} - U_{CME}}{U_{RFEM}} 100 \tag{3.6}$$

3.4 Extension to beam-to-column joint finite element

The usability of the macro-element from Fig. 3.3 was extended and integrated into a beam-to-column joint finite element that considers both tube and connection components. This new joint finite element allows modeling other types of loads and deformations not accounted for explicitly, e.g., transversal deformation and rotation in each connection, as detailed in the next sections.

Table 3.3: Results validation: RFEM vs. CME [mm]

LP	SC	L_{sc}	RFEM				CME				ε_1 [%]			
			U_I	U_{II}	U_{III}	U_{IV}	U_I	U_{II}	U_{III}	U_{IV}	$\varepsilon_{1,I}$	$\varepsilon_{1,II}$	$\varepsilon_{1,III}$	$\varepsilon_{1,IV}$
01	02	20	3.66	26.15	7.91	1.49	3.56	26.24	7.87	1.51	2.84	-0.34	0.55	-0.79
		40	3.22	22.74	5.93	1.05	3.14	22.83	5.90	1.05	2.38	-0.36	0.63	-0.31
		90	1.96	14.32	2.02	0.09	1.93	14.40	1.98	0.03	1.72	-0.56	1.61	67.52
02	02	20	-9.20	21.20	9.20	6.45	-9.31	21.25	9.31	6.50	-1.13	-0.21	-1.13	-0.85
		40	-7.09	18.37	7.09	5.42	-7.17	18.41	7.17	5.46	-1.11	-0.24	-1.11	-0.79
		90	-2.65	11.73	2.65	2.68	-2.69	11.77	2.69	2.66	-1.56	-0.34	-1.56	0.71
03	02	20	11.58	27.65	11.58	27.65	11.43	27.75	11.43	27.75	1.27	-0.36	1.27	-0.36
		40	9.15	23.79	9.15	23.79	9.04	23.88	9.04	23.88	1.24	-0.36	1.24	-0.36
		90	3.97	14.41	3.97	14.41	3.91	14.43	3.91	14.43	1.66	-0.14	1.66	-0.14

Table 3.4: Internal DOFs.

internal DOF	description
iDOF 1 & iDOF 3	linear deformation in Z direction
iDOF 2 & iDOF 4	linear deformation in X direction

Therefore, in addition to the macro-element represented in Fig. 3.3, the beam-to-column joint finite element presents 3D springs with six DOFs corresponding to three linear springs and three rotational springs, allowing to model connections with any desired behavior. Because these springs are 0D elements and are placed in the exact location, it is hard to distinguish them graphically. Therefore a better graphical representation of the joint finite element, in which the connection components are expanded, is shown in Fig. 3.13

The joint finite element consists of five external nodes with six DOFs per node. An additional four internal DOFs are added to ensure kinematic determinacy, resulting in 34 DOFs in total. The numbering for the external DOFs ranges from 1 to 30, whereas the internal DOFs are designated as iDOF1 to iDOF4 (or DOFs 31 to 34). The location and positive direction of the DOFs are presented in Fig. 3.14. Supplementary information regarding the internal DOFs can be found in Tab. 3.4, where the X-Y-Z coordinate system is used as the local system for the joint element's implementation, as shown in Fig. 3.13.

The concept behind the joint element allows the simulation of all three types of joints (i.e., central, edge, and corner), with some nodes potentially not connected to any truss-girder or column 1D finite elements.

The proposed model consists of 32 spring components (i.e., 0D elements) depicted in red in Figs. 3.15 to 3.24. These components are assigned a finite length in all illustrations to facilitate clear representation and discussion. Furthermore, the deformation direction of the spring components is displayed in Tab. 3.5. The behavior of the spring components is described by uniaxial (i.e., single DOF) material objects and can each have a unique load-deformation response history.

3.4.1 Sign convention

To compute the deformations and internal forces in components, the following sign convention is used:

- axial deformation: elongation (+) and shortening (-);
- shear deformation: positive according to the convention of Strength of Materials [201] assuming that the element is oriented according to the axis of the local X-Y-Z coordinate system parallel

Table 3.5: Components deformation direction.

Components	Description
1, 7, 13, 19, 26, 28	linear deformation in X direction
2, 8, 14, 20	linear deformation in Y direction
3, 9, 15, 21, 25, 27	linear deformation in Z direction
29, 30, 31, 32	linear deformation in Z-X plane (tube components: interaction components)
4, 10, 16, 22	rotational deformation after X axis
5, 11, 17, 23	rotational deformation after Y axis
6, 12, 18, 24	rotational deformation after Z axis

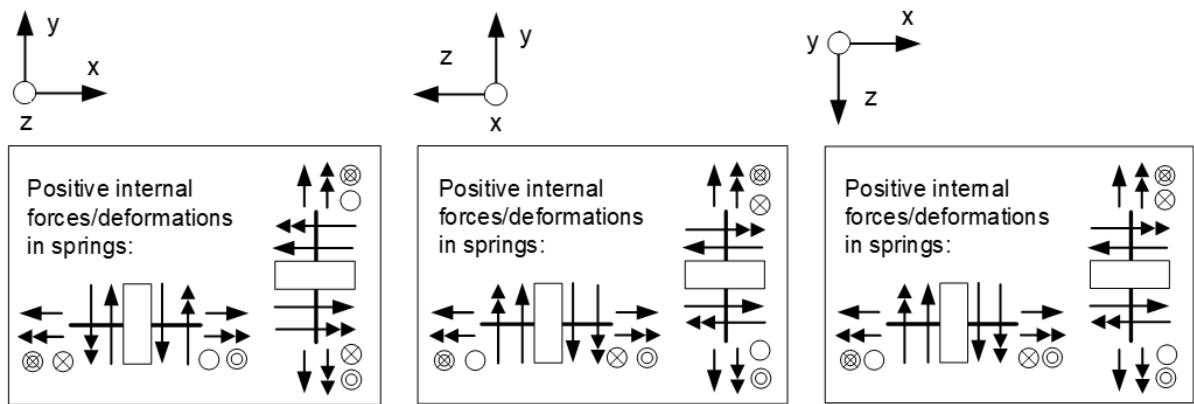


Figure 3.12: Positive sign convention of components.

to it;

- bending deformation: positive according to the convention of Strength of Materials [201] assuming that the element is oriented according to the axis of the local X-Y-Z coordinate system parallel to it;
- torsion deformation: positive if, according to the right-hand rule, the rotation vector points outward from the component and negative if it points inward.

The sign convention for each main plane is presented in Fig. 3.12. The forces and bending moments are represented in the in-plane view by single- and double-headed arrows, while in the plane perpendicular to the viewing plane by a single or double circle. If the single (or double) circle is crossed, the arrow points inward toward the plane, i.e., indicating the direction of entering the represented plane. If the circle is not crossed, the direction of the arrow points outward from the plane, i.e., indicating the direction of exiting the represented plane.

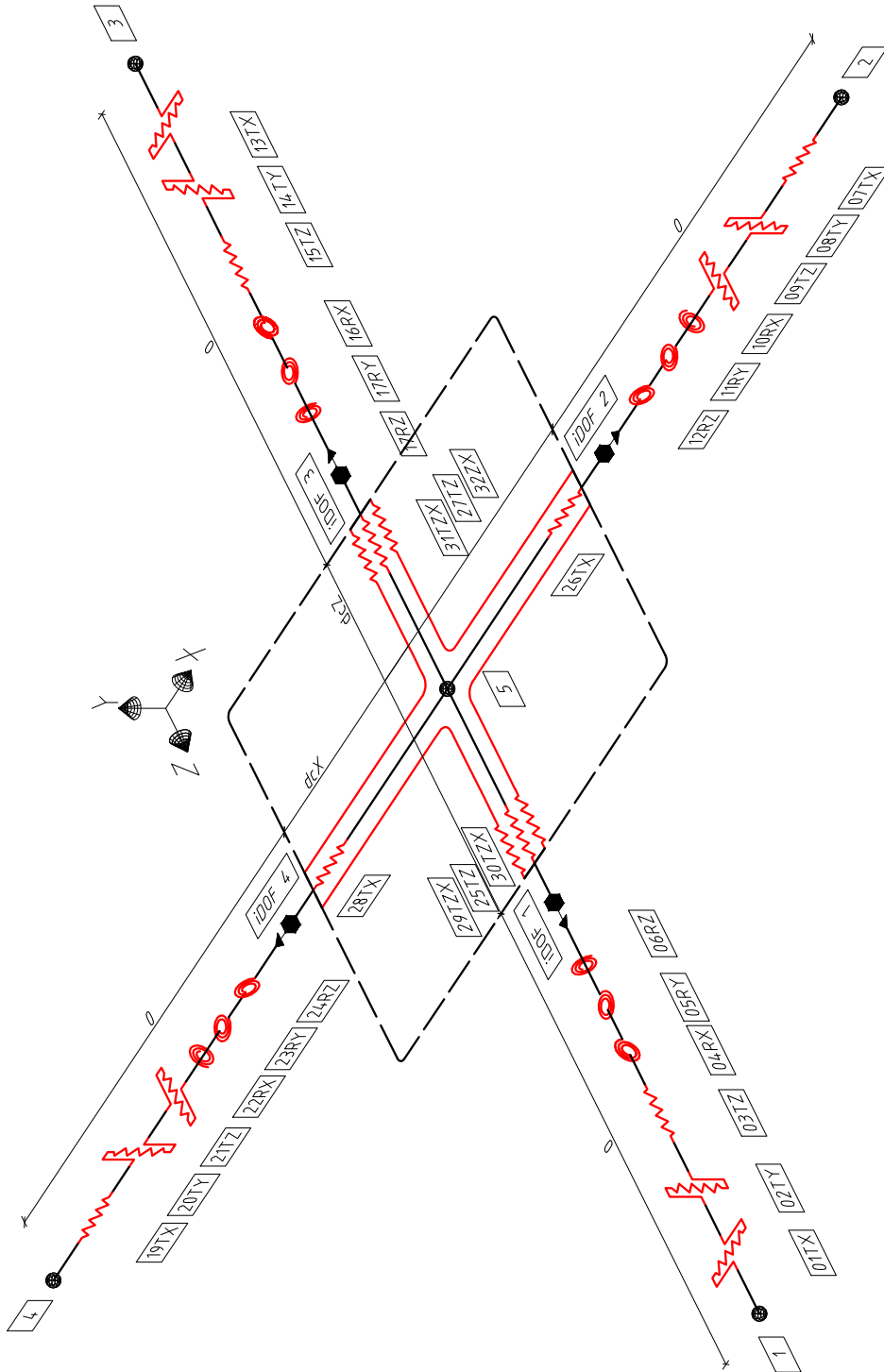


Figure 3.13: Proposed beam-to-column joint finite element: 3D overview.

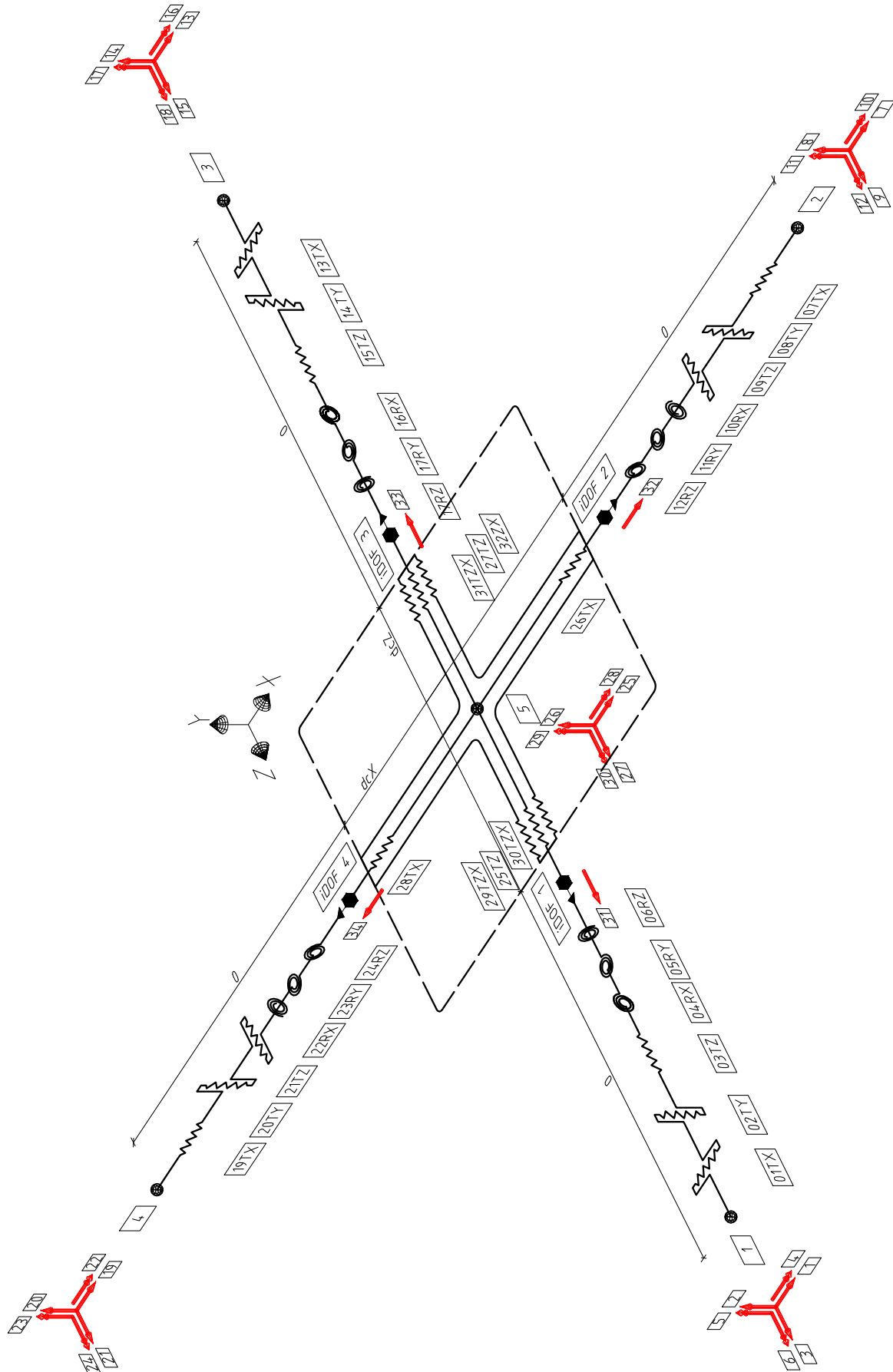


Figure 3.14: Proposed beam-to-column joint finite element: internal and external DOFs.

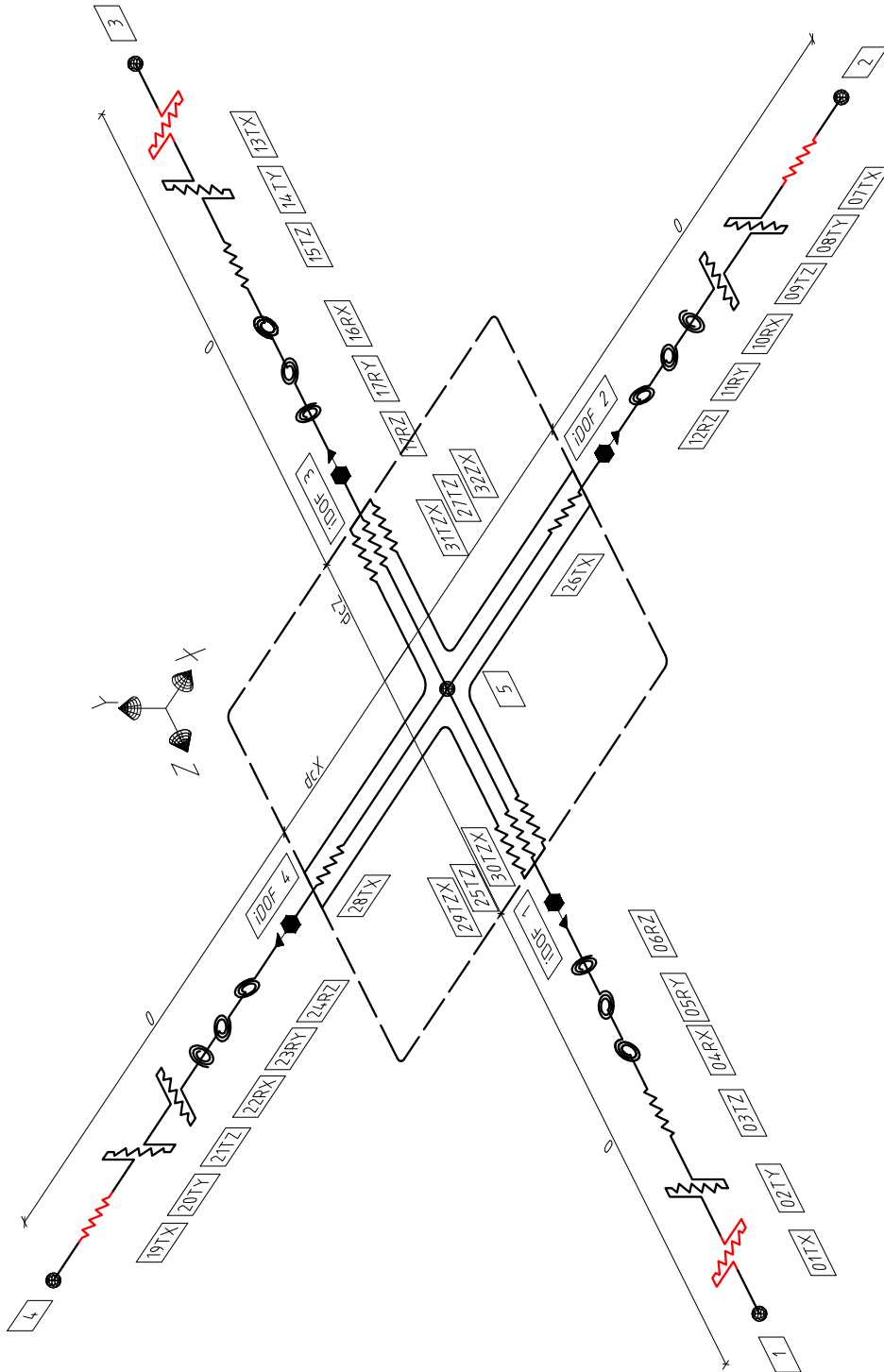


Figure 3.15: Components of the beam-to-column joint finite element: linear deformation in the X direction.

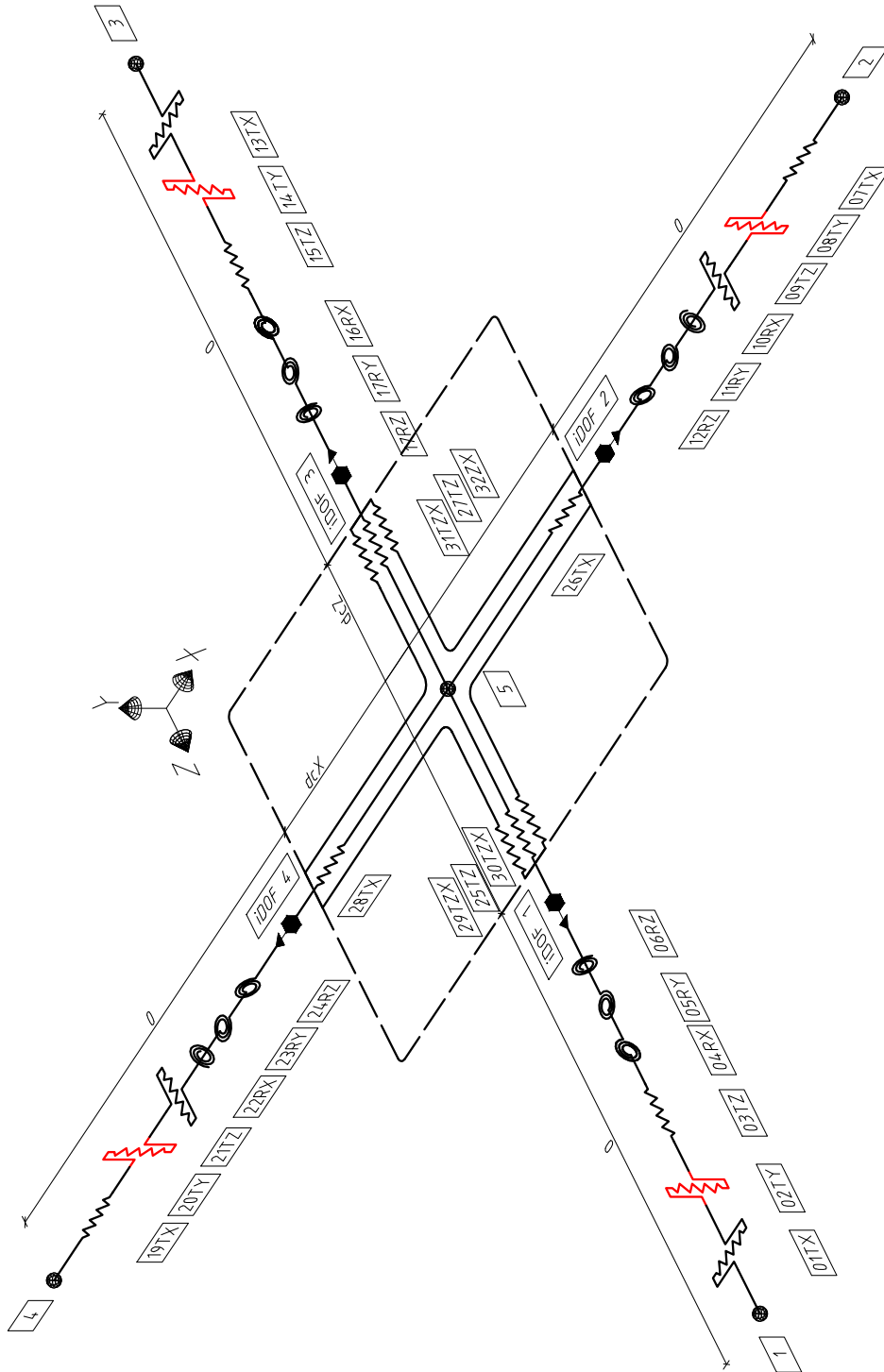


Figure 3.16: Components of the beam-to-column joint finite element: linear deformation in the Y direction.

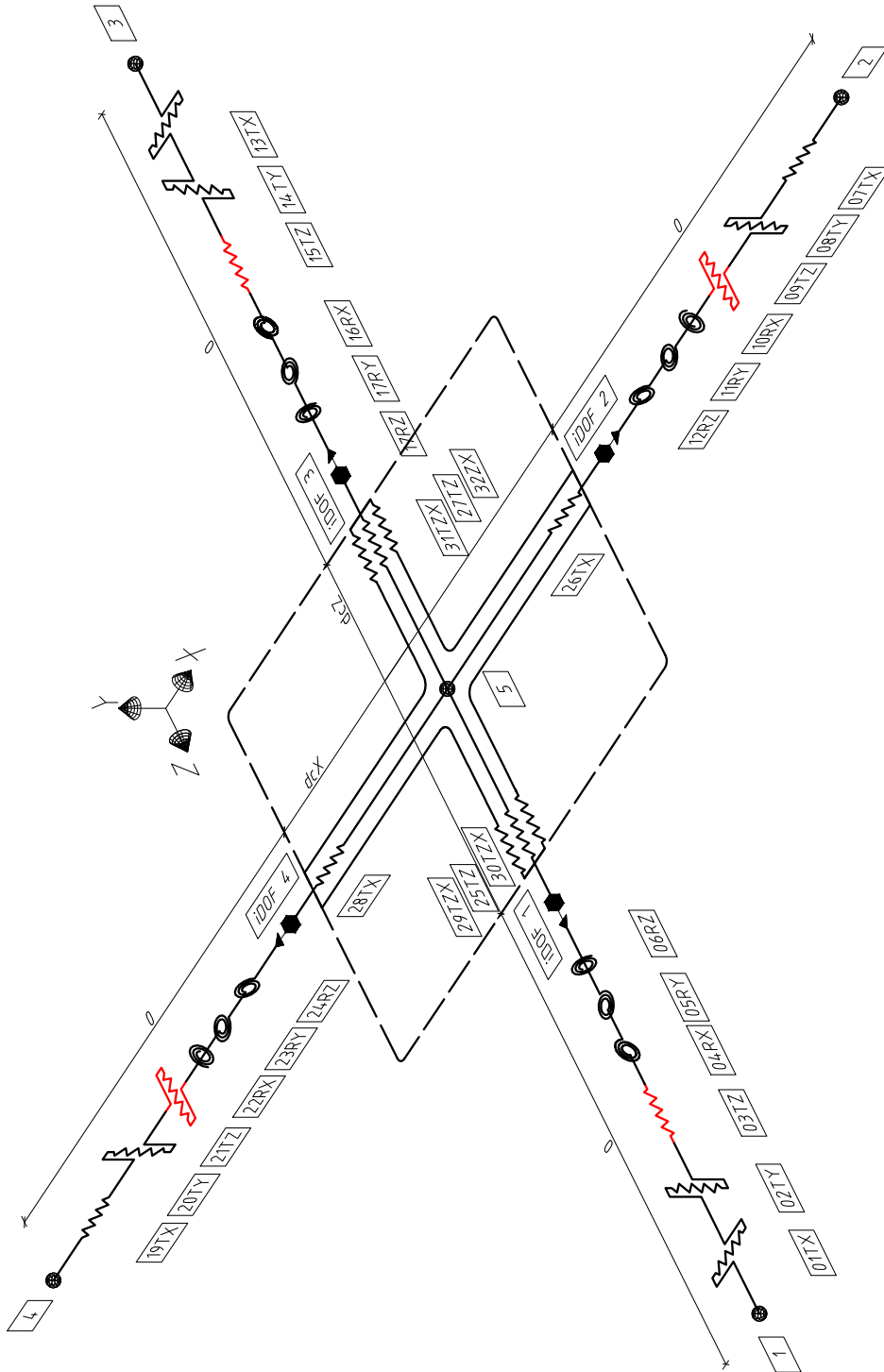


Figure 3.17: Components of the beam-to-column joint finite element: linear deformation in the Z direction.

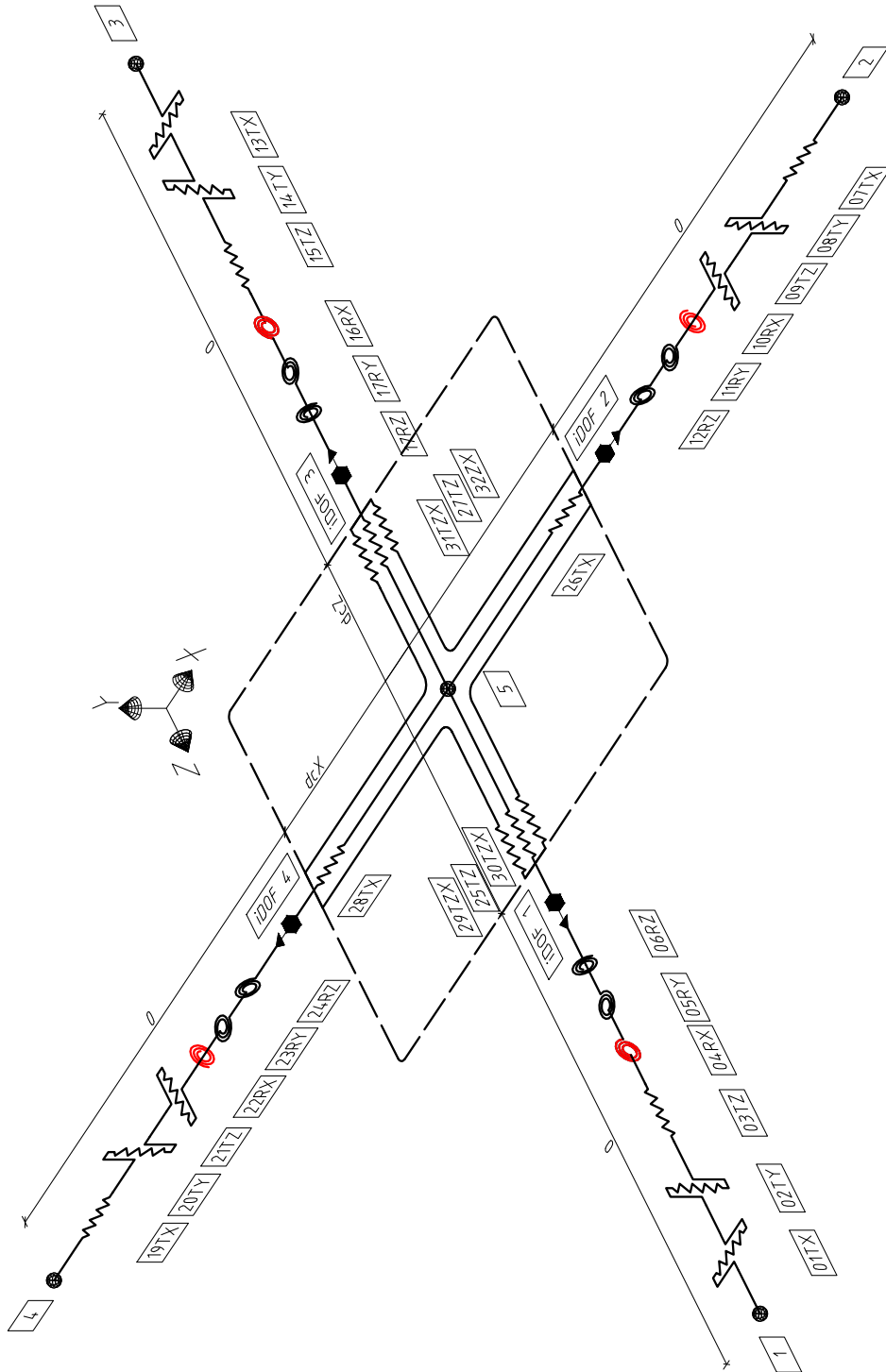


Figure 3.18: Components of the beam-to-column joint finite element: rotational deformation in the X direction.

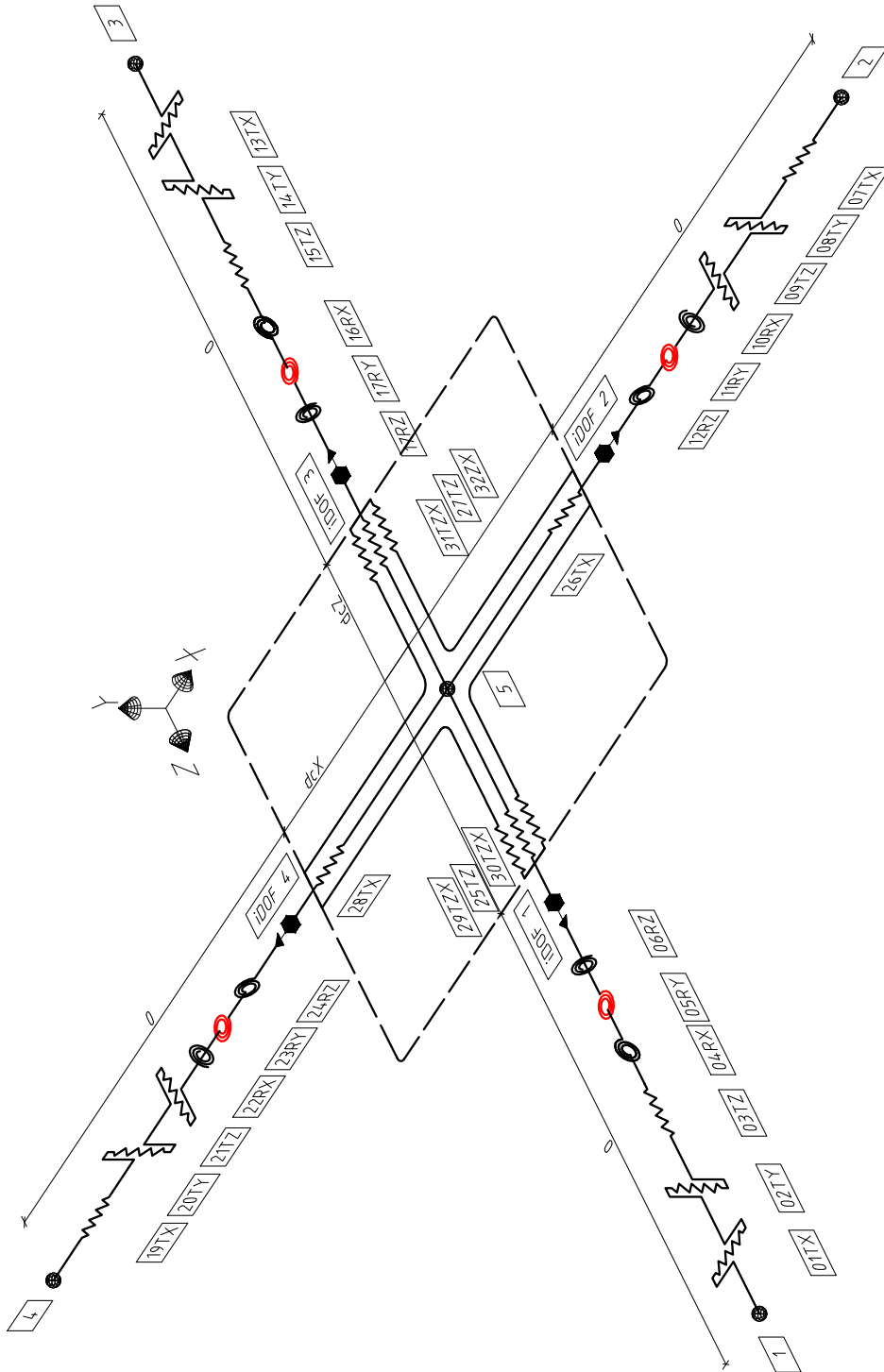


Figure 3.19: Components of the beam-to-column joint finite element: rotational deformation in the Y direction.

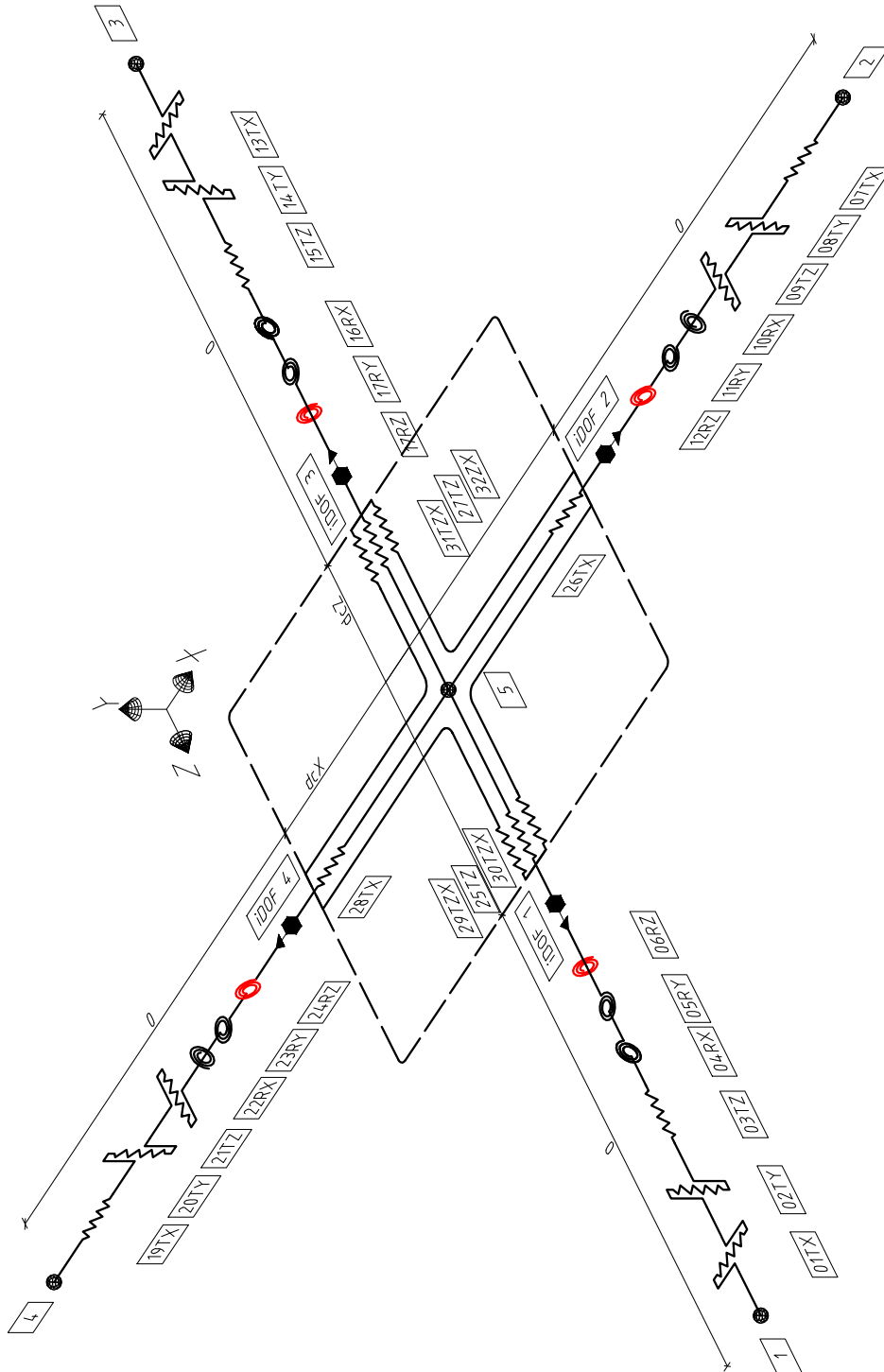


Figure 3.20: Components of the beam-to-column joint finite element: rotational deformation in the Z direction.

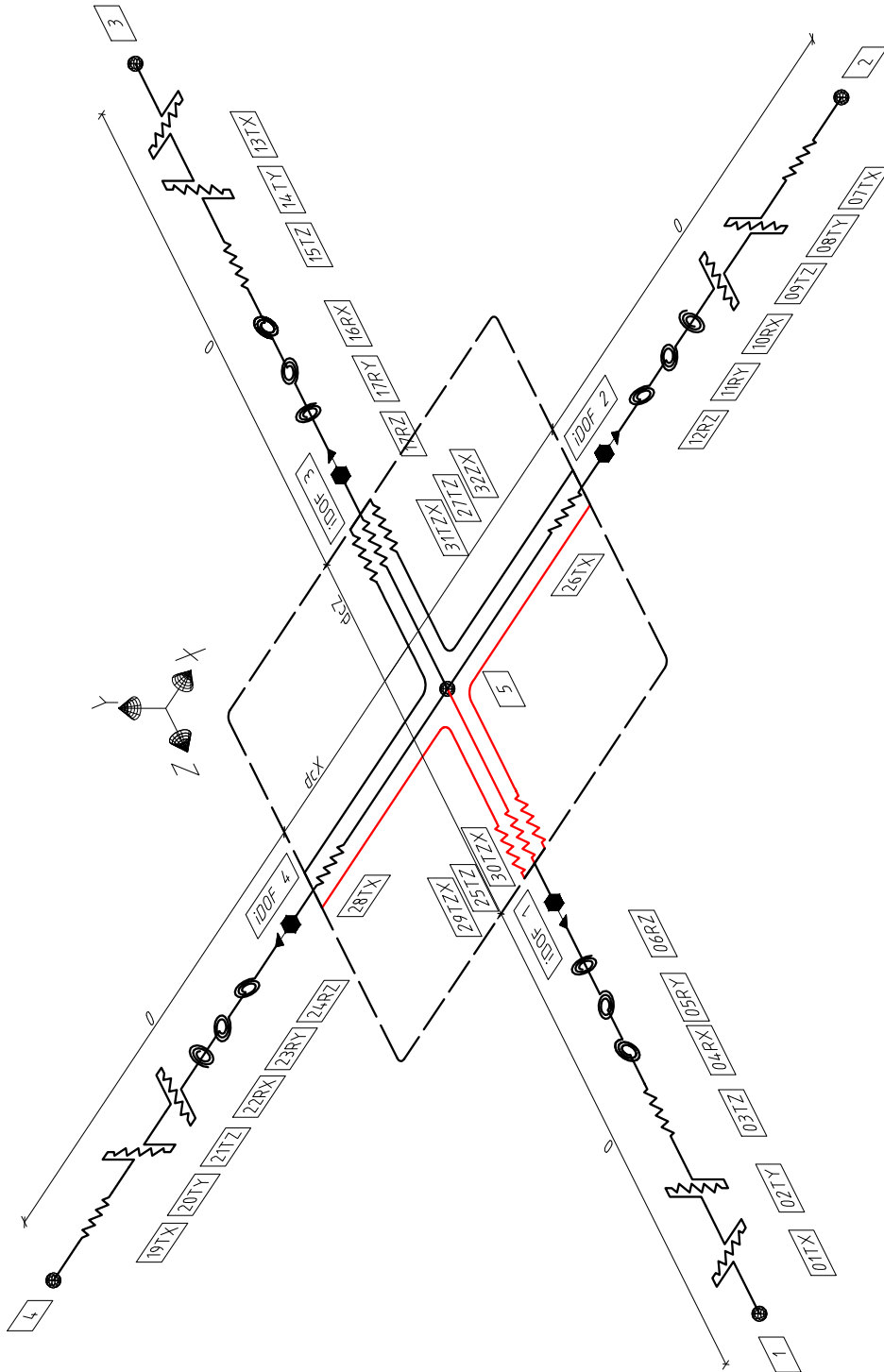


Figure 3.21: Components of the beam-to-column joint finite element: tube components for face 1.

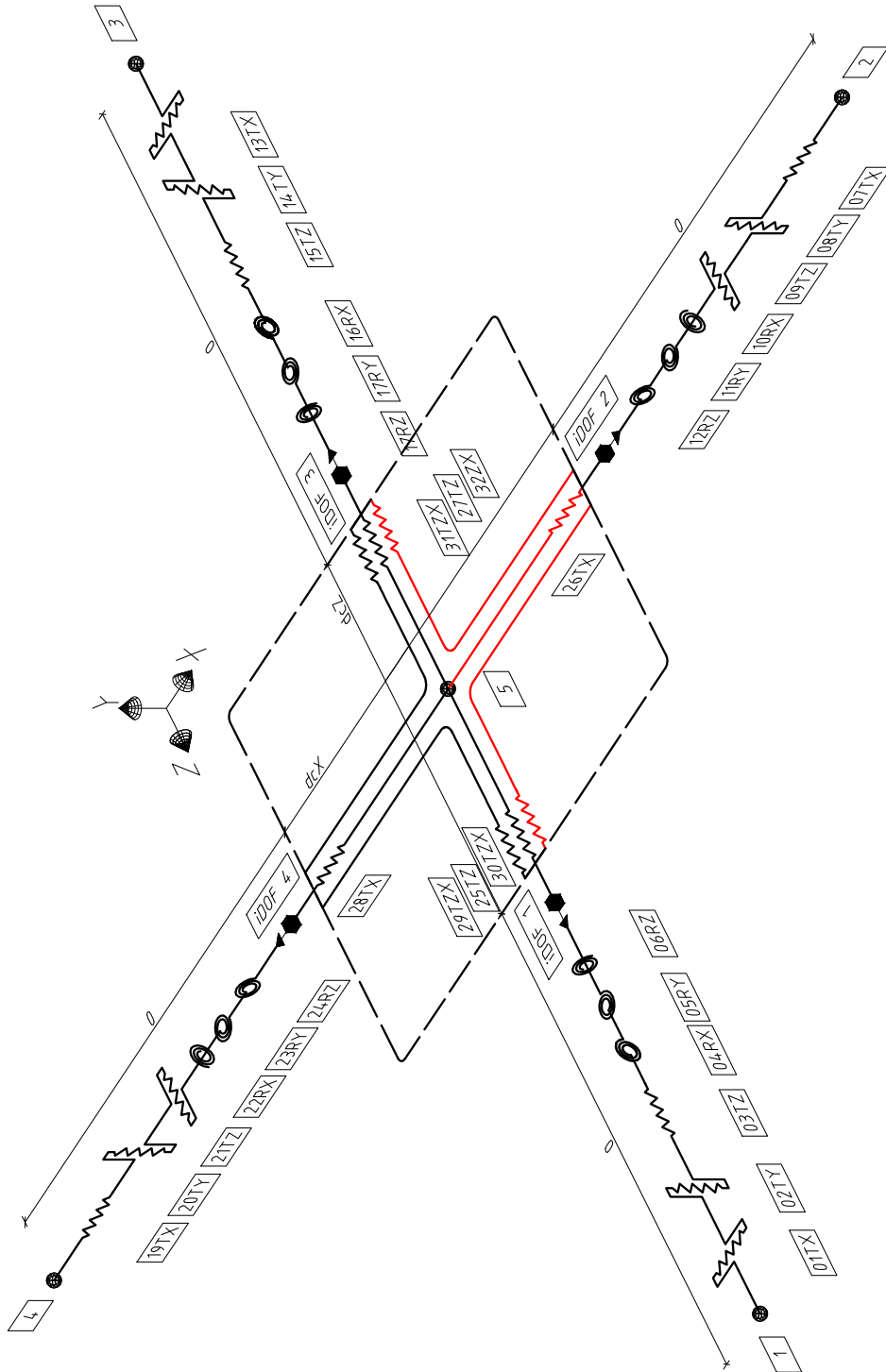


Figure 3.22: Components of the beam-to-column joint finite element: tube components for face 2.

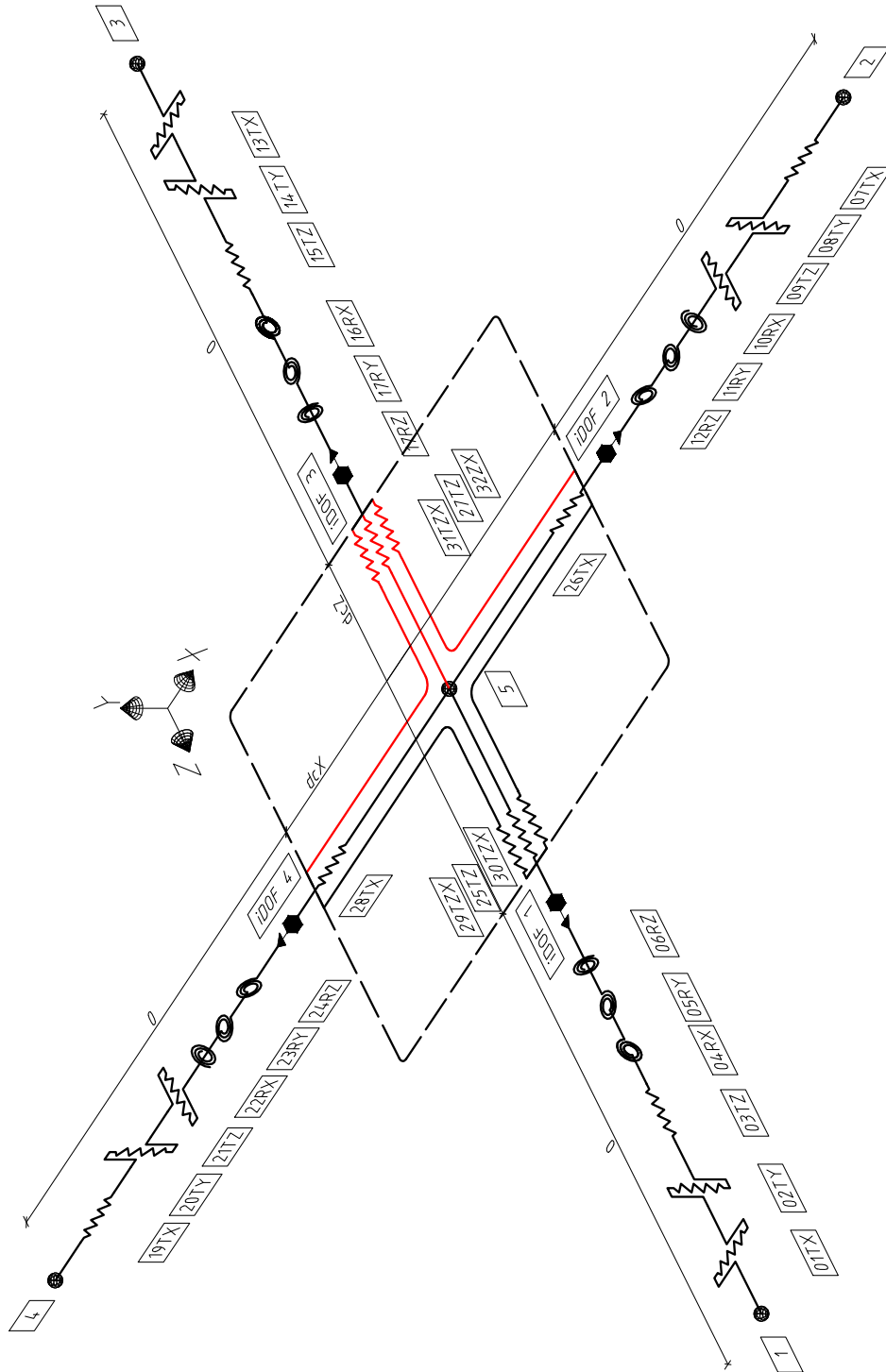


Figure 3.23: Components of the beam-to-column joint finite element: tube components for face 3.

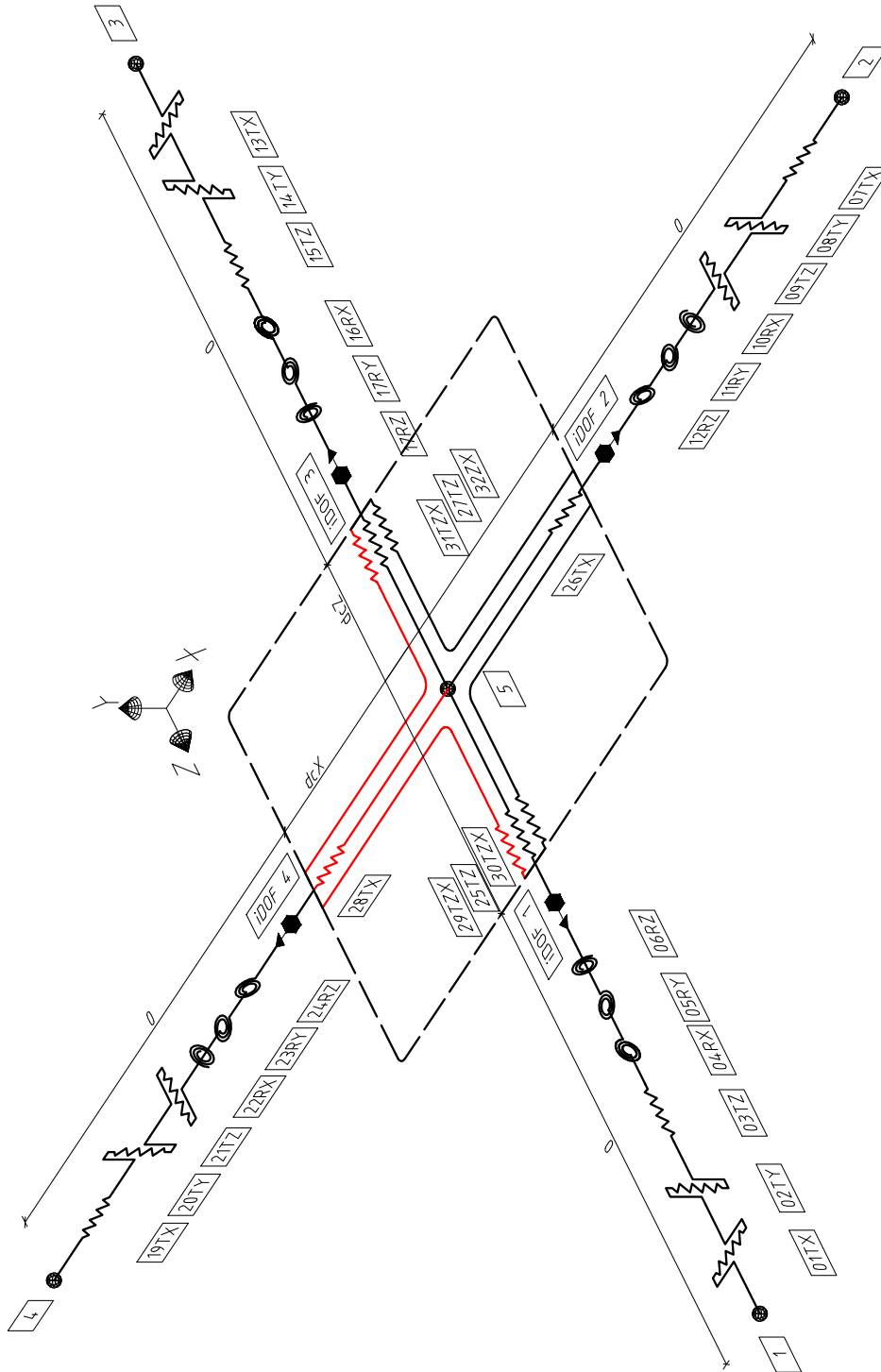


Figure 3.24: Components of the beam-to-column joint finite element: tube components for face 4.

3.4.2 Linear formulation

In the case of a first-order analysis with linear elastic behavior assigned to the beam-to-column joint components, the equilibrium relation between nodal forces and internal forces in the components can be expressed as:

$$\mathbf{f} = \mathbf{B} \mathbf{P} \quad (3.7)$$

where $\mathbf{f}(32 \times 1)$, $\mathbf{B}(32 \times 34)$, and $\mathbf{P}(34 \times 1)$ are the vector of internal forces in components, equilibrium matrix, and vector of nodal forces, respectively. Accordingly,

$$\mathbf{f} = \begin{bmatrix} f_1 & \dots & f_{32} \end{bmatrix}^T \quad (3.8)$$

where f_i is the internal force in component i , with

$$\mathbf{P} = \begin{bmatrix} P_{\text{ext}.1} & \dots & P_{\text{ext}.30} & P_{\text{int}.1} & \dots & P_{\text{int}.4} \end{bmatrix}^T \quad (3.9)$$

where $P_{\text{ext}.i}$ and $P_{\text{int}.j}$ are the nodal force in external DOF i and nodal force in internal DOF j , respectively.

The linearized compatibility relation between the deformations in the components and the nodal displacements can be expressed as:

$$\Delta = \mathbf{A} \mathbf{U} \quad (3.10)$$

where $\Delta(32 \times 1)$, $\mathbf{A}(32 \times 34)$, and $\mathbf{U}(34 \times 1)$ are the vector of deformation in components, compatibility matrix and vector of nodal displacements, respectively. Accordingly,

$$\Delta = \begin{bmatrix} \Delta_1 & \dots & \Delta_{32} \end{bmatrix}^T \quad (3.11)$$






$$\mathbf{U} = \begin{bmatrix} U_{\text{ext}.1} & \dots & U_{\text{ext}.30} & U_{\text{int}.1} & \dots & U_{\text{int}.4} \end{bmatrix}^T \quad (3.12)$$

where Δ_k is the deformation in component k , and $U_{\text{ext}.i}$ and $U_{\text{int}.j}$ are the generalised displacement in external DOF i , and the displacement in internal DOF j , respectively.

The elements, $a_{i,j}$, of the compatibility matrix, \mathbf{A} , are obtained using the procedure presented in Section 3.4.3.

To ease the reading and writing process of the present document, the elements, $a_{i,j}$, of the compatibility matrix, \mathbf{A} , are shown in a tabular form where only the non-zero elements are presented,

Table 3.6: The non-zero elements of the compatibility matrix \mathbf{A} .

Color	Value	Stiffness Coefficient
	1	$a_{1,1}; a_{2,2}; a_{3,3}; a_{5,5}; a_{6,6}; a_{7,7}; a_{9,9}; a_{10,10}; a_{11,11}; a_{12,12}; a_{16,16}; a_{20,20}; a_{8,26}; a_{13,25}; a_{14,26}; a_{16,28}; a_{17,29}; a_{18,30}; a_{21,27}; a_{22,28}; a_{23,29}; a_{24,30}; a_{15,33}; a_{19,34}; a_{25,31}; a_{26,32}; a_{27,27}; a_{28,25}; a_{29,25}; a_{31,25}; a_{31,27}; a_{32,27}; a_{29,31}; a_{32,32}$
	-1	$a_{4,4}; a_{8,8}; a_{13,13}; a_{14,14}; a_{15,15}; a_{17,17}; a_{18,18}; a_{19,19}; a_{21,21}; a_{22,22}; a_{23,23}; a_{24,24}; a_{1,25}; a_{2,26}; a_{4,28}; a_{5,29}; a_{6,30}; a_{9,27}; a_{10,28}; a_{11,29}; a_{12,30}; a_{20,26}; a_{25,27}; a_{26,25}; a_{3,31}; a_{7,32}; a_{29,27}; a_{30,25}; a_{30,27}; a_{32,25}; a_{27,33}; a_{28,34}; a_{29,34}; a_{31,33}; a_{31,34}; a_{32,33}$
	$0.5 dc_X$	$a_{8,30}; a_{9,29}; a_{20,30}; a_{21,29}$
	$0.5 dc_Z$	$a_{2,28}; a_{14,28}$
	$-0.5 dc_Z$	$a_{1,29}; a_{13,29}$

as seen in Tab. 3.6. Moreover, each non-zero value is assigned a distinct color to enhance visibility. A color map illustrating the assignment of colors within the compatibility matrix is presented in Fig. 3.25.

Finally, the internal forces in the components can be expressed by Eq. (3.13):

$$\mathbf{f} = \mathbf{k}_j \Delta \quad (3.13)$$

where $\mathbf{k}_j(32 \times 32)$ is a diagonal matrix, and its elements represent the stiffness of the components, $k_{i,i} = k_{\text{comp},j}$.

In the scope of small deformations, the dual relation between compatibility and equilibrium leads to the following:

$$\mathbf{P} = \mathbf{A}^T \mathbf{f} \quad (3.14)$$

By introducing Eq. (3.10) and Eq. (3.13) into Eq. (3.14), the vector of external forces can be expressed as:

$$\mathbf{P} = \mathbf{A}^T \mathbf{k}_j \mathbf{A} \mathbf{U} = \mathbf{K}_j \mathbf{U} \quad (3.15)$$

from which the stiffness matrix of the beam-to-column joint finite element, $\mathbf{K}_j(34 \times 34)$, is obtained:

$$\mathbf{K}_j = \mathbf{A}^T \mathbf{k} \mathbf{A} \quad (3.16)$$

Knowing that no external forces will be considered in the internal DOFs, the stiffness matrix \mathbf{K}_j can be statically condensed to be expressed explicitly in terms of external DOFs. Thus, the vector of

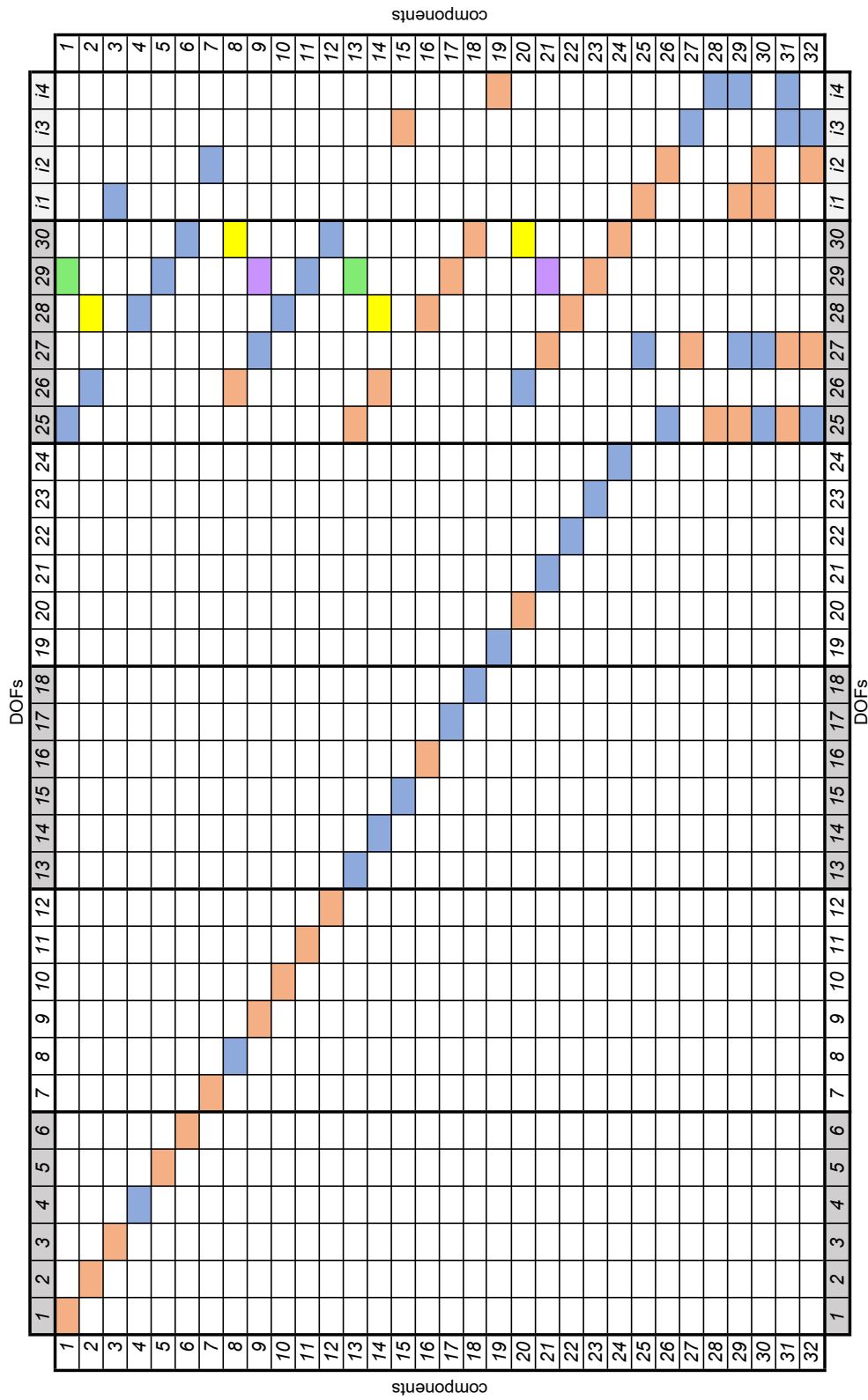


Figure 3.25: Compatibility matrix elements color-coded by values.

Table 3.7: Steps to calculate elements $a_{i,j}$ of \mathbf{A} .

Step no.	Step description
1	select a DOF for which to calculate the deformation in the springs: i ;
2	impose a unit displacement on the selected DOF, while the other DOFs are blocked: $U_i = 1$ with $U_j = 0$;
3	determine the deformations in components: Δ_i ;
4	assign that deformation to the corresponding row and column in the compatibility matrix: $a_{i,j} = \Delta_i$.

nodal forces (Eq. (3.9)) and the vector of nodal displacements (Eq. (3.12)) are split into 2 sub-vectors, as follows:

$$\mathbf{P} = \begin{bmatrix} \mathbf{P}_{\text{ext}} & \mathbf{P}_{\text{int}} \end{bmatrix}^T \quad (3.17)$$

$$\mathbf{U} = \begin{bmatrix} \mathbf{U}_{\text{ext}} & \mathbf{U}_{\text{int}} \end{bmatrix}^T \quad (3.18)$$

where \mathbf{P}_{ext} and \mathbf{U}_{ext} are (30×1) , while \mathbf{P}_{int} and \mathbf{U}_{int} are (4×1) .

Thus, Eq. (3.15) yields into:

$$\mathbf{K}_j \mathbf{U} = \begin{bmatrix} \mathbf{K}_{\text{ext}} & \mathbf{K}_{\text{ie}} \\ \mathbf{K}_{\text{ei}} & \mathbf{K}_{\text{int}} \end{bmatrix} \begin{bmatrix} \mathbf{U}_{\text{ext}} \\ \mathbf{U}_{\text{int}} \end{bmatrix} \quad (3.19)$$

where \mathbf{K}_{ext} is (30×30) , \mathbf{K}_{int} is (4×4) , \mathbf{K}_{ie} is (30×4) and \mathbf{K}_{ei} is (4×30) , from which the condensed stiffness matrix, $\mathbf{K}_j^{\text{cond}}$ (30×30), is derived:

$$\mathbf{K}_j^{\text{cond}} = \mathbf{K}_{\text{ext}} - \mathbf{K}_{\text{ie}} (\mathbf{K}_{\text{int}})^{-1} \mathbf{K}_{\text{ei}} \quad (3.20)$$

3.4.3 Compatibility matrix's elements computation

The determination of the correct compatibility matrix, \mathbf{A} , is both a fundamental step and starting point in the implementation of the new joint element presented in this document. Although at first look, it might seem like a tedious process, in fact, it is a straightforward process that requires the application of the four steps mentioned in Tab. 3.7.

An exemplification of the computation of component deformation caused by a unit load in DOF 2 is provided in Tab. 3.8, while Fig. 3.26 visually represents the resulting deformed components.

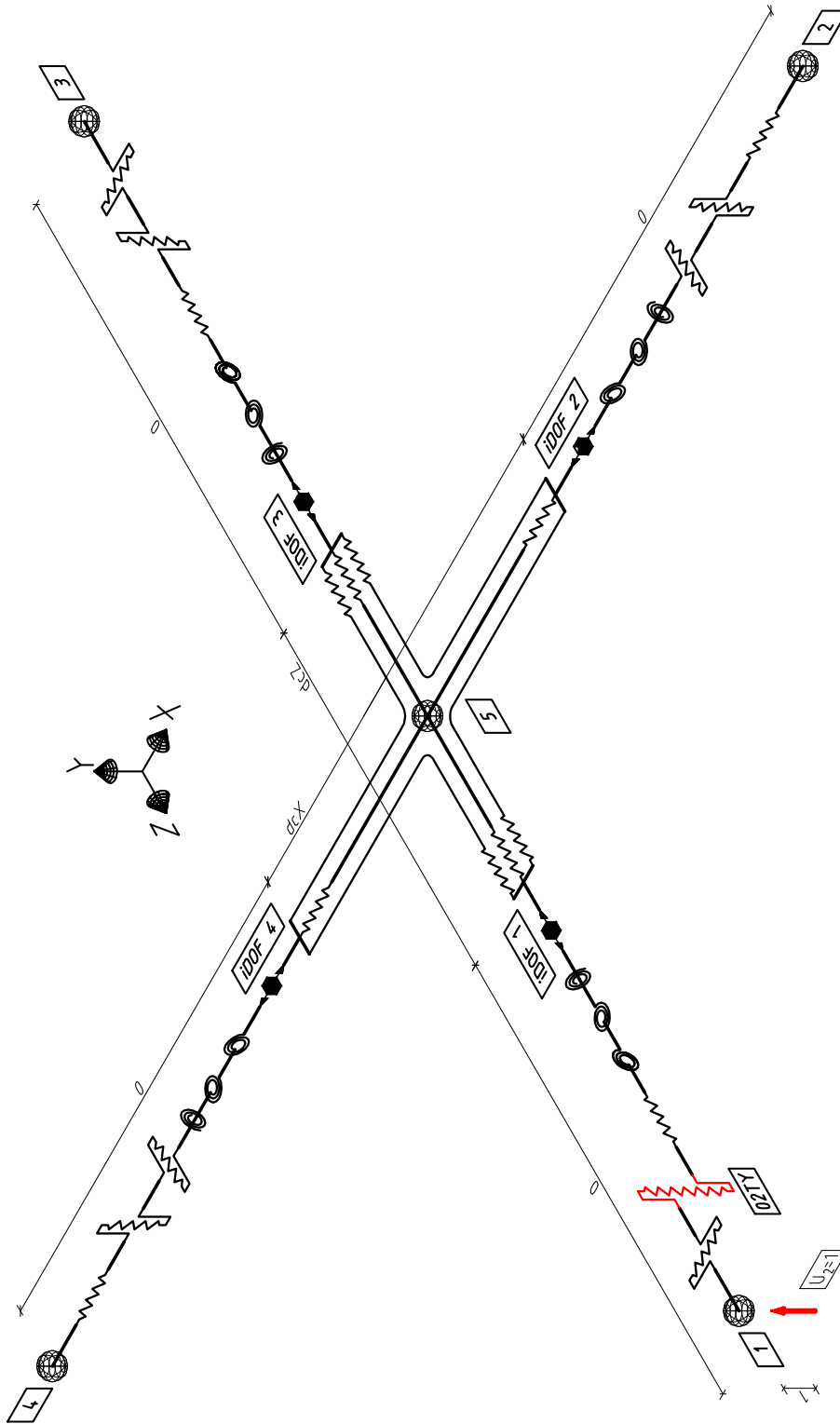


Figure 3.26: Compatibility matrix: element $a_{(2,2)}$ after load application $U_2 = 1$.

Table 3.8: Worked example for DOF 2.

Step no.	Step description
1	select a DOF: $i = 2$;
2	impose a unit displacement on the selected DOF, while the other DOFs are blocked: $U_2 = 1$ with $U_1 = U_3 = U_4 = \dots = U_{34} = 0$
3	determine the deformations in components: $\Delta_2 = 1$;
4	assign that deformation to the corresponding row and column in the compatibility matrix: $a_{2,2} = \Delta_2 = 1$;

Chapter 4

Implementation of the macro-element in OpenSees

4.1 Inno3DPnPJoint Class

The proposed beam-to-column joint finite element's formulation is introduced in the framework of OpenSees as the Inno3DPnPJoint Class, which is a child of the base abstract Element class, as shown in Fig. 4.1. The Element Class consists of several virtual methods defined by the children of the class. These methods dynamically allocate and deallocate memory for an instance of the class, initialize an instance of the class, perform inquiry and access tasks, and generate and return an element tangent matrix and residual vector.

The proposed beam-to-column joint finite element requires an internal solution to determine the internal nodal displacements that satisfy the internal equilibrium of the element. The methods comprising the Inno3DPnPJoint Class are listed in Tab. 4.1 and are adapted from [181]

The order in which the methods are executed for a linear elastic analysis is presented in Fig. 4.2. The flowchart expands both vertically and horizontally. The former represents the move to a new step (i.e., execution of a new method), while the latter implies that in the current step, a method calls another method (i.e., function in function call).

The programming language used to code the proposed beam-to-column joint is C++ [157]. The integrated development environment used to compile the OpenSees source code is Microsoft VisualStudio 2019 ([202]).

For the development of the beam-to-column joint finite element, two files were coded, namely the header file (*.h) and the main (implementation) file (*.cpp). The former defines the interface and

Chapter 4. Implementation of the macro-element in OpenSees

variables for the new class that should be a subclass of the Element class, while the latter explains in detail what the constructors, destructor, and the other methods do.

The presence of the internal DOFs in the proposed model and the nonlinear behavior of the components enforce an internal iteration scheme that needs to be implemented at compilation time (i.e., not at run time).

Table 4.1: Methods Comprising the Inno3DPnPJoint Class.

Method Name	Description
<i>Constructor</i>	
Public: Inno3DPnPJoint(...)	Initializes an object of the class.
<i>Destructor</i>	
Public: Inno3DPnPJoint()	Performs dynamic storage deallocation.
<i>Inquiry and Access Methods</i>	
Public: virtual int getNumExternalNodes()	Returns the number of external nodes of the element.
Public: virtual const ID &getExternalNodes()	Returns pointers to the specified node tags.
Public: virtual getNodePtrs()	Returns pointers to pointers to the specified node tags.
Public: virtual int getNumDOF()	Returns the number of DOFs of the element.
Public: virtual void setDomain()	Required for checking the DOFs and associativity with the node.
Public: virtual const Matrix &getTangentStiff()	Returns the local stiffness matrix of the element at the global assembly stage for all the elements.
Public: virtual getInitialStiff()	Returns the local stiffness matrix of the element at the global assembly stage for all the elements.
Public: virtual const Vector &getResistingForce()	Returns the local residual force vector at the stage of global assembly.
Public: virtual int getResponse(...)	Returns element-specific responses.
Public: virtual setResponse(...)	Contains the valid output(s) for the element.

Continued on next page

Table 4.1: Methods Comprising the Inno3DPnPJoint Class (*continued*).

Method Name	Description
Public: virtual void Print(...)	Prints out element data.
Public: virtual int displaySelf()	Displays element graphically.
<i>Element Solution Methods</i>	
Private: void getGlobalDispls(...)	Returns a set of converged displacements for the five nodes of the element.
Private: void getBCJoint()	Returns the compatibility matrix.
Private: void getdDef_du()	Extracts from the compatibility matrix the rows and columns related to internal DOFs.
Private: void getdg_df()	Transposes the dDef_du matrix.
Private: void matDiag(...)	Takes as input the vector containing the stiffness of the components and converts it to a diagonal matrix of components.
Private: void getMatResponse(...)	Takes as input the displacements and returns the tangent and residual forces based on the material specified by the user.
Private: void formR(...)	Forms the local residual force vector of the element.
Private: void formK(...)	Forms the local stiffness matrix of the element.
Private: void formTransfMat()	Forms the transformation matrix used to transform from global to local coordinates.
Private: double getStepSize(...)	Improves the robustness of the element by determining the step size for line search in case of convergence issues with the internal equilibrium
Public: virtual int commitState()	Commits displacement at each node after meeting the internal equilibrium criterion for the element.
Public: virtual int revertToLastCommit()	Returns to the last committed state if the analysis fails.

Continued on next page

Table 4.1: Methods Comprising the Inno3DPnPJoint Class (continued).

Method Name	Description
Public: virtual int revertToStart()	Returns to the start if the analysis fails.
Public: virtual int update()	Updates the displacements at the external nodes of the element.

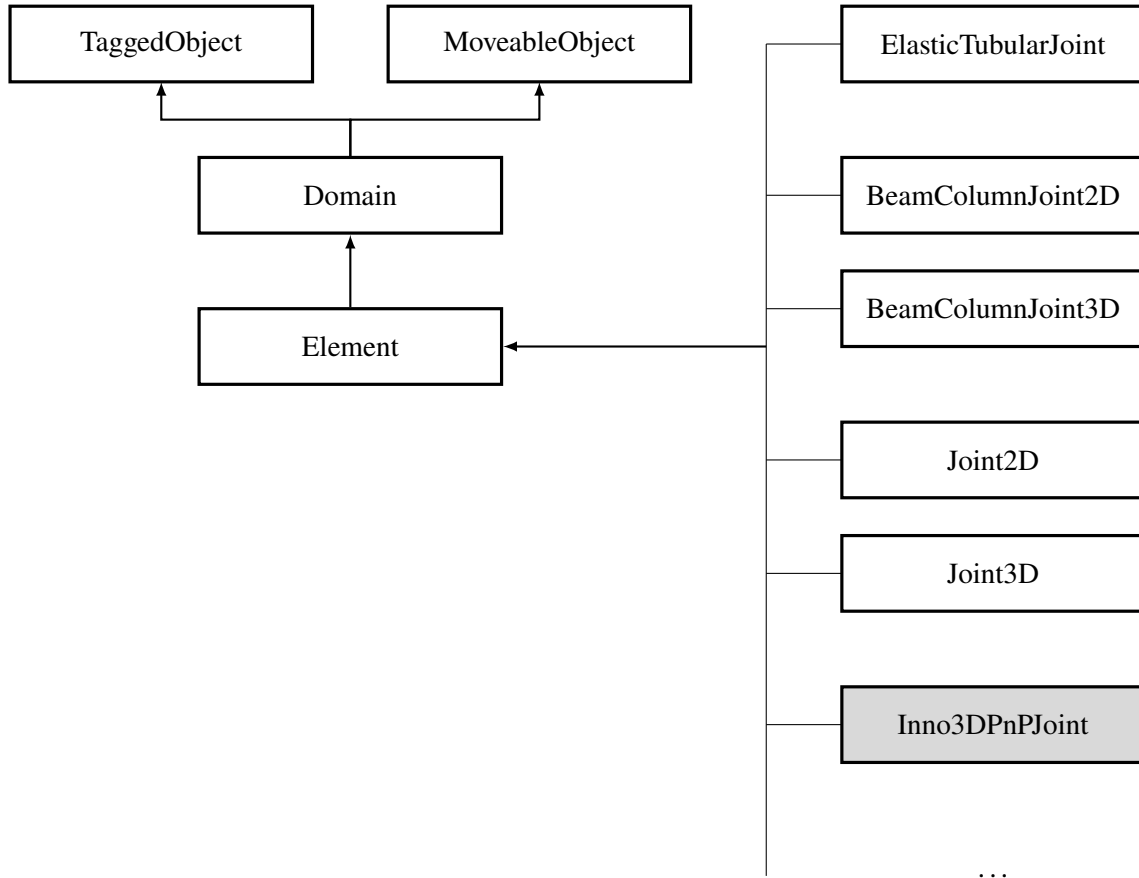


Figure 4.1: Class diagram of the beam-to-column joint finite elements library of OpenSees.

4.2 Transformation matrix

The Inno3DPnPJoint element, although a 3D element, has coordinates that form a 2D plane in 3D space. The requirements for the node coordinates of the finite element are outlined in Section 4.4.4. Additionally, the joint element adheres to the local sign convention presented in Section 3.4.1.

The Inno3DPnPJoint element is intended to facilitate the everyday design of 3D structures rather than serving as a tool exclusively for research purposes. Accordingly, any limitations on the definition of the joint element’s coordinates were eliminated by the incorporation of a transformation matrix into

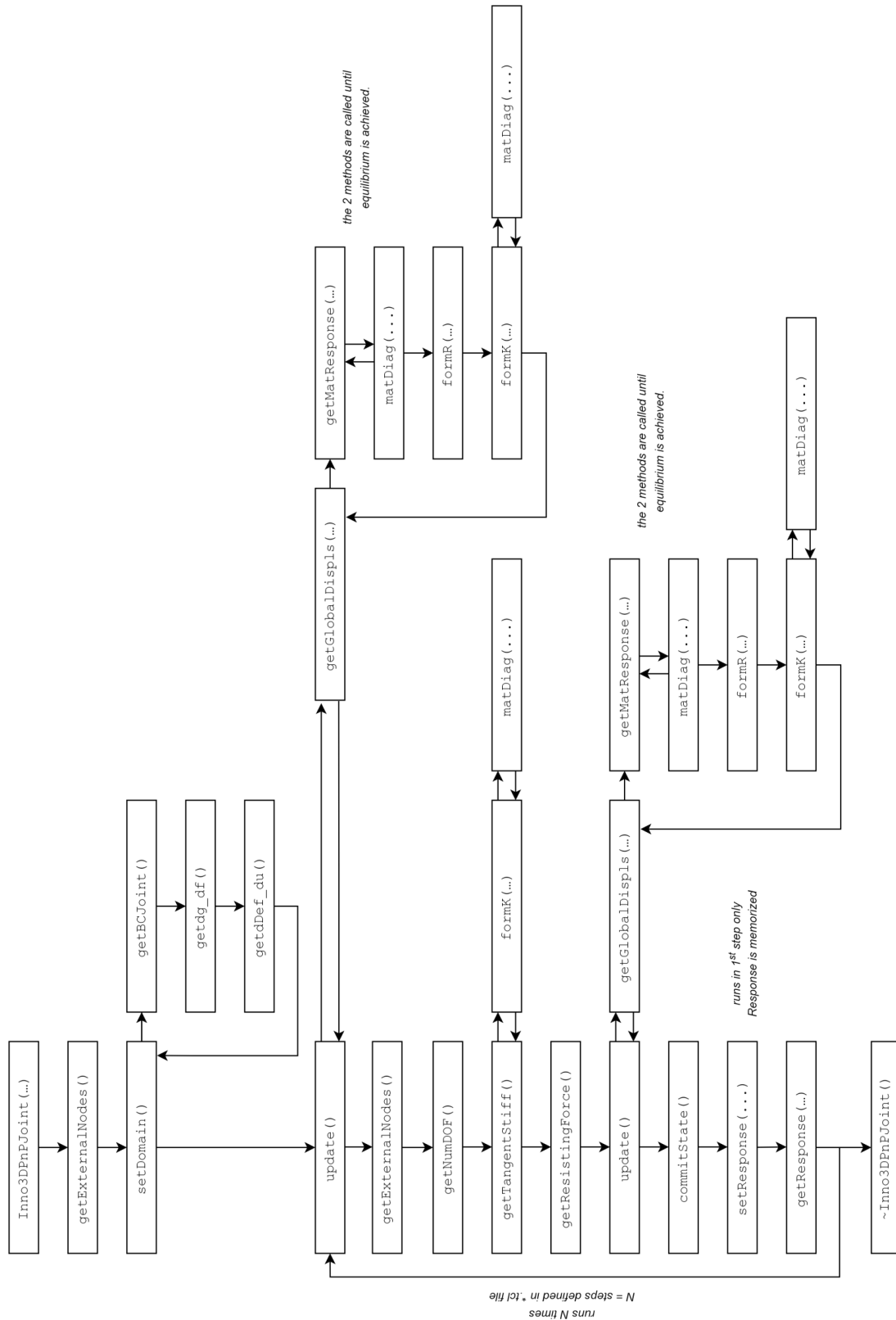


Figure 4.2: Code execution sequence for linear elastic analysis.

the code via the `formTransfMat()` method (Tab. 4.1). This method removes any restrictions related to coordinates or signs, enabling the user to specify the joint element's position in 3D space as desired.

The transformation matrix, **Transf**(30×30), is derived from the vectors containing the coordinates for nodes 1 and 2 (Fig. 3.13), and the coordinates of their cross-product. First, verification is conducted to ensure that the norms of these three vectors are non-zero. Then, a transformation sub-matrix, **Tran**(3×3), is constructed by dividing the coordinates of the three vectors by their norms. Finally, the transformation matrix, **Transf**, is obtained by assembling the sub-matrix, **Tran**, diagonally ten times.

The transformation matrix, **Transf**, is utilized in the following methods:

- `getGlobalDispls(...)` – in the OpenSees input file (i.e., **.tcl* or **.py*), the joint element is defined in the global coordinate system, therefore the coordinates of the five nodes defining the joint element are transformed into the local coordinate system;
- `formR(...)` – the local residual force vector, **R** (34×1), of the element, contains the values related to both the external and internal DOFs, thus, the ones associated with the external DOFs are transformed back, from the local to the global coordinate system;
- `formK(...)` – the condensed local stiffness matrix, **K**, of the element, is transformed from the local to the global coordinate system;
- `getResponse(...)` – the committed displacements associated with the external DOFs are transformed back from the local to the global coordinate system.

4.3 Nonlinear formulation

For the nonlinear analysis, due to the internal DOFs, the proposed beam-to-column joint finite element requires a procedure to determine the internal nodal displacement that satisfies the internal equilibrium of the element for each iteration of the global solution algorithm.

The approach followed by the proposed joint model is a classical Newton-Raphson iteration scheme, which is found in other joint elements of the software's library, such as the `BeamColumJoint` [181].

According to this scheme, the internal node displacements, $\mathbf{u}_{int,t}$, at iteration t associated with the imposed external node displacements, $\mathbf{u}_{ext,t}$, is computed starting from the internal node displacements at iteration $t - 1$ and the material responses of the components according to the following procedure:

1. computation of the first initial trial value of the deformation of each component:

$$\Delta = \mathbf{A} \begin{bmatrix} \mathbf{u}_{\text{ext},t} & \mathbf{u}_{\text{int},t-1} \end{bmatrix}^T \quad (4.1)$$

where $\mathbf{u}_{\text{ext},t}$ and $\mathbf{u}_{\text{int},t-1}$ represent the vectors of displacements of the external and internal nodes, respectively, while Δ and \mathbf{A} are the vector of deformation in the components and compatibility matrix;

2. computation of the internal forces. f_i . and the tangent stiffness. k_i . of the components for Δ , where $i = [1,32]$;

3. computation of the unbalanced nodal forces in the internal nodes \mathbf{P}_{int} :

$$\mathbf{P}_{\text{int}} = \tilde{\mathbf{A}}^T \mathbf{f} \quad (4.2)$$

where \mathbf{f} and \mathbf{P}_{int} stand for the vectors of internal forces in the components and vectors of unbalanced forces in the internal nodes, respectively, and $\tilde{\mathbf{A}}^T$ is the sub-matrix of the compatibility matrix, \mathbf{A} , containing the last four columns (and 32 rows) corresponding to the internal DOFs;

4. iterative internal cycles until the unbalanced forces are small enough (i -th iteration):

- (a) check for convergence:

$$\mathbf{P}_{\text{int}}^i \left((\mathbf{P}_{\text{int}}^i)^T < \text{tolerance} \rightarrow \text{convergence} \rightarrow \text{STOP} \right) \quad (4.3)$$

- (b) computation of the internal node displacements making use of the Newton-Raphson iteration formula:

$$\mathbf{u}_{\text{int}}^{i+1} = \mathbf{u}_{\text{int}}^i - \left(\tilde{\mathbf{A}}^T \mathbf{k} \tilde{\mathbf{A}} \right)^{-1} \mathbf{P}_{\text{int}}^i \quad (4.4)$$

with \mathbf{k} is a diagonal matrix of the components with $k(j, j) = k_{\text{comp},j}$;

- (c) computation of the deformations of the components:

$$\Delta^{i+1} = \mathbf{A} \begin{bmatrix} \mathbf{u}_{\text{ext},t} & \mathbf{u}_{\text{int}}^{i+1} \end{bmatrix}^T \quad (4.5)$$

- (d) computation of the internal forces and the tangent stiffness of the components for Δ^{i+1} ;

(e) computation of the unbalanced nodal forces in the internal nodes:

$$\mathbf{P}_{\text{int}}^{i+1} = \widetilde{\mathbf{A}}^T \mathbf{f} \quad (4.6)$$

(f) move to next iteration $i = i + 1$.

To guarantee convergence of the element for any imposed external nodal displacements, the robustness of the internal solution algorithm was improved. As suggested by Lowes et al. [181], the following modifications were applied with varying degrees of effectiveness:

- modification of the classical Newton-Raphson solution algorithm to include a line-search [203];
- implementation of the classical Modified Newton-Raphson solution algorithm;
- discretization of the imposed external nodal displacement increment to enable internal solution at discrete points along the global solution path.

4.4 Inno3DPnPJoint user manual

4.4.1 Element info

The Inno3DPnPJoint element can be viewed as a 2D plate in a 3D space defined by five external nodes (Fig. 3.14), each having six DOFs. This element configuration is suitable for rectangular and square cross-sections. Furthermore, it allows for the simulation of all types of joints: central, edge, and corner, with some nodes potentially not being connected to any truss-girder or column 1D elements.

4.4.2 Element source code

The Inno3DPnPJoint beam-to-column joint element's C++ source code is available on the OpenSees GitHub repository [204]. Due to the substantial length and the inherent challenges of reading code on paper, particularly when it involves significant indentation, the code is not included in this document. Furthermore, the availability of the code on the GitHub repository allows for modifications to be made by interested parties.

4.4.3 Command line and input arguments

The Inno3DPnPJoint element can be constructed using the command input lines given below with the input arguments listed in Tab. 4.2.

Table 4.2: Input arguments for Inno3DPnPJoint joint finite element.

input \$arg	Description
\$eleTag	An integer tag identifying the element in the domain
\$Node1	An integer tag indicating the node 1
...	
\$Node5	An integer tag indicating the node 5
\$SprMatTag01	An integer tag indicating the uniaxial materials for component 1
...	
\$SprMatTag32	An integer tag indicating the uniaxial materials for component 32

- input line for Tcl (*.tcl) files:

```
element Inno3DPnPJoint $eleTag <$Node1 $Node2 $Node3 $Node4 $Node5>
<$SprMatTag01 ... $SprMatTag32>
```

cmd Example:

```
element Inno3DPnPJoint 99 101 102 103 104 105 1 2 3 4 5 6 7 8 9 10 11 12 13 14 15
16 17 18 19 20 21 22 23 24 25 26 27 28 29 30 31 32

# constructs an Inno3DPnPJoint joint element with element tag 99, that is connected to
nodes 101, 102, 103, 104 and 105 and uses for the components' behaviour the uniaxial
material object tags from 1 to 32.
```

- input line for Python (*.py) files:

```
element('Inno3DPnPJoint', $eleTag, <$eleNode1, $eleNode2, $eleNode3,
$eleNode4>, <$SprMatTag01, ..., $SprMatTag32>)
```

4.4.4 Node definition requirements

The nodes of the element must be defined in a specific order and have coordinates that meet the requirements of coplanarity, perpendicularity, collinearity, centrality, and dimensionality to successfully create the beam-to-column joint finite element. These requirements ensure that the coordinates of the five nodes given as input by the user create a 2D plane in 3D space. These checks can be found in the `setDomain` method (Tab. 4.1).

4.4.4.1 Input Order

The nodes should be defined in a counterclockwise direction. For example, if the element is created in the X-Z plane, the node's input order should be as follows: 1 / bottom, 2 / right, 3 / top, 4 / left, and 5 / center, as shown in Fig. 3.13. However, the joint can be defined in any plane if the node order definition is adapted accordingly.

4.4.4.2 Coplanarity

All nodes should lie in the same plane.

4.4.4.2.1 Verification overview

The equation of the plane passing through nodes 1, 2, and 3 is calculated to ensure that the nodes lie in the same plane. Then, a check is performed to see if nodes 4 and 5 satisfy this equation. If the condition is met, all five nodes are coplanar, and the analysis continues. Conversely, the analysis exits and displays this error message:

ERROR: Inno3DPnPJoint::setDomain – Node 4 does NOT belong to plane created by Node 1, Node 2 and Node 3. Check node coordinate definition.

or

ERROR: Inno3DPnPJoint::setDomain – Node 5 does NOT belong to plane created by Node 1, Node 2 and Node 3. Check node coordinate definition.

4.4.4.2.2 Mathematical description

In a 3D space, a 2D plane can be defined by a point and a vector perpendicular to the plane. The equation representing the plane is given as follows:

$$ax + by + cz + d = 0 \tag{4.7}$$

with $d = -(ax_0 + by_0 + cz_0)$, where (x_0, y_0, z_0) and (a, b, c) represent the coordinates of any point on the plane and the components of the normal vector, \vec{n} , to the plane, respectively.

In a 3D space, a 2D plane is determined by two linearly independent vectors. The cross-product of these vectors is an orthogonal vector to the plane, and any vector orthogonal to this cross-product lies in the plane.

Given the coordinates $N_1 = (x_1, y_1, z_1)$, $N_2 = (x_2, y_2, z_2)$ and $N_3 = (x_3, y_3, z_3)$ for nodes 1, 2, and 3 respectively, the cross-product of the linearly independent vectors resulting from these nodes is expressed as:

$$\begin{aligned}\vec{N}_{21} &= N_2 - N_1 = (x_2 - x_1, y_2 - y_1, z_2 - z_1) = (a_1, b_1, c_1) \\ \vec{N}_{31} &= N_3 - N_1 = (x_3 - x_1, y_3 - y_1, z_3 - z_1) = (a_2, b_2, c_2)\end{aligned}\tag{4.8}$$

Thus, their cross-product, \vec{n} , is expressed as:

$$\begin{aligned}\vec{n} = \vec{N}_{21} \times \vec{N}_{31} &= \begin{vmatrix} a_1 & b_1 & c_1 \\ a_2 & b_2 & c_2 \\ \hat{\mathbf{i}} & \hat{\mathbf{j}} & \hat{\mathbf{k}} \end{vmatrix} = (b_1c_2 - c_1b_2)\hat{\mathbf{i}} + (a_2c_1 - c_2a_1)\hat{\mathbf{j}} + (a_1b_2 - b_1a_2)\hat{\mathbf{k}} \\ &= a\hat{\mathbf{i}} + b\hat{\mathbf{j}} + c\hat{\mathbf{k}}\end{aligned}\tag{4.9}$$

To determine if a node with coordinates (x, y, z) (such as nodes 4 and 5) lies in the plane defined by nodes 1, 2, and 3, the components of the normal vector $\vec{n} = (a, b, c)$ (Eq. (4.9)) and the coordinates of a node on the plane (such as nodes 1, 2 or 3) must be introduced into Eq. (4.7).

Depending on the input values, the equation of the plane (Eq. (4.7)) may not always equal 0. To prevent software failure, an error variable $errorDomain = 1e - 2$ is defined.

4.4.4.3 Perpendicularity

It is mathematically necessary for the vector, represented by the ordered node sequence (1, 5, 3), to be perpendicular to the vector represented by the ordered node sequence (2, 5, 4).

4.4.4.3.1 Verification overview

If the coplanarity requirement is fulfilled, the dot product of the vectors between nodes 1 and 3 and nodes 2 and 4 is calculated. If the result is 0, the two vectors are perpendicular, so the condition is satisfied, and the analysis continues. Conversely, the analysis exits and displays this error message:

ERROR: Inno3DPnPJoint::setDomain – vector of Node 1 & Node 3 not perpendicular to vector of Node 2 & Node 4. Check node coordinate definition.

4.4.4.3.2 Mathematical description

In the realm of algebra, the dot product can be defined as the algebraic summation of the product of corresponding entries of two vector sequences. In this particular case, the vectors in question are represented by \vec{N}_{13} and \vec{N}_{24} , which are comprised of sequences of node coordinates as detailed in Eq. (4.10). The dot product of these vectors is given by Eq. (4.11).

$$\begin{aligned}\vec{N}_{13} &= N_1 - N_3 = (x_1 - x_3, y_1 - y_3, z_1 - z_3) \\ \vec{N}_{24} &= N_2 - N_4 = (x_2 - x_4, y_2 - y_4, z_2 - z_4)\end{aligned}\tag{4.10}$$

$$\vec{N}_{13} \cdot \vec{N}_{24} = \sum_{i=1}^3 \vec{N}_{13}(i) \vec{N}_{24}(i) = 0\tag{4.11}$$

4.4.4.4 Collinearity

The ordered node sequences ((1, 5), (5, 3)) and ((2, 5), (5, 4)) must be collinear to ensure the correct transmission of forces between the components.

4.4.4.4.1 Verification overview

The ordered node sequences of ((1, 5), (5, 3)) and ((2, 5), (5, 4)) must exhibit collinearity to facilitate the computation of cross-products between the center node (node 5) and the edge nodes (nodes 1, 2, 3, and 4). If the cross-product result is equal to zero, it can be concluded that the node sequences are collinear, and the analysis continues. Conversely, the analysis exits and displays this error message:

ERROR: Inno3DPnPJoint::setDomain – Node 1, Node 5 and Node 3 are not collinear.
Check node coordinate definition.

or

ERROR: Inno3DPnPJoint::setDomain – Node 2, Node 5 and Node 4 are not collinear.
Check node coordinate definition.

4.4.4.4.2 Mathematical description

From a mathematical standpoint, if the cross-product of two vectors is equal to zero, the vectors are either parallel to each other, or the angle between them is equal to 0 degrees or 180 degrees. Based on previous assessments, it can be deduced that the angle between the vectors in question is 180 degrees,

thus implying that the nodes are collinear. These vectors are represented by \vec{N}_{51} , \vec{N}_{52} , \vec{N}_{53} , and \vec{N}_{54} , as detailed in Eq. (4.12).

$$\begin{aligned}\vec{N}_{51} &= N_5 - N_1 = (x_5 - x_1, y_5 - y_1, z_5 - z_1) \\ \vec{N}_{52} &= N_5 - N_2 = (x_5 - x_2, y_5 - y_2, z_5 - z_2) \\ \vec{N}_{53} &= N_5 - N_3 = (x_5 - x_3, y_5 - y_3, z_5 - z_3) \\ \vec{N}_{54} &= N_5 - N_4 = (x_5 - x_4, y_5 - y_4, z_5 - z_4)\end{aligned}\tag{4.12}$$

The cross-product, assumed to be zero to meet the requirement of collinearity, is mathematically represented by Eq. (4.13).

$$\begin{aligned}\vec{N}_{153} &= \vec{N}_{51} \times \vec{N}_{53} = 0 \\ \vec{N}_{254} &= \vec{N}_{52} \times \vec{N}_{54} = 0\end{aligned}\tag{4.13}$$

4.4.4.5 Centrality and dimensionality

The edge nodes should be positioned at the center of each column face, so that the norms of the four vectors resulting from the collinearity check can be calculated and compared. There are three potential outcomes of this comparison: (i) if all norms are equal, it indicates that the tube is square, (ii) if two pairs of equal norms are obtained, it suggests that the tube is rectangular, and (iii) if neither of these conditions are met, the analysis exits and displays an error message:

ERROR: Inno3DPnPJoint::setDomain – nodes are not located at the center of the column face. Check node coordinate definition.

Moreover, to prevent division by zero, the dimensions of the joint must be large enough and the norms of the four vectors should be greater than a pre-defined value of $1e-3$. If this criterion is satisfied, the analysis continues. Conversely, the analysis exits and displays this error message:

ERROR: Inno3DPnPJoint::setDomain – length or width $\leq 1e-3$, division by zero occurs. Increase joint size.

4.4.5 Common error messages

In addition to the previously mentioned errors, various error messages may arise for different reasons. However, a summary of the most common ones is presented in Tab. 4.3.

Table 4.3: Common errors.

Description	Displayed error message
number of input arguments is wrong (i.e., different than 38)	WARNING error insufficient. arguments. Want: element Inno3DPnPJoint eleTag? Node1? Node2? Node3? Node4? Node5? Spring01? Spring02? ... Spring32?.
number of external nodes is wrong (i.e., different than 5)	ERROR: Inno3DPnPJoint::Inno3DPnPJoint() eleTag failed to create an ID of size 5.
constructor fails to get copy of material and/or the copy is not valid	ERROR: Inno3DPnPJoint::Constructor failed to get a copy of material matTag.
constructor fails to set pointer to external nodes	ERROR: Inno3DPnPJoint::setDomain. Node pointer is NULL. Node nodeTag does not exit in the domain.
the domain is null	ERROR: Inno3DPnPJoint::setDomain – Domain is null.
number of DOFs is wrong (i.e., different than 6)	ERROR: Inno3DPnPJoint::setDomain – number of DOF associated with the nodes is incorrect.
number of spring requested as output is out of range (1-32)	ERROR: Inno3DPnPJoint::setResponse number of springs out of range: springNo. Spring numbers go from 1 to 32.

4.4.6 Output recorders

The simulation results of the Inno3DPnP beam-to-column joint finite element can be analyzed by defining output records at both the element and component levels.

4.4.6.1 Element level

The outputs at the element level can be requested using the following recorder commands:

- input line for Tcl (*.tcl) files:

```
recorder Element <-file $fileName> <-time> <-ele $eleTag> $arg
```

- input line for Python (*.py) files:

```
recorder('Element', '-file', 'fileName', '-time', '-ele', 'eleTag', '$arg')
```

The list of valid inputs for the argument, \$arg, at the element level, is given by Tab. 4.4.

4.4.6.2 Component level

The outputs at the component level can be requested using the following recorder commands:

Table 4.4: Valid \$arg – at element level.

\$arg	C++ Output Variable		Description
	Name	Size	
extDisp extdisp	UeprCommit_G	30x1	Returns the displacement for the external DOFs.
intDisp intdisp	UeprIntCommit	4x1	Returns the displacement for the internal DOFs.
Disp disp	UeprCommit_G & UeprIntCommit	34x1	Returns the displacement for the external and internal DOFs.
Reaction reaction	R	34x1	Returns the global residual forces for all DOFs.
matStress matstress Stress stress	MaterialPtr->getStress()	32x1	Returns the stress values from the joint components.
matStrain matstrain Strain strain	MaterialPtr->getStrain()	32x1	Returns the strain values from the joint components.
matStressStrain matstressstrain StressStrain stressStrain	MaterialPtr->getStress() MaterialPtr->getStrain()	64x1	Returns the stress and strain values from the joint components.

Table 4.5: Valid \$arg – at component level.

\$arg	C++ Output Variable		Description
	Name	Size	
spring			
-spring material	MaterialPtr[springNo]	1x2	Returns a pair of stress-strain for each time step.
-material			

- input line for Tcl (*.tcl) files:

```
recorder Element <-file $fileName> <-time> <-ele $eleTag> <$arg $sprNo
stressStrain>
```

- input line for Python (*.py) files:

```
recorder('Element', '-file', 'fileName', '-time', '-ele', 'eleTag', '$arg', 'sprNo',
'stressStrain')
```

The list of valid inputs for the argument, \$arg, at component level, is given by Tab. 4.5.

The previous Tcl command only displays the results for a single component; therefore, it must be repeated for each component of interest. A more efficient approach would be to incorporate the command into a loop statement, as demonstrated by the following code sequence using a for-loop:

```

1 # The following code constructs an element recorder command at the
   # component level for the Inno3DPnPJoint element with tag 99. It
   # is integrated into a for-loop to print the results for multiple
   # components (i.e., 1, 2, 3, 25). For each component, a separate
   # output file, designated as "results_Spr_X.out," where X is
   # replaced by the values in the $listSprOutput variable (e.g., X =
   # $SprNo), is created.
2
3 # create an output list with the springs of interest [1<->32]
4 set listSprOutput {1 2 3 25}
5
6 # create an empty string
7 set fileNameOutSpr ""
```

```
8
9 # start the iteration process
10 for {set i 0} {$i < [llength $listSprOutput]} {incr i} {
11     # create a variable that takes the value (number of the spring)
12     # of the current iteration
13     set sprNo [lindex $listSprOutput $i]
14
15     # create separate results files with a different name for each
16     # spring (this step is not mandatory, but it is highly recommended
17     # )
18     set fileNameOutSpr [join [concat "results_Spr_" $sprNo ".out"]
19     ""]
20
21     # element recorder command
22     recorder Element -file $Dir/$fileNameOutSpr -time -ele 99
23     -material $sprNo stressStrain
24 }
```


Chapter 5

Computation of mechanical properties of the macro-element for linear regime

5.1 Introduction

The proposed beam-to-column joint finite element is intended for practical application in routine design practice. As such, in line with linear analysis, the following three essential tasks must be achieved:

1. formulation of the beam-to-column joint model (Chapter 3) and its implementation within general FEM computational tools (Chapter 4);
2. definition of appropriate stiffness parameters leading to realistic internal force distributions;
3. establishment of a strength criterion to evaluate the structural safety of the beam-to-column joint.

Task 1 has already been discussed in previous sections of the document. Task 2 and Task 3, covering the definition of appropriate stiffness parameters and the establishment of a strength criterion, will be addressed in Sections 5.2 to 5.4 and Section 5.5, respectively.

5.2 Analytical definition of stiffness of the components

5.2.1 Introduction

The stiffness of the components of the proposed beam-to-column joint finite element depicted in Fig. 3.13 can be computed using different procedures, such as experimental tests, numerical procedures,

or analytical models. In the current study, given that the beam-to-column joint model is intended for use in routine design processes, a simplified procedure for the computation of the stiffness of the components is sought. To this end, *Equivalent Frame-Model(s)* (EFM(s)), also known in the research field of tubular structures as *ring models* [154], [205], are utilized. The EFMs are a favorable method as they allow for the analytical definition of the stiffness of the components of the beam-to-column joint element.

The fundamental principle underlying the use of the EFMs is the representation of the behavior of the tubular column in the beam-to-column joint region through a planar frame-model, whose Euler-Bernoulli elements represent the faces of the tube. The forces and deformations in the tube faces caused by their interaction with the beams connected to the column are represented by forces applied in the frame-elements and mid-span displacements of these elements, respectively. In these EFMs, the frame-elements are connected at their ends (i.e., at corners) to account for the interaction between the tube faces. The application of Euler-Bernoulli elements in the EFM concept requires the definition of the geometry of the frame-model, the boundary conditions of the frame-model, and a bending stiffness parameter for the linear frame-elements, named equivalent bending stiffness, EI .

The literature review revealed that the existing EFMs are only suitable for square tubular cross-sections [152] and do not consider the size of the "loaded region" of the joint or the bent portion of the tube in the interaction between the column faces. To evaluate the influence of these parameters and incorporate them, four main novel EFMs are presented and developed as follows:

- *Harada frame-model for square cross-sections* (HS-EFM, Fig. 5.4): developed by Harada and Simões da Silva ([153], [154]), and shown here for completeness;
- *Harada extended frame-model for rectangular cross-sections* (HR-EFM, Fig. 5.5): an extension of HS-EFM applicable to both square and rectangular cross-sections developed by the author;
- *Proposed frame-model for square cross-sections* (PS-EFM, Fig. 5.6): based on HS-EFM but modified to account for the connection's size, a feature that makes it suitable for a larger variety of joint dimensions; thus, it is appropriate for the P&PJ beam-to-column connection presented in Section 2.6.4;
- *Proposed frame-model for rectangular cross-sections* (PR-EFM, Fig. 5.8): an extension of the PS-EFM and applies to both square and rectangular cross-sections.

The methodology employed to calculate the bending stiffness parameter for each frame-element in the EFM accounts for the stiffness of each column face independently. Accordingly, in the case of rectangular tubular cross-sections, different bending stiffness parameters are computed for the

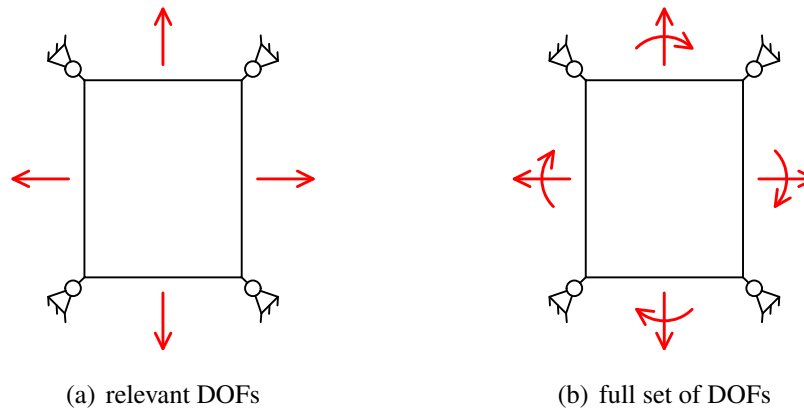


Figure 5.1: Degrees of Freedom in the Displacement Method Application.

column faces with varying dimensions. To assess the feasibility of using similar stiffness parameters in the frame-elements of the same EFM while considering that, in reality, the stiffness of each face is influenced by the stiffness of the other face (i.e., leading to an equivalent stiffness that falls between both), two different scenarios related to the mechanical properties of the frame-elements were examined for rectangular cross-sections, as follows:

- Each column face is assigned its corresponding moment of inertia (IF - inertia full); thus, there are two moments of inertia I_1 (width) and I_2 (length);
- Each column face is assigned the mathematical average of the moments of inertia of the column faces (IEq - inertia equivalent); thus, all faces have the same moment of inertia, which is expressed by Eq. (5.1).

$$I_{eq} = \frac{I_1 + I_2}{2} \quad (5.1)$$

In conclusion, considering the EFMs discussed and the two distinct scenarios related to the mechanical properties of the frame-elements for rectangular tubular cross-sections, a total of six EFMs were examined in the present study.

5.2.2 General procedure to compute the stiffness of the components

The computation of the stiffness of the components for the beam-to-column joints finite element outlined in Section 2.6.5 using EFMs requires, first, the computation of the stiffness matrix associated with the out-of-plane displacements at the mid-span of each frame-element, as depicted in Fig. 5.1(a), hereafter designated with $\mathbf{K}_c^{EFM} (4 \times 4)$.

The analytical calculation of the stiffness matrix for the EFMs can be performed using either classical force or displacement methods [200]. However, the traditional implementation of either

method requires significant computational effort due to the high degree of static and kinematic indeterminacy present in the EFMs, as exemplified by the EFM represented in Fig. 5.1(b), in which both the static and kinematic indeterminacy is 12.

Therefore, instead of calculating the full stiffness matrix of the EFM, $\mathbf{K}^{EFM}(12 \times 12)$, and subsequently condensing it to be only expressed in terms of the out-of-plane translation at the frame-elements' mid-span, $\mathbf{K}_c^{EFM}(4 \times 4)$, an alternative procedure that enables the computation of the condensed stiffness matrix directly has been adopted.

Following the method proposed by Harada and Simões da Silva [154], an alternative procedure for the computation of the condensed stiffness matrix, $\mathbf{K}_c^{EFM}(4 \times 4)$, was developed by selecting four load pattern(s) (LP(s)) that, through symmetry conditions, allow for efficient computation of the out-of-plane mid-span displacements of the frame-elements of the EFM. From the equilibrium between external and internal forces obtained from the displacement method, the condensed stiffness matrix, \mathbf{K}_c^{EFM} , is computed by solving the linear system of equations described by Eq. (5.2). The four LPs are depicted in Fig. 5.2.

$$\begin{bmatrix} P_S & P_E & P_N & P_W \end{bmatrix}^T = \mathbf{K}_c^{EFM} \begin{bmatrix} \delta_S & \delta_E & \delta_N & \delta_W \end{bmatrix}^T \quad (5.2)$$

As previously mentioned, the computation of the mid-span displacements of frame-elements for the LPs represented in Fig. 5.2 was achieved by taking advantage of the symmetry conditions. In other words, the calculation is performed on 1/4 (quadrant) of the EFM, hereafter referred to as *Simplified Equivalent Frame-Model(s)* (SEFM(s)).

The utilization of symmetry conditions necessitates the use of distinct terminology for the location of the calculated displacement. Specifically, the "displacement at the mid-span of the frame-elements of the EFM" before simplification corresponds to the "displacement at the end of the frame-elements of the SEFM" after simplification.

For every SEFM, the mid-span displacements of the frame-elements are also calculated using the classic displacement method, where only the formulae for fixed-fixed and fixed-roller Euler-Bernoulli elements, as presented in Fig. D.2 and Fig. D.1 in Appendix D, are required. The calculation procedure is based on the following steps:

1. identification of the boundary conditions of the SEFM;
2. identification of the kinematic DOFs of the SEFM – in all cases, the SEFM has only one DOF when the fixed-fixed and fixed-roller elements are used: d_1 ;

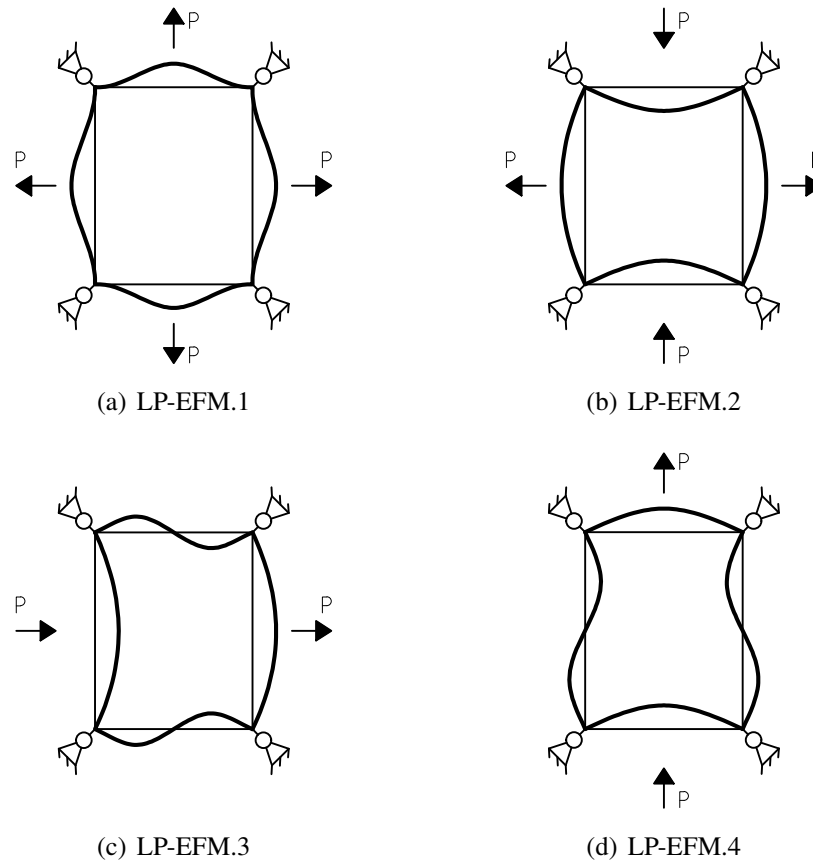


Figure 5.2: Load Patterns for the Equivalent Frame-Models.

3. computation of the stiffness corresponding to the DOF: k_{11} ;
4. computation of the displacement at frame-elements' ends of the SEFM caused by a unit displacement imposed on the DOF d_1 : δ_d ;
5. computation of the fixation forces in the DOF d_1 caused by the LP-EFM: f ;
6. computation of the displacement at the frame-elements' ends of the SEFM caused by the LP-EFM when the DOF is restrained: δ_P ;
7. computation of the displacement in the DOF associated with the LP-EFM: d ;
8. computation of the displacement at the frame-elements' ends of the SEFM caused by the actual displacement: δ_D ;
9. computation of the displacement at the frame-elements' ends of the SEFM using the principle of superposition of effects: δ .

The calculation described previously outputs the displacements at the ends of two frame-elements of the SEFM or at the mid-span of the frame-elements of the EFM. The displacements for the

remaining two frame-elements are derived from symmetry conditions, considering the established sign convention (Section 3.4.1).

Further on, the vectors containing the displacements at the mid-span for each LP-EFM are concatenated to form the matrix \mathbf{F}^{EFM} . Similarly, the matrix of external forces, \mathbf{P} , is obtained, as outlined in Eq. (5.3). In the conducted calculations, the elements of the vectors are defined in a counter-clockwise direction starting from the bottom face. Therefore, by designating the faces of the column in the EFM calculation according to the cardinal directions, the order becomes South-East-North-West (S-E-N-W).

The condensed stiffness matrix of the EFM, \mathbf{K}_c^{EFM} , is obtained by multiplying the matrix of external forces, \mathbf{P}^{EFM} , with the inverse of the matrix \mathbf{F}^{EFM} . Finally, the stiffnesses of the components of the beam-to-column joint finite element are derived.

$$\mathbf{P} = \begin{bmatrix} \mathbf{p}^{LP-EFM.1} & \mathbf{p}^{LP-EFM.2} & \mathbf{p}^{LP-EFM.3} & \mathbf{p}^{LP-EFM.4} \end{bmatrix} = \begin{bmatrix} P & -P & 0 & -P \\ P & P & P & 0 \\ P & -P & 0 & P \\ P & P & -P & 0 \end{bmatrix} \quad (5.3)$$

where

$$\mathbf{p}^{LP-EFM.i} = \begin{bmatrix} p^{LP-EFM.S} & p^{LP-EFM.E} & p^{LP-EFM.N} & p^{LP-EFM.W} \end{bmatrix}^T \quad (5.4)$$

The calculation process is also presented as a flowchart in Fig. 5.3.

5.2.3 Application of the procedure to the EFMs

The calculations for all six EFMs are presented in detail, with each computation following the procedures outlined in Section 5.2.2. Notwithstanding, since the computation methodology remains unchanged for each EFM, to avoid redundancy, the subsequent two sections only provide the EFM's description and the stiffness formulae for the joint components. The detailed step-by-step calculation is exclusively presented in Appendix E according to Tab. 5.1

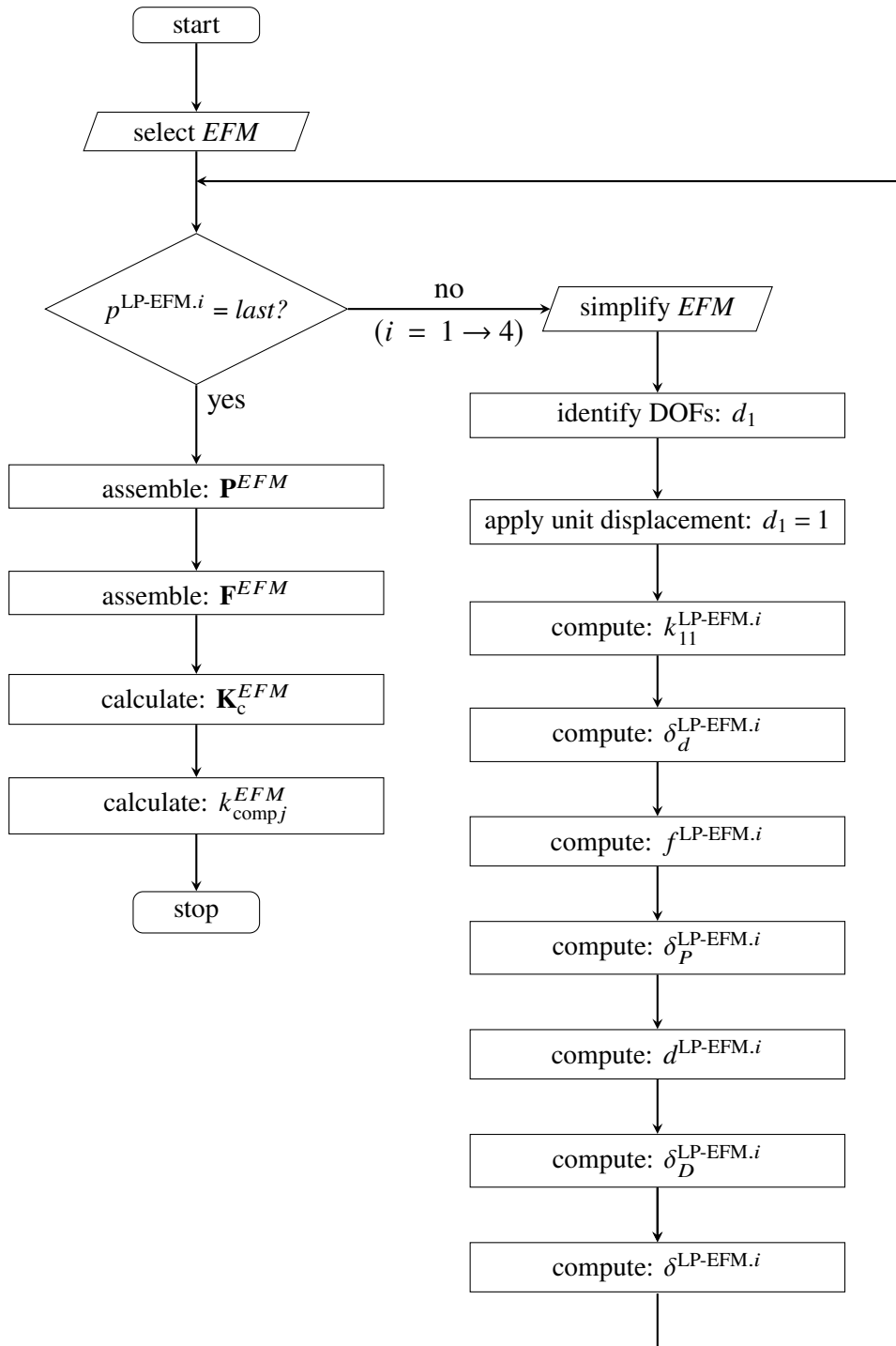


Figure 5.3: General procedure for calculating stiffness of components in all EFMs.

Table 5.1: Index of tables for stiffness calculation.

EFM name	Appendix name	EFM name	Appendix name
HS-EFM	Appendix E.1	PS-EFM	Appendix E.4
HR-EFM-IF	Appendix E.2	PR-EFM-IF	Appendix E.5
HR-EFM-IEq	Appendix E.3	PR-EFM-IEq	Appendix E.6

5.2.4 Description of the EFMs

5.2.4.1 HS-EFM

Harada and Simões da Silva developed the HS-EFM [152]–[154] as a solution for the 3D macro-modeling of beam-to-column joints, particularly under cyclic loading conditions, in which the column cross-sections are square, and the joint's behavior is semi-rigid. Their modeling approach is based on the component method, and its effectiveness has been evaluated through comparison with experimental results. Since the HS-EFM is considered the starting point or simplified approach for computing the stiffness of the components for the proposed macro-element, a brief overview is provided below.

The HS-EFM has four frame-elements of equal dimension, L (width/length), each representing a tube face, with bending stiffness EI , as shown in Fig. 5.4. The thickness of the tube, t_c , is not illustrated graphically; nevertheless, it is assumed to be uniform across all four sides.

The length, L , represents the distance between the exterior face of any two parallel faces. In the case of a tubular member with rounded corners, the length can be reduced to the distance between the radii of one face.

The HS-EFM has four nodes, 1, 2, 3, and 4, representing the EFM's corners. These nodes are restrained in translation to separate the deformations of the EFM from the rigid body motions. It is worth noting that this model prevents overall distortion of the frame-model; thus, the distortion deformation mode of the tube in its cross-section is not considered. Additionally, Harada and Simões da Silva included a roller at the mid-span of each frame-element (i.e., at the center of a column face) to ensure that the column face can only undergo perpendicular out-of-plane displacement.

Thus, the utilization of tables containing stiffness coefficients for fixed-fixed and fixed-roller Euler-Bernoulli (Appendix D) elements results in the need to consider only four rotational DOFs, specifically, d_1 , d_2 , d_3 , and d_4 , as well as four translational DOFs, specifically, δ_S , δ_E , δ_N , and δ_W .

5.2.4.2 HR-EFM-IF

The HR-EFM is an extended version of the HS-EFM, and it offers a more versatile solution because it can be used for both rectangular and square cross-sections. This EFM is similar to the HS-EFM in terms of node numbering, DOFs, and mid-span restraints for each frame-element. However, it differs in the dimensions and bending stiffnesses of the frame-elements, which include two dimensions, L_1 (width) and L_2 (length), as well as two bending stiffnesses, EI_1 and EI_2 .

As stated in Section 5.2.1, two scenarios are considered: one in which each column face is treated with its corresponding stiffness (HR-EFM-IF) and the other in which to all column faces an equivalent

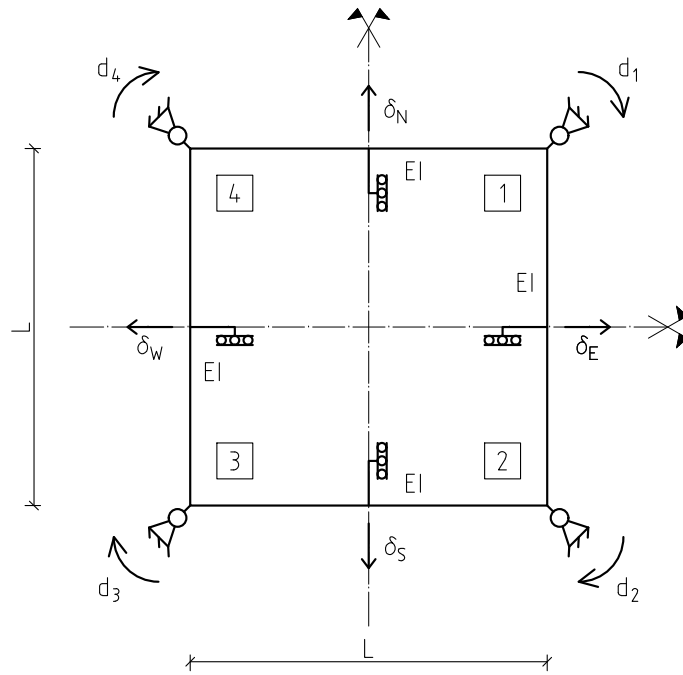


Figure 5.4: HS-EFM: a general overview.

stiffness (Eq. (5.1)) is assigned (HR-EFM-IEq). The procedure outlined in Section 5.2.2 is applied in both scenarios to determine the stiffness matrix of the EFMs.

5.2.4.3 HR-EFM-IEq

The HR-EFM-IEq is identical to the HR-EFM-IF, with the exception that it utilizes an equivalent moment of inertia, I_{eq} , defined by Eq. (5.1), instead of the individual moments of inertia, I_1 and I_2 , throughout the entire calculation. This methodology results in a uniform bending stiffness across all four frame-elements.

5.2.4.4 PS-EFM

The PS-EFM is a modified version of HS-EFM that considers the size of the connection. In the scope of the P&PJ system, which was introduced in Section 2.6.4, the connection size is integrated into the EFM by considering the two contact regions between the socket and the column as rigid areas as illustrated in Fig. 5.16. Despite the existence of two contact regions in the P&PJ configuration, the PS-EFM simplifies the model by considering a single rigid area that accounts for both contact regions and the distance between them, with a finite length denoted as b .

The rigid area is always centered on the frame-elements (i.e., on the tube face), and the same length is assumed for all four faces of the column. This means that truss-girders with identical dimensions are accounted for in both orientations of the structure and are centrally positioned on the column face.

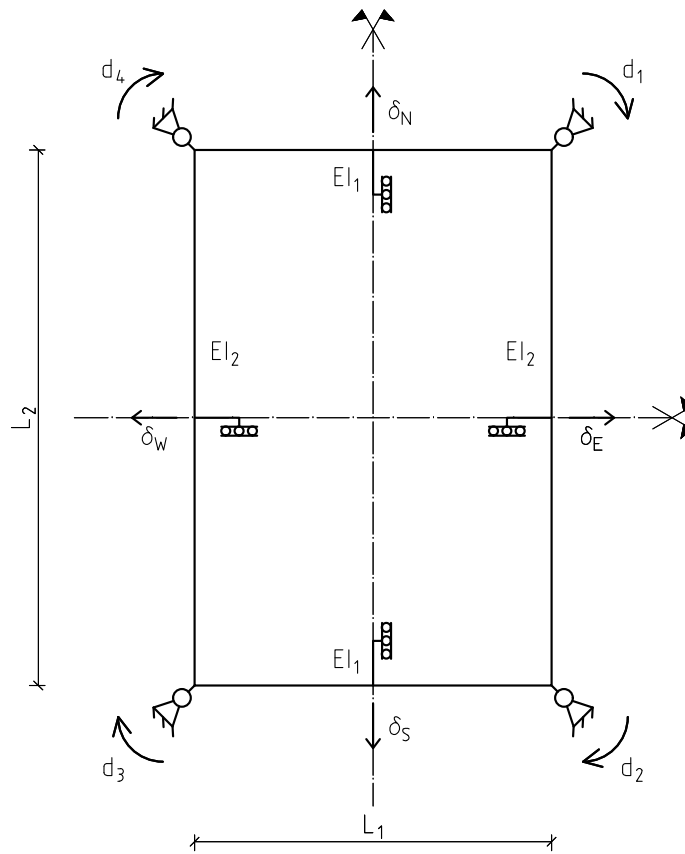


Figure 5.5: HR-EFM-IF: general overview.

Although a more general scenario could involve assigning each column, face a distinct rigid area of varying length, such a scenario would result in impractical analytical solutions and is likely infrequent in design practice.

Furthermore, roller supports are placed at the ends of the rigid element to impose perpendicular out-of-plane displacement on the column face. With this EFM configuration, if five points of interest were assigned to any frame-element (e.g., 1 to 5), the displacement of points 1 and 5, and 2, 3, and 4 would be identical (Fig. 5.7).

5.2.4.5 PR-EFM-IF

The PR-EFM is a more general solution than the PS-EFM since it can be used for both rectangular and square cross-sections. It shares similarities with the PS-EFM in terms of node numbering, DOFs, mid-span restraints for each frame-element, and rigid area length, b . However, it differs in terms of the dimensions and bending stiffnesses of the frame-elements. Specifically, there are two dimensions, L_1 (width) and L_2 (length), as well as two bending stiffnesses, EI_1 and EI_2 . Geometrically, the PR-EFM is a one-sided stretched version of the PS-EFM. The thickness of the tube, t_c , is not shown graphically but is assumed to be the same on all sides. For this EFM configuration, if five points of interest were

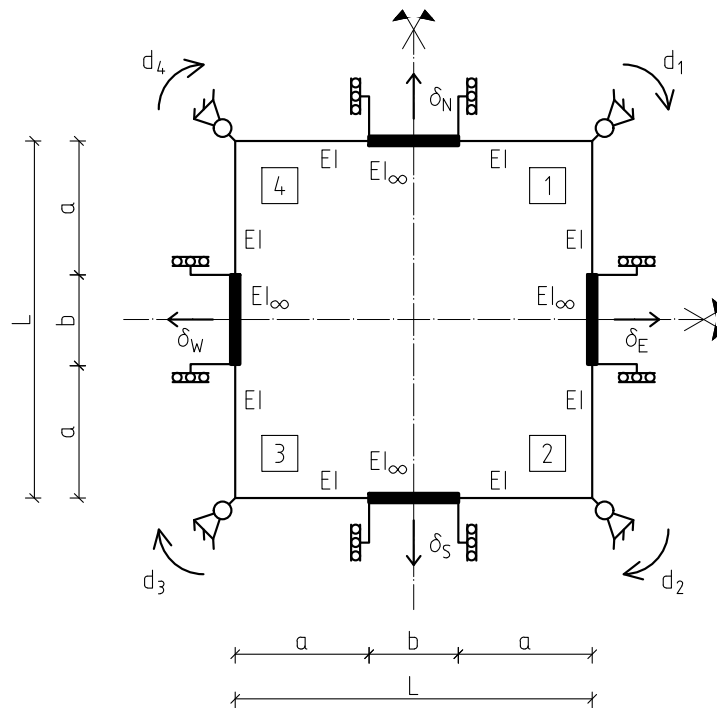


Figure 5.6: PS-EFM: a general overview.

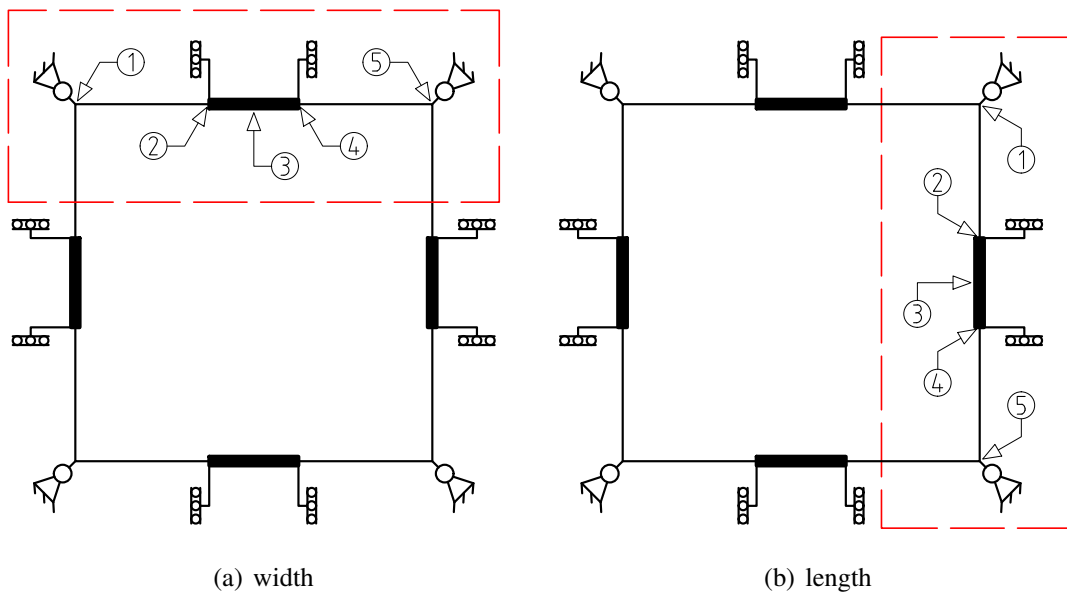


Figure 5.7: Frame-elements divided into points of interest.

assigned to the width (e.g., W1 to W5) or length (e.g., L1 to L5), the displacement of points 1 and 5, and 2, 3, and 4 would be identical for the analyzed face, as illustrated in Fig. 5.9.

Similar to the HR-EFM, the PR-EFM also has two sub-configurations: the first involves assigning each column face its corresponding stiffness (PR-EFM-IF), while the second involves assigning an equivalent stiffness (Eq.(5.1)) to all column faces (PR-EFM-IEq). To determine the out-of-plane displacement and stiffness matrix for both sub-configurations, the methodology outlined in Fig. 5.3 is employed.

5.2.4.6 PR-EFM-IEq

The PR-EFM-IEq is identical to the PR-EFM-IF, with the exception that it utilizes an equivalent moment of inertia, I_{eq} , defined by Eq. (5.1), instead of the individual moments of inertia, I_1 and I_2 , throughout the entire calculation. This methodology results, as in the case of HR-EFM-IEq, in a uniform bending stiffness across all four frame-elements of the EFM.

5.2.5 Stiffness of the tube components of the EFMs

The stiffness equations for the tube components in the beam-to-column joint finite element of an EFM, $k_{comp,j}^{EFM}$, are obtained from the corresponding condensed stiffness matrix, \mathbf{K}_c^{EFM} , as computed and reported in Appendix E. The stiffness formulae of the tube components are presented in the subsequent sections, along with the reference to the corresponding equation number of the stiffness matrix that was used to derive them.

5.2.5.1 HS-EFM

From \mathbf{K}_c^{HS-EFM} (Eq. (E.30)) the stiffness of the tube components becomes:

$$k_{comp.25}^{HS-EFM} = k_{comp.26}^{HS-EFM} = k_{comp.27}^{HS-EFM} = k_{comp.28}^{HS-EFM} = \frac{48 E I}{L^3} \quad (5.5)$$

$$k_{comp.29}^{HS-EFM} = k_{comp.30}^{HS-EFM} = k_{comp.31}^{HS-EFM} = k_{comp.32}^{HS-EFM} = \frac{36 E I}{L^3} \quad (5.6)$$

5.2.5.2 HR-EFM-IF

From $\mathbf{K}_c^{HR-EFM-IF}$ (Eq. (E.60)), the stiffness of the tube components becomes:

$$k_{comp.25}^{HR-EFM-IF} = k_{comp.27}^{HR-EFM-IF} = \frac{48 E I_1 (-3 I_2 L_1^2 + 4 I_2 L_1 L_2 + I_1 L_2^2)}{L_1^3 L_2 (I_1 L_2 + I_2 L_1)} \quad (5.7)$$

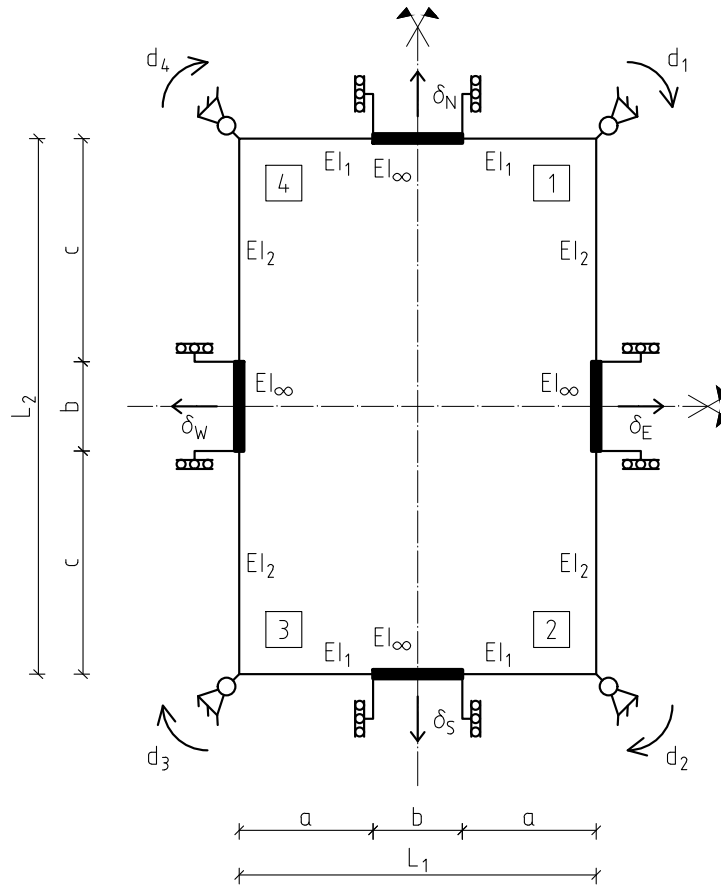


Figure 5.8: PR-EFM-IF: general overview.

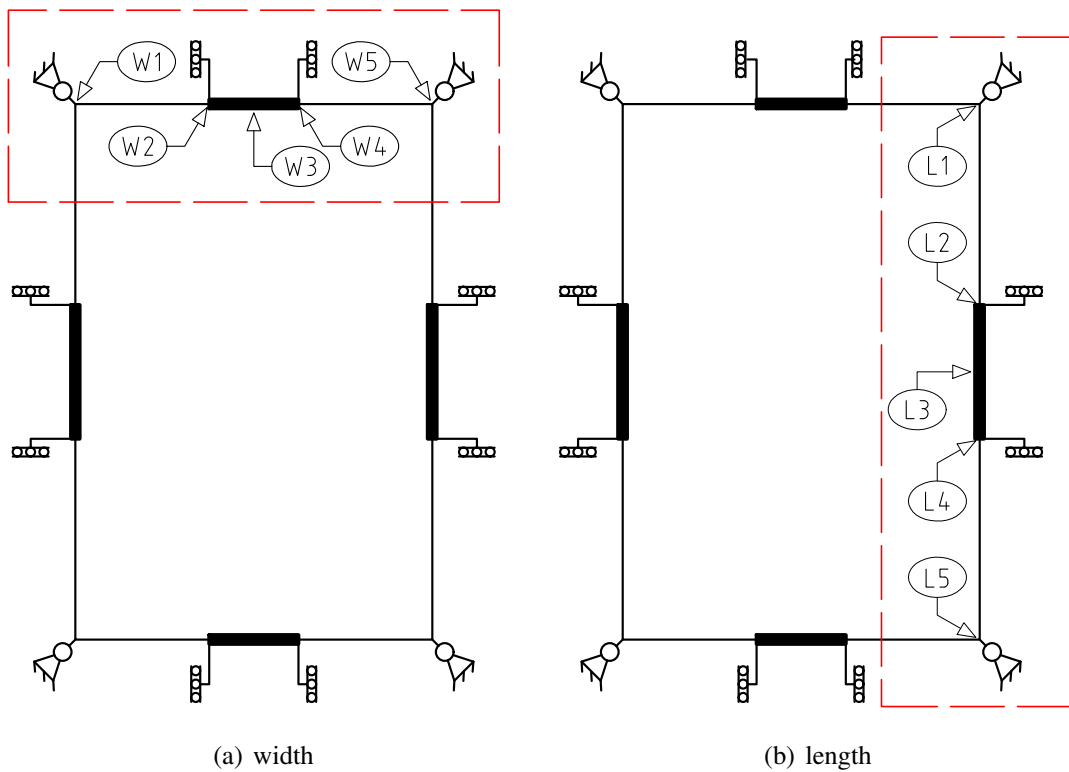


Figure 5.9: Frame-elements divided into points of interest.

$$k_{\text{comp.26}}^{\text{HR-EFM-IF}} = k_{\text{comp.28}}^{\text{HR-EFM-IF}} = \frac{48 E I_2 (I_2 L_1^2 + 4 I_1 L_1 L_2 - 3 I_1 L_2^2)}{L_1 L_2^3 (I_1 L_2 + I_2 L_1)} \quad (5.8)$$

$$k_{\text{comp.29}}^{\text{HR-EFM-IF}} = k_{\text{comp.30}}^{\text{HR-EFM-IF}} = k_{\text{comp.31}}^{\text{HR-EFM-IF}} = k_{\text{comp.32}}^{\text{HR-EFM-IF}} = \frac{72 E I_1 I_2}{L_1 L_2 (I_1 L_2 + I_2 L_1)} \quad (5.9)$$

5.2.5.3 HR-EFM-IEq

From $\mathbf{K}_c^{\text{HR-EFM-IEq}}$ (Eq. (E.65)), the stiffness of the tube components becomes:

$$k_{\text{comp.25}}^{\text{HR-EFM-IEq}} = k_{\text{comp.27}}^{\text{HR-EFM-IEq}} = \frac{48 E I_{eq} (-3 L_1^2 + 4 L_1 L_2 + L_2^2)}{L_1^3 L_2 (L_1 + L_2)} \quad (5.10)$$

$$k_{\text{comp.26}}^{\text{HR-EFM-IEq}} = k_{\text{comp.28}}^{\text{HR-EFM-IEq}} = \frac{48 E I_{eq} (L_1^2 + 4 L_1 L_2 - 3 L_2^2)}{L_1 L_2^3 (L_1 + L_2)} \quad (5.11)$$

$$k_{\text{comp.29}}^{\text{HR-EFM-IEq}} = k_{\text{comp.30}}^{\text{HR-EFM-IEq}} = k_{\text{comp.31}}^{\text{HR-EFM-IEq}} = k_{\text{comp.32}}^{\text{HR-EFM-IEq}} = \frac{72 E I_{eq}}{L_1 L_2 (L_1 + L_2)} \quad (5.12)$$

5.2.5.4 PS-EFM

From $\mathbf{K}_c^{\text{PS-EFM}}$ (Eq. (E.99)), the stiffness of the tube components becomes:

$$k_{\text{comp.25}}^{\text{PS-EFM}} = k_{\text{comp.26}}^{\text{PS-EFM}} = k_{\text{comp.27}}^{\text{PS-EFM}} = k_{\text{comp.28}}^{\text{PS-EFM}} = \frac{6 E I}{a^3} \quad (5.13)$$

$$k_{\text{comp.29}}^{\text{PS-EFM}} = k_{\text{comp.30}}^{\text{PS-EFM}} = k_{\text{comp.31}}^{\text{PS-EFM}} = k_{\text{comp.32}}^{\text{PS-EFM}} = \frac{9 E I}{2 a^3} \quad (5.14)$$

5.2.5.5 PR-EFM-IF

From $\mathbf{K}_c^{\text{PR-EFM-IF}}$ (Eq. (E.129)), the stiffness of the tube components becomes:

$$k_{\text{comp.25}}^{\text{PR-EFM-IF}} = k_{\text{comp.27}}^{\text{PR-EFM-IF}} = \frac{6 E I_1 (-3 I_2 a^2 + 4 I_2 a c + I_1 c^2)}{a^3 c (I_2 a + I_1 c)} \quad (5.15)$$

$$k_{\text{comp.26}}^{\text{PR-EFM-IF}} = k_{\text{comp.28}}^{\text{PR-EFM-IF}} = \frac{6 E I_2 (I_2 a^2 + 4 I_1 a c - 3 I_1 c^2)}{a c^3 (I_2 a + I_1 c)} \quad (5.16)$$

$$k_{\text{comp.29}}^{\text{PR-EFM-IF}} = k_{\text{comp.30}}^{\text{PR-EFM-IF}} = k_{\text{comp.31}}^{\text{PR-EFM-IF}} = k_{\text{comp.32}}^{\text{PR-EFM-IF}} = \frac{9 E I_1 I_2}{a c (I_2 a + I_1 c)} \quad (5.17)$$

5.2.5.6 PR-EFM-IEq

From $\mathbf{K}_c^{\text{PR-EFM-IEq}}$ (Eq. (E.134)), the stiffness of the tube components becomes:

$$k_{\text{comp.25}}^{\text{PR-EFM-IEq}} = k_{\text{comp.27}}^{\text{PR-EFM-IEq}} = \frac{6 E I_{eq} (-3 a^2 + 4 a c + c^2)}{a^3 c (a + c)} \quad (5.18)$$

$$k_{\text{comp.26}}^{\text{PR-EFM-IEq}} = k_{\text{comp.28}}^{\text{PR-EFM-IEq}} = \frac{6 E I_{eq} (a^2 + 4 a c - 3 c^2)}{a c^3 (a + c)} \quad (5.19)$$

$$k_{\text{comp.29}}^{\text{PR-EFM-IEq}} = k_{\text{comp.30}}^{\text{PR-EFM-IEq}} = k_{\text{comp.31}}^{\text{PR-EFM-IEq}} = k_{\text{comp.32}}^{\text{PR-EFM-IEq}} = \frac{9 E I_{eq}}{a c (a + c)} \quad (5.20)$$

5.3 EFM's effective bending stiffness

The mechanical properties of the frame-elements of the EFMs are based on the work done by Gomes, Neves, and Simões da Silva [155], [206]–[208] on the out-of-plane behavior of the column web plate for beam-to-minor-axis column joints.

5.3.1 Neves-Gomes Model

The work of Neves and Gomes referred to as the *Neves-Gomes Model* (NGM), is focused on the out-of-plane force-deformation relation curve for a rectangular plate with two opposite sides fixed and a central region loaded by a rigid-rectangular plate, as shown in Fig. 5.10.

5.3.1.1 Linear elastic regime

According to the NGM, the initial stiffness, S_i , of the out-of-plane force-deformation relation is:

$$S_i = \frac{16 E t_c^3}{L^2} \frac{\alpha + (1 - \beta) \tan \theta}{(1 - \beta)^3 + \frac{10.4 (k_1 - k_2 \beta)}{\mu^2}} \quad (5.21)$$

where:

$$e = (L - f) \tan \theta \quad (5.22)$$

$$l_{eff} = u + (L - f) \tan \theta \quad (5.23)$$

$$\alpha = \frac{u}{L} \quad (5.24)$$

$$\beta = \frac{f}{L} \quad (5.25)$$

$$\mu = \frac{L}{t_c} \quad (5.26)$$

$$\theta = \begin{cases} 35 - 10\beta & , \text{ for } \beta < 0.7 \\ 49 - 30\beta & , \text{ for } \beta = 0.7 \end{cases} \quad (\text{in degrees}) \quad (5.27)$$

$$k_1 = 1.50 \quad (5.28)$$

$$k_2 = 1.63 \quad (5.29)$$

with:

f = width of the rigid area

u = length of the rigid area

t_c = thickness of the column plate

L = width of the column plate

l_{eff} = width of the equivalent strip of the stiffness model

f_y = yield stress of the column plate

E = elastic modulus of the column plate

θ = angle that defines l_{eff}

k_1, k_2 = coefficients obtained from numerical calibration

α, β, μ = non-dimensional parameters

The NGM is valid under the following geometrical conditions:

$$0.05 \leq \alpha \leq 0.20 \quad (5.30)$$

$$0.08 \leq \beta \leq 0.75 \quad (5.31)$$

$$10 \leq \mu \leq 50 \quad (5.32)$$

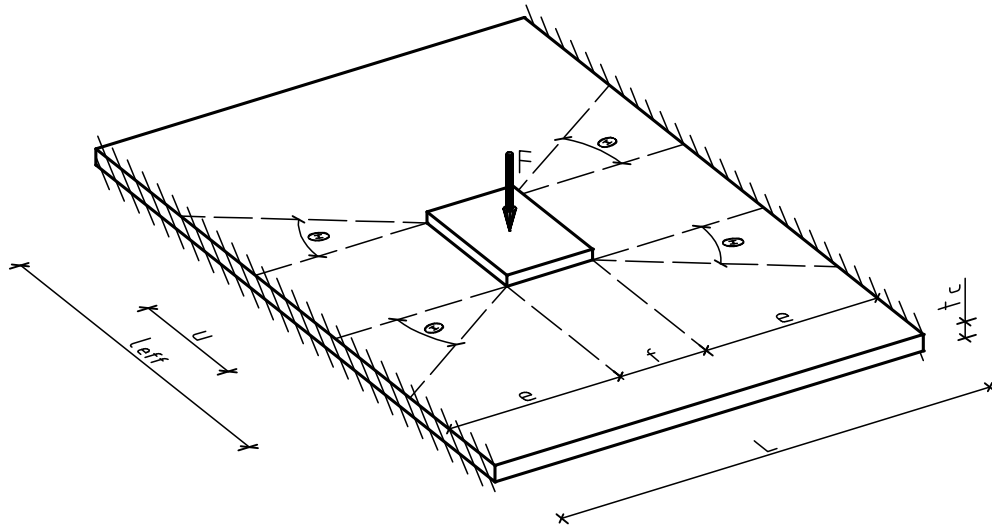


Figure 5.10: Gomes-Neves Model (adapted from [207]).

Although the NGM focuses on the out-of-plane behavior of a single-column plate, it is used in the current research due to the absence of other suitable formulations. Therefore, the tube faces are accounted as four isolated column plates interacting with each other.

5.3.1.1.1 Extension to rectangular cross-sections

The NGM was explicitly developed for the application with single-column plates, such as the web of an I-beam or H-beam profile. Nevertheless, for usage with rectangular sections, it is necessary to modify the variable names in the equation of initial stiffness (Eq. (5.21)) to account for the dimensions of the tube faces, including their width and length. To this end, this document adopts the ensuing modified notations to describe the initial stiffness of the width and length:

$$S_{i.1} = \frac{16 E t_c^3}{L_1^2} \frac{\alpha_1 + (1 - \beta_1) \tan \theta_1}{(1 - \beta_1)^3 + \frac{10.4 (k_1 - k_2 \beta_1)}{\mu_1^2}} \quad (5.33)$$

$$S_{i.2} = \frac{16 E t_c^3}{L_2^2} \frac{\alpha_2 + (1 - \beta_2) \tan \theta_2}{(1 - \beta_2)^3 + \frac{10.4 (k_1 - k_2 \beta_2)}{\mu_2^2}} \quad (5.34)$$

5.3.1.2 Post-elastic regime

In the NGM, the post-elastic regime can be represented by:

$$F = \begin{cases} \left[0.9 + (f_1 + f_2 - 0.9) \frac{\delta}{t_c} \right] F_{pl} & , \text{if } \delta \leq t_c \\ \left(f_1 + f_2 \frac{\delta}{t_c} \right) F_{pl} & , \text{if } \delta > t_c \end{cases} \quad (5.35)$$

where:

$$f_1 = -0.24 \beta - 0.012 \mu + 0.72 \quad (5.36)$$

$$f_2 = 0.55 \beta + 1.07 \alpha + 0.85 \quad (5.37)$$

$$m_{pl} = \frac{t_c^2}{4} f_y \quad (5.38)$$

$$k = \begin{cases} 1 & , \text{if } \alpha + \beta \geq 0.5 \\ 0.7 + 0.6 (\alpha + \beta) & , \text{if } \alpha + \beta < 0.5 \end{cases} \quad (5.39)$$

$$F_{local} = m_{pl} \frac{4}{1 - \frac{f}{L}} \left(\pi \sqrt{1 - \frac{f}{L}} + 2 \frac{u}{L} \right) k = m_{pl} \frac{4}{1 - \beta} \left(\pi \sqrt{1 - \beta} + 2 \alpha \right) k \quad (5.40)$$

$$F_{Q1} = 2 (f + u) t_c \frac{f_y}{\sqrt{3}} = \frac{2}{\sqrt{3}} L^2 f_y \frac{\alpha + \beta}{\mu} \quad (5.41)$$

$$F_{pl} = \min(F_{local}, F_{Q1}) \quad (5.42)$$

with:

k = non-dimensional parameter

F_{pl} = out-of-plane full-plastic strength of the column plate

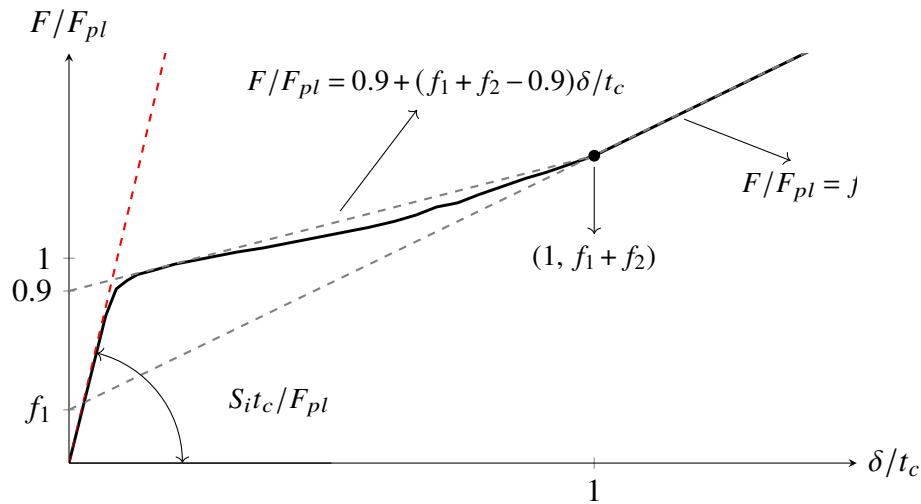


Figure 5.11: Gomes-Neves Model: Out-of-plane force-deformation relation model (adapted from [207]).

F_{local} = plastic flexure strength

F_{Q1} = punching-shear strength

m_{pl} = unitary plastic moment of a column plate

f_1, f_2 = coefficient for membrane model

5.3.2 Effective bending stiffness

The bending stiffness of the frame-elements, EI , of the EFMs is derived so that the displacement of the frame-elements coincides with the out-of-plane deformation of the column plate, according to the model represented in Fig. 5.10. Therefore, the mid-span displacement, δ_1 , of a frame-element, caused by a centrally-applied load P , considering that the frame-element is made of a strip with the second moment of inertia I , is computed by assuming both ends fixed (Fig. D.1(c)). Additionally, depending on the analyzed EFM, a rigid element is incorporated in the center region of the frame-element to represent the socket. As previously stated, for the EFMs where the size of the socket is to be taken into account, the joint region is the region corresponding to the width of the socket faces and the distance between them, as shown in Fig. 5.12.

Under these conditions, if e is the non-rigid part of the frame-element the displacement δ_1 becomes:

$$\delta_1 = \frac{P e^3}{24 E I} \quad (5.43)$$

According to the NGM, for isolated single column plates, the out-of-plane deformation, δ_2 , of the column plate in the linear regime caused by a load P can be derived using the initial stiffness, S_i ,

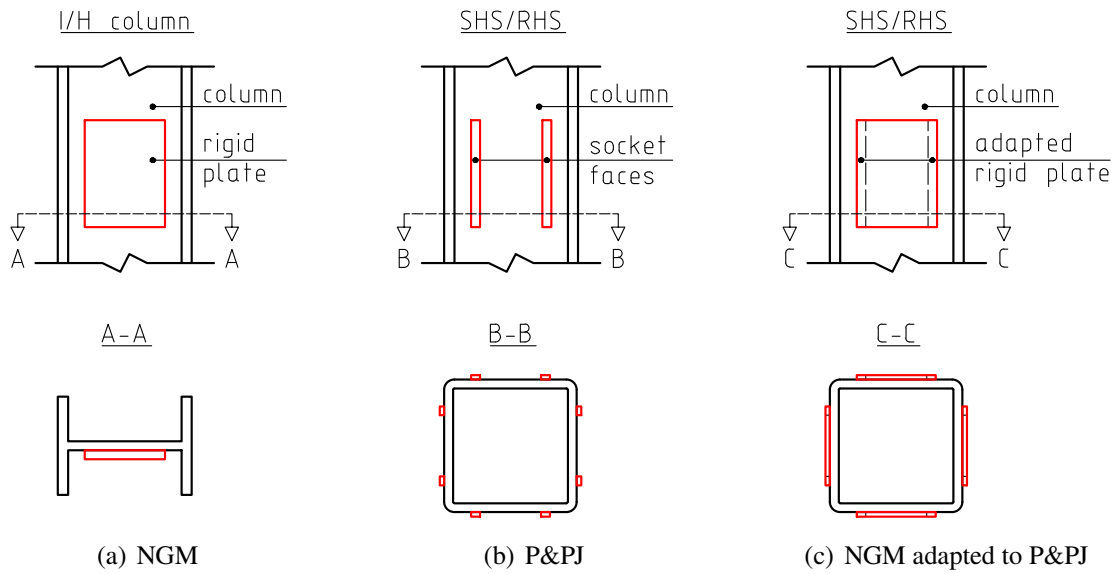


Figure 5.12: Gomes-Neves Model adapted to innovative 3D plug-and-play joint system (schematic representation).

through the following equation:

$$\delta_2 = \frac{P}{S_i} \quad (5.44)$$

By equating the right-hand side of Eq. (5.43) and Eq. (5.44), the bending stiffness of the frame-elements to be considered in the EFM becomes:

$$\delta_1 = \delta_2 \rightarrow EI = \frac{e^3}{24} S_i \quad (5.45)$$

Therefore, by applying this procedure to all the frame-elements of the EFMs, the mid-span displacement of these elements can be calculated for the assumed boundary and load conditions as follows:

$$\delta^{\text{HS-EFM}} = \frac{P L^3}{192 E I^{\text{HS-EFM}}} \quad (5.46)$$

$$\delta^{\text{PS-EFM}} = \frac{P a^3}{24 E I^{\text{PS-EFM}}} \quad (5.47)$$

$$\delta_1^{\text{HR-EFM}} = \frac{P L_1^3}{192 E I_1^{\text{HR-EFM}}} \quad (5.48)$$

$$\delta_2^{\text{HR-EFM}} = \frac{P L_2^3}{192 E I_2^{\text{HR-EFM}}} \quad (5.49)$$

$$\delta_1^{\text{PR-EFM}} = \frac{P a^3}{24 E I_1^{\text{PR-EFM}}} \quad (5.50)$$

$$\delta_2^{\text{PR-EFM}} = \frac{P c^3}{24 E I_2^{\text{PR-EFM}}} \quad (5.51)$$

Thus, the bending stiffness considered in the EFMs becomes:

$$EI^{\text{HS-EFM}} = \frac{L^3}{192} S_i \quad (5.52)$$

$$EI^{\text{PS-EFM}} = \frac{a^3}{24} S_i \quad (5.53)$$

$$EI_1^{\text{HR-EFM}} = \frac{L_1^3}{192} S_{i,1} \quad (5.54)$$

$$EI_2^{\text{HR-EFM}} = \frac{L_2^3}{192} S_{i,2} \quad (5.55)$$

$$EI_1^{\text{PR-EFM}} = \frac{a^3}{24} S_{i,1} \quad (5.56)$$

$$EI_2^{\text{PR-EFM}} = \frac{c^3}{24} S_{i,2} \quad (5.57)$$

5.4 Validation and calibration of EFM's effective bending stiffness

As previously stated, the proposed beam-to-column joint finite element is suitable for use with tubular columns with either square or rectangular cross-sections. To evaluate and validate the accuracy of the stiffness of the components derived from computations utilizing EFMs and the effective bending stiffness from NGM, it is necessary to compare the results from the beam-to-column joint finite element against more precise results. For this purpose, the current study employs high-order finite element models, also referred to as Refined Finite Element Model(s) (RFEM(s)) developed in the Abaqus software package [113]. The validation process involves applying prescribed loads to the joint on one to four faces of the tube to account for their interaction. Then, the results are analyzed and presented in terms of the out-of-plane displacements of the column faces.

The validation process involved a parametric analysis, which entailed the variation of several parameters. In OpenSees, five parameters underwent alteration, namely the column cross-section, LP, socket configuration (SC), EFM, and the impact of rounded corners. Additionally, two scenarios concerning the effective moment of inertia on the RHS were evaluated as specified in Section 5.4.2. In contrast, in Abaqus, only three parameters were altered, namely the column cross-section, LP, and SC, as expounded in Section 5.4.3.

The evaluation of the out-of-plane displacements of the column faces between OpenSees and Abaqus models is performed using the approximation error, ε_2 , and coefficient of determination, R^2 , which are expressed by Eq. (5.58) and Eq. (5.59), respectively.

$$\varepsilon_2 = \frac{\sum_{face=A}^D \left| \left(\delta_{face}^{Abaqus} - \delta_{face}^{OpenSees} \right) \right|}{\sum_{face=A}^D \left| \delta_{face}^{Abaqus} \right|} \quad (5.58)$$

$$R^2 = 1 - \frac{SS_{res}}{SS_{tot}} \quad (5.59)$$

where SS_{res} and SS_{tot} are the residual sum of squares and the total sum of squares (proportional to the variance of the data) of the differences between the out-of-plane displacements from the OpenSees and Abaqus models. The coefficient of determination, R^2 , evaluates how well the output of the joint finite element model compares to the output of the RFEMs. The ideal case is represented by a unitary value of $R^2 = 1$, where the regression line fitting the data set is linear and defined by Eq.(5.60) in the space of $\left(\delta_{face}^{Abaqus} - \delta_{face}^{OpenSees} \right)$.

$$y = m x + b , \text{ with } m = 1 \text{ and } b = 0 \quad (5.60)$$

5.4.1 Load patterns and socket configurations

5.4.1.1 Load patterns

In accordance with the work of Harada and Simões da Silva [154], LPs at the joint level were defined to simulate internal forces originating from the truss-girders in full structures under vertical and horizontal loading scenarios at the upper joint of the P&PJ (i.e., "Joint 1" from Fig. 3.2). Consequently, 10 and 17 LPs were considered for the SHS and RHS, as shown in Tab. 5.2 and Tab. 5.3, respectively. For each LP, the internal forces in a sub-frame bounded by inflection points are depicted in conjunction with the configuration of internal forces at the joint level.

The LPs are named based on the number of beams connected to the column (m01 to m04) and the type of loading on the structure, either vertical (e.g., gravity) or horizontal (e.g., earthquake) denoted as V or H. Corner joints use a preceding letter C (CH or CV). In RHS, LPs are applied considering the column in both possible positions, denoted as 01 or 02 at the end of their names (e.g., H01, CV02). A hypothetical LP named VnVp is also analyzed for both hogging and sagging bending moments.

Table 5.2: LPs considered for the SHS.

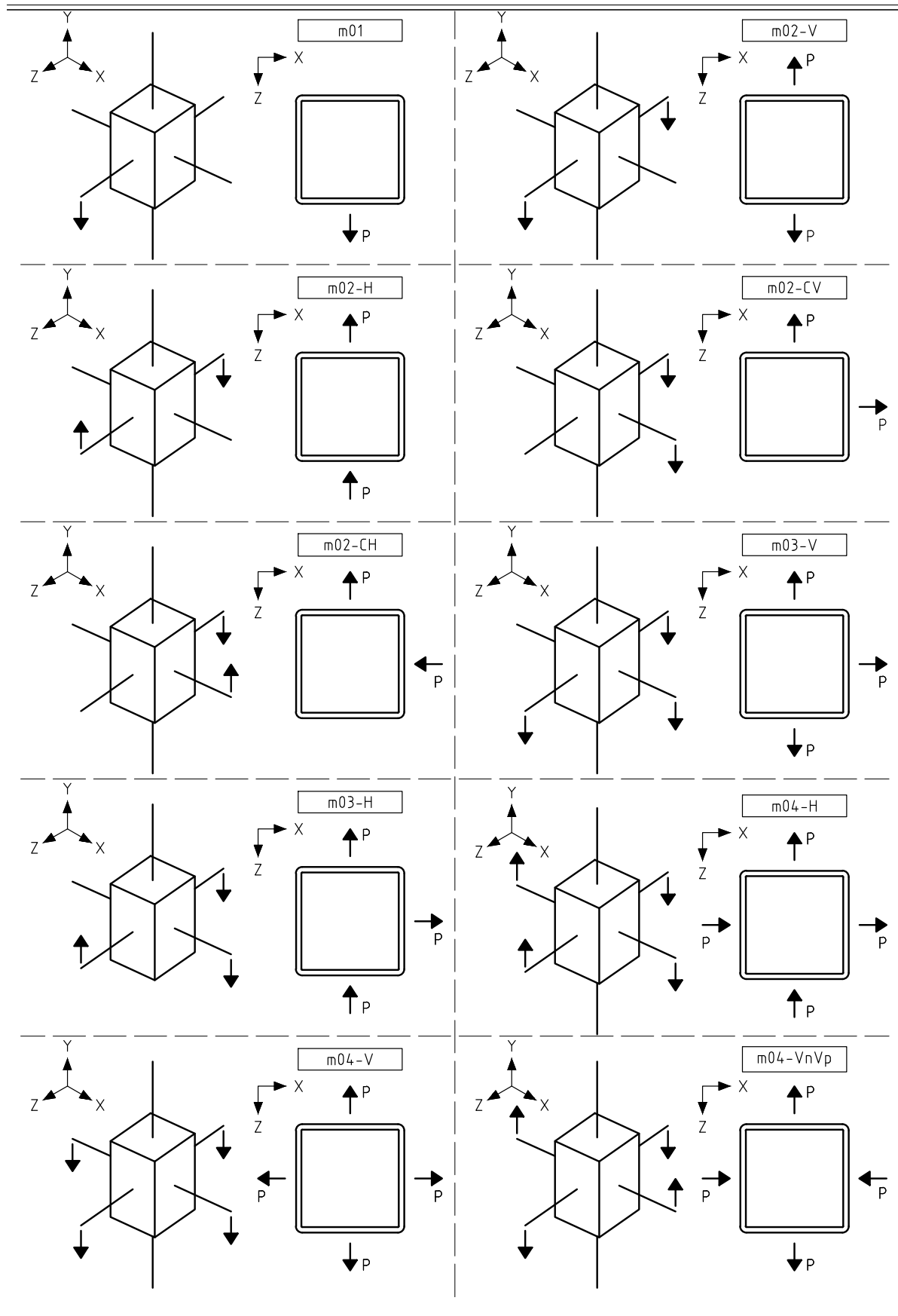
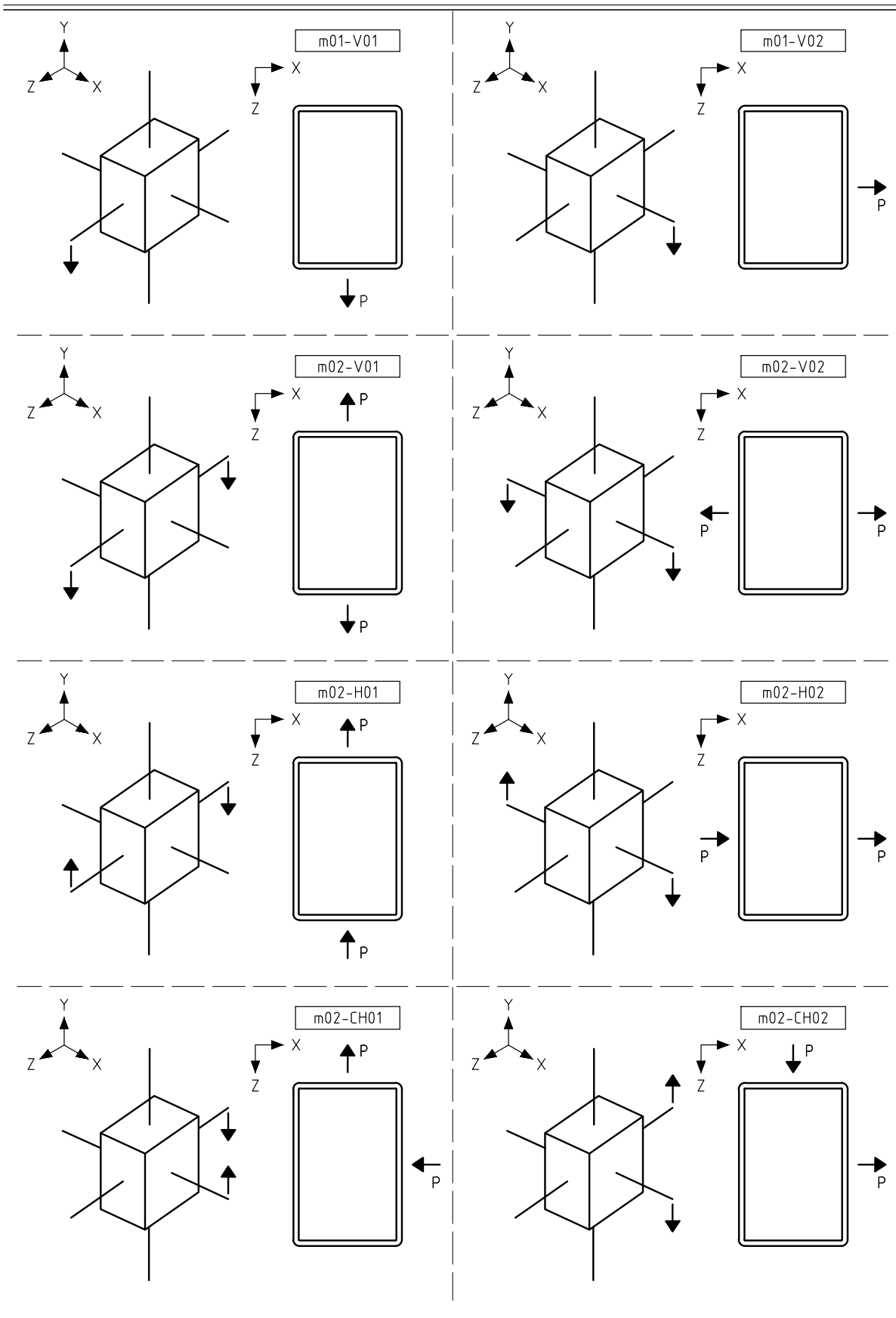
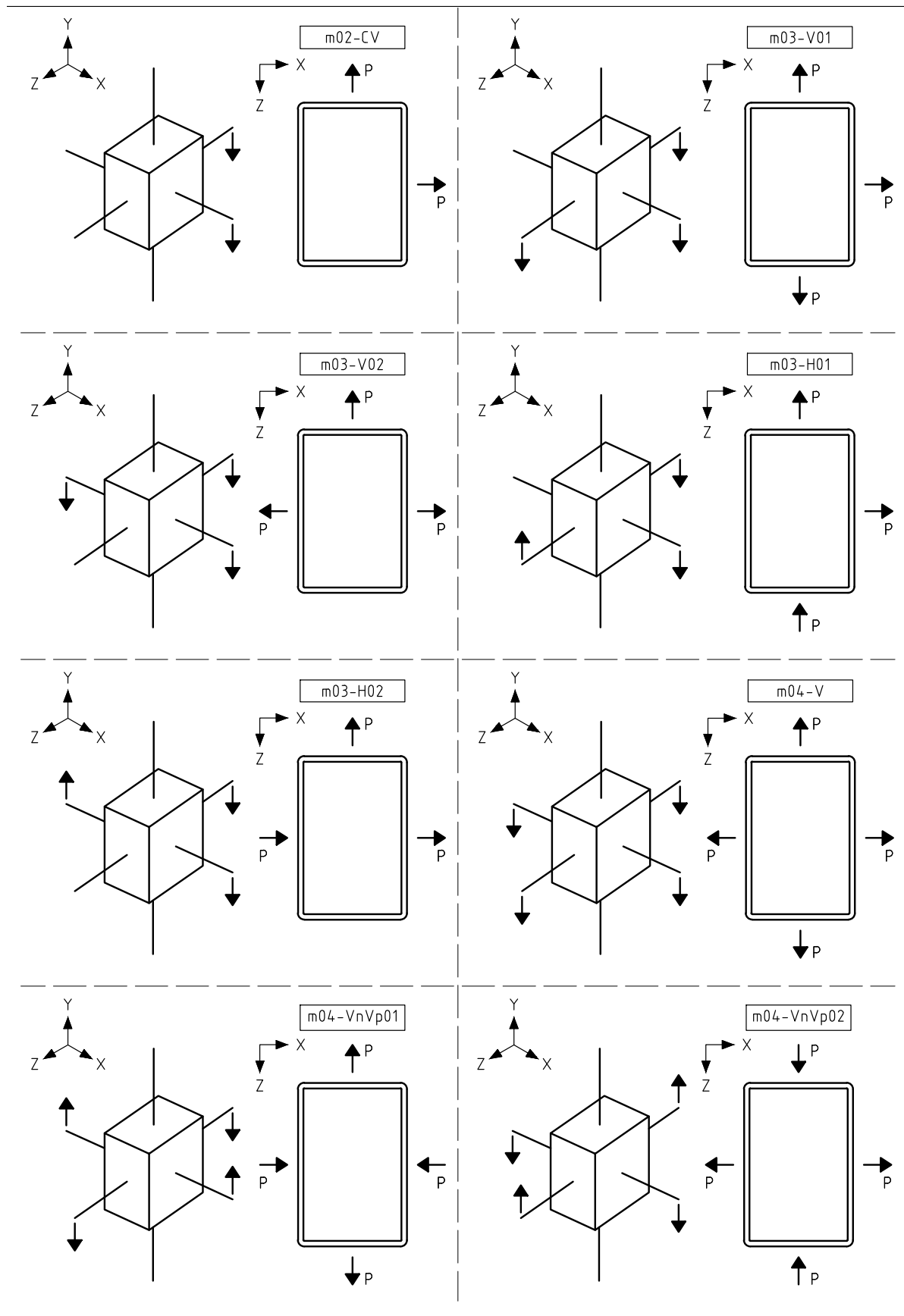


Table 5.3: LPs considered for the RHS.



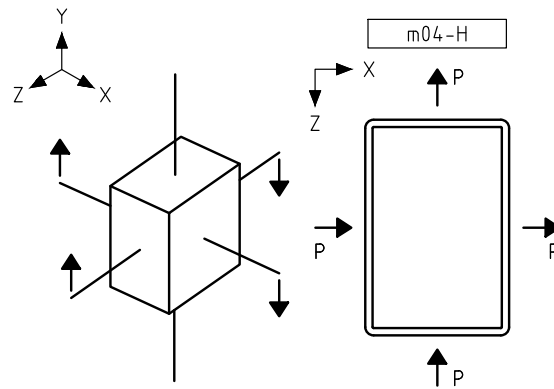
Continued on next page ...

Table 5.3: LPs considered for the RHS (cont.).



Continued on next page ...

Table 5.3: LPs considered for the RHS (*cont.*).



5.4.1.2 Socket configurations

The effect of the distance between the sockets on the out-of-plane deformation of the tube faces was the focus of the SCs considered. The objective was to investigate SCs that range from the scenario where the relative width of the socket region is minimal to the scenario where it is maximal. As a result, four SCs were examined per LP presented in Section 5.4.1.1. However, the socket height remained constant throughout the analysis. It should also be noted that the adopted SC does not fulfill the geometrical condition of the NGM from Eq. (5.30), the height of the socket being too large. This height was selected to replicate the geometry of the experimental specimens [144]. The geometry of the analyzed SCs can be found in Tab. 5.5 and Tab. 5.6 for the SHS and RHS, respectively.

5.4.1.3 Naming convention of the analyzed models

To enhance the readability of this document and the comprehension of the LPs and SCs naming convention, a set of naming examples is provided in Tab. 5.4 for clarification.

5.4.2 OpenSees models

The construction of models within OpenSees is straightforward as it requires only the definition of 5 nodes and the creation of an Inno3DPnPJoint element. The nodes are designated as depicted in Fig. 3.13. The central node (i.e., node 5) is fully fixed, while the edge nodes (i.e., nodes 1 to 4) are subjected to loading as per the designated LP.

The OpenSees models were built varying the following parameters:

1. column cross-sections: 2, namely SHS and RHS (Fig. 5.15);

Table 5.4: LPs and SCs naming examples.

Abbreviated	Detailed
SHS-m04-V-SC01	in a joint configuration where a square hollow section (SHS) column is present with four truss-girders connected to it (m04), a vertical force (V) is applied to the truss-girders. In this scenario, the distance between the socket faces is 0 mm (SC01).
RHS-m02-CH-SC02	in a joint configuration, a rectangular hollow section (RHS) column is present with two truss-girders attached to it (m02) and situated in the corner of a structure (C), a horizontal force (H) is exerted on the truss-girders. In this scenario, the distance between the socket faces is 20 mm (SC02).

Table 5.5: SCs considered for the SHS.

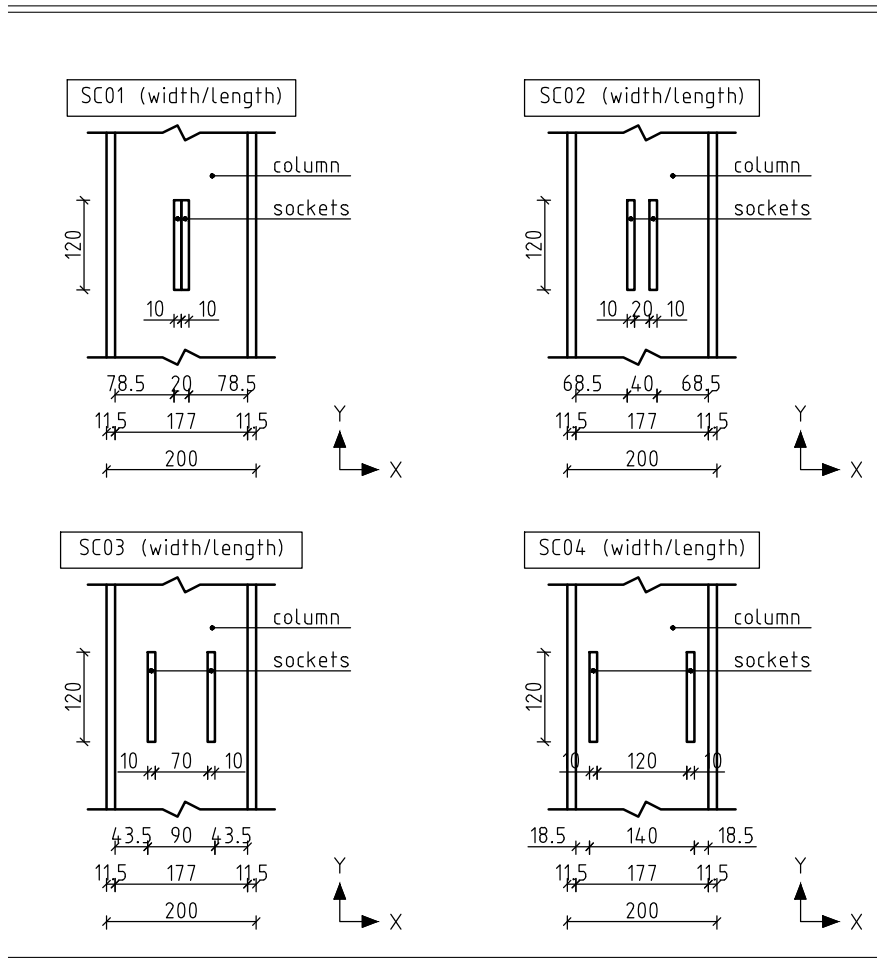
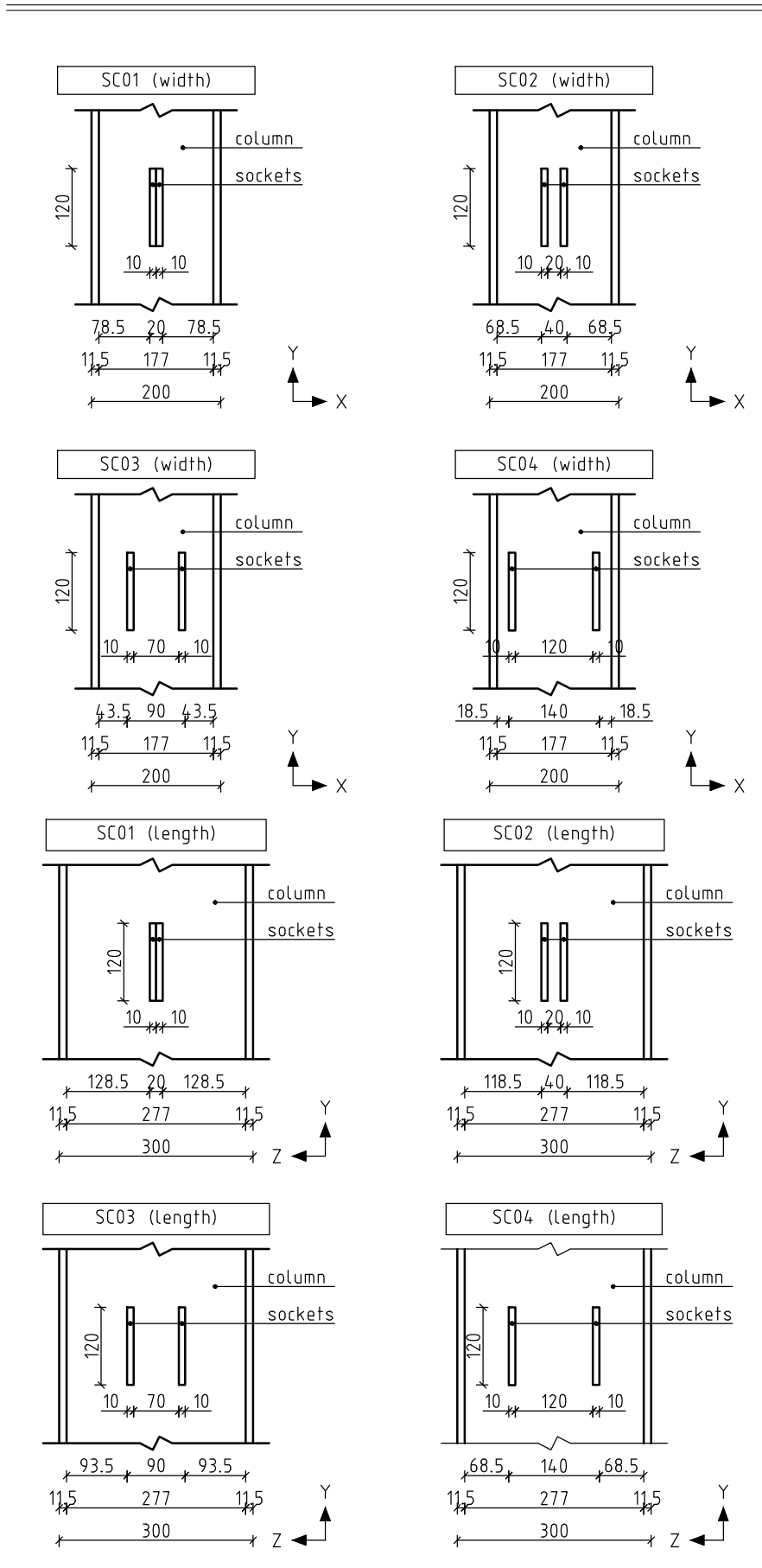


Table 5.6: SCs considered for the RHS.



2. LPs: 10 for SHS (Tab. 5.2) and 17 for RHS (Tab. 5.3);
3. SCs: 4 for both SHS (Tab. 5.5) and RHS (Tab. 5.6);
4. EFMs: 4, namely HS-EFM, PS-EFM, HR-EFM, and PR-EFM;
5. because the rounded corners of the tubular element could lead to uncertainty when it comes to choosing the correct width of the column plate (i.e., L in Fig. 5.10), which is needed in the computation of k_F and k_I for the EFMs, 2 cases were analyzed (Fig. 5.15):
 - (a) R0 – when the assumed width of the column face is the distance between the exterior of any two parallel faces of the column, i.e., the radius is neglected, thus, $L = 200$ mm, and $L_1 = 200$ mm and $L_2 = 300$ mm for the SHS and RHS, respectively;
 - (b) R1 – when the assumed width of the column face is the distance between the radii of a face, i.e., the radius is considered, thus, $L = 177$ mm, and $L_1 = 177$ mm and $L_2 = 277$ mm for the SHS and RHS, respectively;
6. in the RHS, 2 scenarios are considered based on the effective moment of inertia calculated from the variation in the length of the column faces:
 - (a) IF – when to each column face is assigned its corresponding effective moment of inertia bending stiffness: I_1 and I_2 (obtained from Eqs. (5.54) to Eq. (5.57) depending on the EFM);
 - (b) IEq – when to each column face is assigned the average effective moment of inertia (Eq. (5.1)).

A finite element models network is illustrated in Fig. 5.13 and Fig. 5.14 for the SHS and RHS, respectively, to facilitate the interpretation of the analyzed models and their modified features. Each network displays four categories: EFM (which already includes the cross-section type of the column), radius, LP, and SC, and by combining them, a total of 160 and 544 models are obtained for the SHS and RHS, respectively. Each network combination is referred to as *case*. As the primary objective is to assess the 3D interaction between the tube faces, the connection components are considered infinitely stiff in all cases.

An example of an OpenSees model written in Tcl is provided in Appendix F for the PR-EFM-IF-R1 case under m01-V01-SC01.

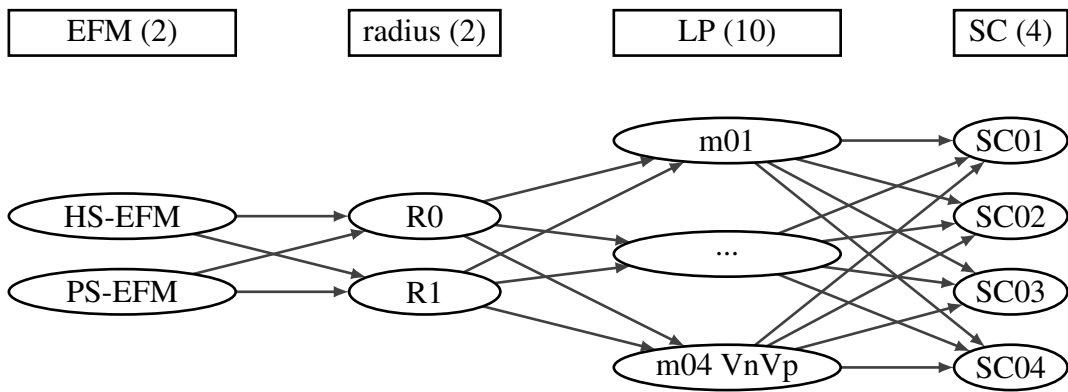


Figure 5.13: OpenSees FEM network for stiffness calculation: SHS (160 cases).

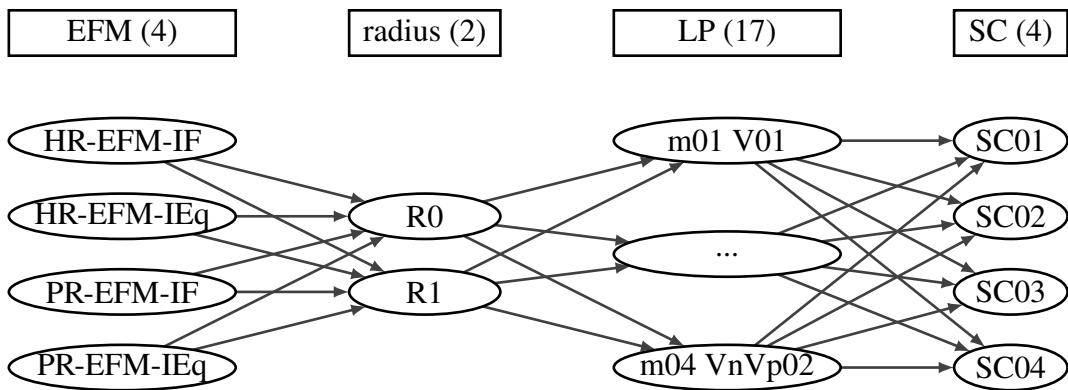


Figure 5.14: OpenSees FEM network for stiffness calculation: RHS (544 cases).

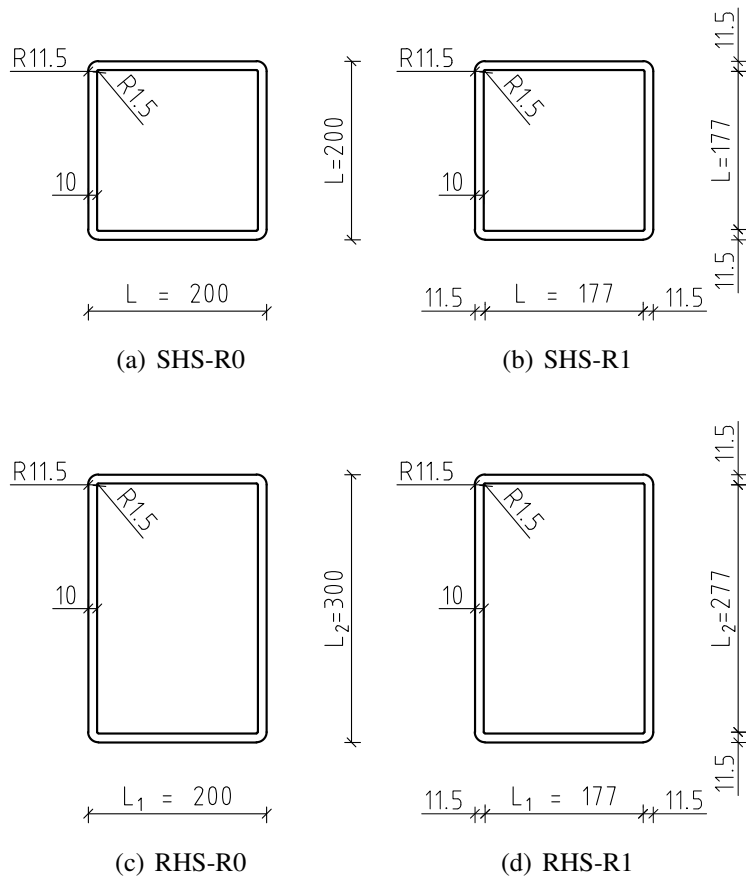


Figure 5.15: Influence of rounded corners on column face dimensions.

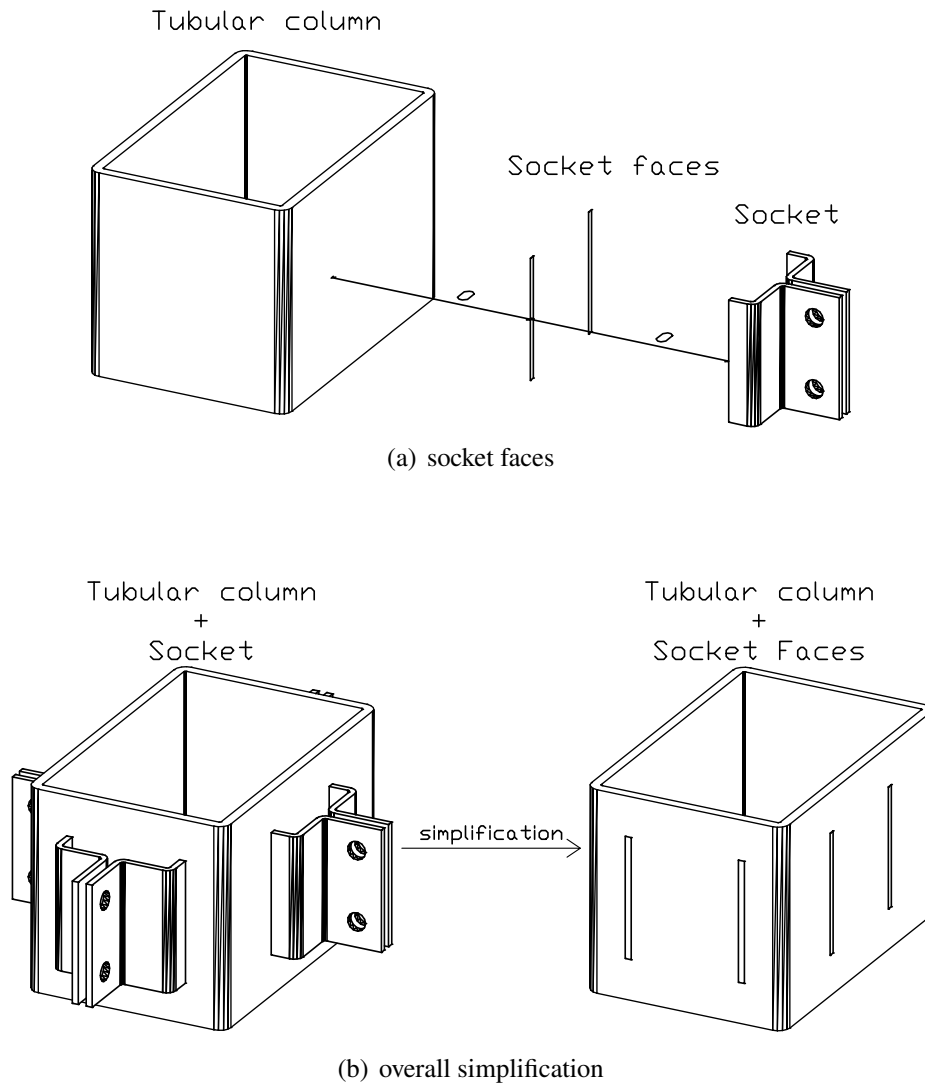


Figure 5.16: Schematic representation of the RFEMs build in Abaqus.

5.4.3 Refined Finite Element Models

5.4.3.1 Description

To evaluate the effectiveness of the developed beam-to-column joint finite element model, Refined Finite Element Model(s) (RFEM(s)) of the tubular column and the joint region were developed using Abaqus [113].

Given the large number of cases considered, the RFEMs were limited to only the tubular column and the two areas corresponding to the contact regions between the socket and column, which will be referred to as the *socket faces*. The graphical representation of the socket faces in the RFEMs can be seen in Fig. 5.16. Additionally, only one joint was modeled in this study (i.e., "Joint 1" from Fig. 3.2).

The RFEMs were developed based on a series of preliminary parametric studies conducted at the beginning of the research. These studies are related to mesh size (Section 5.4.3.2) and geometry and

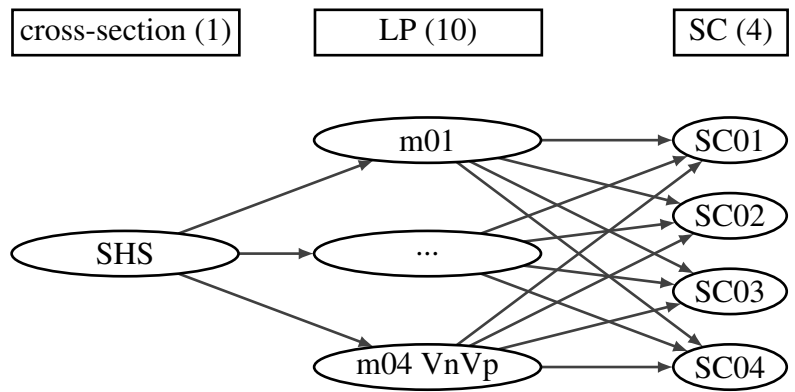


Figure 5.17: Abaqus FEM network for stiffness calculation: SHS (40 cases).

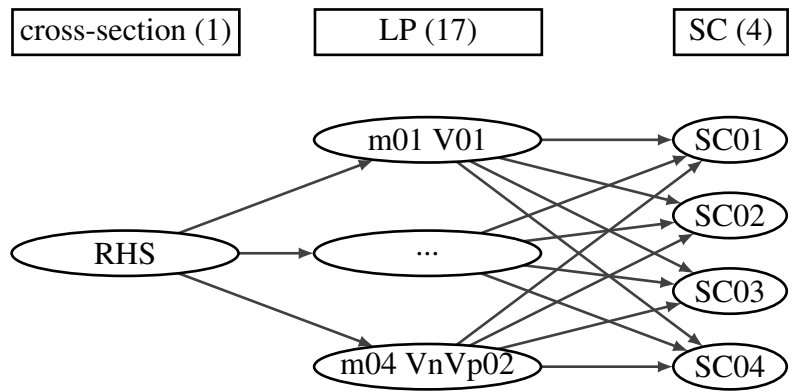


Figure 5.18: Abaqus FEM network for stiffness calculation: RHS (68 cases).

boundary conditions (Section 5.4.3.3). The objective of these studies was to obtain mesh-independent results and make the tube’s local behavior in the joint region independent of boundary conditions and column height.

The Abaqus models were created by modifying the following specific aspects:

1. cross-sections: 2, namely SHS and RHS (Fig. 5.19);
2. LPs: 10 for SHS (Tab. 5.2) and 17 for RHS (Tab. 5.3);
3. SCs: 4 for both SHS (Tab. 5.5) and RHS (Tab. 5.6);

The finite element models networks built in Abaqus are illustrated in Fig. 5.17 and Fig. 5.18 for the SHS, and RHS, respectively. A total of 40 and 68 models are obtained for the SHS and RHS, respectively.

The dimensions of the SHS and RHS columns analyzed in this study are presented in Fig. 5.19. As depicted in Fig. 5.19, the socket faces are located at the mid-height of the column, and the distance between them is varied as described in Section 5.4.1.2.

The tubular column was modeled using solid elements with reduced integration (C3D8R – Fig. 5.20(a)), while the socket faces were modeled using discrete rigid elements (R3D4 – Fig. 5.20(b)).

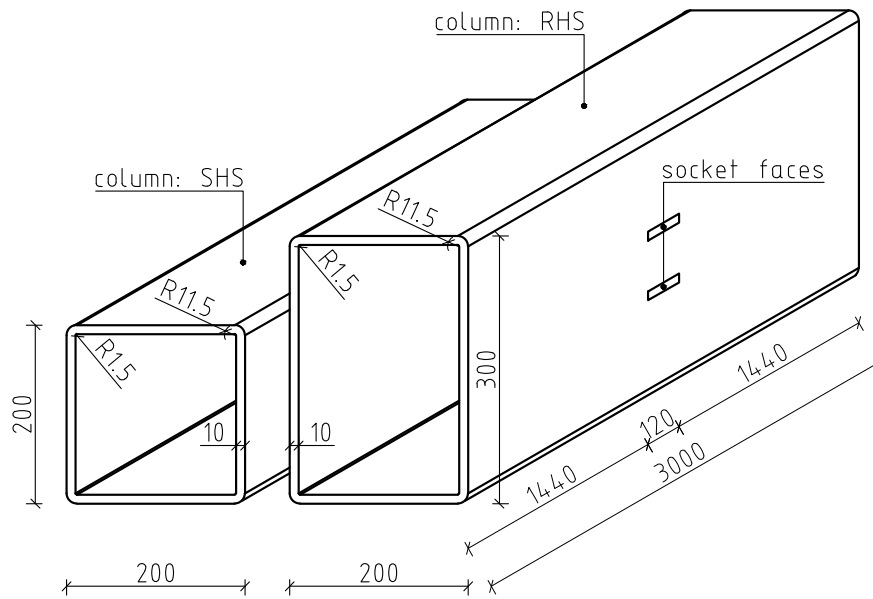


Figure 5.19: Tubular columns (SHS and RHS): height and cross-section dimension.

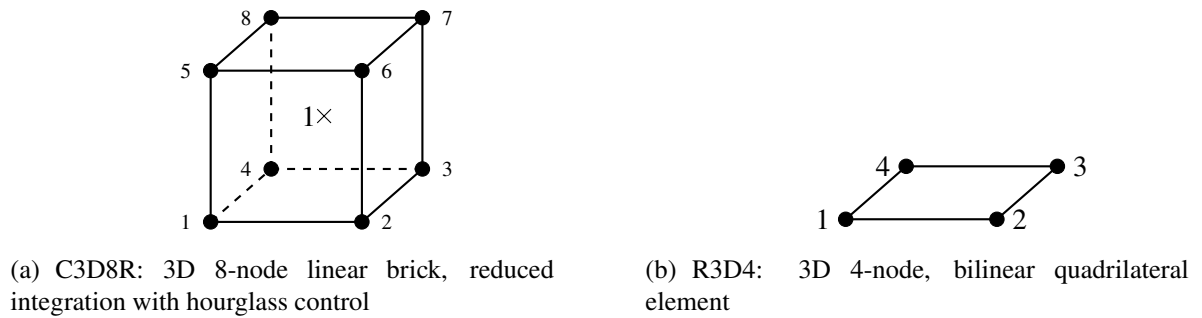


Figure 5.20: Finite Element types used in Abaqus [113]

In compliance with the software requirements, a reference point (RP) was defined on the socket faces to indicate the rigid body reference point; thus, the displacements and internal forces in the socket faces were determined by the displacements and internal forces in the RP.

The column's material constitutive relation was assumed to be linear-elastic and thus only required the definition of Young's modulus of elasticity, E , and Poisson's coefficient, ν . The values of these parameters are listed in Tab. 5.7. As the socket faces were defined with discrete rigid finite elements, no material definition was required for them.

The connection between the tubular column (i.e., solid 3D element) and socket faces (i.e., discrete rigid 2D elements) was established through a surface-to-surface *tie* kinematic constraint, ensuring that

Table 5.7: Linear elastic material characteristics of the tubular column.

E [N/mm ²]	ν
210000	0.3

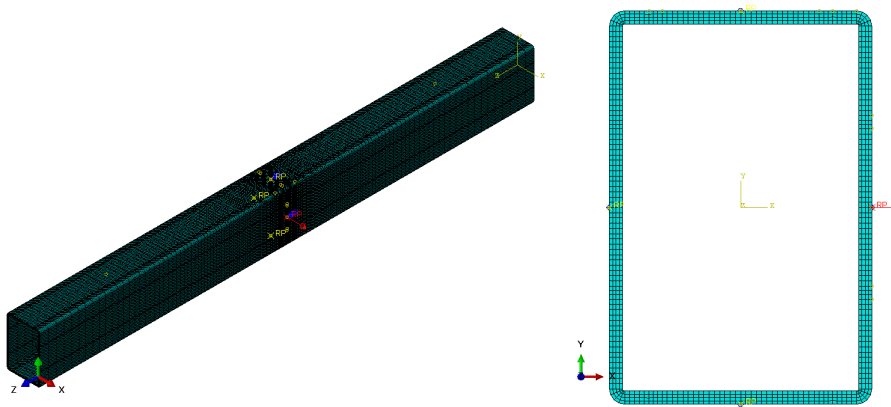


Figure 5.21: Load application: CF on RP.

the faces of the two elements were tied together, with no relative motion between them. As a result, the translational and rotational displacements were equal for the pair of surfaces. Additionally, this constraint fuses the two regions even if the mesh assigned to them is dissimilar.

The load was applied using a concentrated force (CF) assigned to the RP, simulating the internal force transmitted by the T-plug, as depicted in Fig. 5.21.

Although the RFEMs did not consider any nonlinearity to evaluate the results of the beam-to-column joint finite element model in the elastic regime, a nonlinear analysis using the arc length method (*Riks* procedure) as the convergence algorithm was employed in Abaqus [113]. The initial, minimum, and maximum increments were specified as 1, 0.001, and 1, respectively. Furthermore, a maximum of 1000 increments per iteration were defined, and the stopping criterion employed was a maximum load proportionality factor of 1. The use of nonlinear analysis in Abaqus is consistent, in terms of analysis type, with OpenSees, where it is advisable to perform an analysis with an implicit algorithm [209]. The analyses were carried out in load control.

The out-of-plane displacements obtained from the RP are presented in Appendix G, with Tab. G.1 and Tab. G.2 showing the results for the SHS and RHS, respectively. The results are presented for all cases resulting from the combination of each LP and each SC. The deformed shapes of the SHS and RHS for SC02 can be found in Tab. G.3 and Tab. G.4, which are also included in the aforementioned appendix.

5.4.3.2 Mesh sensitivity analysis

A sensitivity analysis was conducted on an SHS column utilizing varying mesh sizes to evaluate the impact of mesh size on the results and determine the lower bound of mesh size that yields accurate results.

The column was modeled with straight corners, neglecting the tube's rounded corners. The

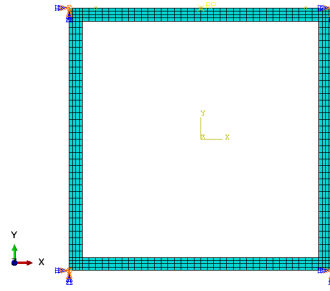


Figure 5.22: BC for mesh sensitivity analysis.

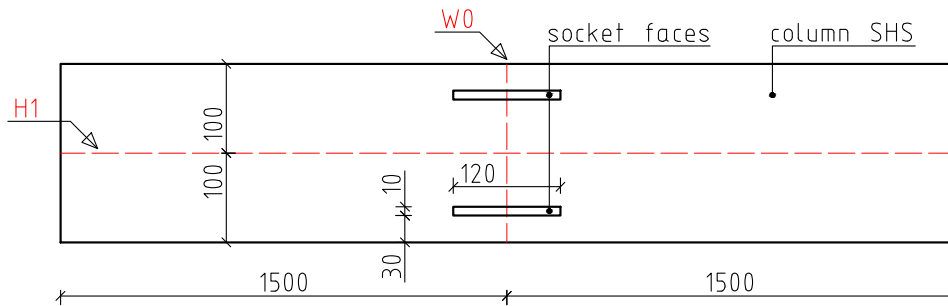


Figure 5.23: Out-of-plane displacement extraction locations for the tubular column face.

considered LP and SC used were m01 and SC04 (Tab. 5.2 and Tab. 5.5). Fully fixed boundary conditions were applied to the edge nodes of the tube to prevent rigid body movement and cross-section distortion, as shown in Fig. 5.22. Three mesh sizes were tested: 10 mm, 5 mm, and 2.5 mm and were referred to as "mesh 10.0", "mesh 5.0", and "mesh 2.5" in their respective RFEMs. Four elements per thickness were utilized in all RFEMs.

For each RFEM, the out-of-plane displacements of tubular column faces are extracted from sections H1 (i.e., along the column height from the center of the loaded column face) and W0 (i.e., through the column cross-section), which are depicted in Fig. 5.23.

The out-of-plane displacements extracted from sections H1 and W0 are presented in Fig. 5.24 and Fig. 5.25(a), respectively. It can be observed that the mesh size that yields objective results in the joint region is provided by the model "mesh 5.0" with a mesh size of 5 mm, a value considered as the lower bound of the mesh size.

Subsequently, the effect of a varying mesh size along the column's height was examined to assess the possibility of reducing the number of finite elements in the RFEMs and thus decreasing the computational time. To accomplish this, a mesh size of 5 mm was used in the joint region, while the mesh size was increased to a maximum of 50 mm towards the column ends by using local *seeds* and *biases* [113]. The out-of-plane displacements extracted for sections H1 and W0 for the model with a uniform mesh size of 5 mm ("mesh 5.0") and the model with a variable mesh size ("mesh 5.0 bias") are plotted in Fig. 5.26 and Fig. 5.25(b), respectively.

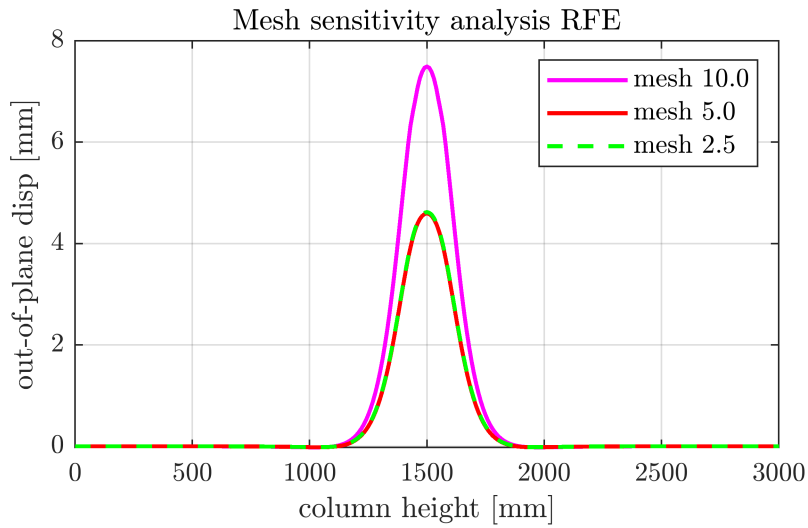


Figure 5.24: Out-of-plane displacements of tube face in section H1 for different mesh sizes.

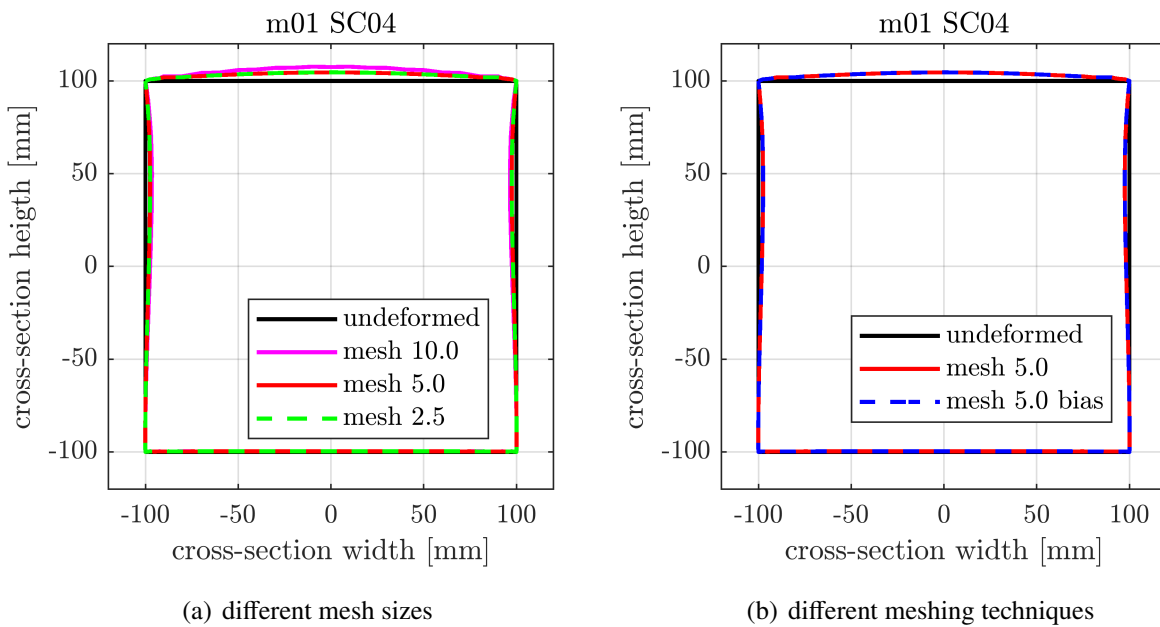


Figure 5.25: Out-of-plane displacements of tube faces in section W0.

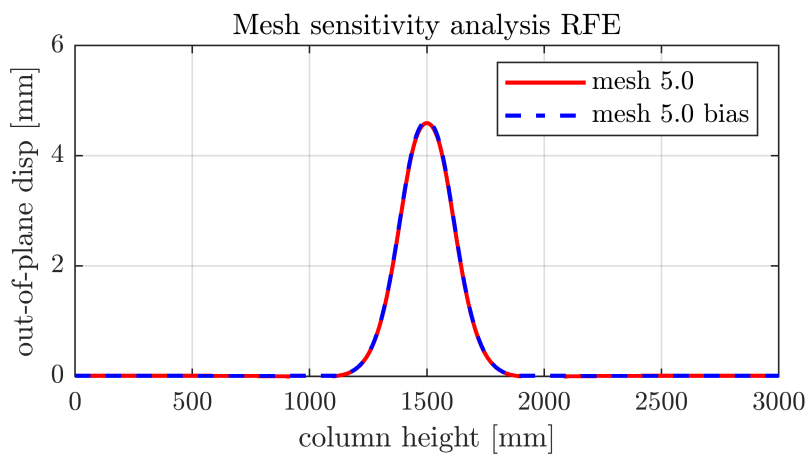


Figure 5.26: Out-of-plane displacements of tube face in section H1 for different meshing techniques.

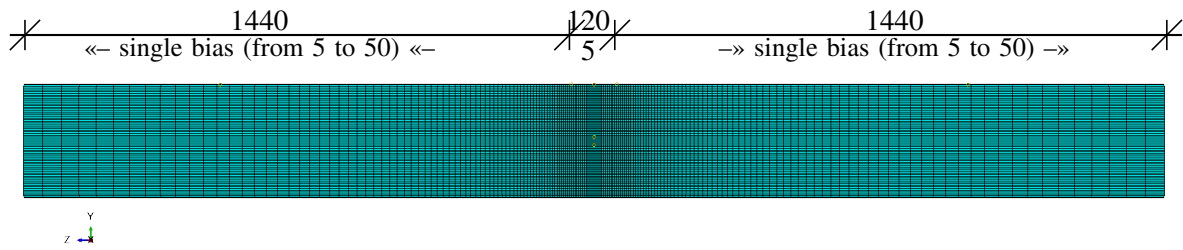


Figure 5.27: Final mesh configuration for tubular columns.

Table 5.8: Number of finite elements for each mesh configuration.

Element type	RFEM name			
	mesh 10.0	mesh 5.0	mesh 2.5	mesh 5.0 bias
tubular column	105600	384000	1459200	114872
socket faces	24	96	384	96

The number of finite elements used to build every RFEM presented in this section is shown in Tab. 5.8.

In conclusion, the results of this study on the column's behavior in the joint region indicated that the column height could be reduced from 3000 mm to 2500 mm or 2000 mm to decrease the computational cost. However, instead of reducing the height, a variable mesh size strategy was implemented to minimize the number of finite elements required. Specifically, a maximum mesh size of 5 mm was utilized in the joint region, while the mesh size gradually increased from 5 mm to 50 mm towards the column ends. Therefore, the final mesh configuration employed in this research is illustrated in Fig. 5.27.

5.4.3.3 Geometry and boundary condition

The effect of modeling the geometry of an SHS column with or without the rounded corners resulting from the manufacturing process (e.g., cold bending) as well as the influence of boundary condition placement on the tube's geometry, were also analyzed. Similar to the previous parametric investigation, the analysis utilized the LP and SC m01 and SC01, respectively (Tab. 5.2 and Tab. 5.5).

Three RFEMs were developed in this parametric investigation, one with straight corners ("w/o RC - BC pt"), and two with rounded corners. The transition from straight to rounded corners introduces ambiguity in the application of boundary conditions; hence, to avoid rigid body movement of the cross-section and preserve the other deformation modes, fixed boundary conditions were tested on two different regions: (i) on the rounded corner part ("w/ RC - BC ln"), and (ii) on the nodes found at the angle bisector of the rounded corner ("w/ RC - BC pt"). The three different boundary conditions

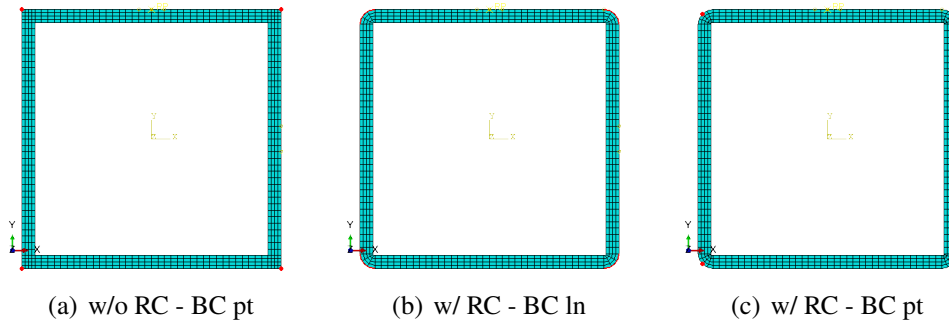


Figure 5.28: Points and regions for BC application.

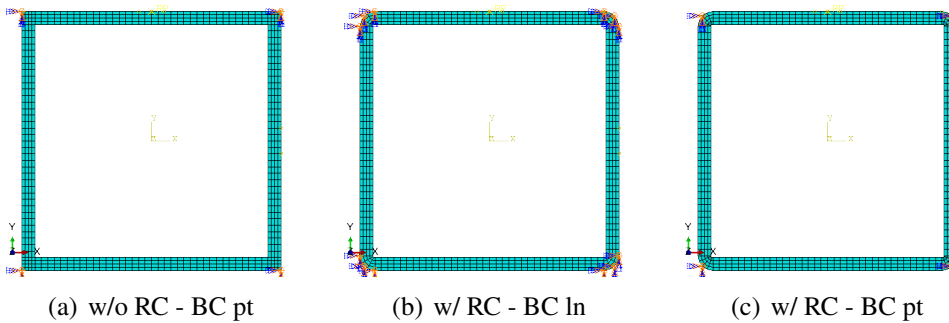


Figure 5.29: Applied BC.

are illustrated in Fig. 5.28 and Fig. 5.29.

Fig. 5.30 depicts the overall deformation of the cross-sections in section W0, which is measured by the U magnitude, i.e., the square root of the sum of squares of all components of the U vector [113].

Fig. 5.31(a) presents a comparison between the RFEM without rounded corners and an undeformed tubular cross-section that also lacks rounded corners ("w/o RC - BC pt" vs. "w/o RC - undef"). This comparison allows for an evaluation of the impact of rounded corners on the results.

Additionally, Fig. 5.31(b) compares the RFEMs with rounded corners and with BCs applied at different locations ("w/ RC - BC ln" vs. "w/ RC - BC pt"). This comparison allows for an assessment of the effect of the location of the boundary conditions on the results.

From Fig. 5.31(b), it can be observed that by constraining the entire rounded corner region ("w/ RC - BC ln"), the interaction between the column faces is impeded, causing the column face to behave as an independently loaded plate instead of a tubular cross-section. As a result, RFEMs with this type of boundary condition were not considered further in this work.

A comparison between the remaining two models ("w/o RC - BC pt" vs. "w/ RC - BC pt") is presented in Fig. 5.32(a). The results of this comparison suggest that the inclusion of rounded corners has a notable impact on the displacements in the loaded column face and, thus, should be considered when conducting further analysis. Specifically, it was found that there was a 7.96% increase in displacement on the loaded face, which also had a ripple effect on the adjacent faces. However,

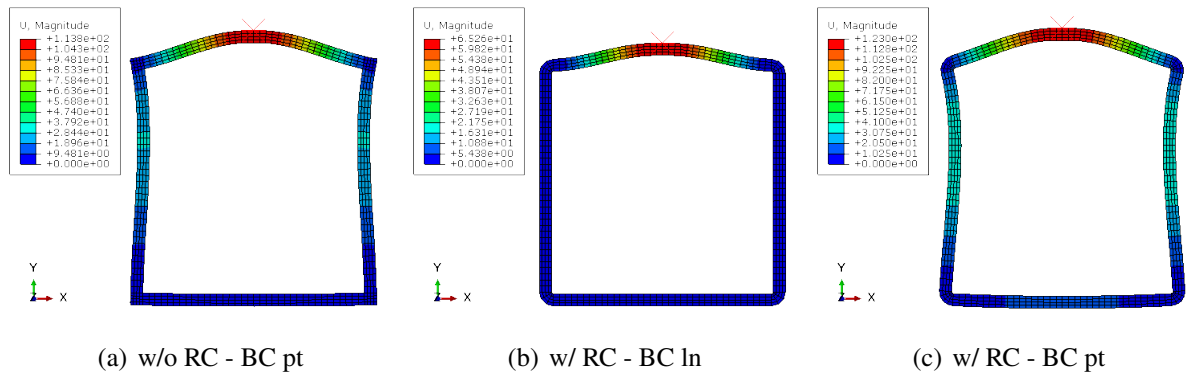


Figure 5.30: Overall deformation of the cross-section of tubes: U Magnitude.

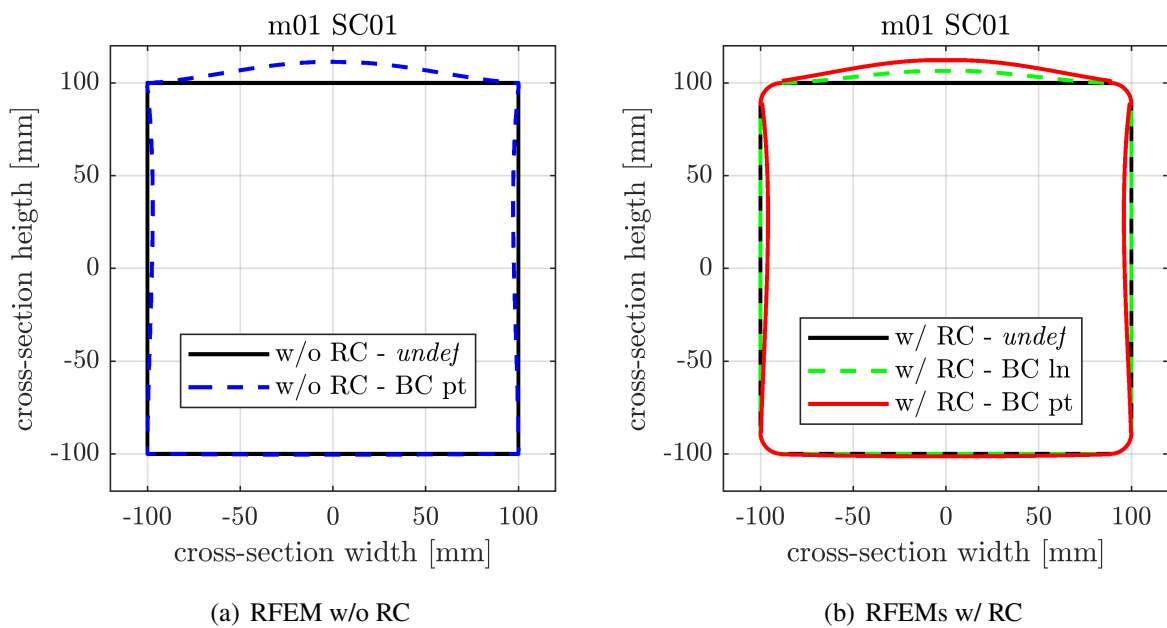


Figure 5.31: Out-of-plane displacement of tube faces in section W0 for different BC.

the RFEM with straight corners presents excessive local distortion in the proximity of the corners. This phenomenon results from using finite elements with a reduced integration scheme (Fig. 5.20(a)) combined with the type and position of the applied boundary condition. As suggested by the software's manual [113], a potential solution to this problem is the use of finite elements with hybrid formulation (i.e., C3D8H). Nevertheless, the model with straight corners is not used beyond this document section.

Furthermore, to ensure that the selected BC ("w/ RC - BC pt") from Fig. 5.29(c) only impedes the rigid body movement of the cross-section, a new model is derived from it ("w/ RC - BC pt E"). In this new model, the BCs are applied to the nodes found at the column ends. For naming consistency, the model with the selected BC is renamed; thus, "w/ RC - BC pt" becomes "w/ RC - BC pt H", as shown in Fig. 5.33. The deformed shapes of the column in 3D and 2D are shown in Fig. 5.34 and Fig. 5.35,

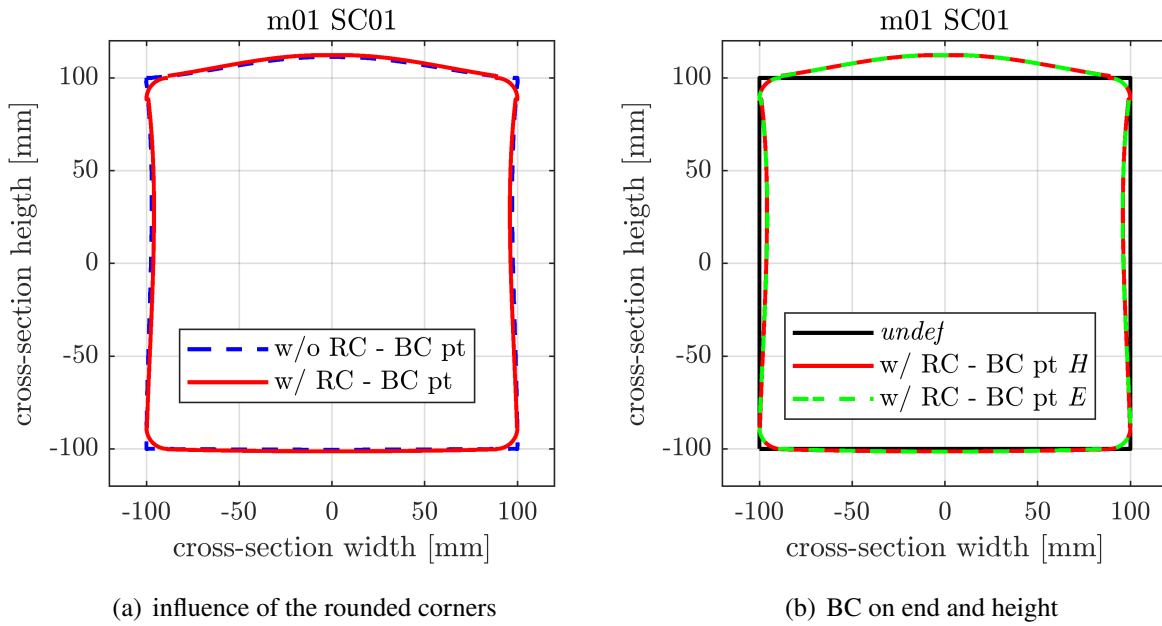


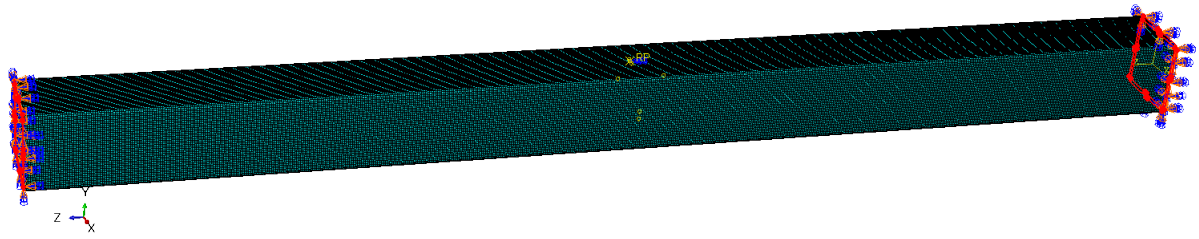
Figure 5.32: Out-of-plane displacements from section W0.

respectively.

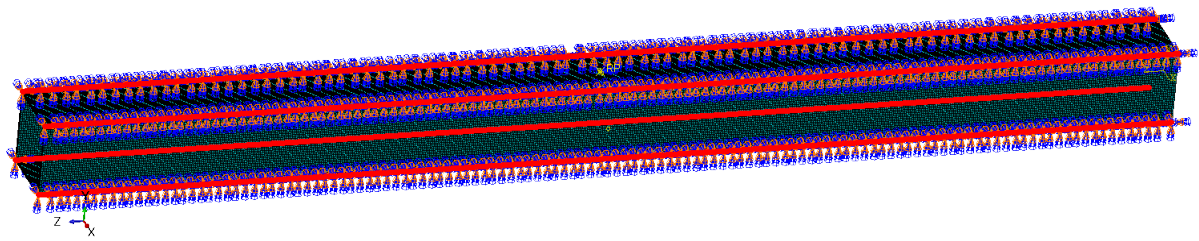
To compare the results obtained from the two boundary condition approaches shown in Fig. 5.33, it is necessary to remove the rigid body movement from the results of the "w/ RC - BC pt *E*" model. This is achieved by assuming that the rigid body movement in any cross-section is represented by the average value of the mean differences calculated at every node of the face between the two models. After subtracting the rigid body movement, the cross-section deformation can be compared with that of the "w/ RC - BC pt *H*" model. The comparison of the cross-section deformation between the two models is presented in Fig. 5.32(b), which shows good agreement between the models.

In summary, these analyses indicate that modeling the tubular column with rounded corners and applying a fully fixed boundary condition on the nodes along the angle bisector of the rounded corner throughout the column height can effectively eliminate rigid body movement. The final configuration of the BCs applied to the tubular column is illustrated in Fig. 5.36. Furthermore, in addition to these BCs, the socket faces, through their RP, are restrained against in-plane rotations.

The generation of Abaqus models, such as those illustrated earlier and applied in the current study, can be readily accomplished using the "abaqTCphd" Abaqus RSG plugin, which was developed by the author and is publicly accessible on GitHub [210]. In addition, a video tutorial demonstrating the usage of this plugin is accessible on YouTube [211].

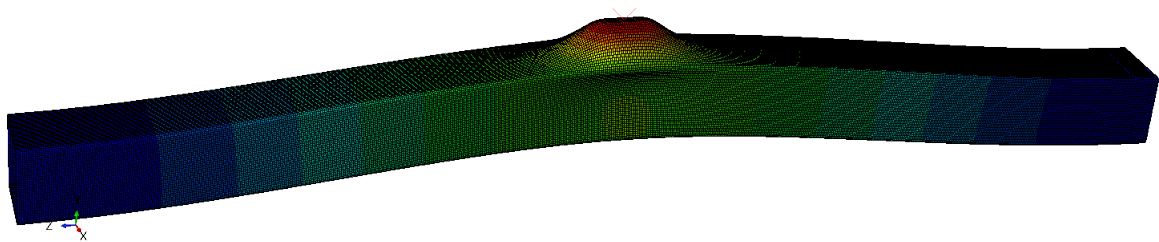


(a) w/ RC - BC pt *E*

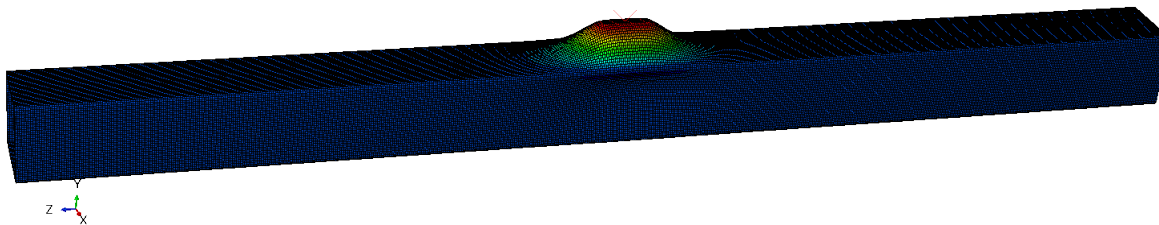


(b) w/ RC - BC pt *H*

Figure 5.33: Applied BC.



(a) w/ RC - BC pt *E*



(b) w/ RC - BC pt *H*

Figure 5.34: Deformed tube in 3D using different BC: U magnitude.

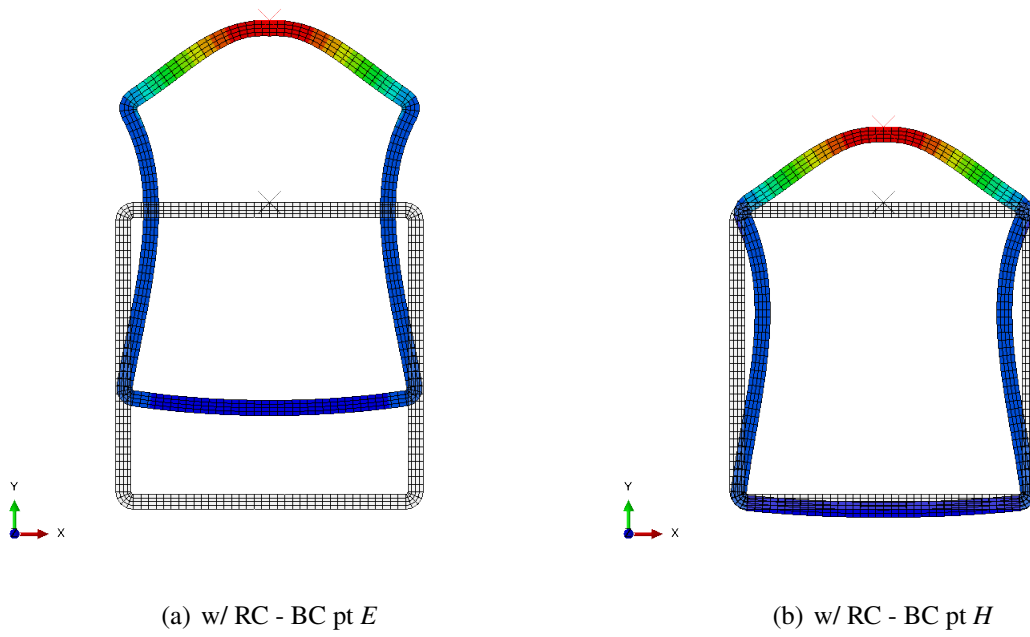


Figure 5.35: Deformed tube in 2D in section W0 using different BC.

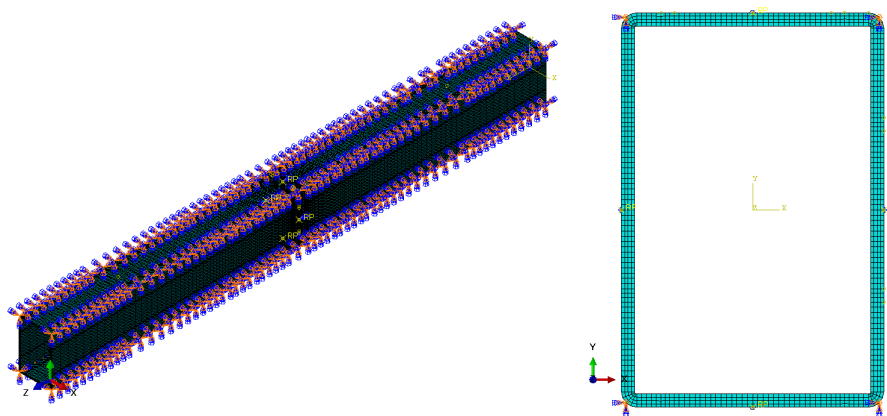


Figure 5.36: Final BC applied to the tubular column.

Table 5.9: Method for results comparison: case examples.

Abaqus		OpenSees	
SHS-m01-SC01	(1)	vs.	HS-EFM-R0-m01-SC01
			HS-EFM-R1-m01-SC01
			PS-EFM-R0-m01-SC01
			PS-EFM-R1-m01-SC01
RHS-m01-V01-SC01	(1)	vs.	HR-EFM-IF-R0-m01-V01-SC01
			HR-EFM-IF-R1-m01-V01-SC01
			HR-EFM-IEq-R0-m01-V01-SC01
			HR-EFM-IEq-R1-m01-V01-SC01
			PR-EFM-IF-R0-m01-V01-SC01
			PR-EFM-IF-R1-m01-V01-SC01
			PR-EFM-IEq-R0-m01-V01-SC01
			PR-EFM-IEq-R1-m01-V01-SC01

5.4.4 Comparison of results

As can be observed from the finite element networks presented in Figs. 5.13, 5.14, 5.17 and 5.18, the models in OpenSees outnumber the models in Abaqus. This phenomenon occurs because the analytical definition of the beam-to-column joint finite element's components allows for greater parameter variation. As a result, four and eight models are developed in OpenSees for each model in Abaqus for the SHS and RHS, respectively. The method for comparing the results is shown in Tab. 5.9 for a randomly picked LP and SC combination.

The results obtained with Abaqus and OpenSees for cases PS-EFM-R1 and PR-EFM-IF-R1 are presented in Tab. 5.10 and Tab. 5.12, respectively, in terms of ε_2 computed according to Eq. (5.58). These tables demonstrate that, in most cases, there is an apparent significant difference in the values of the approximation error between Abaqus and OpenSees. For the SHS case, these differences range from 0.02 (m04-VnVp-SC02) to 0.97 (m04-H-SC04), while for the RHS case, they range from 0.02 (m02-V02-SC03) to 0.73 (m02-H01-SC04). The primary reason for these differences is likely the formulation used to define the tube components' stiffness, specifically the NGM (Section 5.3). However, to the author's best knowledge, currently, there is no other more adequate procedure to define the stiffness of the tube components. The results for the other cases are presented in Appendix H in Tabs. H.2 to H.11.

An alternative method for comparing the results between the Abaqus and OpenSees models is to extract the out-of-plane displacements from the RP of each face individually and plot them against each other. Therefore, these results are plotted for the PS-EFM-R1 and PR-EFM-IF-R1 cases in Fig. 5.37 and Fig. 5.38, respectively, where the names and directions of the column faces are the ones that are

Table 5.10: Results: PS-EFM-R1.

LP	SC	ε_2	LP	SC	ε_2	LP	SC	ε_2
m01	SC01	0.18	m02-H	SC03	0.38	m04-H	SC01	0.17
m01	SC02	0.14	m02-H	SC04	0.67	m04-H	SC02	0.22
m01	SC03	0.30	m02-V	SC01	0.10	m04-H	SC03	0.38
m01	SC04	0.69	m02-V	SC02	0.08	m04-H	SC04	0.67
m02-CH	SC01	0.10	m02-V	SC03	0.30	m04-V	SC01	0.22
m02-CH	SC02	0.11	m02-V	SC04	0.69	m04-V	SC02	0.25
m02-CH	SC03	0.30	m03-H	SC01	0.16	m04-V	SC03	0.37
m02-CH	SC04	0.69	m03-H	SC02	0.20	m04-V	SC04	0.62
m02-CV	SC01	0.17	m03-H	SC03	0.53	m04-VnVp	SC01	0.10
m02-CV	SC02	0.22	m03-H	SC04	0.75	m04-VnVp	SC02	0.02
m02-CV	SC03	0.38	m03-V	SC01	0.15	m04-VnVp	SC03	0.30
m02-CV	SC04	0.67	m03-V	SC02	0.17	m04-VnVp	SC04	0.69
m02-H	SC01	0.17	m03-V	SC03	0.35			
m02-H	SC02	0.22	m03-V	SC04	0.66			

Table 5.11: R^2 for each column face: RHS.

EFM	radius	face A	face B	face C	face D
HR-EFM-IF	R0	0.73	0.85	0.75	0.85
HR-EFM-IEq	R0	0.75	0.83	0.77	0.83
PR-EFM-IF	R0	0.74	0.81	0.76	0.81
PR-EFM-IEq	R0	0.80	0.75	0.82	0.77
HR-EFM-IF	R1	0.95	0.96	0.94	0.96
HR-EFM-IEq	R1	0.95	0.93	0.95	0.94
PR-EFM-IF	R1	0.94	0.97	0.93	0.97
PR-EFM-IEq	R1	0.94	0.96	0.92	0.96

Table 5.12: Results: PR-EFM-IF-R1.

LP	SC	ε_2	LP	SC	ε_2	LP	SC	ε_2
m01-V01	SC01	0.29	m02-H01	SC04	0.73	m03-V01	SC03	0.27
m01-V01	SC02	0.25	m02-H02	SC01	0.04	m03-V01	SC04	0.35
m01-V01	SC03	0.18	m02-H02	SC02	0.07	m03-V02	SC01	0.26
m01-V01	SC04	0.52	m02-H02	SC03	0.15	m03-V02	SC02	0.18
m01-V02	SC01	0.26	m02-H02	SC04	0.24	m03-V02	SC03	0.06
m01-V02	SC02	0.16	m02-V01	SC01	0.20	m03-V02	SC04	0.18
m01-V02	SC03	0.10	m02-V01	SC02	0.18	m04-H	SC01	0.09
m01-V02	SC04	0.23	m02-V01	SC03	0.18	m04-H	SC02	0.13
m02-CH01	SC01	0.24	m02-V01	SC04	0.52	m04-H	SC03	0.21
m02-CH01	SC02	0.15	m02-V02	SC01	0.26	m04-H	SC04	0.31
m02-CH01	SC03	0.12	m02-V02	SC02	0.16	m04-V	SC01	0.23
m02-CH01	SC04	0.30	m02-V02	SC03	0.02	m04-V	SC02	0.20
m02-CH02	SC01	0.24	m02-V02	SC04	0.23	m04-V	SC03	0.11
m02-CH02	SC02	0.15	m03-H01	SC01	0.20	m04-V	SC04	0.11
m02-CH02	SC03	0.12	m03-H01	SC02	0.18	m04-VnVp01	SC01	0.24
m02-CH02	SC04	0.30	m03-H01	SC03	0.20	m04-VnVp01	SC02	0.14
m02-CV	SC01	0.17	m03-H01	SC04	0.28	m04-VnVp01	SC03	0.07
m02-CV	SC02	0.16	m03-H02	SC01	0.10	m04-VnVp01	SC04	0.30
m02-CV	SC03	0.21	m03-H02	SC02	0.10	m04-VnVp02	SC01	0.24
m02-CV	SC04	0.28	m03-H02	SC03	0.17	m04-VnVp02	SC02	0.14
m02-H01	SC01	0.21	m03-H02	SC04	0.29	m04-VnVp02	SC03	0.07
m02-H01	SC02	0.26	m03-V01	SC01	0.15	m04-VnVp02	SC04	0.30
m02-H01	SC03	0.43	m03-V01	SC02	0.17			

Table 5.13: R^2 for each column face: SHS.

EFM	radius	face A	face B	face C	face D
HS-EFM	R0	0.86	0.88	0.70	0.70
PS-EFM	R0	0.86	0.88	0.70	0.70
HS-EFM	R1	0.97	0.97	0.92	0.94
PS-EFM	R1	0.97	0.97	0.92	0.94

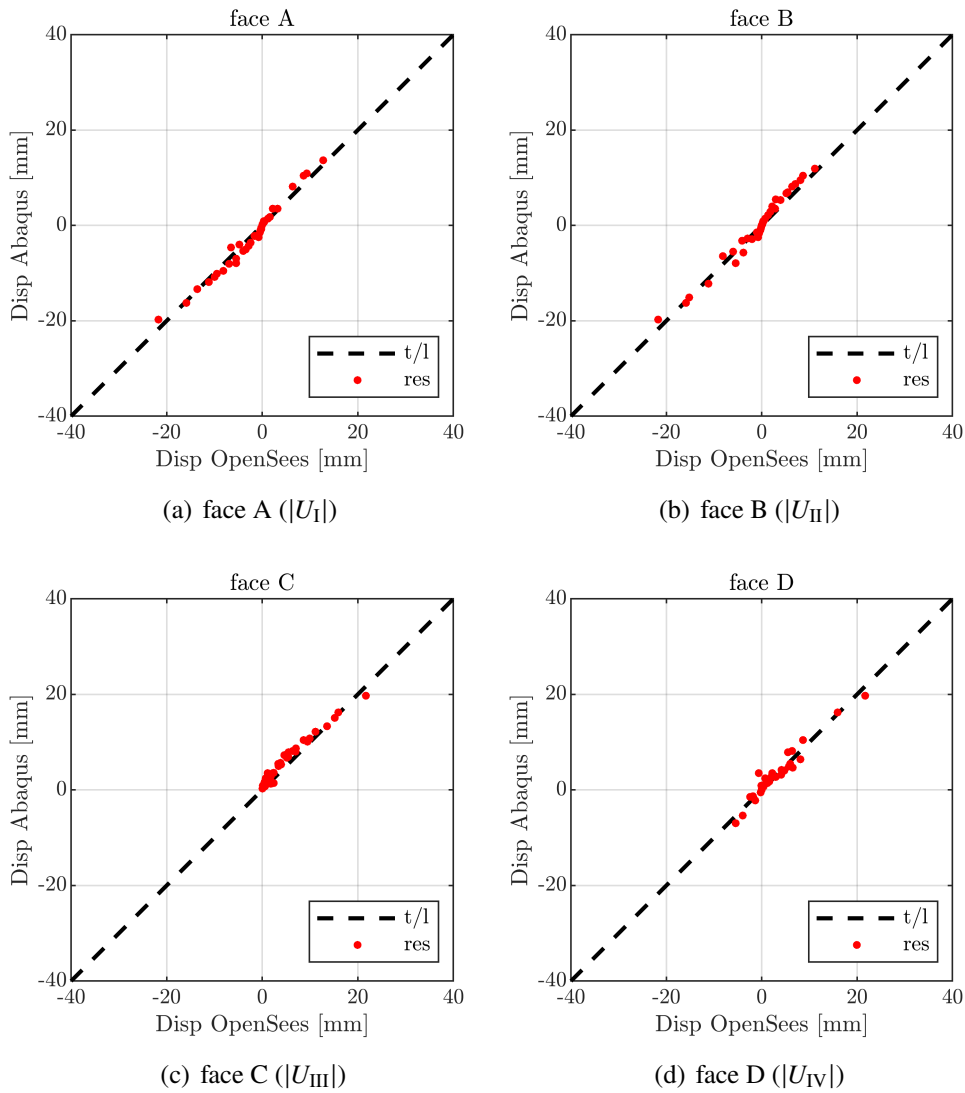


Figure 5.37: PS-EFM-R1.

presented in Fig. 3.3 and in Fig. 3.6(a), respectively. In an "ideal" scenario, the two software would provide identical displacements, and the corresponding dots would be distributed along the line that passes through the origin and has a unitary gradient, $y = x$ (i.e., black dashed line: "t/l"). Although this is not the case, these figures indicate that the displacements obtained from OpenSees using the Inno3DPnPJoint element are in good agreement with the ones obtained from Abaqus.

The plots for the remaining cases are presented in Appendix H in Fig. H.1 to H.10 and provide similar conclusions.

The correlation between the displacement data sets and the linear equation of the line is presented in Tab. 5.13 and Tab. 5.11 for the SHS and RHS, respectively, for every column face individually. The coefficients of determination from Tab. 5.13 and Tab. 5.11 indicate that a higher correlation degree is achieved in the R1 case in both SHS and RHS cases. Furthermore, in the SHS case, both HS-EFM and PS-EFM output the same results. As a result, the joint size (i.e., the socket's size) does not influence

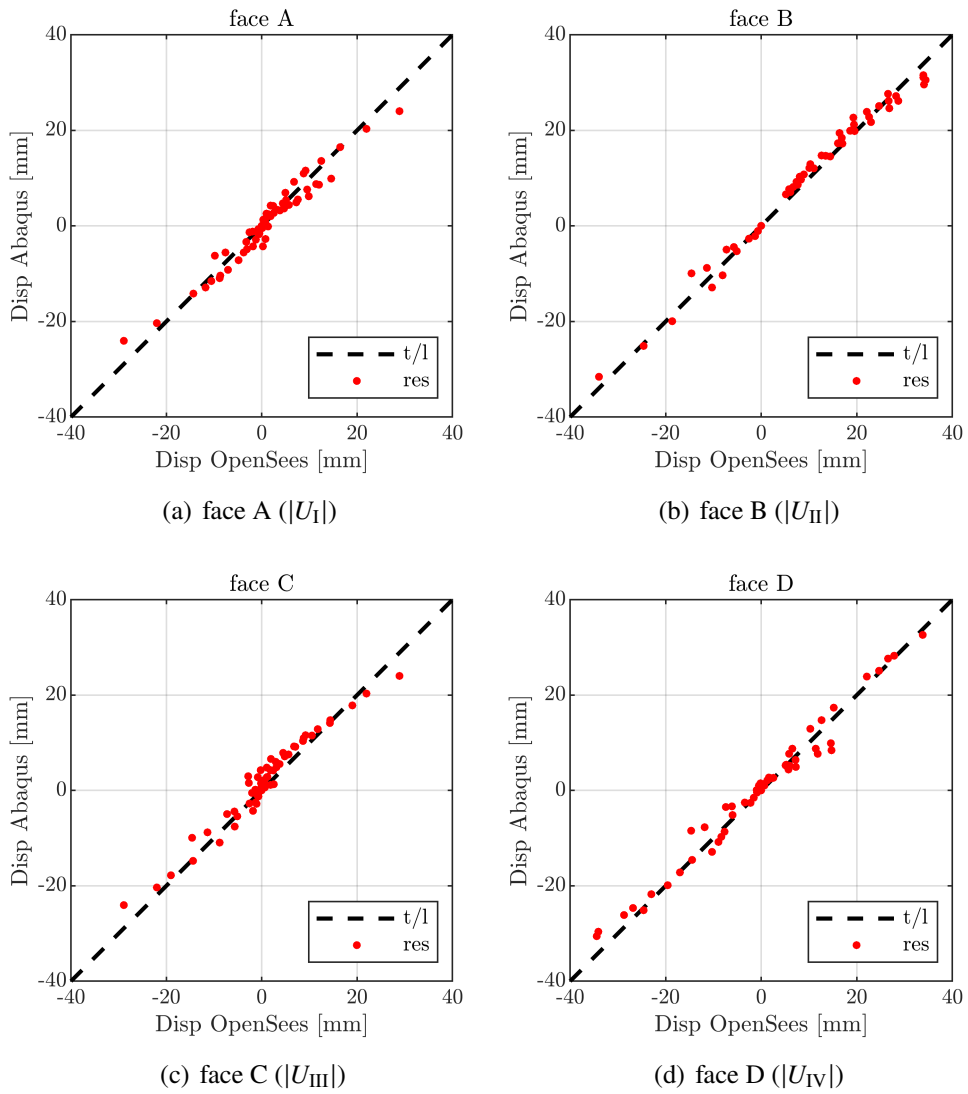


Figure 5.38: PR-EFM-IF-R1.

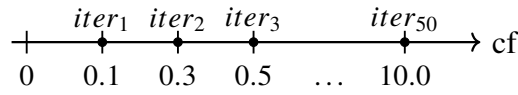


Figure 5.39: Schematic representation of the iterative process for SHS.

the results (Tab. 5.13). Additionally, the RHS cases show a higher correlation degree when using IEq with R0, and IF with R1 (Tab. 5.11).

Analyzing the results through the coefficient of determination provides a broader and more accurate understanding of the displacement spectrum. Therefore, the obtained differences are assumed to be within an acceptable range of error. Although it is not the scope of this research, two analytical methods aiming to improve the accuracy of the results are presented in the following sections.

5.4.5 Calibration of the effective stiffness

5.4.5.1 Method 1: ideal correction factor based correction

5.4.5.1.1 Ideal correction factor

One method to enhance the accuracy of the results is to adjust the initial stiffness, S_i , obtained from the NGM, by a *correction factor*, cf , such that the error is minimized. To achieve this, an iterative process is implemented in which the stiffnesses defined in OpenSees for the tube components are obtained by dividing the initial stiffness by a correction factor.

In the iterative procedure, the correction factor, cf , varies from 0.1 to 10 with a step of 0.2. These values were determined through trial and error. A schematic representation of the iterative processes employed for the SHS and RHS are shown in Fig. 5.39 and Fig. 5.40, respectively. The approximation error, ε_2 (Eq.(5.58)), is calculated and stored at each iteration, allowing for the determination of the minimum value at the end of the process. This minimum value is referred to as the *ideal approximation error*, $\varepsilon_{2,i}$, and is obtained for an *ideal correction factor*, cf_i , as shown in Eq.(5.61).

$$\varepsilon_{2,i} = \min \left(\frac{\sum_{face=A}^D \left| \left(\delta_{face}^{Abaqus} - \delta_{face}^{OpenSees} \left(\frac{S_i}{cf} \right) \right) \right|}{\sum_{face=A}^D \left| \delta_{face}^{Abaqus} \right|} \right) \quad (5.61)$$

For the RHS the displacement in OpenSees from Eq. (5.61) is expressed as a function of $S_{i,1}$ (Eq. (5.33)) and $S_{i,2}$ (Eq. (5.34)), as shown in Eq. (5.62).

$$\delta_{face}^{OpenSees} \left(\frac{S_{i,1}}{cf_{i,1}}, \frac{S_{i,2}}{cf_{i,2}} \right) \quad (5.62)$$

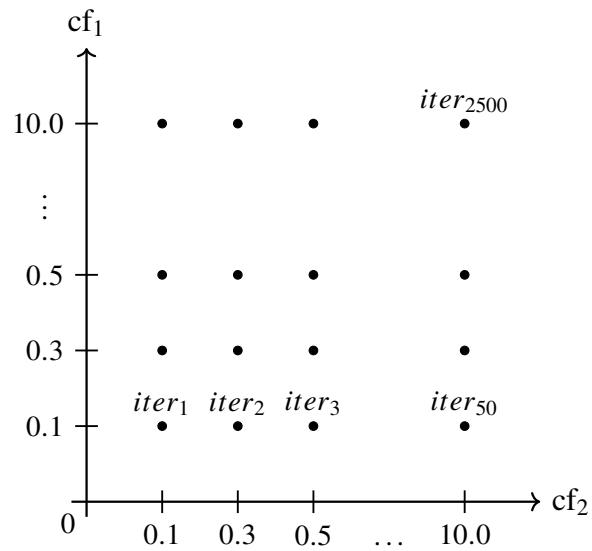


Figure 5.40: Schematic representation of the iterative process for RHS.

This calculation is performed for all cases, and the results for PS-EFM-R1 and PR-EFM-IF-R1 are presented in Tab. 5.14 and Tab. 5.15, respectively. The ideal correction factor ranges from 0.1 to 3.1 in the SHS and from 0.1 to 9.9 in the RHS. In conclusion, it spans the entire analyzed domain.

Table 5.14: PS-EFM-R1: cf_i and $\varepsilon_{2,i}$.

LP	SC	cf_i	$\varepsilon_{2,i}$	LP	SC	cf_i	$\varepsilon_{2,i}$
m01	01	0.9	0.18	m03-H	01	1.1	0.12
m01	02	1.1	0.14	m03-H	02	1.1	0.13
m01	03	1.5	0.06	m03-H	03	1.1	0.49
m01	04	3.1	0.05	m03-H	04	2.3	0.49
m02-CH	01	0.9	0.13	m03-V	01	1.1	0.14
m02-CH	02	1.1	0.08	m03-V	02	1.1	0.12
m02-CH	03	1.5	0.04	m03-V	03	1.5	0.03
m02-CH	04	3.1	0.03	m03-V	04	9.9	0.67
m02-CV	01	1.3	0.08	m04-H	01	1.3	0.08
m02-CV	02	1.3	0.02	m04-H	02	1.3	0.01
m02-CV	03	1.7	0.06	m04-H	03	9.9	0.38
m02-CV	04	2.9	0.06	m04-H	04	9.9	0.67
m02-H	01	1.3	0.08	m04-V	01	1.3	0.02
m02-H	02	1.3	0.01	m04-V	02	1.3	0.03
m02-H	03	1.7	0.06	m04-V	03	1.5	0.05

Continued on next page ...

Table 5.14: PS-EFM-R1: cf_i and $\varepsilon_{2,i}$. (cont.).

LP	SC	cf_i	$\varepsilon_{2,i}$	LP	SC	cf_i	$\varepsilon_{2,i}$
m02-H	04	2.9	0.03	m04-V	04	2.7	0.03
m02-V	01	0.9	0.10	m04-VnVp	01	0.9	0.01
m02-V	02	1.1	0.08	m04-VnVp	02	1.1	0.08
m02-V	03	1.5	0.04	m04-VnVp	03	1.5	0.04
m02-V	04	3.1	0.04	m04-VnVp	04	3.1	0.03

Table 5.15: PR-EFM-IF-R1: $cf_{i,1}$, $cf_{i,2}$ and $\varepsilon_{2,i}$.

LP	SC	$cf_{i,1}$	$cf_{i,2}$	$\varepsilon_{2,i}$	LP	SC	$cf_{i,1}$	$cf_{i,2}$	$\varepsilon_{2,i}$
m01-V01	01	1.5	0.5	0.11	m02-V02	03	1.3	0.9	0.01
m01-V01	02	1.7	0.5	0.07	m02-V02	04	9.9	0.7	0.04
m01-V01	03	2.5	0.5	0.06	m03-H01	01	1.7	0.7	0.14
m01-V01	04	6.1	0.7	0.05	m03-H01	02	2.1	0.7	0.12
m01-V02	01	0.5	1.1	0.08	m03-H01	03	2.7	0.7	0.07
m01-V02	02	0.7	1.1	0.07	m03-H01	04	6.7	0.7	0.07
m01-V02	03	3.3	0.7	0.06	m03-H02	01	0.5	1.3	0.08
m01-V02	04	2.7	0.9	0.07	m03-H02	02	1.3	0.9	0.08
m02-CH01	01	1.1	0.7	0.13	m03-H02	03	1.9	0.9	0.05
m02-CH01	02	0.7	1.1	0.11	m03-H02	04	5.7	0.7	0.02
m02-CH01	03	1.5	0.9	0.07	m03-V01	01	1.3	1.1	0.07
m02-CH01	04	6.9	0.7	0.05	m03-V01	02	1.5	1.1	0.07
m02-CH02	01	1.1	0.7	0.13	m03-V01	03	2.3	0.9	0.03
m02-CH02	02	0.7	1.1	0.11	m03-V01	04	4.7	0.7	0.04
m02-CH02	03	1.5	0.9	0.07	m03-V02	01	1.9	0.7	0.09
m02-CH02	04	6.9	0.7	0.05	m03-V02	02	2.3	0.7	0.05
m02-CV	01	1.7	0.7	0.10	m03-V02	03	3.5	0.7	0.05
m02-CV	02	1.9	0.7	0.10	m03-V02	04	2.3	0.9	0.03
m02-CV	03	2.5	0.7	0.09	m04-H	01	1.5	0.9	0.01
m02-CV	04	5.7	0.7	0.09	m04-H	02	1.7	0.9	0.02
m02-H01	01	0.9	2.5	0.00	m04-H	03	2.1	0.9	0.02

Continued on next page ...

Table 5.15: PR-EFM-IF-R1: $cf_{i,1}$, $cf_{i,2}$ and $\varepsilon_{2,i}$ (cont.).

LP	SC	$cf_{i,1}$	$cf_{i,2}$	$\varepsilon_{2,i}$	LP	SC	$cf_{i,1}$	$cf_{i,2}$	$\varepsilon_{2,i}$
m02-H01	02	0.7	7.7	0.00	m04-H	04	5.5	0.7	0.01
m02-H01	03	1.1	4.9	0.00	m04-V	01	1.9	0.7	0.09
m02-H01	04	2.5	8.5	0.00	m04-V	02	2.1	0.7	0.10
m02-H02	01	0.9	1.1	0.00	m04-V	03	0.1	1.5	0.08
m02-H02	02	7.5	0.5	0.00	m04-V	04	2.1	0.9	0.02
m02-H02	03	2.1	0.9	0.00	m04-VnVp01	01	0.9	0.7	0.03
m02-H02	04	5.5	0.7	0.00	m04-VnVp01	02	1.3	0.7	0.03
m02-V01	01	1.3	0.5	0.06	m04-VnVp01	03	1.3	0.9	0.03
m02-V01	02	1.5	0.5	0.03	m04-VnVp01	04	8.7	0.7	0.01
m02-V01	03	2.1	0.7	0.05	m04-VnVp02	01	0.9	0.7	0.03
m02-V01	04	6.3	0.7	0.04	m04-VnVp02	02	1.3	0.7	0.03
m02-V02	01	0.5	1.1	0.02	m04-VnVp02	03	1.3	0.9	0.03
m02-V02	02	0.9	0.9	0.05	m04-VnVp02	04	8.7	0.7	0.01

5.4.5.1.2 Global correction factor

Since it is impractical to have a correction factor for each case, an *average ideal correction factor*, cf_a , is proposed to reduce the dimension of the data set and the high spread of the ideal correction factors. This factor is obtained by averaging out all cases in terms of LPs. The obtained average ideal correction factors are presented in Tab. 5.16 and Tab. 5.17 for SHS and RHS, respectively.

At this point, the calculation could be continued for each case separately. However, if a correction factor as general and independent of the EFM as possible is desired, an additional step is necessary. A *global correction factor*, cf_p is calculated by taking the mathematical average of the ideal average correction factors presented in Tab. 5.16 and Tab. 5.17, respectively. This global correction factor is defined for each SC and radius combination, as shown in Tab. 5.18 and Tab. 5.19 for the SHS and RHS, respectively. These factors could be directly obtained from the ideal correction factors, eliminating the need for the previously described step of calculating the average ideal correction factor. The data values from Tab. 5.18 and Tab. 5.19 suggest a clear correlation trend between the global correction factors and the width of the socket.

Table 5.16: Average ideal correction factor, cf_a , for SHS.

EFM	radius	SC01	SC02	SC03	SC04
HS-EFM	R0	0.78	0.80	0.88	1.02
HS-EFM	R1	0.78	0.80	0.88	1.02
PS-EFM	R0	1.10	1.18	1.52	2.90
PS-EFM	R1	1.10	1.18	1.52	2.90

Table 5.17: Average ideal correction factors, $cf_{a,1}$ and $cf_{a,2}$, for RHS.

EFM	radius	$cf_{a,1}$				$cf_{a,2}$			
		SC01	SC02	SC03	SC04	SC01	SC02	SC03	SC04
HR-EFM-IF	R0	0.90	0.77	0.77	1.21	0.91	0.98	1.21	1.23
HR-EFM-IEq	R0	1.37	2.29	1.45	2.81	1.88	1.08	2.06	2.38
PR-EFM-IF	R0	0.82	0.94	1.19	1.37	0.90	0.96	1.12	0.98
PR-EFM-IEq	R0	1.56	1.46	3.95	1.69	1.99	1.92	0.51	4.84
HR-EFM-IF	R1	1.46	1.55	1.79	3.19	0.96	1.26	1.10	2.06
HR-EFM-IEq	R1	2.43	2.48	2.83	4.51	2.68	2.78	2.97	4.17
PR-EFM-IF	R1	1.18	1.76	1.95	5.70	0.92	1.21	1.09	1.19
PR-EFM-IEq	R1	1.84	1.35	2.52	3.82	1.48	1.91	2.06	1.36

Table 5.18: Global correction factor, cf_p : SHS.

radius	SC01	SC02	SC03	SC04
R0	0.78	0.80	0.88	1.02
R1	1.10	1.18	1.52	2.90

Table 5.19: Global correction factor, $cf_{p,1}$ and $cf_{p,2}$: RHS.

radius	$cf_{p,1}$				$cf_{p,2}$			
	SC01	SC02	SC03	SC04	SC01	SC02	SC03	SC04
R0	1.16	1.36	1.84	1.77	1.42	1.24	1.23	2.36
R1	1.73	1.78	2.27	4.31	1.51	1.79	1.81	2.20

5.4.5.1.3 Geometry-related correction factors

Based on the correlation trend observed in Tab. 5.18 and Tab. 5.19 between the global correction factor and the joint geometry, *geometry-related correction factors*, cf_G , were computed. Therefore, an attempt was made to introduce the effect of the adjacent column faces on the analyzed column face by considering the correction factors set by Eq. (5.63) and Eq. (5.64) for the SHS and RHS, respectively. In these equations, the variables L , L_1 , and L_2 represent the dimensions of the adjacent column faces, and b represents the length of the rigid area, as illustrated in Fig. 5.6 or Fig. 5.8.

$$cf_G^{SHS} = var_1 \left(var_2 + \frac{b}{L - 2r} \right) \quad (5.63)$$

$$cf_{G.1}^{RHS} = var_1 \left(var_2 + \frac{b}{L_2 - 2r} \right) \quad (5.64)$$

$$cf_{G.2}^{RHS} = var_1 \left(var_2 + \frac{b}{L_1 - 2r} \right)$$

The unknown parameters var_1 and var_2 are determined through an iterative method, where both variables range from 0.05 to 2, with a step of 0.05 similar to the procedure described in Section 5.4.5.1.1, but with the objective of minimizing the difference between the global correction factor, cf_p , and the geometry-related correction factor, cf_G , according to Eq. (5.65) and Eq. (5.66).

$$\varepsilon_3^{SHS} = \min \left(\left| \sum_{i=1}^4 (cf_{p,i} - cf_G^{SHS})_{SC0i} \right| \right) \quad (5.65)$$

$$\varepsilon_3^{RHS} = \min \left(\left| \sum_{i=1}^4 (cf_{p,i} - cf_{G.1}^{RHS} + cf_{p,i} - cf_{G.2}^{RHS})_{SC0i} \right| \right) \quad (5.66)$$

The determined values for the geometry-related correction factors for the SHS and RHS are presented in Tab. 5.20 and Tab. 5.21, respectively. After analyzing the results, it was concluded that the values for var_1 and var_2 should be given by Eq. (5.67). As such, if an improvement in results is desired using an analytical approximation parameter based on geometry-related correction factors, the initial stiffness from the NGM could be expressed for the SHS by Eq. (5.68), and for the RHS by Eq. (5.69) and Eq. (5.70), in conjunction with Eq. (5.67).

Table 5.20: Geometry-related correction factors: ideal values for var_1 and var_2 in SHS.

cross-section	radius	var_1	var_2
SHS	R0	1.70	0.15
SHS	R1	1.95	0.45

Table 5.21: Geometry-related correction factors: ideal values for var_1 and var_2 in RHS.

cross-section	radius	var_1	var_2
RHS	R0	0.70	1.90
RHS	R1	0.80	1.95

$$(var_1; var_2) = \begin{cases} (1.85; 0.30) & , \text{ if } \frac{L_1}{L_2} = 1 \\ (0.80; 1.90) & , \text{ otherwise} \end{cases} \quad (5.67)$$

$$S_i = \frac{16 E t_c^3}{L^2} \frac{\alpha + (1 - \beta) \tan \theta}{(1 - \beta)^3 + \frac{10.4 (k_1 - k_2 \beta)}{\mu^2}} \frac{1}{cf_G^{SHS}} \quad (5.68)$$

$$S_{i.1} = \frac{16 E t_c^3}{L_1^2} \frac{\alpha_1 + (1 - \beta_1) \tan \theta_1}{(1 - \beta_1)^3 + \frac{10.4 (k_1 - k_2 \beta_1)}{\mu_1^2}} \frac{1}{cf_{G.1}^{RHS}} \quad (5.69)$$

$$S_{i.2} = \frac{16 E t_c^3}{L_2^2} \frac{\alpha_2 + (1 - \beta_2) \tan \theta_2}{(1 - \beta_2)^3 + \frac{10.4 (k_1 - k_2 \beta_2)}{\mu_2^2}} \frac{1}{cf_{G.2}^{RHS}} \quad (5.70)$$

Finally, to verify the effectiveness of the geometry-related correction factors, calculations were conducted for all cases, and the out-of-plane displacements for PS-EFM-R1 and PR-EFM-IF-R1 cases are shown in Fig. 5.41 and Fig. 5.42, respectively. In each graph, two sets of data from OpenSees are plotted: (i) red dots "res" – using Eq. (5.21) for SHS, and Eq. (5.33) and Eq. (5.34) for the RHS, respectively; and (ii) green dots "prop" – using Eq. (5.68) for the SHS, and Eq. (5.69) and Eq. (5.70) for the RHS, respectively. The results indicate that the proposed correction factors improve the accuracy of the calculations for SHS but not RHS.

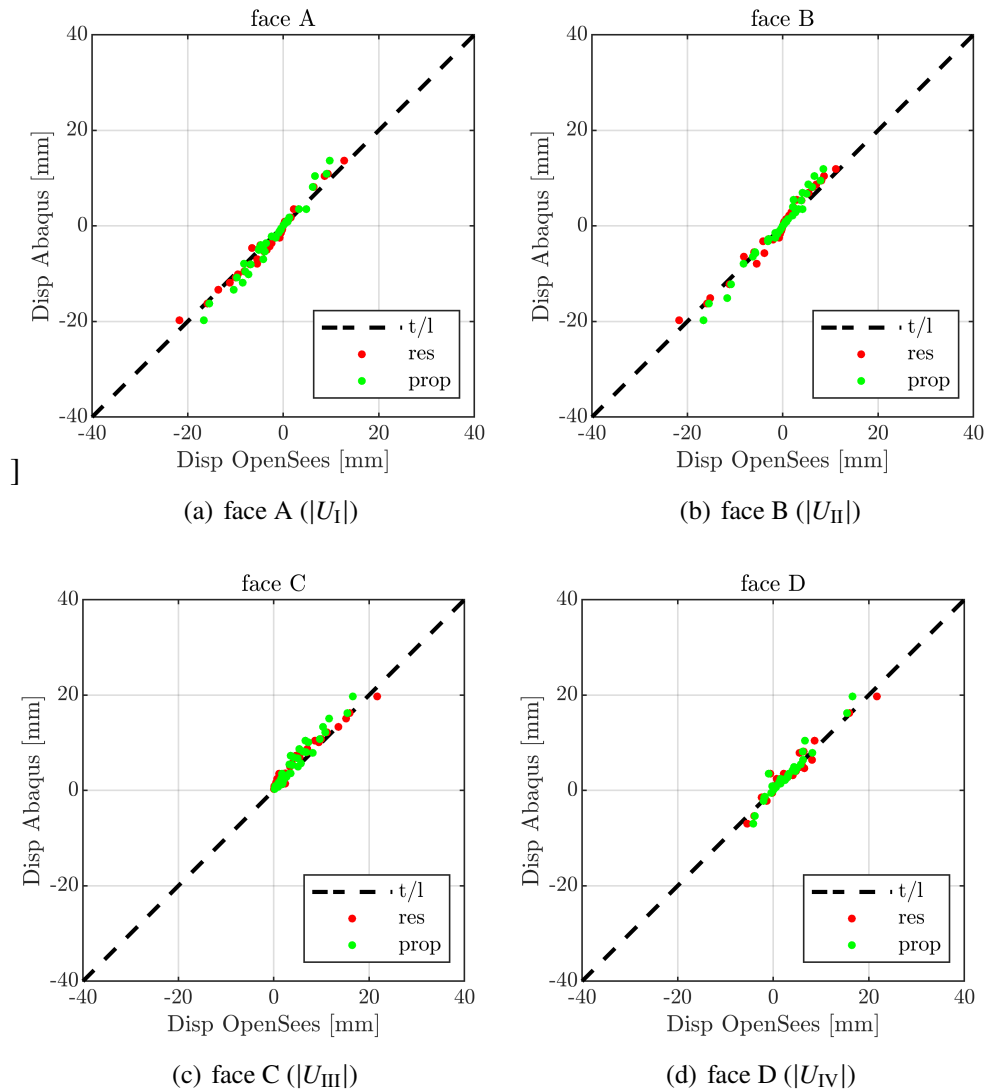


Figure 5.41: PS-EFM-R1 - Method 1.

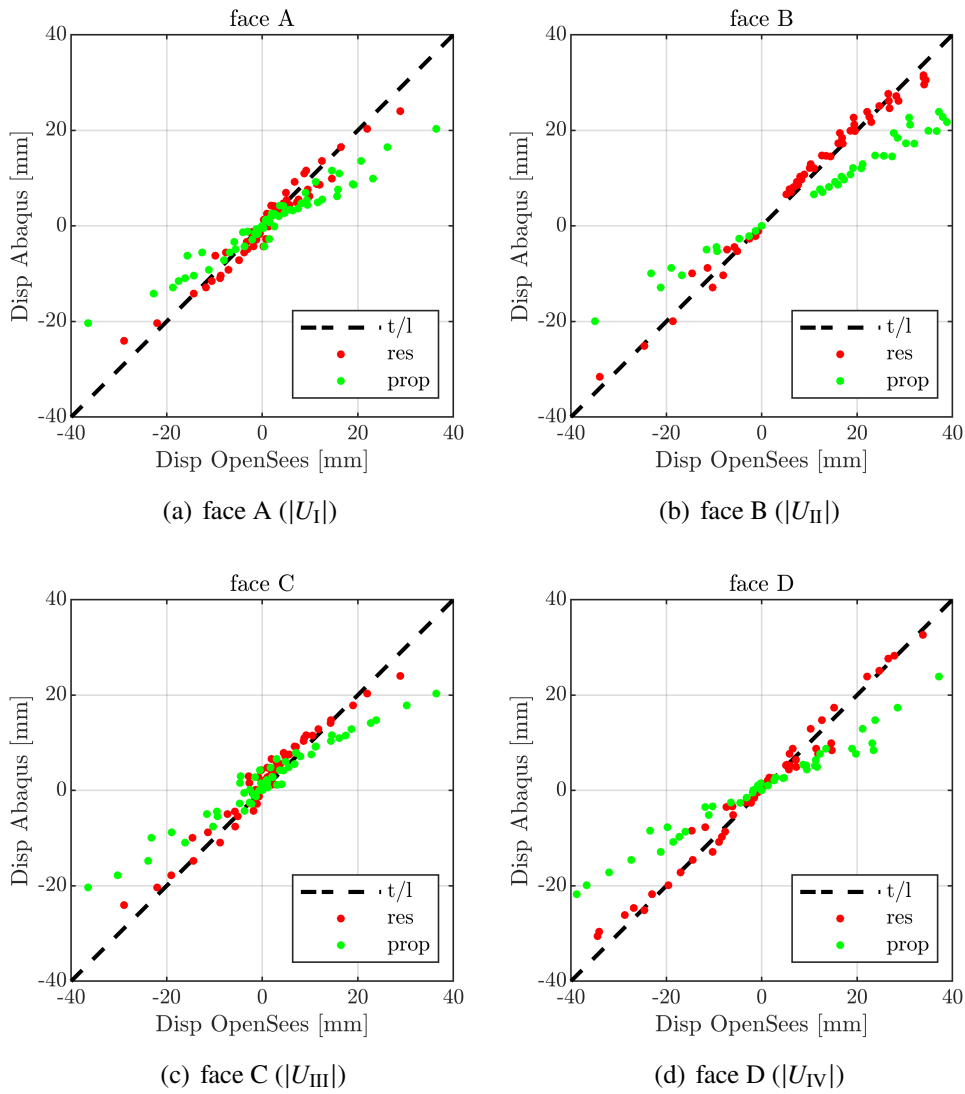


Figure 5.42: PR-EFM-IF-R1 - Method 1.

Table 5.22: R^2 for each column face: SHS-R0.

EFM	radius	face A	face B	face C	face D
HS-EFM	R0	0.98	0.98	0.95	0.94
PS-EFM	R0	0.98	0.98	0.95	0.94
HS-EFM	R1	0.91	0.91	0.76	0.89
PS-EFM	R1	0.91	0.91	0.76	0.89

5.4.5.2 Method 2: matching displacements based correction

As the previous section shows, using an ideal correction factor and then introducing a global correction factor is ineffective. This is likely because the large data set cannot be averaged to provide a single parameter that works well for all EFMs, radii, and SCs.

Therefore, in this section, a new method is developed where the displacements are corrected directly without identifying any correction factor. However, the geometry-related correction factor is still used to adjust the values of the initial stiffnesses (Eq. (5.63) and Eq. (5.64)). Nevertheless, the values of the two parameters, var_1 and var_2 , are determined differently.

In this method, var_1 is assigned a unitary value (i.e., $var_1 = 1$), and var_2 is determined through an iterative process varying 0.1 to 1, with a step of 0.1 similar to the process described in Section 5.4.5.1.1. At each iteration, the coefficient of determination, R^2 (Eq. (5.60)), is calculated. After analyzing the 10 sets of values resulting from the iteration process, it was found that var_2 should be expressed by Eq. (5.71).

$$(var_1; var_2) = \begin{cases} (1; 0.6) & , \text{ for R0} \\ (1; 0.8) & , \text{ for R1} \end{cases} \quad (5.71)$$

The results for the correlation factor for R0 are presented in Tab. 5.22 and Tab. 5.23, and for R1 in Tab. 5.24 and Tab. 5.25. The out-of-plane displacements for the PS-EFM-R1 and PR-EFM-IF-R1 cases are shown in Fig. 5.43 and Fig. 5.44, respectively. In each graph, two sets of data from OpenSees are plotted: (i) red dots "res" – using Eq. (5.21) from SHS, and Eq. (5.33) and Eq. (5.34) for the RHS, respectively; and (ii) green dots "prop" – using Eq. (5.68) for the SHS, and Eq. (5.69) and Eq. (5.70) for the RHS, respectively in conjunction with Eq. (5.71). The results indicate that the proposed correction factors in this method improve the accuracy of the calculations for both SHS and RHS.

Table 5.23: R^2 for each column face: RHS-R0.

EFM	radius	face A	face B	face C	face D
HR-EFM-IF	R0	0.97	0.98	0.96	0.98
HR-EFM-IEq	R0	0.96	0.98	0.95	0.98
PR-EFM-IF	R0	0.96	0.96	0.95	0.96
PR-EFM-IEq	R0	0.96	0.95	0.95	0.96
HR-EFM-IF	R1	0.93	0.93	0.91	0.95
HR-EFM-IEq	R1	0.93	0.90	0.91	0.93
PR-EFM-IF	R1	0.92	0.96	0.89	0.97
PR-EFM-IEq	R1	0.90	0.97	0.87	0.98

Table 5.24: R^2 for each column face: SHS-R1.

EFM	radius	face A	face B	face C	face D
HS-EFM	R0	0.89	0.89	0.77	0.76
PS-EFM	R0	0.89	0.89	0.77	0.76
HS-EFM	R1	0.98	0.98	0.93	0.95
PS-EFM	R1	0.98	0.98	0.93	0.95

Table 5.25: R^2 for each column face: RHS-R1.

EFM	radius	face A	face B	face C	face D
HR-EFM-IF	R0	0.82	0.90	0.83	0.89
HR-EFM-IEq	R0	0.82	0.90	0.83	0.90
PR-EFM-IF	R0	0.83	0.82	0.84	0.83
PR-EFM-IEq	R0	0.87	0.77	0.87	0.80
HR-EFM-IF	R1	0.97	0.99	0.95	0.99
HR-EFM-IEq	R1	0.97	0.96	0.95	0.97
PR-EFM-IF	R1	0.96	0.98	0.94	0.97
PR-EFM-IEq	R1	0.95	0.97	0.93	0.97

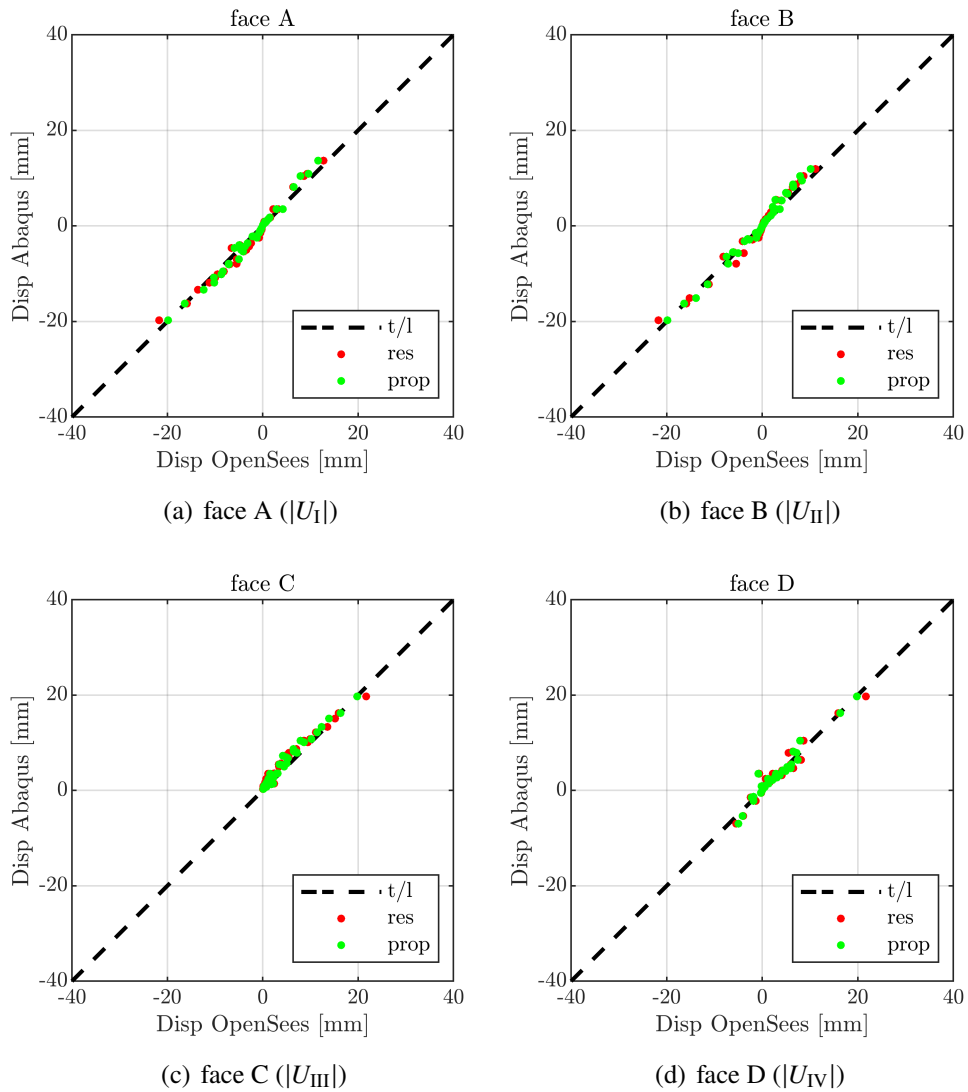


Figure 5.43: PS-EFM-R1 - Method 2.

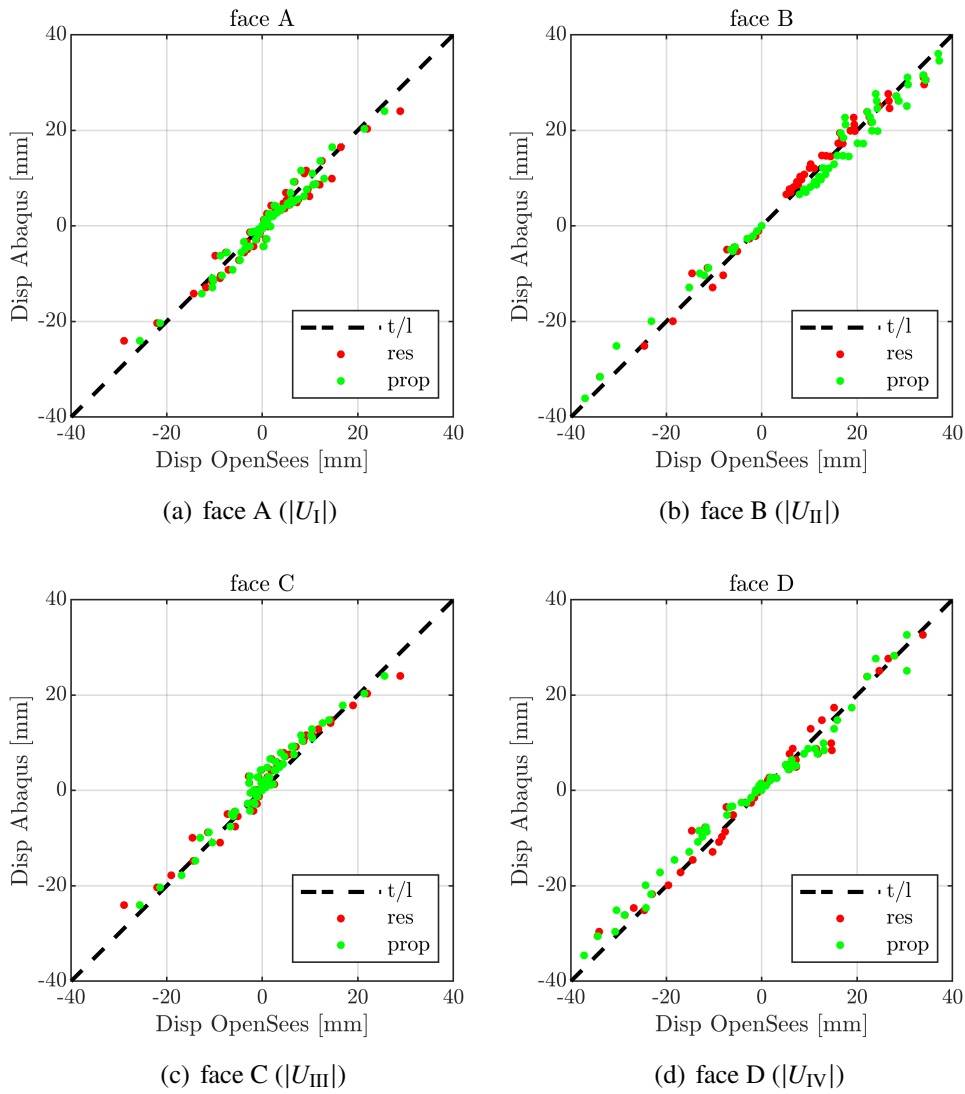


Figure 5.44: PR-EFM-IF-R1 - Method 2.

5.4.5.3 Conclusion

In conclusion, the stiffness definition of the components of the beam-to-column joint finite element implemented in OpenSees was found to be accurate when compared to RFEMs built with Abaqus. The out-of-plane displacements obtained from the two software show good agreements. Although it was not the scope of this research, two analytical methods were presented to improve the accuracy of the results by adjusting the initial stiffness, S_i , from the NGM. While showing better results for the SHS, the first method (Section 5.4.5.1) did not yield good results for RHS; thus, it is not recommended. On the other hand, the second method (Section 5.4.5.2) provided better results for both cross-sections, SHS and RHS.

5.5 Analytical definition of the strength criterion

5.5.1 Introduction

The strength criterion presented in this section for the proposed beam-to-column joint finite element depicted in Fig. 3.13 is also based on the Equivalent Frame-Model (EFM) technique. This strength criterion is a global one because it does not depend on the evaluation of internal forces in a specific component. In the procedures that will be developed for the nonlinear analysis of structures using the beam-to-column joint model (Chapter 6), an alternative strength criterion will be developed that incorporates the traditional approach through the limitation of the internal forces in each component.

5.5.2 General procedure to compute the strength of the components

The strength criterion is established through the definition of equivalent bending strength, M_y , for the frame-elements of the EFMs so that the tube components of the beam-to-column joint element are deemed to be structurally safe if the following equation is fulfilled:

$$|M| \leq |M_y| \quad (5.72)$$

where M is the bending moment in any section of the frame-elements of the EFMs, calculated using analytical expressions that take as input the nodal displacements of the joint model, as described in Section 5.5.6.

The equivalent bending strength of the frame-elements of the EFMs was defined using the Neves-Gomes Model (NGM) outlined in Section 5.3.1. This equivalent bending strength was then adjusted

through a parametric analysis using Refined Finite Element Model(s) (RFEM(s)) developed in Abaqus.

The adjustment process was carried out separately for each EFM and SC combination. Subsequently, a single adjustment factor, α_{min} , was proposed for all the analyzed cases. This adjustment factor was calculated by following the procedure presented below and depicted in Fig. 5.45.

1. development of the RFEM in Abaqus suitable for material nonlinear analysis;
2. definition of the LPs in the joint;
3. incremental application of the LP to the RFEM;
4. identification of the increment y corresponding to the load proportional factor at the beginning of the nonlinear behavior in the relations $F_i - \delta_i$, where F_i and δ_i represent the load applied to the column face i and the out-of-plane displacement of the column face i , respectively;
5. computation of the forces $F_{i,y}$ and out-of-plane displacements $\delta_{i,y}$ corresponding to increment y ;
6. imposition of out-of-plane displacement of the column faces, $\delta_{i,y}$, onto the EFM, as opposed to nodal forces $F_{i,y}$. This approach facilitates the analysis of a specific part of the tube (i.e., a quadrant) and thus simplifies the strength criterion definition;
7. calculation of the bending moments in the predefined critical sections of the EFM, $\mathbf{M}_{crit.s}^{EFM}$;
8. determination the maximum absolute values of the bending moments in the critical sections from all LPs:

$$\mathbf{M}^{EFM} = \max \left(\left| \mathbf{M}_{crit.s}^{EFM} \right| \right) \quad (5.73)$$

9. computation of the equivalent bending strength of the frame-elements of the EFM based on the NGM for the critical sections:

$$\mathbf{M}_y^{EFM} = \left| \mathbf{M}_{y,NGM}^{EFM} \right| \quad (5.74)$$

10. computation of the adjustment factor, $\alpha_{crit.s}^{EFM}$, for the critical sections:

$$\alpha_{crit.s}^{EFM} = \frac{\mathbf{M}^{EFM}}{\mathbf{M}_y^{EFM}} \quad (5.75)$$

11. computation of a maximum adjustment factor, α_{max}^{EFM} , of all critical sections for every EFM and SC combination individually:

$$\alpha_{max}^{EFM} = \max \left(\alpha_{crit.s}^{EFM} \right) \quad (5.76)$$

With the values of α_{max}^{EFM} for each EFM and SC combination, a unique minimum adjustment factor, α_{min} , is computed for all analyzed cases:

$$\alpha_{min} = \min\left(\alpha_{max}^{EFM}\right) \quad (5.77)$$

Finally, the strength criterion defined by Eq. (5.72), expressed in a matrix format that contains the values for all critical sections, becomes:

$$\mathbf{M} \leq \mathbf{M}_y \quad \Rightarrow \quad \mathbf{M}^{EFM} \leq \alpha_{min} \mathbf{M}_y^{EFM} \quad (5.78)$$

The consideration of the maximum value of the adjustment factor specified in Eq. (5.76) guarantees that the section yielded is the one that is being considered for each case. On the other hand, the minimum value of the adjustment factor from Eq. (5.77) provides a conservative limit that ensures safety in all cases.

5.5.3 Critical sections on SEFMs

The bending moment in any section of the frame-elements of the EFMs can be calculated based on the out-of-plane displacements of the quadrant (i.e., 1/4 of EFM) in which the section lies due to the symmetry conditions of the EFMs. For example, the bending moment in section A from Fig. 5.46 can be determined using only the δ_N and δ_E displacements. Accordingly, the analytical computation of bending moments in the sections of the EFM can be performed using the Simplified Equivalent Frame-Models (SEFMs) shown in Fig. 5.47, which only represents a quadrant of the EFMs, where w_1 and w_2 represent the lengths of the non-rigid parts of the frame-elements of the EFMs discussed in Section 5.2.4.

On the other hand, to implement the procedure outlined in Section 5.5.2, it is not necessary to monitor all sections of the SEFM, only the ones where the bending moment may be higher, referred to as *critical sections*. Given that bending moment distributions are linear, the critical sections are located at the ends of the frame-elements elements of the SEFM, as shown in Fig. 5.47. Specifically, sections CA and CB will always produce identical bending moments. However, two sections are considered because their equivalent bending strengths may differ according to the procedure described in Section 5.5.4. Therefore, the vector of bending moments in the critical sections, \mathbf{M}^{EFM} , is:

$$\mathbf{M}^{EFM} = \left[M_A^{EFM} \quad M_{CA}^{EFM} \quad M_{CB}^{EFM} \quad M_B^{EFM} \right]^T \quad (5.79)$$

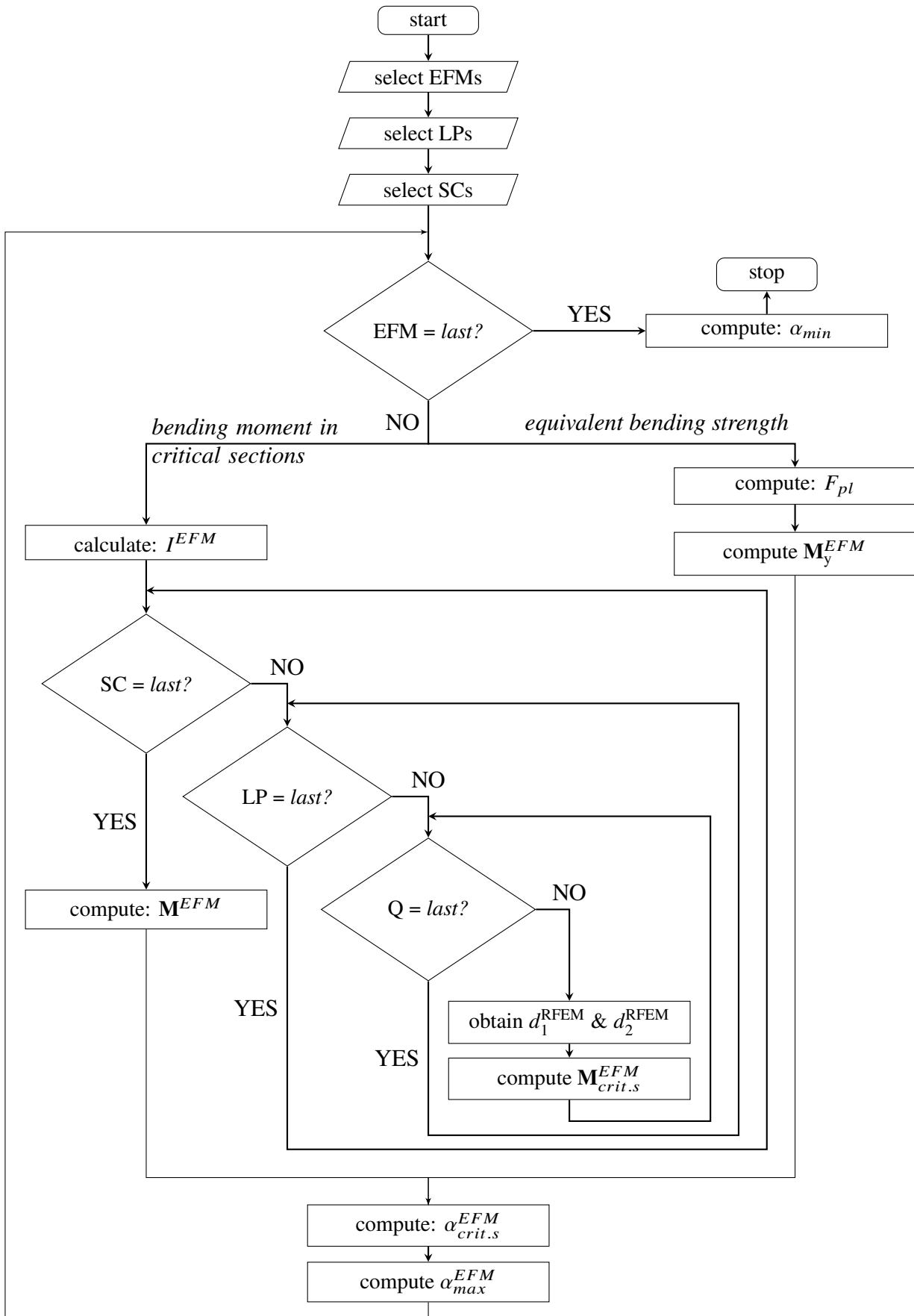


Figure 5.45: General procedure for computing the strength criterion.

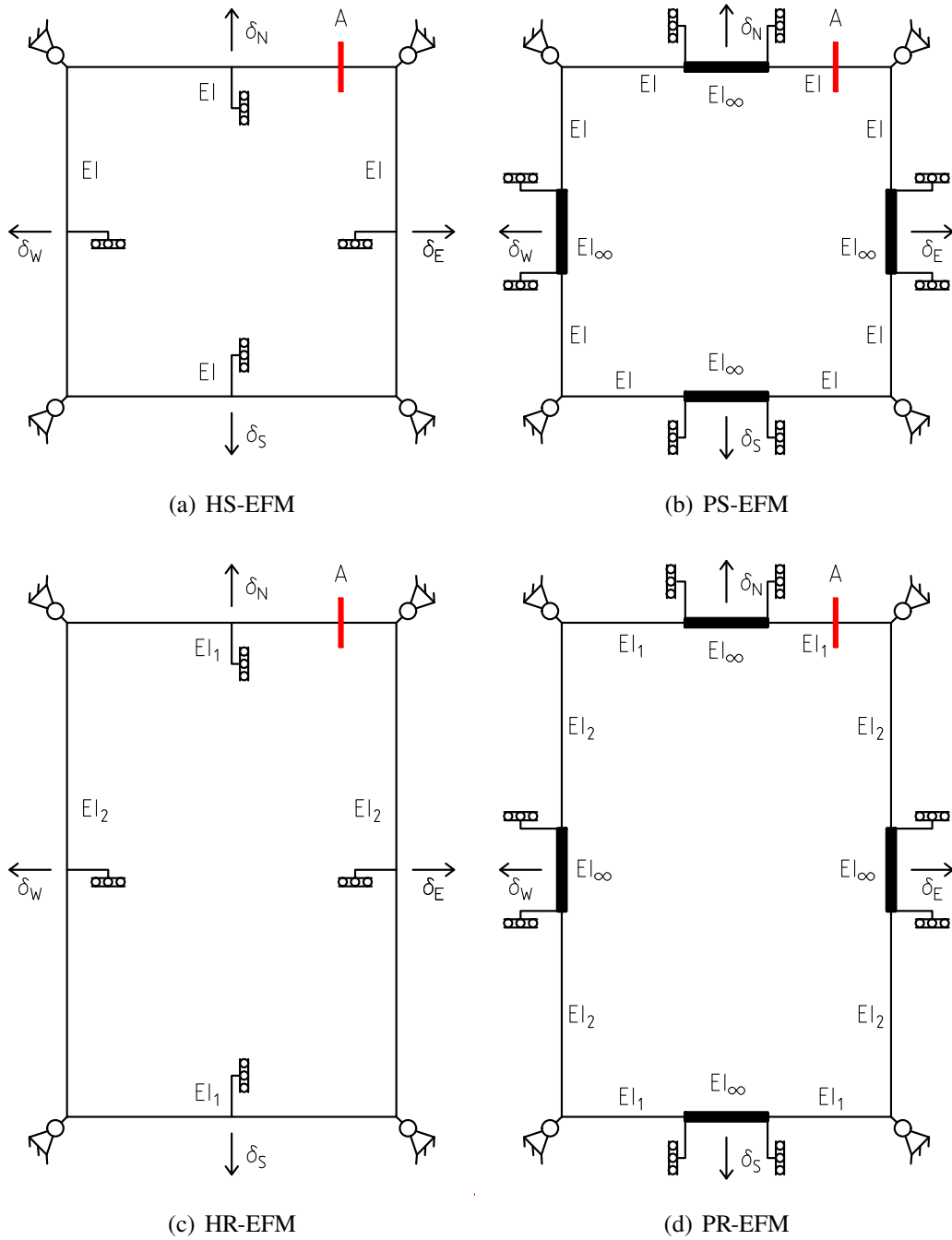


Figure 5.46: Analyzed Equivalent Frame-Models (EFM).

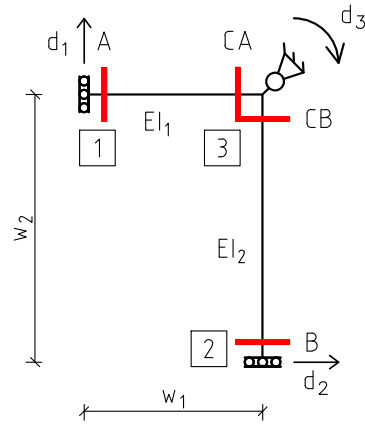


Figure 5.47: Critical sections on a generic Simplified Equivalent Frame-Model (SEFM).

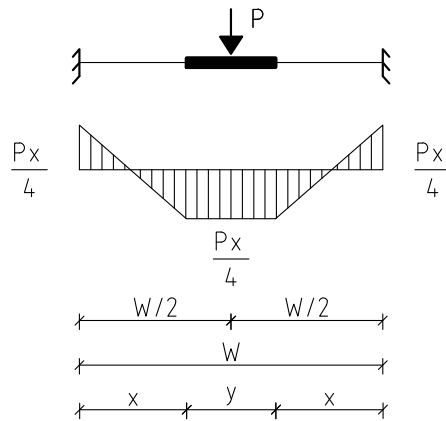


Figure 5.48: Element with fixed-fixed end supports subjected to a concentrated load at mid-span.

where M_A^{EFM} , M_{CA}^{EFM} , M_{CB}^{EFM} and M_B^{EFM} are the bending moments in the critical sections depicted in Fig. 5.47.

5.5.4 Equivalent bending strength

The equivalent bending strength of the frames-elements of the EFM was computed by modeling a fictive 1D element that was fully fixed at both ends and subjected to a load applied at its mid-span, as illustrated in Fig. 5.48. The yielding load of this 1D element was made to match the yielding load computed according to the NGM, F_{pl} (Eq. (5.42)).

In accordance with Fig. 5.48, if the yielding of the fictive 1D element coincides with the yielding of the plate from the NGM, the equivalent bending strength can be expressed as:

$$M_{y,NGM} = \frac{F_{pl} x}{4} \tag{5.80}$$

Given the foregoing, the vector of equivalent bending strengths for the critical sections illustrated in Fig. 5.47 must be calculated while accounting for the potential variation in F_{pl} values between the

Table 5.26: Bilinear elastic-plastic material characteristics of the tubular column.

E [N/mm ²]	ν	f_y [N/mm ²]	f_u [N/mm ²]	ϵ_u
210000	0.3	355	490	0.03

two frame-elements of the SEFM. Therefore, the resulting vector can be expressed as follows:

$$\mathbf{M}_{y.NGM}^{EFM} = \left[M_{y.NGM.A}^{EFM} \quad M_{y.NGM.CA}^{EFM} \quad M_{y.NGM.CB}^{EFM} \quad M_{y.NGM.B}^{EFM} \right]^T \quad (5.81)$$

with:

$$M_{y.NGM.A}^{EFM} = M_{y.NGM.CA}^{EFM} = \frac{F_{pl.1} w_1}{4} \quad (5.82)$$

$$M_{y.NGM.CB}^{EFM} = M_{y.NGM.B}^{EFM} = \frac{F_{pl.2} w_2}{4} \quad (5.83)$$

where $F_{pl.1}$ and $F_{pl.2}$ are the out-of-plane full-plastic strengths of the column plate from the NGM (Eq. (5.42)) for the two frame-elements of the SEFM.

5.5.5 Nonlinear behavior of the beam-to-column joints

The RFEMs utilized in determining the nonlinear behavior of beam-to-column joints were constructed in accordance with the methodology outlined in Section 5.4.3, supplemented by a nonlinear material analysis. In particular, a plasticity model featuring a Mises yield surface with associated plastic flow and isotropic hardening was adopted [212], and the necessary input parameters were supplied as listed in Tab. 5.26.

The nonlinear material analysis required the use of incremental load application. As such, the parameters for the initial, minimum, and maximum increments were set to 0.05, 0.001, and 0.1, respectively. The RFEM's analysis terminated once a column face had reached a displacement of 50 mm, i.e., $\min(L_1, L_2)/4$.

As expected, the yielding of the RFEMs was gradual, making it challenging to determine the transition from the elastic to the post-elastic regime based on the nonlinear $F - \delta$ relationship. Therefore, an energetic criterion was defined to overcome the challenge of identifying this conventional transition. Specifically, a bilinear approximation of the $F - \delta$ relationship was established, ensuring that both the nonlinear and the bilinear approximations shared the same initial tangential stiffness, maximum load and displacement, and potential energy (i.e., the area under the $F - \delta$ curve).

Subsequently, the maximum displacement within the elastic range, δ_{el} , was computed for each column face in the RFEMs through the following procedure:

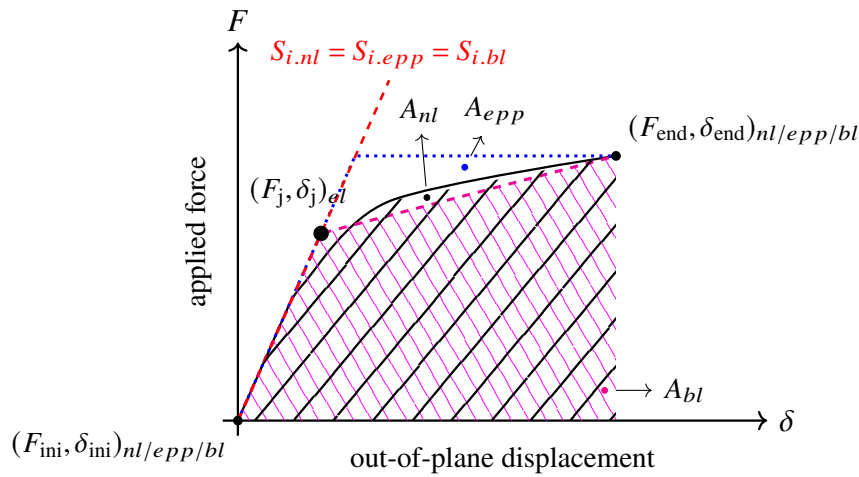


Figure 5.49: Schematic representation of the computation of F_{el} and δ_{el} .

1. extract the nonlinear force - displacement curve, $F - \delta$, from the RFEM (continuous nonlinear black line in Fig. 5.49);
2. calculate the area under the nonlinear curve: A_{nl} ;
3. determine the tangent stiffness, $S_{i,nl}$ – assumed as the secant stiffness at 5% of the ultimate load, F_{end} (red dashed line in Fig. 5.49);
4. construct the elastic-perfect plastic curve using the tangent stiffness, $S_{i,nl}$, and ultimate load, F_{end} (blue dotted line in Fig. 5.49);
5. calculate the area under the elastic-perfect plastic curve, A_{epp} , which is used as a starting point for an iterative process;
6. initiate an iterative process that starts from the elastic-perfect plastic curve and ends when a bilinear curve is found (magenta dashed line in Fig. 5.49) so that the area of the bilinear curve matches the area under the nonlinear curve: $A_{bl} \approx A_{nl}$ while ensuring that the initial and final coordinates of the two curves coincide and have equivalent tangent stiffnesses, $S_{i,nl} = S_{i,bl}$.

This process is schematically illustrated in Fig. 5.49, where "nl", "epp", "bl", and "el" stand for nonlinear (smooth), elastic-perfect plastic, bilinear, and elastic, respectively.

With the (F_{el}, δ_{el}) pairs calculated for all column faces, the vector of limit elastic displacements of the joint is computed as follows:

1. identify the column face ID that has the lowest load proportional factor associated with F_{el} :
 ID_{min} ;

2. set the minimum elastic force, $F_{el.min}$, and its corresponding minimum elastic displacement, $\delta_{el.min}$, as those corresponding to column face ID_{min} for the increment y ;
3. compute the out-of-plane deformation of the column faces, $\delta_{el.min}^i$, for the lowest load proportional factor, i.e., corresponding to increment y ;
4. assemble the vector of limit displacements, $\delta_{el.min}^{RFEM}$:

$$\delta_{el.min}^{RFEM} = \left[\delta_{el.min}^A \quad \delta_{el.min}^B \quad \delta_{el.min}^C \quad \delta_{el.min}^D \right]^T \quad (5.84)$$

To facilitate comprehension of this complex methodology, a detailed calculation for the RHS-m03-H01-SC02 case is presented in Appendix J.

5.5.6 Bending moments in SEFM

The calculation of the bending moments in the critical sections of the SEFMs for the displacements $\delta_{el.min}^{RFEM}$ was performed utilizing the displacement method. Tables for the stiffness coefficients for Euler-Bernoulli elements with both ends fully fixed were utilized (Appendix D) to kinetically define the SEFMs, as illustrated in Fig. 5.47, through the three DOFs, d_1 , d_2 , and d_3 . The vector of nodal displacements \mathbf{d} was established as:

$$\mathbf{d} = \left[d_1 \quad d_2 \quad d_3 \right]^T \quad (5.85)$$

Due to the absence of any load applied in d_3 , it was made dependent on d_1 and d_2 through the application of equilibrium conditions (i.e., static condensation). This resulted in the following equilibrium equation, as determined by the stiffness coefficients from Fig. 5.50:

$$\left[\begin{array}{ccc} -\frac{6EI_1}{w_1^2} & \frac{6EI_2}{w_2^2} & \frac{4EI_1}{w_1} + \frac{4EI_2}{w_2} \end{array} \right] \left[\begin{array}{ccc} d_1 & d_2 & d_3 \end{array} \right]^T = 0 \quad (5.86)$$

which yields:

$$d_3 = \frac{\frac{6EI_1}{w_1^2} d_1 - \frac{6EI_2}{w_2^2} d_2}{\frac{4EI_1}{w_1} + \frac{4EI_2}{w_2}} \quad (5.87)$$

The internal forces in the critical sections (Fig. 5.47) were calculated utilizing the principle of

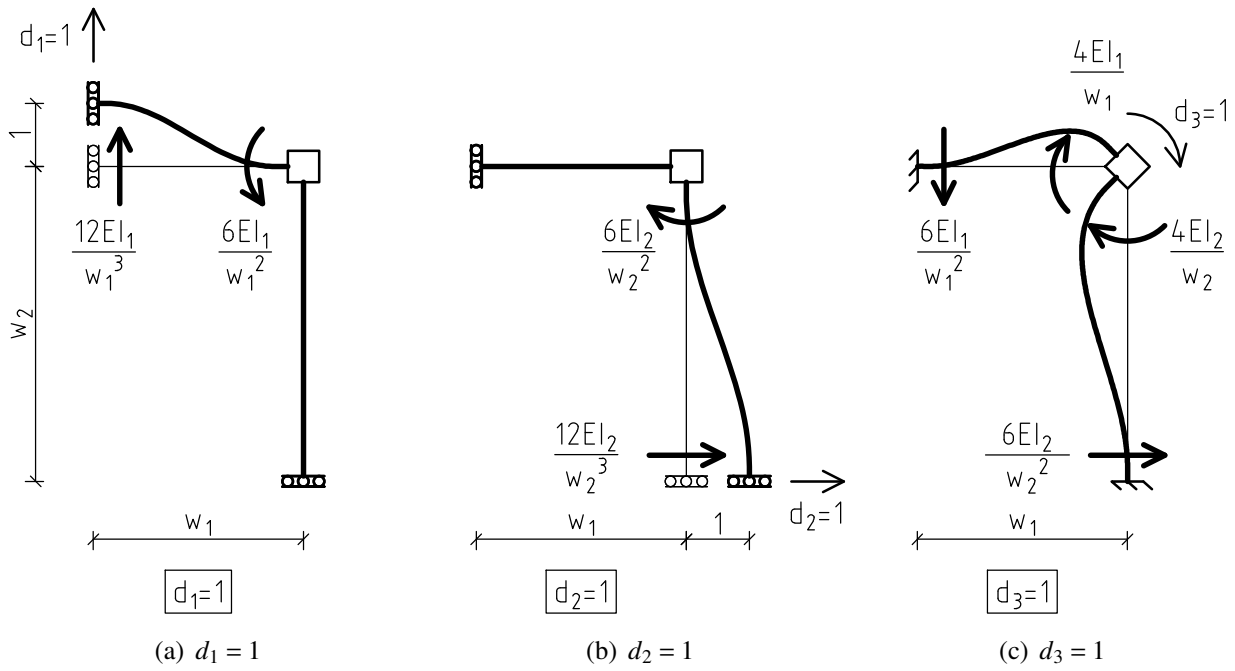


Figure 5.50: Stiffness coefficients associated with the DOFs.

superposition of the effects of the three DOFs displayed in Fig. 5.51. Hence:

$$\mathbf{M}_d^{EFM} = \begin{bmatrix} M_A^{EFM} \\ M_{CA}^{EFM} \\ M_{CB}^{EFM} \\ M_B^{EFM} \end{bmatrix} = \begin{bmatrix} -\frac{6 E I_1}{w_1^2} & 0 & \frac{2 E I_1}{w_1} \\ -\frac{6 E I_1}{w_1^2} & 0 & \frac{4 E I_1}{w_1} \\ 0 & \frac{6 E I_2}{w_2^2} & \frac{4 E I_2}{w_2} \\ 0 & \frac{6 E I_2}{w_2^2} & \frac{2 E I_2}{w_2} \end{bmatrix} \quad (5.88)$$

Therefore the bending moments in the critical sections (Fig. 5.47) of a generic SEFM are expressed by:

$$\mathbf{M}^{EFM} = \mathbf{M}_d^{EFM} \mathbf{d} \quad (5.89)$$

with the following values in each critical section:

$$M_A^{EFM} = -\frac{3 E I_1 (I_2 d_2 w_1^2 + 2 I_2 d_1 w_1 w_2 + I_1 d_1 w_2^2)}{w_1^2 w_2 (I_1 w_2 + I_2 w_1)} \quad (5.90)$$

$$M_{CA}^{EFM} = -\frac{6 E I_1 I_2 (d_1 w_2 + d_2 w_1)}{w_1 w_2 (I_1 w_2 + I_2 w_1)} \quad (5.91)$$

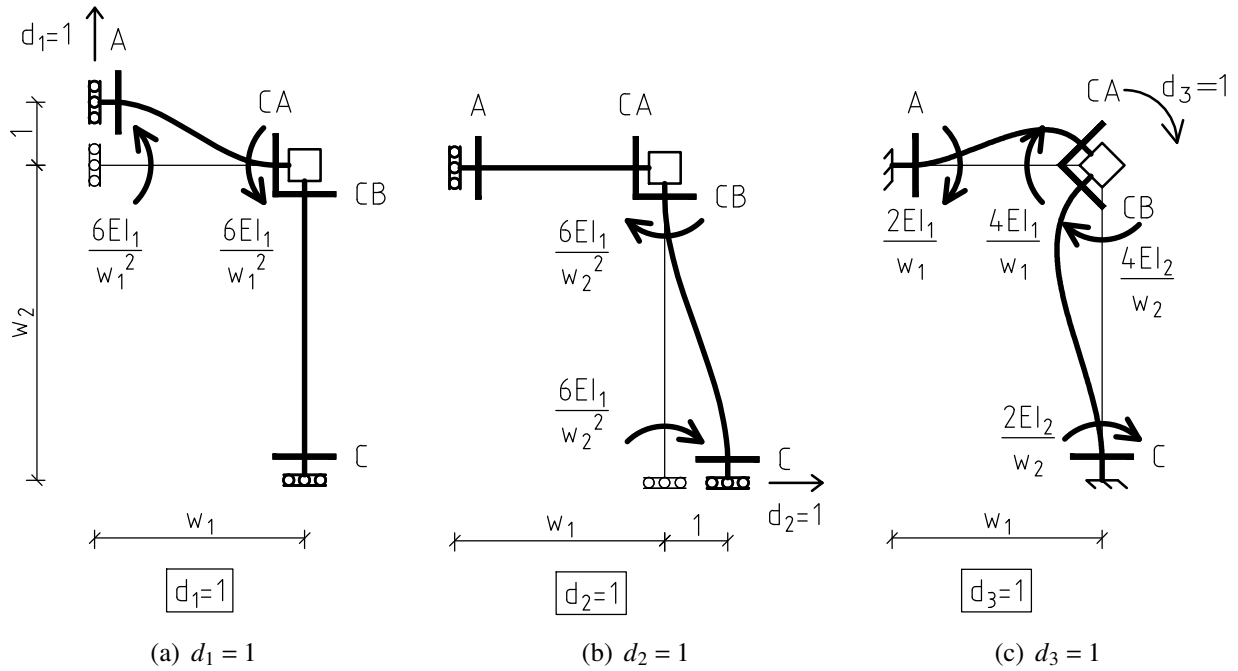


Figure 5.51: Bending moments in critical sections caused by unit load on the DOFs.

$$M_{CB}^{EFM} = \frac{6 E I_1 I_2 (d_1 w_2 + d_2 w_1)}{w_1 w_2 (I_1 w_2 + I_2 w_1)} \quad (5.92)$$

$$M_B^{EFM} = \frac{3 E I_2 (I_2 d_2 w_1^2 + 2 I_1 d_2 w_1 w_2 + I_1 d_1 w_2^2)}{w_1 w_2^2 (I_1 w_2 + I_2 w_1)} \quad (5.93)$$

By substituting the values of the lengths w_1 and w_2 in the equations mentioned above with the lengths of any of the EFM's described in Section 5.2.4, it is possible to directly obtain the bending moments of that particular EFM.

5.5.7 Application of the procedure to the EFM's

To maintain consistency with the stiffness calculation presented in Section 5.2.3 and to align with the goal of this document, which is to provide specific and final calculations for each EFM, the exact values for the dependency of DOF d_3 on DOFs d_1 and d_2 (Eq. (5.87)), the internal forces in the critical sections (Eqs. (5.88) to (5.93)), and the equivalent bending strength (Eqs. (5.81) to (5.83)) are presented for every EFM in Appendix K according to Tab. 5.27. In cases where an equivalent moment of inertia is used (Eq. (5.1)), the results are presented directly to avoid redundancy.

Table 5.27: Index of tables for strength calculation.

EFM name	Appendix name	EFM name	Appendix name
HS-EFM	Appendix K.1	PS-EFM	Appendix K.4
HR-EFM-IF	Appendix K.2	PR-EFM-IF	Appendix K.5
HR-EFM-IEq	Appendix K.3	PR-EFM-IEq	Appendix K.6

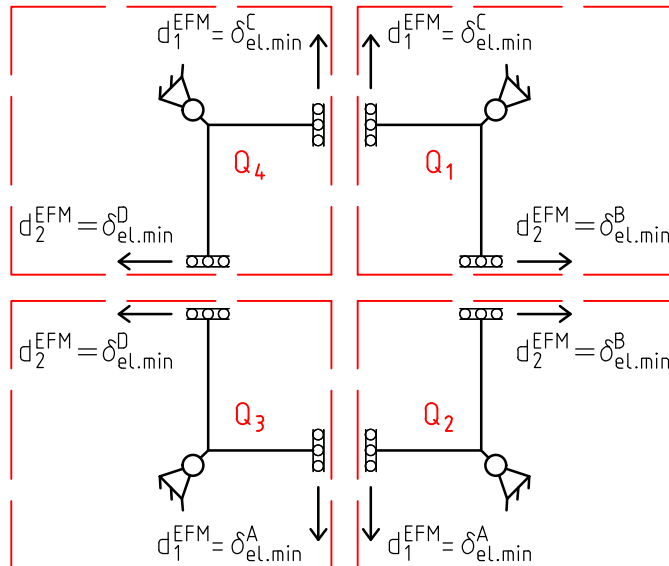


Figure 5.52: Displacements association for quadrant calculations for a generic SEFM.

5.5.8 Adjustment factor

5.5.8.1 Cases considered

The adjustment factor for the strength criterion, α , is determined through a parametric analysis using the same cases employed for calibrating the effective stiffness. However, as not all load patterns and cross-sections are double-symmetric, the full assessment of the joint requires the examination of all four SEFMs at the joint region. To accomplish this, the four displacements from the RFEM (Eq. (5.84)) are grouped into four sets of two displacements, and the calculation is performed for each of the four quadrants at every joint (i.e., Q1 to Q4). The quadrants are depicted in Fig. 5.52. A practical example for RHS-m03-H01-SC02 case, demonstrating the calculation for each quadrant individually, is provided in Appendix L.

A graphical representation of the network for the considered cases is presented in Fig. 5.53 and Fig. 5.54 for the SHS and RHS, respectively, to aid in the interpretation of the analyzed models and their modifications. In addition to the previously mentioned four parameters considered in the evaluation of stiffness in Section 5.4.2 (EFM, radius, LP, and SC), a fifth parameter, namely the quadrant (Q),

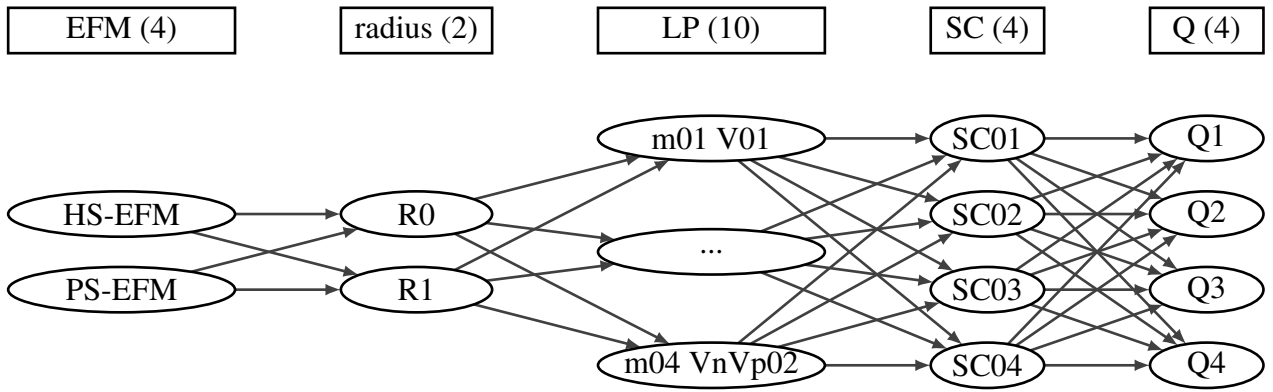


Figure 5.53: Network for strength calculation: SHS (1280 cases).

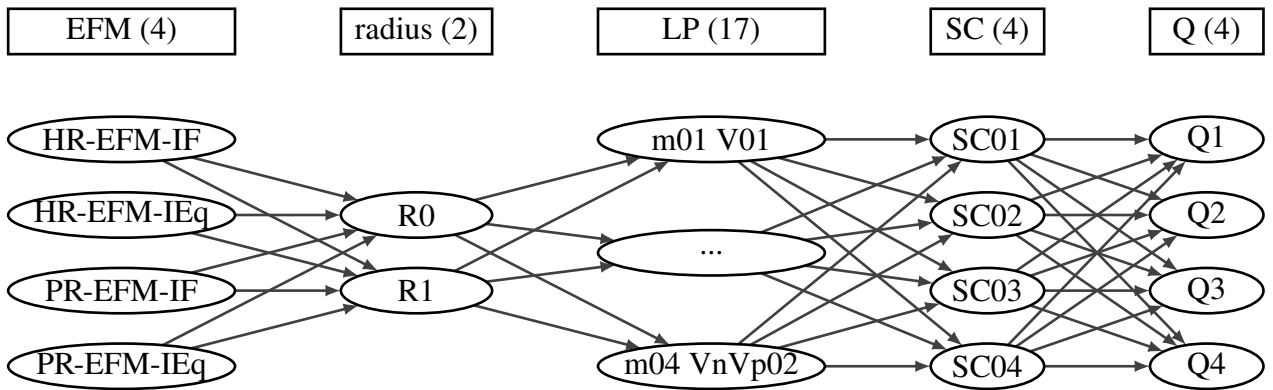


Figure 5.54: Network for strength calculation: RHS (2176 cases).

was added to the network. Combining the five parameters, 1280 and 2176 cases were analyzed and computed for the SHS and RHS, respectively.

5.5.8.2 Results unadjusted

The results for the strength criterion (Eq.(5.72)) are presented for PS-EFM-R1 and PR-EFM-IF-R1, in Tab. 5.28 and Tab. 5.29, respectively. The remaining cases are presented in Appendix M according to Tab. M.1

The tables presented herein contain information on the maximum absolute values of the bending moments in the critical sections, \mathbf{M}^{EFM} (Eq. (5.73)), the equivalent bending strength, \mathbf{M}_y^{EFM} (Eq. (5.74)), in the same sections, the adjustment factor for each critical section, $\alpha_{crit.s}^{EFM}$ (Eq.(5.75)), and the maximum adjustment factor, α_{max}^{EFM} (Eq. (5.76)). Each EFM is displayed in a separate table, and within each table, the results for four SCs are presented.

To ensure the optimal display of the table within the margins of the page, the superscript EFM , which contains the names of the EFMs for the maximum adjustment factor, α_{max}^{EFM} , is excluded from all instances throughout the tables. The components of the bending moment, equivalent bending strength, and adjustment factor vectors are presented in columns, where the name of the critical section (i.e., A,

Table 5.28: Results: PS-EFM-R1 [kNm] (unadjusted).

SC	$M^{PS-EFM-R1}$				$M_{y,NGM}^{PS-EFM-R1}$				$\alpha_{crit.s}^{PS-EFM-R1}$				α_{max}
	A	CA	CB	B	A	CA	CB	B	A	CA	CB	B	
01	8.75	8.57	8.57	8.57	3.39	3.39	3.39	3.39	2.6	2.5	2.5	2.5	2.6
02	8.30	8.18	8.18	8.18	3.24	3.24	3.24	3.24	2.6	2.5	2.5	2.5	2.6
03	7.40	7.40	7.40	7.40	2.79	2.79	2.79	2.79	2.6	2.6	2.6	2.6	2.6
04	7.76	7.76	7.76	7.76	2.19	2.19	2.19	2.19	3.5	3.5	3.5	3.5	3.5

Table 5.29: Results: PR-EFM-IF-R1 [kNm] (unadjusted).

SC	$M^{PR-EFM-IF-R1}$				$M_{y,NGM}^{PR-EFM-IF-R1}$				$\alpha_{crit.s}^{PR-EFM-IF-R1}$				α_{max}
	A	CA	CB	B	A	CA	CB	B	A	CA	CB	B	
01	9.01	8.99	8.99	8.98	3.39	3.39	4.78	4.78	2.7	2.7	1.9	1.9	2.7
02	8.53	8.53	8.53	8.54	3.24	3.24	4.64	4.64	2.6	2.6	1.8	1.8	2.6
03	7.64	7.52	7.52	7.41	2.79	2.79	4.24	4.24	2.7	2.7	1.8	1.7	2.7
04	7.63	6.80	6.80	6.67	2.19	2.19	3.78	3.78	3.5	3.1	1.8	1.8	3.5

CA, CB, and B) is used as the header for each respective column.

Upon analyzing the outcomes in regards to the values of the maximum adjustment factor, α_{max} , it is observed that this factor varies between 2.0 and 3.5 for the SHS, while for RHS, it varies between 1.8 and 5.6, and therefore an adjustment factor is needed.

5.5.8.3 Results adjusted

The unique minimum adjustment factor, α_{min} (Eq. (5.77)) leads to Eq. (5.94). These minimum values are obtained for the SHS and RHS from the cases HS-EFM-R1-SC01 and HR-EFM-IF-R0-SC04, respectively.

$$\alpha_{min} = \begin{cases} 2.0 & , \text{if } \frac{L_1}{L_2} = 1 \\ 1.8 & , \text{otherwise} \end{cases} \quad (5.94)$$

The results with the unique minimum adjustment factor, α_{min} , incorporated in the equivalent bending strength (Eq.(5.78)) are presented for PS-EFM-R1 and PR-EFM-IF-R1, in Tab. 5.30 and Tab. 5.31, respectively. The remaining cases are presented in Appendix N in accordance with Tab. N.1. The adjustment factor for the critical section was recalculated, providing a clearer representation of

Table 5.30: Results: PS-EFM-R1 [kNm] (adjusted).

SC	$M^{PS-EFM-R1}$				$M_{y.NGM}^{PS-EFM-R1}$				$\alpha_{crit.s}^{PS-EFM-R1}$			
	A	CA	CB	B	A	CA	CB	B	A	CA	CB	B
01	8.75	8.57	8.57	8.57	6.81	6.81	6.81	6.81	1.3	1.3	1.3	1.3
02	8.30	8.18	8.18	8.18	6.50	6.50	6.50	6.50	1.3	1.3	1.3	1.3
03	7.40	7.40	7.40	7.40	5.62	5.62	5.62	5.62	1.3	1.3	1.3	1.3
04	7.76	7.76	7.76	7.76	4.41	4.41	4.41	4.41	1.8	1.8	1.8	1.8

the critical section's behavior. Specifically, values at or below unity indicate that the critical section is in the elastic range, whereas values above unity indicate that the critical section has entered the post-elastic range.

Table 5.31: Results: PR-EFM-IF-R1 [kNm] (adjusted).

SC	$M^{PR-EFM-IF-R1}$				$M_{y.NGM}^{PR-EFM-IF-R1}$				$\alpha_{crit.s}^{PR-EFM-IF-R1}$			
	A	CA	CB	B	A	CA	CB	B	A	CA	CB	B
01	9.01	8.99	8.99	8.98	6.24	6.24	8.80	8.80	1.4	1.4	1.0	1.0
02	8.53	8.53	8.53	8.54	5.95	5.95	8.53	8.53	1.4	1.4	1.0	1.0
03	7.64	7.52	7.52	7.41	5.14	5.14	7.80	7.80	1.5	1.5	1.0	0.9
04	7.63	6.80	6.80	6.67	4.04	4.04	6.96	6.96	1.9	1.7	1.0	1.0

5.5.9 Conclusion

In conclusion, a strength criterion based on a unique minimum adjustment factor with global applicability that does not depend on the evaluation of internal forces in a specific component was defined for the components of the beam-to-column joint finite element implemented in OpenSees. Although it presents a conservative threshold, it guarantees safety across all considered scenarios.

Chapter 6

Conceptual framework for nonlinear analysis

6.1 Introduction

The conventional method to address nonlinear behavior in component-based methods is to consider the nonlinearity at each 0D element that reflects the actual nonlinear behavior of the component and assume independent behavior for each component. This typically involves characterizing the nonlinear behavior of each component through experimental tests or Refined Finite Element Model(s) (RFEM(s)) of the isolated components, matching each 0D element. Alternatively, a small number of components can be tested together to characterize individual components when it is possible to assess the internal forces and deformations in each component and assume no interaction between them.

In the present study, this approach was followed for most components in the context of the INNO3DJOINTS project, as presented in Section 2.6. However, when dealing with the tube components considered in the beam-to-column macro-element, this traditional approach cannot be applied because the components do not have a similar meaning to those assigned to components in the component method, where a component is typically defined as a part of a joint under an internal force, e.g., column web in tension. The traditional procedure is also feasible when the component accounts for internal forces coming from multiple 1D elements but has only one possible deformation mode. In this case, a single internal force condenses the contributions of the internal forces coming from the multiple 1D elements connected to the joint, e.g., column web in shear.

However, in the developed macro-element, the joint is subject to four internal forces, with one force acting on each column face. These internal forces cannot be condensed into a single static variable. Therefore, to account for the various possible deformation patterns and the interaction between the column faces, multiple 0D elements are required. Consequently, the stiffness of each 0D element

in the column macro-element is associated with the global deformation pattern of the entire tube in the joint region, as opposed to a part of the joint, as in the traditional approach. By applying the principle of superposition of effects, all relevant deformation and load patterns can be represented. Therefore, the stiffness of a face component is not exclusively related to a specific face but accounts for the deformation of the entire tube.

Given these conceptual differences, a different approach was required to account for the nonlinear behavior of the P&PJ making use of the macro-element developed in the scope of the current work.

6.2 Conceptual framework

The conceptual framework of nonlinearity was investigated by analyzing the behavior of the tubular column within the joint region using RFEMs developed in Abaqus. The findings demonstrated that the onset of yielding occurs near the socket faces for all socket configurations (SCs), as depicted in Fig. 6.1. These observations suggest that the nonlinearity of the tube in the joint region begins as a local phenomenon.

Based on the previous evidence, it may be stated that the initiation of nonlinear behavior can be captured by assigning the nonlinear behavior to a component of the beam-to-column joint finite element that captures the total force applied on each column face, including the force installed in the face component and the interaction components on each face, e.g., component 03 in Fig. 3.13. However, despite being simple and straightforward, this approach may yield unsatisfactory results due to its failure to consider the integration effect of all column faces in the strength analysis.

In order to consider the interaction between the column faces in terms of the strength of each component and to account for the local onset of nonlinearity, one approach is to define the onset of yielding in terms of the deformation of the column face, i.e., in terms of the deformation of each face component.

On the other hand, as defined in Chapter 3, the stiffness of a face component can be set as the force required to produce a unitary out-of-plane displacement on one column face when unitary out-of-plane displacements are simultaneously imposed on the adjacent column faces (k_F , Fig. 6.2(a)). The stiffness of an interaction component can be defined as the force required to maintain null out-of-plane displacements on one column face when a unitary out-of-plane displacement is imposed on an adjacent column face (k_I , Fig. 6.2(b)). Thus, the stiffness of a face component can be considered to have two contributions: the force required to produce a unitary out-of-plane displacement on one column face when null out-of-plane displacements are imposed on the adjacent column faces (k_A , Fig. 6.2(c)), and the force required to maintain null out-of-plane displacements on the same column face when unitary

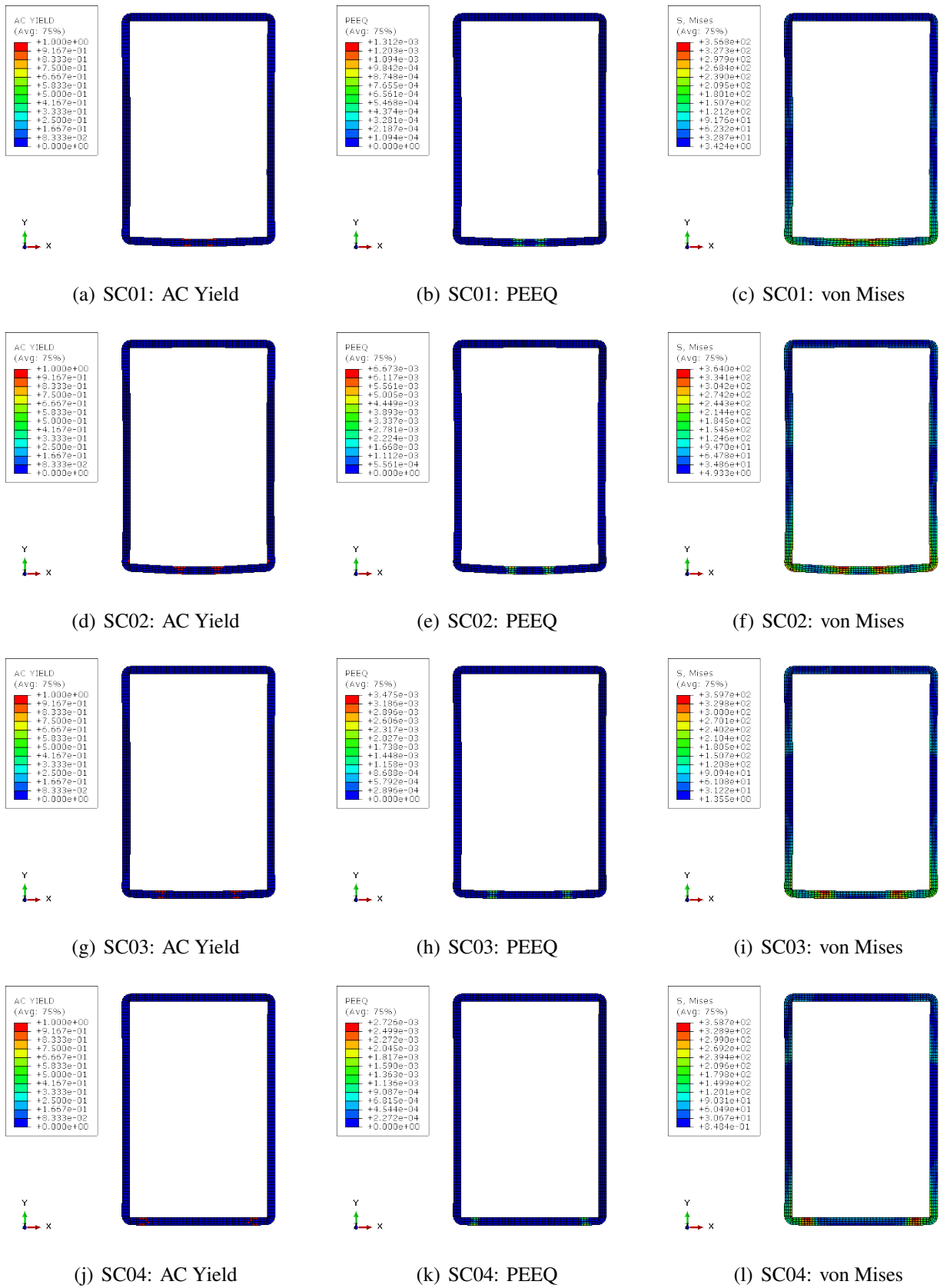


Figure 6.1: Stress and plasticity related results at the joint region gathered from RFEMs: actively yielding (AC yield), equivalent plastic strain (PEEQ), and Mises equivalent stress (von Mises).

out-of-plane displacements are imposed on both adjacent column faces ($2 k_I$, Fig. 6.2(d)). Hence,

$$k_F = k^A - 2k_I \quad (6.1)$$

as previously mentioned.

Based on the above approach, the hypothesis that the onset of the nonlinear behavior can be defined accurately enough only by a force at each face related to the deformation mode represented in Fig. 6.2(c) was employed in the current work. The load for the case represented in Fig. 6.2(c) that would lead to the onset of the linear behavior is defined as F_y . The onset of the nonlinear behavior for any load configuration occurs when the deformation of a column face reaches the deformation d_y . In the case of face A, this value is expressed as follows:

$$d_y^A = \frac{F_y^A}{k^A} \quad (6.2)$$

With regard to the post-yielding behavior, the principle of superposition of effects becomes invalid. As a result, there is no assurance that the validity of Eq. (6.1) will persist in the post-yielding regime. However, in order to establish an approximate procedure for defining the nonlinear behavior of components in the nonlinear regime, assuming a bilinear behavior for the deformation modes illustrated in Fig. 6.2(b) and Fig. 6.2(c), Eq. (6.1) was considered valid in the post-yielding regime. Within the confines of this framework, the following hypotheses were considered:

- Hypothesis 1: the nonlinearity is present only in association with the deformation mode shown in Fig. 6.2(c), where the face component undergoes nonlinear behavior while the interaction components remain in the elastic regime. This results in the constitutive laws represented in Fig. 6.3(a);
- Hypothesis 2: the nonlinearity is present in association with both deformation modes shown in Fig. 6.2(b) and Fig. 6.2(c) simultaneously, where the face component undergoes nonlinear behavior together with the interaction components. This results in the constitutive laws represented in Fig. 6.3(b).
- Hypothesis 3: the nonlinearity is present in association with both deformation modes shown in Fig. 6.2(b) and Fig. 6.2(c), but the nonlinearity associated with the mode represented in Fig. 6.2(b) manifests itself only after the nonlinearity associated with the mode represented in Fig. 6.2(c). This means that the face component undergoes nonlinear behavior while the interaction components remain temporarily in the elastic regime, resulting in the constitutive

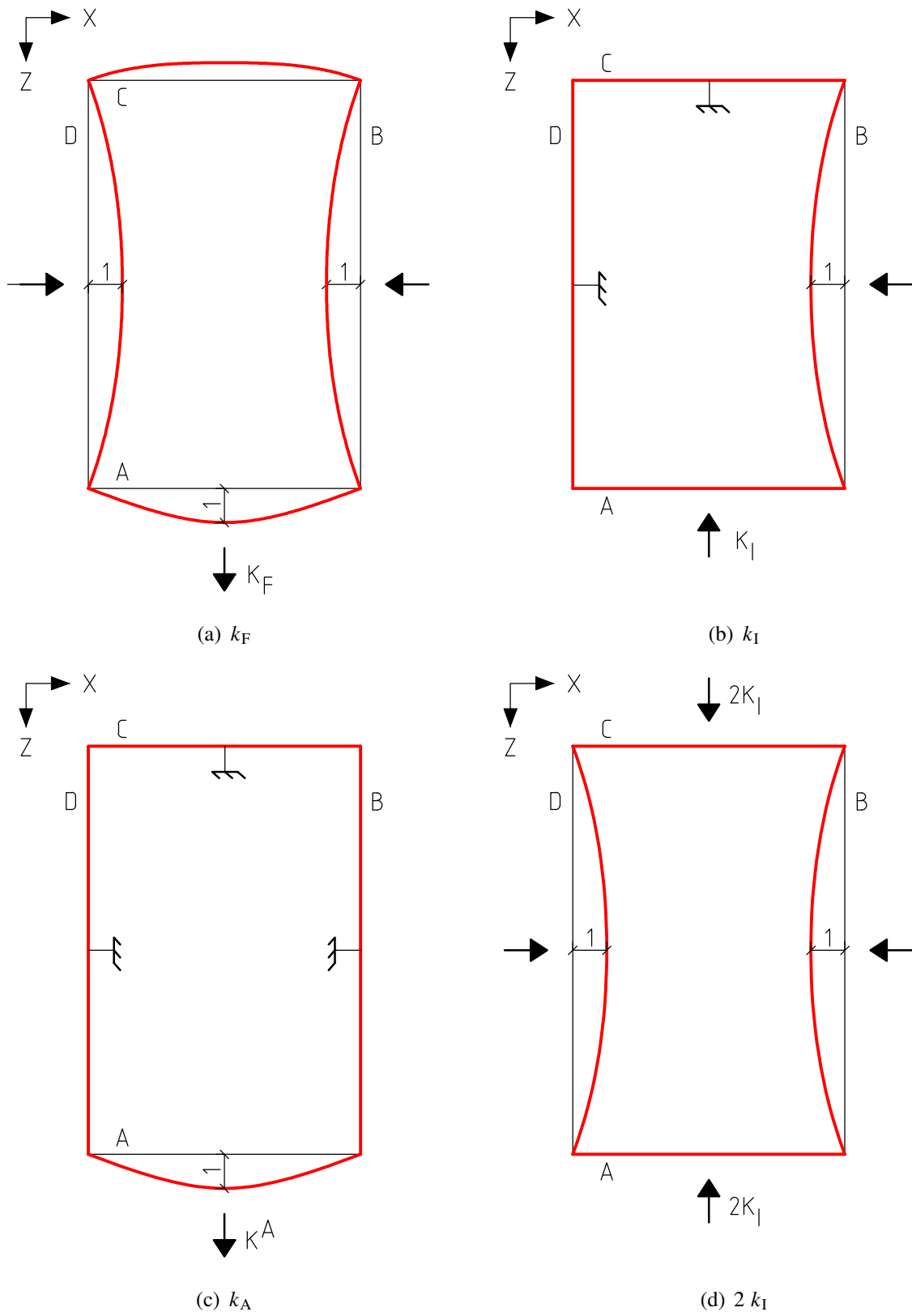


Figure 6.2: Stiffness of the tube components (generic).

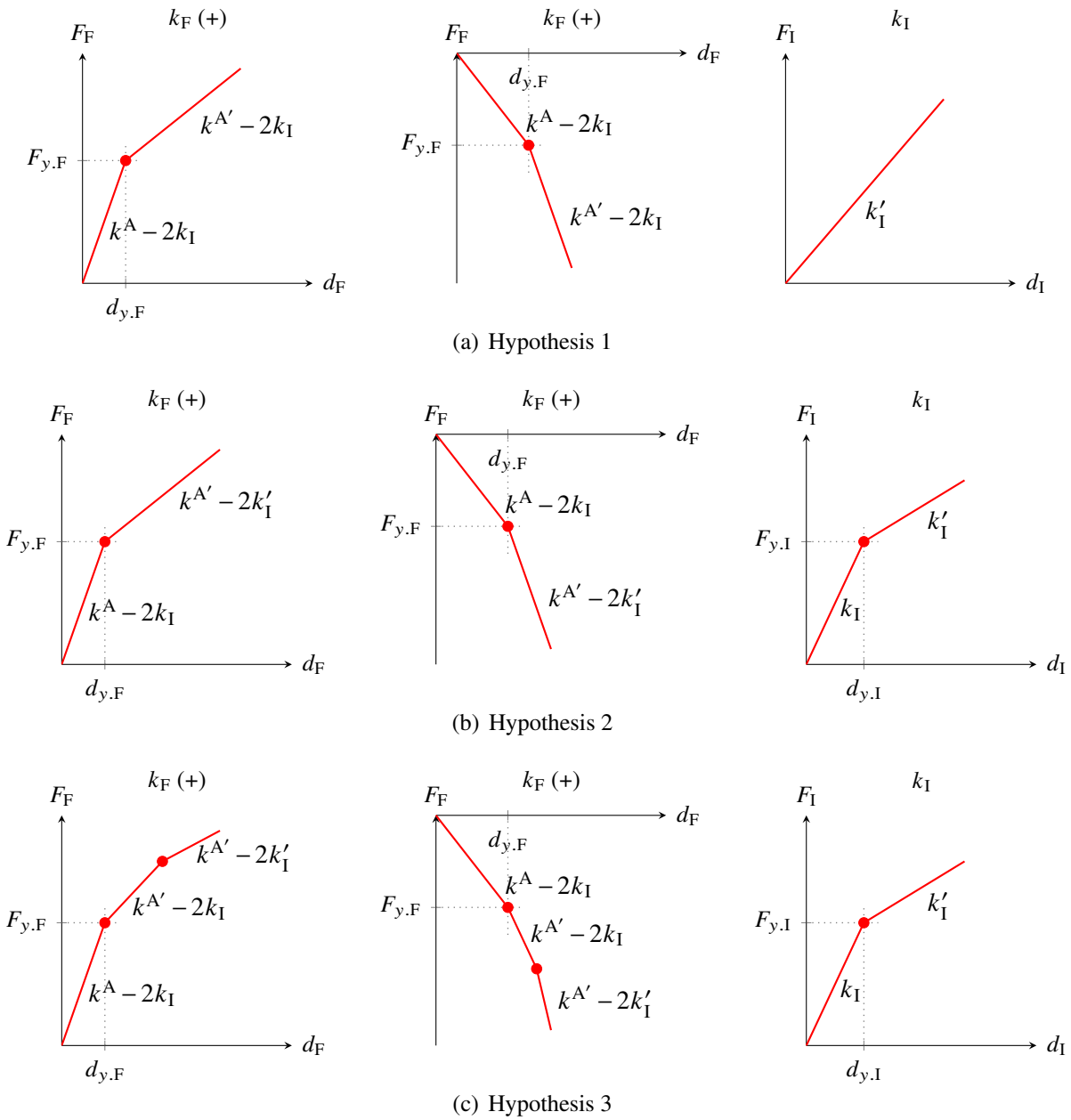


Figure 6.3: Constitutive relations for components.

laws represented in Fig. 6.3(a).

where k'_A represents the post-elastic stiffness associated with the deformation mode shown in Fig. 6.2(c), and k'_I denotes the post-elastic stiffness corresponding to the deformation mode depicted in Fig. 6.2(b).

To determine which of the three hypotheses accurately describes the behavior of the column tube in the joint region, the reference case presented in Fig. 6.4 was analyzed.

For the given boundary conditions illustrated in Fig. 6.4, the macro-element has only one DOF, d , and the corresponding stiffness can be expressed as:

$$k = k_F + 2 k_I = k^A - 2 k_I + 2 k_I = k^A \quad (6.3)$$

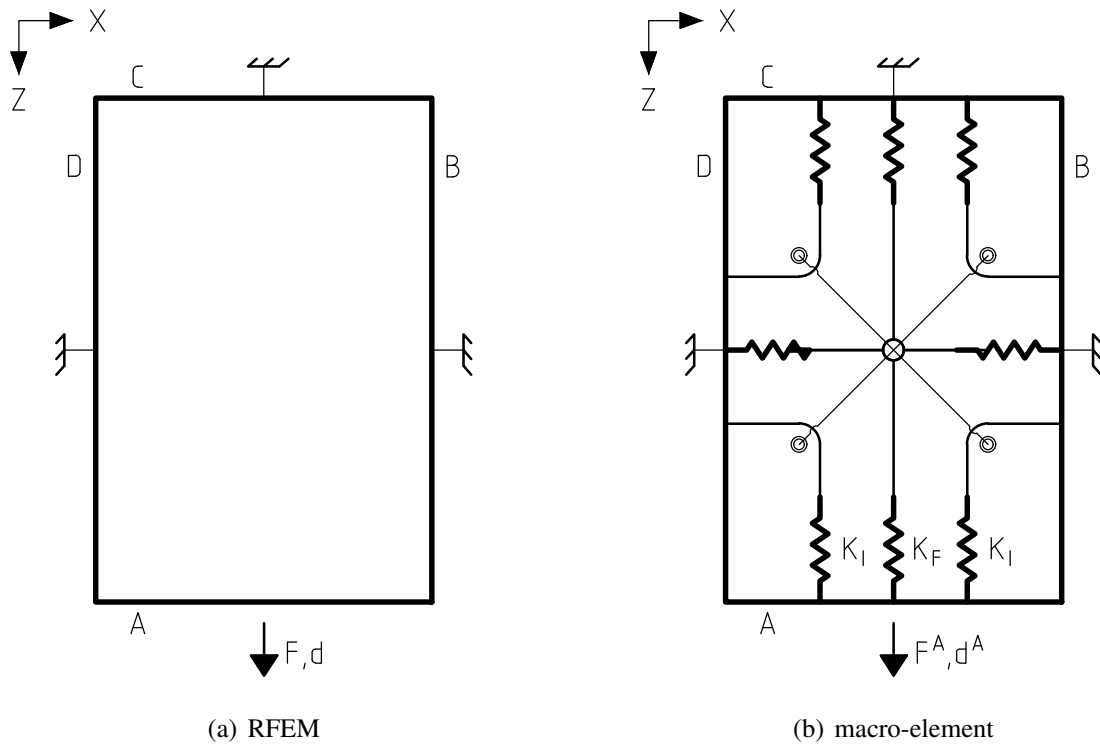


Figure 6.4: Reference case to set the nonlinear modeling approach.

Consequently, the $F - d$ relation is associated with the deformation mode represented in Fig. 6.2(c), while the $R - d$ relation is related to the deformation mode depicted in Fig. 6.2(d). This enables a comparison of the plausibility of the three hypotheses. These curves were extracted from an RFEM build in Abaqus for the reference case shown in Fig. 6.4. The model is as the ones described in Section 5.5.5. Thus, the two curves are plotted in Fig. 6.5.

Based on the previous findings, hypothesis 2 is the most plausible within the scope of the approximate approach discussed. This implies that the face component and the interaction component enter the post-yielding regime simultaneously.

However, the formulation of the beam-to-column joint finite element presented in Chapter 4

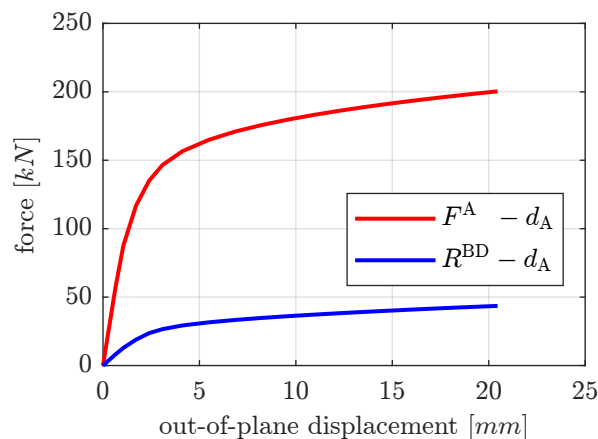


Figure 6.5: Curves for the reference case: $F^A - d^A$ and $R^{BD} - d^A$.

requires the explicit definition of constitutive relations for each component as input and does not allow for the automatic incorporation of constitutive relations from different components during the analysis. Consequently, the current implementation of the joint finite element cannot ensure that two distinct components, which may exhibit different levels of deformation due to the interaction of the column faces, will enter the nonlinear regime simultaneously. To address this limitation, the interaction component's nonlinear behavior needs to be established on a relationship between the deformation of the interaction component and the deformation of the face component for each iteration of the analysis.

Although the formulation of the beam-to-column joint finite element can be upgraded to incorporate this feature, it is beyond the scope of the current study. Instead, a simplified approach is adopted whereby the interaction component enters the post-yielding regime once it reaches the yield regime designated for the corresponding face components, that is, $d_{y,I} = d_{y,F}$ as shown in Fig. 6.3.

6.3 Predictive capability of NGM nonlinear formulation for P&PJ setup

A parametric analysis was conducted to evaluate the capability of the NGM nonlinear formulation to predict and characterize the nonlinear behavior of the components of the P&PJ.

The analysis involved comparing the out-of-plane force-displacement curve (Eq. (5.35)) obtained using the NGM formulation for a rectangular plate with two opposite sides fixed and a central area loaded by two rigid-rectangular plates (i.e., socket faces) to the results obtained using RFEMs for the same situation.

The study varied three geometrical parameters, specifically, the width of the column plate, L , the width, f , and length, u , of the rigid area, as depicted in Fig. 5.10. It is noteworthy that configurations with a socket height greater than 40 mm do not satisfy the geometric condition outlined in Eq. (5.30). The values of these parameters and their corresponding combinations, as well as the case network, are presented in Fig. 6.6. The thickness of the column plate was held constant at $t_c = 10$ mm for all cases.

RFEMs were developed using Abaqus [113] for each column plate, representing one face of the RHS columns analyzed in Section 5.4.3. As such, Tab. 5.26 and Fig. 5.27 outline the material properties and mesh configuration used in these models. The models are novel in that they feature variations in the height of the socket faces and fully fixed boundary conditions applied longitudinally to the column plate thickness. The stopping criterion for the analysis was set at 20 mm for the out-of-plane deformation of the plate (i.e., $10\% \min(L)$). The assembly and mesh assignment of an RFEM are illustrated in Fig. 6.7, while Fig. 6.8 displays the deformed shape in the loaded region.

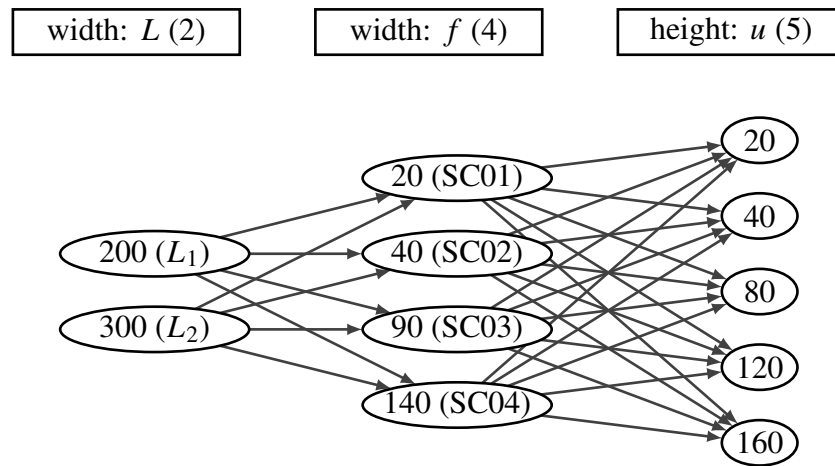


Figure 6.6: Network for F_{pl} calculation from the NGM (40 cases) [mm].

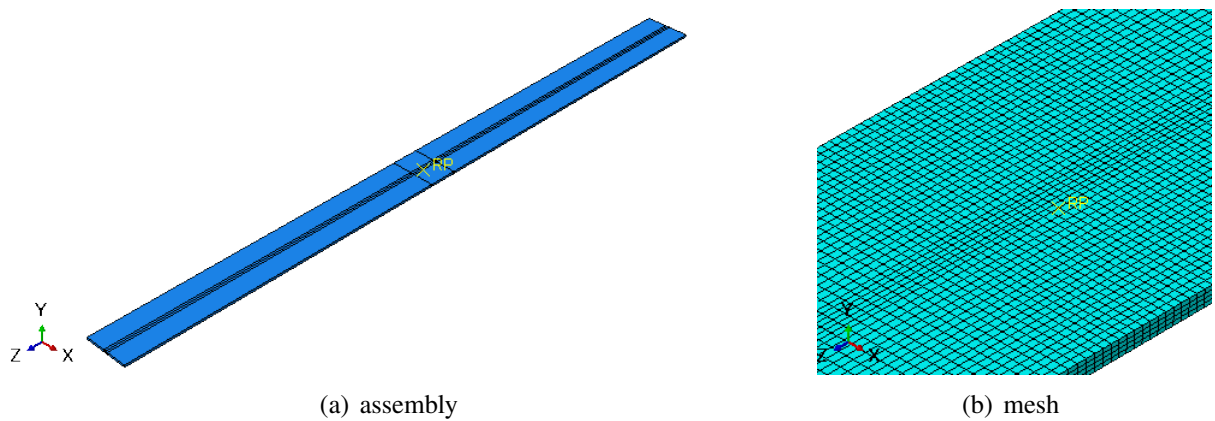


Figure 6.7: RFEM of a column plate: assembly and discretization.

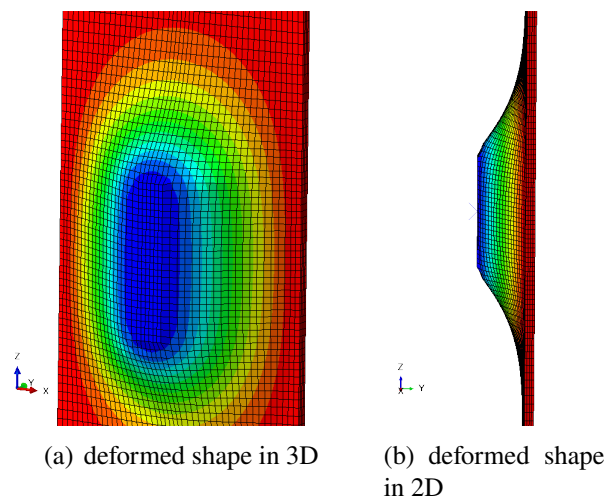


Figure 6.8: RFEM of a column plate: deformation in the loaded region.

The nonlinear behavior of the NGM is characterized by two distinct branches that are dependent on the ratio of displacement-to-plate thickness, δ/t_c . The first branch corresponds to the plastic behavior regime, which is defined by a ratio of less than one. In this regime, the membrane effects are negligible and can be ignored. The second branch is associated with the plastic regime region where the ratio is greater than one. In this regime, the membrane effect becomes significant, and this behavior is outside the scope of the present study.

The end of the elastic range in the $(F/F_{pl} - \delta/t_c)$ space is determined by the intersection of the initial stiffness line, S_i , with the branch that characterizes the plastic range without of membrane effects. These three branches are depicted in Fig. 6.9. Additionally, it is evident from the figure that the force that corresponds to the formation of the full-plastic mechanism of the plate F_{pl} is not a precise representation of the onset of the nonlinear behavior in certain configurations. Consequently, to obtain a better representation of the transition from the elastic to the post-elastic region, a new parameter, namely NGM yield force, F_{NGM} , is introduced, as illustrated in Fig. 6.9. This yield force corresponds to the intersection of the initial stiffness branch with the plastic branch. The ratio of F_{NGM}/F_{pl} ranges from 0.92 to 1.23, as presented in Tab. 6.1, based on the analyzed cases. When considering only the cases that satisfy the geometric condition (Eq. (5.30)), the ratio varies from 0.92 to 1.05. Therefore, in this study, F_{NGM} is employed to ensure consistency and accuracy. The present document does not delve into a detailed analysis of the underlying causes that contribute to a ratio exceeding unity.

The force-displacement curves obtained from the NGM and RFEM analyses are presented in Fig. 6.10 and Fig. 6.11. Each figure corresponds to a specific combination of length and socket height ($L - u$ pairs), displaying the curves for four socket configurations. In addition, the nonlinear curve obtained from the RFEM is approximated as a bilinear curve using the equal potential energy criterion, as explained in Section 5.5.5. The graphs showing the remaining combination are presented in Appendix O. The ratio between the NGM yield force, F_{NGM} , and that obtained from the RFEM, F_y^{RFEM} , varies from 0.70 to 1.56, as reported in Tab. 6.1. When considering only the cases that satisfy the geometric condition (Eq. (5.30)), this ratio ranges from 0.76 to 1.24.

In absolute terms, these results lack significant meaning; however, they offer a framework for evaluating the accuracy of the beam-to-column joint finite element's results when characterizing component behavior using the NGM.

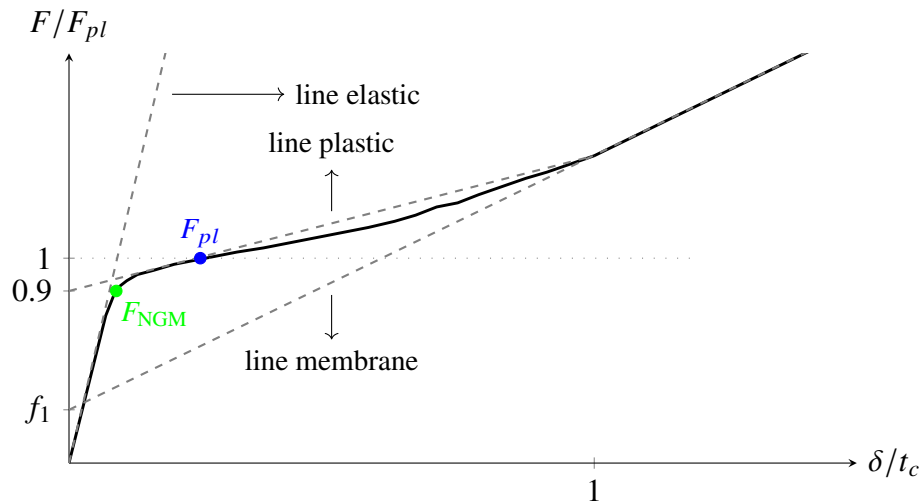


Figure 6.9: Schematic representation of the yielding force (adapted from [207]).

Table 6.1: Comparing yield strengths obtained by different methods.

L [mm]	f [mm]	u [mm]	S_i [kNm]	F_{pl} [kN]	F_{NGM} [kN]	F_y^{RFEM} [kN]	$\frac{F_{NGM}}{F_{pl}}$	$\frac{F_{NGM}}{F_y^{RFEM}}$
200	20	20	77763.5	102.9	100.1	101.1	0.97	0.99
200	20	40	88761.7	117.3	115.9	112.2	0.99	1.03
200	20	80	110758.1	149.1	152.4	132.8	1.02	1.15
200	20	120	132754.5	164.9	171.9	152.8	1.04	1.13
200	20	160	154750.9	180.7	192.2	174.4	1.06	1.10
200	40	20	95922.4	117.5	114.1	113.9	0.97	1.00
200	40	40	111405.6	133.9	131.7	126.9	0.98	1.04
200	40	80	142371.9	160.2	160.9	149.9	1.00	1.07
200	40	120	173338.3	177.9	181.3	174.5	1.02	1.04
200	40	160	204304.7	195.7	202.3	198.7	1.03	1.02
200	90	20	191160.0	163.3	156.0	153.2	0.96	1.02
200	90	40	236247.6	176.2	168.4	173.9	0.96	0.97
200	90	80	326422.8	202.0	193.9	213.1	0.96	0.91
200	90	120	416598.0	227.8	219.5	253.5	0.96	0.87
200	90	160	506773.2	253.7	245.8	286.2	0.97	0.86
200	140	20	599963.6	227.3	210.6	225.8	0.93	0.93
200	140	40	831152.0	251.0	231.9	271.6	0.92	0.85
200	140	80	1293528.9	298.3	275.5	362.0	0.92	0.76

Continued on next page ...

Table 6.1: Values test (*cont.*)

L	f	u	S_i	F_{pl}	F_{NGM}	F_y^{RFEM}	$\frac{F_{NGM}}{F_{pl}}$	$\frac{F_{NGM}}{F_y^{RFEM}}$
[mm]	[mm]	[mm]	[kNm]	[kN]	[kN]	[kN]		
200	140	120	1755905.7	345.6	319.6	452.6	0.92	0.71
200	140	160	2218282.5	393.0	363.8	517.0	0.93	0.70
300	20	20	31706.0	94.0	96.0	80.3	1.02	1.20
300	20	40	34707.8	103.0	107.8	89.2	1.05	1.21
300	20	80	40711.5	122.2	134.9	99.4	1.10	1.36
300	20	120	46715.3	143.0	167.6	113.1	1.17	1.48
300	20	160	52719.0	156.0	191.5	122.7	1.23	1.56
300	40	20	36108.0	102.7	105.1	89.3	1.02	1.18
300	40	40	39846.3	112.4	117.5	95.5	1.05	1.23
300	40	80	47322.9	133.1	146.0	110.4	1.10	1.32
300	40	120	54799.4	152.6	175.4	122.2	1.15	1.43
300	40	160	62276.0	163.5	194.1	135.2	1.19	1.44
300	90	20	53058.2	128.9	131.1	108.1	1.02	1.21
300	90	40	60075.4	141.0	145.5	117.5	1.03	1.24
300	90	80	74109.8	160.3	169.6	133.5	1.06	1.27
300	90	120	88144.3	173.9	187.1	151.4	1.08	1.24
300	90	160	102178.7	187.4	205.3	166.6	1.10	1.23
300	140	20	88235.9	161.6	160.9	132.7	1.00	1.21
300	140	40	103767.5	170.5	170.1	144.9	1.00	1.17
300	140	80	134830.6	188.2	188.9	168.2	1.00	1.12
300	140	120	165893.7	206.0	208.2	191.3	1.01	1.09
300	140	160	196956.9	223.7	227.9	211.3	1.02	1.08

6.4 Strength reduction factor of the NGM yield force

As previously mentioned, the NGM presents an analytical approach to calculate the yielding force of a plate with two opposite sides fixed and a central region loaded. However, utilizing this model to estimate the yielding force of a column face for the deformation mode illustrated in Fig. 6.2(d), within the scope of the framework presented in Section 6.2, is unsuitable due to the border limitations of the

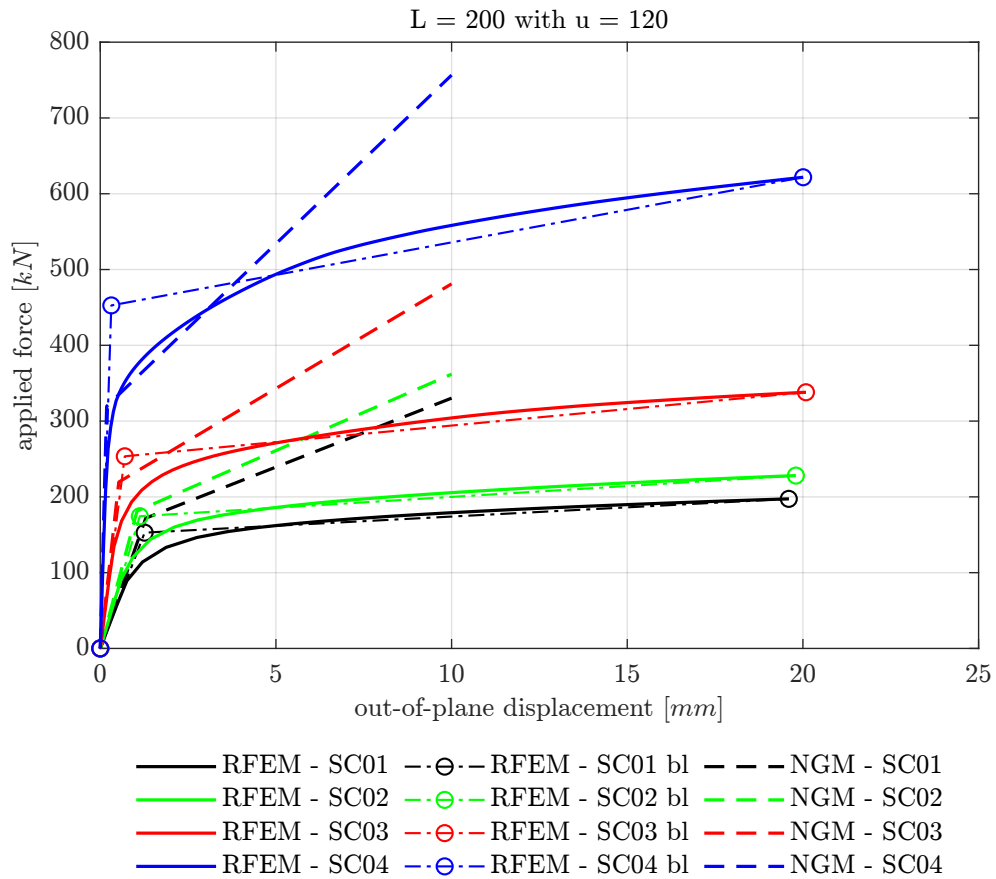


Figure 6.10: $F - \delta$ comparison between RFEM and NGM for $L_1 = 200$ and $u = 120$ and all SCs.

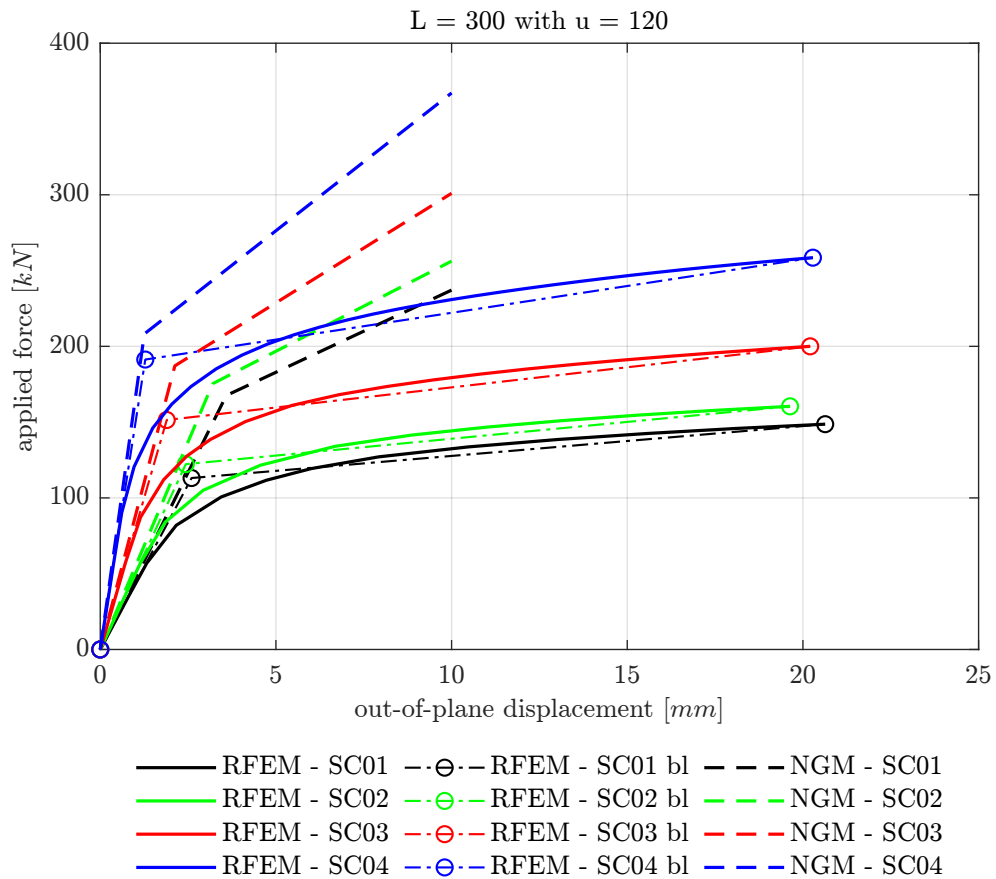


Figure 6.11: $F - \delta$ comparison between RFEM and NGM for $L_2 = 300$ and $u = 120$ and all SCs.

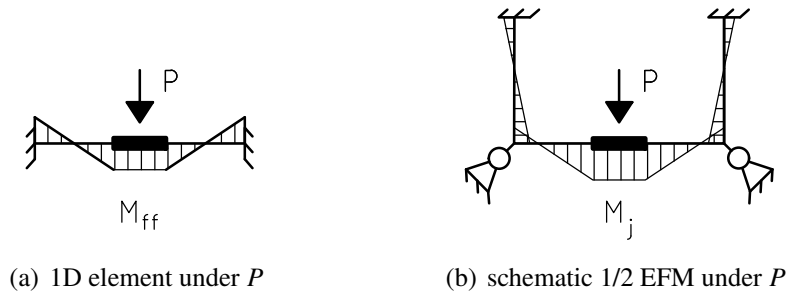


Figure 6.12: Analogy between a 1D element and 1/2 EFM for the strength reduction factor.

column face. Although the column face borders are not entirely fixed, they are not free to rotate either. Hence, a smaller yielding force is expected to be observed in the case of the tube face.

Accordingly, a reduction factor for the yielding force associated with the deformation mode illustrated in Fig. 6.2(d) was computed using an analogy for the EFM depicted in Fig. 6.12. Since the bending moment generated by a force P on the 1D element with fully fixed ends, M_{ff} , is smaller than the bending moment obtained by applying the same force to the EFM, M_j , a *strength reduction factor* (*SRF*) for the NGM yielding force of the column face is defined as the ratio between the bending moments using a 1D frame-element that is fully fixed at both ends and the bending moment calculated on 1/2 of an EFM. This ratio is expressed as follows:

$$SRF = \frac{M_{ff}}{M_j} \tag{6.4}$$

where M_{ff} and M_j are defined in Fig. 6.12. Consequently, the yielding force associated with the deformation mode illustrated in Fig. 6.2(d) will be deemed as:

$$F_y^A = F_{NGM}^{SRF} = SRF F_{NGM} \tag{6.5}$$

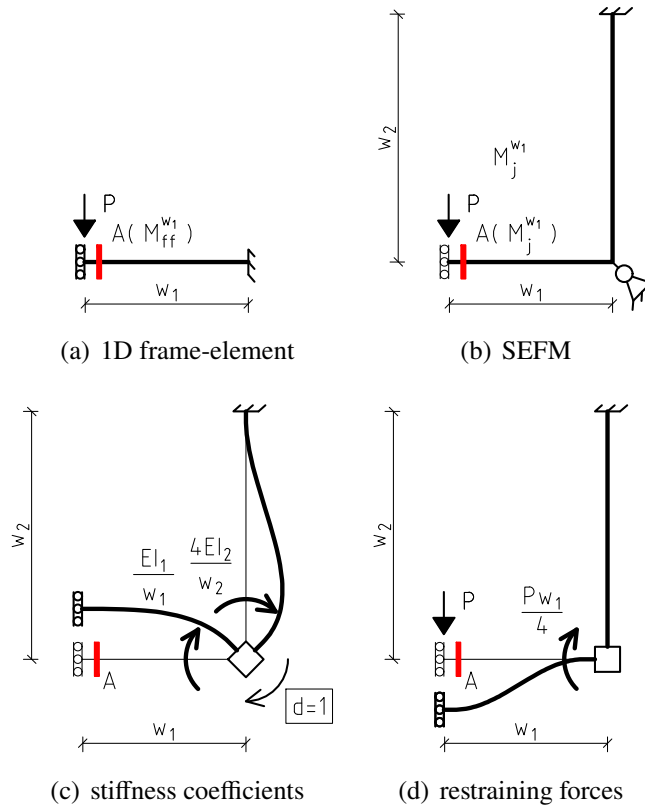
The computation of the strength reduction factor can be made using a 1/4 of an EFM as represented in Fig. 6.13 and Fig. 6.14.

The strength reduction factor, SRF^{w_1} , for the width (i.e., shorter column face) of the EFM is determined by calculating the ratio between bending moments calculated in section A, as shown in Fig. 6.13(a) and Fig. 6.13(b).

The bending moment in section A for the fully fixed 1D frame-element is:

$$M_{ff}^{w_1} = \frac{P w_1}{4} \tag{6.6}$$

The stiffness coefficient and fixation force for the DOF d , as shown in Fig. 6.13(c) and Fig. 6.13(d),


 Figure 6.13: Strength reduction factor for the shorter column face (w_1).

as well as the displacement in the DOF associated with P , are represented by Eqs. (6.7) through (6.9).

$$k^{w_1} = \frac{E I_1}{w_1} + \frac{4 E I_2}{w_2} \quad (6.7)$$

$$f^{w_1} = \frac{P w_1}{4} \quad (6.8)$$

$$d^{w_1} = (k^{w_1})^{-1} (-f^{w_1}) \quad (6.9)$$

Therefore, the bending moment in section A for 1/4 EFM is:

$$M_j^{w_1} = M_{ff}^{w_1} - d^{w_1} \frac{E I_1}{w_1} \quad (6.10)$$

Thus, the SRF for the shorter column face, w_1 , is:

$$SRF^{w_1} = \frac{M_{ff}^{w_1}}{M_j^{w_1}} \quad (6.11)$$

Similarly, the determination of the strength reduction factor for the length of the EFM, SRF^{w_2} , involves the computation of the ratio between bending moments calculated in section B, as illustrated in Fig. 6.14(a) and Fig. 6.14(b). Employing a methodology akin to the aforementioned, utilizing

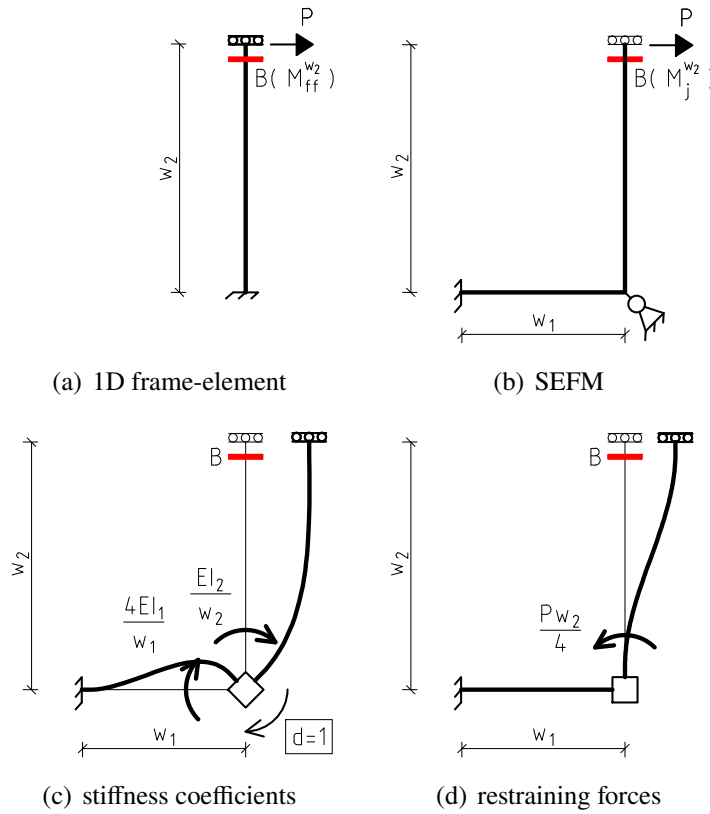


Figure 6.14: Strength reduction factor for the longer column face (w_2).

Fig. 6.14(c) and Fig. 6.14(d), and Eqs. (6.12) to (6.16). Thus, the *SRF* for the shorter column face, w_2 , is expressed as per Eq. (6.17).

$$M_{ff}^{w_2} = \frac{P w_2}{4} \quad (6.12)$$

$$k^{w_2} = \frac{E I_2}{w_2} + \frac{4 E I_1}{w_1} \quad (6.13)$$

$$f^{w_2} = \frac{P w_2}{4} \quad (6.14)$$

$$d^{w_2} = (k^{w_2})^{-1} (f^{w_2}) \quad (6.15)$$

$$M_j^{w_2} = M_{ff}^{w_2} + d^{w_2} \frac{E I_2}{w_2} \quad (6.16)$$

$$SRF^{w_2} = \frac{M_{ff}^{w_2}}{M_j^{w_2}} \quad (6.17)$$

To demonstrate the impact of the adjustment, the values of F_{NGM} , F_{NGM}^{SRF} , and *SRF* were solely computed for the RHS case. The values of F_{pl} are tabulated in Tab. 6.2, while the values of F_{NGM}^{SRF} and *SRF* for R0 and R1 are presented in Tab. 6.3 and Tab. 6.4, respectively.

Table 6.2: Values of F_{NGM} for RHS [kN].

radius	face dimension	SC01	SC02	SC03	SC04
R0	L1	171.92	181.31	219.55	319.57
R0	L2	167.57	175.36	187.13	208.20
R1	L1	175.50	187.64	242.57	433.16
R1	L2	170.75	174.89	189.91	217.71

Table 6.3: Values of SRF for RHS-R0.

EFM	F_{NGM}^{SRF}				SRF			
	SC01	SC02	SC03	SC04	SC01	SC02	SC03	SC04
HR-EFM-IF-R0-L1	148.02	149.32	144.11	91.82	0.86	0.82	0.66	0.29
HR-EFM-IF-R0-L2	147.90	156.01	173.58	203.84	0.88	0.89	0.93	0.98
HR-EFM-IEq-R0-L1	143.01	145.64	155.45	171.23	0.83	0.80	0.71	0.54
HR-EFM-IEq-R0-L2	151.79	158.19	169.32	195.20	0.91	0.90	0.90	0.94
PR-EFM-IF-R0-L1	139.63	146.26	171.63	227.19	0.81	0.81	0.78	0.71
PR-EFM-IF-R0-L2	143.61	150.77	163.14	187.61	0.86	0.86	0.87	0.90
PR-EFM-IEq-R0-L1	134.22	139.73	159.78	193.14	0.78	0.77	0.73	0.60
PR-EFM-IEq-R0-L2	148.02	155.73	169.43	195.76	0.88	0.89	0.91	0.94

Table 6.4: Values of SRF for RHS-R1.

EFM	F_{NGM}^{SRF}				SRF			
	SC01	SC02	SC03	SC04	SC01	SC02	SC03	SC04
HR-EFM-IF-R1-L1	156.25	159.76	157.81	82.44	0.89	0.85	0.65	0.19
HR-EFM-IF-R1-L2	151.13	156.21	177.96	215.14	0.89	0.89	0.94	0.99
HR-EFM-IEq-R1-L1	150.89	155.97	178.34	248.95	0.86	0.83	0.74	0.57
HR-EFM-IEq-R1-L2	155.90	158.25	170.19	201.55	0.91	0.90	0.90	0.93
PR-EFM-IF-R1-L1	142.90	151.98	192.13	330.35	0.81	0.81	0.79	0.76
PR-EFM-IF-R1-L2	145.85	149.77	164.29	191.05	0.85	0.86	0.87	0.88
PR-EFM-IEq-R1-L1	136.89	144.53	176.80	264.81	0.78	0.77	0.73	0.61
PR-EFM-IEq-R1-L2	150.78	155.28	171.97	204.77	0.88	0.89	0.91	0.94

6.5 Validation of the framework for nonlinearity

A series of nonlinear analyses were conducted on the proposed beam-to-column joint finite element using nonlinear behavior ascribed to the tube components in OpenSees and Abaqus to verify and validate the assumptions outlined in the preceding sections.

6.5.1 OpenSees models

The OpenSees models are described in Section 5.4.2. An exemplar OpenSees model file can be found in Appendix F.1, while a joint definition model file for the nonlinear behavior (bilinear) can be found in Section F.3.

The analysis was conducted for the PR-EFM-IF-R0-SC01 case. In this scenario, the behavior of the elastic component was determined using Eqs. (5.15) to (5.17).

The nonlinear behavior was achieved by assigning a uniaxialMaterial Steel01 material type to the tube components, which required the input of the yield strength, the initial elastic tangent, and the strain-hardening ratio (i.e., the ratio between the post-yield tangent and initial elastic tangent) which was assumed to be 1 ‰. Moreover, the analysis was carried out in displacement control.

To determine the yield strength, the maximum elastic displacement was first determined for each column face using the following method:

$$d^A = d^C = \frac{F_{\text{NGM}}^{\text{SRF}}}{k_{\text{comp.25}}^{\text{PR-EFM-IF}} + 2 k_{\text{comp.29}}^{\text{PR-EFM-IF}}} \quad (6.18)$$

$$d^B = d^D = \frac{F_{\text{NGM}}^{\text{SRF}}}{k_{\text{comp.26}}^{\text{PR-EFM-IF}} + 2 k_{\text{comp.29}}^{\text{PR-EFM-IF}}} \quad (6.19)$$

Then the yielding strength of the face components is then derived as follows:

$$F_{y.25} = F_{y.27} = k_{\text{comp.25}}^{\text{PR-EFM-IF}} d^A \quad (6.20)$$

$$F_{y.26} = F_{y.28} = k_{\text{comp.26}}^{\text{PR-EFM-IF}} d^B \quad (6.21)$$

In reference to the interaction components, according to Hypothesis 2 in Section 6.2, they should enter the plastic range simultaneously with the first adjacent face component. However, as previously mentioned, this cannot be achieved with the current beam-to-column joint finite element implementation. Consequently, two alternative versions are being considered:

- Version 1: The yield strength of the interaction component will be reached at the same

deformation as that of the face component on the shorter column face (i.e., width or face A/C).

- Version 2: The yield strength of the interaction component will be reached at the same deformation as that of the face component on the longer column face (i.e., width or face B/D) in the other.

This aspect leads to the following interaction components definitions:

$$F_{y.29}^{v1} = F_{y.30}^{v1} = F_{y.31}^{v1} = F_{y.32}^{v1} = k_{\text{comp.29}}^{\text{PR-EFM-IF}} \frac{F_{y.25}}{k_{\text{comp.25}}^{\text{PR-EFM-IF}}} \quad (6.22)$$

$$F_{y.29}^{v2} = F_{y.30}^{v2} = F_{y.31}^{v2} = F_{y.32}^{v2} = k_{\text{comp.29}}^{\text{PR-EFM-IF}} \frac{F_{y.26}}{k_{\text{comp.26}}^{\text{PR-EFM-IF}}} \quad (6.23)$$

Fig. 6.15 shows the nonlinear behavior used as input in OpenSees for the PR-EFM-IF-R0-SC01 case, specifically for the two face components and the interaction component. It is important to note that the values on the vertical axis for the longer column face, as shown in Fig. 6.15(b), indicate a lower magnitude based on the performed calculation. In each figure, vertical lines passing through the displacements that mark the onset of post-elastic behavior are included beside the force-displacement curves. These vertical lines will be implemented in the plots showcased in Section 6.5.4. The indices "v1" and "v2" correspond to the previously presented versions.

6.5.2 RFEMs build with Abaqus

The validation of the results is done in comparison with RFEMs developed in Abaqus. The RFEMs geometry, boundary condition, and mesh assignment are described in Sections 5.4.3 and the material properties and type of analysis in Section 5.5.5.

6.5.3 Load Patterns

The LPs considered for this section are presented in Fig. 6.16.

6.5.4 Results

The results of the nonlinear analysis are shown in terms of applied force-displacement and applied force-deformation curves for the column faces and tube components, respectively, for the LPs depicted in Fig. 6.16. The outcomes are graphically depicted in Figs. 6.17 to 6.24 for the LP0*i*-L1, with $i = [1, 4]$.

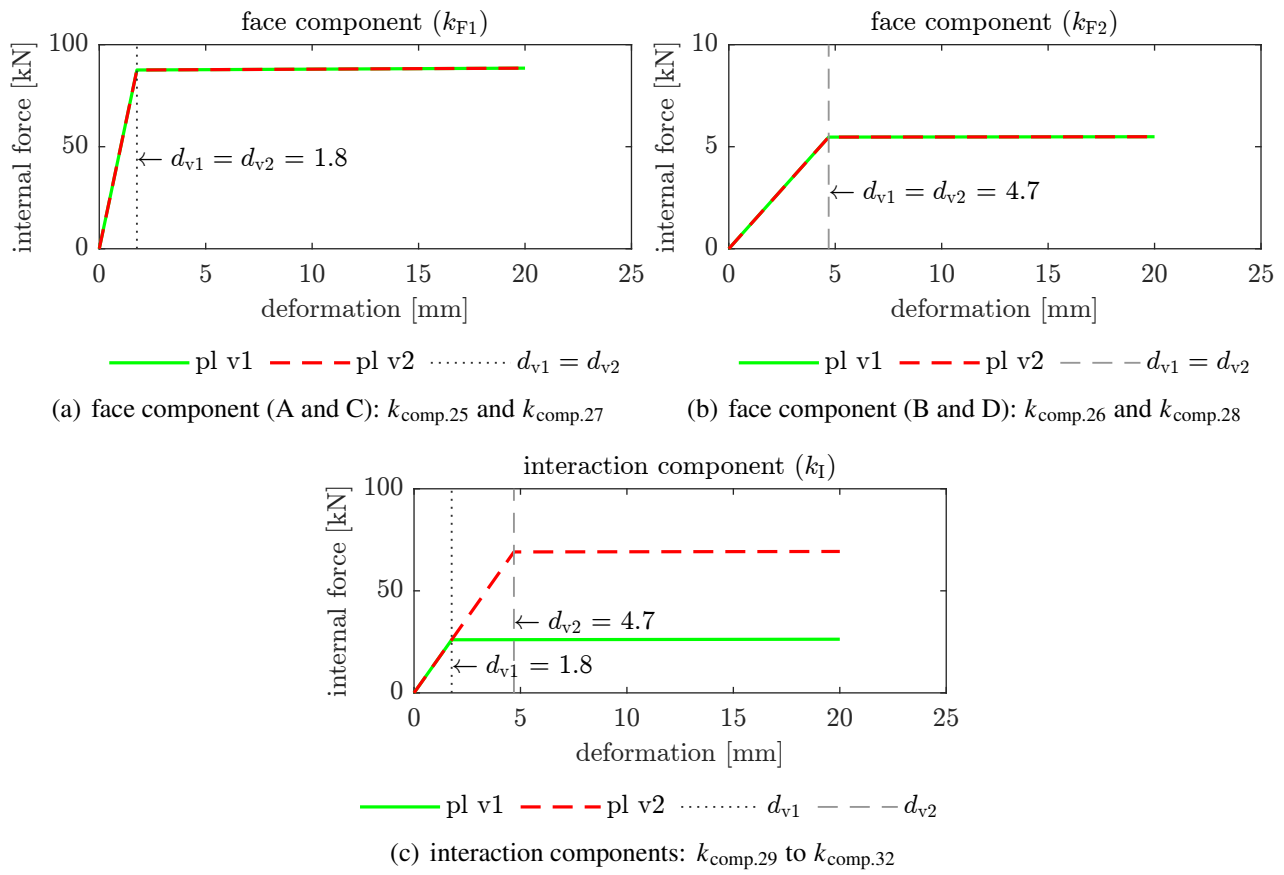


Figure 6.15: Force-deformation curves used as input in OpenSees for the PR-EFM-IF-R0-SC01 case.

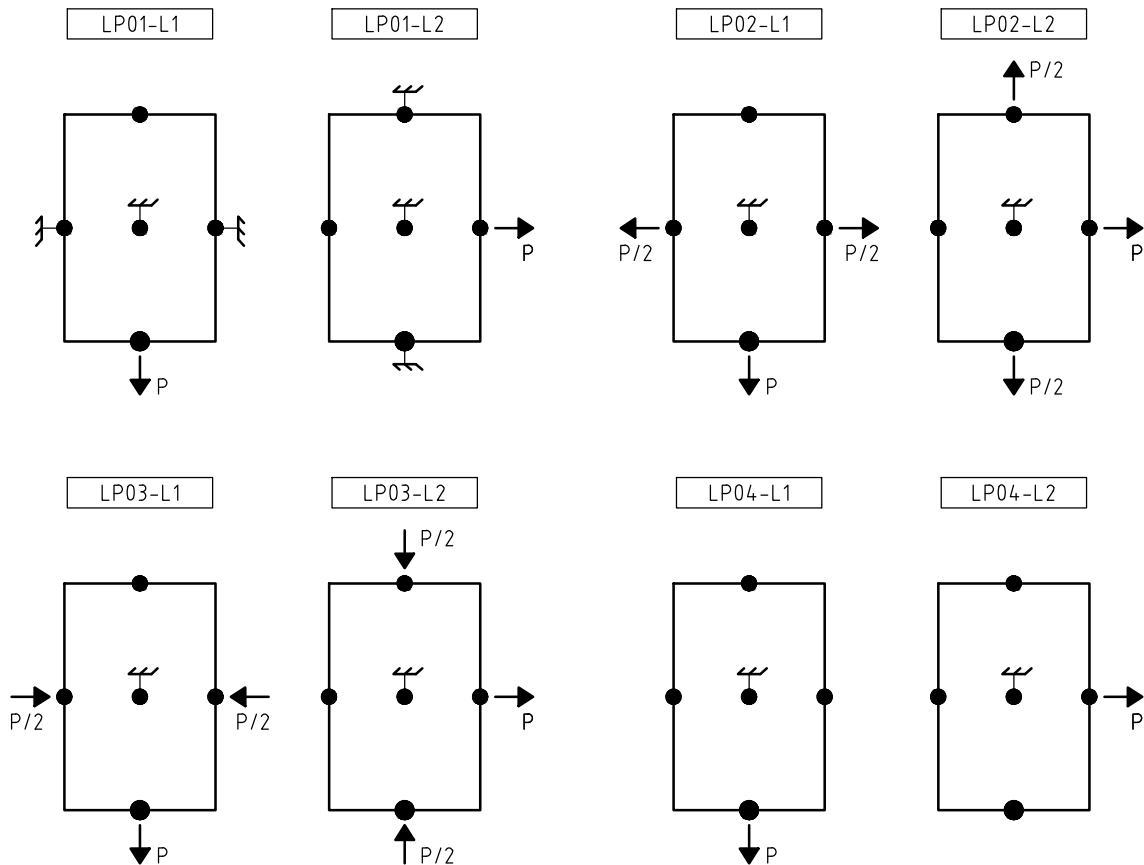


Figure 6.16: Load Patterns for the nonlinear calculation.

The figures are generated solely for relevant column faces and tube components in accordance with the applied LP. The results for LP0*i*-L2, with $i = [1, 4]$ are presented in Appendix P.

Regarding the applied force-displacement curves of the column faces, four curves are presented: (i) the bilinear idealization of the RFEM's nonlinear curve (black continuous line: "RFEM"), (ii) the linear elastic curve obtained from OpenSees by assigning linear elastic behavior to the components (blue continuous curve: "el"), (iii) the curve obtained from OpenSees by deriving the interaction component from Eq. (6.22) (green continuous line: "pl v1"), and (iv) the curve obtained from OpenSees by deriving the interaction component from Eq. (6.23) (red dashed line: "pl v2").

In terms of the applied force-deformation curves of the tube components, the figures exhibit the same curves as previously presented, with the exception of the one obtained from the RFEMs (i.e., there are no components in RFEMs). Additionally, the figures contain two vertical lines, d_{v1} and d_{v2} that were discussed in Section 6.5.1, to help identify the onset of the post-elastic behavior.

6.6 Conclusions

The case analyses presented in the preceding section demonstrate that the elastic behavior of joints can be accurately evaluated, as evidenced in Section 5.2. Nevertheless, "pl v1" models usually underestimate the post-yielding behavior, while "pl v2" models overestimate it.

By examining the applied force-deformation relationship of the components, it is observed that the results for the LP01 case (Fig. 6.18 and Fig. P.2) are consistent with expectations, indicating that both the face and interaction components enter the post-elastic range simultaneously, thus confirming the hypothesis presented in the previous sections.

This observation is further validated by the LP04-L1 case (Fig. 6.24), where the interaction components enter the nonlinear range concurrently with face components 26 and 28. However, both components reach the nonlinear range earlier than anticipated (Fig. 6.24), suggesting that the constitutive relation for face component 25 underestimates the yield force.

Accurately determining the initiation of the plastic range of the interaction components is crucial for obtaining reasonable estimates for joints in the nonlinear range. If the interaction component enters the plastic range before the face components, the joint's strength is significantly underestimated (e.g., LP02-L1: components 31 and 32 Fig. 6.20).

However, if the boundary condition permits avoiding this situation (e.g., LP01-L1 with "pl v1" and LP01-L2 with "pl v2"), the accuracy match between Abaqus and OpenSees is similar to the analysis conducted in Section 6.3. This indicates that improving the definition of the yielding force of the face components is necessary.

Therefore, it can be concluded that an alternative procedure is required for defining the interaction component's yield strength. Section 7.3 offers suggestions in this regard.

Furthermore, it is evident that an elastic-perfect plastic behavior for components is inadequate, and further investigation is necessary to model the post-yielding regime.

The presented examples demonstrate that the proposed approach provides a safe strength criterion when the "pl v1" modeling strategy is employed for interaction components, assuming that the elastic limit represents the maximum load allowable for the joint. Consequently, the initiation of the nonlinear behavior of the components serves as an alternative to the strength criteria set forth in Section 5.5.

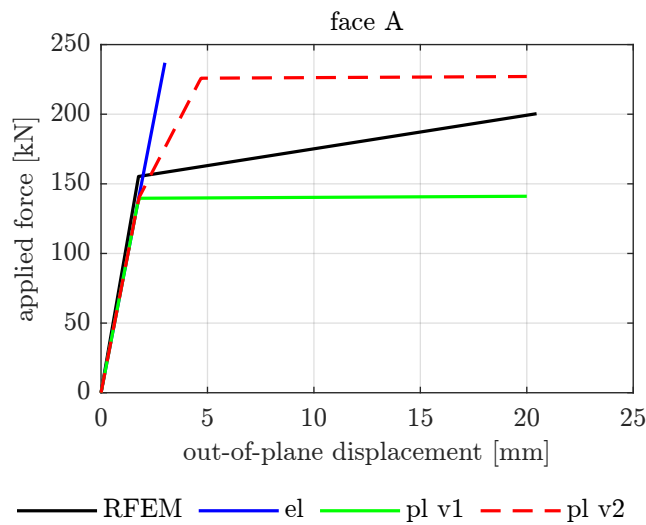


Figure 6.17: Force-displacement under LP01-L1.

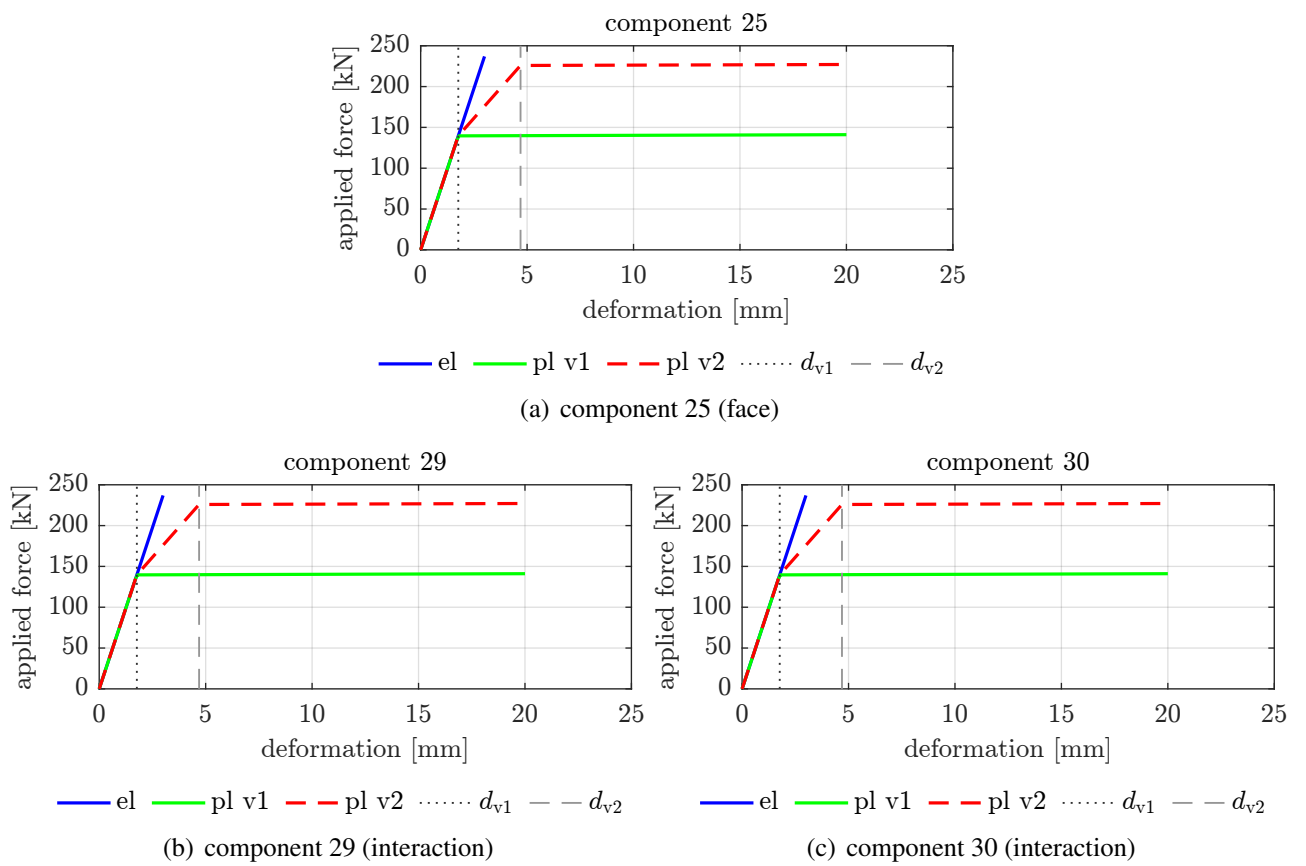


Figure 6.18: Force-deformation curves in the tube components under LP01-L1.

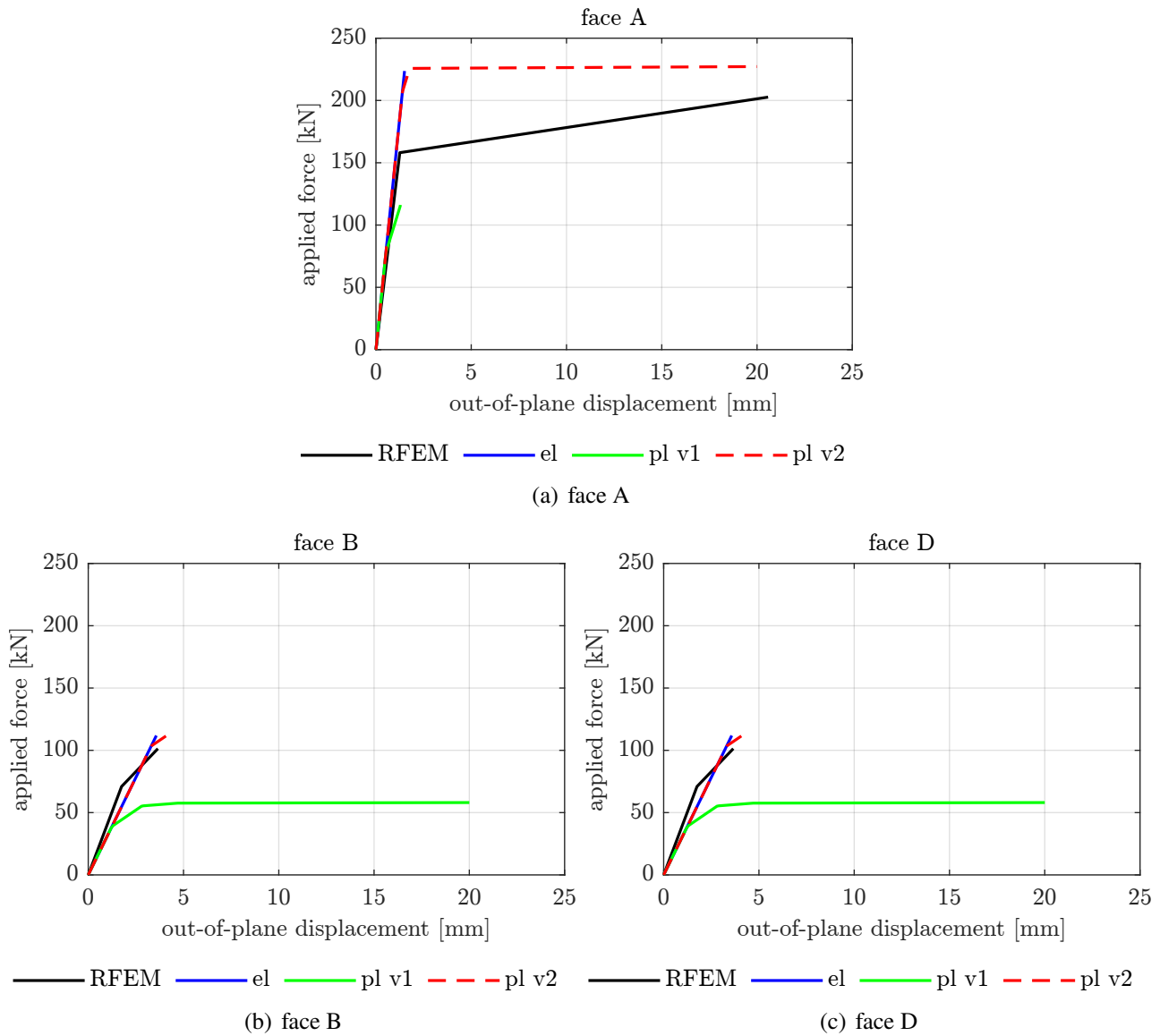


Figure 6.19: Force-displacement under LP02-L1.

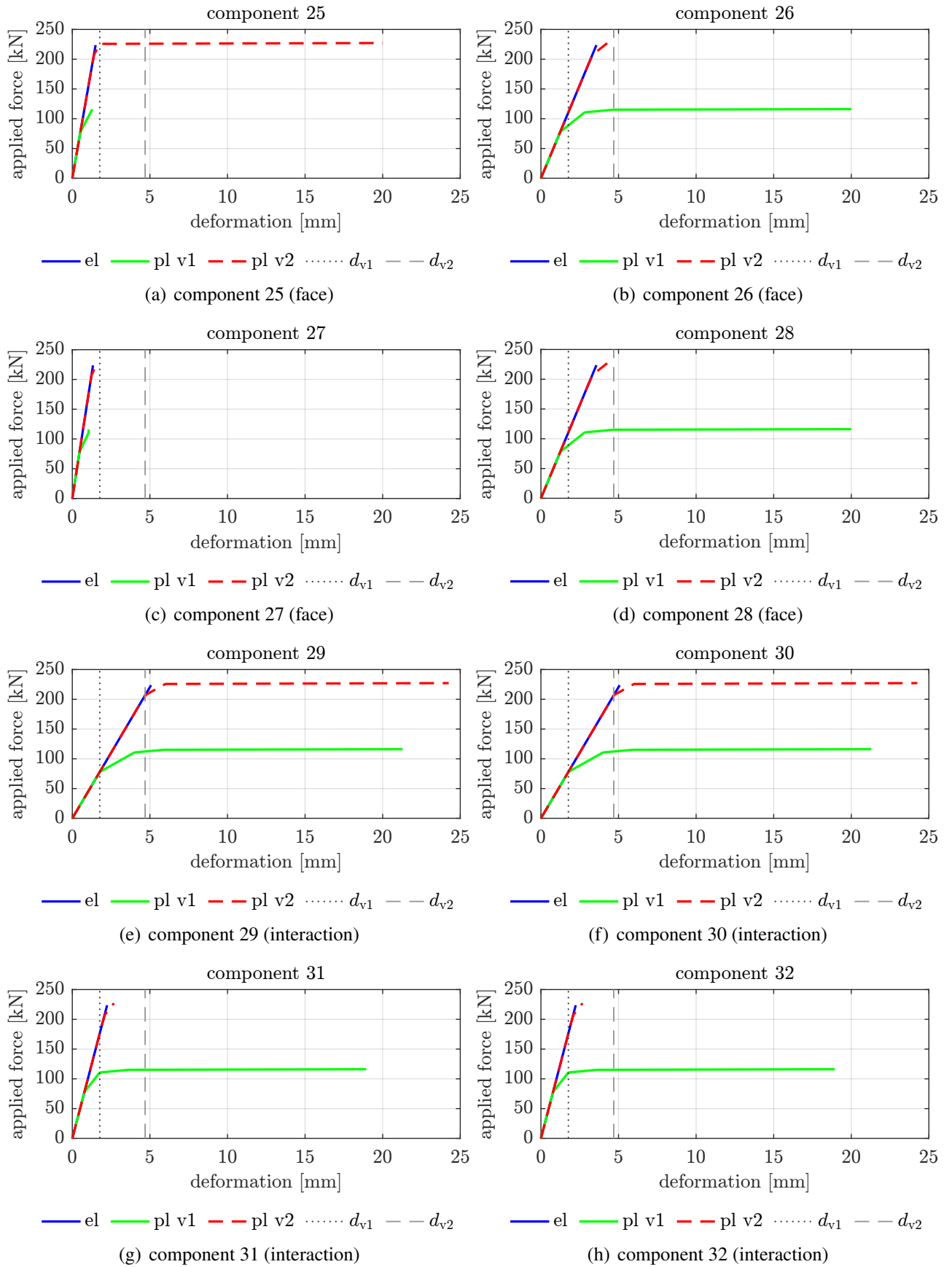


Figure 6.20: Force-deformation curves in the tube components under LP02-L1.

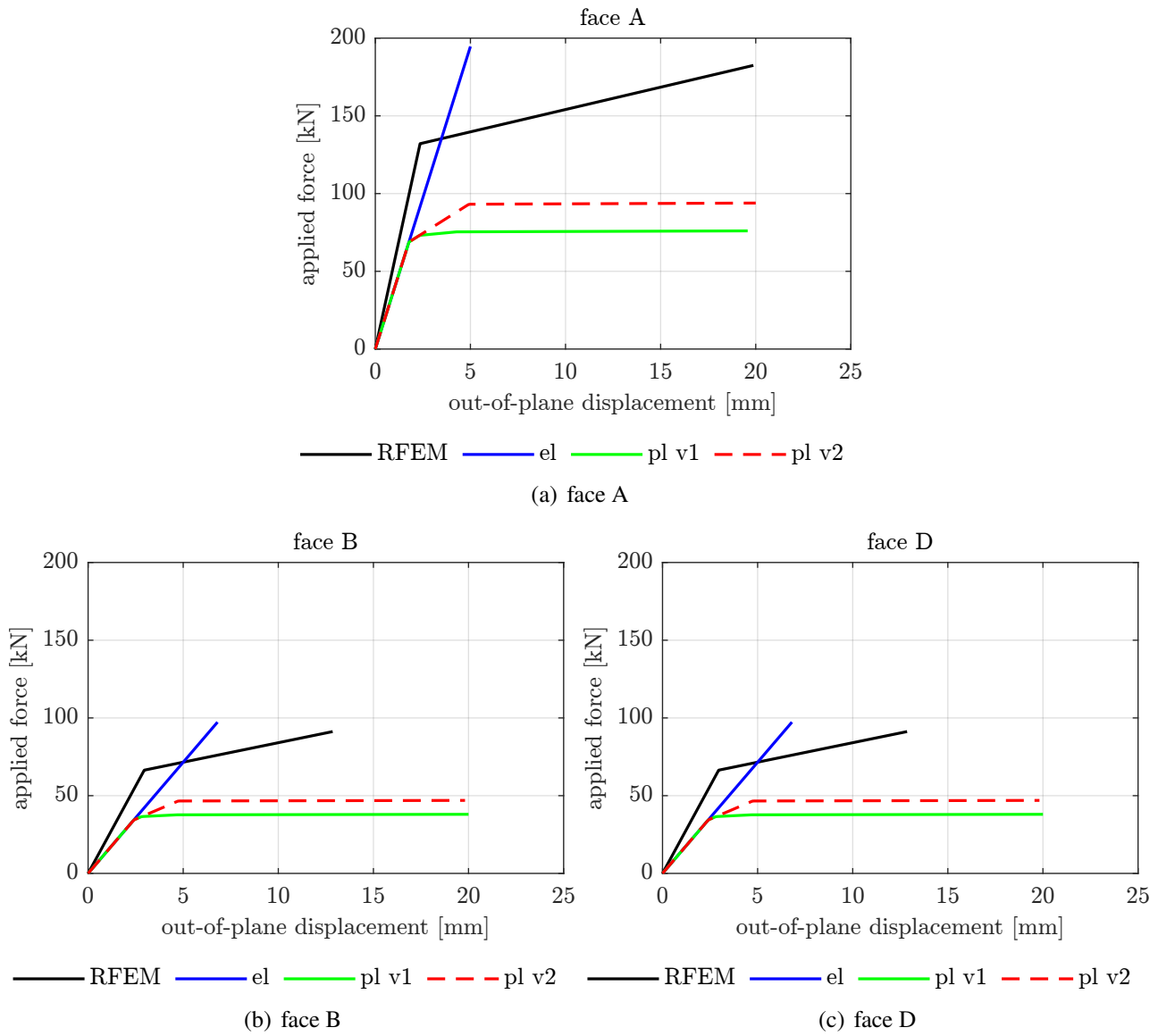


Figure 6.21: Force-displacement under LP03-L1.

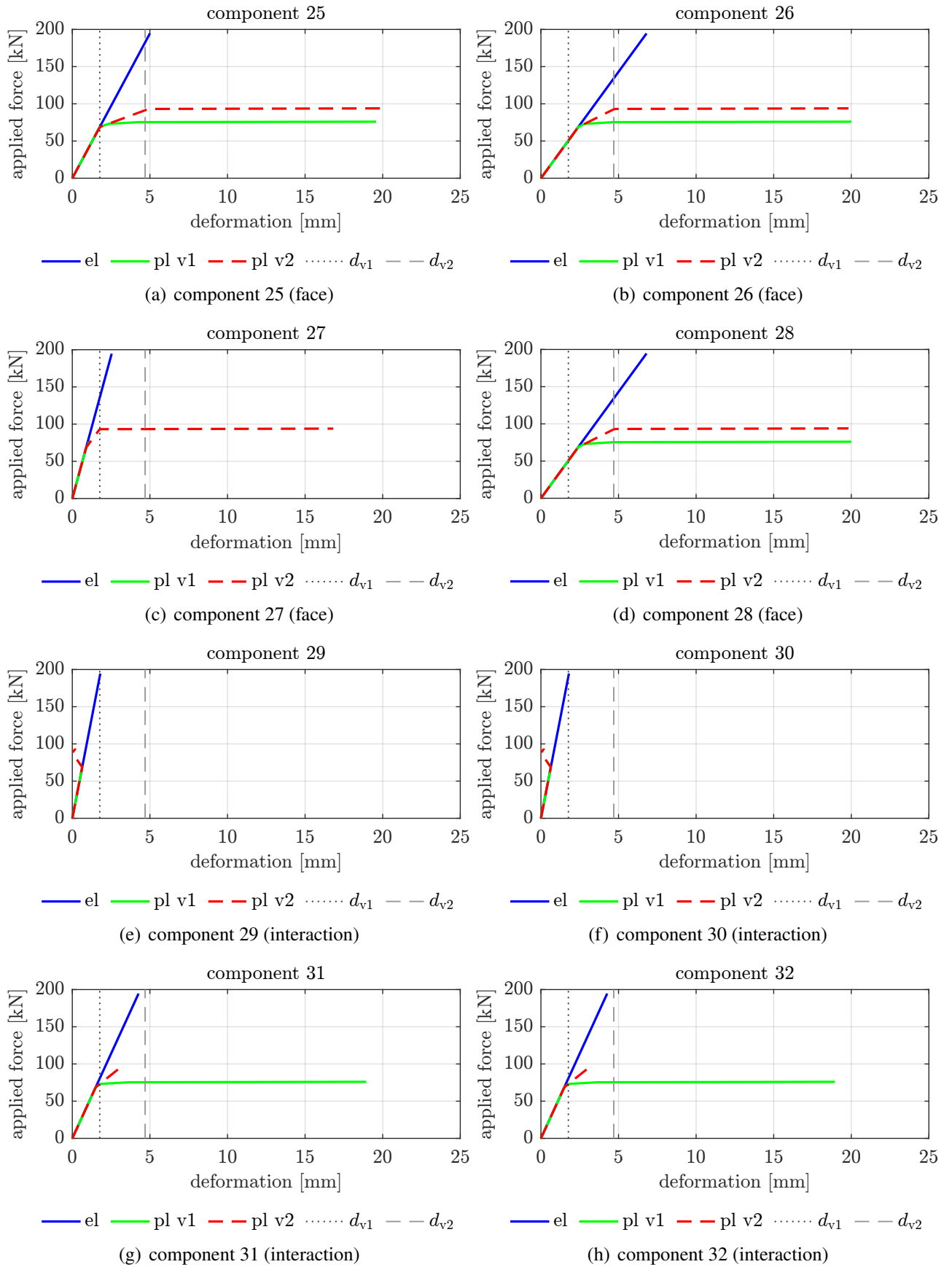


Figure 6.22: Force-deformation curves in the tube components under LP03-L1.

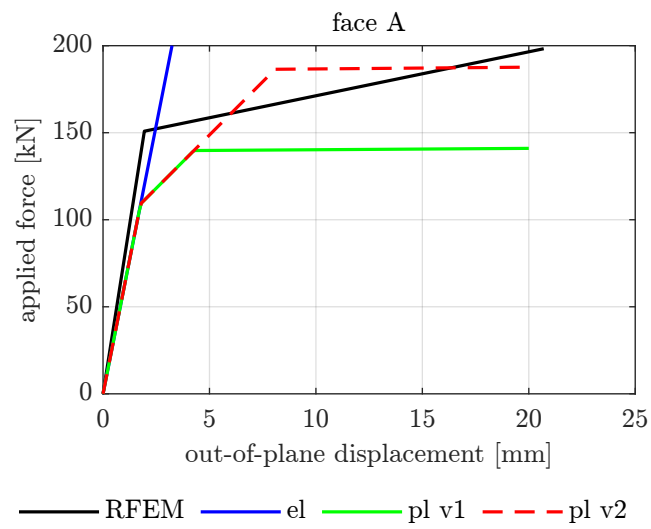


Figure 6.23: Force-displacement under LP04-L1.

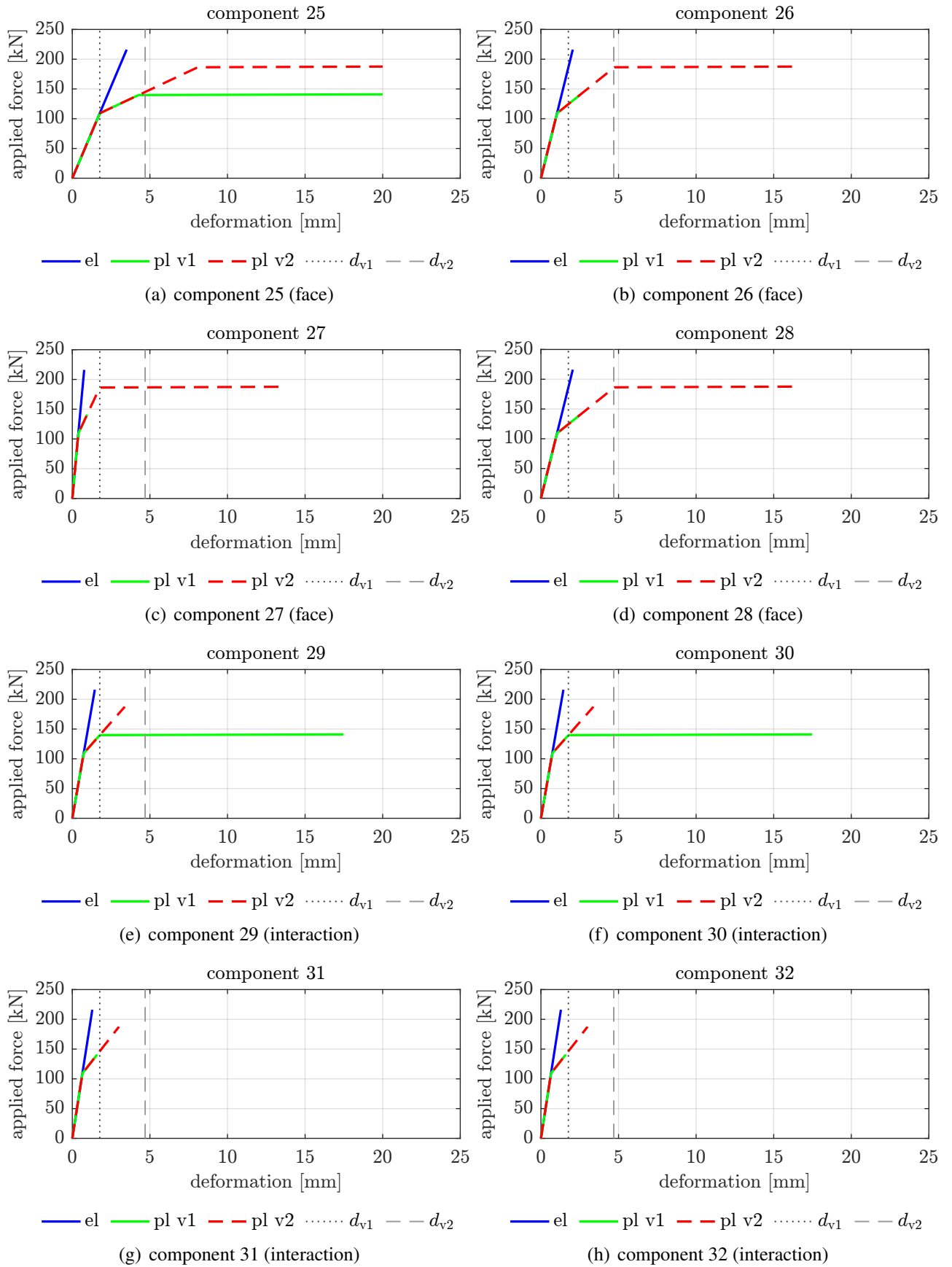


Figure 6.24: Force-deformation curves in the tube components under LP04-L1.

Chapter 7

Conclusions and future lines of investigations

7.1 Summary of the work

Modular construction has become popular due to its benefits, but this type of construction also faces a few challenges, such as limited design flexibility and building code restrictions. Joints are critical in achieving modular construction advantages, and plug-and-play joints have become attractive. However, challenges such as structural integrity and compatibility need to be addressed. To capitalize on the advantages of modular systems and plug-and-play joints but mainly to tackle the existing challenges, the INNO3DJOINTS project [5] developed an innovative 3D plug-and-play joint system for hybrid tubular construction.

The research presented in this manuscript originated as part of the INNO3DJOINTS project. This system connects tubular columns with cold-formed lightweight steel truss-girders and cross-laminated timber slabs, yielding a highly efficient structural system. Furthermore, the project involved creating, formulating, and applying a macro-element to examine and design plug-and-play beam-to-column joints. The work developed for this Ph.D. thesis offers an alternative macro-element for using 3D component-based macro-element modeling for beam-to-column steel joints. The procedure utilized in this thesis aimed to create a flexible, physically meaningful, and comprehensible approach for designers, resulting in a more transparent model that is highly probable to be embraced by designers.

Accordingly, the current study focused on creating, developing, implementing, and calibrating a macro-element for an innovative 3D plug-and-play joint (P&PJ) system. The macro-element comprises three essential aspects: (i) is based on the component method, (ii) accounts for the 3D interaction between the faces of the tubular column, and (iii) the mechanical characteristics of its components have a clear physical meaning. The development of the macro-element was based on previous

research [153], [154], [199], which presented experimental and numerical results demonstrating that simultaneous loading of the different tube faces results in out-of-plane deformations that differ from those observed when each load is applied individually to each face. This phenomenon indicates the presence of an interaction between the tube faces.

The macro-element outlined in this document comprises connection components and tube components, which are further divided into face and interaction components. The validation of the macro-element involved a proof of concept validation using Refined Finite Element Model(s) (RFEM(s)) developed in Abaqus [113]. The results were favorable, and the macro-element was subsequently implemented in the OpenSees framework [115] as a standalone beam-to-column joint finite element, referred to as the Inno3DPnPJoint Class [180].

The primary objective of the beam-to-column joint finite element was to simplify the design of 3D structures, and its development was not exclusively limited to research purposes. To achieve this goal, the incorporation of a transformation matrix into the code removed any constraints on the definition of the joint element's coordinates. The mathematical formulation of the element, both linear and nonlinear, was presented, and a comprehensive user manual was provided to assist users in utilizing the element effectively.

This study determined the mechanical properties of the proposed macro-element in the linear regime regarding stiffness and strength. The beam-to-column joint finite element needed suitable stiffness parameters for realistic internal force distributions and a strength criterion for evaluating the joint's structural safety to meet practical requirements.

The stiffness of the components was analytically defined using Equivalent Frame Models (EFMs), also referred to as ring models in the field of research on tubular structures [154], [205]. The basic principle underlying the use of EFMs is to represent the behavior of the tubular column in the beam-to-column joint region through a planar frame-model, in which the frame-elements (i.e., Euler-Bernoulli elements) represent the faces of the tube. The forces and deformations in the tube faces caused by the interaction of the beams connected with the column are represented by forces applied in the frame-elements and mid-span displacements of these elements, respectively.

Upon conducting a literature review, it was found that existing EFMs only consider square tubular cross-sections, neglecting the size of the "loaded region" of the joint and the bent portion of the tube in the interaction between the column faces [152]. To address these limitations, four EFMs were presented: (i) the Harada frame-model for square cross-sections (HS-EFM) for 3D macro-modeling of beam-to-column joints under cyclic loading [152]–[154], (ii) the Harada extended frame-model for rectangular cross-sections (HR-EFM), an extension of the HS-EFM for both square and rectangular cross-sections, (iii) the Proposed frame-model for square cross-sections (PS-EFM) that considers the

connection's size, suitable for the P&PJ system, and (iv) the Proposed frame-model for rectangular cross-sections (PR-EFM), an extension of the PS-EFM for both square and rectangular cross-sections. To assess the feasibility of incorporating equivalent stiffness parameters in the EFM while accounting for the mutual influence of the stiffness of each face, resulting in an equivalent stiffness between both, two scenarios were tested for rectangular cross-sections: (i) assigning each face its corresponding moment of inertia (IF), and (ii) assigning each face the mathematical average of the moments of inertia of the column faces (IEq). Therefore, a total of six EFMs were evaluated.

The stiffness equations for the tube components of the proposed beam-to-column joint element were calculated in the current investigation, and the mechanical properties of the EFMs' frame-elements were derived from the Neves-Gomes Model (NGM) [155], [206]–[208]. Despite the NGM primarily being focused on the out-of-plane behavior of a single-column plate, it was utilized in the present study due to a lack of other appropriate formulations. The tube faces were considered as four separate column plates that interact with each other.

The bending stiffness of the EFMs' frame-elements was derived such that the frame-element displacement coincides with the out-of-plane deformation of the column plate. The validation and calibration of the EFMs' effective bending stiffness were conducted using RFEMs. The validation process entailed a parametric analysis that involved varying several parameters. Four parameters were considered in OpenSees: the column cross-section, load pattern (LP), socket configuration (SC), EFM type, and the impact of rounded corners (radius). In comparison, only three parameters were altered in Abaqus: the column cross-section, LP, and SC. While improving the accuracy of the results by adjusting the initial stiffness from the NGM was not the main focus of this study, two analytical approaches were proposed to achieve this objective.

The strength criterion developed in this study is based on the EFM technique, and it is a global criterion as it does not depend on assessing internal forces in any specific component. The criterion was established by defining the equivalent bending strength for the frame-elements of the EFMs, with the tube components of the beam-to-column joint finite element being considered structurally safe if the bending moment in any section of the frame-elements was lower than the equivalent bending strength. The equivalent bending strength was determined using the NGM and subsequently adjusted through a parametric analysis using RFEMs.

The conceptual framework for modeling the nonlinear behavior of the beam-to-column joint was investigated by analyzing the behavior of a tubular column within the joint region using RFEMs. As tube components do not possess the same physical meaning as components in traditional nonlinear analysis using the components method, a new strategy was established for using the macro-element's multiple OD elements to account for the various deformation patterns and interactions among the

column faces in the nonlinear regime focusing on the onset of post-yielding behavior. This involved the use of bilinear behavior curves for the tube components. Multiple hypotheses were tested, and the study concluded that the face component exhibited nonlinear behavior in conjunction with the interaction components, and the onset of their inelastic regime should be simultaneous. Subsequently, this hypothesis was validated using RFEMs, resulting in safe-sided results for identifying the beginning of the nonlinear regime. New developments necessary for improved modeling of the nonlinear regime were also identified.

7.2 Conclusions

The study presented in this document is a natural continuation of prior research conducted by the author's research group in the field of macro-modeling of beam-to-column joints. The principal conclusions of this study may be summarized as follows:

- the proposed macro-element developed for the modeling of the innovative 3D plug-and-play joint system has been successfully validated against RFEMs. This macro-element has been integrated to effectively replicate the 3D deformation of tubular columns by considering the interaction between the faces of the column;
- extending the macro-element to a beam-to-column joint finite element implemented within the OpenSees framework was a logical progression that provides widespread accessibility to all users. Moreover, the addition of the source code to the GitHub repository of OpenSees [180] enables modifications and enhancements from researchers worldwide;
- the stiffness definition of the joint element's components using the NGM approach yields satisfactory results and may be utilized in the absence of alternative methods;
- the strength criterion defined makes the tube components of the beam-to-column joint element deemed structurally safe;
- the nonlinearity behavior definition of the tube components is complex and requires further research to establish a clear and straightforward procedure.

7.3 Future lines of investigation

The doctoral thesis presents a macro-model that provides significant insights into various lines of research. Therefore, future studies may explore the following:

- investigating the behavior of the macro-element using alternative procedures to define the stiffness of the tube components based on their physical meaning other than EFM and/or the NGM developed for single-loaded plates;
- conducting extensive parametric studies to examine the impacts of socket height and column thickness, both within and beyond the bounds of the NGM;
- conducting 3D analysis on full structures with the beam-column joint finite element to assess improvement needs.

Furthermore, potential improvements to the beam-to-column joint finite element can be achieved through the following means:

- incorporating the nonlinear behavior of the interaction components dependent on the nonlinear behavior of the face components by modifying the interaction components to be defined within the source code rather than relying on user input;
- developing extended versions of the macro-element to account for the possibility of uncoupled movement of each socket part, particularly in situations where minor bending moments in truss-girders occur and no slab is present to absorb the minor bending moments;
- designing a user-friendly interface that directly defines the mechanical properties of the components based on the joint geometry and the mechanical characteristics of the steel, eliminating the need for post-processing work to compute the mechanical properties of components;
- utilizing, developing, and comparing various advanced material models for the behavior of the components.

As the study of beam-to-column joints in structures continues to advance, numerous potential areas remain for future investigation. These include exploring the ideas suggested previously, as well as other possible lines of inquiry. Such endeavors could yield more reliable and precise models for simulating joint behavior, thereby enhancing the comprehension of these critical structural elements. Through the pursuit of these research paths, scholars can push the limits of the field, promote knowledge growth, and contribute to the creation of safer and more resilient structures.

Appendices

Appendix A: P&PJ's components under tension and/or compression

The computation of the strength and stiffness of the components identified for the INNO3DJOINTS plug-and-play joint system [5], specifically in the simplest configuration of the P&PJ where a single truss-girder is connected to the column and subjected to tension or compression forces [197], are thoroughly presented hereinafter.

A.1 Column side wall

A.1.1 Strength

The strengths of the column side wall under tensile and compressive forces are determined according to [213], as shown in Fig. A.1. This method is planned to be used in the next revision of Eurocode 3 Part 1-8 (see the latest draft [214]).

The design resistance against tensile force, $N_{t,csw}$, for the column side wall is:

$$N_{t,csw} = \frac{2 f_{y0} t_0 b_w Q_f}{\gamma_{M0}} \quad (\text{A.1})$$

The effective breadth, b_w , for the side wall failure in tension is:

$$b_w = h_s + 5 t_0 \quad (\text{A.2})$$

The chord stress factor, Q_f , for the side wall failure in tension is:

$$Q_f = (1 - |n|)^{C_1} \quad (\text{A.3})$$

with:

$$n = \frac{N_0}{N_{pl,0}} + \frac{M_0}{M_{pl,0}} \quad (\text{A.4})$$

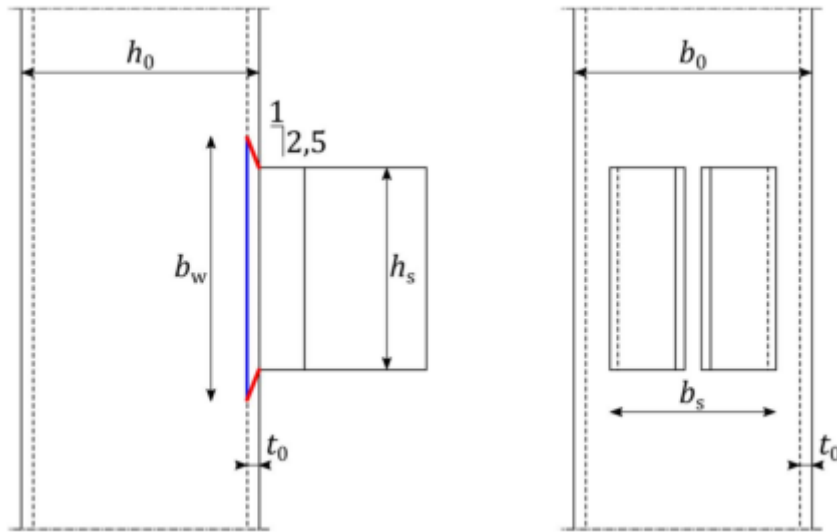


Figure A.1: Column side wall under tensile or compressive force.

and

$$C_1 = \begin{cases} 0.1 & , 0 \leq n \text{ (tension)} \\ 0.6 - \frac{b_s}{b_0} & , n < 0 \text{ (compression)} \end{cases} \quad (\text{A.5})$$

where:

N_0 = axial force in the column (tension > 0).

$N_{pl,0}$ = axial plastic strength of the column.

M_0 = bending moment in the column.

$M_{pl,0}$ = bending moment strength of the column.

The design resistance against compressive force, $N_{c,sw}$, for the column side wall is:

$$N_{c,sw} = \frac{2 k_{cx} \chi f_{y0} t_0 b_w Q_f}{\gamma_{M1}} \quad (\text{A.6})$$

where:

k_{cx} = correction factor equal to 0.8 if a socket is also provided on the column face opposite to the analyzed socket, and equal to 1.0 if not.

χ = reduction factor in accordance with [215] considering the curve "c" ($\alpha = 0.49$), and the following relative slenderness:

$$\bar{\lambda} = 3.46 \frac{\frac{h_0}{t_0} - 2}{\pi \sqrt{\frac{E}{f_{y0}}}} \quad (\text{A.7})$$

A.1.2 Stiffness

The stiffness of the column side wall under tensile or compressive forces is determined according to reference [216]. A stiffness factor equal to the component's stiffness divided by the steel's elasticity modulus is used, as in Eurocode 3 Part 1-8 [28].

The stiffness factor, k_{csw} , for the column side wall is:

$$k_{csw} = 2 \frac{0.7 b_w t_0}{h_0} \quad (\text{A.8})$$

A.2 Column face

A.2.1 Strength

The strengths of the column face under tensile and compressive forces are determined according to reference [213]. This method is planned to be used in the next revision of Eurocode 3 Part 1-8 (see the last draft [214]). Two failure modes are considered for this component, as presented in Fig. A.2:

(a) face plastification under bending

(b) face failure by punching shear

(a) Face plastification under bending:

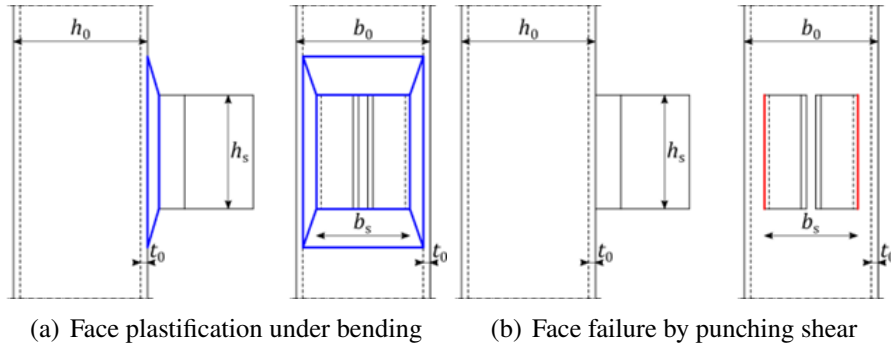


Figure A.2: Column face under tensile or compressive force.

The design resistance against tensile force, $N_{t,cb}$, for the column face plastification in bending is:

$$N_{t,cb} = \frac{Q_u Q_f f_{y0} t_0^2}{\gamma_{M0}} \quad (\text{A.9})$$

with Q_f defined by Eq. (A.3).

The mechanism factor, Q_u , for the face plastification is:

$$Q_u = \left(\frac{2\eta}{1-\beta} + \frac{4}{\sqrt{1-\beta}} \right) \quad (\text{A.10})$$

The design resistance against compressive force, $N_{c,cb}$, for the column face plastification in bending has the same value:

$$N_{c,cb} = N_{t,cb} \quad (\text{A.11})$$

(b) Face failure by punching shear:

The design resistance against tensile force, $N_{t,cps}$, for the column face in punching shear is:

$$N_{t,cps} = \frac{f_{y0}}{\sqrt{3} \gamma_{M0}} t_0 l_{p,eff} \quad (\text{A.12})$$

The effective length, $l_{p,eff}$, for the face in punching shear is:

$$l_{p,eff} = 2 h_s \quad (\text{A.13})$$

The design resistance against compressive force, $N_{c,cps}$, for the column face failure in punching shear has the same value:

$$N_{c,cps} = N_{t,cps} \quad (\text{A.14})$$

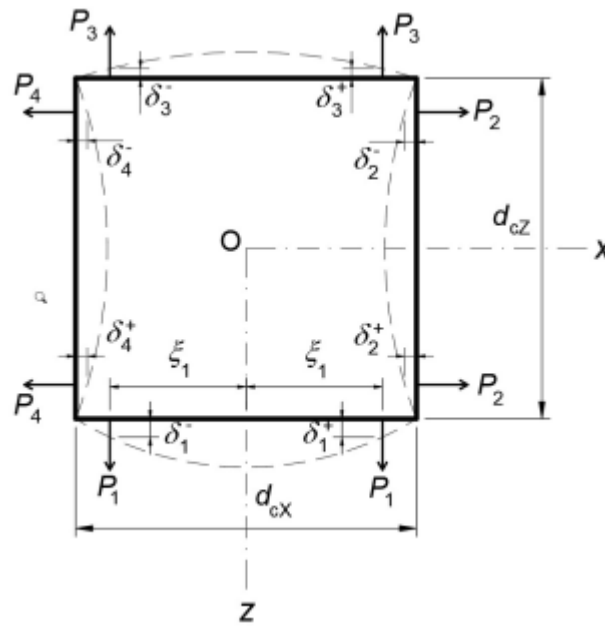


Figure A.3: Calculation model for tubular section [197].

A.2.2 Stiffness

(a) Face deformation under bending

An approach to macro-modeling of 3D tubular column-to-beam joint has been presented previously [152], [216]. The cross-section of the SHS column is modeled by a square plane rigid frame with four identical members (same length and same flexural stiffness). The cross-section is simply supported at its four corners. It is loaded concentrically at the center of only one column face. The out-of-plane deformation of the four column faces is then derived.

This strategy is adopted in the current project but for a more general case where the RHS cross-section is loaded by two symmetrically concentrated forces at each column face due to the geometry of the socket (Fig. A.3). Each load is applied over a rectangular of dimensions $h_s \times t_s$, where: h_s and t_s are the length and thickness of the socket, respectively (Fig. A.6). The center of the rectangle is located at $\xi = (b_s - t_s)/2$ from the axis of the column face where: b_s is the socket width (Fig. A.7). Since only one type of socket is used for all the column faces, parameters h_s , t_s , ξ are the same for all the column faces.

When the cross-section is only loaded at face 1, the out-of-plane displacements of the four column sides at the load application point ($x = a/2$ and $y = \xi$) in Fig. A.4 are determined by:

$$\begin{aligned} \delta_1 &= b_1 P_1 \\ \delta_2 &= \delta_4 = b_2 P_1 \end{aligned} \quad (\text{A.15})$$

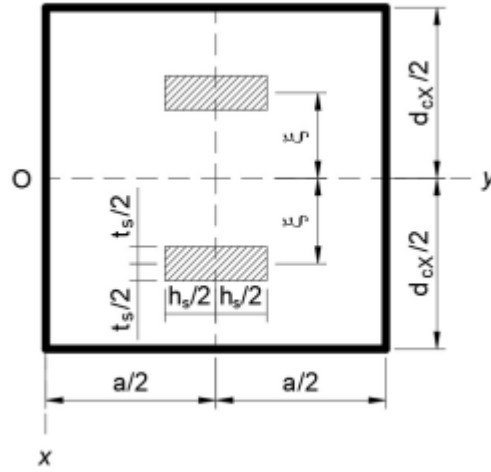


Figure A.4: Face of the tubular column [197].

$$\delta_3 = b_3 P_1$$

where:

$$b_1 = \frac{1}{h_s t_s} \sum_{m=1,3,\dots}^9 \left\{ a_m + \left[A_m^+ + A_{m,r}^- + (D_m^+ + D_{m,r}^-) \gamma_m - \alpha_m \tanh \alpha_m B_m^{(1)} \right] \cosh \gamma_m + \dots \right. \\ \left. \dots + \left[(B_m^+ + B_{m,r}^- + B_m^{(1)}) \gamma_m + C_m^+ + C_{m,r}^- \right] \sinh \gamma_m \right\} \sin(0.5 m \pi)$$

$$b_2 = \frac{1}{h_s t_s} \sum_{m=1,3,\dots}^9 \left[B_m^{(2)} (\gamma_m \sinh \gamma_m - \beta_m \tanh \beta_m \cosh \gamma_m) \right] \sin(m \pi (0.5 - d))$$

$$b_3 = \frac{1}{h_s t_s} \sum_{m=1,3,\dots}^9 \left[B_m^{(3)} (-\alpha_m \tanh \alpha_m \cosh \gamma_m + \gamma_m \sinh \gamma_m) \right] \sin(0.5 m \pi)$$

with:

α = is a length parameter, defined by: $a = \max \{5 d c_x; 5 d c_z\}$.

d = is a length parameter, defined by: $d = |d b_x - d b_z|/a$, but with $d \leq 0.5$.

$$A_m^+ = \frac{a_m}{4 \cosh^2 \alpha_m} \left\{ \cosh \alpha_m \left[-\gamma_{m,p}^+ \sinh (\alpha_m - \gamma_{m,p}^+) - 2 \cosh (\alpha_m - \gamma_{m,p}^+) + \dots \right. \right. \\ \left. \dots + \gamma_{m,m}^+ \sinh (\alpha_m + \gamma_{m,m}^+) - 2 \cosh (\alpha_m + \gamma_{m,m}^+) \right] + \dots \\ \left. \dots + \alpha_m (\sinh \gamma_{m,m}^+ - \sinh \gamma_{m,p}^+) \right\}$$

$$B_m^+ = \frac{a_m}{4 \cosh \alpha_m} \left[\cosh (\alpha_m - \gamma_{m,p}^+) + \cosh (\alpha_m + \gamma_{m,m}^+) \right]$$

$$C_m^+ = \frac{a_m}{4 \sinh^2 \alpha_m} \left\{ \sinh \alpha_m \left[-\gamma_{m,p}^+ \sinh \left(\alpha_m - \gamma_{m,p}^+ \right) - 2 \cosh \left(\alpha_m - \gamma_{m,p}^+ \right) - \dots \right. \right. \\ \left. \left. \dots - \gamma_{m,m}^+ \sinh \left(\alpha_m + \gamma_{m,m}^+ \right) + 2 \cosh \left(\alpha_m + \gamma_{m,m}^+ \right) \right] + \dots \right. \\ \left. \dots + \alpha_m \left(\cosh \gamma_{m,m}^+ - \cosh \gamma_{m,p}^+ \right) \right\}$$

$$D_m^+ = \frac{a_m}{4 \sinh \alpha_m} \left[\cosh \left(\alpha_m - \gamma_{m,p}^+ \right) - \cosh \left(\alpha_m + \gamma_{m,m}^+ \right) \right]$$

$$A_{m,r}^\pm = \frac{a_m}{4 \cosh^2 \alpha_m} \left\{ \cosh \alpha_m \left[-\gamma_{m,p}^\pm \sinh \left(\alpha_m + \gamma_{m,p}^\pm \right) + 2 \cosh \left(\alpha_m + \gamma_{m,p}^\pm \right) + \dots \right. \right. \\ \left. \left. \dots + \gamma_{m,m}^\pm \sinh \left(\alpha_m + \gamma_{m,m}^\pm \right) - 2 \cosh \left(\alpha_m + \gamma_{m,m}^\pm \right) \right] + \dots \right. \\ \left. \dots + \alpha_m \left(\sinh \gamma_{m,m}^\pm - \sinh \gamma_{m,p}^\pm \right) \right\}$$

$$B_{m,r}^\pm = \frac{a_m}{4 \cosh \alpha_m} \left[-\cosh \left(\alpha_m + \gamma_{m,p}^\pm \right) + \cosh \left(\alpha_m + \gamma_{m,m}^\pm \right) \right]$$

$$C_{m,r}^\pm = \frac{a_m}{4 \sinh^2 \alpha_m} \left\{ \sinh \alpha_m \left[\gamma_{m,p}^\pm \sinh \left(\alpha_m + \gamma_{m,p}^\pm \right) - 2 \cosh \left(\alpha_m + \gamma_{m,p}^\pm \right) - \dots \right. \right. \\ \left. \left. \dots - \gamma_{m,m}^\pm \sinh \left(\alpha_m + \gamma_{m,m}^\pm \right) + 2 \cosh \left(\alpha_m + \gamma_{m,m}^\pm \right) \right] + \dots \right. \\ \left. \dots + \alpha_m \left(\cosh \gamma_{m,m}^\pm - \cosh \gamma_{m,p}^\pm \right) \right\}$$

$$D_{m,r}^\pm = \frac{a_m}{4 \sinh \alpha_m} \left[\cosh \left(\alpha_m + \gamma_{m,p}^\pm \right) - \cosh \left(\alpha_m + \gamma_{m,m}^\pm \right) \right]$$

with:

$$\alpha_m = \frac{m \pi d_c X}{2 a}$$

$$\beta_m = \frac{m \pi d_c Z}{2 a}$$

$$\gamma_m = \frac{m \pi \xi}{a}$$

$$a_m = \frac{4 a^4}{\pi^5 D m^5} (-1)^{\frac{m-1}{2}} \sin \frac{m \pi u}{2 a}$$

$$D = \frac{E t^3}{12 (1 - \nu^2)}$$

$$\nu = 0.3$$

$$\gamma_{m,m}^{\pm} = \frac{(\pm 2 \xi - \nu) m \pi}{2 a}$$

$$\gamma_{m,p}^{\pm} = \frac{(\pm 2 \xi + \nu) m \pi}{2 a}$$

$$B_m^{(1)} = \frac{d_{m,11} [d_{m,22} (d_{m,14} d_{m,23} + d_{m,13} d_{m,24}) - 2 d_{m,23} d_{m,12} d_{m,24}]}{2 (d_{m,13} d_{m,22} - d_{m,23} d_{m,12}) (d_{m,14} d_{m,22} - d_{m,12} d_{m,24})}$$

$$B_m^{(2)} = \frac{d_{m,11} d_{m,22}}{2 (d_{m,13} d_{m,22} - d_{m,23} d_{m,12})}$$

$$B_m^{(3)} = \frac{d_{m,11} d_{m,22} (d_{m,14} d_{m,23} - d_{m,13} d_{m,24})}{2 (d_{m,13} d_{m,22} - d_{m,23} d_{m,12}) (d_{m,14} d_{m,22} - d_{m,12} d_{m,24})}$$

$$C_m^{(2)} = \frac{d_{m,11} d_{m,22}}{2 (d_{m,14} d_{m,22} - d_{m,12} d_{m,24})}$$

$$d_{m,12} = \sinh \alpha_m + \frac{\alpha_m}{\cosh \alpha_m}$$

$$d_{m,13} = -\sinh \beta_m - \frac{\beta_m}{\cosh \beta_m}$$

$$d_{m,14} = \frac{1}{\cosh \beta_m} - \frac{\sinh \beta_m}{\beta_m}$$

$$d_{m,22} = 2 \cosh \alpha_m$$

$$d_{m,23} = 2 \cosh \beta_m$$

$$d_{m,24} = \frac{2}{\beta_m} \frac{\sinh^2 \beta_m}{\cosh \beta_m}$$

When the cross-section is only loaded at face 3, the out-of-plane displacements of the four column sides at the load application point ($x = a/2$ and $y = \xi$) are determined by:

$$\delta_3 = b_1 P_3$$

$$\delta_2 = \delta_4 = b_2 P_3 \tag{A.16}$$

$$\delta_1 = b_3 P_3$$

When the cross-section is only loaded at face 2, the out-of-plane displacements of the four column

sides at the load application point ($x = a/2$ and $y = \xi$) are determined by:

$$\begin{aligned}\delta_2 &= h_1 P_2 \\ \delta_1 &= \delta_3 = h_2 P_2 \\ \delta_4 &= h_3 P_2\end{aligned}\tag{A.17}$$

where:

$$\begin{aligned}\alpha_m &= \frac{m \pi d_{cZ}}{2 a} \\ \beta_m &= \frac{m \pi d_{cX}}{2 a}\end{aligned}$$

$$\begin{aligned}h_1 &= \frac{1}{h_s t_s} \sum_{m=1,3,\dots}^9 \left\{ a_m + \left[A_m^+ + A_{m,r}^- + (D_m^+ + D_{m,r}^-) \gamma_m - \alpha_m \tanh \alpha_m B_m^{(1)} \right] \cosh \gamma_m + \dots \right. \\ &\quad \left. \dots + \left[(B_m^+ + B_{m,r}^- + B_m^{(1)}) \gamma_m + C_m^+ + C_{m,r}^- \right] \sinh \gamma_m \right\} \sin(0.5 m \pi)\end{aligned}$$

$$h_2 = \frac{1}{h_s t_s} \sum_{m=1,3,\dots}^9 \left[B_m^{(2)} (\gamma_m \sinh \gamma_m - \beta_m \tanh \beta_m \cosh \gamma_m) \right] \sin(m \pi (0.5 - d))$$

$$h_3 = \frac{1}{h_s t_s} \sum_{m=1,3,\dots}^9 \left[B_m^{(3)} (-\alpha_m \tanh \alpha_m \cosh \gamma_m + \gamma_m \sinh \gamma_m) \right] \sin(0.5 m \pi)$$

When the cross-section is only loaded at face 4, the out-of-plane displacements of the four column sides at the load application point ($x = a/2$ and $y = \xi$) are determined by:

$$\begin{aligned}\delta_4 &= h_1 P_4 \\ \delta_1 &= \delta_3 = h_2 P_4 \\ \delta_2 &= h_3 P_4\end{aligned}\tag{A.18}$$

By superposing the solutions from Eqs. (A.15) to (A.18) for all column faces, we obtain the following matrix equation that describes the interaction among out-of-plane force-deformation

relationships of four column faces:

$$\begin{bmatrix} \delta_1 \\ \delta_3 \\ \delta_2 \\ \delta_4 \end{bmatrix} = \begin{bmatrix} b_1 & b_3 & h_2 & h_2 \\ b_3 & b_1 & h_2 & h_2 \\ b_2 & b_2 & h_1 & h_3 \\ b_2 & b_2 & h_3 & h_1 \end{bmatrix} \begin{bmatrix} P_1 \\ P_3 \\ P_2 \\ P_4 \end{bmatrix} = \mathbf{D} \begin{bmatrix} P_1 \\ P_3 \\ P_2 \\ P_4 \end{bmatrix} \quad (\text{A.19})$$

It can be rewritten as follows:

$$\begin{bmatrix} P_1 \\ P_3 \\ P_2 \\ P_4 \end{bmatrix} = \mathbf{K} \begin{bmatrix} \delta_1 \\ \delta_3 \\ \delta_2 \\ \delta_4 \end{bmatrix} = \begin{bmatrix} k_{b1} & k_{b3} & k_{h2} & k_{h2} \\ k_{b3} & k_{b1} & k_{h2} & k_{h2} \\ k_{b2} & k_{b2} & k_{h1} & k_{h3} \\ k_{b2} & k_{b2} & k_{h3} & k_{h1} \end{bmatrix} \begin{bmatrix} \delta_1 \\ \delta_3 \\ \delta_2 \\ \delta_4 \end{bmatrix} \quad (\text{A.20})$$

Where: $\mathbf{K} = \mathbf{D}^{-1}$ is the stiffness matrix:

$$\begin{aligned} k_{b1} &= \frac{2 b_2 h_2 - b_1 (h_1 + h_3)}{(b_1 - b_3) [4 b_2 h_2 - (b_1 + b_3) (h_1 + h_3)]} \\ k_{b3} &= \frac{b_3 (h_1 + h_3) - 2 b_2 h_2}{(b_1 - b_3) [4 b_2 h_2 - (b_1 + b_3) (h_1 + h_3)]} \\ k_{b2} &= \frac{b_2}{4 b_2 h_2 - (b_1 + b_3) (h_1 + h_3)} \\ k_{h1} &= \frac{2 b_2 h_2 - h_1 (b_1 + b_3)}{(h_1 - h_3) [4 b_2 h_2 - (b_1 + b_3) (h_1 + h_3)]} \\ k_{h3} &= \frac{h_3 (b_1 + b_3) - 2 b_2 h_2}{(h_1 - h_3) [4 b_2 h_2 - (b_1 + b_3) (h_1 + h_3)]} \\ k_{h2} &= \frac{h_2}{4 b_2 h_2 - (b_1 + b_3) (h_1 + h_3)} \end{aligned} \quad (\text{A.21})$$

It can be observed that the matrix \mathbf{K} is not symmetrical. The interaction between two axes is represented by the terms $K_{1,3}$ and $K_{3,1}$. Since $K_{1,3} \neq K_{3,1}$, this interaction cannot be modeled by a spring. However, when multiplying two displacement components δ_2 and δ_4 with h_2/b_2 the

matrix equation Eq. (A.19) becomes:

$$\begin{bmatrix} \delta_1 \\ \delta_3 \\ \delta_2 (h_2/b_2) \\ \delta_4 (h_2/b_2) \end{bmatrix} = \begin{bmatrix} \bar{\delta}_1 \\ \bar{\delta}_3 \\ \bar{\delta}_2 \\ \bar{\delta}_4 \end{bmatrix} = \begin{bmatrix} b_1 & b_3 & h_2 & h_2 \\ b_3 & b_1 & h_2 & h_2 \\ h_2 & h_2 & h_1 h_2/b_2 & h_3 h_2/b_2 \\ h_2 & h_2 & h_3 h_2/b_2 & h_1 h_2/b_2 \end{bmatrix} \begin{bmatrix} P_1 \\ P_3 \\ P_2 \\ P_4 \end{bmatrix} = \bar{\mathbf{D}} \begin{bmatrix} P_1 \\ P_3 \\ P_2 \\ P_4 \end{bmatrix}$$

It can be observed that the new flexibility matrix $[\bar{\mathbf{D}}]$ is a symmetrical one. The matrix equation becomes:

$$\begin{bmatrix} P_1 \\ P_3 \\ P_2 \\ P_4 \end{bmatrix} = \bar{\mathbf{K}} \begin{bmatrix} \bar{\delta}_1 \\ \bar{\delta}_3 \\ \bar{\delta}_2 \\ \bar{\delta}_4 \end{bmatrix} = \begin{bmatrix} \bar{k}_{b1} & \bar{k}_{b3} & \bar{k}_{h2} & \bar{k}_{h2} \\ \bar{k}_{b3} & \bar{k}_{b1} & \bar{k}_{h2} & \bar{k}_{h2} \\ \bar{k}_{b2} & \bar{k}_{b2} & \bar{k}_{h1} & \bar{k}_{h3} \\ \bar{k}_{b2} & \bar{k}_{b2} & \bar{k}_{h3} & \bar{k}_{h1} \end{bmatrix} \begin{bmatrix} \bar{\delta}_1 \\ \bar{\delta}_3 \\ \bar{\delta}_2 \\ \bar{\delta}_4 \end{bmatrix} \quad (\text{A.22})$$

where:

$$\begin{aligned} \bar{k}_{b1} &= k_{b1} = \frac{2 b_2 h_2 - b_1 (h_1 + h_3)}{(b_1 - b_3) [4 b_2 h_2 - (b_1 + b_3) (h_1 + h_3)]} \\ \bar{k}_{b3} &= k_{b3} = \frac{b_3 (h_1 + h_3) - 2 b_2 h_2}{(b_1 - b_3) [4 b_2 h_2 - (b_1 + b_3) (h_1 + h_3)]} \\ \bar{k}_{b2} &= k_{b2} = \frac{b_2}{4 b_2 h_2 - (b_1 + b_3) (h_1 + h_3)} \\ \bar{k}_{h1} &= k_{h1} \frac{b_2}{h_2} = \frac{2 b_2 h_2 - h_1 (b_1 + b_3)}{(h_1 - h_3) [4 b_2 h_2 - (b_1 + b_3) (h_1 + h_3)]} \frac{b_2}{h_2} \\ \bar{k}_{h3} &= k_{h3} \frac{b_2}{h_2} = \frac{h_3 (b_1 + b_3) - 2 b_2 h_2}{(h_1 - h_3) [4 b_2 h_2 - (b_1 + b_3) (h_1 + h_3)]} \frac{b_2}{h_2} \\ \bar{k}_{h2} &= k_{h2} \frac{b_2}{h_2} = \frac{k_{b2}}{4 b_2 h_2 - (b_1 + b_3) (h_1 + h_3)} \end{aligned} \quad (\text{A.23})$$

Finally, the equation may be modeled by a system of springs as presented in Fig. A.5 where the

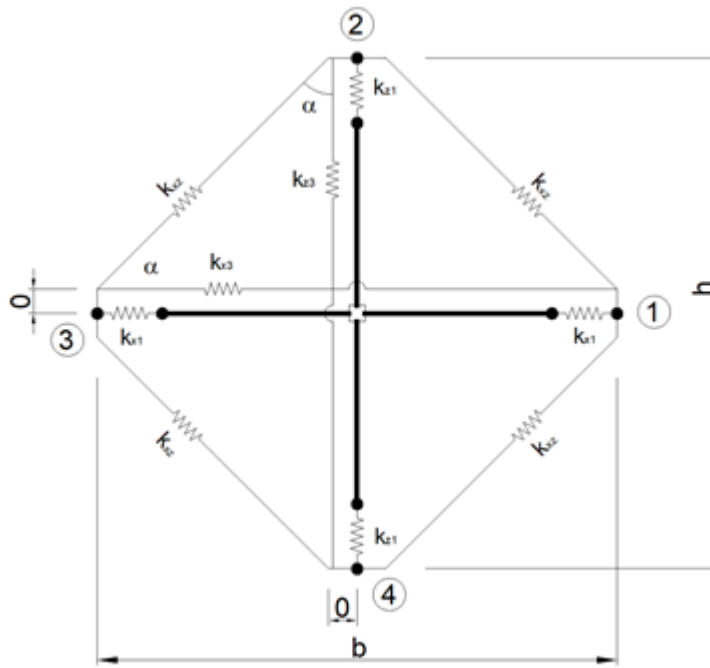


Figure A.5: Springs model [197].

stiffness of springs is given by:

$$\begin{aligned}
 k_{x1} &= \bar{k}_{b1} - \bar{k}_{b3} - 2 k_{xz} (\sin \alpha)^2 \\
 k_{x3} &= \bar{k}_{b3} \bar{k}_{h2} = \frac{\bar{k}_{b2}}{\sin \alpha \cos \alpha} \\
 k_{xz} &= \frac{\sin \alpha \cos \alpha}{k_{z1}} = \bar{k}_{h1} - \bar{k}_{h3} - 2 k_{xz} (\cos \alpha)^2 \\
 k_{x3} &= \bar{k}_{h3}
 \end{aligned}
 \tag{A.24}$$

where:

$$(\sin \alpha)^2 = \frac{b^2}{b^2 + h^2}$$

and

$$(\cos \alpha)^2 = \frac{h^2}{b^2 + h^2}$$

In order to check if the matrix Eq. (A.22) may be obtained from the springs model, a concentrated force P_i is applied at the node i of the model. The obtained displacement of the node i is $\bar{\delta}_i$. Forces in springs that are connected to node 1 are calculated as follows:

$$\text{Spring } k_{x1} : k_{x1} \bar{\delta}_1$$

$$\text{Spring } k_{x3} : k_{x3} (\bar{\delta}_1 + \bar{\delta}_3)$$

$$\text{Spring } k_{xz} \text{ (top)} : k_{xz} (\bar{\delta}_2 \cos \alpha + \bar{\delta}_1 \sin \alpha)$$

$$\text{Spring } k_{xz} \text{ (bottom)} : k_{xz} (\bar{\delta}_4 \cos \alpha + \bar{\delta}_1 \sin \alpha)$$

The total horizontal force at node 1 is:

$$\begin{aligned} P_1 &= k_{x1} \bar{\delta}_1 + k_{x3} (\bar{\delta}_1 + \bar{\delta}_3) + k_{xz} (\bar{\delta}_2 \cos \alpha + \bar{\delta}_1 \sin \alpha) \sin \alpha + k_{xz} (\bar{\delta}_4 \cos \alpha + \bar{\delta}_1 \sin \alpha) \sin \alpha \\ \Rightarrow P_1 &= [\bar{k}_{b1} - \bar{k}_{b3} - 2 k_{xz} (\sin \alpha)^2] \bar{\delta}_1 + \bar{k}_{b3} (\bar{\delta}_1 + \bar{\delta}_3) + [(k_{xz} \cos \alpha \sin \alpha) \bar{\delta}_2 + \dots \\ &\quad \dots k_{xz} (\sin \alpha)^2 \bar{\delta}_1] + [(k_{xz} \cos \alpha \sin \alpha) \bar{\delta}_4 + k_{xz} (\sin \alpha)^2 \bar{\delta}_1] \\ \Rightarrow P_1 &= \bar{k}_{b1} \bar{\delta}_1 + \bar{k}_{b3} \bar{\delta}_3 + \bar{k}_{h2} \bar{\delta}_2 + \bar{k}_{h2} \bar{\delta}_4 \end{aligned}$$

The above equation is exactly the first row of the matrix Eq. (A.22). The same equations for the other nodes can be easily obtained in the same way.

(b) Punching shear The stiffness of the column face in punching shear is taken as infinity:

$$k_{cps} = \infty \quad (\text{A.25})$$

A.3 Welds between column and socket

A.3.1 Strength

The strengths of the socket welds on the column under tensile and compressive forces are determined according to Eurocode 3 Part 1-8 [28], and the latest draft of the revision [214] (simplified method).

The design resistance against tensile or compressive force, $N_{t,w}$ or $N_{c,w}$, for the welds is:

$$N_{t,w} = N_{c,w} = L_w a_w \frac{f_u}{\sqrt{3} \beta_w \gamma_{M2}} \quad (\text{A.26})$$

with:

f_u = ultimate tensile strength in tension of the lower welded steel grade (f_{u0} for the column or f_{us} for the socket).

β_w = correlation factor depending on the lower welded steel grade (column or socket), see [28] or [214].

The weld length, L_w , between the socket and the column is:

$$L_w = 2 (h_s - 2a_w) \quad (\text{A.27})$$

A.3.2 Stiffness

The stiffness factor of the welds is taken as infinity [28] or [214]:

$$k_w = \infty \quad (\text{A.28})$$

A.4 Socket

A.4.1 Strength

(a) Socket in bending

The design resistance of the socket in bending against tensile force, $N_{t, sb}$, is:

$$N_{t, sb} = \frac{4 M_{pl, s}}{m_s} = \frac{t_s^2 h_s C_{sh, s} f_{ys}}{m_s \gamma_{M0}} \quad (\text{A.29})$$

with:

m_s = socket lever arm in bending, as shown in Fig. A.6

$M_{pl, s}$ = plastic moment in the socket, defined as follows:

$$M_{pl, s} = \frac{t_s^2 h_s C_{sh, s} f_{ys}}{4\gamma_{M0}} \quad (\text{A.30})$$

with:

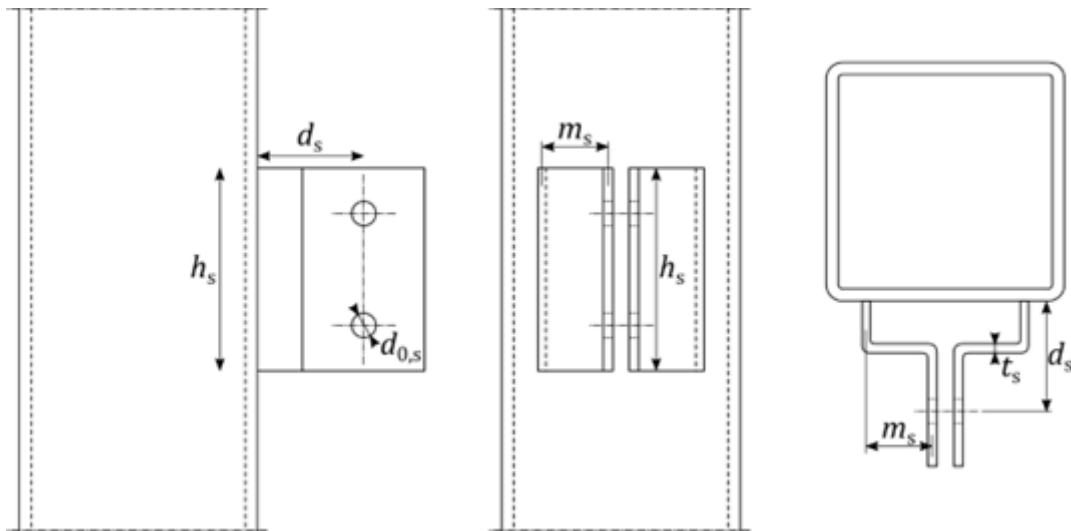


Figure A.6: Symbols for the socket's strength and stiffness [197].

$C_{sh,s}$ = coefficient accounting of the strain hardening in the socket, according to WP3 results:

$$C_{sh,s} = 3$$

The design resistance against compressive force, $N_{c,sb}$, for the socket in bending has the same value:

$$N_{c,sb} = N_{t,sb} \quad (\text{A.31})$$

(b) Socket gross and net section

The design resistance of the socket gross section against tensile force, $N_{t,sg}$, is:

$$N_{t,sg} = \frac{2 t_s h_s f_{ys}}{\gamma_{M0}} \quad (\text{A.32})$$

The characteristic resistance against compressive force, $N_{c,sg}$, for the socket gross section has the same value:

$$N_{c,sg} = N_{c,sg} \quad (\text{A.33})$$

The design resistance of the socket net section against tensile force, $N_{t,su}$, is:

$$N_{t,su} = 2 \cdot 0.9 t_s (h_s - n_b d_{0,s}) \frac{f_{us}}{\gamma_{M2}} \quad (\text{A.34})$$

with:

$d_{0,s}$ = hole diameter

This failure mode is not relevant under compressive force:

$$N_{c,su} = \infty \quad (\text{A.35})$$

A.4.2 Stiffness

(a) Socket in bending

The stiffness of the socket in bending is defined with a similar formulation as the equivalent T-stub [214], with a specific correction factor.

The stiffness factor, k_{sb} , for the socket in bending:

$$k_{sb} = C_{sb} \frac{h_s t_s^3}{m_s^3} \quad (\text{A.36})$$

with:

C_{sb} = correction factor for INNO3DJOINTS socket in bending, according to WP3 results:

$$C_{sb} = 1$$

(b) Socket elongation/contraction

The stiffness of the socket gross section in tension or compression is defined with a similar formula as the equivalent T-stub in [3], with a specific correction factor.

The stiffness factor, k_{sg} , for the socket gross section:

$$k_{sg} = C_{sg} \frac{h_s t_s}{d_s} \quad (\text{A.37})$$

with:

C_{sg} = correction factor for INNO3DJOINTS socket in tension, according to WP3 results:

$$C_{sg} = 1$$

d_s = socket depth from the bolt axis to the weld on the column, as shown in Fig. A.6

A.5 Bearing in the socket

A.5.1 Strength

The strengths of the bolt in bearing are determined according to the latest draft of the next revision of Eurocode 3 Part 1-8 [214].

The design resistance against tensile or compressive force, $N_{t,bb}$ or $N_{c,bb}$, for the bolt in bearing is:

$$N_{bb} = 2 n_b F_{b,Rd} \quad (\text{A.38})$$

The design resistance of one bolt in bearing, $F_{b,Rd}$, is:

$$F_{b,Rd} = \frac{k_m \alpha_b f_u d t}{\gamma_{M2}} \quad (\text{A.39})$$

with:

k_m = factor equal to 0.9 for steel grades equal or greater than S460, and equal to 1.0 otherwise.

f_u = nominal ultimate strength in tension of the steel grade ($f_u = f_{us}$ in the socket)

t = thickness of the material ($t = t_s$ in the socket)

The α_b factor is currently defined by the following [214]:

$$\begin{aligned} \text{for end bolts} &\Rightarrow \alpha_b = \min \left\{ \frac{e_1}{d_0} ; 3 \frac{f_{ub}}{f_u} ; 3 \right\} \\ \text{for inner bolts} &\Rightarrow \alpha_b = \min \left\{ \frac{p_1}{d_0} - \frac{1}{2} ; 3 \frac{f_{ub}}{f_u} ; 3 \right\} \end{aligned} \quad (\text{A.40})$$

with:

d_0 = hole diameter ($d_0 = d_{0,s}$ in the socket).

p_1 = pitch distance between bolts in the direction of the force ($p_1 = \infty$ for the socket)

For the bolt bearing in the socket, the edge distance, e_1 , in the direction of the force is the distance shown in Fig. A.7 ($e_{1,s}$) for tensile force, and $e_1 = \infty$ for compressive force.

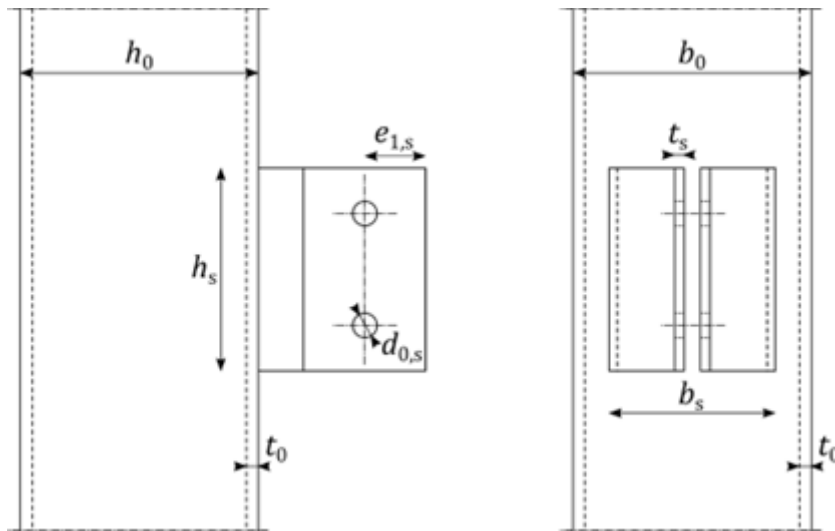


Figure A.7: Edge distance e_1 for the socket under tensile force [197].

A.5.2 Stiffness

The bearing bolt's stiffness is determined in accordance with the Eurocode 3 Part 1-8 method, using a stiffness factor that divides the component's stiffness by the steel's elasticity modulus [214].

The stiffness factor, k_{bb} , for the bolts in bearing:

$$k_{bb} = \frac{2 \bar{S}_b n_b t f_u}{E} \quad (\text{A.41})$$

with:

\bar{S}_b = relative (non-dimensional) bearing stress. For the sake of simplicity, the constant value $\bar{S}_b = 12$ is considered, see [214].

A.6 Bolt between the socket and the T-plug in shear

A.6.1 Strength

The strength of the bolts in shear is determined according to Eurocode 3 Part 1-8 [28], and the last draft of the next revision [214] (same methods). The design resistance against tensile or compressive force, $N_{t,bs}$ or $N_{c,bs}$, for the bolt in shear is:

$$N_{bs} = n_b F_{v,Rd} \quad (\text{A.42})$$

with:

n_b = number of bolts

The design resistance of one bolt in shear, $F_{v,Rd}$, is:

$$F_{v,Rd} = \frac{\alpha_v f_{ub} A_s}{\gamma_{M2}} \quad (\text{A.43})$$

with:

α_v = factor equal to 0.6 for property classes 4.6, 5.6, or 8.8, and 0.5 otherwise

A_s = tensile stress area of the bolt

A.6.2 Stiffness

The stiffness of the bolts in shear is determined according to Eurocode 3 Part 1-8 [28], and the last draft of the next revision [214] (same methods). A stiffness factor equal to the component's stiffness divided by the steel's elasticity modulus is used, as in Eurocode 3 Part 1-8 method [28].

The stiffness factor, k_{bs} , for the bolts in shear:

$$k_{bs} = \frac{16 n_b d^2 f_{ub}}{E d_{M16}} \quad (\text{A.44})$$

with:

d_{M16} = nominal diameter of an M16 bolt

A.7 Bearing in the T-plug

As in Section A.5, with:

$$N_{bb} = n_b F_{b,Rd} \quad (\text{A.45})$$

$$k_{bb} = \frac{\bar{S}_b n_b t f_u}{E} \quad (\text{A.46})$$

where:

f_u = nominal ultimate stress in tension of the steel grade ($f_u = f_{uT}$ in T-plug)

t = thickness of the material ($t = t_T$ in T-plug)

d_0 = hole diameter ($d_0 = d_{0,T}$ in T-plug)

e_1 = edge distance of the bolts in the direction of the force ($e_1 = \infty$ for the T-plug, for tension or compression)

p_1 = pitch distance between bolts in the direction of the force ($p_1 = \infty$ for the T-plug)

A.8 T-plug

A.8.1 Strength

The design resistance of the T-plug gross section against tensile force, $N_{t,Tg}$, is:

$$N_{t,Tg} = \frac{t_T h_T f_{yT}}{\gamma_{M0}} \quad (\text{A.47})$$

The design resistance T-plug gross section against compressive force $N_{c,Tg}$, is:

$$N_{c,Tg} = \frac{\chi t_T h_T f_{yT}}{\gamma_{M1}} \quad (\text{A.48})$$

with:

χ = reduction factor in accordance with [156] considering the curve "c" ($\alpha = 0.49$), and the following relative slenderness:

$$\bar{\lambda} = C_{Tbl} \frac{\frac{d_T}{t_T / \sqrt{12}}}{93.9 \varepsilon} = C_{Tbl} \frac{d_T / t_T}{27.1 \varepsilon} \quad (\text{A.49})$$

where:

d_T = T-plug depth, as shown in Fig. A.8

C_{Tbl} = buckling length correction factor for the T-plug, according to WP3 results: $C_{Tbl} = 1$

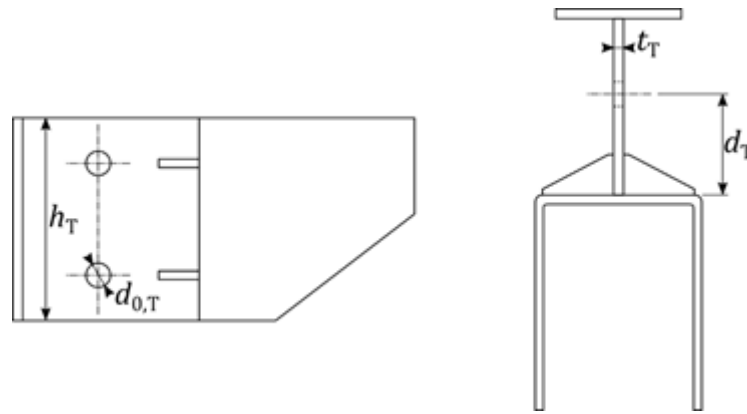


Figure A.8: Symbols for the T-plug strength and stiffness [197].

The partial factor used to calculate the design resistance for this failure mode is γ_{M0} under tension and γ_{M1} under compression.

The design resistance of the T-plug net section against tensile force, $N_{t,Tu}$, is:

$$N_{t,Tu} = 0.9 t_T (h_T - n_b d_0) \frac{f_{uT}}{\gamma_{M2}} \quad (\text{A.50})$$

with:

d_0 = hole diameter ($d_0 = d_{0,T}$ in the T-plug)

This failure mode is not relevant under compressive force:

$$N_{c,Tu} = \infty \quad (\text{A.51})$$

A.8.2 Stiffness

The stiffness of the T-plug gross section in tension is defined with a similar formula as the equivalent T-stub [214], with a specific correction factor.

The stiffness factor, k_{Tg} , for the T-plug in bending:

$$k_{Tg} = C_{Tg} \frac{h_T t_T}{d_T} \quad (\text{A.52})$$

with:

C_{Tg} = correction factor for INNO3DJOINTS T-plug in tension or compression, according to WP3 results: $C_{Tg} = 1$

A.9 Welds between T-plug and clipping part

As in Section A.3, with:

f_u = ultimate stress in the tension of the lower welded steel grade (f_{uT} for the T-plug or f_{uY} for the Y-part)

β_w = correlation factor depending on the lower welded steel grade (T-plug or Y-part), see [28] or [214]

The weld length, L_w , between the T-plug and the clipping part is:

$$L_w = 2 h_T \quad (\text{A.53})$$

A.10 Y-part (clip on the CFS)

A.10.1 Strength

(a) Y-part in bending:

The design resistance of the socket in bending against tensile force, $N_{t,Yb}$, is:

$$N_{t,Yb} = \frac{4 M_{pl,Y}}{m_Y} = \frac{t_Y^2 l_{eff,Y} C_{sh,Y} f_{yY}}{m_Y \gamma_{M0}} \quad (\text{A.54})$$

with:

m_Y = Y-part lever arm in bending, as shown in Fig. A.9

$M_{pl,Y}$ = plastic moment resistance in the Y-part, defined as follows:

$$M_{pl,1} = \frac{t_Y^2 l_{eff,Y} C_{sh,Y} f_{yY}}{4 \gamma_{M0}} \quad (\text{A.55})$$

where:

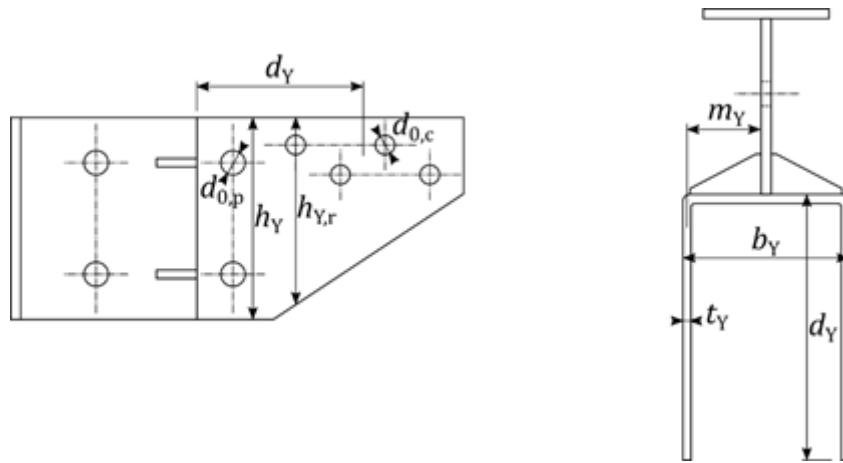


Figure A.9: Symbols for the Y-part strength and stiffness [197].

$C_{sh,Y}$ = coefficient accounting of the strain hardening in the Y-part, according to WP3 results:

$$C_{sh,Y} = 1$$

$l_{eff,Y}$ = effective length for the Y-part in bending, as follows:

with 0 stiffener: $l_{eff,Y} = h_Y$

with 1 stiffener: $l_{eff,Y} = h_Y + b_Y$ (A.56)

with 2 stiffener: $l_{eff,Y} = h_Y + 2 b_Y$

The design resistance against compressive force, $N_{c,Yb}$, for the Y-part has the same value:

$$N_{c,Yb} = N_{t,Yb} \quad (A.57)$$

(b) Y-part in gross and net section:

The design resistance of the Y-part gross section against tensile force, $N_{t,Yg}$, is:

$$N_{t,Yg} = \frac{2 t_Y h_{Y,r} f_{yY}}{\gamma_{M0}} \quad (A.58)$$

with:

$h_{Y,r}$ = reduced Y-part height (measured at the position of the first bolt on the chord, as shown in Fig. A.9)

The design resistance against compressive force, $N_{c,Yg}$, for the Y-part gross section has the same value:

$$N_{c,Yg} = N_{t,Yg} \quad (\text{A.59})$$

The design resistance of the Y-part net section against tensile force, $N_{t,Yu}$, is:

$$N_{t,Yu} = 2 \cdot 0.9 t_Y \frac{f_{uY}}{\gamma_{M2}} \cdot \min \{ h_Y - n_{b,p} d_{0,p}; \quad h_{Y,r} - n_{b,c} d_{0,c} \} \quad (\text{A.60})$$

with:

$n_{b,p}$ = number of bolts in the in the vertical post

$d_{0,p}$ = hole diameter, for bolt arrangement in the vertical post

$n_{b,c}$ = number of bolts crossed by the net section in the chord

$d_{0,c}$ = hole diameter, for bolt arrangement in the chord

This failure mode is not relevant under compressive force:

$$N_{c,Yu} = \infty \quad (\text{A.61})$$

A.10.2 Stiffness

(a) Y-part in bending:

The stiffness of the Y-part in bending is defined with a similar formula as the equivalent T-stub [214], with a specific correction factor.

The stiffness factor, k_{Yb} , for the socket in bending:

$$k_{Yb} = C_{Yb} \frac{h_Y t_Y^3}{m_Y^3} \quad (\text{A.62})$$

with:

C_{Yb} = correction factor for INNO3DJOINTS Y-part in bending, according to WP3 results:

$$C_{Yb} = 1$$

(b) Y-part in elongation/contraction:

The stiffness of the Y-part gross section in tension or compression is defined with a similar formulation to the equivalent T-stub [214], with a specific correction factor.

The stiffness factor, k_{Yg} , for the Y-part gross section:

$$k_{Yg} = C_{Yg} \frac{h_{Y,r} t_Y}{d_Y} \quad (\text{A.63})$$

with:

C_{Yg} = correction factor for INNO3DJOINTS Y-part in tension, according to WP3 results:

$$C_{Yg} = 1$$

d_Y = Y-part depth from the center of the bolts' arrangement on the chord, as shown in Fig. A.9

A.11 Bearing of the Y-part

As in Section A.5, with:

f_u = nominal ultimate stress in tension of the steel grade (f_{uY} for the Y-part)

t = thickness of the material (t_Y for the Y-part)

e_1 = edge distance of the bolts in the direction of the force ($e_1 = e_{1,c}$ for the Y-part on the chord, as shown in Fig. A.10)

p_1 = pitch distance between bolts in the direction of the force ($p_1 = p_{1,c}$ for the Y-part on the chord connection, as shown in Fig. A.10)

The vertical pitch, $p_{2,c}$, in the case of staggered holes, have to conform to the following requirements:

$$p_{2,c} \geq 1.2 d_{0,c} \quad (\text{A.64})$$

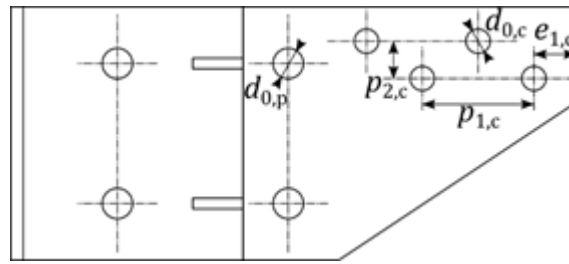


Figure A.10: Edge distance, e_1 , and pitch distance, p_1 , for the Y-part [197].

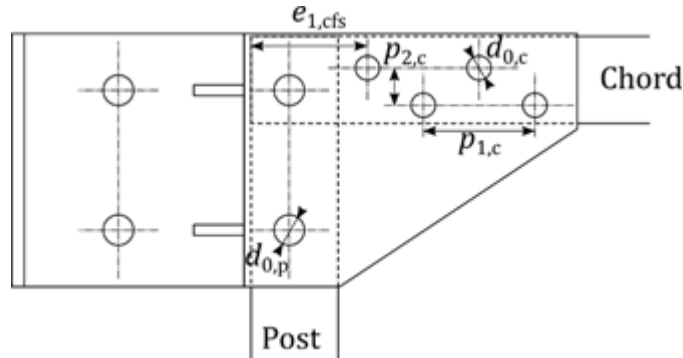


Figure A.11: Edge distance, e_1 , and pitch distance, p_1 , for the CFS chord [197].

A.12 Bolt between the clipping part and the cold-formed member in shear

As in Section A.6

A.13 Bearing of cold-formed member (chord)

As in Section A.5, with:

f_u = nominal ultimate stress in tension of the steel grade (f_{uc} for the CFS chord)

t = thickness of the material

e_1 = edge distance of the bolts in the direction of the force ($e_1 = e_{1,cfs}$ for the Y-part on the chord connection, as shown in Fig. A.11)

p_1 = pitch distance between bolts in the direction of the force ($p_1 = p_{1,c}$ for the Y-part on the chord connection, as shown in Fig. A.11)

A.14 Gross and net section of cold-formed member (chord)

The design resistance of the CFS chord gross section against tensile force, $N_{t,cg}$, is:

$$N_{t,cg} = \frac{A_{g,c} f_{yc}}{\gamma_{M0}} \quad (\text{A.65})$$

The design resistance against compressive force, $N_{c,cg}$, for the CFS chord gross section has the same value:

$$N_{c,cg} = N_{t,cg} \quad (\text{A.66})$$

The design resistance of the Y-part net section against tensile force, $N_{t,cu}$, is:

$$N_{t,cu} = \frac{0.9 A_{net,c} f_{uc}}{\gamma_{M2}} \quad (\text{A.67})$$

This failure mode is not relevant under compressive force:

$$N_{c,cu} = \infty \quad (\text{A.68})$$

Appendix B: P&PJ's components under vertical shear load

The computation of the strength of the components identified for the INNO3DJOINTS plug-and-play joint system [5], specifically in the simplest configuration of the P&PJ where a single truss-girder is connected to the column and subjected to vertical shear load [197], are presented in detail hereinafter.

B.1 Column side wall

The design resistance against shear load, V_{csw} , for the column side wall is:

$$V_{csw} = 2 \frac{f_{y0}}{\sqrt{3} \gamma_{M0}} t_0 b_w \quad (\text{B.1})$$

with:

b_w = effective breadth in column side wall, see Section A.1.1

B.2 Column face

(a) face plastification under bending

Component not considered in pure shear.

(b) face failure by punching shear

The design resistance against shear load, V_{cps} , for the column face in punching shear is:

$$V_{cps} = \frac{f_{y0}}{\sqrt{3} \gamma_{M0}} t_0 l_{p,eff} \quad (\text{B.2})$$

with:

$l_{p,eff}$ = effective length for punching shear, see Section A.2.1

B.3 Welds between column and socket

The design resistance against shear load, V_w , for the welds is:

$$V_w = N_{t,w} \quad (\text{B.3})$$

with:

$N_{t,w}$ = tensile resistance of the weld between the column and the socket, see Section A.3.1

B.4 Socket

(a) Socket in bending

Component not considered in pure shear.

(b) Socket gross and net section

The design resistance of the socket gross section against shear load, V_{sg} , is:

$$V_{sg} = 2 t_s h_s \frac{f_{ys}}{\sqrt{3} \gamma_{M0}} \quad (\text{B.4})$$

The design resistance of the socket net section against tensile force, V_{su} , is:

$$V_{su} = 2 \cdot 0.9 t_s (h_s - n_b d_{0,s}) \frac{f_{us}}{\sqrt{3} \gamma_{M2}} \quad (\text{B.5})$$

with:

$d_{0,s}$ = hole diameter in the socket

B.5 Bearing in the socket

The strength of the bolt in the bearing is determined according to the last draft of the next revision of Eurocode 3 Part 1-8 [214]. The design resistance against shear load, V_{bb} , for the bolt in the bearing is:

$$V_{bb} = 2 n_b F_{b,Rd} \quad (\text{B.6})$$

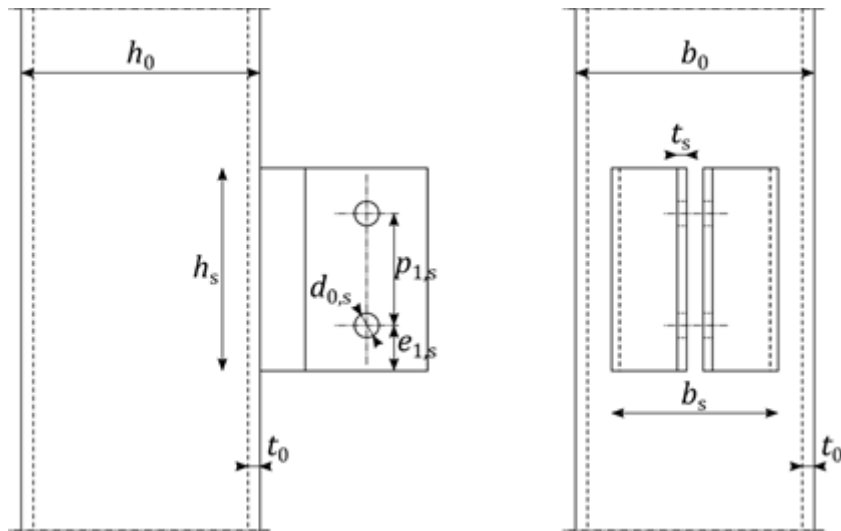


Figure B.1: Pitch distance, p_1 , and edge distance, e_1 , for the socket under shear load [197].

with:

$F_{b,Rd}$ = design resistance of one bolt in bearing, see Section A.5.1 and considering the following pitch and edge distances

p_1 = pitch distance between bolts in the direction of the force ($p_1 = p_{1,s}$ for the socket, as shown in Fig. B.1)

e_1 = pitch distance between bolts in the direction of the force ($e_1 = e_{1,s}$ for the socket, as shown in Fig. B.1)

B.6 Bolt between the socket and the T-plug in shear

The strength of the bolts in shear is determined according to Eurocode 3 Part 1-8 [28], and the last draft of the next revision [214]. The design resistance against shear load, V_{bs} , for the bolt in shear is:

$$V_{bs} = n_b F_{v,Rd} \quad (\text{B.7})$$

with:

$F_{v,Rd}$ = design resistance of one bolt in shear, see Section A.6.1

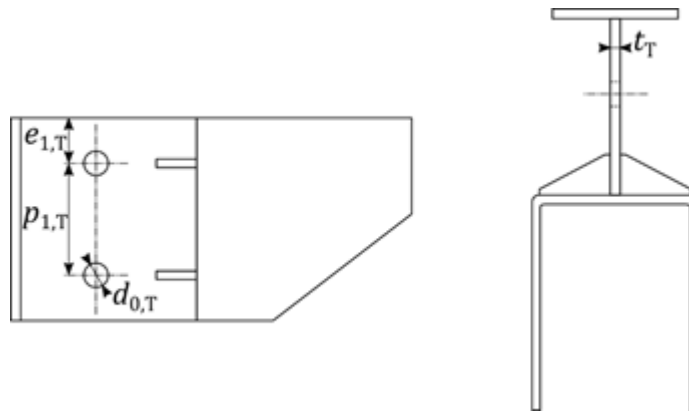


Figure B.2: Pitch distance, p_1 , and edge distance, e_1 , for the T-plug under shear load [197].

B.7 Bearing in the T-plug

As in Section B.5, with:

$$V_{bb} = n_b F_{b,Rd} \quad (\text{B.8})$$

where:

p_1 = pitch distance between bolts in the direction of the force ($p_1 = p_{1,T}$ for the T-plug, as shown in Fig. B.2)

e_1 = pitch distance between bolts in the direction of the force ($e_1 = e_{1,T}$ for the T-plug, as shown in Fig. B.2)

B.8 T-plug

(a) T-plug in bending

Component not considered in pure shear

(b) T-plug gross and net section

The design resistance of the T-plug gross section against shear load, V_{Tg} , is:

$$V_{Tg} = t_T h_T \frac{f_{yT}}{\sqrt{3} \gamma_{M0}} \quad (\text{B.9})$$

The design resistance of the T-plug net section against shear load, V_{Tu} , is:

$$V_{Tu} = 0.9 t_T (h_T - n_b d_0) \frac{f_{uT}}{\sqrt{3} \gamma_{M2}} \quad (\text{B.10})$$

with:

d_0 = hole diameter ($d_0 = d_{0,T}$ in the T-plug)

B.9 Welds between T-plug and Y-part

As in Section B.3, with:

L_w = weld effective length, as follows:

$$L_w = 2 h_T \quad (\text{B.11})$$

B.10 Y-part

The design resistance of the Y-part gross section against shear load, V_{Yg} , is:

$$V_{Yg} = 2 t_Y h_Y \frac{f_{yY}}{\sqrt{3} \gamma_{M0}} \quad (\text{B.12})$$

The design resistance of the Y-part net section against shear load, V_{Yu} , is:

$$V_{Yu} = 2 \cdot 0.9 t_Y \frac{f_{uY}}{\sqrt{3} \gamma_{M2}} \min \{ h_Y - n_{b,p} d_{0,p}; \quad h_{Y,r} - n_{b,c} d_{0,c} \} \quad (\text{B.13})$$

$n_{b,p}$ = number of bolts in the in the vertical post

$d_{0,p}$ = hole diameter, for bolt arrangement in the vertical post

$n_{b,c}$ = number of bolts crossed by the net section in the chord

$d_{0,c}$ = hole diameter, for bolt arrangement in the chord

B.11 Bearing in the Y-part

As in Section B.5, with:

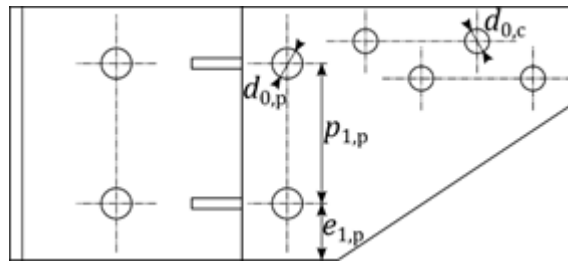


Figure B.3: Pitch distance, p_1 , and edge distance, e_1 , for the Y-part [197].

e_1 = edge distance of the bolts in the direction of the force ($e_1 = e_{1,p}$ for the Y-part on the end post, as shown in Fig. B.3)

p_1 = pitch distance between bolts in the direction of the force ($p_1 = p_{1,p}$ for the Y-part on the end post, as shown in Fig. B.3)

B.12 Bolt between the Y-part and the cold-formed member in shear

As in Section B.6

B.13 Bearing of cold-formed member (truss)

As in Section B.5, with:

e_1 = edge distance of the bolts in the direction of the force ($e_1 = e_{1,cfs}$ for the Y-part on the end post, as shown in Fig. B.4)

p_1 = pitch distance between bolts in the direction of the force ($p_1 = p_{1,cfs}$ for the Y-part on the end post, as shown in Fig. B.4)

B.14 Gross and net section of the CFS end post

The design resistance of the CFS end post gross section against vertical shear load, V_{cg} , is:

$$V_{cg} = \frac{A_{g,p} f_{yp}}{\gamma_{M0}} \quad (\text{B.14})$$

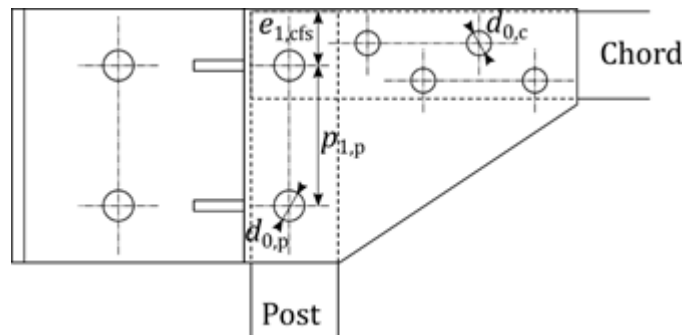


Figure B.4: Pitch distance, p_1 , and edge distance, e_1 , for the Y-part [197].

The design resistance of the CFS end post net section against vertical shear load, V_{cu} , is:

$$V_{cu} = \frac{0.9 A_{net,p} f_{up}}{\gamma_{M2}} \quad (\text{B.15})$$

Appendix C: Macro-element developed within the INNO3DJOINTS project

C.1 The element formulation

C.1.1 Sign convention

The deformation and internal forces of the components in the macro-element developed within the INNO3DJOINTS project [5] adhere to the sign convention expounded in Section 3.4.1.

C.1.2 Linear formulation

In the case of a first-order analysis with linear elastic behavior assigned to the beam-to-column joint components, the macro-element developed within the INNO3DJOINTS project [5] follows the methodology presented in Section 3.4.2. However, it should be noted that the dimensions of the matrices within the analysis are adjusted to suit this particular model. As expected, a new compatibility matrix, \mathbf{A} (38×44), is employed in the calculation process. The details of the compatibility matrix will be presented in the next section.

Furthermore, in this case, the constitutive relation matrix, \mathbf{k}_j , which contains the stiffness of the beam-to-column joint components listed in Tab. 2.4 and is expressed by Eq. (3.13), is not a diagonal matrix. Instead, it includes non-zero off-diagonal elements that account for the 3D interaction between the components. Specifically, the matrix elements adhere to the following conditions:

- $k_{i,j} = 0$, if $i \neq j$;
- $k_{i,j} = k_i$, if $i = j$, where k_i is the stiffness of component i ;
- additional elements are added to the matrix to account for the 3D interaction between the components.

The additional elements outside of the diagonal are:

$$k_{2,5} = k_{5,2} = k_{1,4} = k_{4,1} = k_{b3} \quad (\text{C.1})$$

$$k_{23,26} = k_{26,23} = k_{22,25} = k_{25,22} = k_{h3} \quad (\text{C.2})$$

$$k_{2,23} = k_{2,26} = k_{5,23} = k_{5,26} = k_{1,22} = k_{1,25} = k_{4,22} = k_{4,25} = k_{h2} \quad (\text{C.3})$$

$$k_{23,2} = k_{26,2} = k_{23,5} = k_{26,5} = k_{22,1} = k_{25,1} = k_{22,4} = k_{25,4} = k_{b2} \quad (\text{C.4})$$

where k_{b3} , k_{h3} , k_{h2} and k_{b2} are expressed by Eq. (A.21).

C.1.3 Compatibility matrix

The non-zero elements, $a_{i,j}$, of the compatibility matrix, **A**, for the macro-element developed in the context of the INNO3DJOINTS project [5], are presented in Tab. C.1. Furthermore, each non-zero value is associated with a unique color to enhance the visibility of the color-coded representation of the compatibility matrix, as illustrated in Fig. C.1.

In Tab. C.1 presents the dimensions of the structural members in the X and Z directions, denoted by dbX , dbZ , dcX , and dcZ , as well as the angles θ_{YX} and θ_{YZ} , which are defined as $\theta_{YX} = \arctan(dbX/dcX)$ and $\theta_{YZ} = \arctan(dbZ/dcZ)$, respectively. The elements, $a_{i,j}$, of the compatibility matrix represent the deformation in component i caused by a unit displacement in DOF j . The computation of these elements follows the same methodology presented in Section 3.4.3.

C.2 Implementation in OpenSees

























C.2.1 Inno3DJointND Class

The proposed beam-to-column joint finite element formulation is introduced in the framework of OpenSees as the Inno3DJointND Class and is a child of the base abstract Element class.

C.2.2 Nonlinear formulation

In order to conduct nonlinear analysis, the beam-to-column joint finite element suggested in this study requires a methodology for determining the internal nodal displacement that satisfies the internal equilibrium of the element for each iteration of the global solution algorithm due to the presence of internal degrees of freedom. This approach is based on the methodology outlined in Section 4.3.

Table C.1: The non-zero elements of the compatibility matrix **A**.

Color	Value	Stiffness Coefficient
	1	$a_{4,1}; a_{25,3}; a_{18,4}; a_{9,6}; a_{1,7}; a_{2,7}; a_{12,9}; a_{13,10}; a_{14,11}; a_{3,12};$ $a_{5,13}; a_{10,14}; a_{27,15}; a_{21,17}; a_{36,20}; a_{29,25}; a_{37,26}; a_{22,27};$ $a_{23,27}; a_{30,29}; a_{31,30}; a_{27,34}; a_{35,37}; a_{20,39}; a_{17,40}; a_{19,40};$ $a_{33,40}; a_{3,41}; a_{24,43};$
	- 1	$a_{1,1}; a_{8,2}; a_{22,3}; a_{19,5}; a_{35,8}; a_{2,13}; a_{23,15}; a_{20,16}; a_{11,18}; a_{4,19};$ $a_{5,19}; a_{15,21}; a_{16,22}; a_{17,23}; a_{6,24}; a_{24,28}; a_{32,31}; a_{38,32}; a_{25,33};$ $a_{26,33}; a_{33,35}; a_{34,36}; a_{36,38}; a_{18,39}; a_{14,40}; a_{21,40}; a_{30,40}; a_{6,42};$ $a_{27,44};$
	0.5	$a_{32,1}; a_{15,3}; a_{31,13}; a_{15,15}; a_{8,37}; a_{38,37}; a_{8,38}; a_{38,38};$
	- 0.5	$a_{29,1}; a_{12,3}; a_{29,13}; a_{12,15}; a_{10,37}; a_{37,37}; a_{10,38}; a_{37,38};$
	$\cos(\theta_{YX})$	$a_{7,13};$
	- $\cos(\theta_{YX})$	$a_{7,1};$
	$\cos(\theta_{YZ})$	$a_{28,15};$
	- $\cos(\theta_{YZ})$	$a_{28,3};$
	1 dbZ	$a_{34,1}; a_{31,13};$
	- 1 dbZ	$a_{31,1}; a_{34,13};$
	1 dbX	$a_{13,3}; a_{16,15};$
	- 1 dbX	$a_{16,3}; a_{13,15};$
	$\sin(\theta_{YX})$	$a_{7,37};$
	- $\sin(\theta_{YX})$	$a_{7,38};$
	1 dcX	$a_{11,37}; a_{9,38};$
	- 1 dcX	$a_{9,37}; a_{11,38};$
	- $dbZ \cos(\theta_{YZ})$	$a_{28,39};$
	0.5 dcX	$a_{12,40}; a_{15,40};$
	0.5 dcZ	$a_{37,39}; a_{38,39};$
	- 0.5 dcZ	$a_{29,40}; a_{32,40};$
	0.5 dbX	$a_{2,41}; a_{4,42};$
	- 0.5 dbX	$a_{1,41}; a_{5,42};$
	0.5 dbZ	$a_{23,42}; a_{25,44};$
	- 0.5 dbZ	$a_{22,43}; a_{26,44};$

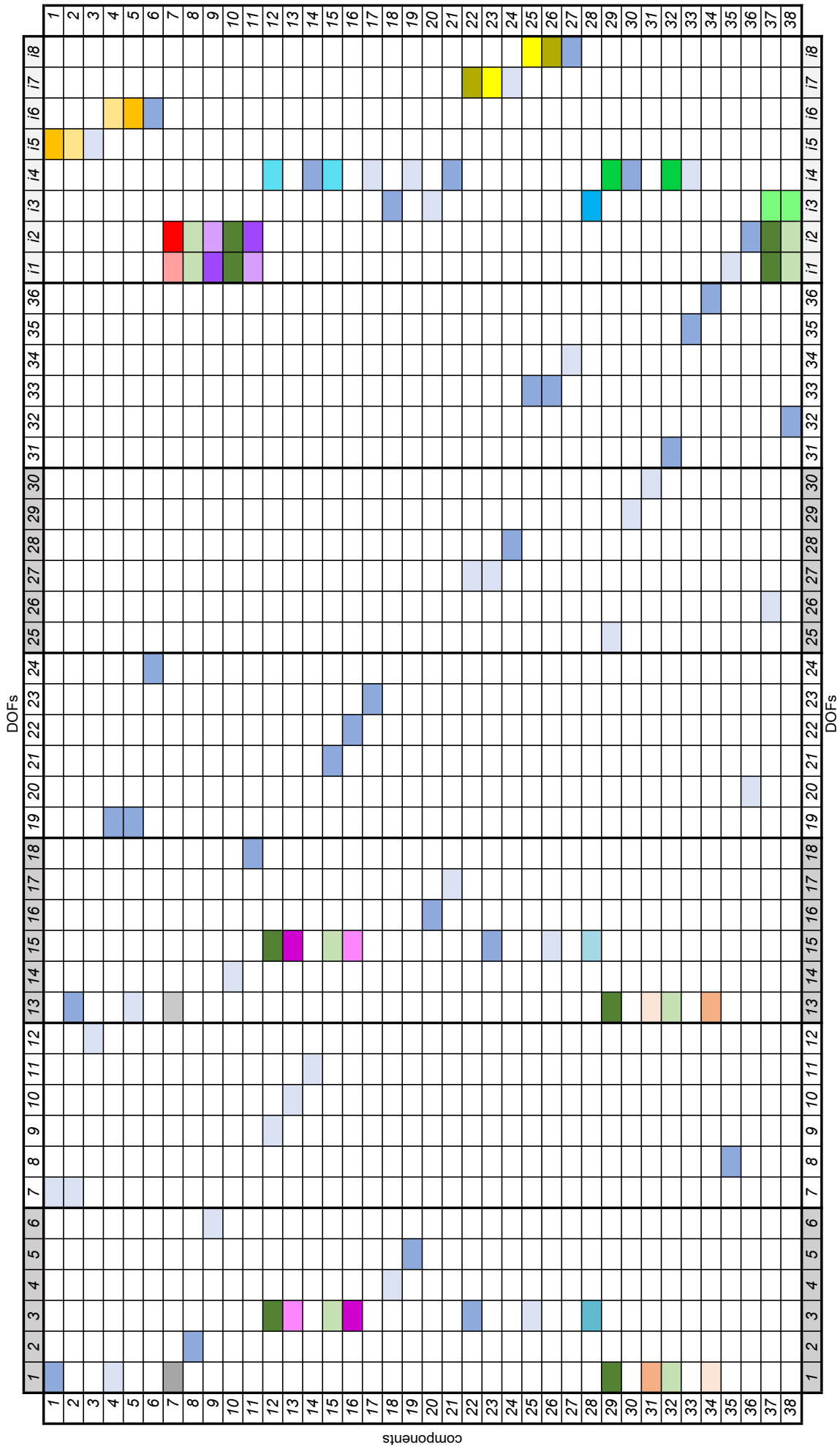


Figure C.1: Compatibility matrix elements color-coded by values.

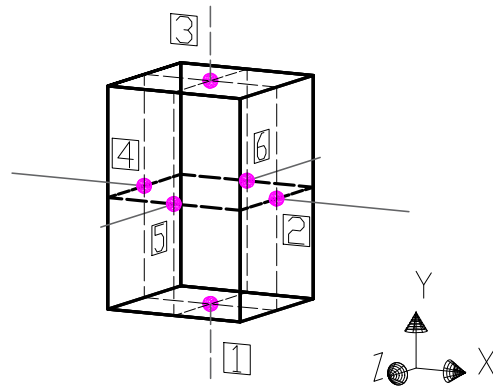


Figure C.2: Proposed beam-to-column joint finite element within the INNO3DJOINTS project [5]: Inno3DJointND element's schematic representation.

C.2.3 Inno3DJointND user manual

C.2.3.1 Element info

The Inno3DJointND joint finite element is defined in a 3D domain with six nodal DOFs. To construct a rectangular cuboid, which represents the joint, perpendicular planes are drawn to the beam and column ends, as illustrated in Fig. C.2. All six external nodes need to be defined regardless of the analyzed types of joints, namely central, edge, and corner, though some of these nodes may or may not be connected to any beam-to-column 1D element.

C.2.3.2 Element source code

The C++ source code of the Inno3DJointND element has not been made available to the general public due to legal restrictions imposed by the European project under which it was developed. Nonetheless, interested parties can request access to this source code by contacting Professor Luís Alberto Proença Simões da Silva via email at luisss@dec.uc.pt.

C.2.3.3 Command line and input arguments

The Inno3DJointND beam-to-column joint finite element can be constructed using the command input lines given below with the input arguments listed in Tab. C.2.

- input line for Tcl (*.tcl) files:

```
element Inno3DJointND $eleTag <$Node1 $Node2 $Node3 $Node4 $Node5$Node6>
<$SprMatTag01 ... $SprMatTag62>
```

- input line for Python (*.py) files:

Table C.2: Input arguments for Inno3DJointND joint finite element.

Input \$arg	Description
\$eleTag	An integer tag identifying the element in the domain
\$Node1	An integer tag indicating the node 1
...	
\$Node5	An integer tag indicating the node 5
\$SprMatTag01	An integer tag indicating the uniaxial materials for component 1
...	
\$SprMatTag62	An integer tag indicating the uniaxial materials for component 62

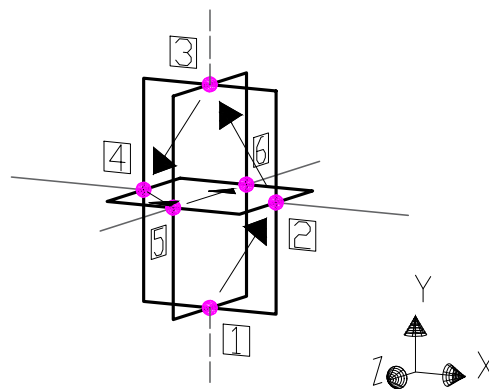


Figure C.3: Proposed beam-to-column joint finite element within the INNO3DJOINTS project [5]: Inno3DJointND element’s node input order.

```
element('Inno3DJointND', $eleTag, <$eleNode1, $eleNode2, $eleNode3, $eleNode4
$eleNode5>, <$SprMatTag01, ..., $SprMatTag62>)
```

C.2.3.4 Input requirements

The Inno3DJointND element is a 3D domain defined by six external nodes with six DOFs each. The nodes need to be defined in a specific order: 1/ bottom, 2/ right, 3 / top, 4/ left, 5 / front, and 6 / back, as shown in Fig. C.3.

The dimensions of the joint, as illustrated in Fig. C.4, must satisfy the criterion defined by Eq. (C.5) in all directions, irrespective of the units utilized by the user, given that OpenSees is a unitless software package. Otherwise, division by 0 occurs.

$$\min (dcX, dcZ, dbX, dbZ) \geq 1e - 12 \tag{C.5}$$

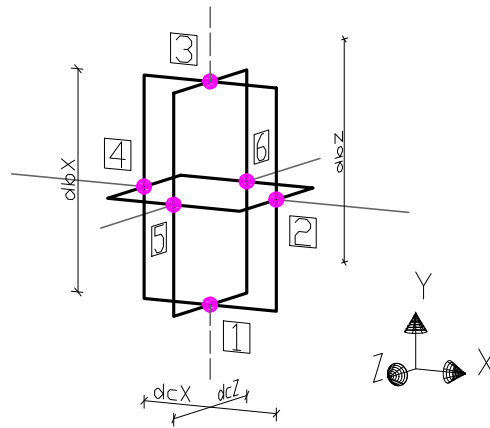


Figure C.4: Proposed beam-to-column joint finite element within the INNO3DJOINTS project [5]: Inno3DJointND element's dimensions.

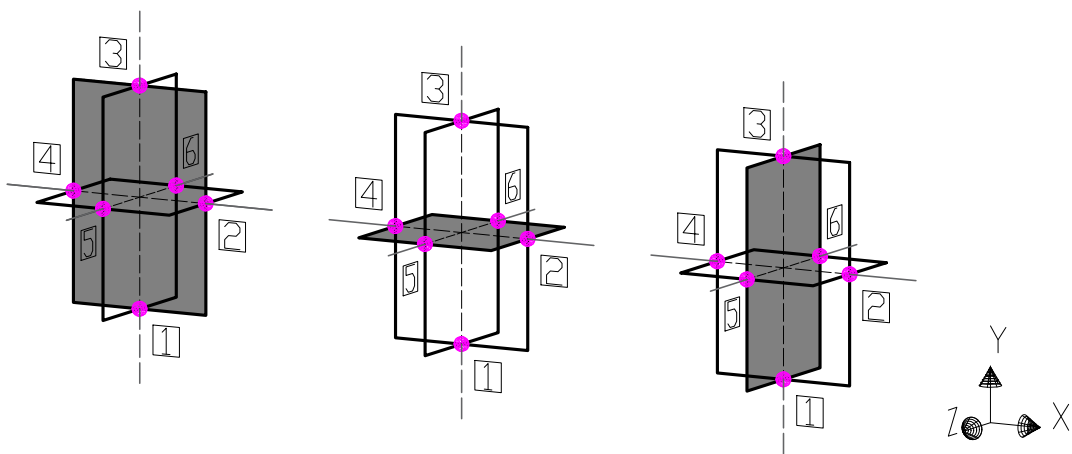


Figure C.5: Proposed beam-to-column joint finite element within the INNO3DJOINTS project [5]: Inno3DJointND element's dimensions.

To guarantee the formation of a rectangular cuboid through the use of the six external nodes, it is essential to adhere to the following guidelines when defining the three internal rectangular planes:

- each plane must be parallel to the primary planes - YX, YZ, and ZX - and must include only four external nodes of the joint, as illustrated in Fig. C.5;
- the mid-planes of the rectangular cuboid must correspond to the defined planes.

In other words, the coordinates of the nodes must satisfy the conditions from Tab. C.3.

C.2.3.5 Common errors messages

If the input requirements outlined in the previous section are not met, the software's framework console will exhibit the messages shown in Tab. C.4, and the domain will not be created:

Table C.3: Conditions for node coordinates.

Plane/Direction	Condition
Y-X plane	$x_4 < x_1 = x_3 = x_5 = x_6 < x_2$
Y-Z plane	$y_1 < y_2 = y_4 = y_5 = y_6 < y_3$
Z-X plane	$z_5 < z_1 = z_2 = z_3 = z_4 < z_6$
X direction	$ x_2 - x_1 = x_1 - x_4 = dcX/2$
Y direction	$ y_1 - y_2 = y_2 - y_3 = dbX/2$
Z direction	$ z_6 - z_1 = z_1 - z_5 = dcZ/2$

where (x_i, y_i, z_i) are the (x, y, z) coordinate of nodes.

Table C.4: Common errors.

Error source	Displayed error message
number of input arguments is wrong (i.e., different than 69)	WARNING error insufficient. arguments. Want: element Inno3DJointND eleTag? Node1? Node2? Node3? Node4? Node5? Node6? Spring01? Spring02? ... Spring62?.
number of DOFs/node is wrong (i.e., different than 6)	ERROR: Inno3DJointND::setDomain – number of DOFs associated with the node is incorrect.
joint size is too small	ERROR: Inno3DJointND::setDomain – height, length or width not correct, division by zero occurs. ERROR: Inno3DJointND::setDomain – All dimensions (distances between nodes) should be greater than 1e-12.
coordinate X (Y-Z plane)	ERROR: Inno3DJointND::setDomain – Incorrect X coordinates. Nodes 1, 3, 5 and 6 must have the same X-coordinate.
coordinate Z (Y-X plane)	ERROR: Inno3DJointND::setDomain – Incorrect Z coordinates. Nodes 1, 2, 3 and 4 must have the same Z-coordinate.
coordinate Y (Z-X plane)	ERROR: Inno3DJointND::setDomain – Incorrect Y coordinates. Nodes 2, 4, 5 and 6 must have the same Y-coordinate.
coordinate X (mid-line)	ERROR: Inno3DJointND::setDomain – Incorrect X coordinates. The absolute distance from node 4 to nodes 1 and 3 must be equal to the absolute distance from node 2 to nodes 1 and 3.
coordinate Z (mid-line)	ERROR: Inno3DJointND::setDomain – Incorrect Z coordinates. The absolute distance from node 5 to nodes 1 and 3 must be equal to the absolute distance from node 6 to nodes 1 and 3.
coordinate Y (mid-line)	ERROR: Inno3DJointND::setDomain – Incorrect Y coordinates. The absolute distance from node 1 to nodes 2 and 4 must be equal to the absolute distance from node 3 to nodes 3 and 2.

C.2.4 Output recorders

The Inno3DJointND joint finite element simulation outcomes can be analyzed by specifying output records at the component and element levels. To obtain such output records, input line commands for either Tcl or Python outputs are presented in Section 4.4.6, for both cases. The list of permissible inputs for the argument, \$arg, at the element level, is provided in Tab. C.5. Similarly, the list of permissible inputs for the argument, \$arg, at the component level is provided in Tab. C.6.

Table C.5: Valid \$arg – at element level.

\$arg	C++ Output Variable		Description
	Name	Size	
extDisp extdisp	UeprCommit	36×1	Returns the displacement in the external DOFs.
intDisp intdisp	UeprIntCommit	8×1	Returns the displacement in the internal DOFs.
Disp disp	UeprCommit UeprIntCommit	44×1	Returns the displacement in all DOFs.
Reaction reaction	R	44×1	Returns the global residual forces for all DOFs.
matStress matstress Stress stress	MaterialPtr->getStress()	62×1	Returns the stress values of the components.
matStrain matstrain Strain strain	MaterialPtr->getStrain()	62×1	Returns the strain values of the components.
matStressStrain matstressstrain StressStrain stressStrain	MaterialPtr->getStress() MaterialPtr->getStrain()	124×1	Returns the stress and strain values of the components.

Table C.6: Valid \$arg – at component level.

\$arg	C++ Output Variable		Description
	Name	Size	
spring			
-spring material	MaterialPtr[springNo]	1x2	Returns a pair of stress-strain for each time step.
-material			

Appendix D: Values of the parameters used in the calculation for the Euler-Bernoulli elements

The calculation presented in this document utilizes the displacement method to calculate the stiffness coefficient and restraining forces for various configurations. Therefore, to facilitate the reader's comprehension and avoid the necessity of consulting additional resources, the formulae for a 1D element with fixed-roller and fixed-fixed end supports are presented in Fig. D.1 and Fig. D.2, respectively.

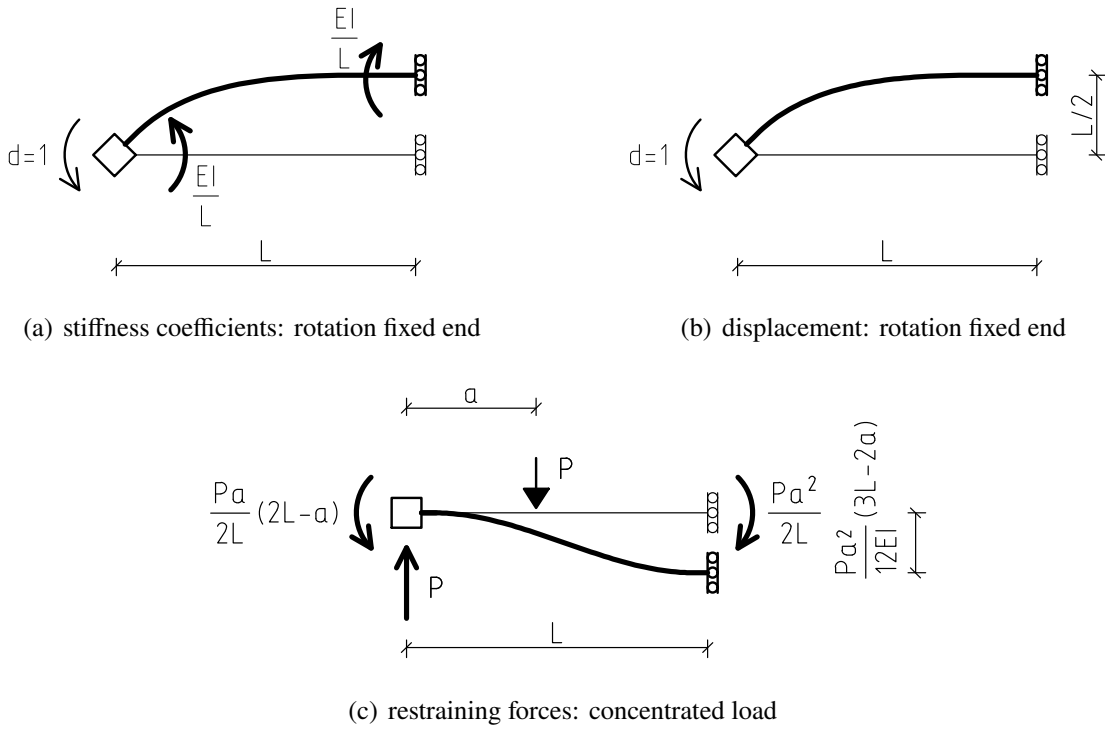


Figure D.1: 1D element with fixed-roller end supports.

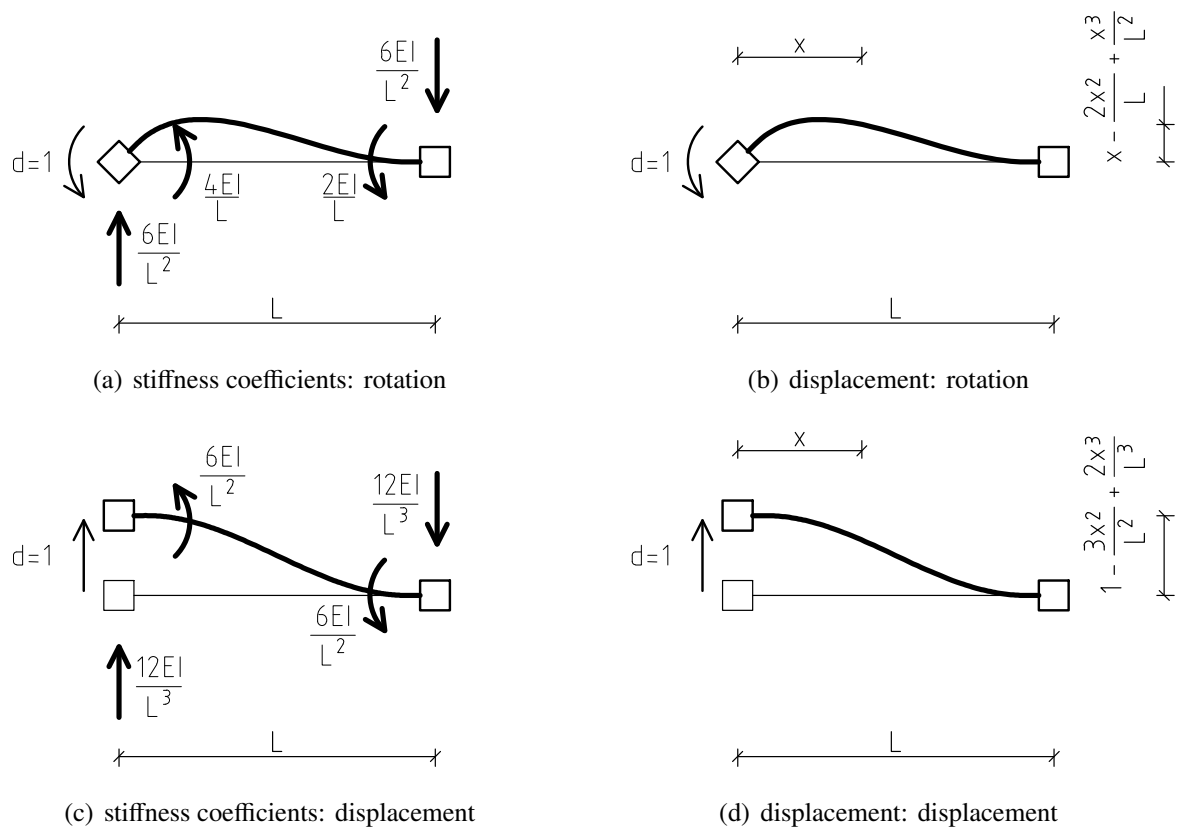


Figure D.2: 1D element with fixed-fixed end supports.

Appendix E: Detailed analytical computation of the condensed stiffness matrix of the EFMs

The analytical computation of the condensed stiffness matrix, \mathbf{K}_c^{EFM} (4×4) for the beam-to-column joint finite element presented in Section 2.6.5 is presented in detail for all six EFMs in separate sections. Each calculation follows the steps described in Section 5.2.2.

E.1 HS-EFM

The following four sections present detailed calculations for each LP-EFM shown in Fig. 5.2, as applied to the HS-EFM. These calculations follow the procedures outlined in Section 5.2.2. A separate section is dedicated to the condensed stiffness matrix of the HS-EFM, \mathbf{K}_c^{HS-EFM} .

E.1.1 LP-EFM.1

The deformation of HS-EFM under LP-EFM.1, the SEFM due to symmetry conditions, the stiffness coefficients, and the corresponding restraining forces are presented in Fig. E.1(a), Fig. E.1(b) Fig. E.1(c), and Fig. E.1(d), respectively. Eqs. (E.1) to (E.7) present the results from the application of the procedure described in Section 5.2.2.

$$k_{11}^{LP-EFM.1} = \frac{EI}{L/2} + \frac{EI}{L/2} \quad (E.1)$$

$$\delta_d^{LP-EFM.1} = \begin{bmatrix} \delta_d^{LP-EFM.1.N} \\ \delta_d^{LP-EFM.1.E} \end{bmatrix} = \begin{bmatrix} \frac{L/2}{2} \\ -\frac{L/2}{2} \end{bmatrix} \quad (E.2)$$

$$f^{LP-EFM.1} = \begin{bmatrix} -\frac{PL}{8} + \frac{PL}{8} \end{bmatrix} \quad (E.3)$$

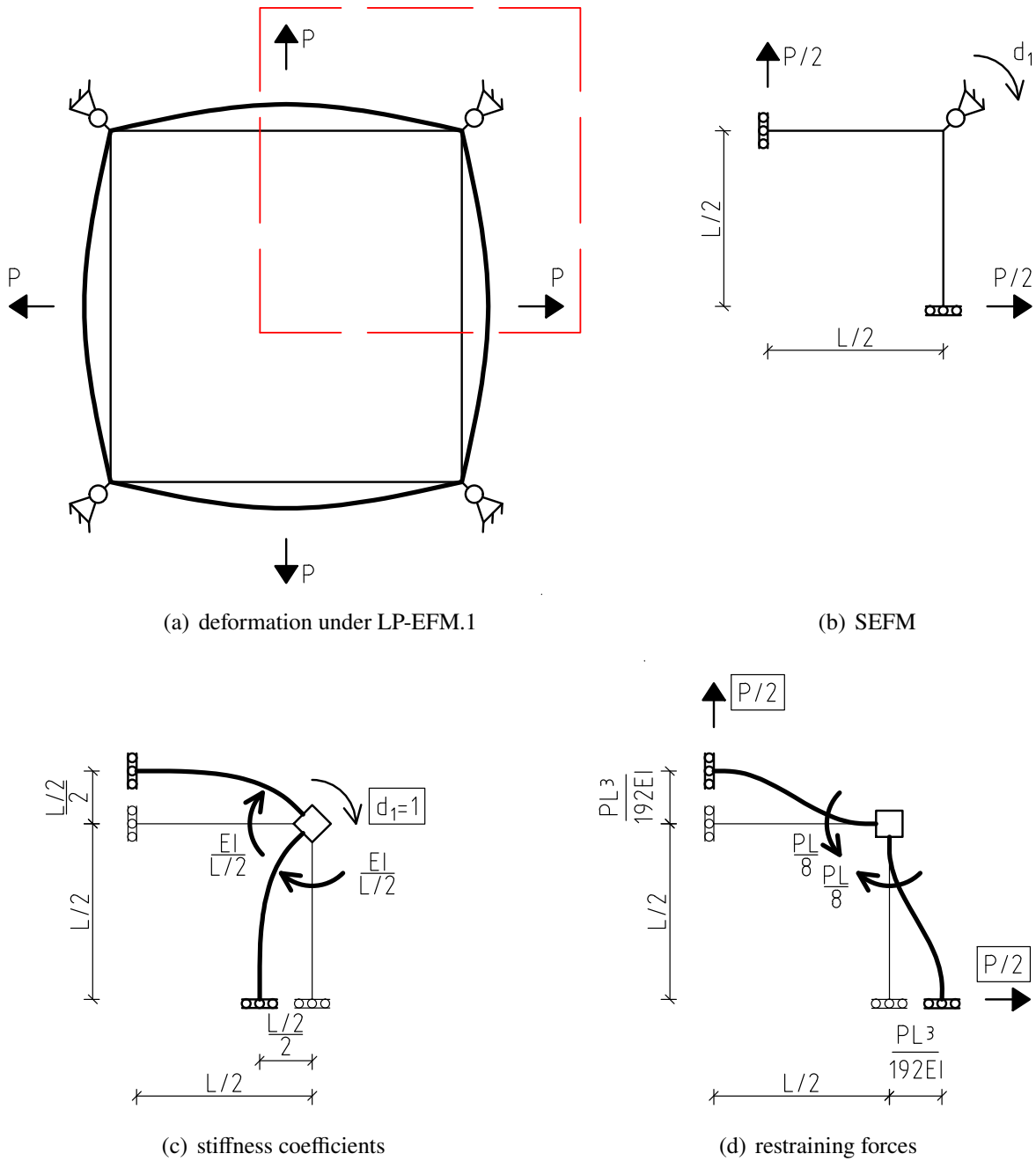


Figure E.1: HS-EFM under LP-EFM.1.

$$\delta_P^{\text{LP-EFM.1}} = \begin{bmatrix} \delta_P^{\text{LP-EFM.1.N}} \\ \delta_P^{\text{LP-EFM.1.E}} \end{bmatrix} = \begin{bmatrix} \frac{P L^3}{192 E I} \\ \frac{P L^3}{192 E I} \end{bmatrix} \quad (\text{E.4})$$

$$d^{\text{LP-EFM.1}} = \left(k_{11}^{\text{LP-EFM.1}} \right)^{-1} \left(-f^{\text{LP-EFM.1}} \right) = 0 \quad (\text{E.5})$$

$$\delta_D^{\text{LP-EFM.1}} = \delta_d^{\text{LP-EFM.1}} d^{\text{LP-EFM.1}} = \begin{bmatrix} \delta_D^{\text{LP-EFM.1.N}} \\ \delta_D^{\text{LP-EFM.1.E}} \end{bmatrix} = \begin{bmatrix} 0 \\ 0 \end{bmatrix} \quad (\text{E.6})$$

$$\delta^{\text{LP-EFM.1}} = \delta_D^{\text{LP-EFM.1}} + \delta_P^{\text{LP-EFM.1}} = \begin{bmatrix} \delta^{\text{LP-EFM.1.N}} \\ \delta^{\text{LP-EFM.1.E}} \end{bmatrix} = \begin{bmatrix} \frac{P L^3}{192 E I} \\ \frac{P L^3}{192 E I} \end{bmatrix} \quad (\text{E.7})$$

E.1.2 LP-EFM.2

The deformation of HS-EFM under LP-EFM.2, the SEFM due to symmetry conditions, the stiffness coefficients, and the corresponding restraining forces are presented in Fig. E.2(a), Fig. E.2(b) Fig. E.2(c), and Fig. E.2(d), respectively. Eqs. (E.8) to (E.14) present the results from the application of the procedure described in Section 5.2.2.

$$k_{11}^{\text{LP-EFM.2}} = \frac{E I}{L/2} + \frac{E I}{L/2} \quad (\text{E.8})$$

$$\delta_d^{\text{LP-EFM.2}} = \begin{bmatrix} \delta_d^{\text{LP-EFM.2.N}} \\ \delta_d^{\text{LP-EFM.2.E}} \end{bmatrix} = \begin{bmatrix} \frac{L/2}{2} \\ -\frac{L/2}{2} \end{bmatrix} \quad (\text{E.9})$$

$$f^{\text{LP-EFM.2}} = \begin{bmatrix} \frac{P L}{8} + \frac{P L}{8} \end{bmatrix} \quad (\text{E.10})$$

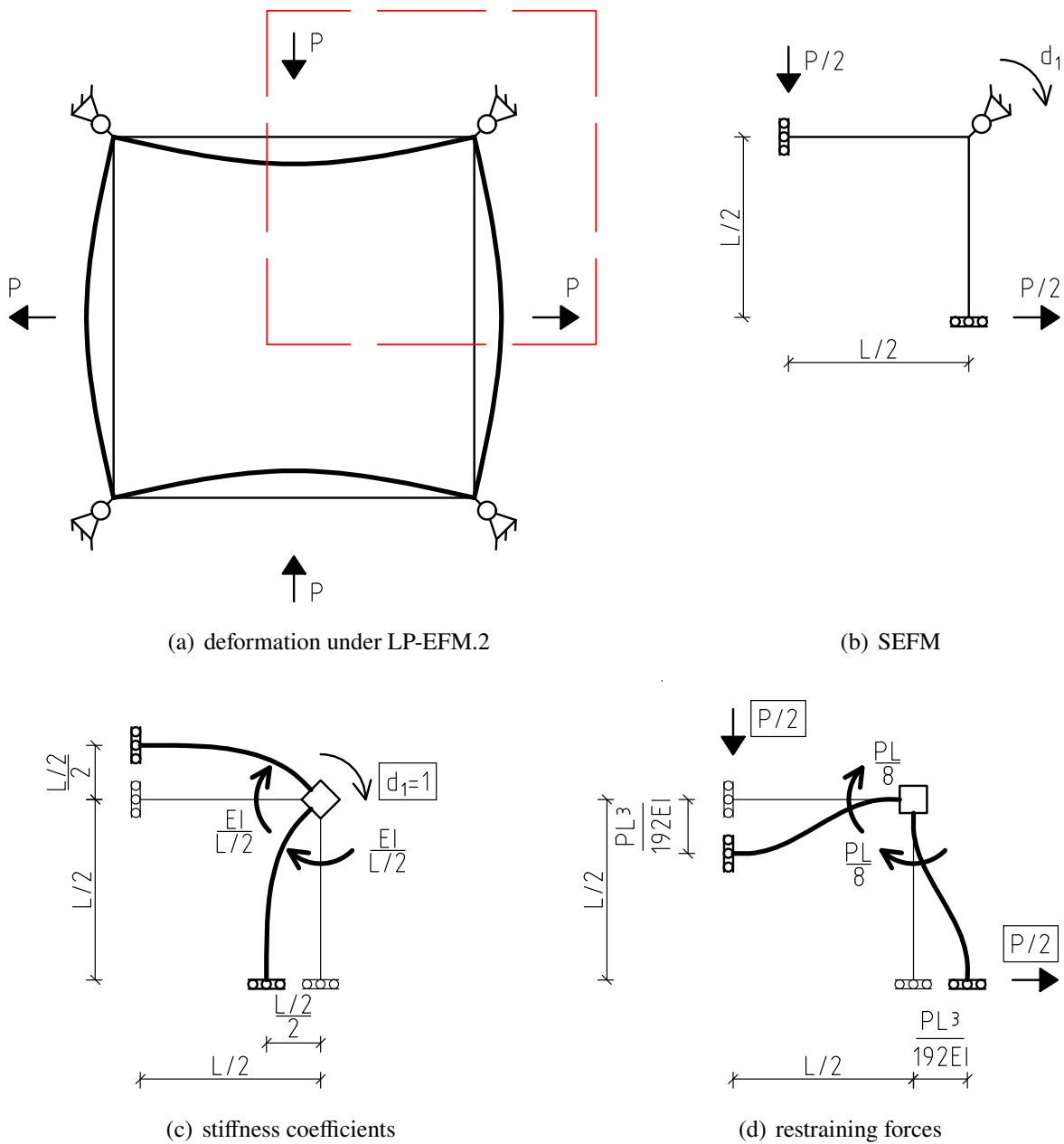


Figure E.2: HS-EFM under LP-EFM.2.

$$\delta_P^{\text{LP-EFM.2}} = \begin{bmatrix} \delta_P^{\text{LP-EFM.2.N}} \\ \delta_P^{\text{LP-EFM.2.E}} \end{bmatrix} = \begin{bmatrix} -\frac{P L^3}{192 E I} \\ \frac{P L^3}{192 E I} \end{bmatrix} \quad (\text{E.11})$$

$$d^{\text{LP-EFM.2}} = \left(k_{11}^{\text{LP-EFM.2}} \right)^{-1} \left(-f^{\text{LP-EFM.2}} \right) = -\frac{P L^2}{16 E I} \quad (\text{E.12})$$

$$\delta_D^{\text{LP-EFM.2}} = \delta_d^{\text{LP-EFM.2}} d^{\text{LP-EFM.2}} = \begin{bmatrix} \delta_D^{\text{LP-EFM.2.N}} \\ \delta_D^{\text{LP-EFM.2.E}} \end{bmatrix} = \begin{bmatrix} -\frac{P L^3}{64 E I} \\ \frac{P L^3}{64 E I} \end{bmatrix} \quad (\text{E.13})$$

$$\delta^{\text{LP-EFM.2}} = \delta_D^{\text{LP-EFM.2}} + \delta_P^{\text{LP-EFM.2}} = \begin{bmatrix} \delta^{\text{LP-EFM.2.N}} \\ \delta^{\text{LP-EFM.2.E}} \end{bmatrix} = \begin{bmatrix} -\frac{P L^3}{48 E I} \\ \frac{P L^3}{48 E I} \end{bmatrix} \quad (\text{E.14})$$

E.1.3 LP-EFM.3

The deformation of HS-EFM under LP-EFM.3, the SEFM due to symmetry conditions, the stiffness coefficients, and the corresponding restraining forces are presented in Fig. E.3(a), Fig. E.3(b) Fig. E.3(c), and Fig. E.3(d), respectively. Eqs. (E.15) to (E.21) present the results from the application of the procedure described in Section 5.2.2.

$$k_{11}^{\text{LP-EFM.3}} = \frac{4 E I}{L/2} + \frac{E I}{L/2} \quad (\text{E.15})$$

$$\delta_d^{\text{LP-EFM.3}} = \begin{bmatrix} \delta_d^{\text{LP-EFM.3.N}} \\ \delta_d^{\text{LP-EFM.3.E}} \end{bmatrix} = \begin{bmatrix} 0 \\ -\frac{L/2}{2} \end{bmatrix} \quad (\text{E.16})$$

$$f^{\text{LP-EFM.3}} = \begin{bmatrix} \frac{P L}{8} \end{bmatrix} \quad (\text{E.17})$$

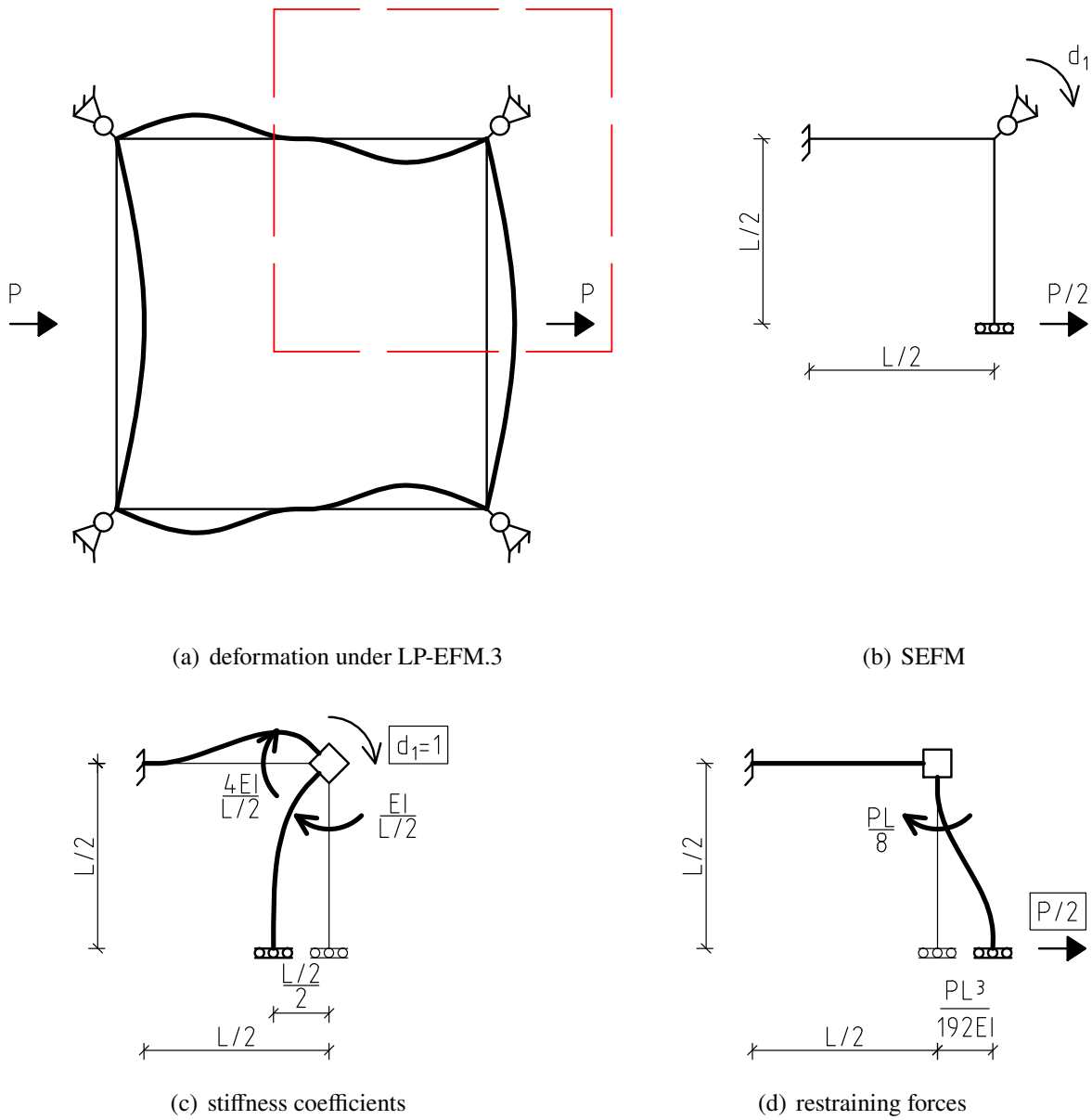


Figure E.3: HS-EFM under LP-EFM.3.

$$\delta_P^{\text{LP-EFM.3}} = \begin{bmatrix} \delta_P^{\text{LP-EFM.3.N}} \\ \delta_P^{\text{LP-EFM.3.E}} \end{bmatrix} = \begin{bmatrix} 0 \\ \frac{P L^3}{192 E I} \end{bmatrix} \quad (\text{E.18})$$

$$d^{\text{LP-EFM.3}} = \left(k_{11}^{\text{LP-EFM.3}} \right)^{-1} \left(-f^{\text{LP-EFM.3}} \right) = -\frac{P L^2}{80 E I} \quad (\text{E.19})$$

$$\delta_D^{\text{LP-EFM.3}} = \delta_d^{\text{LP-EFM.3}} d^{\text{LP-EFM.3}} = \begin{bmatrix} \delta_D^{\text{LP-EFM.3.N}} \\ \delta_D^{\text{LP-EFM.3.E}} \end{bmatrix} = \begin{bmatrix} 0 \\ \frac{P L^3}{320 E I} \end{bmatrix} \quad (\text{E.20})$$

$$\delta^{\text{LP-EFM.3}} = \delta_d^{\text{LP-EFM.3}} + \delta_P^{\text{LP-EFM.3}} = \begin{bmatrix} \delta^{\text{LP-EFM.3.N}} \\ \delta^{\text{LP-EFM.3.E}} \end{bmatrix} = \begin{bmatrix} 0 \\ \frac{P L^3}{120 E I} \end{bmatrix} \quad (\text{E.21})$$

E.1.4 LP-EFM.4

The deformation of HS-EFM under LP-EFM.4, the SEFM due to symmetry conditions, the stiffness coefficients, and the corresponding restraining forces are presented in Fig. E.4(a), Fig. E.4(b) Fig. E.4(c), and Fig. E.4(d), respectively. Eqs. (E.22) to (E.28) present the results from the application of the procedure described in Section 5.2.2.

$$k_{11}^{\text{LP-EFM.4}} = \frac{E I}{L/2} + \frac{4 E I}{L/2} \quad (\text{E.22})$$

$$\delta_d^{\text{LP-EFM.4}} = \begin{bmatrix} \delta_d^{\text{LP-EFM.4.N}} \\ \delta_d^{\text{LP-EFM.4.E}} \end{bmatrix} = \begin{bmatrix} \frac{L/2}{2} \\ 0 \end{bmatrix} \quad (\text{E.23})$$

$$f^{\text{LP-EFM.4}} = \begin{bmatrix} -\frac{P L}{8} \end{bmatrix} \quad (\text{E.24})$$

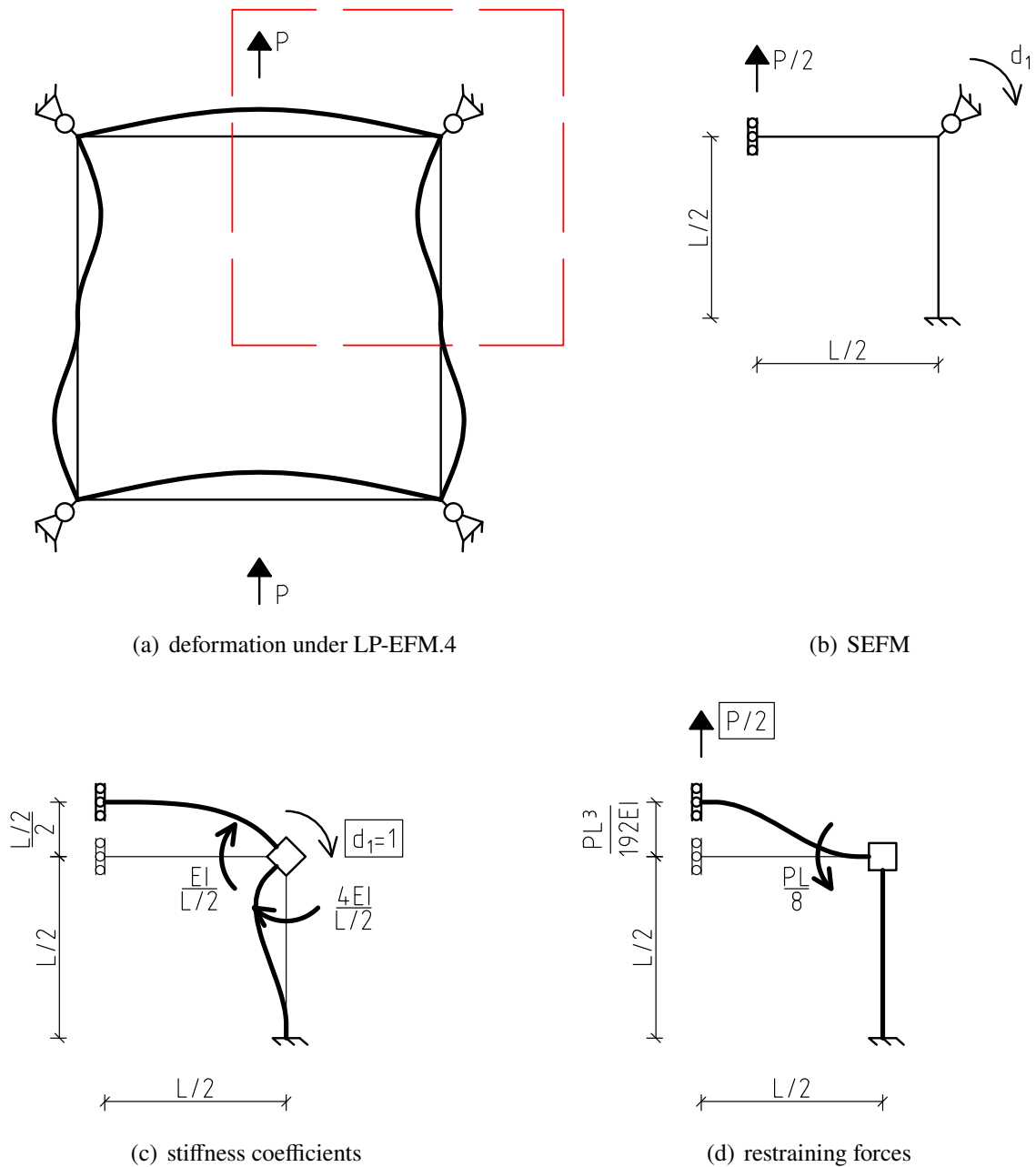


Figure E.4: HS-EFM under LP-EFM.4.

$$\delta_P^{\text{LP-EFM.4}} = \begin{bmatrix} \delta_P^{\text{LP-EFM.4.N}} \\ \delta_P^{\text{LP-EFM.4.E}} \end{bmatrix} = \begin{bmatrix} \frac{P L^3}{192 E I} \\ 0 \end{bmatrix} \quad (\text{E.25})$$

$$d^{\text{LP-EFM.4}} = \left(k_{11}^{\text{LP-EFM.4}} \right)^{-1} \left(-f^{\text{LP-EFM.4}} \right) = \frac{P L^2}{80 E I} \quad (\text{E.26})$$

$$\delta_D^{\text{LP-EFM.4}} = \delta_d^{\text{LP-EFM.4}} d^{\text{LP-EFM.4}} = \begin{bmatrix} \delta_D^{\text{LP-EFM.4.N}} \\ \delta_D^{\text{LP-EFM.4.E}} \end{bmatrix} = \begin{bmatrix} \frac{P L^3}{320 E I} \\ 0 \end{bmatrix} \quad (\text{E.27})$$

$$\delta^{\text{LP-EFM.4}} = \delta_D^{\text{LP-EFM.4}} + \delta_P^{\text{LP-EFM.4}} = \begin{bmatrix} \delta^{\text{LP-EFM.4.N}} \\ \delta^{\text{LP-EFM.4.E}} \end{bmatrix} = \begin{bmatrix} \frac{P L^3}{120 E I} \\ 0 \end{bmatrix} \quad (\text{E.28})$$

E.1.5 Condensed stiffness matrix of HS-EFM

As already mentioned, the matrix $\mathbf{F}^{\text{HS-EFM}}$ is constructed for the full EFM by concatenating the displacement vectors of each LP-EFM, $\delta^{\text{LP-EFM.}i}$. Eq. (E.7), (E.14), (E.21), and (E.28) provide two of the four displacements, with the remaining two derived from symmetry conditions with respect to the sign convention, yielding the results shown in Eq. (E.29).

$$\mathbf{F}^{\text{HS-EFM}} = \begin{bmatrix} \delta^{\text{LP-EFM.1.N}} & \delta^{\text{LP-EFM.2.N}} & \delta^{\text{LP-EFM.3.N}} & -\delta^{\text{LP-EFM.4.N}} \\ \delta^{\text{LP-EFM.1.E}} & \delta^{\text{LP-EFM.2.E}} & \delta^{\text{LP-EFM.3.E}} & \delta^{\text{LP-EFM.4.E}} \\ \delta^{\text{LP-EFM.1.N}} & \delta^{\text{LP-EFM.2.N}} & \delta^{\text{LP-EFM.3.N}} & \delta^{\text{LP-EFM.4.N}} \\ \delta^{\text{LP-EFM.1.E}} & \delta^{\text{LP-EFM.2.E}} & -\delta^{\text{LP-EFM.3.E}} & \delta^{\text{LP-EFM.4.E}} \end{bmatrix} \quad (\text{E.29})$$

The condensed stiffness matrix of the HS-EFM, $\mathbf{K}_c^{\text{HS-EFM}}$, is obtained by multiplying the matrix

of external forces, \mathbf{P} (Eq. (5.3)), with the inverse of $\mathbf{F}^{\text{HS-EFM}}$ (Eq. (E.29)), leading to Eq. (E.30).

$$\mathbf{K}_c^{\text{HS-EFM}} = \mathbf{P} \left(\mathbf{F}^{\text{HS-EFM}} \right)^{-1} = \begin{bmatrix} \frac{120 E I}{L^3} & \frac{36 E I}{L^3} & 0 & \frac{36 E I}{L^3} \\ \frac{36 E I}{L^3} & \frac{120 E I}{L^3} & \frac{36 E I}{L^3} & 0 \\ 0 & \frac{36 E I}{L^3} & \frac{120 E I}{L^3} & \frac{36 E I}{L^3} \\ \frac{36 E I}{L^3} & 0 & \frac{36 E I}{L^3} & \frac{120 E I}{L^3} \end{bmatrix} \quad (\text{E.30})$$

E.2 HR-EFM-IF

The subsequent four sections provide detailed calculations for each LP-EFM depicted in Fig. 5.2 when applied to the HR-EFM-IF, using the procedures outlined in Section 5.2.2. Following these sections, a final section is designated for the stiffness matrix of the HR-EFM-IF, $\mathbf{K}_c^{\text{HR-EFM-IF}}$.

E.2.1 LP-EFM.1

The deformation of HR-EFM under LP-EFM.1, the SEFM due to symmetry conditions, the stiffness coefficients, and the corresponding restraining forces are presented in Fig. E.5(a), Fig. E.5(b) Fig. E.5(c), and Fig. E.5(d), respectively. Eqs. (E.31) to (E.37) present the results from the application of the procedure described in Section 5.2.2.

$$k_{11}^{\text{LP-EFM.1}} = \frac{E I_1}{L_1/2} + \frac{E I_2}{L_2/2} \quad (\text{E.31})$$

$$\delta_d^{\text{LP-EFM.1}} = \begin{bmatrix} \delta_d^{\text{LP-EFM.1.N}} \\ \delta_d^{\text{LP-EFM.1.E}} \end{bmatrix} = \begin{bmatrix} \frac{L_1/2}{2} \\ -\frac{L_2/2}{2} \end{bmatrix} \quad (\text{E.32})$$

$$f^{\text{LP-EFM.1}} = \begin{bmatrix} -\frac{P L_1}{8} + \frac{P L_2}{8} \end{bmatrix} \quad (\text{E.33})$$

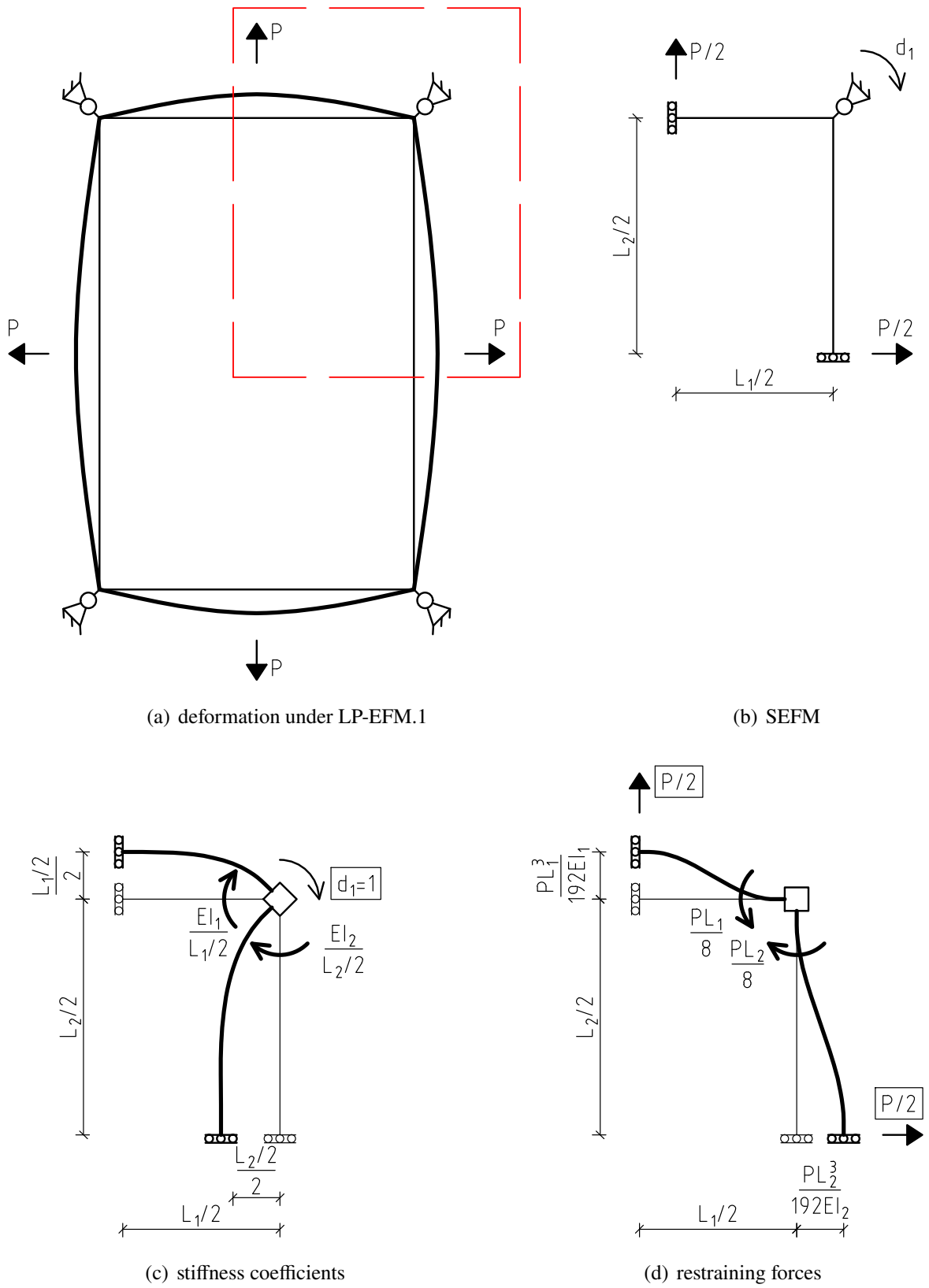


Figure E.5: HR-EFM under LP-EFM.1.

$$\delta_P^{\text{LP-EFM.1}} = \begin{bmatrix} \delta_P^{\text{LP-EFM.1.N}} \\ \delta_P^{\text{LP-EFM.1.E}} \end{bmatrix} = \begin{bmatrix} \frac{P L_1^3}{192 E I_1} \\ \frac{P L_2^3}{192 E I_2} \end{bmatrix} \quad (\text{E.34})$$

$$d^{\text{LP-EFM.1}} = \left(k_{11}^{\text{LP-EFM.1}} \right)^{-1} \left(-f^{\text{LP-EFM.1}} \right) = \frac{L_1 L_2 P (L_1 - L_2)}{16 E (I_1 L_2 + I_2 L_1)} \quad (\text{E.35})$$

$$\delta_D^{\text{LP-EFM.1}} = \delta_d^{\text{LP-EFM.1}} d^{\text{LP-EFM.1}} = \begin{bmatrix} \delta_D^{\text{LP-EFM.1.N}} \\ \delta_D^{\text{LP-EFM.1.E}} \end{bmatrix} = \begin{bmatrix} \frac{L_1^2 L_2 P (L_1 - L_2)}{64 E (I_1 L_2 + I_2 L_1)} \\ -\frac{L_1 L_2^2 P (L_1 - L_2)}{64 E (I_1 L_2 + I_2 L_1)} \end{bmatrix} \quad (\text{E.36})$$

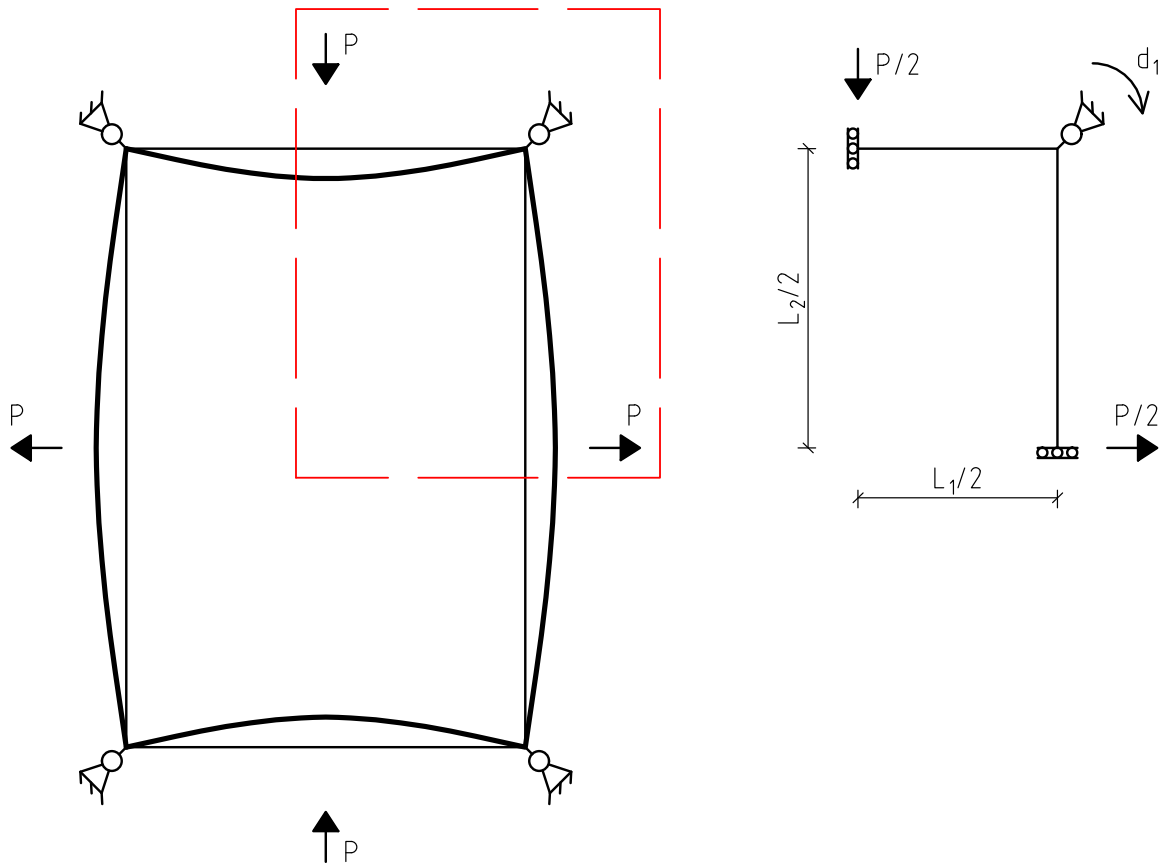
$$\delta^{\text{LP-EFM.1}} = \delta_D^{\text{LP-EFM.1}} + \delta_P^{\text{LP-EFM.1}} = \begin{bmatrix} \delta^{\text{LP-EFM.1.N}} \\ \delta^{\text{LP-EFM.1.E}} \end{bmatrix} = \begin{bmatrix} \frac{L_1^2 P (I_2 L_1^2 + 4 I_1 L_1 L_2 - 3 I_1 L_2^2)}{192 E I_1 (I_1 L_2 + I_2 L_1)} \\ \frac{L_2^2 P (-3 I_2 L_1^2 + 4 I_2 L_1 L_2 + I_1 L_2^2)}{192 E I_2 (I_1 L_2 + I_2 L_1)} \end{bmatrix} \quad (\text{E.37})$$

E.2.2 LP-EFM.2

The deformation of HR-EFM under LP-EFM.2, the SEFM due to symmetry conditions, the stiffness coefficients, and the corresponding restraining forces are presented in Fig. E.6(a), Fig. E.6(b) Fig. E.6(c), and Fig. E.6(d), respectively. Eqs. (E.38) to (E.44) present the results from the application of the procedure described in Section 5.2.2.

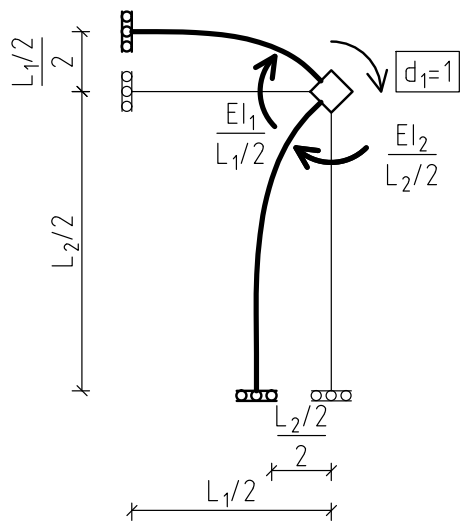
$$k_{11}^{\text{LP-EFM.2}} = \frac{E I_1}{L_1/2} + \frac{E I_2}{L_2/2} \quad (\text{E.38})$$

$$\delta_d^{\text{LP-EFM.2}} = \begin{bmatrix} \delta_d^{\text{LP-EFM.2.N}} \\ \delta_d^{\text{LP-EFM.2.E}} \end{bmatrix} = \begin{bmatrix} \frac{L_1/2}{2} \\ -\frac{L_2/2}{2} \end{bmatrix} \quad (\text{E.39})$$

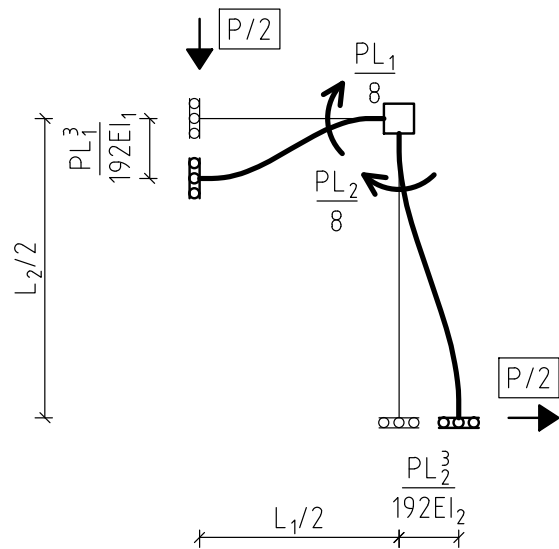


(a) deformation under LP-EFM.2

(b) SEFM



(c) stiffness coefficients



(d) restraining forces

Figure E.6: HR-EFM under LP-EFM.2.

$$f^{\text{LP-EFM.2}} = \left[\frac{P L_1}{8} + \frac{P L_2}{8} \right] \quad (\text{E.40})$$

$$\delta_P^{\text{LP-EFM.2}} = \begin{bmatrix} \delta_P^{\text{LP-EFM.2.N}} \\ \delta_P^{\text{LP-EFM.2.E}} \end{bmatrix} = \begin{bmatrix} -\frac{P L_1^3}{192 E I_1} \\ \frac{P L_2^3}{192 E I_2} \end{bmatrix} \quad (\text{E.41})$$

$$d^{\text{LP-EFM.2}} = \left(k_{11}^{\text{LP-EFM.2}} \right)^{-1} \left(-f^{\text{LP-EFM.2}} \right) = -\frac{L_1 L_2 P (L_1 + L_2)}{16 E (I_1 L_2 + I_2 L_1)} \quad (\text{E.42})$$

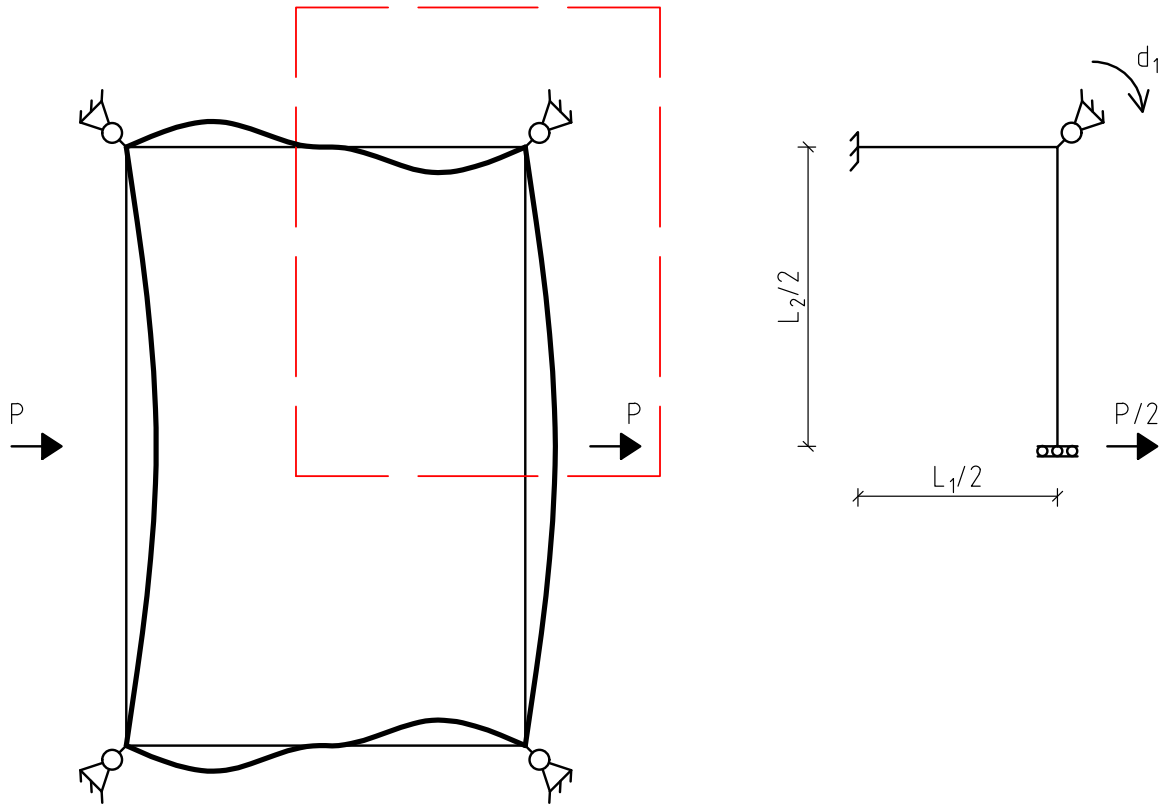
$$\delta_D^{\text{LP-EFM.2}} = \delta_d^{\text{LP-EFM.2}} d^{\text{LP-EFM.2}} = \begin{bmatrix} \delta_D^{\text{LP-EFM.2.N}} \\ \delta_D^{\text{LP-EFM.2.E}} \end{bmatrix} = \begin{bmatrix} -\frac{L_1^2 L_2 P (L_1 + L_2)}{64 E (I_1 L_2 + I_2 L_1)} \\ \frac{L_1 L_2^2 P (L_1 + L_2)}{64 E (I_1 L_2 + I_2 L_1)} \end{bmatrix} \quad (\text{E.43})$$

$$\begin{aligned} \delta^{\text{LP-EFM.2}} &= \delta_D^{\text{LP-EFM.2}} + \delta_P^{\text{LP-EFM.2}} = \begin{bmatrix} \delta^{\text{LP-EFM.2.N}} \\ \delta^{\text{LP-EFM.2.E}} \end{bmatrix} \\ &= \begin{bmatrix} -\frac{L_1^2 P (I_2 L_1^2 + 4 I_1 L_1 L_2 + 3 I_1 L_2^2)}{192 E I_1 (I_1 L_2 + I_2 L_1)} \\ \frac{L_2^2 P (3 I_2 L_1^2 + 4 I_2 L_1 L_2 + I_1 L_2^2)}{192 E I_2 (I_1 L_2 + I_2 L_1)} \end{bmatrix} \end{aligned} \quad (\text{E.44})$$

E.2.3 LP-EFM.3

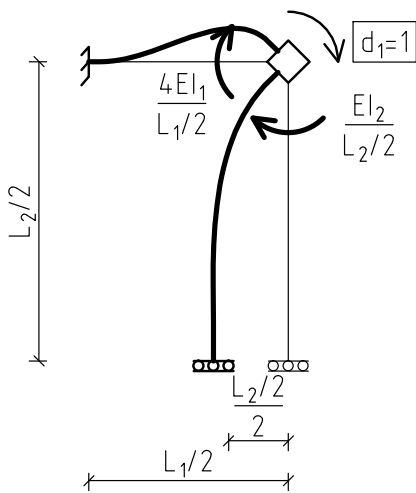
The deformation of HR-EFM under LP-EFM.3, the SEFM due to symmetry conditions, the stiffness coefficients, and the corresponding restraining forces are presented in Fig. E.7(a), Fig. E.7(b) Fig. E.7(c), and Fig. E.7(d), respectively. Eqs. (E.45) to (E.51) present the results from the application of the procedure described in Section 5.2.2.

$$k_{11}^{\text{LP-EFM.3}} = \frac{4 E I_1}{L_1/2} + \frac{E I_2}{L_2/2} \quad (\text{E.45})$$

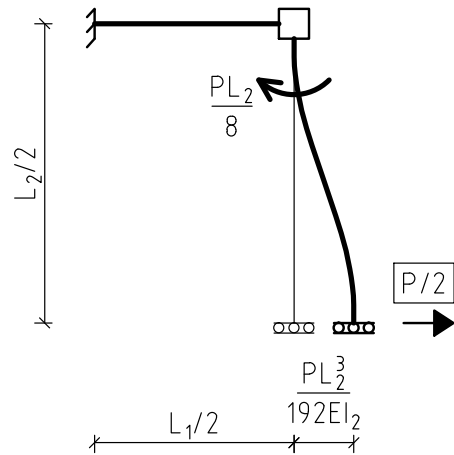


(a) deformation under LP-EFM.3

(b) SEFM



(c) stiffness coefficients



(d) restraining forces

Figure E.7: HR-EFM under LP-EFM.3.

$$\delta_d^{\text{LP-EFM.3}} = \begin{bmatrix} \delta_d^{\text{LP-EFM.3.N}} \\ \delta_d^{\text{LP-EFM.3.E}} \end{bmatrix} = \begin{bmatrix} 0 \\ -\frac{L_2/2}{2} \end{bmatrix} \quad (\text{E.46})$$

$$f^{\text{LP-EFM.3}} = \begin{bmatrix} \frac{P L_2}{8} \end{bmatrix} \quad (\text{E.47})$$

$$\delta_P^{\text{LP-EFM.3}} = \begin{bmatrix} \delta_P^{\text{LP-EFM.3.N}} \\ \delta_P^{\text{LP-EFM.3.E}} \end{bmatrix} = \begin{bmatrix} 0 \\ \frac{P L_2^3}{192 E I_2} \end{bmatrix} \quad (\text{E.48})$$

$$d^{\text{LP-EFM.3}} = \left(k_{11}^{\text{LP-EFM.3}} \right)^{-1} \left(-f^{\text{LP-EFM.3}} \right) = -\frac{L_1 L_2^2 P}{16 E (4 I_1 L_2 + I_2 L_1)} \quad (\text{E.49})$$

$$\delta_D^{\text{LP-EFM.3}} = \delta_d^{\text{LP-EFM.3}} d^{\text{LP-EFM.3}} = \begin{bmatrix} \delta_D^{\text{LP-EFM.3.N}} \\ \delta_D^{\text{LP-EFM.3.E}} \end{bmatrix} = \begin{bmatrix} 0 \\ \frac{L_1 L_2^3 P}{64 E (4 I_1 L_2 + I_2 L_1)} \end{bmatrix} \quad (\text{E.50})$$

$$\delta^{\text{LP-EFM.3}} = \delta_D^{\text{LP-EFM.3}} + \delta_P^{\text{LP-EFM.3}} = \begin{bmatrix} \delta^{\text{LP-EFM.3.N}} \\ \delta^{\text{LP-EFM.3.E}} \end{bmatrix} = \begin{bmatrix} 0 \\ \frac{L_2^3 P (I_1 L_2 + I_2 L_1)}{48 E I_2 (4 I_1 L_2 + I_2 L_1)} \end{bmatrix} \quad (\text{E.51})$$

E.2.4 LP-EFM.4

The deformation of HR-EFM under LP-EFM.4, the SEFM due to symmetry conditions, the stiffness coefficients, and the corresponding restraining forces are presented in Fig. E.8(a), Fig. E.8(b) Fig. E.8(c), and Fig. E.8(d), respectively. Eqs. (E.52) to (E.58) present the results from the application of the procedure described in Section 5.2.2.

$$k_{11}^{\text{LP-EFM.4}} = \frac{E I_1}{L_1/2} + \frac{4 E_2 I}{L_2/2} \quad (\text{E.52})$$

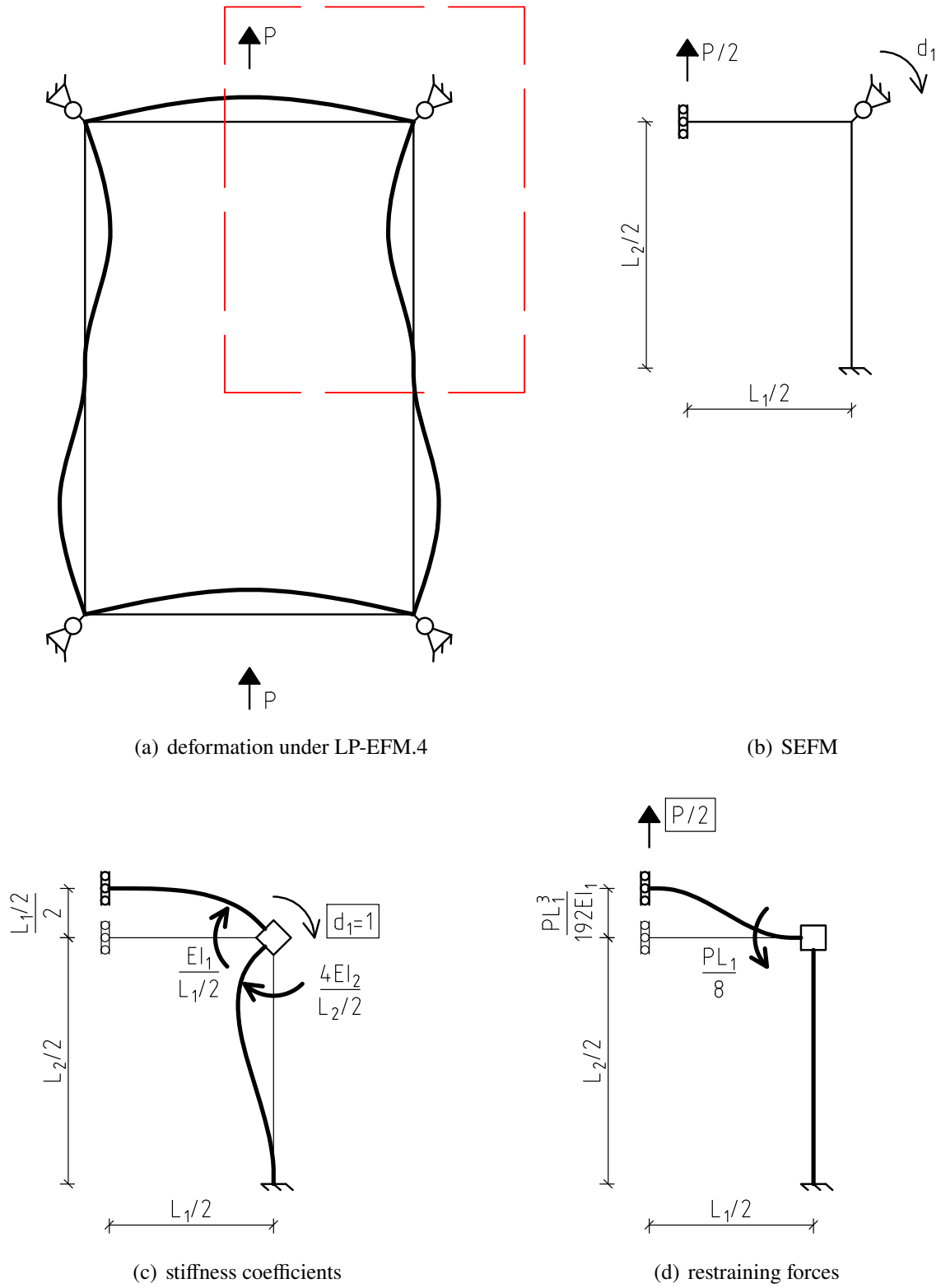


Figure E.8: HR-EFM under LP-EFM.4.

$$\delta_d^{\text{LP-EFM.4}} = \begin{bmatrix} \delta_d^{\text{LP-EFM.4.N}} \\ \delta_d^{\text{LP-EFM.4.E}} \end{bmatrix} = \begin{bmatrix} \frac{L_1/2}{2} \\ 0 \end{bmatrix} \quad (\text{E.53})$$

$$f^{\text{LP-EFM.4}} = \begin{bmatrix} -\frac{P L_1}{8} \end{bmatrix} \quad (\text{E.54})$$

$$\delta_P^{\text{LP-EFM.4}} = \begin{bmatrix} \delta_P^{\text{LP-EFM.4.N}} \\ \delta_P^{\text{LP-EFM.4.E}} \end{bmatrix} = \begin{bmatrix} \frac{P L_1^3}{192 E I_1} \\ 0 \end{bmatrix} \quad (\text{E.55})$$

$$d^{\text{LP-EFM.4}} = \left(k_{11}^{\text{LP-EFM.4}} \right)^{-1} \left(-f^{\text{LP-EFM.4}} \right) = \frac{L_1^2 L_2 P}{16 E (I_1 L_2 + 4 I_2 L_1)} \quad (\text{E.56})$$

$$\delta_D^{\text{LP-EFM.4}} = \delta_d^{\text{LP-EFM.4}} d^{\text{LP-EFM.4}} = \begin{bmatrix} \delta_D^{\text{LP-EFM.4.N}} \\ \delta_D^{\text{LP-EFM.4.E}} \end{bmatrix} = \begin{bmatrix} \frac{L_1^3 L_2 P}{64 E (I_1 L_2 + 4 I_2 L_1)} \\ 0 \end{bmatrix} \quad (\text{E.57})$$

$$\delta^{\text{LP-EFM.4}} = \delta_D^{\text{LP-EFM.4}} + \delta_P^{\text{LP-EFM.4}} = \begin{bmatrix} \delta^{\text{LP-EFM.4.N}} \\ \delta^{\text{LP-EFM.4.E}} \end{bmatrix} = \begin{bmatrix} \frac{L_1^3 P (I_1 L_2 + I_2 L_1)}{48 E I_1 (I_1 L_2 + 4 I_2 L_1)} \\ 0 \end{bmatrix} \quad (\text{E.58})$$

E.2.5 Condensed stiffness matrix of HR-EFM-IF

The matrix $\mathbf{F}^{\text{HR-EFM-IF}}$ is generated for the full EFM by concatenating the displacement vectors of each LP-EFM, described by Eqs. (E.37), (E.44), (E.51), and (E.58), and the two additional displacements

obtained from symmetry conditions, resulting in Eq. (E.59).

$$\mathbf{F}^{\text{HR-EFM-IF}} = \begin{bmatrix} \delta^{\text{LP-EFM.1.N}} & \delta^{\text{LP-EFM.2.N}} & \delta^{\text{LP-EFM.3.N}} & -\delta^{\text{LP-EFM.4.N}} \\ \delta^{\text{LP-EFM.1.E}} & \delta^{\text{LP-EFM.2.E}} & \delta^{\text{LP-EFM.3.E}} & \delta^{\text{LP-EFM.4.E}} \\ \delta^{\text{LP-EFM.1.N}} & \delta^{\text{LP-EFM.2.N}} & \delta^{\text{LP-EFM.3.N}} & \delta^{\text{LP-EFM.4.N}} \\ \delta^{\text{LP-EFM.1.E}} & \delta^{\text{LP-EFM.2.E}} & -\delta^{\text{LP-EFM.3.E}} & \delta^{\text{LP-EFM.4.E}} \end{bmatrix} \quad (\text{E.59})$$

The condensed stiffness matrix of the HR-EFM-IF, $\mathbf{K}_c^{\text{HR-EFM-IF}}$, is obtained by multiplying the matrix of external forces, \mathbf{P} (Eq. (5.3)), with the inverse of $\mathbf{F}^{\text{HR-EFM-IF}}$ (Eq. (E.59)), leading to Eq. (E.60).

$$\mathbf{K}_c^{\text{HR-EFM-IF}} = \mathbf{P} \left(\mathbf{F}^{\text{HR-EFM-IF}} \right)^{-1} = \begin{bmatrix} k_{11}^{\text{HR-EFM-IF}} & k_{12}^{\text{HR-EFM-IF}} & k_{13}^{\text{HR-EFM-IF}} & k_{14}^{\text{HR-EFM-IF}} \\ k_{21}^{\text{HR-EFM-IF}} & k_{22}^{\text{HR-EFM-IF}} & k_{23}^{\text{HR-EFM-IF}} & k_{24}^{\text{HR-EFM-IF}} \\ k_{31}^{\text{HR-EFM-IF}} & k_{32}^{\text{HR-EFM-IF}} & k_{33}^{\text{HR-EFM-IF}} & k_{34}^{\text{HR-EFM-IF}} \\ k_{41}^{\text{HR-EFM-IF}} & k_{42}^{\text{HR-EFM-IF}} & k_{43}^{\text{HR-EFM-IF}} & k_{44}^{\text{HR-EFM-IF}} \end{bmatrix} \quad (\text{E.60})$$

where:

$$k_{11}^{\text{HR-EFM-IF}} = k_{33}^{\text{HR-EFM-IF}} = \frac{48 E I_1 (I_1 L_2 + 4 I_2 L_1)}{L_1^3 (I_1 L_2 + I_2 L_1)} \quad (\text{E.61})$$

$$k_{22}^{\text{HR-EFM-IF}} = k_{44}^{\text{HR-EFM-IF}} = \frac{48 E I_2 (4 I_1 L_2 + I_2 L_1)}{L_2^3 (I_1 L_2 + I_2 L_1)} \quad (\text{E.62})$$

$$\begin{aligned} k_{12}^{\text{HR-EFM-IF}} &= k_{14}^{\text{HR-EFM-IF}} = k_{21}^{\text{HR-EFM-IF}} = k_{23}^{\text{HR-EFM-IF}} = k_{32}^{\text{HR-EFM-IF}} = k_{34}^{\text{HR-EFM-IF}} = \dots \\ \dots &= k_{41}^{\text{HR-EFM-IF}} = k_{43}^{\text{HR-EFM-IF}} = \frac{72 E I_1 I_2}{L_1 L_2 (I_1 L_2 + I_2 L_1)} \end{aligned} \quad (\text{E.63})$$

$$k_{13}^{\text{HR-EFM-IF}} = k_{24}^{\text{HR-EFM-IF}} = k_{31}^{\text{HR-EFM-IF}} = k_{42}^{\text{HR-EFM-IF}} = 0 \quad (\text{E.64})$$

E.3 HR-EFM-IEq

As previously noted, the HR-EFM-IEq and HR-EFM-IF are identical, except for the usage of an equivalent moment of inertia, I_{eq} , as defined by Eq. (5.1), in place of individual moments of inertia, I_1 and I_2 . Consequently, the condensed stiffness matrix, $\mathbf{K}_c^{\text{HR-EFM-IEq}}$, is explicitly presented to eliminate the need for repetitive calculations and figure displays.

E.3.1 Condensed stiffness matrix of HR-EFM-IEq

The stiffness matrix, $\mathbf{K}_c^{\text{HR-EFM-IEq}}$, of the HR-EFM-IEq is:

$$\mathbf{K}_c^{\text{HR-EFM-IEq}} = \begin{bmatrix} k_{11}^{\text{HR-EFM-IEq}} & k_{12}^{\text{HR-EFM-IEq}} & k_{13}^{\text{HR-EFM-IEq}} & k_{14}^{\text{HR-EFM-IEq}} \\ k_{21}^{\text{HR-EFM-IEq}} & k_{22}^{\text{HR-EFM-IEq}} & k_{23}^{\text{HR-EFM-IEq}} & k_{24}^{\text{HR-EFM-IEq}} \\ k_{31}^{\text{HR-EFM-IEq}} & k_{32}^{\text{HR-EFM-IEq}} & k_{33}^{\text{HR-EFM-IEq}} & k_{34}^{\text{HR-EFM-IEq}} \\ k_{41}^{\text{HR-EFM-IEq}} & k_{42}^{\text{HR-EFM-IEq}} & k_{43}^{\text{HR-EFM-IEq}} & k_{44}^{\text{HR-EFM-IEq}} \end{bmatrix} \quad (\text{E.65})$$

where:

$$k_{11}^{\text{HR-EFM-IEq}} = k_{33}^{\text{HR-EFM-IEq}} = \frac{48 E I_{eq} (4 L_1 + L_2)}{L_1^3 (L_1 + L_2)} \quad (\text{E.66})$$

$$k_{22}^{\text{HR-EFM-IEq}} = k_{44}^{\text{HR-EFM-IEq}} = \frac{48 E I_{eq} (L_1 + 4 L_2)}{L_2^3 (L_1 + L_2)} \quad (\text{E.67})$$

$$\begin{aligned} k_{12}^{\text{HR-EFM-IEq}} &= k_{14}^{\text{HR-EFM-IEq}} = k_{21}^{\text{HR-EFM-IEq}} = k_{23}^{\text{HR-EFM-IEq}} = k_{32}^{\text{HR-EFM-IEq}} = \dots \\ \dots &= k_{34}^{\text{HR-EFM-IEq}} = k_{41}^{\text{HR-EFM-IEq}} = k_{43}^{\text{HR-EFM-IEq}} = \frac{72 E I_{eq}}{L_1 L_2 (L_1 + L_2)} \end{aligned} \quad (\text{E.68})$$

$$k_{13}^{\text{HR-EFM-IEq}} = k_{24}^{\text{HR-EFM-IEq}} = k_{31}^{\text{HR-EFM-IEq}} = k_{42}^{\text{HR-EFM-IEq}} = 0 \quad (\text{E.69})$$

E.4 PS-EFM

Each of the following four sections provides detailed calculations for each LP-EFM illustrated in Fig. 5.2, applied to the PS-EFM, following the steps outlined in Section 5.2.2.

E.4.1 LP-EFM.1

The deformation of PS-EFM under LP-EFM.1, the SEFM due to symmetry conditions, the stiffness coefficients, and the corresponding restraining forces are presented in Fig. E.9(a), Fig. E.9(b) Fig. E.9(c), and Fig. E.9(d), respectively. Eqs. (E.70) to (E.76) present the results from the application of the procedure described in Section 5.2.2.

$$k_{11}^{\text{LP-EFM.1}} = \frac{E I}{a} + \frac{E I}{a} \quad (\text{E.70})$$

$$\delta_d^{\text{LP-EFM.1}} = \begin{bmatrix} \delta_d^{\text{LP-EFM.1.N}} \\ \delta_d^{\text{LP-EFM.1.E}} \end{bmatrix} = \begin{bmatrix} \frac{a}{2} \\ -\frac{a}{2} \end{bmatrix} \quad (\text{E.71})$$

$$f^{\text{LP-EFM.1}} = \begin{bmatrix} -\frac{P a}{4} + \frac{P a}{4} \end{bmatrix} \quad (\text{E.72})$$

$$\delta_P^{\text{LP-EFM.1}} = \begin{bmatrix} \delta_P^{\text{LP-EFM.1.N}} \\ \delta_P^{\text{LP-EFM.1.E}} \end{bmatrix} = \begin{bmatrix} \frac{P a^3}{24 E I} \\ \frac{P a^3}{24 E I} \end{bmatrix} \quad (\text{E.73})$$

$$d^{\text{LP-EFM.1}} = \left(k_{11}^{\text{LP-EFM.1}} \right)^{-1} \left(-f^{\text{LP-EFM.1}} \right) = 0 \quad (\text{E.74})$$

$$\delta_D^{\text{LP-EFM.1}} = \delta_d^{\text{LP-EFM.1}} d^{\text{LP-EFM.1}} = \begin{bmatrix} \delta_D^{\text{LP-EFM.1.N}} \\ \delta_D^{\text{LP-EFM.1.E}} \end{bmatrix} = \begin{bmatrix} 0 \\ 0 \end{bmatrix} \quad (\text{E.75})$$

$$\delta^{\text{LP-EFM.1}} = \delta_D^{\text{LP-EFM.1}} + \delta_P^{\text{LP-EFM.1}} = \begin{bmatrix} \delta^{\text{LP-EFM.1.N}} \\ \delta^{\text{LP-EFM.1.E}} \end{bmatrix} = \begin{bmatrix} \frac{P a^3}{24 E I} \\ \frac{P a^3}{24 E I} \end{bmatrix} \quad (\text{E.76})$$

E.4.2 LP-EFM.2

The deformation of PS-EFM under LP-EFM.2, the SEFM due to symmetry conditions, the stiffness coefficients, and the corresponding restraining forces are presented in Fig. E.10(a), Fig. E.10(b)

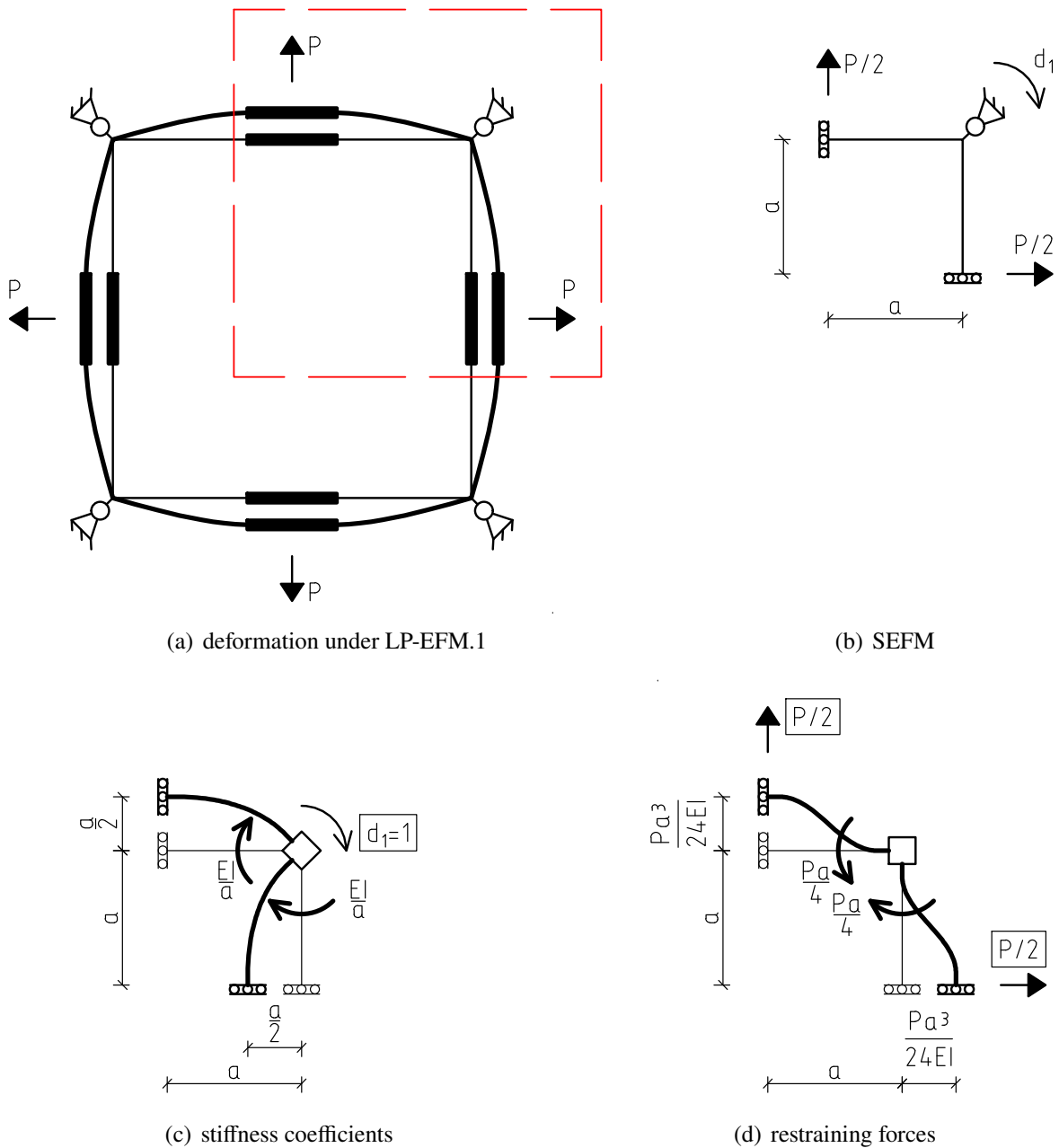


Figure E.9: PS-EFM under LP-EFM.1.

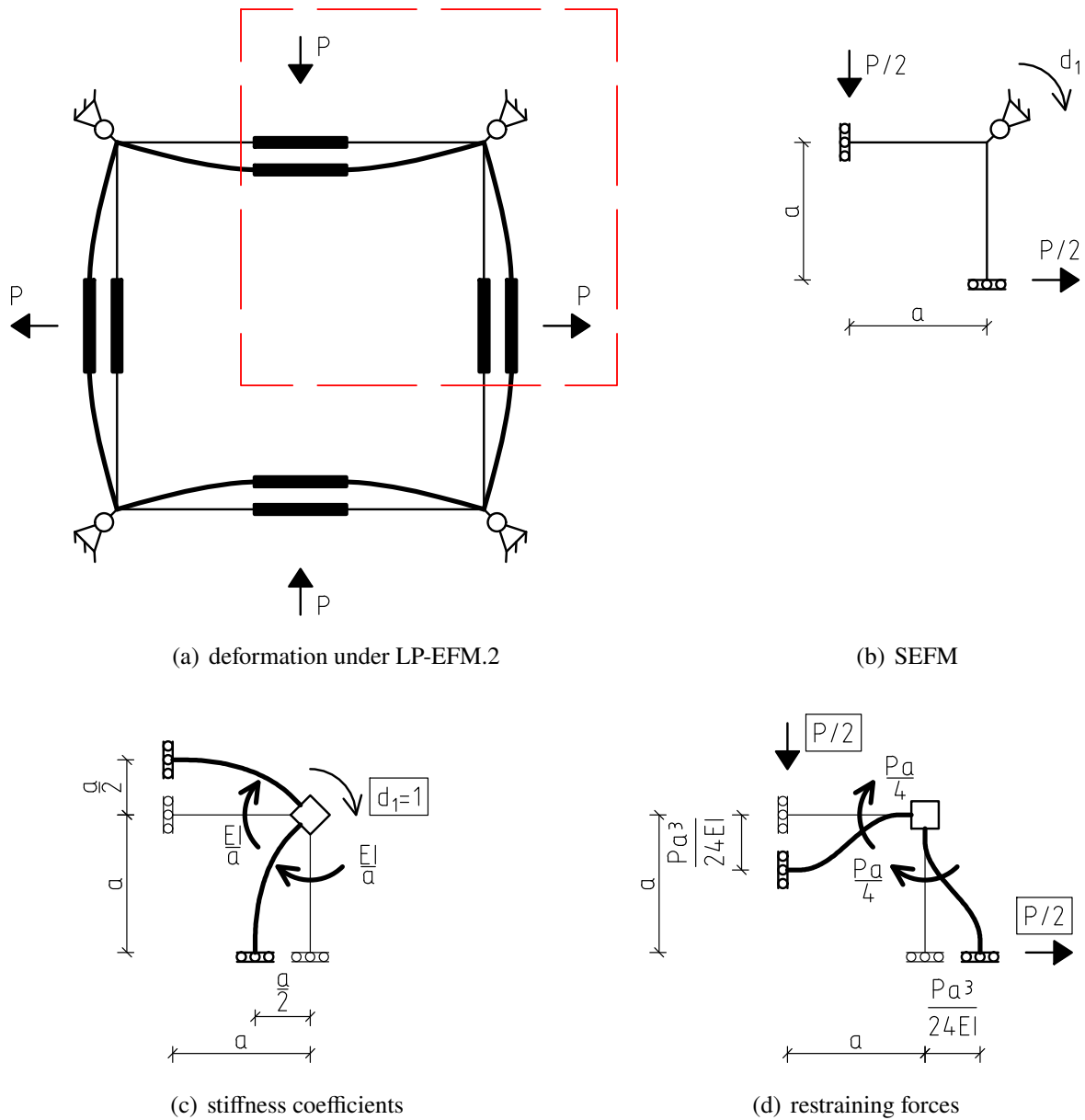


Figure E.10: PS-EFM under LP-EFM.2.

Fig. E.10(c), and Fig. E.10(d), respectively. Eqs. (E.77) to (E.83) present the results from the application of the procedure described in Section 5.2.2.

$$k_{11}^{\text{LP-EFM.2}} = \frac{E I}{a} + \frac{E I}{a} \quad (\text{E.77})$$

$$\delta_d^{\text{LP-EFM.2}} = \begin{bmatrix} \delta_d^{\text{LP-EFM.2.N}} \\ \delta_d^{\text{LP-EFM.2.E}} \end{bmatrix} = \begin{bmatrix} \frac{a}{2} \\ -\frac{a}{2} \end{bmatrix} \quad (\text{E.78})$$

$$f^{\text{LP-EFM.2}} = \left[\frac{P a}{4} + \frac{P a}{4} \right] \quad (\text{E.79})$$

$$\delta_P^{\text{LP-EFM.2}} = \begin{bmatrix} \delta_P^{\text{LP-EFM.2.N}} \\ \delta_P^{\text{LP-EFM.2.E}} \end{bmatrix} = \begin{bmatrix} -\frac{P a^3}{24 E I} \\ \frac{P a^3}{24 E I} \end{bmatrix} \quad (\text{E.80})$$

$$d^{\text{LP-EFM.2}} = \left(k_{11}^{\text{LP-EFM.2}} \right)^{-1} \left(-f^{\text{LP-EFM.2}} \right) = -\frac{P a^2}{4 E I} \quad (\text{E.81})$$

$$\delta_D^{\text{LP-EFM.2}} = \delta_d^{\text{LP-EFM.2}} d^{\text{LP-EFM.2}} = \begin{bmatrix} \delta_D^{\text{LP-EFM.2.N}} \\ \delta_D^{\text{LP-EFM.2.E}} \end{bmatrix} = \begin{bmatrix} -\frac{P a^3}{8 E I} \\ \frac{P a^3}{8 E I} \end{bmatrix} \quad (\text{E.82})$$

$$\delta^{\text{LP-EFM.2}} = \delta_D^{\text{LP-EFM.2}} + \delta_P^{\text{LP-EFM.2}} = \begin{bmatrix} \delta^{\text{LP-EFM.2.N}} \\ \delta^{\text{LP-EFM.2.E}} \end{bmatrix} = \begin{bmatrix} -\frac{P a^3}{6 E I} \\ \frac{P a^3}{6 E I} \end{bmatrix} \quad (\text{E.83})$$

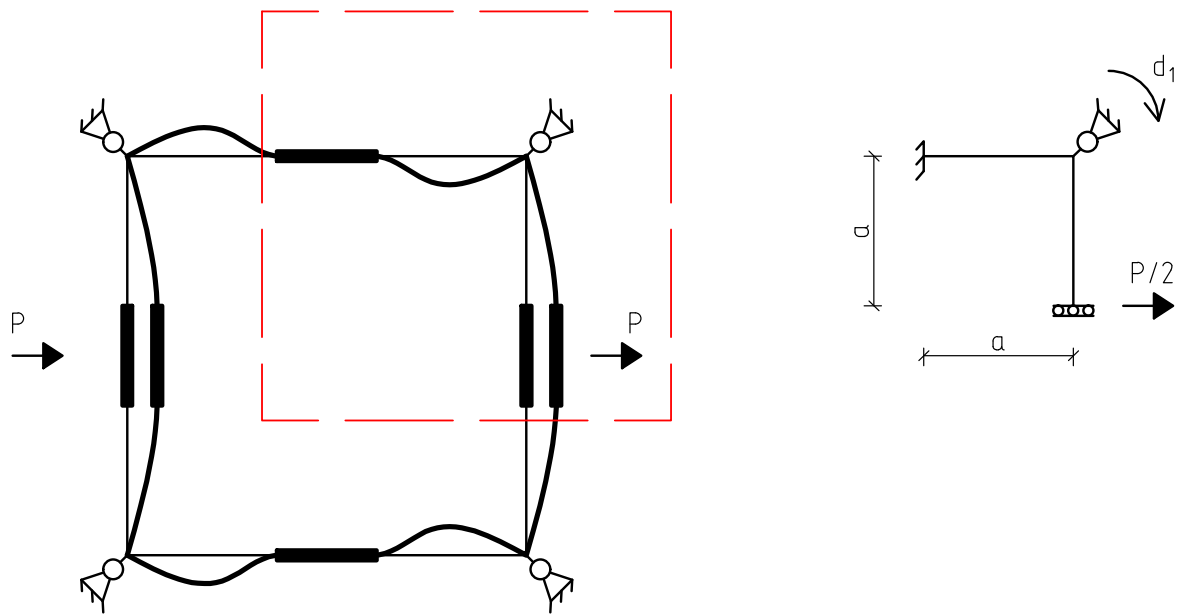
E.4.3 LP-EFM.3

The deformation of PS-EFM under LP-EFM.3, the SEFM due to symmetry conditions, the stiffness coefficients, and the corresponding restraining forces are presented in Fig. E.11(a), Fig. E.11(b) Fig. E.11(c), and Fig. E.11(d), respectively. Eqs. (E.84) to (E.90) present the results from the application of the procedure described in Section 5.2.2.

$$k_{11}^{\text{LP-EFM.3}} = \frac{4 E I}{a} + \frac{E I}{a} \quad (\text{E.84})$$

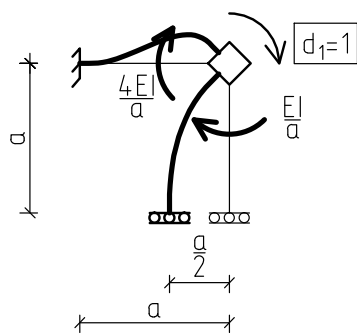
$$\delta_d^{\text{LP-EFM.3}} = \begin{bmatrix} \delta_d^{\text{LP-EFM.3.N}} \\ \delta_d^{\text{LP-EFM.3.E}} \end{bmatrix} = \begin{bmatrix} 0 \\ -\frac{a}{2} \end{bmatrix} \quad (\text{E.85})$$

$$f^{\text{LP-EFM.3}} = \left[\frac{P a}{4} \right] \quad (\text{E.86})$$

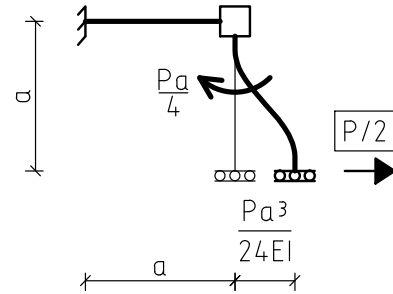


(a) deformation under LP-EFM.3

(b) SEFM



(c) stiffness coefficients



(d) restraining forces

Figure E.11: PS-EFM under LP-EFM.3.

$$\delta_P^{\text{LP-EFM.3}} = \begin{bmatrix} \delta_P^{\text{LP-EFM.3.N}} \\ \delta_P^{\text{LP-EFM.3.E}} \end{bmatrix} = \begin{bmatrix} 0 \\ \frac{P a^3}{24 E I} \end{bmatrix} \quad (\text{E.87})$$

$$d^{\text{LP-EFM.3}} = \left(k_{11}^{\text{LP-EFM.3}} \right)^{-1} \left(-f^{\text{LP-EFM.3}} \right) = -\frac{P a^2}{20 E I} \quad (\text{E.88})$$

$$\delta_D^{\text{LP-EFM.3}} = \delta_d^{\text{LP-EFM.3}} d^{\text{LP-EFM.3}} = \begin{bmatrix} \delta_D^{\text{LP-EFM.3.N}} \\ \delta_D^{\text{LP-EFM.3.E}} \end{bmatrix} = \begin{bmatrix} 0 \\ \frac{P a^3}{40 E I} \end{bmatrix} \quad (\text{E.89})$$

$$\delta^{\text{LP-EFM.3}} = \delta_D^{\text{LP-EFM.3}} + \delta_P^{\text{LP-EFM.3}} = \begin{bmatrix} \delta^{\text{LP-EFM.3.N}} \\ \delta^{\text{LP-EFM.3.E}} \end{bmatrix} = \begin{bmatrix} 0 \\ \frac{P a^3}{15 E I} \end{bmatrix} \quad (\text{E.90})$$

E.4.4 LP-EFM.4

The deformation of PS-EFM under LP-EFM.4, the SEFM due to symmetry conditions, the stiffness coefficients, and the corresponding restraining forces are presented in Fig. E.12(a), Fig. E.12(b) Fig. E.12(c), and Fig. E.12(d), respectively. Eqs. (E.91) to (E.97) present the results from the application of the procedure described in Section 5.2.2.

$$k_{11}^{\text{LP-EFM.4}} = \frac{E I}{a} + \frac{4 E I}{a} \quad (\text{E.91})$$

$$\delta_d^{\text{LP-EFM.4}} = \begin{bmatrix} \delta_d^{\text{LP-EFM.4.N}} \\ \delta_d^{\text{LP-EFM.4.E}} \end{bmatrix} = \begin{bmatrix} \frac{a}{2} \\ 0 \end{bmatrix} \quad (\text{E.92})$$

$$f^{\text{LP-EFM.4}} = \begin{bmatrix} -\frac{P a}{4} \end{bmatrix} \quad (\text{E.93})$$

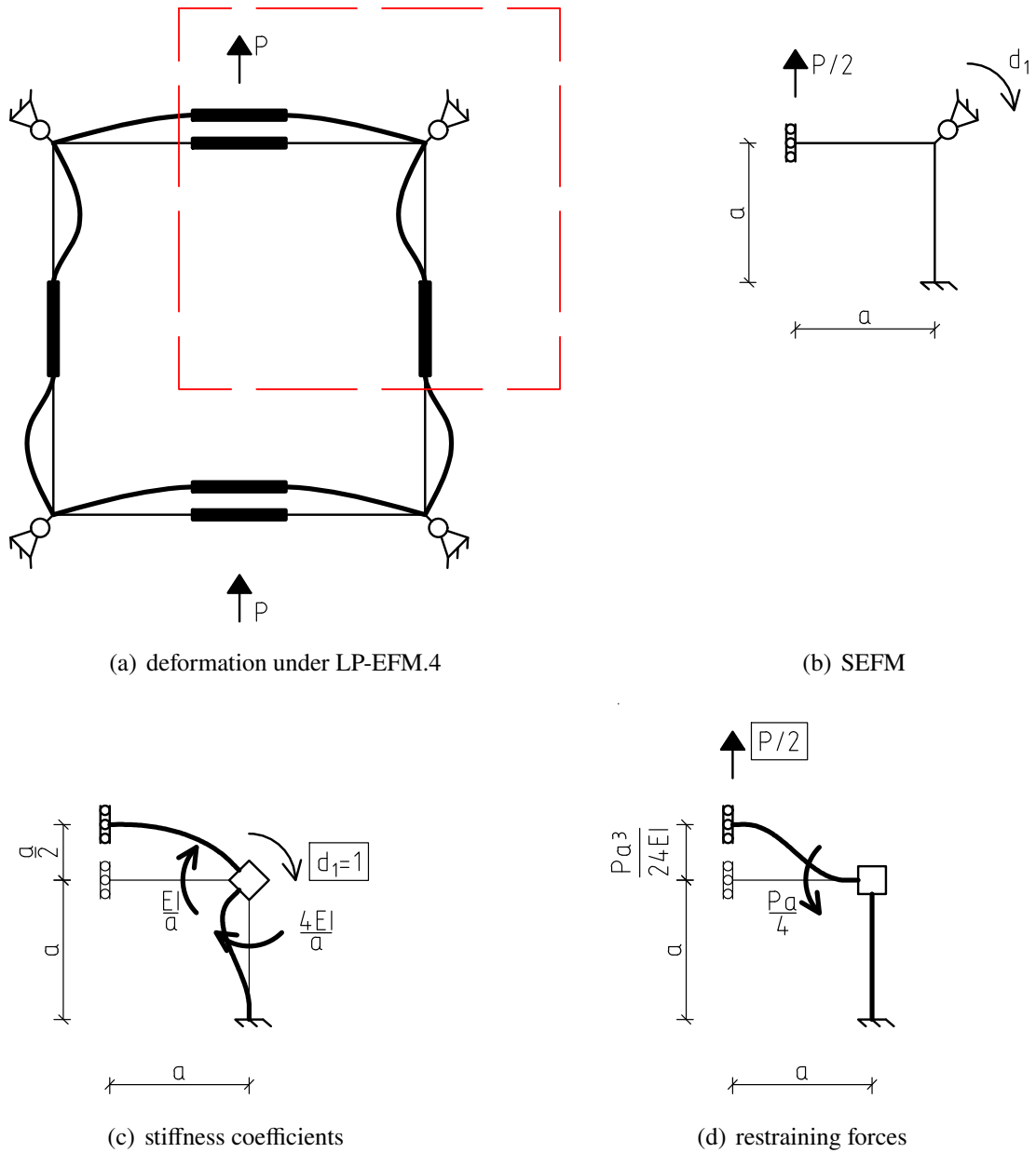


Figure E.12: PS-EFM under LP-EFM.4.

$$\delta_P^{\text{LP-EFM.4}} = \begin{bmatrix} \delta_P^{\text{LP-EFM.4.N}} \\ \delta_P^{\text{LP-EFM.4.E}} \end{bmatrix} = \begin{bmatrix} \frac{P a^3}{24 E I} \\ 0 \end{bmatrix} \quad (\text{E.94})$$

$$d^{\text{LP-EFM.4}} = \left(k_{11}^{\text{LP-EFM.4}} \right)^{-1} \left(-f^{\text{LP-EFM.4}} \right) = \frac{P a^2}{20 E I} \quad (\text{E.95})$$

$$\delta_D^{\text{LP-EFM.4}} = \delta_d^{\text{LP-EFM.4}} d^{\text{LP-EFM.4}} = \begin{bmatrix} \delta_D^{\text{LP-EFM.4.N}} \\ \delta_D^{\text{LP-EFM.4.E}} \end{bmatrix} = \begin{bmatrix} \frac{P a^3}{40 E I} \\ 0 \end{bmatrix} \quad (\text{E.96})$$

$$\delta^{\text{LP-EFM.4}} = \delta_D^{\text{LP-EFM.4}} + \delta_P^{\text{LP-EFM.4}} = \begin{bmatrix} \delta^{\text{LP-EFM.4.N}} \\ \delta^{\text{LP-EFM.4.E}} \end{bmatrix} = \begin{bmatrix} \frac{P a^3}{15 E I} \\ 0 \end{bmatrix} \quad (\text{E.97})$$

E.4.5 Condensed stiffness matrix of PS-EFM

The matrix $\mathbf{F}^{\text{PS-EFM}}$ is generated for the full EFM by concatenating the displacement vectors of each LP-EFM, described by Eqs. (E.76), (E.83), (E.90), and (E.97), and the two additional displacements obtained from symmetry conditions, resulting in Eq. (E.98).

$$\mathbf{F}^{\text{PS-EFM}} = \begin{bmatrix} \delta^{\text{LP-EFM.1.N}} & \delta^{\text{LP-EFM.2.N}} & \delta^{\text{LP-EFM.3.N}} & -\delta^{\text{LP-EFM.4.N}} \\ \delta^{\text{LP-EFM.1.E}} & \delta^{\text{LP-EFM.2.E}} & \delta^{\text{LP-EFM.3.E}} & \delta^{\text{LP-EFM.4.E}} \\ \delta^{\text{LP-EFM.1.N}} & \delta^{\text{LP-EFM.2.N}} & \delta^{\text{LP-EFM.3.N}} & \delta^{\text{LP-EFM.4.N}} \\ \delta^{\text{LP-EFM.1.E}} & \delta^{\text{LP-EFM.2.E}} & -\delta^{\text{LP-EFM.3.E}} & \delta^{\text{LP-EFM.4.E}} \end{bmatrix} \quad (\text{E.98})$$

The condensed stiffness matrix of the PS-EFM, $\mathbf{K}_c^{\text{PS-EFM}}$, is obtained by multiplying the matrix of external forces, \mathbf{P} (Eq. (5.3)), with the inverse of $\mathbf{F}^{\text{PS-EFM}}$ (Eq. (E.98)), leading to Eq. (E.99).

$$\mathbf{K}_c^{\text{PS-EFM}} = \mathbf{P} \left(\mathbf{F}^{\text{PS-EFM}} \right)^{-1} = \begin{bmatrix} \frac{15 E I}{a^3} & \frac{9 E I}{2 a^3} & 0 & \frac{9 E I}{2 a^3} \\ \frac{9 E I}{2 a^3} & \frac{15 E I}{a^3} & \frac{9 E I}{2 a^3} & 0 \\ 0 & \frac{9 E I}{2 a^3} & \frac{15 E I}{a^3} & \frac{9 E I}{2 a^3} \\ \frac{9 E I}{2 a^3} & 0 & \frac{9 E I}{2 a^3} & \frac{15 E I}{a^3} \end{bmatrix} \quad (\text{E.99})$$

E.5 PR-EFM-IF

The next four sections comprise detailed calculations for each LP-EFM shown in Fig. 5.2, applied to the PR-EFM-IF, according to the procedures outlined in Section 5.2.2. A separate section is dedicated to presenting the stiffness matrix, $\mathbf{K}_c^{\text{PR-EFM-IF}}$.

E.5.1 LP-EFM.1

The deformation of PR-EFM under LP-EFM.1, the SEFM due to symmetry conditions, the stiffness coefficients, and the corresponding restraining forces are presented in Fig. E.13(a), Fig. E.13(b) Fig. E.13(c), and Fig. E.13(d), respectively. Eqs. (E.100) to (E.106) present the results from the application of the procedure described in Section 5.2.2.

$$k_{11}^{\text{LP-EFM.1}} = \frac{E I_1}{a} + \frac{E I_2}{c} \quad (\text{E.100})$$

$$\delta_d^{\text{LP-EFM.1}} = \begin{bmatrix} \delta_d^{\text{LP-EFM.1.N}} \\ \delta_d^{\text{LP-EFM.1.E}} \end{bmatrix} = \begin{bmatrix} \frac{a}{2} \\ -\frac{c}{2} \end{bmatrix} \quad (\text{E.101})$$

$$f^{\text{LP-EFM.1}} = \begin{bmatrix} -\frac{P a}{4} + \frac{P c}{4} \end{bmatrix} \quad (\text{E.102})$$

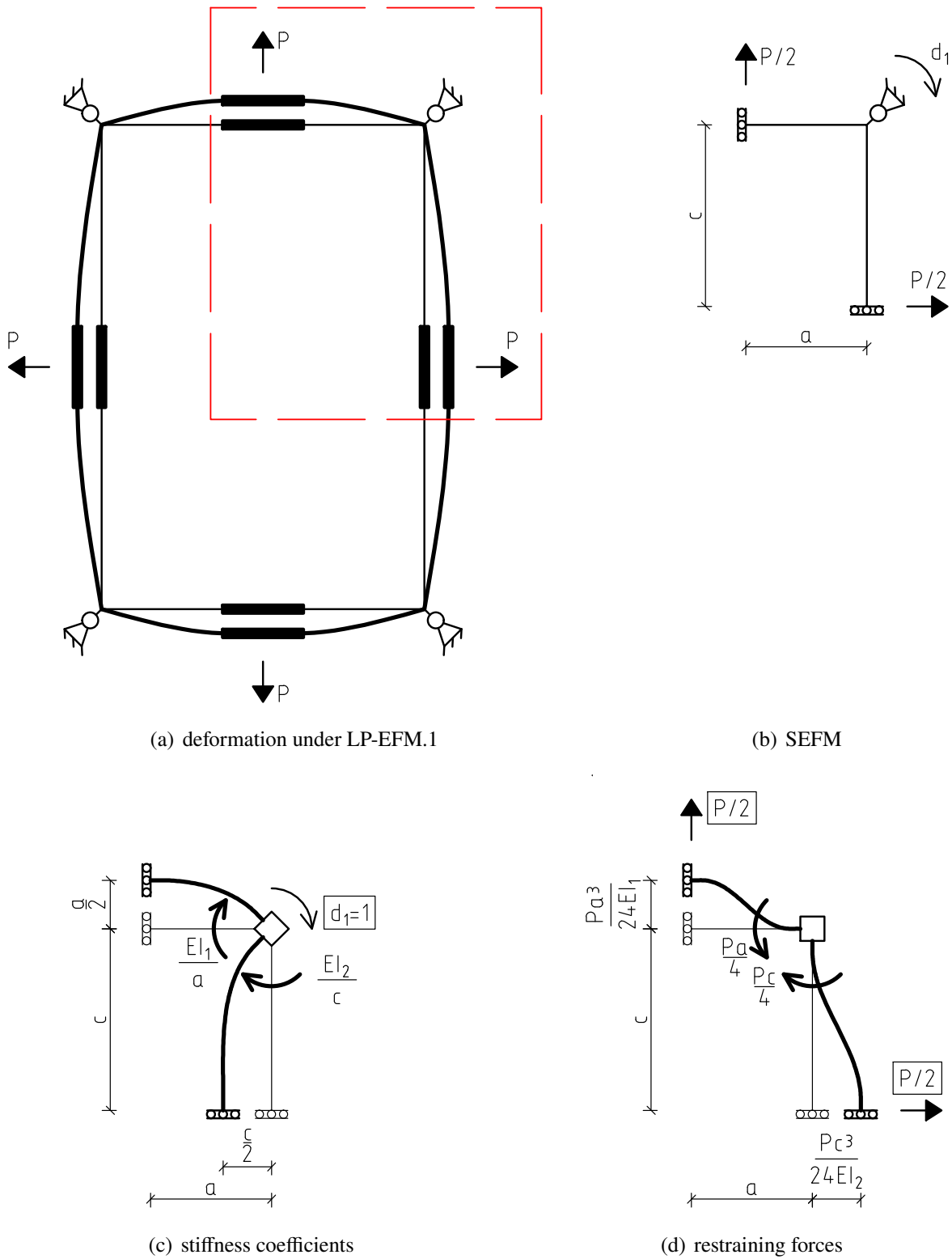


Figure E.13: PR-EFM under LP-EFM.1.

$$\delta_P^{\text{LP-EFM.1}} = \begin{bmatrix} \delta_P^{\text{LP-EFM.1.N}} \\ \delta_P^{\text{LP-EFM.1.E}} \end{bmatrix} = \begin{bmatrix} \frac{P a^3}{24 E I_1} \\ \frac{P c^3}{24 E I_2} \end{bmatrix} \quad (\text{E.103})$$

$$d^{\text{LP-EFM.1}} = \left(k_{11}^{\text{LP-EFM.1}} \right)^{-1} \left(-f^{\text{LP-EFM.1}} \right) = \frac{P a c (a - c)}{4 E (I_2 a + I_1 c)} \quad (\text{E.104})$$

$$\delta_D^{\text{LP-EFM.1}} = \delta_d^{\text{LP-EFM.1}} d^{\text{LP-EFM.1}} = \begin{bmatrix} \delta_D^{\text{LP-EFM.1.N}} \\ \delta_D^{\text{LP-EFM.1.E}} \end{bmatrix} = \begin{bmatrix} \frac{P a^2 c (a - c)}{8 E (I_2 a + I_1 c)} \\ -\frac{P a c^2 (a - c)}{8 E (I_2 a + I_1 c)} \end{bmatrix} \quad (\text{E.105})$$

$$\begin{aligned} \delta^{\text{LP-EFM.1}} &= \delta_D^{\text{LP-EFM.1}} + \delta_P^{\text{LP-EFM.1}} = \begin{bmatrix} \delta^{\text{LP-EFM.1.N}} \\ \delta^{\text{LP-EFM.1.E}} \end{bmatrix} \\ &= \begin{bmatrix} \frac{P a^2 (I_2 a^2 + 4 I_1 a c - 3 I_1 c^2)}{24 E I_1 (I_2 a + I_1 c)} \\ \frac{P c^2 (-3 I_2 a^2 + 4 I_2 a c + I_1 c^2)}{24 E I_2 (I_2 a + I_1 c)} \end{bmatrix} \end{aligned} \quad (\text{E.106})$$

E.5.2 LP-EFM.2

The deformation of PR-EFM under LP-EFM.2, the SEFM due to symmetry conditions, the stiffness coefficients, and the corresponding restraining forces are presented in Fig. E.14(a), Fig. E.14(b) Fig. E.14(c), and Fig. E.14(d), respectively. Eqs. (E.107) to (E.113) present the results from the application of the procedure described in Section 5.2.2.

$$k_{11}^{\text{LP-EFM.2}} = \frac{E I_1}{a} + \frac{E I_2}{c} \quad (\text{E.107})$$

$$\delta_d^{\text{LP-EFM.2}} = \begin{bmatrix} \delta_d^{\text{LP-EFM.2.N}} \\ \delta_d^{\text{LP-EFM.2.E}} \end{bmatrix} = \begin{bmatrix} \frac{a}{2} \\ -\frac{c}{2} \end{bmatrix} \quad (\text{E.108})$$

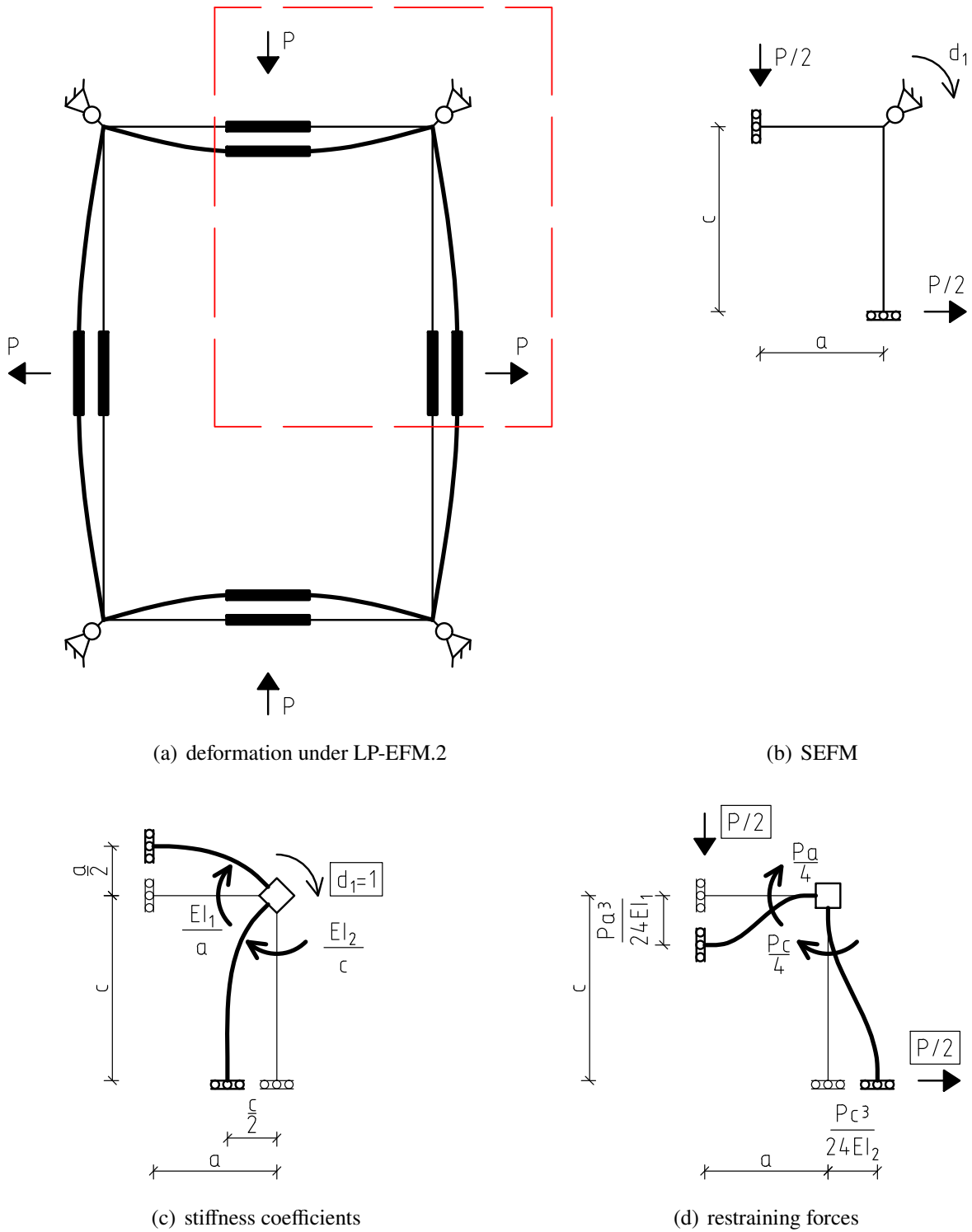


Figure E.14: PR-EFM under LP-EFM.2.

$$f^{\text{LP-EFM.2}} = \left[\frac{P a}{4} + \frac{P c}{4} \right] \quad (\text{E.109})$$

$$\delta_P^{\text{LP-EFM.2}} = \begin{bmatrix} \delta_P^{\text{LP-EFM.2.N}} \\ \delta_P^{\text{LP-EFM.2.E}} \end{bmatrix} = \begin{bmatrix} -\frac{P a^3}{24 E I_1} \\ \frac{P c^3}{24 E I_2} \end{bmatrix} \quad (\text{E.110})$$

$$d^{\text{LP-EFM.2}} = \left(k_{11}^{\text{LP-EFM.2}} \right)^{-1} \left(-f^{\text{LP-EFM.2}} \right) = -\frac{P a c (a + c)}{4 E (I_2 a + I_1 c)} \quad (\text{E.111})$$

$$\delta_D^{\text{LP-EFM.2}} = \delta_d^{\text{LP-EFM.2}} d^{\text{LP-EFM.2}} = \begin{bmatrix} \delta_D^{\text{LP-EFM.2.N}} \\ \delta_D^{\text{LP-EFM.2.E}} \end{bmatrix} = \begin{bmatrix} -\frac{P a^2 c (a + c)}{8 E (I_2 a + I_1 c)} \\ \frac{P a c^2 (a + c)}{8 E (I_2 a + I_1 c)} \end{bmatrix} \quad (\text{E.112})$$

$$\begin{aligned} \delta^{\text{LP-EFM.2}} &= \delta_D^{\text{LP-EFM.2}} + \delta_P^{\text{LP-EFM.2}} = \begin{bmatrix} \delta^{\text{LP-EFM.2.N}} \\ \delta^{\text{LP-EFM.2.E}} \end{bmatrix} \\ &= \begin{bmatrix} -\frac{P a^2 (I_2 a^2 + 4 I_1 a c + 3 I_1 c^2)}{24 E I_1 (I_2 a + I_1 c)} \\ \frac{P c^2 (3 I_2 a^2 + 4 I_2 a c + I_1 c^2)}{24 E I_2 (I_2 a + I_1 c)} \end{bmatrix} \end{aligned} \quad (\text{E.113})$$

E.5.3 LP-EFM.3

The deformation of PR-EFM under LP-EFM.3, the SEFM due to symmetry conditions, the stiffness coefficients, and the corresponding restraining forces are presented in Fig. E.15(a), Fig. E.15(b) Fig. E.15(c), and Fig. E.15(d), respectively. Eqs. (E.114) to (E.120) present the results from the application of the procedure described in Section 5.2.2.

$$k_{11}^{\text{LP-EFM.3}} = \frac{4 E I_1}{a} + \frac{E I_2}{c} \quad (\text{E.114})$$

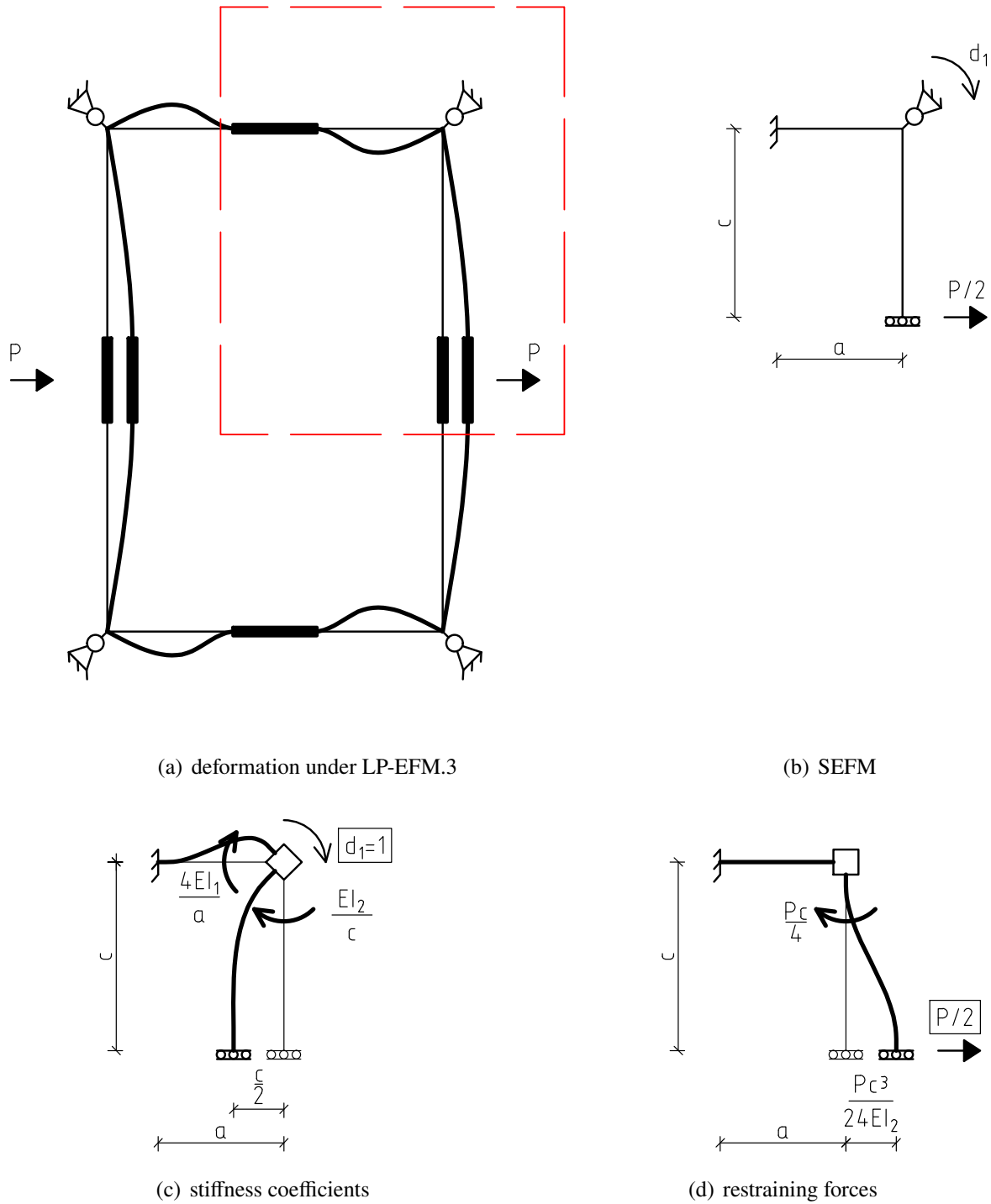


Figure E.15: PR-EFM under LP-EFM.3.

$$\delta_d^{\text{LP-EFM.3}} = \begin{bmatrix} \delta_d^{\text{LP-EFM.3.N}} \\ \delta_d^{\text{LP-EFM.3.E}} \end{bmatrix} = \begin{bmatrix} 0 \\ -\frac{c}{2} \end{bmatrix} \quad (\text{E.115})$$

$$f^{\text{LP-EFM.3}} = \begin{bmatrix} P c \\ 4 \end{bmatrix} \quad (\text{E.116})$$

$$\delta_P^{\text{LP-EFM.3}} = \begin{bmatrix} \delta_P^{\text{LP-EFM.3.N}} \\ \delta_P^{\text{LP-EFM.3.E}} \end{bmatrix} = \begin{bmatrix} 0 \\ \frac{P c^3}{24 E I_2} \end{bmatrix} \quad (\text{E.117})$$

$$d^{\text{LP-EFM.3}} = \left(k_{11}^{\text{LP-EFM.3}} \right)^{-1} \left(-f^{\text{LP-EFM.3}} \right) = -\frac{P a c^2}{4 E (I_2 a + 4 I_1 c)} \quad (\text{E.118})$$

$$\delta_D^{\text{LP-EFM.3}} = \delta_d^{\text{LP-EFM.3}} d^{\text{LP-EFM.3}} = \begin{bmatrix} \delta_D^{\text{LP-EFM.3.N}} \\ \delta_D^{\text{LP-EFM.3.E}} \end{bmatrix} = \begin{bmatrix} 0 \\ \frac{P a c^3}{8 E (I_2 a + 4 I_1 c)} \end{bmatrix} \quad (\text{E.119})$$

$$\delta_{\text{LP-EFM.3}} = \delta_D^{\text{LP-EFM.3}} + \delta_P^{\text{LP-EFM.3}} = \begin{bmatrix} \delta^{\text{LP-EFM.3.N}} \\ \delta^{\text{LP-EFM.3.E}} \end{bmatrix} = \begin{bmatrix} 0 \\ \frac{P c^3 (I_2 a + I_1 c)}{6 E I_2 (I_2 a + 4 I_1 c)} \end{bmatrix} \quad (\text{E.120})$$

E.5.4 LP-EFM.4

The deformation of PR-EFM under LP-EFM.4, the SEFM due to symmetry conditions, the stiffness coefficients, and the corresponding restraining forces are presented in Fig. E.16(a), Fig. E.16(b) Fig. E.16(c), and Fig. E.16(d), respectively. Eqs. (E.121) to (E.127) present the results from the application of the procedure described in Section 5.2.2.

$$k_{11}^{\text{LP-EFM.4}} = \frac{E I_1}{a} + \frac{4 E_2 I}{c} \quad (\text{E.121})$$

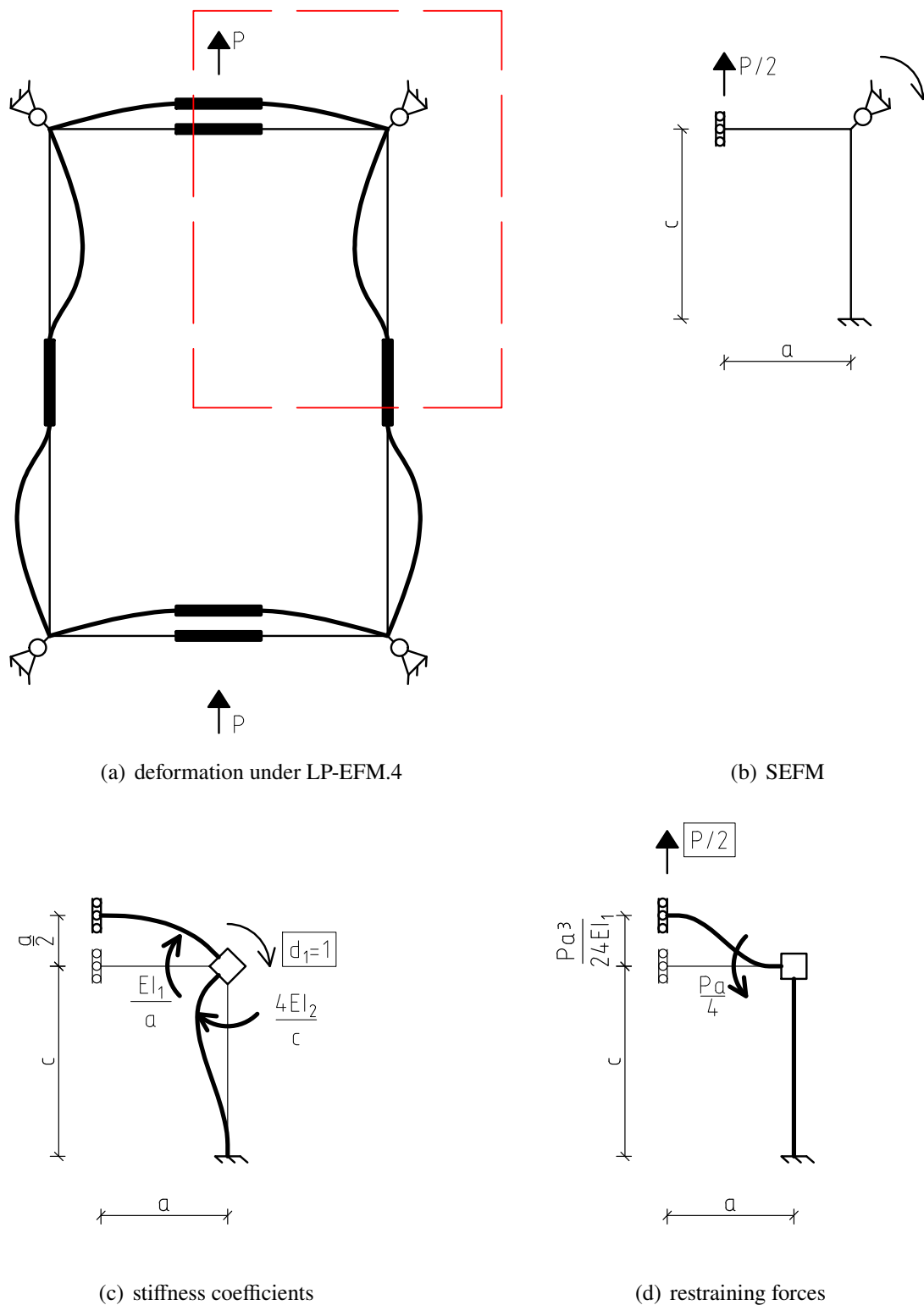


Figure E.16: PR-EFM under LP-EFM.4.

$$\delta_d^{\text{LP-EFM.4}} = \begin{bmatrix} \delta_d^{\text{LP-EFM.4.N}} \\ \delta_d^{\text{LP-EFM.4.E}} \end{bmatrix} = \begin{bmatrix} \frac{a}{2} \\ 0 \end{bmatrix} \quad (\text{E.122})$$

$$f^{\text{LP-EFM.4}} = \begin{bmatrix} -\frac{P a}{4} \end{bmatrix} \quad (\text{E.123})$$

$$\delta_P^{\text{LP-EFM.4}} = \begin{bmatrix} \delta_P^{\text{LP-EFM.4.N}} \\ \delta_P^{\text{LP-EFM.4.E}} \end{bmatrix} = \begin{bmatrix} \frac{P a^3}{24 E I_1} \\ 0 \end{bmatrix} \quad (\text{E.124})$$

$$d^{\text{LP-EFM.4}} = \left(k_{11}^{\text{LP-EFM.4}} \right)^{-1} \left(-f^{\text{LP-EFM.4}} \right) = \frac{P a^2 c}{4 E (4 I_2 a + I_1 c)} \quad (\text{E.125})$$

$$\delta^{D.DM4} = \delta_d^{\text{LP-EFM.4}} d^{\text{LP-EFM.4}} = \begin{bmatrix} \delta_D^{\text{LP-EFM.4.N}} \\ \delta_D^{\text{LP-EFM.4.E}} \end{bmatrix} = \begin{bmatrix} \frac{P a^3 c}{8 E (4 I_2 a + I_1 c)} \\ 0 \end{bmatrix} \quad (\text{E.126})$$

$$\delta^{\text{LP-EFM.4}} = \delta_D^{\text{LP-EFM.4}} + \delta_P^{\text{LP-EFM.4}} = \begin{bmatrix} \delta^{\text{LP-EFM.4.N}} \\ \delta^{\text{LP-EFM.4.E}} \end{bmatrix} = \begin{bmatrix} \frac{P a^3 (I_2 a + I_1 c)}{6 E I_1 (4 I_2 a + I_1 c)} \\ 0 \end{bmatrix} \quad (\text{E.127})$$

E.5.5 Condensed stiffness matrix of PR-EFM-IF

The matrix $\mathbf{F}^{\text{PR-EFM-IF}}$ is generated for the full EFM by concatenating the displacement vectors of each LP-EFM, described by Eqs. (E.106), (E.113), (E.120), and (E.127), and the two additional

displacements obtained from symmetry conditions, resulting in Eq. (E.128).

$$\mathbf{F}^{\text{PR-EFM-IF}} = \begin{bmatrix} \delta^{\text{LP-EFM.1.N}} & \delta^{\text{LP-EFM.2.N}} & \delta^{\text{LP-EFM.3.N}} & -\delta^{\text{LP-EFM.4.N}} \\ \delta^{\text{LP-EFM.1.E}} & \delta^{\text{LP-EFM.2.E}} & \delta^{\text{LP-EFM.3.E}} & \delta^{\text{LP-EFM.4.E}} \\ \delta^{\text{LP-EFM.1.N}} & \delta^{\text{LP-EFM.2.N}} & \delta^{\text{LP-EFM.3.N}} & \delta^{\text{LP-EFM.4.N}} \\ \delta^{\text{LP-EFM.1.E}} & \delta^{\text{LP-EFM.2.E}} & -\delta^{\text{LP-EFM.3.E}} & \delta^{\text{LP-EFM.4.E}} \end{bmatrix} \quad (\text{E.128})$$

The condensed stiffness matrix of the PR-EFM-IF, $\mathbf{K}_c^{\text{PR-EFM-IF}}$, is obtained by multiplying the matrix of external forces, \mathbf{P} (Eq. (5.3)), with the inverse of $\mathbf{F}^{\text{PR-EFM-IF}}$ (Eq. (E.128)), leading to Eq. (E.129).

$$\mathbf{K}_c^{\text{PR-EFM-IF}} = \mathbf{P} \left(\mathbf{F}^{\text{PR-EFM-IF}} \right)^{-1} = \begin{bmatrix} k_{11}^{\text{PR-EFM-IF}} & k_{12}^{\text{PR-EFM-IF}} & k_{13}^{\text{PR-EFM-IF}} & k_{14}^{\text{PR-EFM-IF}} \\ k_{21}^{\text{PR-EFM-IF}} & k_{22}^{\text{PR-EFM-IF}} & k_{23}^{\text{PR-EFM-IF}} & k_{24}^{\text{PR-EFM-IF}} \\ k_{31}^{\text{PR-EFM-IF}} & k_{32}^{\text{PR-EFM-IF}} & k_{33}^{\text{PR-EFM-IF}} & k_{34}^{\text{PR-EFM-IF}} \\ k_{41}^{\text{PR-EFM-IF}} & k_{42}^{\text{PR-EFM-IF}} & k_{43}^{\text{PR-EFM-IF}} & k_{44}^{\text{PR-EFM-IF}} \end{bmatrix} \quad (\text{E.129})$$

where:

$$k_{11}^{\text{PR-EFM-IF}} = k_{33}^{\text{PR-EFM-IF}} = \frac{6 E I_1 (4 I_2 a + I_1 c)}{a^3 (I_2 a + I_1 c)} \quad (\text{E.130})$$

$$k_{22}^{\text{PR-EFM-IF}} = k_{44}^{\text{PR-EFM-IF}} = \frac{6 E I_2 (I_2 a + 4 I_1 c)}{c^3 (I_2 a + I_1 c)} \quad (\text{E.131})$$

$$\begin{aligned} k_{12}^{\text{PR-EFM-IF}} &= k_{14}^{\text{PR-EFM-IF}} = k_{21}^{\text{PR-EFM-IF}} = k_{23}^{\text{PR-EFM-IF}} = k_{32}^{\text{PR-EFM-IF}} = k_{34}^{\text{PR-EFM-IF}} = \dots \\ \dots &= k_{41}^{\text{PR-EFM-IF}} = k_{43}^{\text{PR-EFM-IF}} = \frac{9 E I_1 I_2}{a c (I_2 a + I_1 c)} \end{aligned} \quad (\text{E.132})$$

$$k_{13}^{\text{PR-EFM-IF}} = k_{24}^{\text{PR-EFM-IF}} = k_{31}^{\text{PR-EFM-IF}} = k_{42}^{\text{PR-EFM-IF}} = 0 \quad (\text{E.133})$$

E.6 PR-EFM-IEq

In the PR-EFM-IEq, the individual moments of inertia I_1 and I_2 from PR-EFM-IF are substituted with the equivalent moment of inertia I_{eq} , as defined in Eq. (5.1), throughout the entire calculation. As a result, the full calculation is omitted to prevent redundancy. However, the stiffness matrix, $\mathbf{K}_c^{\text{PR-EFM-IEq}}$, is presented in the subsequent section.

E.6.1 Condensed stiffness matrix of PR-EFM-IEq

The stiffness matrix, $\mathbf{K}_c^{\text{PR-EFM-IEq}}$, of the PR-EFM-IEq is:

$$\mathbf{K}_c^{\text{PR-EFM-IEq}} = \begin{bmatrix} k_{11}^{\text{PR-EFM-IEq}} & k_{12}^{\text{PR-EFM-IEq}} & k_{13}^{\text{PR-EFM-IEq}} & k_{14}^{\text{PR-EFM-IEq}} \\ k_{21}^{\text{PR-EFM-IEq}} & k_{22}^{\text{PR-EFM-IEq}} & k_{23}^{\text{PR-EFM-IEq}} & k_{24}^{\text{PR-EFM-IEq}} \\ k_{31}^{\text{PR-EFM-IEq}} & k_{32}^{\text{PR-EFM-IEq}} & k_{33}^{\text{PR-EFM-IEq}} & k_{34}^{\text{PR-EFM-IEq}} \\ k_{41}^{\text{PR-EFM-IEq}} & k_{42}^{\text{PR-EFM-IEq}} & k_{43}^{\text{PR-EFM-IEq}} & k_{44}^{\text{PR-EFM-IEq}} \end{bmatrix} \quad (\text{E.134})$$

where:

$$k_{11}^{\text{PR-EFM-IEq}} = k_{33}^{\text{PR-EFM-IEq}} = \frac{6 E I_{eq} (4 a + c)}{a^3 (a + c)} \quad (\text{E.135})$$

$$k_{22}^{\text{PR-EFM-IEq}} = k_{44}^{\text{PR-EFM-IEq}} = \frac{6 E I_{eq} (a + 4 c)}{c^3 (a + c)} \quad (\text{E.136})$$

$$\begin{aligned} k_{12}^{\text{PR-EFM-IEq}} &= k_{14}^{\text{PR-EFM-IEq}} = k_{21}^{\text{PR-EFM-IEq}} = k_{23}^{\text{PR-EFM-IEq}} = k_{32}^{\text{PR-EFM-IEq}} = \dots \\ \dots &= k_{34}^{\text{PR-EFM-IEq}} = k_{41}^{\text{PR-EFM-IEq}} = k_{43}^{\text{PR-EFM-IEq}} = \frac{9 E I_{eq}}{a c (a + c)} \end{aligned} \quad (\text{E.137})$$

$$k_{13}^{\text{PR-EFM-IEq}} = k_{24}^{\text{PR-EFM-IEq}} = k_{31}^{\text{PR-EFM-IEq}} = k_{42}^{\text{PR-EFM-IEq}} = 0 \quad (\text{E.138})$$

Appendix F: OpenSees model file example for Tcl

This section presents an OpenSees file model coded in the Tool Command Language (Tcl). The OpenSees model comprises two discrete files, namely the main file and a secondary file dedicated to defining joint stiffness. A succinct overview of the contents of these files is subsequently provided.

F.1 Main file

The design of the main file is optimized to enable the swift achievement of any desired load pattern. In order to achieve a specific load pattern, the user only needs to modify the magnitude and orientation (i.e., sign) of the applied forces in the main file, denoted as *jointModel.tcl*. As an illustration, the OpenSees model main file utilized for the validation and calibration of the effective bending stiffness of EFM in Section 5.4 for the PR-EFM-IF-R1 case under the RHS-m01-V01-SC01 load patterns and socket configuration is presented below.

jointModel.tcl:

```
1 # INNO3DJOINT (Linear and Elastic)
2 # Abaqus (RFE): stiffness validation
3 # Units: N, mm, sec
4 # -----
5 # Analyzed case: PR-EFM-IF-R1
6 # LP: m01 V01
7 # SC: SC01
8 # -----
9
10 # Remove existing model
11 wipe
12
13 # Display message
14 puts "Analysis: START!"
15
16 # Create data directory:
```

```
17 set Dir "res_PR_EFM_IF_R1_m01_v01_SC01";
18 file mkdir $Dir;
19
20 # INPUTS
21 # -----
22 # Set the forces
23 # Y dir
24 set Fy101 -1000000.
25 set Fy103 0.
26
27 # X dir
28 set Fx102 0.
29 set Fx104 0.
30
31 # Set BC node tag
32 set bcNode 105
33
34 # Set force node tag
35 set forceNode101 101
36 set forceNode102 102
37 set forceNode103 103
38 set forceNode104 104
39
40 # Set column dimmesions
41 set dcX 200.0;
42 set dcZ 300.0;
43
44
45 # BUILD MODEL
46 # -----
47 # Create ModelBuilder (in 3D with 6 DOFs/node):
48 model BasicBuilder -ndm 3 -ndf 6
49
50 # Define nodes coordinates:
```

```
51 node 101 0.0 [expr -$dcZ/2] 0.0
52 node 102 [expr $dcX/2] 0.0 0.0
53 node 103 0.0 [expr $dcZ/2] 0.0
54 node 104 [expr -$dcX/2] 0.0 0.0
55 node 105 0.0 0.0 0.0
56
57 # Apply BC
58 fix $bcNode 1 1 1 1 1 1
59
60 # Create joint finite element
61 source src_jDef_PR_EFM_IF_R1_m01_v01_SC01.tcl
62
63 # Create a Linear TimeSeries:
64 timeSeries Linear 1
65
66 # Create a Plain LP with a linear TimeSeries:
67 pattern Plain 1 1 {
68     load $forceNode101 0 $Fy101 0 0 0 0
69     load $forceNode102 $Fx102 0 0 0 0
70     load $forceNode103 0 $Fy103 0 0 0 0
71     load $forceNode104 $Fx104 0 0 0 0
72 }
73
74
75 # CREATE RECORDERS
76 # -----
77 # element level
78 recorder Element -file $Dir/Element99Disp_ALL.out -time -ele 99
79     disp
80 recorder Element -file $Dir/Element99React_ALL.out -time -ele 99
81     reaction
82
83 # element component level
84 recorder Element -file $Dir/springs_stress.out -time -ele 99
```



```
matStress
83 recorder Element -file $Dir/springs_strain.out -time -ele 99
matStrain
84
85
86 # DEFINE ANALYSIS
87 # -----
88 # constraint handler
89 constraints Plain
90
91 # DOF numberer
92 numberer Plain
93
94 # system of equation
95 system FullGeneral
96
97 # norm displacement increment test
98 set tol 1.0e-1;
99 set ite 1000;
100 test NormDispIncr $tol $ite;
101
102 # solution algorithm,
103 algorithm ModifiedNewton
104
105 # integration scheme
106 integrator LoadControl 1
107
108 # analysis object:
109 analysis Static
110
111 # perform the analysis (1 step):
112 analyze 1
113
114
```

```
115 # -----
116 # Print element
117 print -ele; # print all elements
118
119 # Display message
120 puts "Analysis: END!"
121
122 # Remove existing model
123 wipe
```

F.2 Beam-to-column joint element definition file for the elastic case

The secondary file, containing the joint definition in the linear elastic regime for the PR-EFM-IF-R1 case, subjected to the RHS-m01-V01-SC01 load patterns and socket configuration, is provided hereafter.

src_jDef_PR_EFM_IF_R1_m01_v01_SC01.tcl:

```
1 # INNO3DJJOINT (Linear and Elastic)
2 # Abaqus (RFE): stiffness validation
3 # Units: N, mm, sec
4 # -----
5 # Analyzed case: PR-EFM-IF-R1
6 # LP: m01 V01
7 # SC: SC01
8 # -----
9
10 # Define stiffness for components:
11 # define stiffness for tube components: face components
12 set k_25 7.04E+04;
13 set k_26 -6.25E+02;
14 set k_27 7.04E+04;
```

```
15 set k_28 -6.25E+02;
16
17 # define stiffness for tube components: interaction components
18 set k_29 1.91E+04;
19 set k_30 1.91E+04;
20 set k_31 1.91E+04;
21 set k_32 1.91E+04;
22
23 # define stiffness for connection components (infinitely stiff)
24 set kLin 1E+11;
25 set kRot $kLin;
26
27 # assign stiffness to connection components: face A
28 set valK01 $kLin;
29 set valK02 $kLin;
30 set valK03 $kLin;
31
32 set valK04 $kRot;
33 set valK05 $kRot;
34 set valK06 $kRot;
35
36 # assign stiffness to connection components: face B
37 set valK07 $kLin;
38 set valK08 $kLin;
39 set valK09 $kLin;
40
41 set valK10 $kRot;
42 set valK11 $kRot;
43 set valK12 $kRot;
44
45 # assign stiffness to connection components: face C
46 set valK13 $kLin;
47 set valK14 $kLin;
48 set valK15 $kLin;
```

```
49
50 set valK16 $kRot;
51 set valK17 $kRot;
52 set valK18 $kRot;
53
54 # assign stiffness to connection components: face D
55 set valK19 $kLin;
56 set valK20 $kLin;
57 set valK21 $kLin;
58
59 set valK22 $kRot;
60 set valK23 $kRot;
61 set valK24 $kRot;
62
63 # assign stiffness to tube components
64 # face components
65 set valK25 $k_25;
66 set valK26 $k_26;
67 set valK27 $k_27;
68 set valK28 $k_28;
69
70 # interaction components
71 set valK29 $k_29;
72 set valK30 $k_30;
73 set valK31 $k_31;
74 set valK32 $k_32;
75
76 # Define Uniaxial elastic material:
77 uniaxialMaterial Elastic 1 $valK01;
78 uniaxialMaterial Elastic 2 $valK02;
79 uniaxialMaterial Elastic 3 $valK03;
80 uniaxialMaterial Elastic 4 $valK04;
81 uniaxialMaterial Elastic 5 $valK05;
82 uniaxialMaterial Elastic 6 $valK06;
```

Appendix F. OpenSees model file example for Tcl

```
83 uniaxialMaterial Elastic 7 $valK07;
84 uniaxialMaterial Elastic 8 $valK08;
85 uniaxialMaterial Elastic 9 $valK09;
86 uniaxialMaterial Elastic 10 $valK10;
87 uniaxialMaterial Elastic 11 $valK11;
88 uniaxialMaterial Elastic 12 $valK12;
89 uniaxialMaterial Elastic 13 $valK13;
90 uniaxialMaterial Elastic 14 $valK14;
91 uniaxialMaterial Elastic 15 $valK15;
92 uniaxialMaterial Elastic 16 $valK16;
93 uniaxialMaterial Elastic 17 $valK17;
94 uniaxialMaterial Elastic 18 $valK18;
95 uniaxialMaterial Elastic 19 $valK19;
96 uniaxialMaterial Elastic 20 $valK20;
97 uniaxialMaterial Elastic 21 $valK21;
98 uniaxialMaterial Elastic 22 $valK22;
99 uniaxialMaterial Elastic 23 $valK23;
100 uniaxialMaterial Elastic 24 $valK24;
101 uniaxialMaterial Elastic 25 $valK25;
102 uniaxialMaterial Elastic 26 $valK26;
103 uniaxialMaterial Elastic 27 $valK27;
104 uniaxialMaterial Elastic 28 $valK28;
105 uniaxialMaterial Elastic 29 $valK29;
106 uniaxialMaterial Elastic 30 $valK30;
107 uniaxialMaterial Elastic 31 $valK31;
108 uniaxialMaterial Elastic 32 $valK32;
109
110 # Create Inno3DJointND Element:
111 element Inno3DPnPJoint 99 101 102 103 104 105 1 2 3 4 5 6 7 8 9 10
    11 12 13 14 15 16 17 18 19 20 21 22 23 24 25 26 27 28 29 30 31 3
    2;
```

F.3 Beam-to-column joint element definition file for the elastic-plastic case

The elastic-plastic analysis involves the division of the secondary file that comprises the joint definition in the linear elastic-plastic regime for the PR-EFM-IF-R0-SC01 case into two distinct files. The first file includes the tube components' hard-coded values, while the second file encompasses the joint element definition. The ensuing files are provided below for reference.

src_defTC_PR_EFM_IF_R0_v1.tcl:

```
1 #####
2 ##### BASED ON F_NGM #####
3 #####
4
5 # face COMPONENTS
6
7 # spring 25:
8 set matTag25 25;
9 set Fy_25 87590.77273;
10 set E0_25 49542.0
11 set b_25 0.001;
12
13 # spring 26:
14 set matTag26 26;
15 set Fy_26 5471.005557;
16 set E0_26 1166.0;
17 set b_26 0.001;
18
19 # spring 27:
20 set matTag27 27;
21 set Fy_27 87590.77273;
22 set E0_27 49542.0;
23 set b_27 0.001;
24
25 # spring 28:
```

```
26 set matTag28 28;
27 set Fy_28 5471.005557;
28 set E0_28 1166.0;
29 set b_28 0.001;
30
31
32 # interaction COMPONENTS
33
34 # spring 29, 30, 31 and 32
35 set disp [expr $Fy_25/$E0_25];
36
37 set matTag29 29;
38 set matTag30 30;
39 set matTag31 31;
40 set matTag32 32;
41
42 set E0_kI 14718;
43 set Fy_kI [expr $disp*$E0_kI];
44 set b_kI 0.001;
```

src_defJ_PR_EFM_IF_R0_v1.tcl:

```
1 # SET Stiffness for Springs:
2 source src_defTC_PR_EFM_IF_R0_v1.tcl
3
4 # ## CONNECTION COMPONENTS
5 # #####
6 set kLin 1E+11;
7 set kRot [expr $kLin*1E+0];
8 puts $kLin
9 puts $kRot
10
11 # # branch 1
12 set valK01 $kLin;
```

```
13 set valK02 $kLin;
14 set valK03 $kLin;
15
16 set valK04 $kRot;
17 set valK05 $kRot;
18 set valK06 $kRot;
19
20 # # branch 2
21 set valK07 $kLin;
22 set valK08 $kLin;
23 set valK09 $kLin;
24
25 set valK10 $kRot;
26 set valK11 $kRot;
27 set valK12 $kRot;
28
29 # # branch 3
30 set valK13 $kLin;
31 set valK14 $kLin;
32 set valK15 $kLin;
33
34 set valK16 $kRot;
35 set valK17 $kRot;
36 set valK18 $kRot;
37
38 # # branch 4
39 set valK19 $kLin;
40 set valK20 $kLin;
41 set valK21 $kLin;
42
43 set valK22 $kRot;
44 set valK23 $kRot;
45 set valK24 $kRot;
46
```



```
47
48 # Define UniAxial Elastic Material:
49 uniaxialMaterial Elastic 1 $valK01;
50 uniaxialMaterial Elastic 2 $valK02;
51 uniaxialMaterial Elastic 3 $valK03;
52 uniaxialMaterial Elastic 4 $valK04;
53 uniaxialMaterial Elastic 5 $valK05;
54 uniaxialMaterial Elastic 6 $valK06;
55 uniaxialMaterial Elastic 7 $valK07;
56 uniaxialMaterial Elastic 8 $valK08;
57 uniaxialMaterial Elastic 9 $valK09;
58 uniaxialMaterial Elastic 10 $valK10;
59 uniaxialMaterial Elastic 11 $valK11;
60 uniaxialMaterial Elastic 12 $valK12;
61 uniaxialMaterial Elastic 13 $valK13;
62 uniaxialMaterial Elastic 14 $valK14;
63 uniaxialMaterial Elastic 15 $valK15;
64 uniaxialMaterial Elastic 16 $valK16;
65 uniaxialMaterial Elastic 17 $valK17;
66 uniaxialMaterial Elastic 18 $valK18;
67 uniaxialMaterial Elastic 19 $valK19;
68 uniaxialMaterial Elastic 20 $valK20;
69 uniaxialMaterial Elastic 21 $valK21;
70 uniaxialMaterial Elastic 22 $valK22;
71 uniaxialMaterial Elastic 23 $valK23;
72 uniaxialMaterial Elastic 24 $valK24;
73
74
75 # ## TUBE COMPONENTS
76 # #####
77
78 # face COMPONENTS (SHORT FACE) -- spring 25 and 27
79
80 # PLASTIC
```

```

81 uniaxialMaterial Steel01 $matTag25 $Fy_25 $E0_25 $b_25;
82 uniaxialMaterial Steel01 $matTag27 $Fy_27 $E0_27 $b_27;
83
84
85 # face COMPONENTS (LONG FACE) -- spring 26 and 28
86
87 # PLASTIC
88 uniaxialMaterial Steel01 $matTag26 $Fy_26 $E0_26 $b_26;
89 uniaxialMaterial Steel01 $matTag28 $Fy_28 $E0_28 $b_28;
90
91
92 # interaction COMPONENTS
93
94 # PLASTIC
95 uniaxialMaterial Steel01 $matTag29 $Fy_kI $E0_kI $b_kI;
96 uniaxialMaterial Steel01 $matTag30 $Fy_kI $E0_kI $b_kI;
97 uniaxialMaterial Steel01 $matTag31 $Fy_kI $E0_kI $b_kI;
98 uniaxialMaterial Steel01 $matTag32 $Fy_kI $E0_kI $b_kI;
99
100
101 # # CREATE Inno3DPnPJoint Element:
102 # #####
103 element Inno3DPnPJoint 99 101 102 103 104 105 1 2 3 4 5 6 7 8 9 10
    11 12 13 14 15 16 17 18 19 20 21 22 23 24 25 26 27 28 29 30 31 3
    2;

```


Appendix G: Results RFEMs - material elastic

The results of the out-of-plane displacement from the center of each column face, δ_i , where i represents the column faces {A, B, C, D}, obtained from the RFEMs developed in Abaqus, which are described in Section 5.4.3, are presented for both the SHS and RHS in Tab. G.1 and Tab. G.2, respectively. Furthermore, the deformed shapes of the SHS and RHS cross-sections under the SC02 configuration are displayed in Tab. G.3 and Tab. G.4, respectively, for all load pattern(s) (LP(s)).

Table G.1: Values of displacements δ_i for SHS.

LP	SC	δ_A	δ_B	δ_C	δ_D
m01	SC01	-11.90	-3.20	1.43	3.20
m01	SC02	-9.49	-2.73	1.30	2.73
m01	SC03	-4.27	-1.43	0.75	1.43
m01	SC04	-1.20	-0.49	0.28	0.49
m02-CH	SC01	-4.63	-15.10	15.10	4.63
m02-CH	SC02	-4.03	-12.22	12.22	4.03
m02-CH	SC03	-2.18	-5.70	5.70	2.18
m02-CH	SC04	-0.76	-1.68	1.68	0.76
m02-CV	SC01	1.77	8.70	8.70	1.77
m02-CV	SC02	1.43	6.76	6.76	1.43
m02-CV	SC03	0.67	2.84	2.84	0.67
m02-CV	SC04	0.21	0.71	0.71	0.21
m02-H	SC01	10.46	0.00	10.46	0.00
m02-H	SC02	8.19	0.00	8.19	0.00
m02-H	SC03	3.52	0.00	3.52	0.00
m02-H	SC04	0.92	0.00	0.92	0.00
m02-V	SC01	-13.33	-6.40	13.33	6.40
m02-V	SC02	-10.79	-5.46	10.79	5.46
m02-V	SC03	-5.02	-2.85	5.02	2.85
m02-V	SC04	-1.47	-0.97	1.47	0.97
m03-H	SC01	13.66	11.90	7.26	-1.43

Continued on next page ...

Table G.1: Values of displacements δ_i for SHS (*cont.*).

LP	SC	δ_A	δ_B	δ_C	δ_D
m03-H	SC02	10.92	9.49	5.46	-1.30
m03-H	SC03	3.52	3.52	3.52	3.52
m03-H	SC04	0.92	0.92	0.92	0.92
m03-V	SC01	-10.13	5.50	10.13	4.97
m03-V	SC02	-8.06	4.03	8.06	4.16
m03-V	SC03	-3.60	1.42	3.60	2.10
m03-V	SC04	-9.89	2.24	9.89	6.92
m04-H	SC01	10.46	10.46	10.46	10.46
m04-H	SC02	8.19	8.19	8.19	8.19
m04-H	SC03	35.18	35.18	35.18	35.18
m04-H	SC04	9.17	9.17	9.17	9.17
m04-V	SC01	-6.93	6.93	6.93	-6.93
m04-V	SC02	-5.33	5.33	5.33	-5.33
m04-V	SC03	-2.17	2.17	2.17	-2.17
m04-V	SC04	-0.50	0.50	0.50	-0.50
m04-VnVp	SC01	-19.73	-19.73	19.73	19.73
m04-VnVp	SC02	-16.25	-16.25	16.25	16.25
m04-VnVp	SC03	-7.88	-7.88	7.88	7.88
m04-VnVp	SC04	-2.45	-2.45	2.45	2.45

Table G.2: Values of displacements δ_i for RHS.

LP	SC	δ_A	δ_B	δ_C	δ_D
m01-V01	01	-12.87	-4.95	1.29	4.95
m01-V01	02	-10.38	-4.38	1.16	4.38
m01-V01	03	-4.88	-2.63	0.66	2.63
m01-V01	04	-1.52	-1.07	0.22	1.07
m01-V02	01	4.95	31.10	-4.95	-3.46
m01-V02	02	4.40	27.20	-4.40	-3.33
m01-V02	03	2.71	17.30	-2.71	-2.54

Continued on next page ...

Table G.2: Values of displacements δ_i for RHS (*cont.*).

LP	SC	δ_A	δ_B	δ_C	δ_D
m01-V02	04	1.27	9.24	-1.27	-1.53
m02-CH01	01	-6.24	-36.05	17.82	8.41
m02-CH01	02	-5.56	-31.58	14.78	7.71
m02-CH01	03	-3.37	-19.93	7.59	5.17
m02-CH01	04	-1.49	-10.31	2.80	2.60
m02-CH02	01	6.24	36.05	-17.82	-8.41
m02-CH02	02	5.56	31.58	-14.78	-7.71
m02-CH02	03	3.37	19.93	-7.59	-5.17
m02-CH02	04	1.49	10.31	-2.80	-2.60
m02-CV	01	3.66	26.15	7.91	1.49
m02-CV	02	3.23	22.82	5.99	1.05
m02-CV	03	2.05	14.67	2.18	0.09
m02-CV	04	1.05	8.17	0.25	-0.46
m02-H01	01	11.58	0.00	11.58	0.00
m02-H01	02	9.22	0.00	9.22	0.00
m02-H01	03	4.23	0.00	4.23	0.00
m02-H01	04	1.30	0.00	1.30	0.00
m02-H02	01	0.00	27.65	0.00	27.65
m02-H02	02	0.00	23.87	0.00	23.87
m02-H02	03	0.00	14.76	0.00	14.76
m02-H02	04	0.00	7.71	0.00	7.71
m02-V01	01	-14.16	-9.90	14.16	9.90
m02-V01	02	-11.55	-8.76	11.55	8.76
m02-V01	03	-5.54	-5.26	5.54	5.26
m02-V01	04	-1.75	-2.14	1.75	2.14
m02-V02	01	9.90	34.56	-9.90	-34.56
m02-V02	02	8.79	30.53	-8.79	-30.53
m02-V02	03	5.41	19.84	-5.41	-19.84
m02-V02	04	2.54	10.77	-2.54	-10.77
m03-H01	01	16.53	31.10	6.62	-3.46

Continued on next page ...

Table G.2: Values of displacements δ_i for RHS (*cont.*).

LP	SC	δ_A	δ_B	δ_C	δ_D
m03-H01	02	13.62	27.20	4.82	-3.33
m03-H01	03	6.93	17.30	1.52	-2.54
m03-H01	04	2.57	9.24	0.03	-1.53
m03-H02	01	-1.29	22.70	12.87	32.60
m03-H02	02	-1.16	19.48	10.38	28.25
m03-H02	03	-0.66	12.12	4.88	17.39
m03-H02	04	-0.22	6.64	1.52	8.78
m03-V01	01	-9.20	21.20	9.20	6.45
m03-V01	02	-7.15	18.44	7.15	5.43
m03-V01	03	-2.84	12.04	2.84	2.72
m03-V01	04	-0.47	7.10	0.47	0.61
m03-V02	01	8.61	29.61	2.96	-29.61
m03-V02	02	7.63	26.15	1.59	-26.15
m03-V02	03	4.75	17.21	-0.53	-17.21
m03-V02	04	2.32	9.70	-1.02	-9.70
m04-H	01	11.58	27.65	11.58	27.65
m04-H	02	9.22	23.87	9.22	23.87
m04-H	03	4.23	14.76	4.23	14.76
m04-H	04	1.30	7.71	1.30	7.71
m04-V	01	-4.25	24.66	4.25	-24.66
m04-V	02	-2.75	21.77	2.75	-21.77
m04-V	03	-0.13	14.58	0.13	-14.58
m04-V	04	0.80	8.64	-0.80	-8.64
m04-VnVp01	01	-24.06	-44.46	24.06	44.46
m04-VnVp01	02	-20.34	-39.29	20.34	39.29
m04-VnVp01	03	-10.96	-25.10	10.96	25.10
m04-VnVp01	04	-4.29	-12.91	4.29	12.91
m04-VnVp02	01	24.06	44.46	-24.06	-44.46
m04-VnVp02	02	20.34	39.29	-20.34	-39.29
m04-VnVp02	03	10.96	25.10	-10.96	-25.10

Continued on next page ...

Table G.2: Values of displacements δ_i for RHS (*cont.*).

LP	SC	δ_A	δ_B	δ_C	δ_D
m04-VnVp02	04	4.29	12.91	-4.29	-12.91

Table G.3: Deformed shape for SHS for all LPs with SC02.

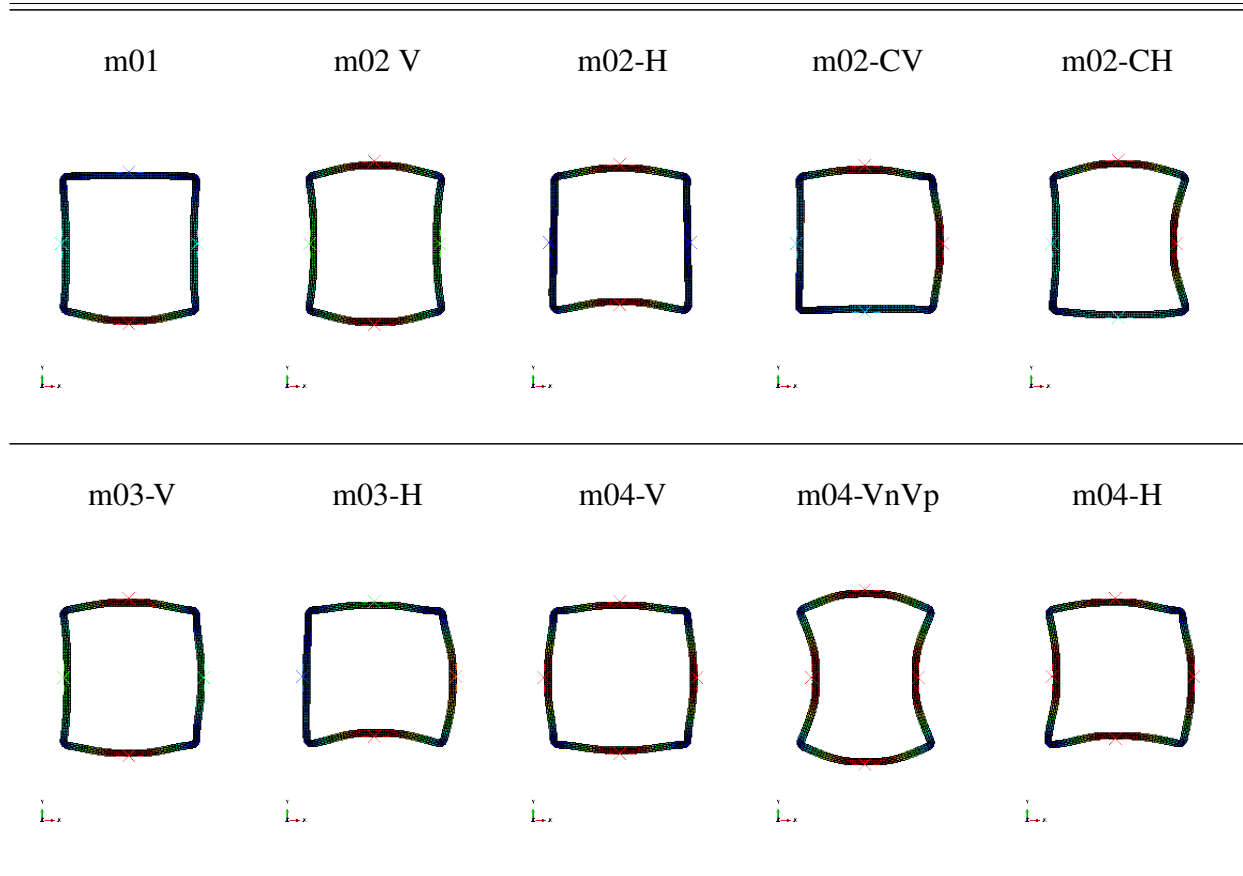
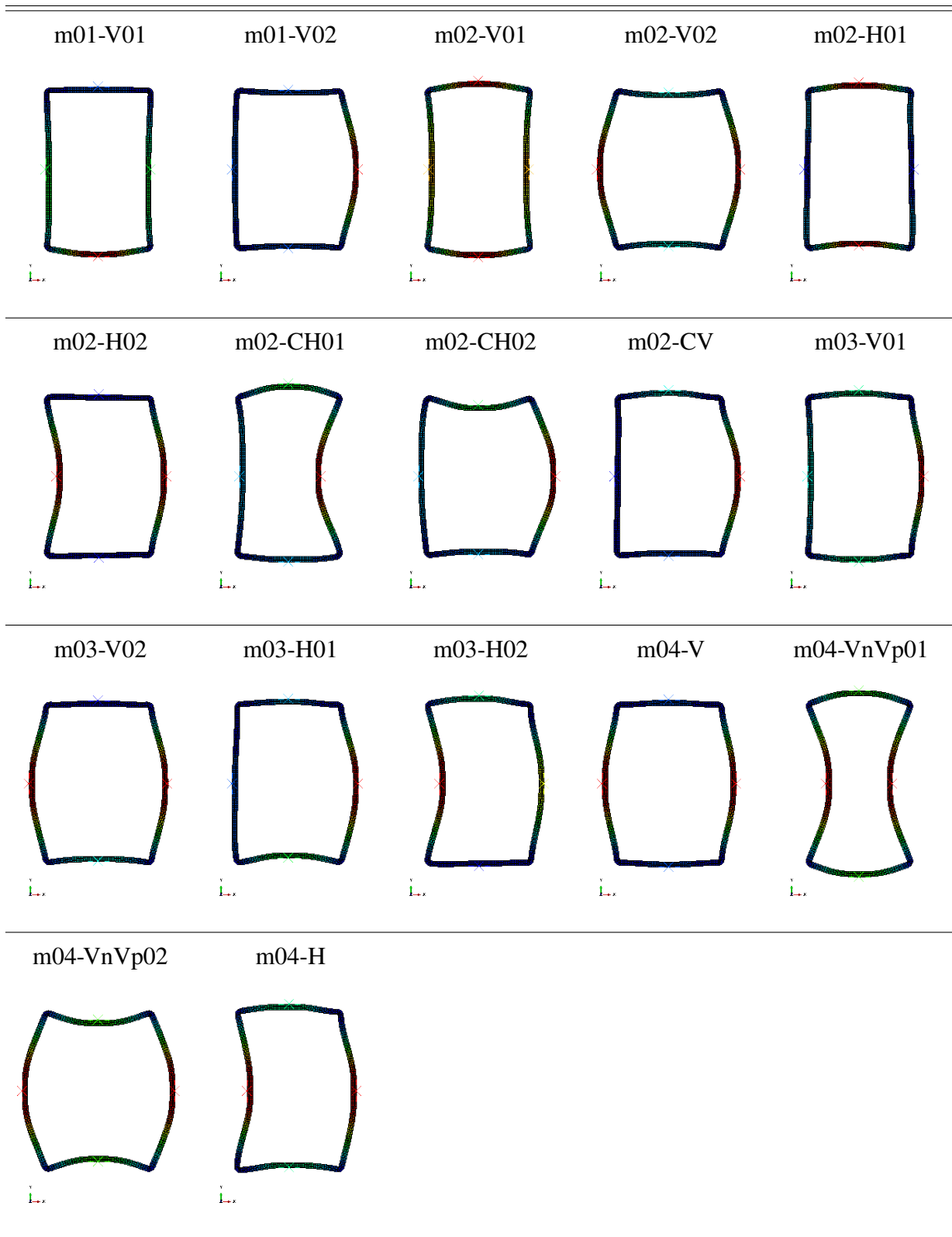


Table G.4: Deformed shape for RHS for all LP with SC02.



Appendix H: Results stiffness

The comparison of the out-of-plane displacements of the column faces between OpenSees and Abaqus models is presented in two ways: mathematically, using the approximation error parameter, ε_2 , defined in Eq. (5.58) as outlined in Section 5.4; and graphically, by plotting the results of the two software against each other. The results are presented in this section, in accordance with Tab. H.1.

Table H.1: Index of tables for stiffness results.

Case	Table no.	Figure no.
HS-EFM-R0	Tab. H.2	Fig. H.1
HS-EFM-R1	Tab. H.3	Fig. H.2
PS-EFM-R0	Tab. H.4	Fig. H.3
PS-EFM-R1	Tab. 5.10*	Fig. 5.37*
HR-EFM-IF-R0	Tab. H.5	Fig. H.4
HR-EFM-IEq-R0	Tab. H.6	Fig. H.5
HR-EFM-IF-R1	Tab. H.7	Fig. H.6
HR-EFM-IEq-R1	Tab. H.8	Fig. H.7
PR-EFM-IF-R0	Tab. H.9	Fig. H.8
PR-EFM-IEq-R0	Tab. H.10	Fig. H.9
PR-EFM-IF-R1	Tab. 5.12*	Fig. 5.38*
PR-EFM-IEq-R1	Tab. H.11	Fig. H.10

* see Section 5.4.4

Table H.2: Results: HS-EFM-R0.

LP	SC	ε_2	LP	SC	ε_2	LP	SC	ε_2
m01	SC01	0.53	m02-H	SC03	0.09	m04-H	SC01	0.15
m01	SC02	0.42	m02-H	SC04	0.01	m04-H	SC02	0.13
m01	SC03	0.22	m02-V	SC01	0.53	m04-H	SC03	0.09
m01	SC04	0.07	m02-V	SC02	0.42	m04-H	SC04	0.01
m02-CH	SC01	0.53	m02-V	SC03	0.22	m04-V	SC01	0.09
m02-CH	SC02	0.42	m02-V	SC04	0.07	m04-V	SC02	0.08
m02-CH	SC03	0.22	m03-H	SC01	0.30	m04-V	SC03	0.11
m02-CH	SC04	0.07	m03-H	SC02	0.25	m04-V	SC04	0.13
m02-CV	SC01	0.15	m03-H	SC03	0.68	m04-VnVp	SC01	0.53
m02-CV	SC02	0.13	m03-H	SC04	0.62	m04-VnVp	SC02	0.42
m02-CV	SC03	0.09	m03-V	SC01	0.34	m04-VnVp	SC03	0.22
m02-CV	SC04	0.07	m03-V	SC02	0.28	m04-VnVp	SC04	0.07
m02-H	SC01	0.15	m03-V	SC03	0.16			
m02-H	SC02	0.13	m03-V	SC04	0.07			

Table H.3: Results: HS-EFM-R1.

LP	SC	ε_2	LP	SC	ε_2	LP	SC	ε_2
m01	SC01	0.18	m02-H	SC03	0.38	m04-H	SC01	0.17
m01	SC02	0.14	m02-H	SC04	0.67	m04-H	SC02	0.22
m01	SC03	0.30	m02-V	SC01	0.10	m04-H	SC03	0.38
m01	SC04	0.69	m02-V	SC02	0.08	m04-H	SC04	0.67
m02-CH	SC01	0.10	m02-V	SC03	0.30	m04-V	SC01	0.22
m02-CH	SC02	0.11	m02-V	SC04	0.69	m04-V	SC02	0.25
m02-CH	SC03	0.30	m03-H	SC01	0.16	m04-V	SC03	0.37
m02-CH	SC04	0.69	m03-H	SC02	0.20	m04-V	SC04	0.62
m02-CV	SC01	0.17	m03-H	SC03	0.53	m04-VnVp	SC01	0.10
m02-CV	SC02	0.22	m03-H	SC04	0.75	m04-VnVp	SC02	0.02
m02-CV	SC03	0.38	m03-V	SC01	0.15	m04-VnVp	SC03	0.30
m02-CV	SC04	0.67	m03-V	SC02	0.17	m04-VnVp	SC04	0.69
m02-H	SC01	0.17	m03-V	SC03	0.35			
m02-H	SC02	0.22	m03-V	SC04	0.66			

Table H.4: Results: PS-EFM-R0.

LP	SC	ε_2	LP	SC	ε_2	LP	SC	ε_2
m01	SC01	0.53	m02-H	SC03	0.09	m04-H	SC01	0.15
m01	SC02	0.42	m02-H	SC04	0.01	m04-H	SC02	0.13
m01	SC03	0.22	m02-V	SC01	0.53	m04-H	SC03	0.09
m01	SC04	0.07	m02-V	SC02	0.42	m04-H	SC04	0.01
m02-CH	SC01	0.53	m02-V	SC03	0.22	m04-V	SC01	0.09
m02-CH	SC02	0.42	m02-V	SC04	0.07	m04-V	SC02	0.08
m02-CH	SC03	0.22	m03-H	SC01	0.30	m04-V	SC03	0.11
m02-CH	SC04	0.07	m03-H	SC02	0.25	m04-V	SC04	0.13
m02-CV	SC01	0.15	m03-H	SC03	0.68	m04-VnVp	SC01	0.53
m02-CV	SC02	0.13	m03-H	SC04	0.62	m04-VnVp	SC02	0.42
m02-CV	SC03	0.09	m03-V	SC01	0.34	m04-VnVp	SC03	0.22
m02-CV	SC04	0.07	m03-V	SC02	0.28	m04-VnVp	SC04	0.07
m02-H	SC01	0.15	m03-V	SC03	0.16			
m02-H	SC02	0.13	m03-V	SC04	0.07			

Table H.5: Results: HR-EFM-IF-R0.

LP	SC	ε_2	LP	SC	ε_2	LP	SC	ε_2
m01-V01	SC01	0.62	m02-H01	SC04	0.15	m03-V01	SC03	0.16
m01-V01	SC02	0.53	m02-H02	SC01	0.16	m03-V01	SC04	0.28
m01-V01	SC03	0.35	m02-H02	SC02	0.11	m03-V02	SC01	0.47
m01-V01	SC04	0.07	m02-H02	SC03	0.01	m03-V02	SC02	0.37
m01-V02	SC01	0.55	m02-H02	SC04	0.10	m03-V02	SC03	0.13
m01-V02	SC02	0.43	m02-V01	SC01	0.62	m03-V02	SC04	0.19
m01-V02	SC03	0.17	m02-V01	SC02	0.53	m04-H	SC01	0.15
m01-V02	SC04	0.15	m02-V01	SC03	0.35	m04-H	SC02	0.11
m02-CH01	SC01	0.57	m02-V01	SC04	0.07	m04-H	SC03	0.05
m02-CH01	SC02	0.46	m02-V02	SC01	0.55	m04-H	SC04	0.11
m02-CH01	SC03	0.23	m02-V02	SC02	0.43	m04-V	SC01	0.32
m02-CH01	SC04	0.10	m02-V02	SC03	0.17	m04-V	SC02	0.25
m02-CH02	SC01	0.57	m02-V02	SC04	0.15	m04-V	SC03	0.04
m02-CH02	SC02	0.46	m03-H01	SC01	0.42	m04-V	SC04	0.23
m02-CH02	SC03	0.23	m03-H01	SC02	0.34	m04-VnVp01	SC01	0.57
m02-CH02	SC04	0.10	m03-H01	SC03	0.16	m04-VnVp01	SC02	0.46
m02-CV	SC01	0.24	m03-H01	SC04	0.15	m04-VnVp01	SC03	0.23
m02-CV	SC02	0.18	m03-H02	SC01	0.22	m04-VnVp01	SC04	0.10
m02-CV	SC03	0.06	m03-H02	SC02	0.18	m04-VnVp02	SC01	0.57
m02-CV	SC04	0.22	m03-H02	SC03	0.11	m04-VnVp02	SC02	0.46
m02-H01	SC01	0.12	m03-H02	SC04	0.10	m04-VnVp02	SC03	0.23
m02-H01	SC02	0.11	m03-V01	SC01	0.16	m04-VnVp02	SC04	0.10
m02-H01	SC03	0.15	m03-V01	SC02	0.13			

Table H.6: Results: HR-EFM-IEq-R0.

LP	SC	ε_2	LP	SC	ε_2	LP	SC	ε_2
m01-V01	SC01	0.57	m02-H01	SC04	0.21	m03-V01	SC03	0.30
m01-V01	SC02	0.51	m02-H02	SC01	0.20	m03-V01	SC04	0.73
m01-V01	SC03	0.43	m02-H02	SC02	0.13	m03-V02	SC01	0.52
m01-V01	SC04	0.22	m02-H02	SC03	0.08	m03-V02	SC02	0.39
m01-V02	SC01	0.57	m02-H02	SC04	0.46	m03-V02	SC03	0.06
m01-V02	SC02	0.44	m02-V01	SC01	0.57	m03-V02	SC04	0.44
m01-V02	SC03	0.13	m02-V01	SC02	0.51	m04-H	SC01	0.17
m01-V02	SC04	0.34	m02-V01	SC03	0.43	m04-H	SC02	0.12
m02-CH01	SC01	0.57	m02-V01	SC04	0.22	m04-H	SC03	0.11
m02-CH01	SC02	0.46	m02-V02	SC01	0.57	m04-H	SC04	0.42
m02-CH01	SC03	0.21	m02-V02	SC02	0.44	m04-V	SC01	0.40
m02-CH01	SC04	0.27	m02-V02	SC03	0.12	m04-V	SC02	0.28
m02-CH02	SC01	0.57	m02-V02	SC04	0.34	m04-V	SC03	0.10
m02-CH02	SC02	0.46	m03-H01	SC01	0.44	m04-V	SC04	0.58
m02-CH02	SC03	0.21	m03-H01	SC02	0.35	m04-VnVp01	SC01	0.57
m02-CH02	SC04	0.27	m03-H01	SC03	0.12	m04-VnVp01	SC02	0.46
m02-CV	SC01	0.29	m03-H01	SC04	0.37	m04-VnVp01	SC03	0.21
m02-CV	SC02	0.21	m03-H02	SC01	0.23	m04-VnVp01	SC04	0.27
m02-CV	SC03	0.12	m03-H02	SC02	0.18	m04-VnVp02	SC01	0.57
m02-CV	SC04	0.55	m03-H02	SC03	0.14	m04-VnVp02	SC02	0.46
m02-H01	SC01	0.08	m03-H02	SC04	0.45	m04-VnVp02	SC03	0.21
m02-H01	SC02	0.10	m03-V01	SC01	0.15	m04-VnVp02	SC04	0.27
m02-H01	SC03	0.21	m03-V01	SC02	0.13			

Table H.7: Results: HR-EFM-IF-R1.

LP	SC	ε_2	LP	SC	ε_2	LP	SC	ε_2
m01-V01	SC01	0.28	m02-H01	SC04	0.55	m03-V01	SC03	0.27
m01-V01	SC02	0.22	m02-H02	SC01	0.06	m03-V01	SC04	0.41
m01-V01	SC03	0.17	m02-H02	SC02	0.12	m03-V02	SC01	0.22
m01-V01	SC04	0.61	m02-H02	SC03	0.26	m03-V02	SC02	0.10
m01-V02	SC01	0.23	m02-H02	SC04	0.42	m03-V02	SC03	0.22
m01-V02	SC02	0.14	m02-V01	SC01	0.21	m03-V02	SC04	0.52
m01-V02	SC03	0.19	m02-V01	SC02	0.14	m04-H	SC01	0.10
m01-V02	SC04	0.53	m02-V01	SC03	0.17	m04-H	SC02	0.15
m02-CH01	SC01	0.22	m02-V01	SC04	0.61	m04-H	SC03	0.27
m02-CH01	SC02	0.10	m02-V02	SC01	0.23	m04-H	SC04	0.44
m02-CH01	SC03	0.18	m02-V02	SC02	0.11	m04-V	SC01	0.18
m02-CH01	SC04	0.55	m02-V02	SC03	0.19	m04-V	SC02	0.15
m02-CH02	SC01	0.22	m02-V02	SC04	0.53	m04-V	SC03	0.26
m02-CH02	SC02	0.10	m03-H01	SC01	0.18	m04-V	SC04	0.50
m02-CH02	SC03	0.18	m03-H01	SC02	0.14	m04-VnVp01	SC01	0.22
m02-CH02	SC04	0.55	m03-H01	SC03	0.23	m04-VnVp01	SC02	0.10
m02-CV	SC01	0.15	m03-H01	SC04	0.53	m04-VnVp01	SC03	0.18
m02-CV	SC02	0.17	m03-H02	SC01	0.10	m04-VnVp01	SC04	0.55
m02-CV	SC03	0.27	m03-H02	SC02	0.13	m04-VnVp02	SC01	0.22
m02-CV	SC04	0.48	m03-H02	SC03	0.26	m04-VnVp02	SC02	0.10
m02-H01	SC01	0.18	m03-H02	SC04	0.44	m04-VnVp02	SC03	0.18
m02-H01	SC02	0.21	m03-V01	SC01	0.15	m04-VnVp02	SC04	0.55
m02-H01	SC03	0.30	m03-V01	SC02	0.17			

Table H.8: Results: HR-EFM-IEq-R1.

LP	SC	ε_2	LP	SC	ε_2	LP	SC	ε_2
m01-V01	SC01	0.28	m02-H01	SC04	0.54	m03-V01	SC03	0.32
m01-V01	SC02	0.22	m02-H02	SC01	0.03	m03-V01	SC04	0.69
m01-V01	SC03	0.14	m02-H02	SC02	0.11	m03-V02	SC01	0.25
m01-V01	SC04	0.52	m02-H02	SC03	0.38	m03-V02	SC02	0.11
m01-V02	SC01	0.25	m02-H02	SC04	0.77	m03-V02	SC03	0.30
m01-V02	SC02	0.13	m02-V01	SC01	0.18	m03-V02	SC04	0.76
m01-V02	SC03	0.25	m02-V01	SC02	0.14	m04-H	SC01	0.08
m01-V02	SC04	0.73	m02-V01	SC03	0.10	m04-H	SC02	0.14
m02-CH01	SC01	0.22	m02-V01	SC04	0.52	m04-H	SC03	0.35
m02-CH01	SC02	0.11	m02-V02	SC01	0.25	m04-H	SC04	0.74
m02-CH01	SC03	0.20	m02-V02	SC02	0.11	m04-V	SC01	0.24
m02-CH01	SC04	0.68	m02-V02	SC03	0.25	m04-V	SC02	0.14
m02-CH02	SC01	0.22	m02-V02	SC04	0.73	m04-V	SC03	0.37
m02-CH02	SC02	0.11	m03-H01	SC01	0.20	m04-V	SC04	0.81
m02-CH02	SC03	0.20	m03-H01	SC02	0.14	m04-VnVp01	SC01	0.22
m02-CH02	SC04	0.68	m03-H01	SC03	0.28	m04-VnVp01	SC02	0.10
m02-CV	SC01	0.17	m03-H01	SC04	0.72	m04-VnVp01	SC03	0.20
m02-CV	SC02	0.17	m03-H02	SC01	0.10	m04-VnVp01	SC04	0.68
m02-CV	SC03	0.35	m03-H02	SC02	0.13	m04-VnVp02	SC01	0.22
m02-CV	SC04	0.77	m03-H02	SC03	0.35	m04-VnVp02	SC02	0.10
m02-H01	SC01	0.21	m03-H02	SC04	0.74	m04-VnVp02	SC03	0.20
m02-H01	SC02	0.22	m03-V01	SC01	0.14	m04-VnVp02	SC04	0.68
m02-H01	SC03	0.26	m03-V01	SC02	0.17			

Table H.9: Results: PR-EFM-IF-R0.

LP	SC	ε_2	LP	SC	ε_2	LP	SC	ε_2
m01-V01	SC01	0.61	m02-H01	SC04	0.21	m03-V01	SC03	0.13
m01-V01	SC02	0.50	m02-H02	SC01	0.18	m03-V01	SC04	0.21
m01-V01	SC03	0.32	m02-H02	SC02	0.16	m03-V02	SC01	0.51
m01-V01	SC04	0.22	m02-H02	SC03	0.14	m03-V02	SC02	0.46
m01-V02	SC01	0.57	m02-H02	SC04	0.12	m03-V02	SC03	0.35
m01-V02	SC02	0.49	m02-V01	SC01	0.61	m03-V02	SC04	0.22
m01-V02	SC03	0.34	m02-V01	SC02	0.50	m04-H	SC01	0.16
m01-V02	SC04	0.20	m02-V01	SC03	0.32	m04-H	SC02	0.13
m02-CH01	SC01	0.59	m02-V01	SC04	0.19	m04-H	SC03	0.11
m02-CH01	SC02	0.49	m02-V02	SC01	0.57	m04-H	SC04	0.13
m02-CH01	SC03	0.34	m02-V02	SC02	0.49	m04-V	SC01	0.37
m02-CH01	SC04	0.20	m02-V02	SC03	0.34	m04-V	SC02	0.36
m02-CH02	SC01	0.59	m02-V02	SC04	0.20	m04-V	SC03	0.36
m02-CH02	SC02	0.49	m03-H01	SC01	0.44	m04-V	SC04	0.24
m02-CH02	SC03	0.34	m03-H01	SC02	0.39	m04-VnVp01	SC01	0.59
m02-CH02	SC04	0.20	m03-H01	SC03	0.31	m04-VnVp01	SC02	0.49
m02-CV	SC01	0.28	m03-H01	SC04	0.23	m04-VnVp01	SC03	0.34
m02-CV	SC02	0.27	m03-H02	SC01	0.23	m04-VnVp01	SC04	0.18
m02-CV	SC03	0.28	m03-H02	SC02	0.19	m04-VnVp02	SC01	0.59
m02-CV	SC04	0.23	m03-H02	SC03	0.15	m04-VnVp02	SC02	0.49
m02-H01	SC01	0.09	m03-H02	SC04	0.12	m04-VnVp02	SC03	0.34
m02-H01	SC02	0.06	m03-V01	SC01	0.15	m04-VnVp02	SC04	0.18
m02-H01	SC03	0.01	m03-V01	SC02	0.12			

Table H.10: Results: PR-EFM-IEq-R0.

LP	SC	ε_2	LP	SC	ε_2	LP	SC	ε_2
m01-V01	SC01	0.53	m02-H01	SC04	0.31	m03-V01	SC03	0.24
m01-V01	SC02	0.42	m02-H02	SC01	0.25	m03-V01	SC04	0.41
m01-V01	SC03	0.23	m02-H02	SC02	0.23	m03-V02	SC01	0.58
m01-V01	SC04	0.18	m02-H02	SC03	0.23	m03-V02	SC02	0.53
m01-V02	SC01	0.61	m02-H02	SC04	0.26	m03-V02	SC03	0.42
m01-V02	SC02	0.52	m02-V01	SC01	0.53	m03-V02	SC04	0.30
m01-V02	SC03	0.38	m02-V01	SC02	0.42	m04-H	SC01	0.18
m01-V02	SC04	0.26	m02-V01	SC03	0.21	m04-H	SC02	0.17
m02-CH01	SC01	0.58	m02-V01	SC04	0.18	m04-H	SC03	0.20
m02-CH01	SC02	0.49	m02-V02	SC01	0.61	m04-H	SC04	0.27
m02-CH01	SC03	0.33	m02-V02	SC02	0.52	m04-V	SC01	0.50
m02-CH01	SC04	0.24	m02-V02	SC03	0.38	m04-V	SC02	0.49
m02-CH02	SC01	0.58	m02-V02	SC04	0.26	m04-V	SC03	0.49
m02-CH02	SC02	0.49	m03-H01	SC01	0.47	m04-V	SC04	0.35
m02-CH02	SC03	0.33	m03-H01	SC02	0.42	m04-VnVp01	SC01	0.58
m02-CH02	SC04	0.24	m03-H01	SC03	0.34	m04-VnVp01	SC02	0.49
m02-CV	SC01	0.36	m03-H01	SC04	0.31	m04-VnVp01	SC03	0.33
m02-CV	SC02	0.36	m03-H02	SC01	0.26	m04-VnVp01	SC04	0.24
m02-CV	SC03	0.38	m03-H02	SC02	0.23	m04-VnVp02	SC01	0.58
m02-CV	SC04	0.35	m03-H02	SC03	0.21	m04-VnVp02	SC02	0.49
m02-H01	SC01	0.03	m03-H02	SC04	0.26	m04-VnVp02	SC03	0.33
m02-H01	SC02	0.01	m03-V01	SC01	0.15	m04-VnVp02	SC04	0.24
m02-H01	SC03	0.09	m03-V01	SC02	0.17			

Table H.11: Results: PR-EFM-IEq-R1.

LP	SC	ε_2	LP	SC	ε_2	LP	SC	ε_2
m01-V01	SC01	0.29	m02-H01	SC04	0.79	m03-V01	SC03	0.28
m01-V01	SC02	0.25	m02-H02	SC01	0.02	m03-V01	SC04	0.25
m01-V01	SC03	0.27	m02-H02	SC02	0.01	m03-V02	SC01	0.31
m01-V01	SC04	0.64	m02-H02	SC03	0.06	m03-V02	SC02	0.24
m01-V02	SC01	0.29	m02-H02	SC04	0.10	m03-V02	SC03	0.10
m01-V02	SC02	0.19	m02-V01	SC01	0.21	m03-V02	SC04	0.14
m01-V02	SC03	0.07	m02-V01	SC02	0.20	m04-H	SC01	0.09
m01-V02	SC04	0.21	m02-V01	SC03	0.27	m04-H	SC02	0.10
m02-CH01	SC01	0.23	m02-V01	SC04	0.64	m04-H	SC03	0.16
m02-CH01	SC02	0.18	m02-V02	SC01	0.29	m04-H	SC04	0.20
m02-CH01	SC03	0.11	m02-V02	SC02	0.19	m04-V	SC01	0.33
m02-CH01	SC04	0.31	m02-V02	SC03	0.06	m04-V	SC02	0.30
m02-CH02	SC01	0.23	m02-V02	SC04	0.21	m04-V	SC03	0.20
m02-CH02	SC02	0.18	m03-H01	SC01	0.25	m04-V	SC04	0.03
m02-CH02	SC03	0.11	m03-H01	SC02	0.23	m04-VnVp01	SC01	0.23
m02-CH02	SC04	0.31	m03-H01	SC03	0.18	m04-VnVp01	SC02	0.13
m02-CV	SC01	0.24	m03-H01	SC04	0.25	m04-VnVp01	SC03	0.09
m02-CV	SC02	0.22	m03-H02	SC01	0.10	m04-VnVp01	SC04	0.31
m02-CV	SC03	0.18	m03-H02	SC02	0.08	m04-VnVp02	SC01	0.23
m02-CV	SC04	0.18	m03-H02	SC03	0.12	m04-VnVp02	SC02	0.13
m02-H01	SC01	0.26	m03-H02	SC04	0.17	m04-VnVp02	SC03	0.09
m02-H01	SC02	0.32	m03-V01	SC01	0.14	m04-VnVp02	SC04	0.31
m02-H01	SC03	0.49	m03-V01	SC02	0.19			

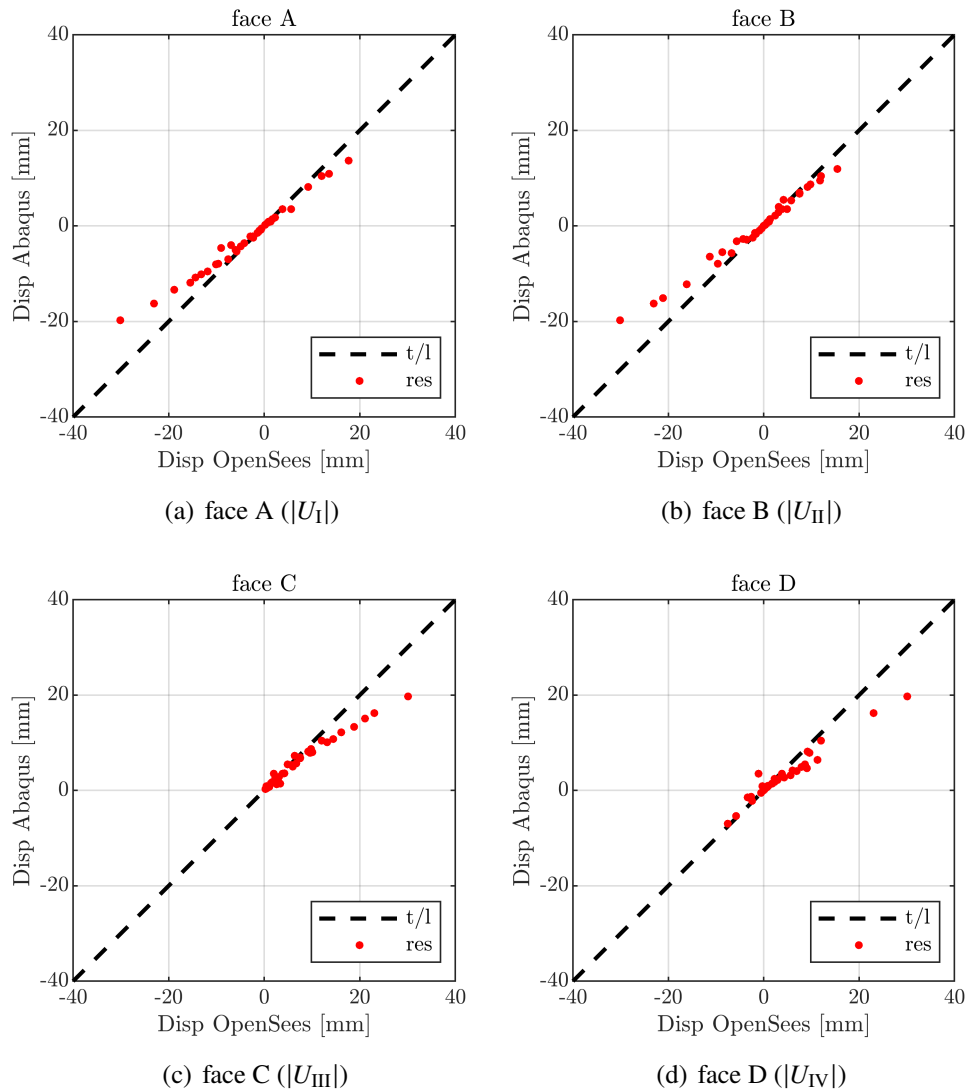


Figure H.1: HS-EFM-R0.

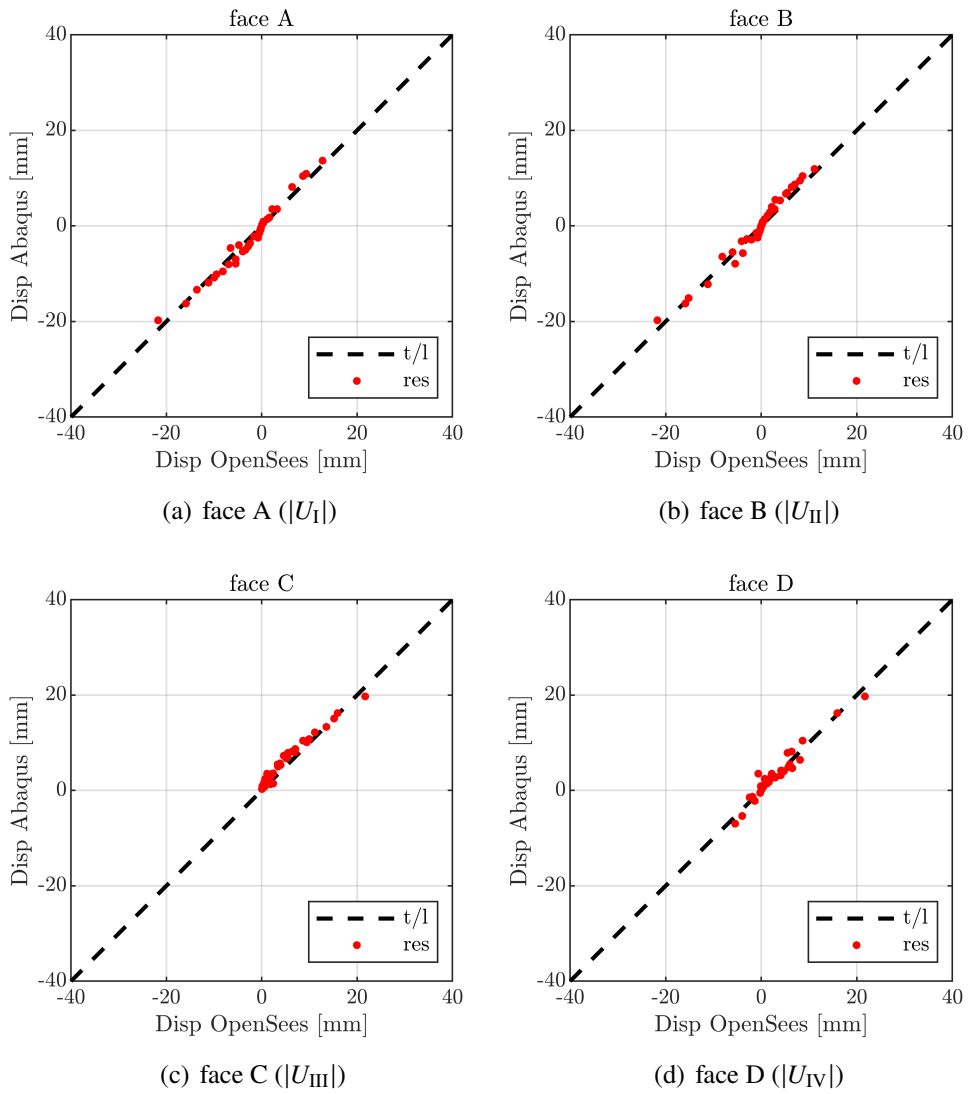


Figure H.2: HS-EFM-R1.

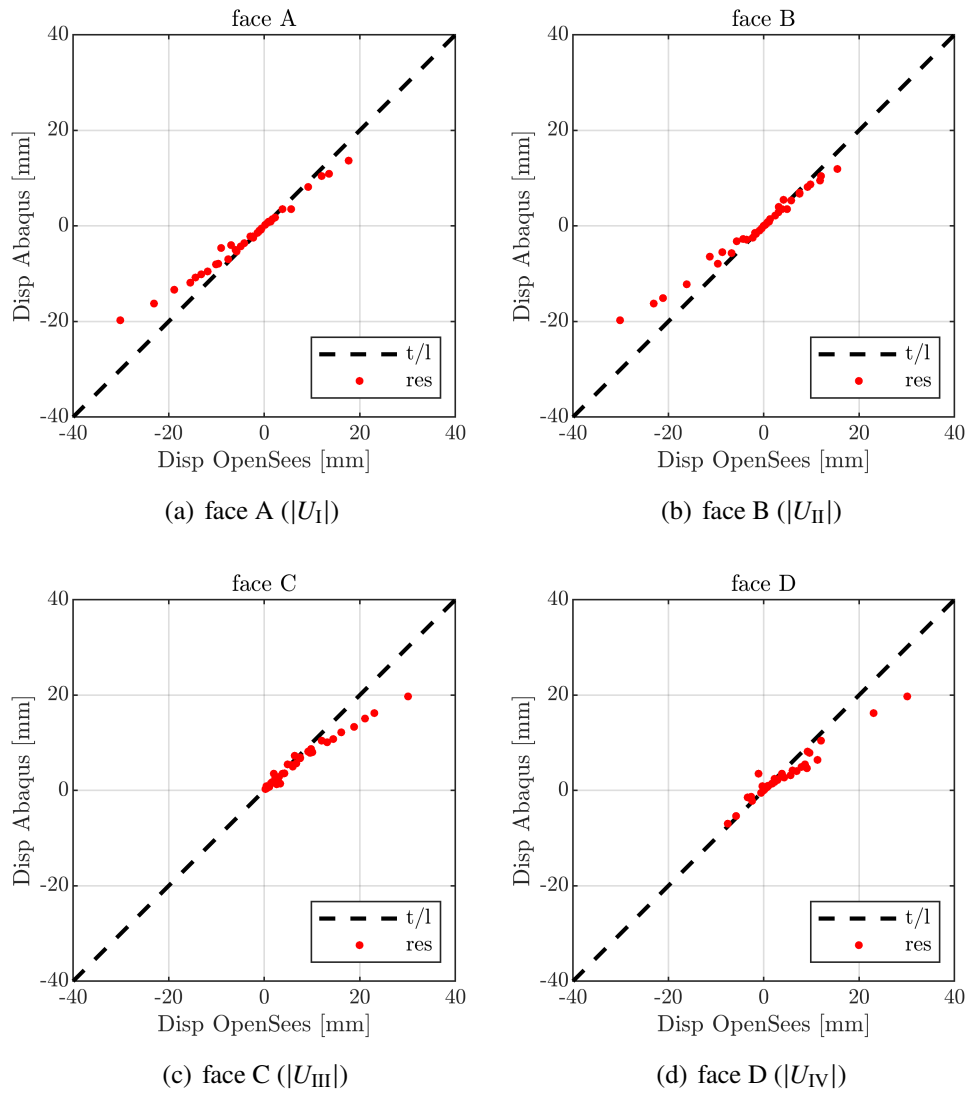


Figure H.3: PS-EFM-R0.

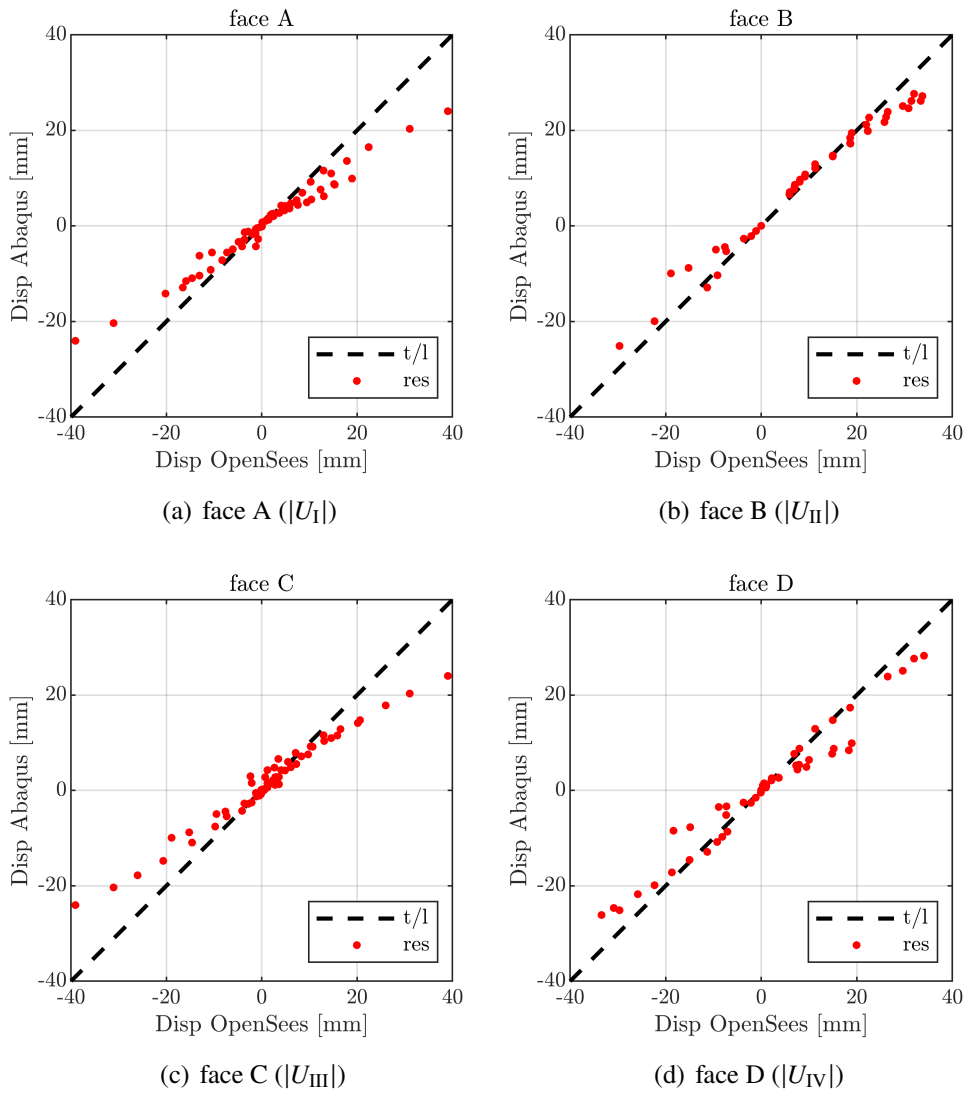


Figure H.4: HR-EFM-IF-R0.

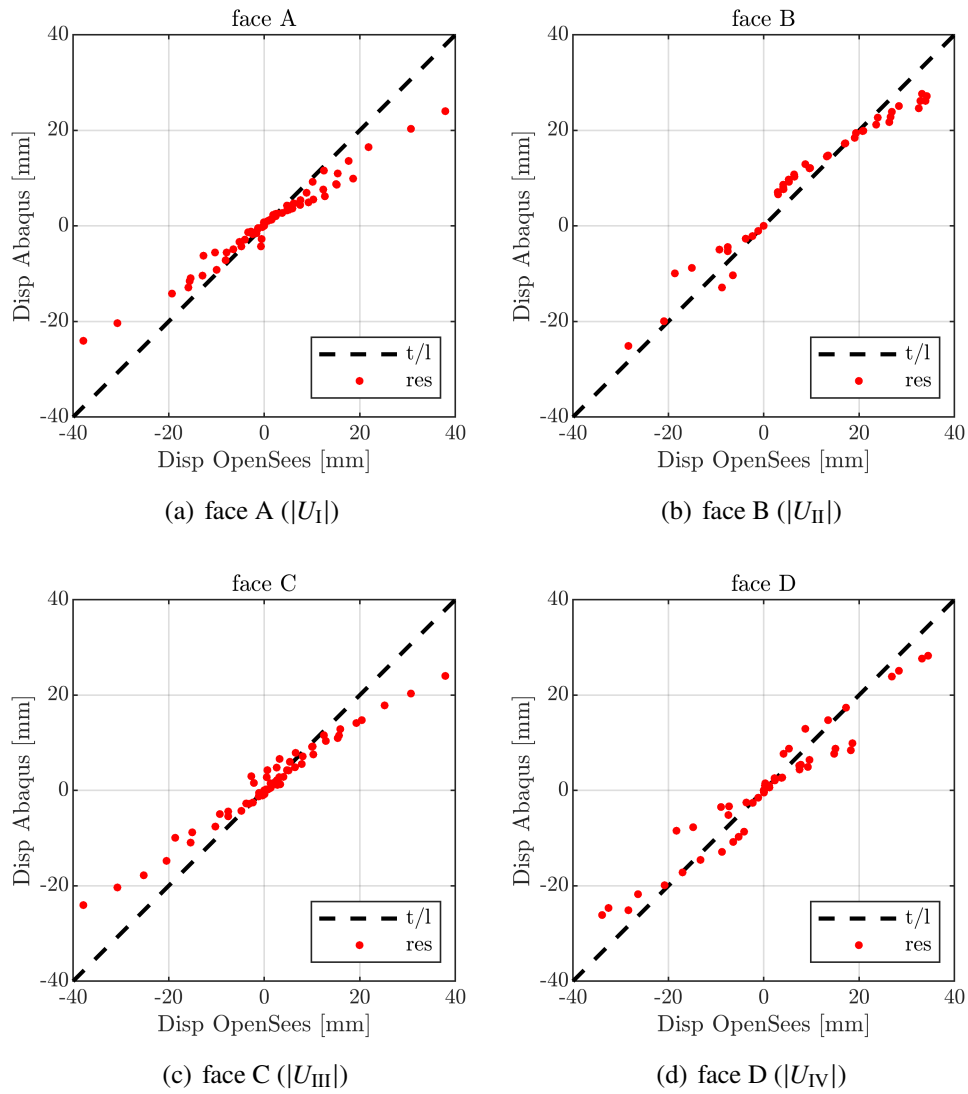


Figure H.5: HR-EFM-IEq-R0.

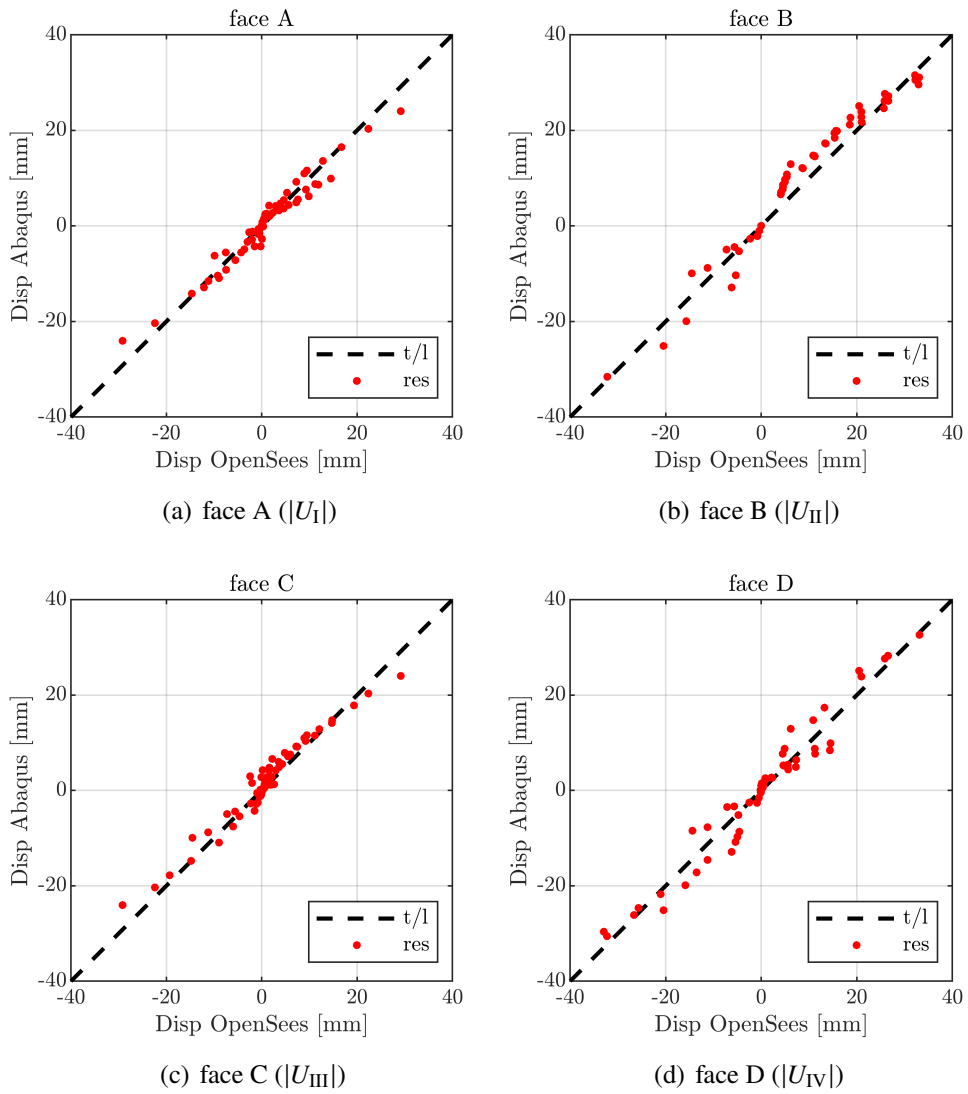


Figure H.6: HR-EFM-IF-R1.

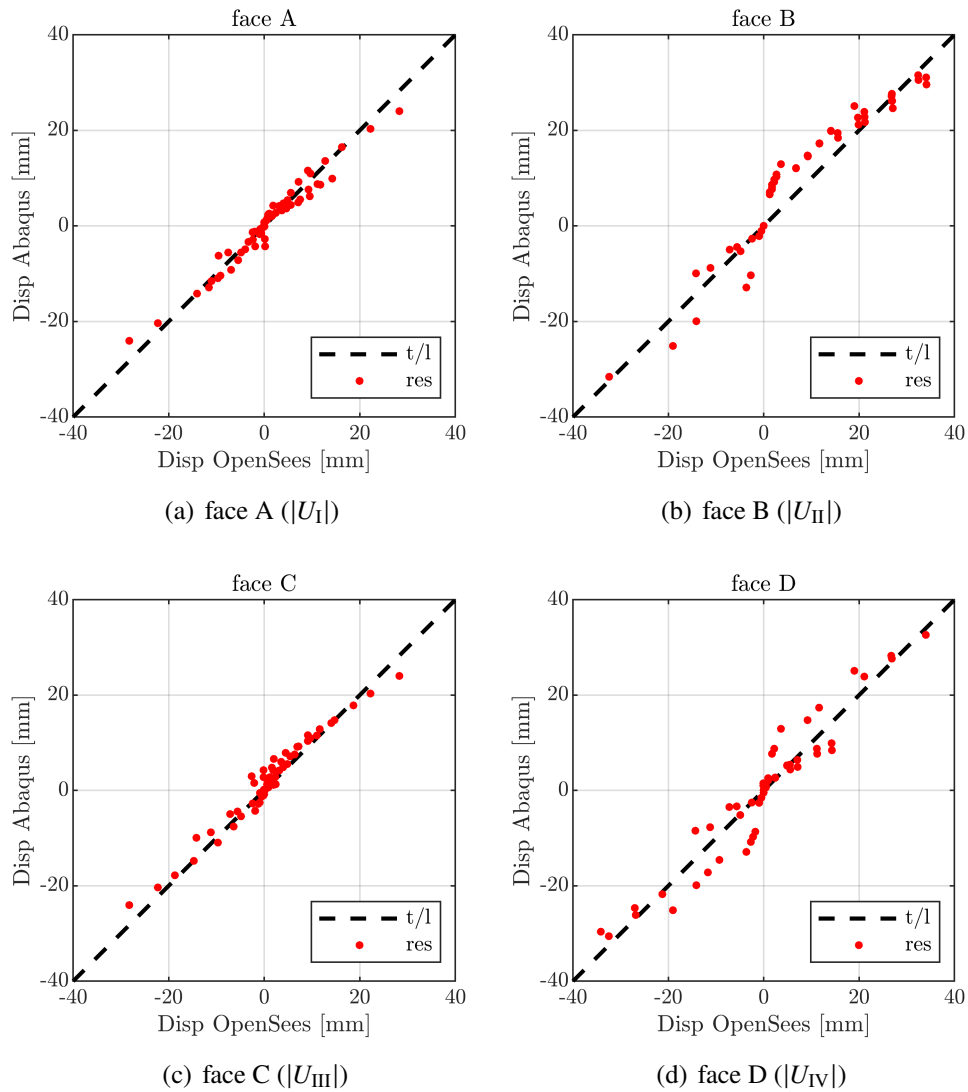


Figure H.7: HR-EFM-IEq-R1.

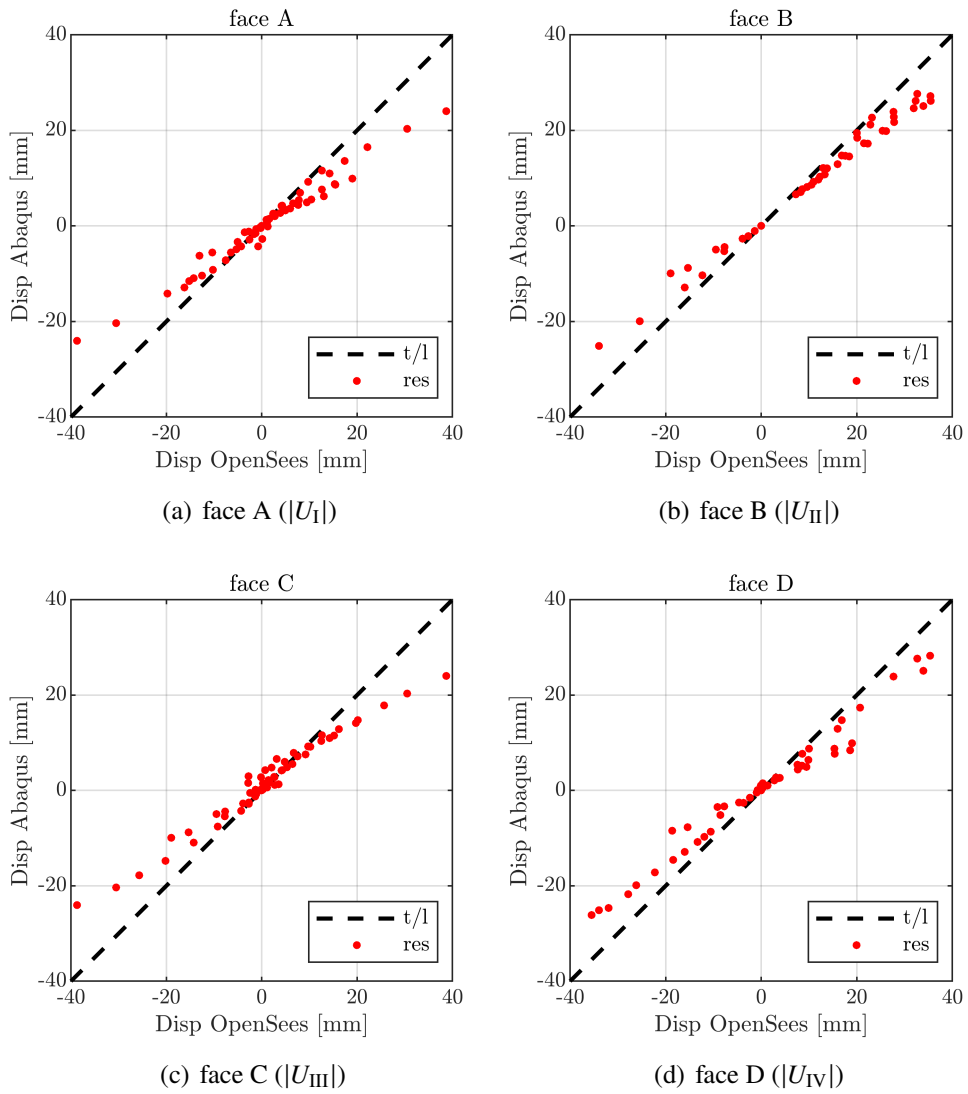


Figure H.8: PR-EFM-IF-R0.

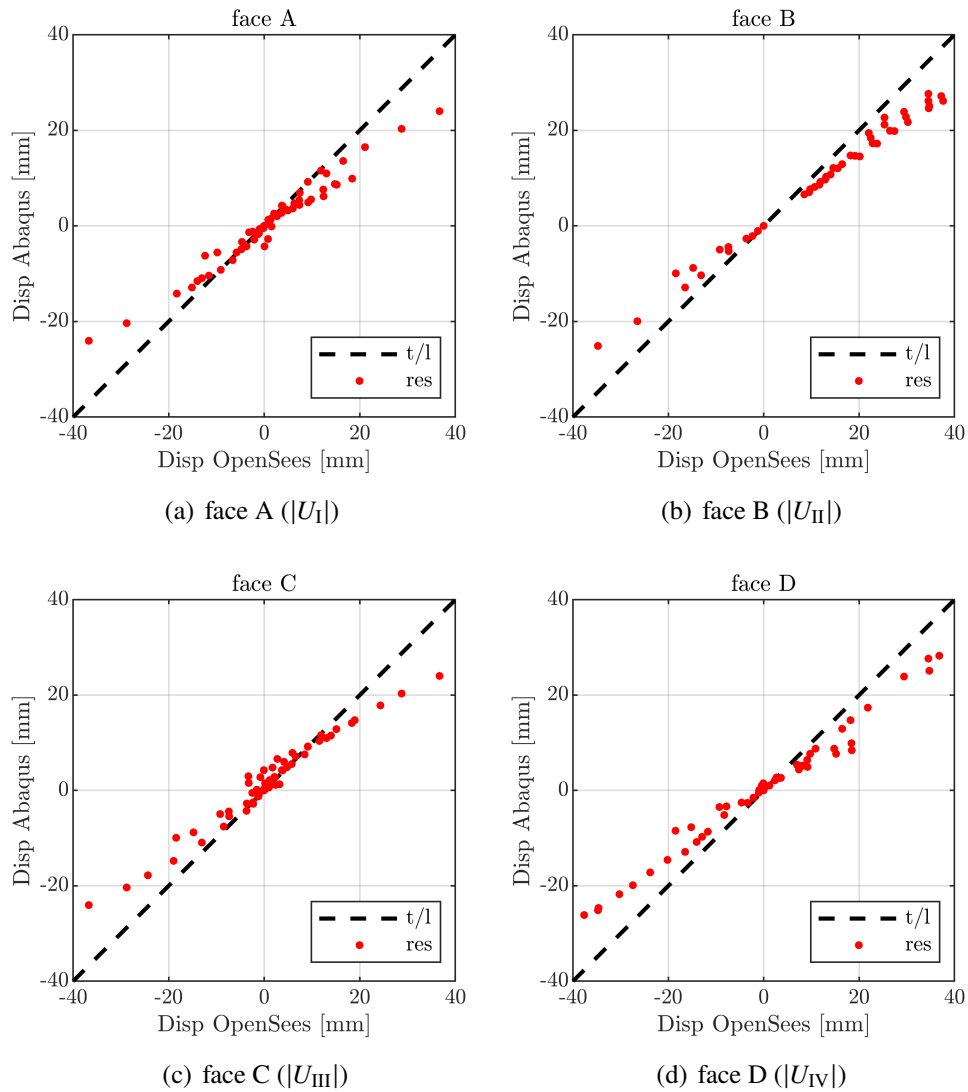


Figure H.9: PR-EFM-IEq-R0.

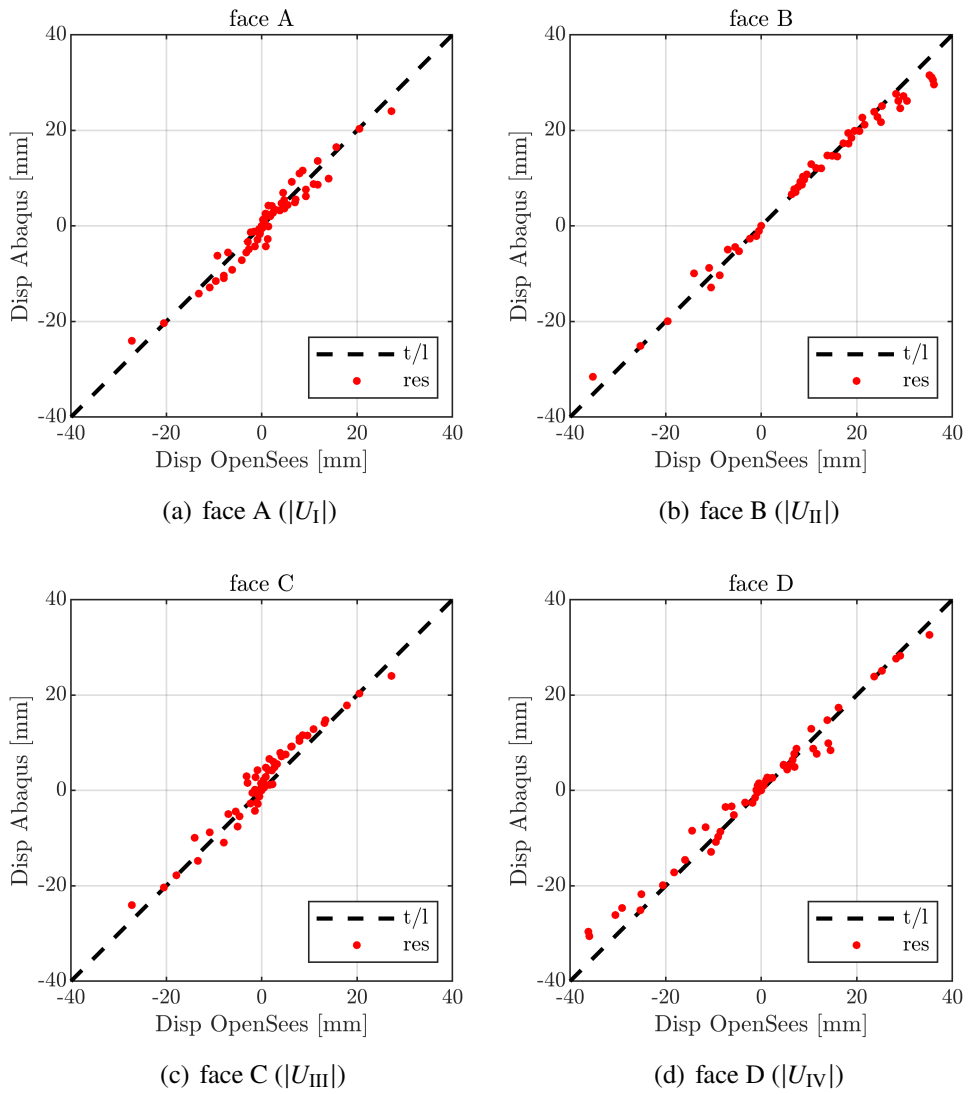


Figure H.10: PR-EFM-IEq-R1.

Appendix I: Results RFEMs - material elastic-plastic

The values of the elastic displacement, δ_{el}^i , and minimum elastic displacement, $\delta_{el.min}^i$, where i represents the column face {A, B, C, D}, obtained using the methodology presented in Section 5.5.5, are presented for all cases for the SHS and RHS in Tab. I.1 and Tab. I.2, respectively.

Table I.1: Values of displacements δ_{el}^i and $\delta_{el.min}^i$ for SHS.

LP	SC	δ_{el}				$\delta_{el.min}$			
		δ_{el}^A	δ_{el}^B	δ_{el}^C	δ_{el}^D	$\delta_{el.min}^A$	$\delta_{el.min}^B$	$\delta_{el.min}^C$	$\delta_{el.min}^D$
m01	01	-2.07	0.00	0.00	0.00	-2.07	-0.56	0.25	0.56
m01	02	-1.88	0.00	0.00	0.00	-1.88	-0.54	0.26	0.54
m01	03	-1.21	0.00	0.00	0.00	-1.21	-0.40	0.21	0.40
m01	04	-0.54	0.00	0.00	0.00	-0.54	-0.22	0.13	0.22
m02-CH	01	0.00	-2.15	2.15	0.00	-0.66	-2.15	2.15	0.66
m02-CH	02	0.00	-1.96	1.96	0.00	-0.65	-1.96	1.96	0.65
m02-CH	03	0.00	-1.26	1.26	0.00	-0.48	-1.26	1.26	0.48
m02-CH	04	0.00	-0.55	0.55	0.00	-0.25	-0.55	0.55	0.25
m02-CV	01	0.00	1.55	1.55	0.00	0.31	1.55	1.55	0.31
m02-CV	02	0.00	1.37	1.37	0.00	0.29	1.37	1.37	0.29
m02-CV	03	0.00	0.82	0.82	0.00	0.20	0.82	0.82	0.20
m02-CV	04	0.00	0.33	0.33	0.00	0.10	0.33	0.33	0.10
m02-H	01	1.84	0.00	1.84	0.00	1.84	0.00	1.84	0.00
m02-H	02	1.64	0.00	1.64	0.00	1.64	0.00	1.64	0.00
m02-H	03	1.01	0.00	1.01	0.00	1.01	0.00	1.01	0.00
m02-H	04	0.42	0.00	0.42	0.00	0.42	0.00	0.42	0.00
m02-V	01	-2.25	0.00	2.25	0.00	-2.25	-1.08	2.25	1.08
m02-V	02	-2.06	0.00	2.06	0.00	-2.06	-1.04	2.06	1.04
m02-V	03	-1.32	0.00	1.32	0.00	-1.32	-0.75	1.32	0.75
m02-V	04	-0.57	0.00	0.57	0.00	-0.57	-0.37	0.57	0.37
m03-H	01	2.33	2.03	1.33	0.00	2.33	2.03	1.24	-0.24
m03-H	02	2.11	1.83	1.14	0.00	2.11	1.83	1.05	-0.25

Continued on next page ...

Table I.1: Values of displacements δ_{el}^i and $\delta_{el.min}^i$ for SHS (*cont.*).

LP	SC	δ_{el}				$\delta_{el.min}$			
		δ_{el}^A	δ_{el}^B	δ_{el}^C	δ_{el}^D	$\delta_{el.min}^A$	$\delta_{el.min}^B$	$\delta_{el.min}^C$	$\delta_{el.min}^D$
m03-H	03	1.35	1.16	0.63	0.00	1.16	1.16	1.16	1.16
m03-H	04	0.54	0.46	0.18	0.00	0.46	0.46	0.46	0.46
m03-V	01	-1.77	0.96	1.77	0.00	-1.77	0.96	1.77	0.87
m03-V	02	-1.60	0.80	1.60	0.00	-1.60	0.80	1.60	0.83
m03-V	03	-1.00	0.39	1.00	0.00	-1.00	0.39	1.00	0.58
m03-V	04	-0.42	0.09	0.42	0.00	-0.42	0.10	0.42	0.29
m04-H	01	1.53	1.53	1.53	1.53	1.53	1.53	1.53	1.53
m04-H	02	1.35	1.35	1.35	1.35	1.35	1.35	1.35	1.35
m04-H	03	0.80	0.80	0.80	0.80	0.80	0.80	0.80	0.80
m04-H	04	0.32	0.32	0.32	0.32	0.32	0.32	0.32	0.32
m04-V	01	-1.26	1.26	1.26	-1.26	-1.26	1.26	1.26	-1.26
m04-V	02	-1.11	1.11	1.11	-1.11	-1.11	1.11	1.11	-1.11
m04-V	03	-0.64	0.64	0.64	-0.64	-0.64	0.64	0.64	-0.64
m04-V	04	-0.24	0.24	0.24	-0.24	-0.24	0.24	0.24	-0.24
m04-VnVp	01	-2.21	-2.21	2.21	2.21	-2.21	-2.21	2.21	2.21
m04-VnVp	02	-2.01	-2.01	2.01	2.01	-2.01	-2.01	2.01	2.01
m04-VnVp	03	-1.29	-1.29	1.29	1.29	-1.29	-1.29	1.29	1.29
m04-VnVp	04	-0.55	-0.55	0.55	0.55	-0.55	-0.55	0.55	0.55

Table I.2: Values of displacements δ_{el}^i and $\delta_{el.min}^i$ for RHS.

LP	SC	δ_{el}				$\delta_{el.min}$			
		δ_{el}^A	δ_{el}^B	δ_{el}^C	δ_{el}^D	$\delta_{el.min}^A$	$\delta_{el.min}^B$	$\delta_{el.min}^C$	$\delta_{el.min}^D$
m01-V01	01	-2.20	0.00	0.00	0.00	-2.20	-0.85	0.22	0.85
m01-V01	02	-2.01	0.00	0.00	0.00	-2.01	-0.85	0.23	0.85
m01-V01	03	-1.34	0.00	0.00	0.00	-1.34	-0.72	0.18	0.72
m01-V01	04	-0.63	0.00	0.00	0.00	-0.63	-0.44	0.09	0.44
m01-V02	01	0.00	4.07	0.00	0.00	0.65	4.07	-0.65	-0.45
m01-V02	02	0.00	3.88	0.00	0.00	0.63	3.88	-0.63	-0.47

Continued on next page ...

Table I.2: Values of displacements δ_{el}^i and $\delta_{el.min}^i$ for RHS (*cont.*).

LP	SC	δ_{el}				$\delta_{el.min}$			
		δ_{el}^A	δ_{el}^B	δ_{el}^C	δ_{el}^D	$\delta_{el.min}^A$	$\delta_{el.min}^B$	$\delta_{el.min}^C$	$\delta_{el.min}^D$
m01-V02	03	0.00	2.99	0.00	0.00	0.47	2.99	-0.47	-0.44
m01-V02	04	0.00	1.97	0.00	0.00	0.27	1.97	-0.27	-0.33
m02-CH01	01	0.00	-4.28	2.10	0.00	-0.74	-4.28	2.11	1.00
m02-CH01	02	0.00	-4.06	1.89	0.00	-0.71	-4.06	1.90	0.99
m02-CH01	03	0.00	-3.21	1.17	0.00	-0.52	-3.07	1.17	0.80
m02-CH01	04	0.00	-2.09	0.46	0.00	-0.25	-1.71	0.46	0.43
m02-CH02	01	0.00	4.28	-2.10	0.00	0.74	4.28	-2.11	-1.00
m02-CH02	02	0.00	4.06	-1.89	0.00	0.71	4.06	-1.90	-0.99
m02-CH02	03	0.00	3.21	-1.17	0.00	0.52	3.07	-1.17	-0.80
m02-CH02	04	0.00	2.09	-0.46	0.00	0.25	1.71	-0.46	-0.43
m02-CV	01	0.00	3.44	0.98	0.00	0.45	3.24	0.98	0.19
m02-CV	02	0.00	3.25	0.76	0.00	0.41	2.90	0.76	0.13
m02-CV	03	0.00	2.56	0.28	0.00	0.26	1.87	0.28	0.01
m02-CV	04	0.00	1.75	0.00	0.00	0.22	1.75	0.05	-0.10
m02-H01	01	2.01	0.00	2.01	0.00	2.01	0.00	2.01	0.00
m02-H01	02	1.81	0.00	1.81	0.00	1.81	0.00	1.81	0.00
m02-H01	03	1.17	0.00	1.17	0.00	1.17	0.00	1.17	0.00
m02-H01	04	0.54	0.00	0.54	0.00	0.54	0.00	0.54	0.00
m02-H02	01	0.00	3.66	0.00	3.66	0.00	3.66	0.00	3.66
m02-H02	02	0.00	3.40	0.00	3.40	0.00	3.40	0.00	3.40
m02-H02	03	0.00	2.57	0.00	2.57	0.00	2.57	0.00	2.57
m02-H02	04	0.00	1.65	0.00	1.65	0.00	1.65	0.00	1.65
m02-V01	01	-2.37	0.00	2.37	0.00	-2.37	-1.66	2.37	1.66
m02-V01	02	-2.19	0.00	2.19	0.00	-2.19	-1.66	2.19	1.66
m02-V01	03	-1.46	0.00	1.46	0.00	-1.46	-1.38	1.46	1.38
m02-V01	04	-0.68	0.00	0.68	0.00	-0.68	-0.83	0.68	0.83
m02-V02	01	0.00	4.43	0.00	-4.43	1.27	4.43	-1.27	-4.43
m02-V02	02	0.00	4.23	0.00	-4.23	1.22	4.23	-1.22	-4.23
m02-V02	03	0.00	3.30	0.00	-3.30	0.90	3.30	-0.90	-3.30

Continued on next page ...

Table I.2: Values of displacements δ_{el}^i and $\delta_{el.min}^i$ for RHS (*cont.*).

LP	SC	δ_{el}				$\delta_{el.min}$			
		δ_{el}^A	δ_{el}^B	δ_{el}^C	δ_{el}^D	$\delta_{el.min}^A$	$\delta_{el.min}^B$	$\delta_{el.min}^C$	$\delta_{el.min}^D$
m02-V02	04	0.00	2.14	0.00	-2.14	0.50	2.14	-0.50	-2.14
m03-H01	01	1.97	3.70	0.72	0.00	1.80	3.39	0.72	-0.38
m03-H01	02	1.76	3.52	0.53	0.00	1.50	3.00	0.53	-0.37
m03-H01	03	1.08	2.80	0.15	0.00	0.69	1.73	0.15	-0.25
m03-H01	04	0.43	1.89	0.00	0.00	0.16	0.58	0.00	-0.10
m03-H02	01	0.00	3.03	1.71	4.36	-0.17	3.01	1.71	4.32
m03-H02	02	0.00	2.81	1.49	4.10	-0.17	2.80	1.49	4.05
m03-H02	03	0.00	2.14	0.83	3.09	-0.11	2.06	0.83	2.95
m03-H02	04	0.00	1.43	0.27	1.90	-0.04	1.18	0.27	1.56
m03-V01	01	-1.13	2.80	1.13	0.00	-1.13	2.61	1.13	0.79
m03-V01	02	-0.92	2.64	0.92	0.00	-0.92	2.37	0.92	0.70
m03-V01	03	-0.39	2.10	0.39	0.00	-0.39	1.67	0.39	0.38
m03-V01	04	-0.05	1.52	0.05	0.00	-0.05	0.80	0.05	0.07
m03-V02	01	0.00	3.83	0.37	-3.83	1.09	3.73	0.37	-3.73
m03-V02	02	0.00	3.68	0.19	-3.68	0.90	3.08	0.19	-3.08
m03-V02	03	0.00	2.92	0.13	-2.92	0.81	2.92	-0.09	-2.92
m03-V02	04	0.00	1.99	0.20	-1.99	0.48	1.99	-0.21	-1.99
m04-H	01	1.40	3.32	1.40	3.32	1.39	3.32	1.39	3.32
m04-H	02	1.20	3.12	1.20	3.12	1.21	3.12	1.21	3.12
m04-H	03	0.66	2.43	0.66	2.43	0.66	2.31	0.66	2.31
m04-H	04	0.22	1.60	0.22	1.60	0.22	1.30	0.22	1.30
m04-V	01	-0.58	3.24	0.58	-3.24	-0.56	3.24	0.56	-3.24
m04-V	02	-0.39	3.10	0.39	-3.10	-0.39	3.06	0.39	-3.06
m04-V	03	-0.01	2.53	0.01	-2.53	-0.02	2.53	0.02	-2.53
m04-V	04	-0.16	1.84	0.16	-1.84	0.17	1.84	-0.17	-1.84
m04-VnVp01	01	-2.27	-4.21	2.27	4.21	-2.27	-4.19	2.27	4.19
m04-VnVp01	02	-2.08	-4.05	2.08	4.05	-2.08	-4.01	2.08	4.01
m04-VnVp01	03	-1.35	-3.22	1.35	3.22	-1.35	-3.10	1.35	3.10
m04-VnVp01	04	-0.58	-2.10	0.58	2.10	-0.58	-1.75	0.58	1.75

Continued on next page ...

Table I.2: Values of displacements δ_{el}^i and $\delta_{el.min}^i$ for RHS (*cont.*).

LP	SC	δ_{el}				$\delta_{el.min}$			
		δ_{el}^A	δ_{el}^B	δ_{el}^C	δ_{el}^D	$\delta_{el.min}^A$	$\delta_{el.min}^B$	$\delta_{el.min}^C$	$\delta_{el.min}^D$
m04-VnVp02	01	2.32	4.36	-2.32	-4.36	2.32	4.29	-2.32	-4.29
m04-VnVp02	02	2.10	4.10	-2.10	-4.10	2.10	4.05	-2.10	-4.05
m04-VnVp02	03	1.35	3.22	-1.35	-3.22	1.35	3.10	-1.35	-3.10
m04-VnVp02	04	0.58	2.10	-0.58	-2.10	0.58	1.75	-0.58	-1.75

Appendix J: Attainment of $F_{el} - \delta_{el}$

The results of δ_{el}^i and $\delta_{el.min}^i$ for each case, where i represents the column faces {A, B, C, D}, are shown in Appendix I in Tab. I.1 and Tab. I.2 for the SHS and RHS, respectively.

A worked example for the RHS-m03-H01-SC02 case is provided below:

1. extract the nonlinear force - out-of-plane displacement curve, $F - \delta$, from Abaqus from the RP for all column faces: continuous black lines in Fig. J.1;
2. calculate area under the nonlinear curve, A_{nl} ;
3. determine the tangent stiffness, $S_{i.nl}$ – secant stiffness at 5% of the ultimate load, F_{end} : red dotted line in Fig. J.1;
4. construct the elastic-perfect plastic curve using the tangent stiffness, $S_{i.nl}$, and ultimate load, F_{end} ; blue dashed line in Fig. J.1;
5. calculate the area under the elastic-perfect plastic curve, A_{epp} which is used as a starting point for the iterative process;
6. initiate an iterative process that starts from the elastic-perfect plastic curve and ends when a bilinear curve is found so that the area of the bilinear curve is close to the area under the nonlinear curve: $A_{bl} \approx A_{nl}$ while ensuring that the initial and final coordinates of the two curves coincide and have equivalent tangent stiffnesses, $S_{i.nl} = S_{i.bl}$.
7. construct the bilinear curve maintaining the tangent stiffness, $S_{i.nl}$ and ultimate load, F_{end} : magenta dashed line in Fig. J.1;
8. identify the elastic force, F_{el} , and the elastic displacement, δ_{el} , from the bilinear curve: green "x" markers in Fig. J.1; if the face of the column is not loaded (i.e., $A_{nl} = 0$), then $F_{el} = \delta_{el} = 0$;

For the analyzed case, the values of the elastic forces and displacements in absolute values are:

$$F_{el}^A = 129.51 \text{ kN} \quad F_{el}^B = 128.68 \text{ kN} \quad F_{el}^C = 111.27 \text{ kN} \quad F_{el}^D = 0.00 \text{ kN} \quad (\text{J.1})$$

$$\delta_{el}^A = 1.76 \text{ mm} \quad \delta_{el}^B = 3.52 \text{ mm} \quad \delta_{el}^C = 0.53 \text{ mm} \quad \delta_{el}^D = 0.00 \text{ mm} \quad (\text{J.2})$$

thus, the minimum elastic force and its corresponding elastic displacements and face ID are:

$$F_{el.min} = \min(F_{el}^A, F_{el}^B, F_{el}^C, F_{el}^D) = F_{el}^C \quad (= 111.27 \text{ kN}) \quad (\text{J.3})$$

$$\delta_{el.min} = \delta_{el}^C \quad (= 0.53 \text{ mm}) \quad (\text{J.4})$$

and the face ID:

$$\text{ID}_{min} = \text{C} \quad (\text{J.5})$$

From the RFEMs developed for the stiffness case, the displacements are (shown in Tab. G.2 in Appendix G):

$$\delta_A = 13.62 \text{ mm} \quad \delta_B = 27.20 \text{ mm} \quad \delta_C = 4.82 \text{ mm} \quad \delta_D = -3.33 \text{ mm} \quad (\text{J.6})$$

Knowing that the computation of the limit elastic displacement for each face of the column is made using the ratio between the elastic out-of-plane displacements:

$$\delta_{el.min}^i = \frac{\delta_i}{\delta_{\text{ID}_{min}}} \delta_{el.min} \quad , \text{ with } i \in \{A, B, C, D\} \quad (\text{J.7})$$

where δ_i is the elastic displacement in column face i and $\delta_{\text{ID}_{min}}$ is the elastic displacement in column face, ID_{min} , for the arbitrary load parameter computed using RFEMs.

By applying Eq. (J.7), the minimum elastic of each column face becomes:

$$\delta_{el.min}^A = \frac{\delta_A}{\delta_C} \delta_{el.min} = 1.50 \text{ mm} \quad (\text{J.8})$$

$$\delta_{el.min}^B = \frac{\delta_B}{\delta_C} \delta_{el.min} = 3.00 \text{ mm} \quad (\text{J.9})$$

$$\delta_{el.min}^C = \frac{\delta_C}{\delta_C} \delta_{el.min} = 0.53 \text{ mm} \quad (\text{J.10})$$

$$\delta_{el.min}^D = \frac{\delta_D}{\delta_C} \delta_{el.min} = -0.37 \text{ mm} \quad (\text{J.11})$$

Therefore, the vector containing the minimum elastic displacements, $\delta_{el,min}$, for the RHS-m03-H01-SC02 case is:

$$\delta_{el,min}^{RFEM} = \begin{bmatrix} 1.50 & 3.00 & 0.53 & -0.37 \end{bmatrix}^T \quad (J.12)$$

The values for the remaining cases are presented in Appendix I in Tab. I.1 and Tab. I.2 for the SHS and RHS, respectively.

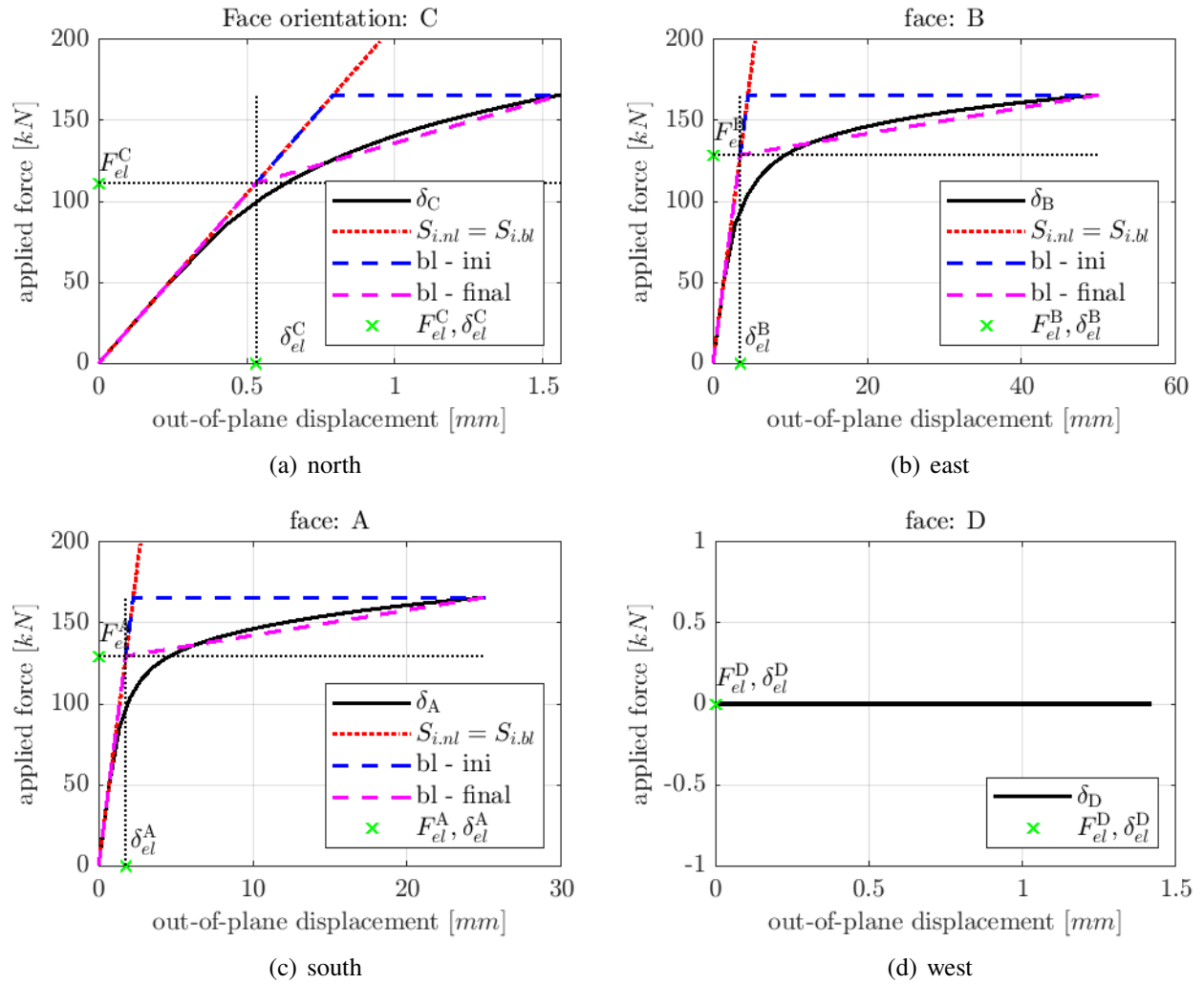


Figure J.1: $F_{el} - \delta_{el}$ (absolute value) curve: for RHS-m03-H01-SC02.

Appendix K: Detailed analytical computation of the strength criterion of the EFMs

The analytical computation of the strength criterion for the beam-to-column joint finite element discussed in Section 2.6.5 is presented in detail in the subsequent sections for all six EFMs separately. It is worth noting that each computation follows the methodology outlined in Section 5.5.

K.1 HS-EFM

Fig. K.1(a) and Fig. K.1(b) present the HS-EFM and its SEFM with critical sections. Furthermore, the relationship between the stiffness coefficients associated with DOF d_3 and the dependency on DOFs d_1 and d_2 is depicted in Fig. K.2 and mathematically expressed in Eqs. (K.1) to (K.3).

Additionally, the bending moments in the critical sections caused by a unit load applied to the DOFs are shown in Fig. K.3 and described by Eqs. (K.4) to (K.9). Finally, Fig. K.4 depicts the equivalent bending strengths for the critical sections, expressed by Eq. (K.10).

$$\mathbf{d}^{\text{HS.EFM}} = \begin{bmatrix} d_1^{\text{HS.EFM}} & d_2^{\text{HS.EFM}} & d_3^{\text{HS.EFM}} \end{bmatrix}^T \quad (\text{K.1})$$

$$0 = \begin{bmatrix} -\frac{6EI}{(L/2)^2} & \frac{6EI}{(L/2)^2} & \frac{4EI}{(L/2)} + \frac{4EI}{(L/2)} \end{bmatrix} \mathbf{d}^{\text{HS.EFM}} \quad (\text{K.2})$$

$$d_3^{\text{HS.EFM}} = \frac{3d_1^{\text{HS.EFM}} - 3d_2^{\text{HS.EFM}}}{2L} \quad (\text{K.3})$$

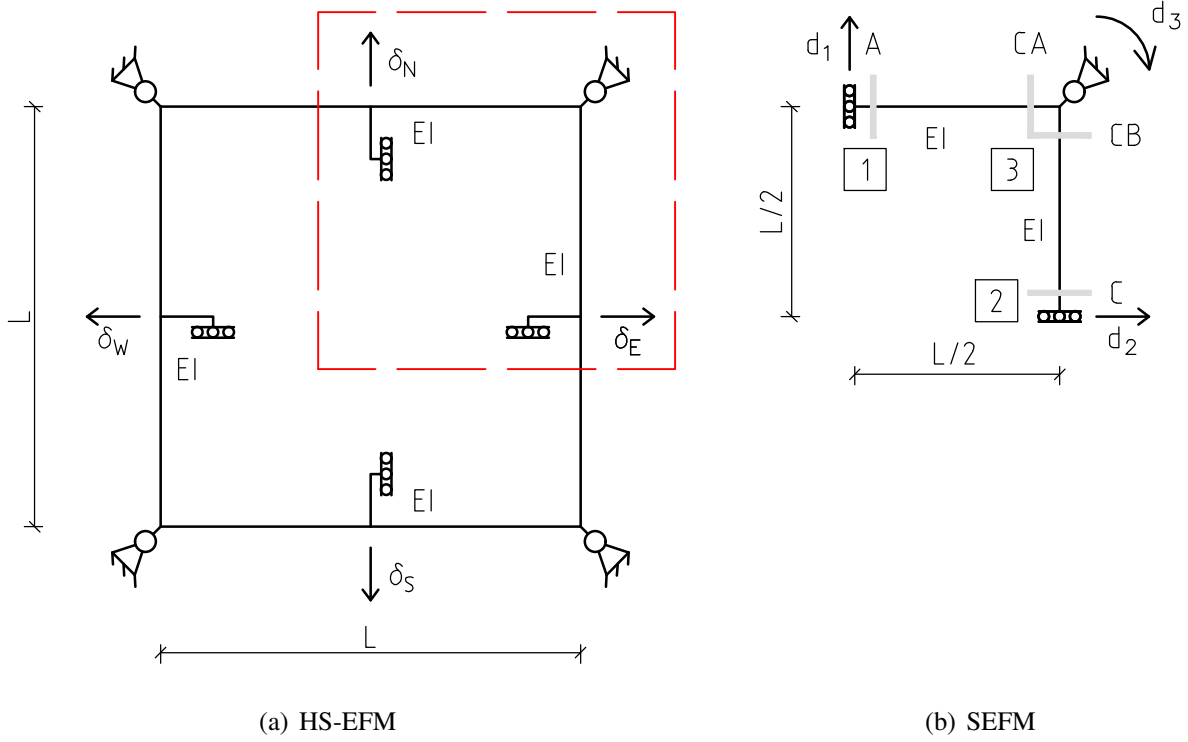


Figure K.1: HS-EFM and its SEFM with the critical sections.

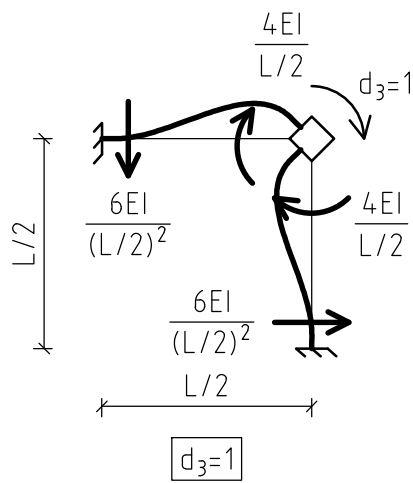


Figure K.2: Stiffness coefficients associated to d_3 for the HS-EFM.

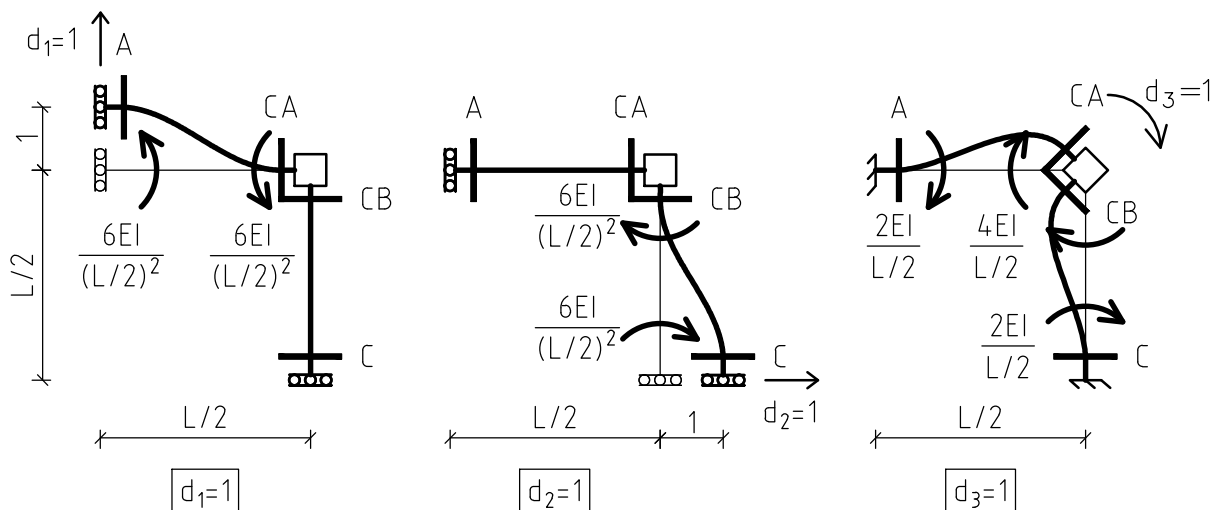


Figure K.3: Bending moments in critical sections under unit load in DOFs for the HS-EFM.

$$\mathbf{M}_d^{\text{HS.EFM}} = \begin{bmatrix} M_A^{d_1} & M_A^{d_2} & M_A^{d_3} \\ M_{CA}^{d_1} & M_{CA}^{d_2} & M_{CA}^{d_3} \\ M_{CB}^{d_1} & M_{CB}^{d_2} & M_{CB}^{d_3} \\ M_B^{d_1} & M_B^{d_2} & M_B^{d_3} \end{bmatrix} = \begin{bmatrix} -\frac{6EI}{(L/2)^2} & 0 & \frac{2EI}{L/2} \\ -\frac{6EI}{(L/2)^2} & 0 & \frac{4EI}{L/2} \\ 0 & \frac{6EI}{(L/2)^2} & \frac{4EI}{L/2} \\ 0 & \frac{6EI}{(L/2)^2} & \frac{2EI}{L/2} \end{bmatrix} \quad (\text{K.4})$$

$$\mathbf{M}^{\text{HS.EFM}} = \mathbf{M}_d^{\text{HS.EFM}} \mathbf{d}^{\text{HS.EFM}} = \begin{bmatrix} M_A^{\text{HS.EFM}} & M_{CA}^{\text{HS.EFM}} & M_{CB}^{\text{HS.EFM}} & M_B^{\text{HS.EFM}} \end{bmatrix}^T \quad (\text{K.5})$$

$$M_A^{\text{HS.EFM}} = -\frac{6EI(3d_1^{\text{HS.EFM}} + d_2^{\text{HS.EFM}})}{L^2} \quad (\text{K.6})$$

$$M_{CA}^{\text{HS.EFM}} = -\frac{12EI(d_1^{\text{HS.EFM}} + d_2^{\text{HS.EFM}})}{L^2} \quad (\text{K.7})$$

$$M_{CB}^{\text{HS.EFM}} = \frac{12EI(d_1^{\text{HS.EFM}} + d_2^{\text{HS.EFM}})}{L^2} \quad (\text{K.8})$$

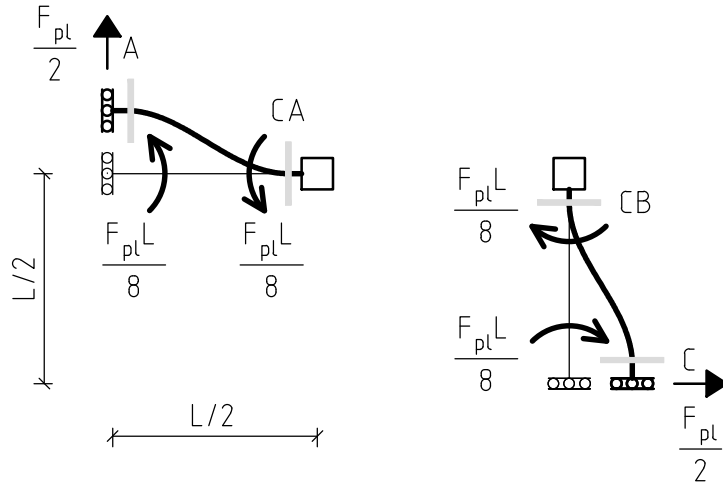


Figure K.4: Bending moments in critical sections under unit load in DOFs for the HS-EFM.

$$M_B^{HS.EFM} = \frac{6 E I (d_1^{HS.EFM} + 3 d_2^{HS.EFM})}{L^2} \quad (K.9)$$

$$\begin{aligned} \mathbf{M}_{y.NGM}^{HS.EFM} &= \begin{bmatrix} M_{y.NGM.A}^{HS.EFM} & M_{y.NGM.CA}^{HS.EFM} & M_{y.NGM.CB}^{HS.EFM} & M_{y.NGM.B}^{HS.EFM} \end{bmatrix}^T \\ &= \begin{bmatrix} -\frac{F_{pl} L}{8} & -\frac{F_{pl} L}{8} & \frac{F_{pl} L}{8} & \frac{F_{pl} L}{8} \end{bmatrix}^T \end{aligned} \quad (K.10)$$

K.2 HR-EFM-IF

Fig. K.5(a) and Fig. K.5(b) present the HR-EFM and its SEFM with critical sections. Furthermore, the relationship between the stiffness coefficients associated with DOF d_3 and the dependency on DOFs d_1 and d_2 is depicted in Fig. K.6 and mathematically expressed in Eqs. (K.11) to (K.13).

Additionally, the bending moments in the critical sections caused by a unit load applied to the DOFs are shown in Fig. K.7 and described by Eqs. (K.14) to (K.19). Finally, Fig. K.8 depicts the equivalent bending strengths for the critical sections, which are expressed by Eq. (K.20).

$$\mathbf{d}^{HR.EFM.IF} = \begin{bmatrix} d_1^{HR.EFM.IF} & d_2^{HR.EFM.IF} & d_3^{HR.EFM.IF} \end{bmatrix}^T \quad (K.11)$$

$$0 = \begin{bmatrix} -\frac{6 E I_1}{(L_1/2)^2} & \frac{6 E I_2}{(L_2/2)^2} & \frac{4 E I_1}{(L_1/2)} + \frac{4 E I_2}{(L_2/2)} \end{bmatrix} \mathbf{d}^{HR.EFM.IF} \quad (K.12)$$

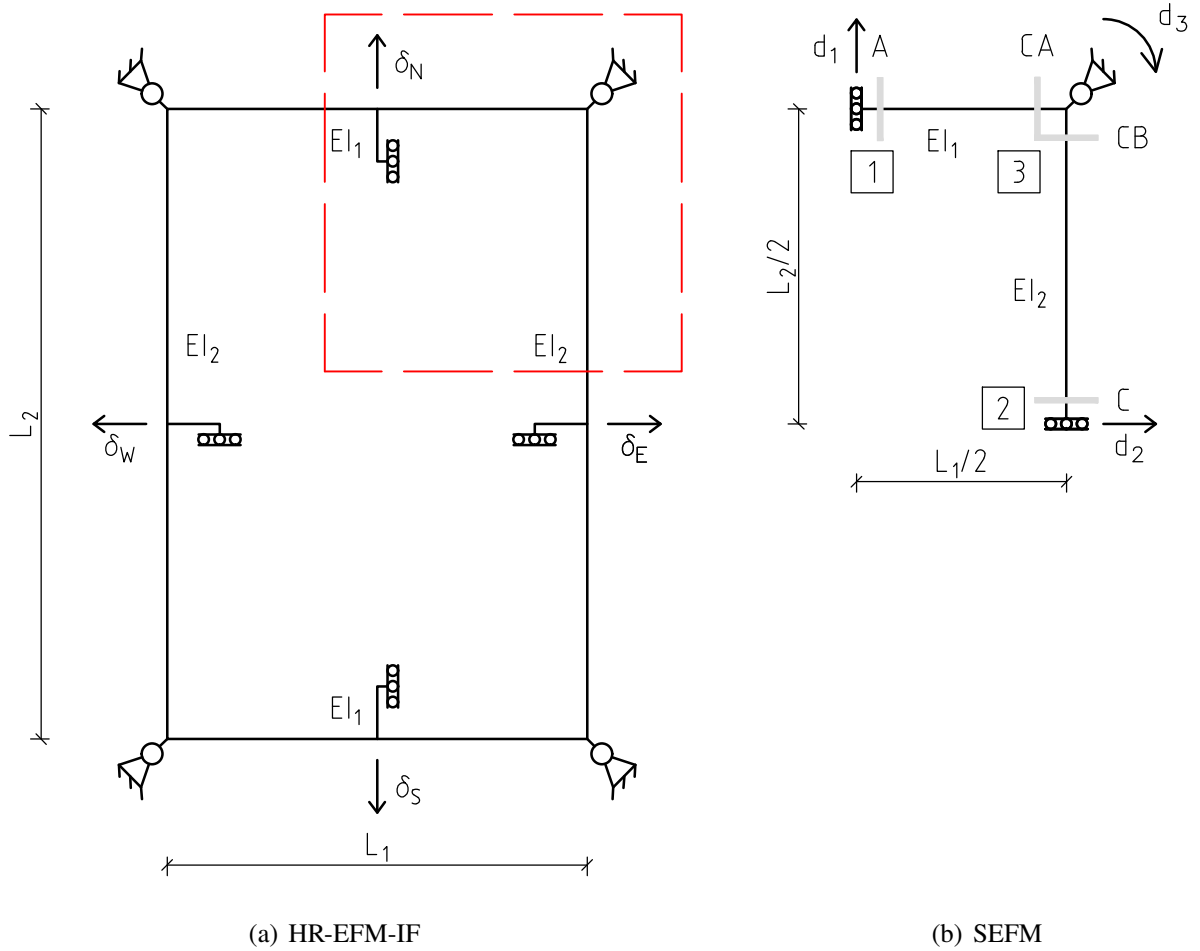


Figure K.5: HR-EFM and its SEFM with the critical sections.

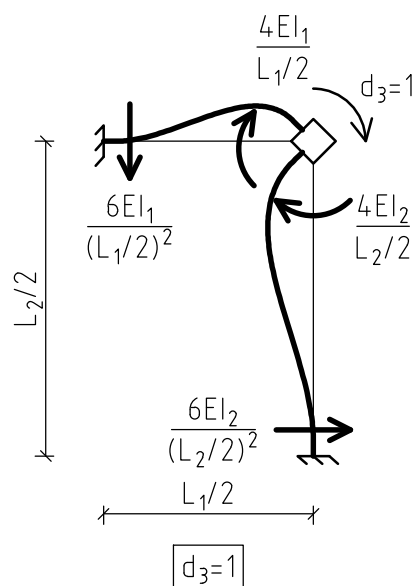


Figure K.6: Stiffness coefficients associated to d_3 for the HR-EFM-IF.

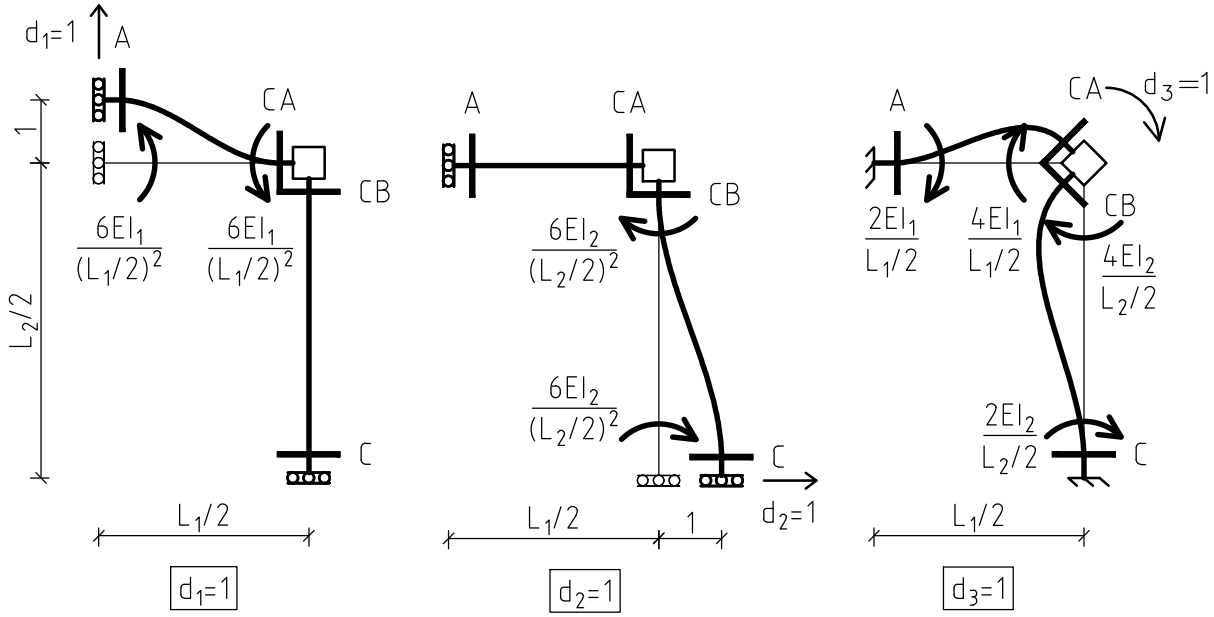


Figure K.7: Bending moments in critical sections under unit load in DOFs for the HR-EFM-IF.

$$d_3^{\text{HR.EFM.IF}} = \frac{-3 I_2 d_2^{\text{HR.EFM.IF}} L_1^2 + 3 I_1 d_1^{\text{HR.EFM.IF}} L_2^2}{L_1 L_2 (I_1 L_2 + I_2 L_1)} \quad (\text{K.13})$$

$$\mathbf{M}_d^{\text{HR.EFM.IF}} = \begin{bmatrix} M_A^{d_1} & M_A^{d_2} & M_A^{d_3} \\ M_{CA}^{d_1} & M_{CA}^{d_2} & M_{CA}^{d_3} \\ M_{CB}^{d_1} & M_{CB}^{d_2} & M_{CB}^{d_3} \\ M_B^{d_1} & M_B^{d_2} & M_B^{d_3} \end{bmatrix} = \begin{bmatrix} -\frac{6 E I_1}{(L_1/2)^2} & 0 & \frac{2 E I_1}{L_1/2} \\ -\frac{6 E I_1}{(L_1/2)^2} & 0 & \frac{4 E I_1}{L_1/2} \\ 0 & \frac{6 E I_2}{(L_2/2)^2} & \frac{4 E I_2}{L_2/2} \\ 0 & \frac{6 E I_2}{(L_2/2)^2} & \frac{2 E I_2}{L_2/2} \end{bmatrix} \quad (\text{K.14})$$

$$\begin{aligned} \mathbf{M}^{\text{HR.EFM.IF}} &= \mathbf{M}_d^{\text{HR.EFM.IF}} \mathbf{d}^{\text{HR.EFM.IF}} \\ &= \begin{bmatrix} M_A^{\text{HR.EFM.IF}} & M_{CA}^{\text{HR.EFM.IF}} & M_{CB}^{\text{HR.EFM.IF}} & M_B^{\text{HR.EFM.IF}} \end{bmatrix}^T \end{aligned} \quad (\text{K.15})$$

$$M_A^{\text{HR.EFM.IF}} = -\frac{12 E I_1 (I_2 d_2^{\text{HR.EFM.IF}} L_1^2 + 2 I_2 d_1^{\text{HR.EFM.IF}} L_1 L_2 + I_1 d_1^{\text{HR.EFM.IF}} L_2^2)}{L_1^2 L_2 (I_1 L_2 + I_2 L_1)} \quad (\text{K.16})$$

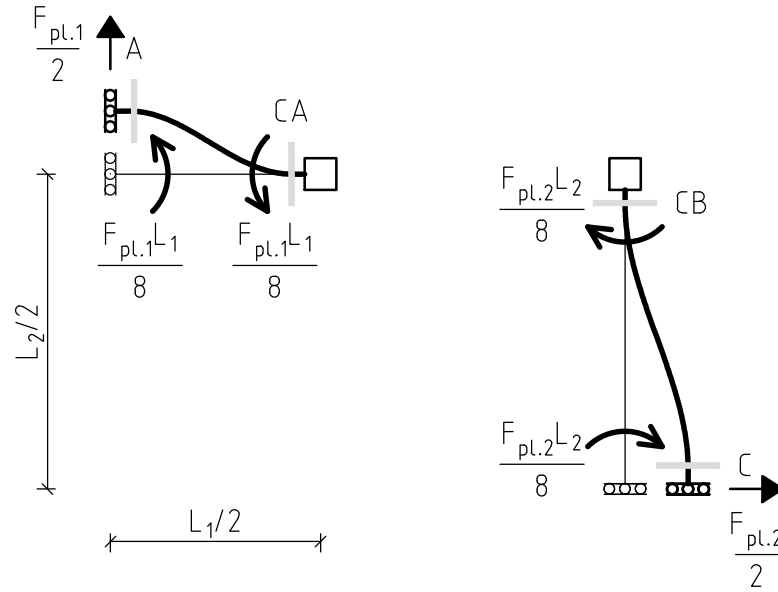


Figure K.8: Bending moments in critical sections under unit load in DOFs for the HR-EFM-IF.

$$M_{CA}^{HR.EFM.IF} = - \frac{24 E I_1 I_2 (L_1 d_2^{HR.EFM.IF} + L_2 d_1^{HR.EFM.IF})}{L_1 L_2 (I_1 L_2 + I_2 L_1)} \quad (K.17)$$

$$M_{CB}^{HR.EFM.IF} = \frac{24 E I_1 I_2 (L_1 d_2^{HR.EFM.IF} + L_2 d_1^{HR.EFM.IF})}{L_1 L_2 (I_1 L_2 + I_2 L_1)} \quad (K.18)$$

$$M_B^{HR.EFM.IF} = \frac{12 E I_2 (I_2 d_2^{HR.EFM.IF} L_1^2 + 2 I_1 d_2^{HR.EFM.IF} L_1 L_2 + I_1 d_1^{HR.EFM.IF} L_2^2)}{L_1 L_2^2 (I_1 L_2 + I_2 L_1)} \quad (K.19)$$

$$\begin{aligned} \mathbf{M}_{y.NGM}^{HR.EFM.IF} &= \begin{bmatrix} M_{y.NGM.A}^{HR.EFM.IF} & M_{y.NGM.CA}^{HR.EFM.IF} & M_{y.NGM.CB}^{HR.EFM.IF} & M_{y.NGM.B}^{HR.EFM.IF} \end{bmatrix}^T \\ &= \begin{bmatrix} -\frac{F_{pl.1} L_1}{8} & -\frac{F_{pl.1} L_1}{8} & \frac{F_{pl.2} L_2}{8} & \frac{F_{pl.2} L_2}{8} \end{bmatrix}^T \end{aligned} \quad (K.20)$$

K.3 HR-EFM-IEq

The relationship between DOF d_3 and DOFs d_1 and d_2 is given by Eq. (K.21). The bending moments in the critical sections are expressed by Eqs. (K.22) to (K.25). The equivalent bending strengths for the critical sections is outlined in Eq. (K.26).

$$d_3^{HR.EFM.IEq} = - \frac{12 E I_{eq} (d_2^{HR.EFM.IEq} L_1^2 + 2 d_1^{HR.EFM.IEq} L_1 L_2 + d_1^{HR.EFM.IEq} L_2^2)}{L_1^2 L_2 (L_1 + L_2)} \quad (K.21)$$

$$M_A^{\text{HR.EFM.IEq}} = - \frac{12 E I_{eq} \left(d_2^{\text{HR.EFM.IEq}} L_1^2 + 2 d_1^{\text{HR.EFM.IEq}} L_1 L_2 + d_1^{\text{HR.EFM.IEq}} L_2^2 \right)}{L_1^2 L_2 (L_1 + L_2)} \quad (\text{K.22})$$

$$M_{CA}^{\text{HR.EFM.IEq}} = - \frac{24 E I_{eq} \left(L_1 d_2^{\text{HR.EFM.IEq}} + L_2 d_1^{\text{HR.EFM.IEq}} \right)}{L_1 L_2 (L_1 + L_2)} \quad (\text{K.23})$$

$$M_{CB}^{\text{HR.EFM.IEq}} = \frac{24 E I_{eq} \left(L_1 d_2^{\text{HR.EFM.IEq}} + L_2 d_1^{\text{HR.EFM.IEq}} \right)}{L_1 L_2 (L_1 + L_2)} \quad (\text{K.24})$$

$$M_B^{\text{HR.EFM.IEq}} = \frac{12 E I_{eq} \left(d_2^{\text{HR.EFM.IEq}} L_1^2 + 2 d_2^{\text{HR.EFM.IEq}} L_1 L_2 + d_1^{\text{HR.EFM.IEq}} L_2^2 \right)}{L_1 L_2^2 (L_1 + L_2)} \quad (\text{K.25})$$

$$\mathbf{M}_{y,\text{NGM}}^{\text{HR.EFM.IEq}} = \mathbf{M}_{y,\text{NGM}}^{\text{HR.EFM.IF}} \quad (\text{K.26})$$

K.4 PS-EFM

Fig. K.9(a) and Fig. K.9(b) present the PS-EFM and its SEFM with critical sections. Furthermore, the relationship between the stiffness coefficients associated with DOF d_3 and the dependency on DOFs d_1 and d_2 is depicted in Fig. K.10 and mathematically expressed in Eqs. (K.27) to (K.29).

Additionally, the bending moments in the critical sections caused by a unit load applied to the DOFs are shown in Fig. K.11 and described by Eqs. (K.30) to (K.35). Finally, Fig. K.12 depicts the equivalent bending strengths for the critical sections, which are expressed by Eq. (K.36).

$$\mathbf{d}^{\text{PS.EFM}} = \left[d_1^{\text{PS.EFM}} \quad d_2^{\text{PS.EFM}} \quad d_3^{\text{PS.EFM}} \right]^T \quad (\text{K.27})$$

$$0 = \left[-\frac{6 E I}{a^2} \quad \frac{6 E I}{a^2} \quad \frac{4 E I}{a} + \frac{4 E I}{a} \right] \mathbf{d}^{\text{PS.EFM}} \quad (\text{K.28})$$

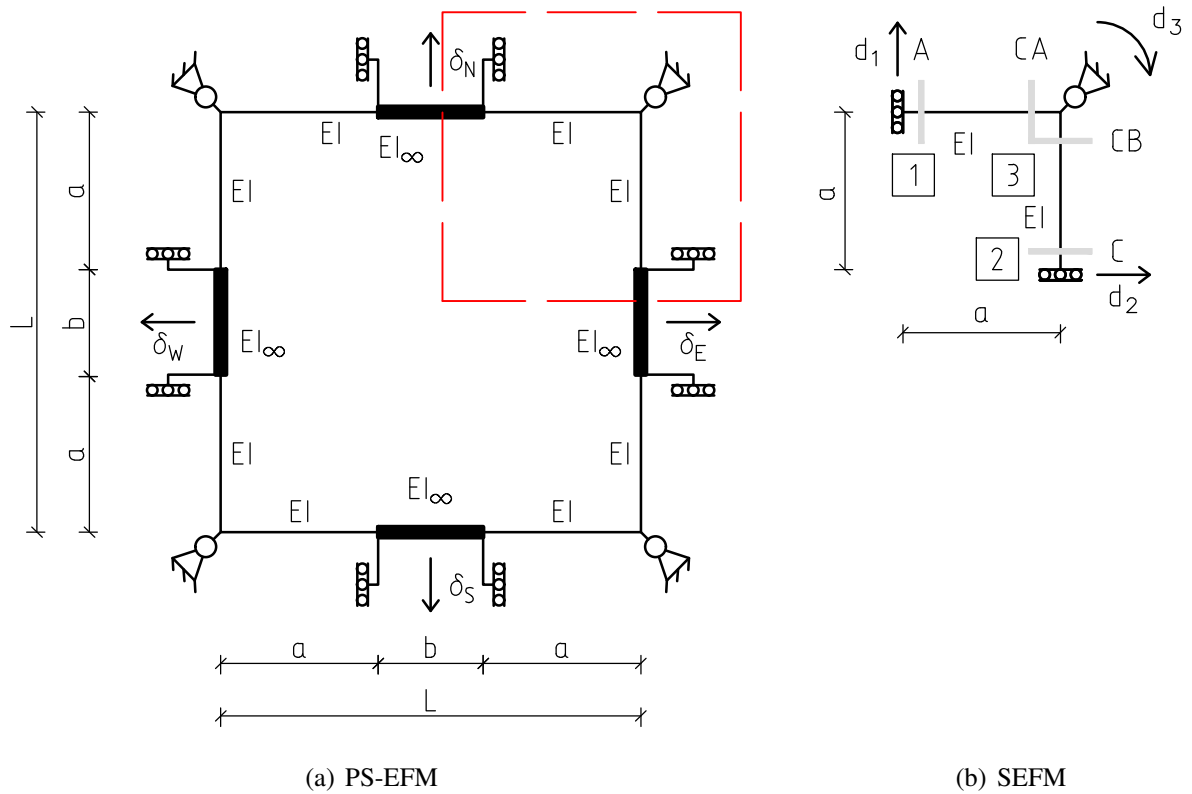


Figure K.9: PS-EFM and its SEFM with the critical sections.

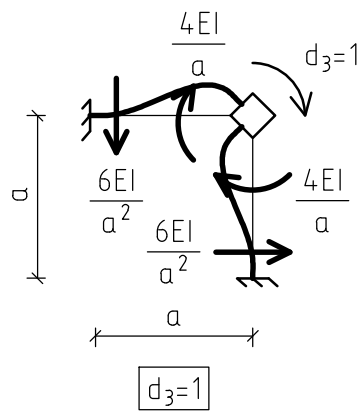


Figure K.10: Stiffness coefficients associated to d_3 for the PS-EFM.

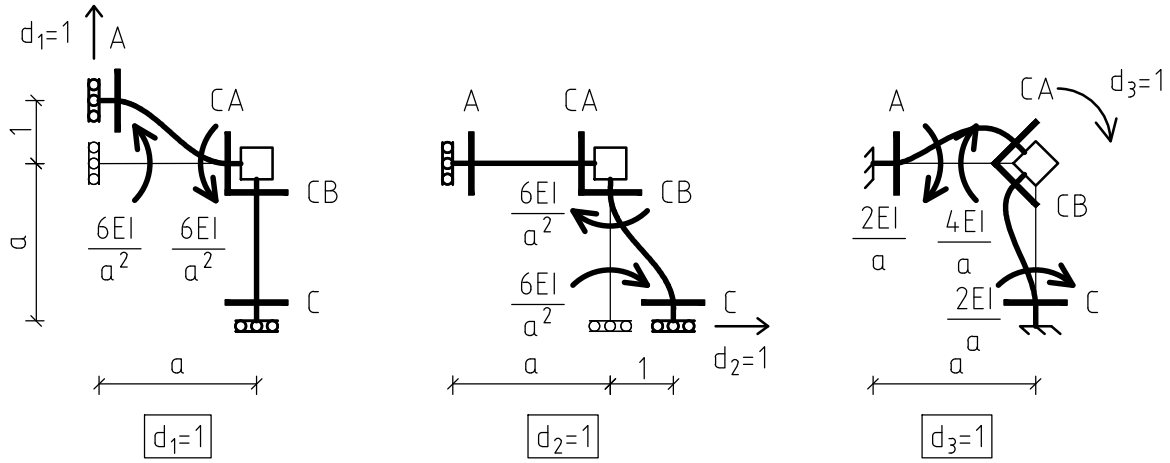


Figure K.11: Bending moments in critical sections under unit load in DOFs for the PS-EFM.

$$d_3^{\text{PS.EFM}} = \frac{3 d_1^{\text{PS.EFM}} - 3 d_2^{\text{PS.EFM}}}{4 a} \quad (\text{K.29})$$

$$\mathbf{M}_d^{\text{PS.EFM}} = \begin{bmatrix} M_A^{d_1} & M_A^{d_2} & M_A^{d_3} \\ M_{CA}^{d_1} & M_{CA}^{d_2} & M_{CA}^{d_3} \\ M_{CB}^{d_1} & M_{CB}^{d_2} & M_{CB}^{d_3} \\ M_B^{d_1} & M_B^{d_2} & M_B^{d_3} \end{bmatrix} = \begin{bmatrix} -\frac{6 E I}{a^2} & 0 & \frac{2 E I}{a} \\ -\frac{6 E I}{a^2} & 0 & \frac{4 E I}{a} \\ 0 & \frac{6 E I}{a^2} & \frac{4 E I}{a} \\ 0 & \frac{6 E I}{a^2} & \frac{2 E I}{a} \end{bmatrix} \quad (\text{K.30})$$

$$\mathbf{M}^{\text{PS.EFM}} = \mathbf{M}_d^{\text{PS.EFM}} \mathbf{d}^{\text{PS.EFM}} = \begin{bmatrix} M_A^{\text{PS.EFM}} & M_{CA}^{\text{PS.EFM}} & M_{CB}^{\text{PS.EFM}} & M_B^{\text{PS.EFM}} \end{bmatrix}^T \quad (\text{K.31})$$

$$M_A^{\text{PS.EFM}} = -\frac{3 E I (3 d_1^{\text{PS.EFM}} + d_2^{\text{PS.EFM}})}{2 a^2} \quad (\text{K.32})$$

$$M_{CA}^{\text{PS.EFM}} = -\frac{3 E I (d_1^{\text{PS.EFM}} + d_2^{\text{PS.EFM}})}{a^2} \quad (\text{K.33})$$

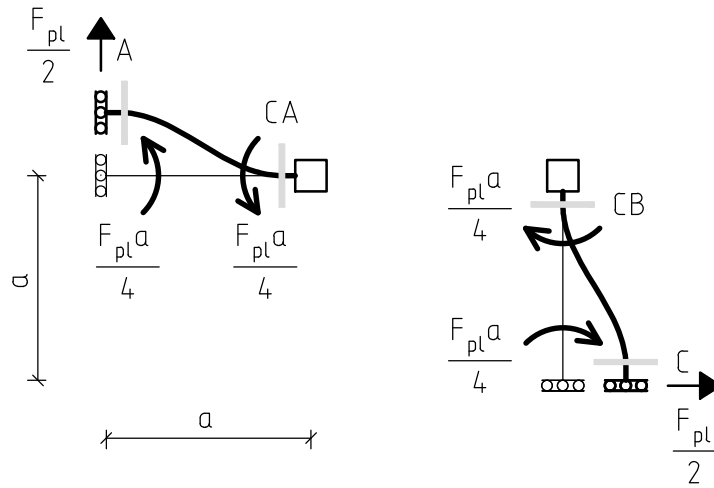


Figure K.12: Bending moments in critical sections under unit load in DOFs for the PS-EFM.

$$M_{CB}^{PS.EFM} = \frac{3 E I (d_1^{PS.EFM} + d_2^{PS.EFM})}{a^2} \quad (K.34)$$

$$M_B^{PS.EFM} = \frac{3 E I (d_1^{PS.EFM} + 3 d_2^{PS.EFM})}{2 a^2} \quad (K.35)$$

$$\begin{aligned} \mathbf{M}_{y.NGM}^{PS.EFM} &= \left[M_{y.NGM.A}^{PS.EFM} \quad M_{y.NGM.CA}^{PS.EFM} \quad M_{y.NGM.CB}^{PS.EFM} \quad M_{y.NGM.B}^{PS.EFM} \right]^T \\ &= \left[-\frac{F_{pl} a}{4} \quad -\frac{F_{pl} a}{4} \quad \frac{F_{pl} a}{4} \quad \frac{F_{pl} a}{4} \right]^T \end{aligned} \quad (K.36)$$

K.5 PR-EFM-IF

Fig. K.13(a) and Fig. K.13(b) present the PR-EFM and its SEFM with critical sections. Furthermore, the relationship between the stiffness coefficients associated with DOF d_3 and the dependency on DOFs d_1 and d_2 is depicted in Fig. K.14 and mathematically expressed in Eqs. (K.37) to (K.39).

Additionally, the bending moments in the critical sections caused by a unit load applied to the DOFs are shown in Fig. K.15 and described by Eqs. (K.40) to (K.45). Finally, Fig. K.16 depicts the equivalent bending strengths for the critical sections, which are expressed by Eq. (K.46).

$$\mathbf{d}^{PR.EFM.IF} = \left[d_1^{PR.EFM.IF} \quad d_2^{PR.EFM.IF} \quad d_3^{PR.EFM.IF} \right]^T \quad (K.37)$$

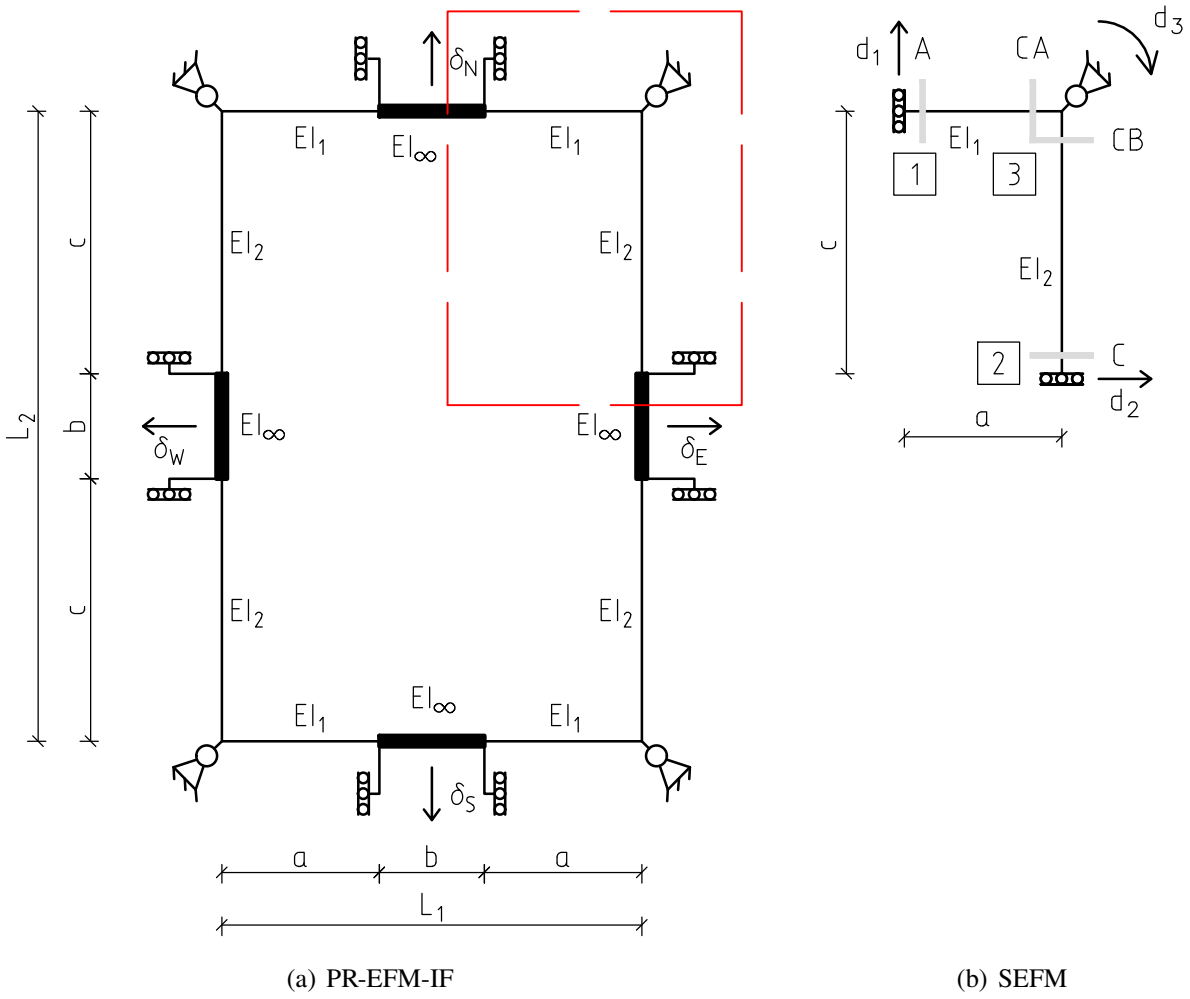


Figure K.13: PR-EFM and its SEFM with the critical sections.

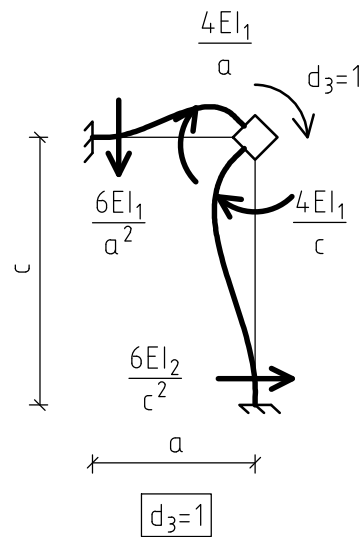


Figure K.14: Stiffness coefficients associated to d_3 for the PR-EFM-IF.

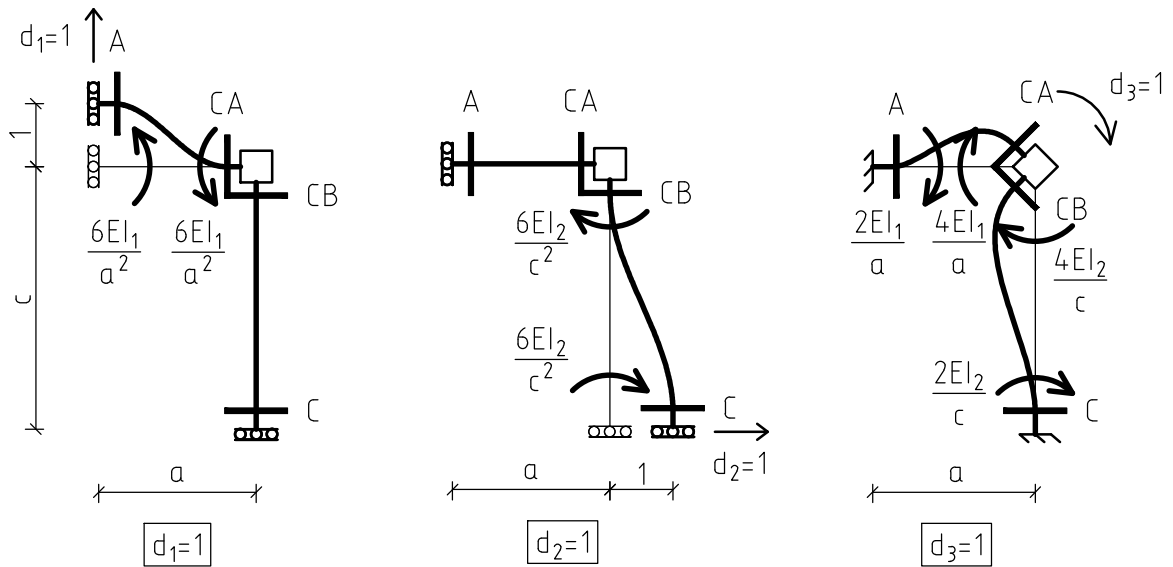


Figure K.15: Bending moments in critical sections under unit load in DOFs for the PR-EFM-IF.

$$0 = \left[-\frac{6 E I_1}{a^2} \quad \frac{6 E I_2}{c^2} \quad \frac{4 E I_1}{a} + \frac{4 E I_2}{c} \right] \mathbf{d}^{\text{PR.EFM-IF}} \quad (\text{K.38})$$

$$d_3^{\text{PR.EFM-IF}} = -\frac{3 I_2 d_2^{\text{PR.EFM-IF}} a^2 - 3 I_1 d_1^{\text{PR.EFM-IF}} c^2}{2 a c (I_2 a + I_1 c)} \quad (\text{K.39})$$

$$\mathbf{M}_d^{\text{PR.EFM-IF}} = \begin{bmatrix} M_A^{d_1} & M_A^{d_2} & M_A^{d_3} \\ M_{CA}^{d_1} & M_{CA}^{d_2} & M_{CA}^{d_3} \\ M_{CB}^{d_1} & M_{CB}^{d_2} & M_{CB}^{d_3} \\ M_B^{d_1} & M_B^{d_2} & M_B^{d_3} \end{bmatrix} = \begin{bmatrix} -\frac{6 E I_1}{a^2} & 0 & \frac{2 E I_1}{a} \\ -\frac{6 E I_1}{a^2} & 0 & \frac{4 E I_1}{a} \\ 0 & \frac{6 E I_2}{c^2} & \frac{4 E I_2}{c} \\ 0 & \frac{6 E I_2}{c^2} & \frac{2 E I_2}{c} \end{bmatrix} \quad (\text{K.40})$$

$$\mathbf{M}^{\text{PR.EFM-IF}} = \mathbf{M}_d^{\text{PR.EFM-IF}} \mathbf{d}^{\text{PR.EFM-IF}} = \begin{bmatrix} M_A^{\text{PR.EFM-IF}} & M_{CA}^{\text{PR.EFM-IF}} & M_{CB}^{\text{PR.EFM-IF}} & M_B^{\text{PR.EFM-IF}} \end{bmatrix}^T \quad (\text{K.41})$$

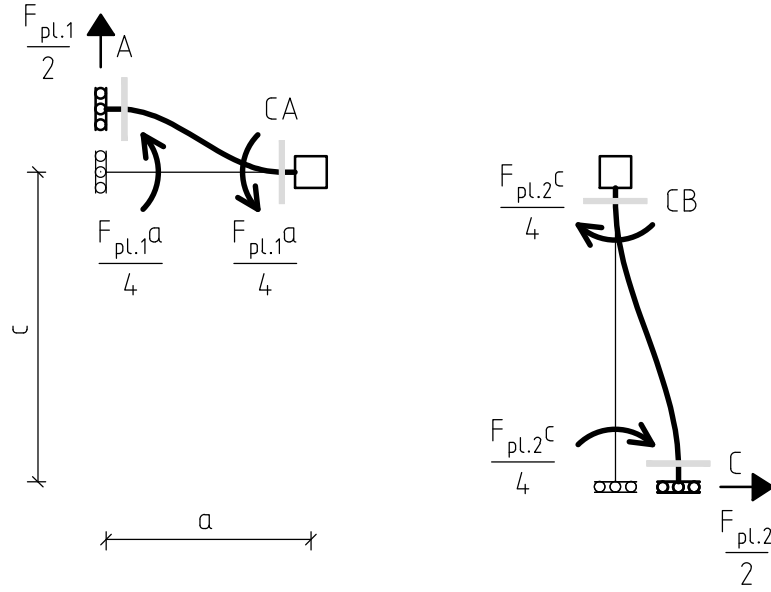


Figure K.16: Bending moments in critical sections under unit load in DOFs for the PR-EFM-IF.

$$M_A^{\text{PR.EFM.IF}} = - \frac{3 E I_1 (I_2 d_2^{\text{PR.EFM.IF}} a^2 + 2 I_2 d_1^{\text{PR.EFM.IF}} a c + I_1 d_1^{\text{PR.EFM.IF}} c^2)}{a^2 c (I_2 a + I_1 c)} \quad (\text{K.42})$$

$$M_{CA}^{\text{PR.EFM.IF}} = - \frac{6 E I_1 I_2 (a d_2^{\text{PR.EFM.IF}} + c d_1^{\text{PR.EFM.IF}})}{a c (I_2 a + I_1 c)} \quad (\text{K.43})$$

$$M_{CB}^{\text{PR.EFM.IF}} = \frac{6 E I_1 I_2 (a d_2^{\text{PR.EFM.IF}} + c d_1^{\text{PR.EFM.IF}})}{a c (I_2 a + I_1 c)} \quad (\text{K.44})$$

$$M_B^{\text{PR.EFM.IF}} = \frac{3 E I_2 (I_2 d_2^{\text{PR.EFM.IF}} a^2 + 2 I_1 d_2^{\text{PR.EFM.IF}} a c + I_1 d_1^{\text{PR.EFM.IF}} c^2)}{a c^2 (I_2 a + I_1 c)} \quad (\text{K.45})$$

$$\begin{aligned} \mathbf{M}_{y,\text{NGM}}^{\text{PR.EFM.IF}} &= \left[M_{y,\text{NGM}.A}^{\text{PR.EFM.IF}} \quad M_{y,\text{NGM}.CA}^{\text{PR.EFM.IF}} \quad M_{y,\text{NGM}.CB}^{\text{PR.EFM.IF}} \quad M_{y,\text{NGM}.B}^{\text{PR.EFM.IF}} \right]^T \\ &= \left[-\frac{F_{pl.1} a}{4} \quad -\frac{F_{pl.1} a}{4} \quad \frac{F_{pl.2} c}{4} \quad \frac{F_{pl.2} c}{4} \right]^T \end{aligned} \quad (\text{K.46})$$

K.6 PR-EFM-IEq

The relationship between DOF d_3 and DOFs d_1 and d_2 is given by Eq. (K.47). The bending moments in the critical sections are expressed by Eqs. (K.48) to (K.51). The equivalent bending strengths for

the critical sections is outlined in Eq. (K.52).

$$d_3^{\text{PR.EFM.IEq}} = - \frac{3 d_2^{\text{PR.EFM.IEq}} a^2 - 3 d_1^{\text{PR.EFM.IEq}} c^2}{2 a c (a + c)} \quad (\text{K.47})$$

$$M_A^{\text{PR.EFM.IEq}} = - \frac{3 E I_{eq} \left(d_2 a^2 + 2 d_1^{\text{PR.EFM.IEq}} a c + d_1^{\text{PR.EFM.IEq}} c^2 \right)}{a^2 c (a + c)} \quad (\text{K.48})$$

$$M_{CA}^{\text{PR.EFM.IEq}} = - \frac{6 E I_{eq} \left(a d_2^{\text{PR.EFM.IEq}} + c d_1^{\text{PR.EFM.IEq}} \right)}{a c (a + c)} \quad (\text{K.49})$$

$$M_{CB}^{\text{PR.EFM.IEq}} = \frac{6 E I_{eq} \left(a d_2^{\text{PR.EFM.IEq}} + c d_1^{\text{PR.EFM.IEq}} \right)}{a c (a + c)} \quad (\text{K.50})$$

$$M_B^{\text{PR.EFM.IEq}} = \frac{3 E I_{eq} \left(d_2^{\text{PR.EFM.IEq}} a^2 + 2 d_2 a c + d_1^{\text{PR.EFM.IEq}} c^2 \right)}{a c^2 (a + c)} \quad (\text{K.51})$$

$$\mathbf{M}_{y,\text{NGM}}^{\text{PR.EFM.IEq}} = \mathbf{M}_{y,\text{NGM}}^{\text{PR.EFM.IF}} \quad (\text{K.52})$$

Appendix L: Quadrant Calculation

The cross-section of the tubular column is divided into four quadrants (i.e., Q1 to Q4), and their behavior is expressed through three DOFs, d_1 , d_2 , and d_3 , as presented in Eq.(5.85). However, as explained in Section 5.5.6, d_3 , it was made dependent on d_1 and d_2 by applying Eq.(5.87). Thus, four calculations are performed for every EFM.

According to Tab. I.2 from Appendix I, the vector containing the minimum elastic displacements, $\delta_{el.min}$, for the RHS-m03-H01-SC02 case is:

$$\delta_{el.min}^{RFEM} = \begin{bmatrix} 1.50 & 3.00 & 0.53 & -0.37 \end{bmatrix}^T \quad (L.1)$$

The EFM is partitioned into four quadrants, as depicted in Fig. 5.52, and the values of d_1^{EFM} and d_2^{EFM} are presented in Tab. L.1.

Table L.1: Values of d_1^{EFM} and d_2^{EFM} for RHS-m01-V01-SC01.

Displacement	Q ₁	Q ₂	Q ₃	Q ₄
d_1^{EFM}	0.53	1.50	1.50	0.53
d_2^{EFM}	3.00	3.00	-0.37	-0.37

Appendix M: Results strength - unadjusted

The unadjusted results for the strength criterion (Eq.(5.72) are expressed in accordance with Tab. M.1.

Table M.1: Index of tables for unadjusted strength results.

Case name	Table no.
HS-EFM-R0	Tab. M.2
HS-EFM-R1	Tab. M.3
PS-EFM-R0	Tab. M.4
PS-EFM-R1	Tab. 5.28*
HR-EFM-IF-R0	Tab. M.5
HR-EFM-IEq-R0	Tab. M.6
HR-EFM-IF-R1	Tab. M.7
HR-EFM-IEq-R1	Tab. M.8
PR-EFM-IF-R0	Tab. M.9
PR-EFM-IEq-R0	Tab. M.10
PR-EFM-IF-R1	Tab. 5.29*
PR-EFM-IEq-R1	Tab. M.11

* see Section 5.5.8.2

Table M.2: Results: HS-EFM-R0 [kNm] (unadjusted).

SC	$M^{HS-EFM-R0}$				$M_{y.GNM}^{HS-EFM-R0}$				$\alpha_{crit.s}^{HS-EFM-R0}$				α_{max}
	A	CA	CB	B	A	CA	CB	B	A	CA	CB	B	
01	10.67	10.46	10.46	10.46	4.12	4.12	4.12	4.12	2.6	2.5	2.5	2.5	2.6
02	11.06	10.90	10.90	10.90	4.45	4.45	4.45	4.45	2.5	2.5	2.5	2.5	2.5
03	12.78	12.78	12.78	12.78	5.70	5.70	5.70	5.70	2.2	2.2	2.2	2.2	2.2
04	18.56	18.56	18.56	18.56	8.64	8.64	8.64	8.64	2.1	2.1	2.1	2.1	2.1

Appendix M. Results strength - unadjusted

Table M.3: Results: HS-EFM-R1 [kNm] (unadjusted).

SC	$M^{HS-EFM-R1}$				$M_{y.GNM}^{HS-EFM-R1}$				$\alpha_{crit.s}^{HS-EFM-R1}$				α_{max}
	A	CA	CB	B	A	CA	CB	B	A	CA	CB	B	
01	7.72	7.57	7.57	7.57	3.82	3.82	3.82	3.82	2.0	2.0	2.0	2.0	2.0
02	8.40	8.28	8.28	8.28	4.18	4.18	4.18	4.18	2.0	2.0	2.0	2.0	2.0
03	11.79	11.79	11.79	11.79	5.69	5.69	5.69	5.69	2.1	2.1	2.1	2.1	2.1
04	29.09	29.09	29.09	29.09	10.49	10.49	10.49	10.49	2.8	2.8	2.8	2.8	2.8

Table M.4: Results: PS-EFM-R0 [kNm] (unadjusted).

SC	$M^{PS-EFM-R0}$				$M_{y.GNM}^{PS-EFM-R0}$				$\alpha_{crit.s}^{PS-EFM-R0}$				α_{max}
	A	CA	CB	B	A	CA	CB	B	A	CA	CB	B	
01	9.60	9.41	9.41	9.41	3.71	3.71	3.71	3.71	2.6	2.5	2.5	2.5	2.6
02	8.85	8.72	8.72	8.72	3.56	3.56	3.56	3.56	2.5	2.5	2.5	2.5	2.5
03	7.03	7.03	7.03	7.03	3.13	3.13	3.13	3.13	2.2	2.2	2.2	2.2	2.2
04	5.57	5.57	5.57	5.57	2.59	2.59	2.59	2.59	2.1	2.1	2.1	2.1	2.1

Table M.5: Results: HR-EFM-IF-R0 [kNm] (unadjusted).

SC	$M^{HR-EFM-IF-R0}$				$M_{y.GNM}^{HR-EFM-IF-R0}$				$\alpha_{crit.s}^{HR-EFM-IF-R0}$				α_{max}
	A	CA	CB	B	A	CA	CB	B	A	CA	CB	B	
01	11.09	11.16	11.16	11.22	4.12	4.12	5.36	5.36	2.7	2.7	2.1	2.1	2.7
02	11.36	11.36	11.36	11.36	4.45	4.45	5.72	5.72	2.6	2.6	2.0	2.0	2.6
03	12.77	12.12	12.12	11.75	5.70	5.70	6.52	6.52	2.2	2.1	1.9	1.8	2.2
04	15.92	13.39	13.39	12.92	8.64	8.64	7.72	7.72	1.8	1.6	1.7	1.7	1.8

Table M.6: Results: HR-EFM-IEq-R0 [kNm] (unadjusted).

SC	$M^{HR-EFM-IEq-R0}$				$M_{y.GNM}^{HR-EFM-IEq-R0}$				$\alpha_{crit.s}^{HR-EFM-IEq-R0}$				α_{max}
	A	CA	CB	B	A	CA	CB	B	A	CA	CB	B	
01	11.71	11.05	11.05	10.61	4.12	4.12	5.36	5.36	2.8	2.7	2.1	2.0	2.8
02	11.77	11.25	11.25	10.90	4.45	4.45	5.72	5.72	2.6	2.5	2.0	1.9	2.6
03	12.37	12.44	12.44	12.49	5.70	5.70	6.52	6.52	2.2	2.2	1.9	1.9	2.2
04	15.04	18.08	18.08	20.16	8.64	8.64	7.72	7.72	1.7	2.1	2.3	2.6	2.6

Table M.7: Results: HR-EFM-IF-R1 [kNm] (unadjusted).

SC	$M^{HR-EFM-IF-R1}$				$M_{y.GNM}^{HR-EFM-IF-R1}$				$\alpha_{crit.s}^{HR-EFM-IF-R1}$				α_{max}
	A	CA	CB	B	A	CA	CB	B	A	CA	CB	B	
01	8.04	8.11	8.11	8.17	3.82	3.82	5.16	5.16	2.1	2.1	1.6	1.6	2.1
02	8.59	8.56	8.56	8.53	4.18	4.18	5.42	5.42	2.1	2.0	1.6	1.6	2.1
03	11.31	10.25	10.25	9.73	5.69	5.69	6.28	6.28	2.0	1.8	1.6	1.6	2.0
04	22.19	13.28	13.28	12.27	10.49	10.49	7.64	7.64	2.1	1.3	1.7	1.6	2.1

Table M.8: Results: HR-EFM-IEq-R1 [kNm] (unadjusted).

SC	$M^{HR-EFM-IEq-R1}$				$M_{y.GNM}^{HR-EFM-IEq-R1}$				$\alpha_{crit.s}^{HR-EFM-IEq-R1}$				α_{max}
	A	CA	CB	B	A	CA	CB	B	A	CA	CB	B	
01	8.51	8.03	8.03	7.71	3.82	3.82	5.16	5.16	2.2	2.1	1.6	1.5	2.2
02	8.88	8.48	8.48	8.22	4.18	4.18	5.42	5.42	2.1	2.0	1.6	1.5	2.1
03	10.77	10.83	10.83	10.87	5.69	5.69	6.28	6.28	1.9	1.9	1.7	1.7	1.9
04	20.79	24.98	24.98	27.86	10.49	10.49	7.64	7.64	2.0	2.4	3.3	3.6	3.6

Table M.9: Results: PR-EFM-IF-R0 [kNm] (unadjusted).

SC	$M^{PR-EFM-IF-R0}$				$M_{y.GNM}^{PR-EFM-IF-R0}$				$\alpha_{crit.s}^{PR-EFM-IF-R0}$				α_{max}
	A	CA	CB	B	A	CA	CB	B	A	CA	CB	B	
01	10.07	10.24	10.24	10.38	3.71	3.71	5.00	5.00	2.7	2.8	2.0	2.1	2.8
02	9.29	9.48	9.48	9.66	3.56	3.56	4.96	4.96	2.6	2.7	1.9	1.9	2.7
03	7.54	7.69	7.69	7.83	3.13	3.13	4.56	4.56	2.4	2.5	1.7	1.7	2.5
04	5.78	5.95	5.95	6.30	2.59	2.59	4.12	4.12	2.2	2.3	1.4	1.5	2.3

Table M.10: Results: PR-EFM-IEq-R0 [kNm] (unadjusted).

SC	$M^{PR-EFM-IEq-R0}$				$M_{y.GNM}^{PR-EFM-IEq-R0}$				$\alpha_{crit.s}^{PR-EFM-IEq-R0}$				α_{max}
	A	CA	CB	B	A	CA	CB	B	A	CA	CB	B	
01	11.00	10.14	10.14	9.60	3.71	3.71	5.00	5.00	3.0	2.7	2.0	1.9	3.0
02	10.33	9.40	9.40	8.82	3.56	3.56	4.96	4.96	2.9	2.6	1.9	1.8	2.9
03	8.81	7.59	7.59	6.95	3.13	3.13	4.56	4.56	2.8	2.4	1.7	1.5	2.8
04	7.64	5.74	5.74	5.29	2.59	2.59	4.12	4.12	2.9	2.2	1.4	1.3	2.9

Table M.11: Results: PR-EFM-IEq-R1 [kNm] (unadjusted).

SC	$M^{PR-EFM-IEq-R1}$				$M_{y.GNM}^{PR-EFM-IEq-R1}$				$\alpha_{crit.s}^{PR-EFM-IEq-R1}$				α_{max}
	A	CA	CB	B	A	CA	CB	B	A	CA	CB	B	
01	9.95	8.89	8.89	8.24	3.39	3.39	4.78	4.78	2.9	2.6	1.9	1.7	2.9
02	9.66	8.43	8.43	7.73	3.24	3.24	4.64	4.64	3.0	2.6	1.8	1.7	3.0
03	9.31	7.37	7.37	6.47	2.79	2.79	4.24	4.24	3.3	2.6	1.7	1.5	3.3
04	12.21	6.45	6.45	5.41	2.19	2.19	3.78	3.78	5.6	2.9	1.7	1.4	5.6

Appendix N: Results strength - adjusted

The results with the unique minimum adjustment factor, α_{min} , incorporated in the equivalent bending stiffness in the strength criterion (Eq.(5.78) are presented in accordance with Tab. N.1.

Table N.1: Index of tables for adjusted strength results.

Case name	Table no.
HS-EFM-R0	Tab. N.2
HS-EFM-R1	Tab. N.3
PS-EFM-R0	Tab. N.4
PS-EFM-R1	Tab. 5.30*
HR-EFM-IF-R0	Tab. N.5
HR-EFM-IEq-R0	Tab. N.6
HR-EFM-IF-R1	Tab. N.7
HR-EFM-IEq-R1	Tab. N.8
PR-EFM-IF-R0	Tab. N.9
PR-EFM-IEq-R0	Tab. N.10
PR-EFM-IF-R1	Tab. 5.31*
PR-EFM-IEq-R1	Tab. N.11

* see Section 5.5.8.3

Table N.2: Results: HS-EFM-R0 [kNm] (adjusted).

SC	$M^{HS-EFM-R0}$				$M_{y,GNM}^{HS-EFM-R0}$				$\alpha_{crit.s}^{HS-EFM-R0}$			
	A	CA	CB	B	A	CA	CB	B	A	CA	CB	B
01	10.67	10.46	10.46	10.46	8.29	8.29	8.29	8.29	1.3	1.3	1.3	1.3
02	11.06	10.90	10.90	10.90	8.94	8.94	8.94	8.94	1.2	1.2	1.2	1.2
03	12.78	12.78	12.78	12.78	11.45	11.45	11.45	11.45	1.1	1.1	1.1	1.1
04	18.56	18.56	18.56	18.56	17.37	17.37	17.37	17.37	1.1	1.1	1.1	1.1

Appendix N. Results strength - adjusted

Table N.3: Results: HS-EFM-R1 [kNm] (adjusted).

SC	$M^{HS-EFM-R1}$				$M_{y.GNM}^{HS-EFM-R1}$				$\alpha_{crit.s}^{HS-EFM-R1}$			
	A	CA	CB	B	A	CA	CB	B	A	CA	CB	B
01	7.72	7.57	7.57	7.57	7.68	7.68	7.68	7.68	1.0	1.0	1.0	1.0
02	8.40	8.28	8.28	8.28	8.40	8.40	8.40	8.40	1.0	1.0	1.0	1.0
03	11.79	11.79	11.79	11.79	11.43	11.43	11.43	11.43	1.0	1.0	1.0	1.0
04	29.09	29.09	29.09	29.09	21.09	21.09	21.09	21.09	1.4	1.4	1.4	1.4

Table N.4: Results: PS-EFM-R0 [kNm] (adjusted).

SC	$M^{PS-EFM-R0}$				$M_{y.GNM}^{PS-EFM-R0}$				$\alpha_{crit.s}^{PS-EFM-R0}$			
	A	CA	CB	B	A	CA	CB	B	A	CA	CB	B
01	9.60	9.41	9.41	9.41	7.46	7.46	7.46	7.46	1.3	1.3	1.3	1.3
02	8.85	8.72	8.72	8.72	7.15	7.15	7.15	7.15	1.2	1.2	1.2	1.2
03	7.03	7.03	7.03	7.03	6.30	6.30	6.30	6.30	1.1	1.1	1.1	1.1
04	5.57	5.57	5.57	5.57	5.21	5.21	5.21	5.21	1.1	1.1	1.1	1.1

Table N.5: Results: HR-EFM-IF-R0 [kNm] (adjusted).

SC	$M^{HR-EFM-IF-R0}$				$M_{y.GNM}^{HR-EFM-IF-R0}$				$\alpha_{crit.s}^{HR-EFM-IF-R0}$			
	A	CA	CB	B	A	CA	CB	B	A	CA	CB	B
01	11.09	11.16	11.16	11.22	7.59	7.59	9.86	9.86	1.5	1.5	1.1	1.1
02	11.36	11.36	11.36	11.36	8.19	8.19	10.53	10.53	1.4	1.4	1.1	1.1
03	12.77	12.12	12.12	11.75	10.48	10.48	12.00	12.00	1.2	1.2	1.0	1.0
04	15.92	13.39	13.39	12.92	15.90	15.90	14.21	14.21	1.0	0.8	0.9	0.9

Table N.6: Results: HR-EFM-IEq-R0 [kNm] (adjusted).

SC	$M^{HR-EFM-IEq-R0}$				$M_{y.GNM}^{HR-EFM-IEq-R0}$				$\alpha_{crit.s}^{HR-EFM-IEq-R0}$			
	A	CA	CB	B	A	CA	CB	B	A	CA	CB	B
01	11.71	11.05	11.05	10.61	7.59	7.59	9.86	9.86	1.5	1.5	1.1	1.1
02	11.77	11.25	11.25	10.90	8.19	8.19	10.53	10.53	1.4	1.4	1.1	1.0
03	12.37	12.44	12.44	12.49	10.48	10.48	12.00	12.00	1.2	1.2	1.0	1.0
04	15.04	18.08	18.08	20.16	15.90	15.90	14.21	14.21	0.9	1.1	1.3	1.4

Table N.7: Results: HR-EFM-IF-R1 [kNm] (adjusted).

SC	$M^{HR-EFM-IF-R1}$				$M_{y.GNM}^{HR-EFM-IF-R1}$				$\alpha_{crit.s}^{HR-EFM-IF-R1}$			
	A	CA	CB	B	A	CA	CB	B	A	CA	CB	B
01	8.04	8.11	8.11	8.17	7.03	7.03	9.49	9.49	1.1	1.2	0.9	0.9
02	8.59	8.56	8.56	8.53	7.69	7.69	9.97	9.97	1.1	1.1	0.9	0.9
03	11.31	10.25	10.25	9.73	10.46	10.46	11.55	11.55	1.1	1.0	0.9	0.8
04	22.19	13.28	13.28	12.27	19.30	19.30	14.07	14.07	1.1	0.7	0.9	0.9

Table N.8: Results: HR-EFM-IEq-R1 [kNm] (adjusted).

SC	$M^{HR-EFM-IEq-R1}$				$M_{y.GNM}^{HR-EFM-IEq-R1}$				$\alpha_{crit.s}^{HR-EFM-IEq-R1}$			
	A	CA	CB	B	A	CA	CB	B	A	CA	CB	B
01	8.51	8.03	8.03	7.71	7.03	7.03	9.49	9.49	1.2	1.1	0.8	0.8
02	8.88	8.48	8.48	8.22	7.69	7.69	9.97	9.97	1.2	1.1	0.9	0.8
03	10.77	10.83	10.83	10.87	10.46	10.46	11.55	11.55	1.0	1.0	0.9	0.9
04	20.79	24.98	24.98	27.86	19.30	19.30	14.07	14.07	1.1	1.3	1.8	2.0

Table N.9: Results: PR-EFM-IF-R0 [kNm] (adjusted).

SC	$M^{PR-EFM-IF-R0}$				$M_{y.GNM}^{PR-EFM-IF-R0}$				$\alpha_{crit.s}^{PR-EFM-IF-R0}$			
	A	CA	CB	B	A	CA	CB	B	A	CA	CB	B
01	10.07	10.24	10.24	10.38	6.83	6.83	9.21	9.21	1.5	1.5	1.1	1.1
02	9.29	9.48	9.48	9.66	6.55	6.55	9.12	9.12	1.4	1.4	1.0	1.1
03	7.54	7.69	7.69	7.83	5.76	5.76	8.40	8.40	1.3	1.3	0.9	0.9
04	5.78	5.95	5.95	6.30	4.77	4.77	7.58	7.58	1.2	1.2	0.8	0.8

Table N.10: Results: PR-EFM-IEq-R0 [kNm] (adjusted).

SC	$M^{PR-EFM-IEq-R0}$				$M_{y.GNM}^{PR-EFM-IEq-R0}$				$\alpha_{crit.s}^{PR-EFM-IEq-R0}$			
	A	CA	CB	B	A	CA	CB	B	A	CA	CB	B
01	11.00	10.14	10.14	9.60	6.83	6.83	9.21	9.21	1.6	1.5	1.1	1.0
02	10.33	9.40	9.40	8.82	6.55	6.55	9.12	9.12	1.6	1.4	1.0	1.0
03	8.81	7.59	7.59	6.95	5.76	5.76	8.40	8.40	1.5	1.3	0.9	0.8
04	7.64	5.74	5.74	5.29	4.77	4.77	7.58	7.58	1.6	1.2	0.8	0.7

Table N.11: Results: PR-EFM-IEq-R1 [kNm] (adjusted).

SC	$M^{\text{PR-EFM-IEq-R1}}$				$M_{y,\text{GNM}}^{\text{PR-EFM-IEq-R1}}$				$\alpha_{\text{crit},s}^{\text{PR-EFM-IEq-R1}}$			
	A	CA	CB	B	A	CA	CB	B	A	CA	CB	B
01	9.95	8.89	8.89	8.24	6.24	6.24	8.80	8.80	1.6	1.4	1.0	0.9
02	9.66	8.43	8.43	7.73	5.95	5.95	8.53	8.53	1.6	1.4	1.0	0.9
03	9.31	7.37	7.37	6.47	5.14	5.14	7.80	7.80	1.8	1.4	0.9	0.8
04	12.21	6.45	6.45	5.41	4.04	4.04	6.96	6.96	3.0	1.6	0.9	0.8

Appendix O: Force-displacement curves for a column plate

The force-displacement curves obtained from the NGM and RFEM analyses are presented in Figs. O.1 to O.8. Each figure corresponds to a specific combination of length and socket height ($L - u$ pairs), displaying the curves for four socket configurations. In addition, the nonlinear curve obtained from the RFEM is approximated as a bilinear curve using the equal potential energy criterion, as explained in Section 5.5.5.

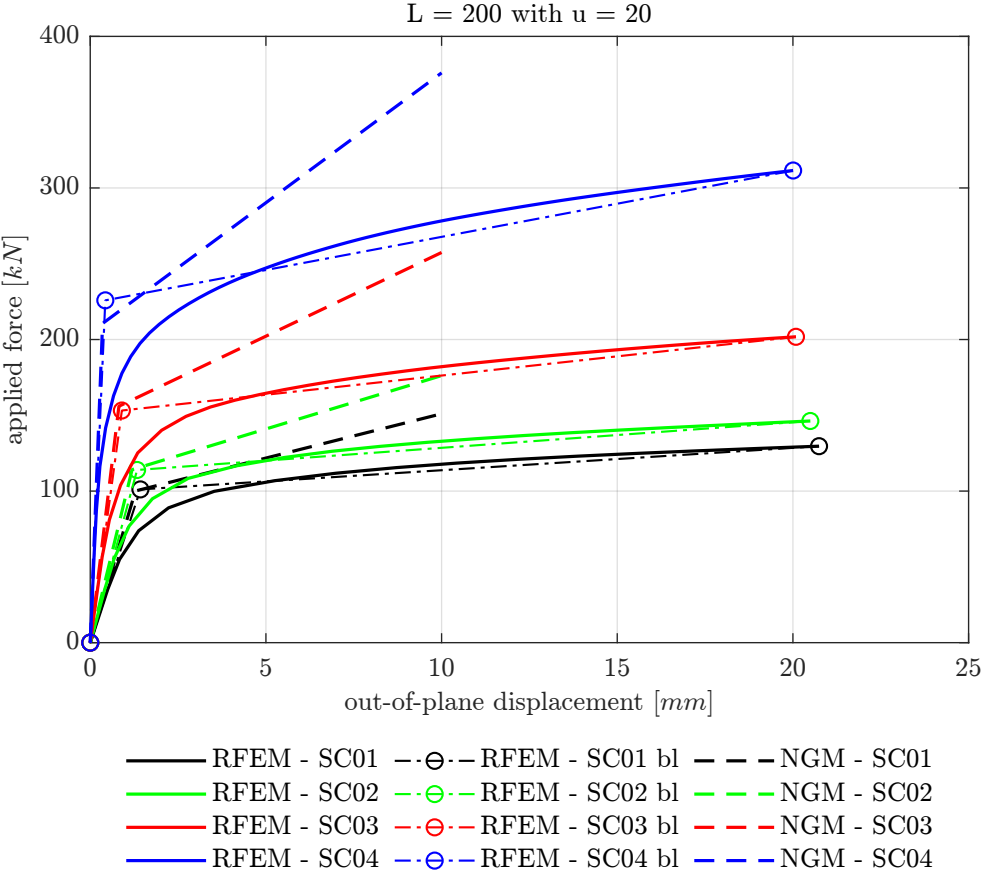


Figure O.1: $F - \delta$ comparison between RFEM and NGM for $L_1 = 200$ and $u = 20$ and all SCs.

Appendix O. Force-displacement curves for a column plate

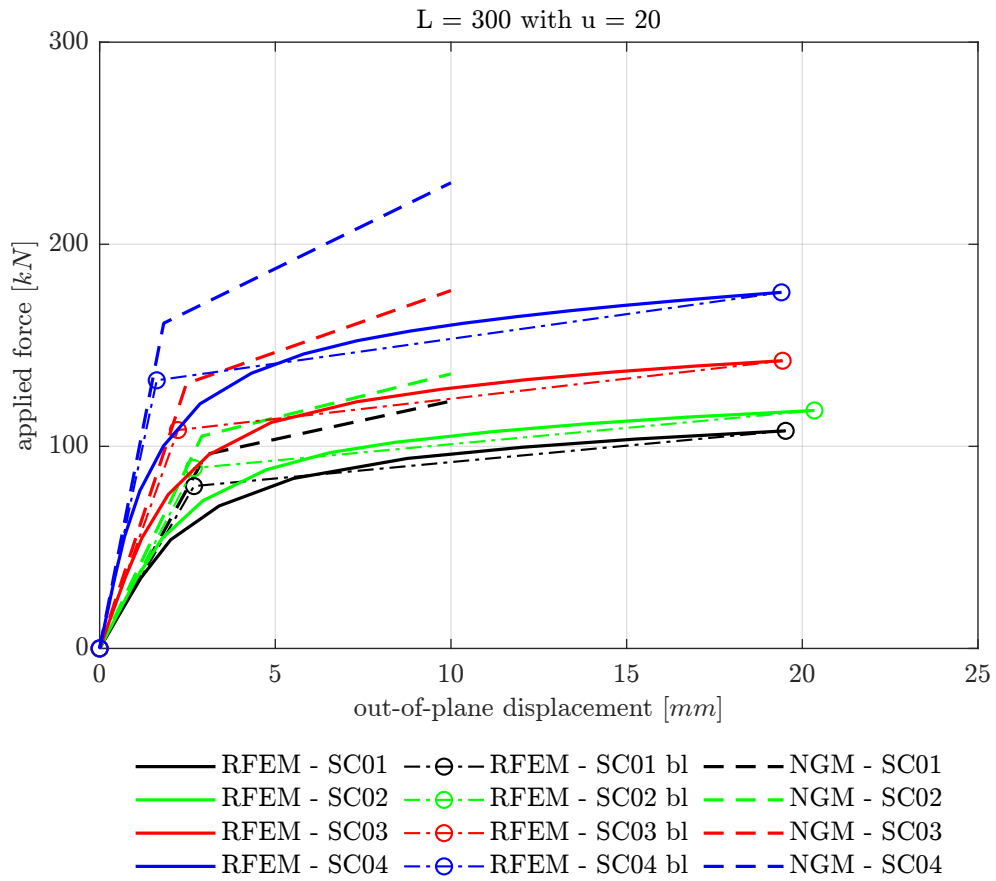


Figure O.2: $F - \delta$ comparison between RFEM and NGM for $L_2 = 300$ and $u = 20$ and all SCs.

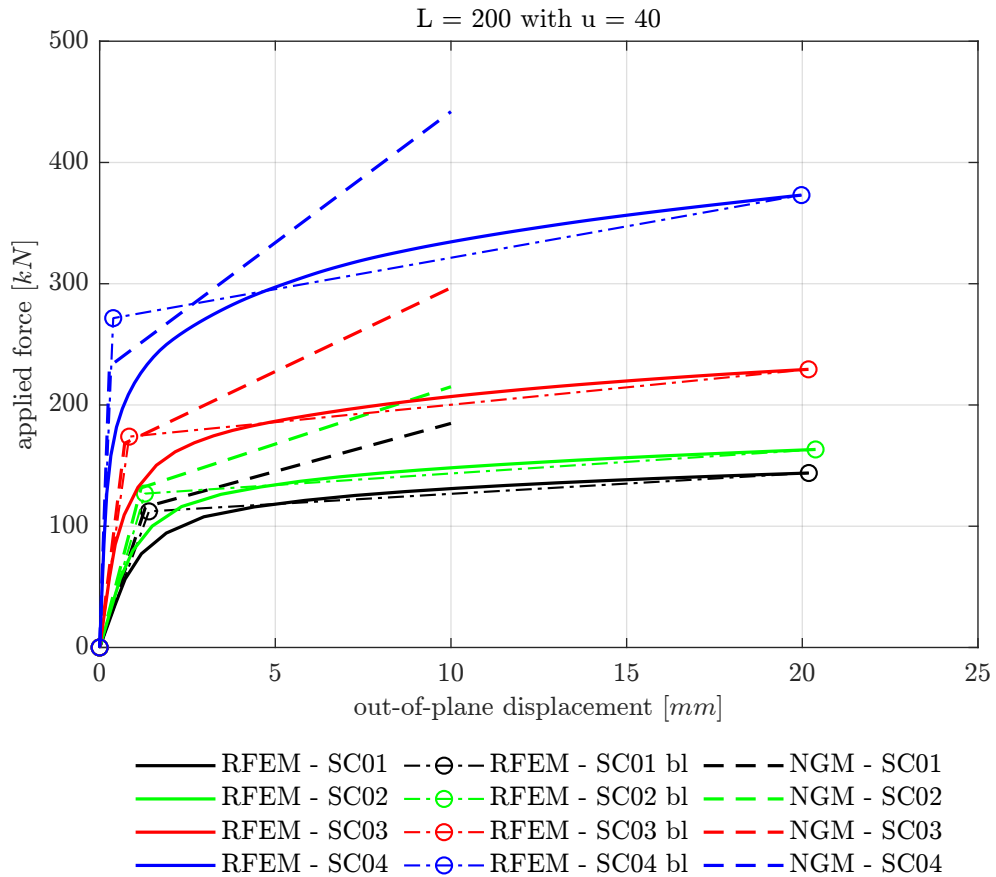


Figure O.3: $F - \delta$ comparison between RFEM and NGM for $L_1 = 200$ and $u = 40$ and all SCs.

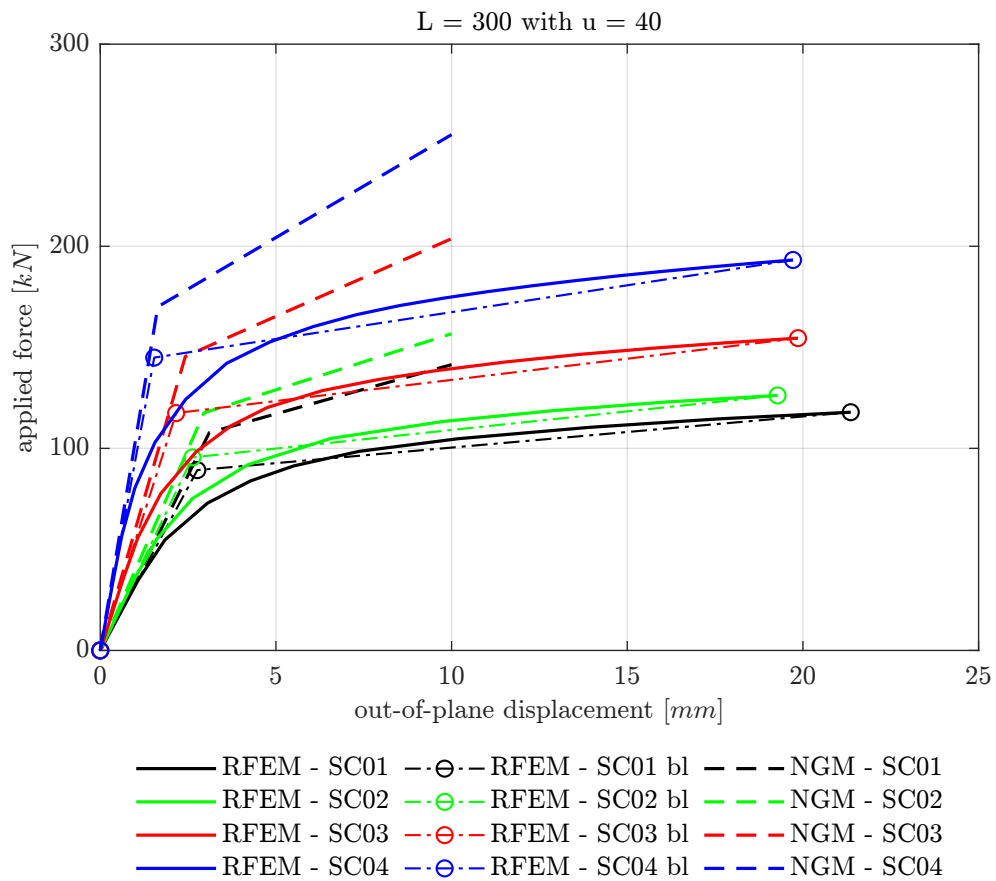


Figure O.4: $F - \delta$ comparison between RFEM and NGM for $L_2 = 300$ and $u = 40$ and all SCs.

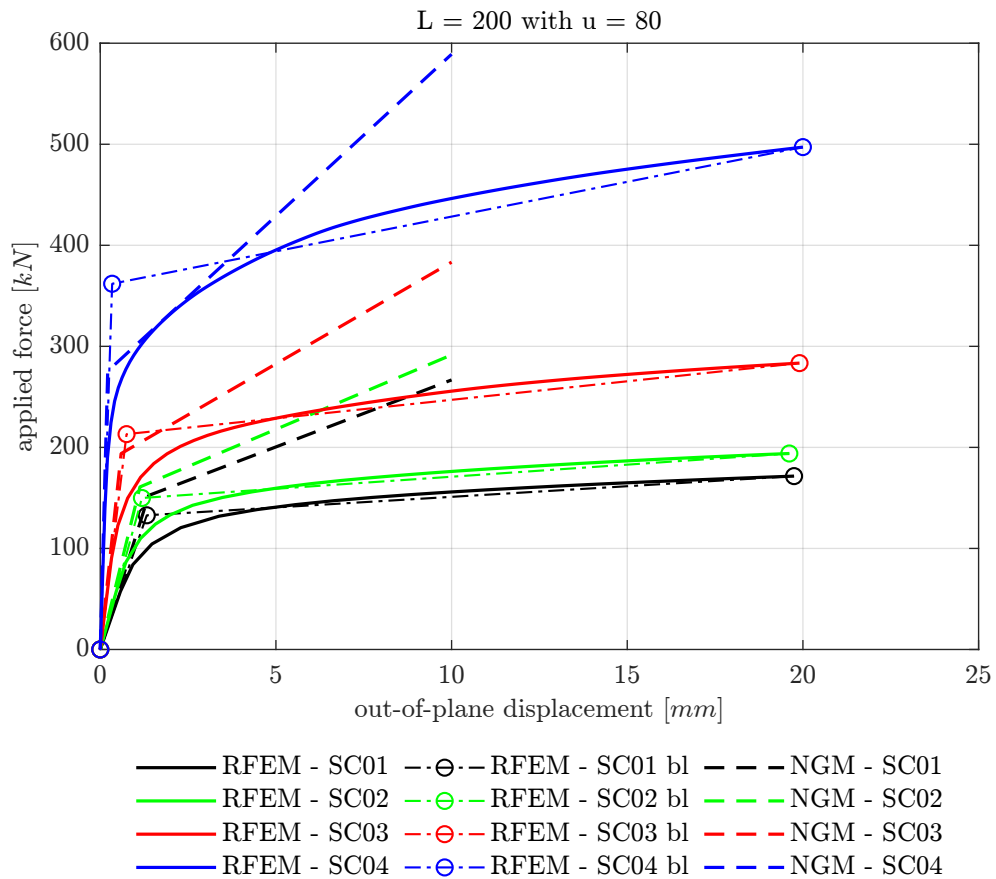


Figure O.5: $F - \delta$ comparison between RFEM and NGM for $L_1 = 200$ and $u = 80$ and all SCs.

Appendix O. Force-displacement curves for a column plate

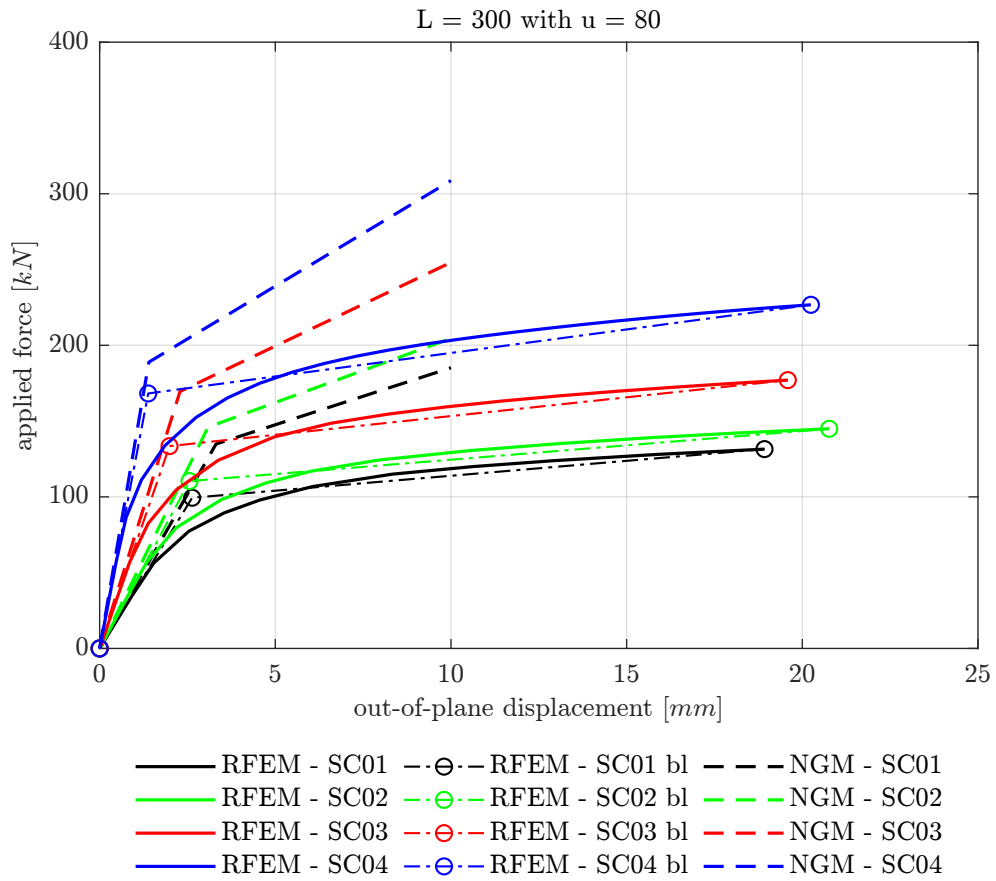


Figure O.6: $F - \delta$ comparison between RFEM and NGM for $L_2 = 300$ and $u = 80$ and all SCs.

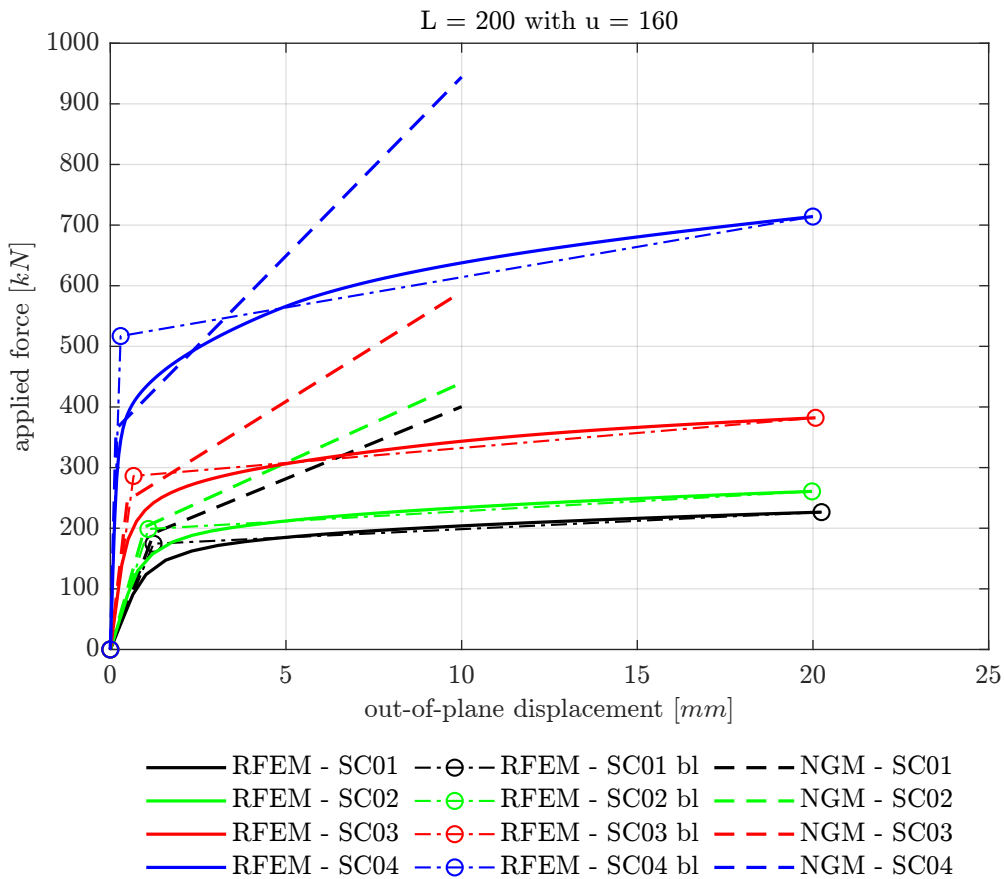


Figure O.7: $F - \delta$ comparison between RFEM and NGM for $L_1 = 200$ and $u = 190$ and all SCs.

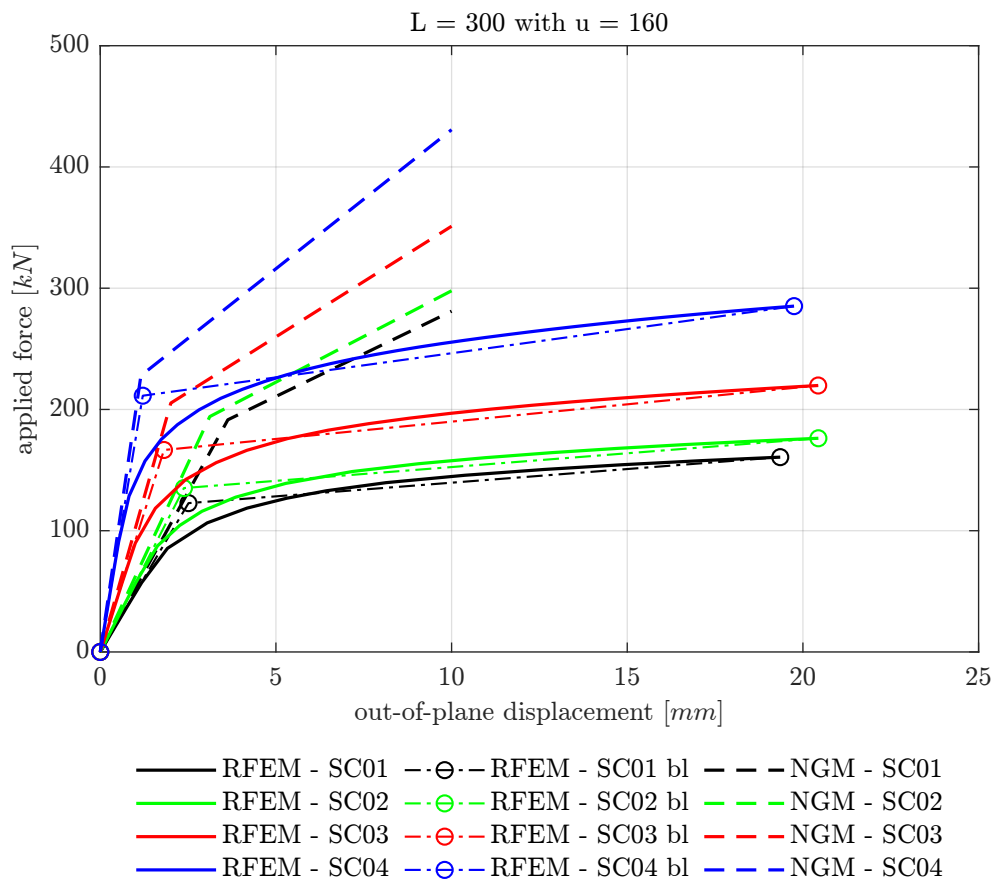


Figure O.8: $F - \delta$ comparison between RFEM and NGM for $L_2 = 300$ and $u = 160$ and all SCs.

Appendix P: Results nonlinearity

The results of the nonlinear analysis introduced in Chapter 6 are presented through applied force-displacement and applied force-deformation curves for the column faces and tube components, respectively. The analysis focuses on the load patterns illustrated in Fig. 6.16, particularly on LP0*i*-L2, with $i = [1, 4]$. These graphical representations are shown in Figs. P.1 to P.8.

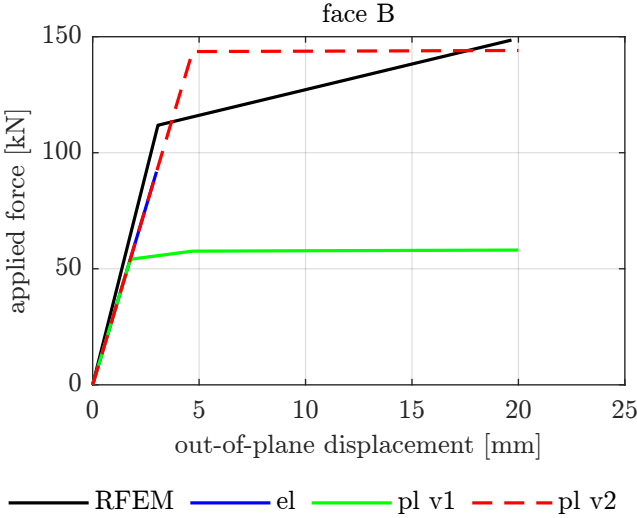


Figure P.1: Force-displacement under LP01-L2.

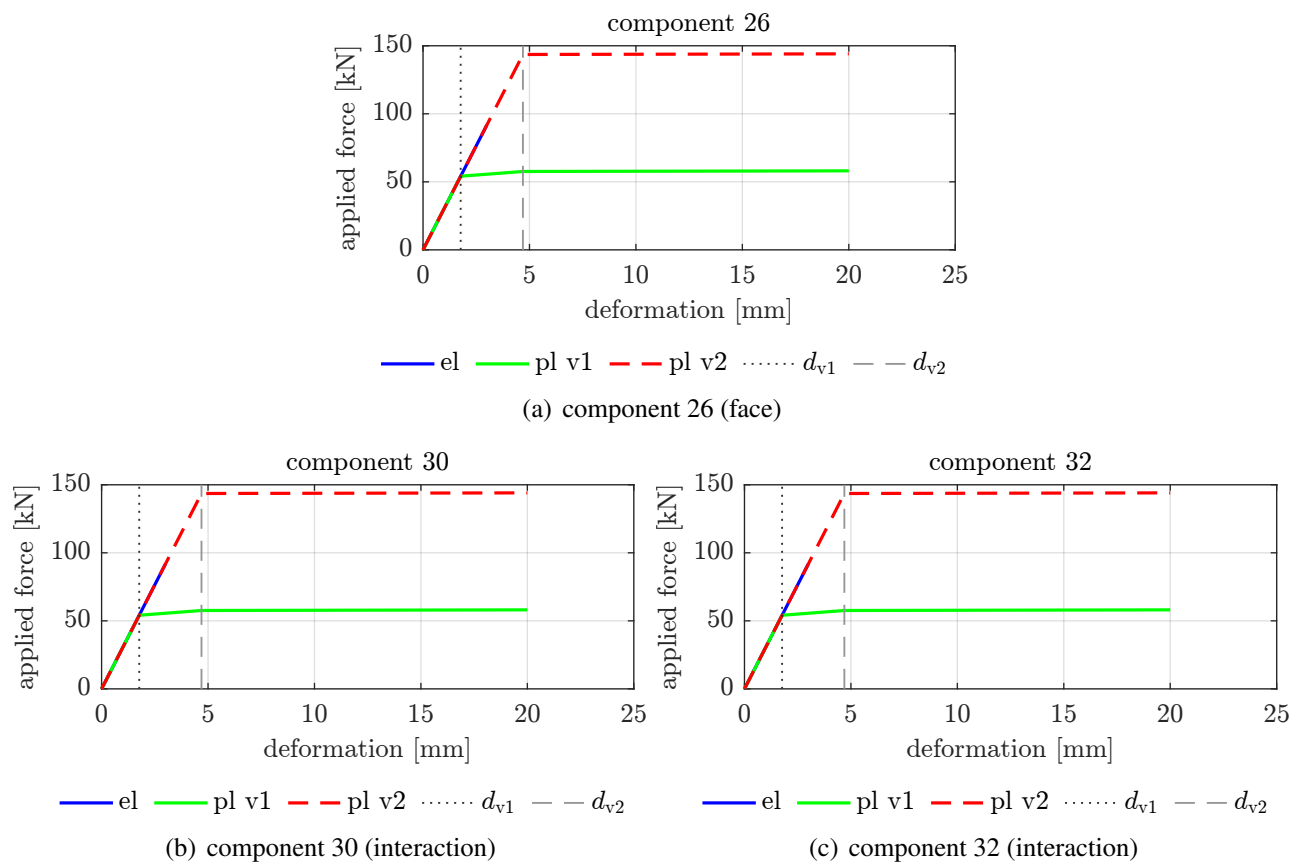


Figure P.2: Force-deformation curves in the tube components under LP01-L2.

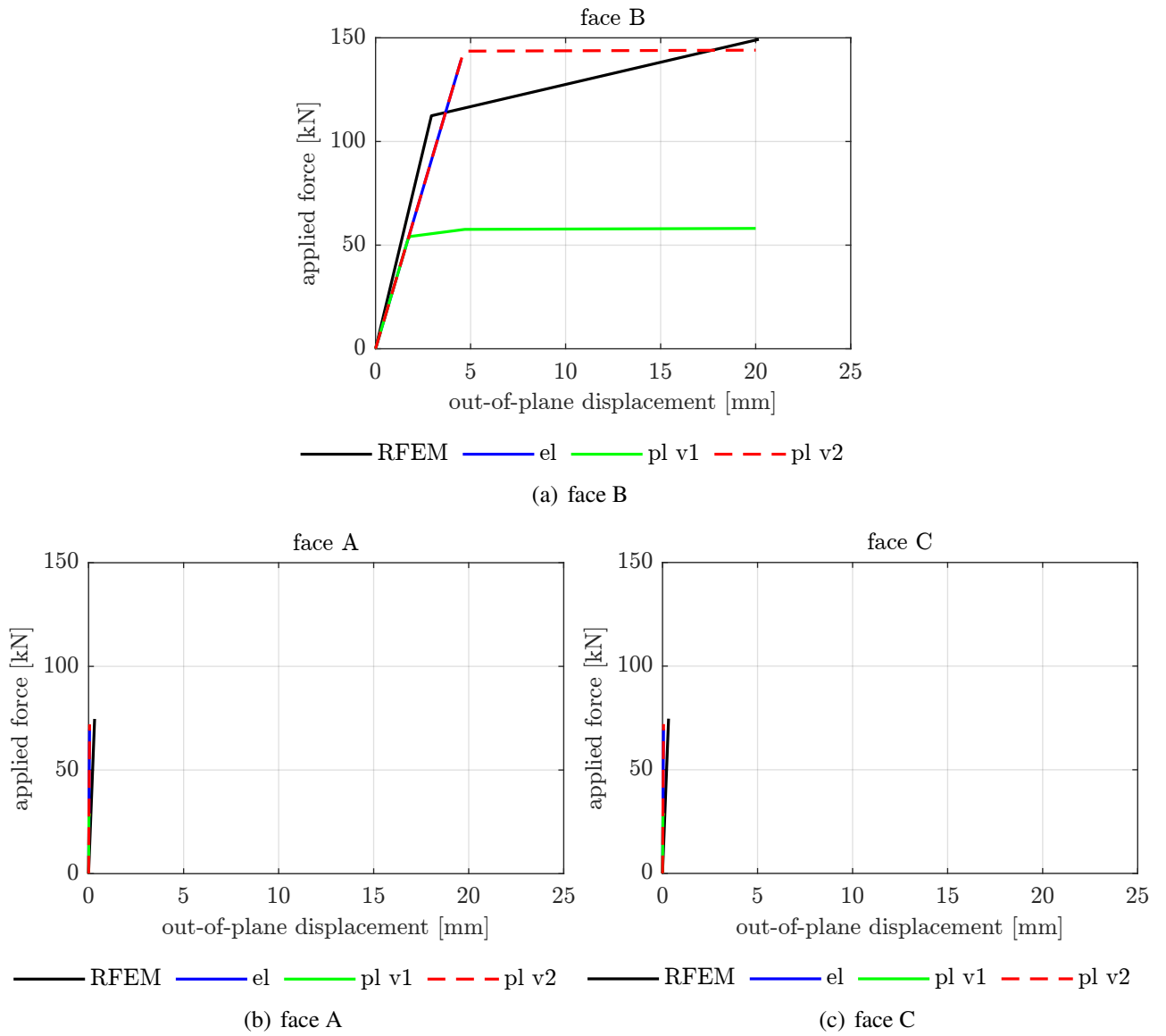


Figure P.3: Force-displacement under LP02-L2.

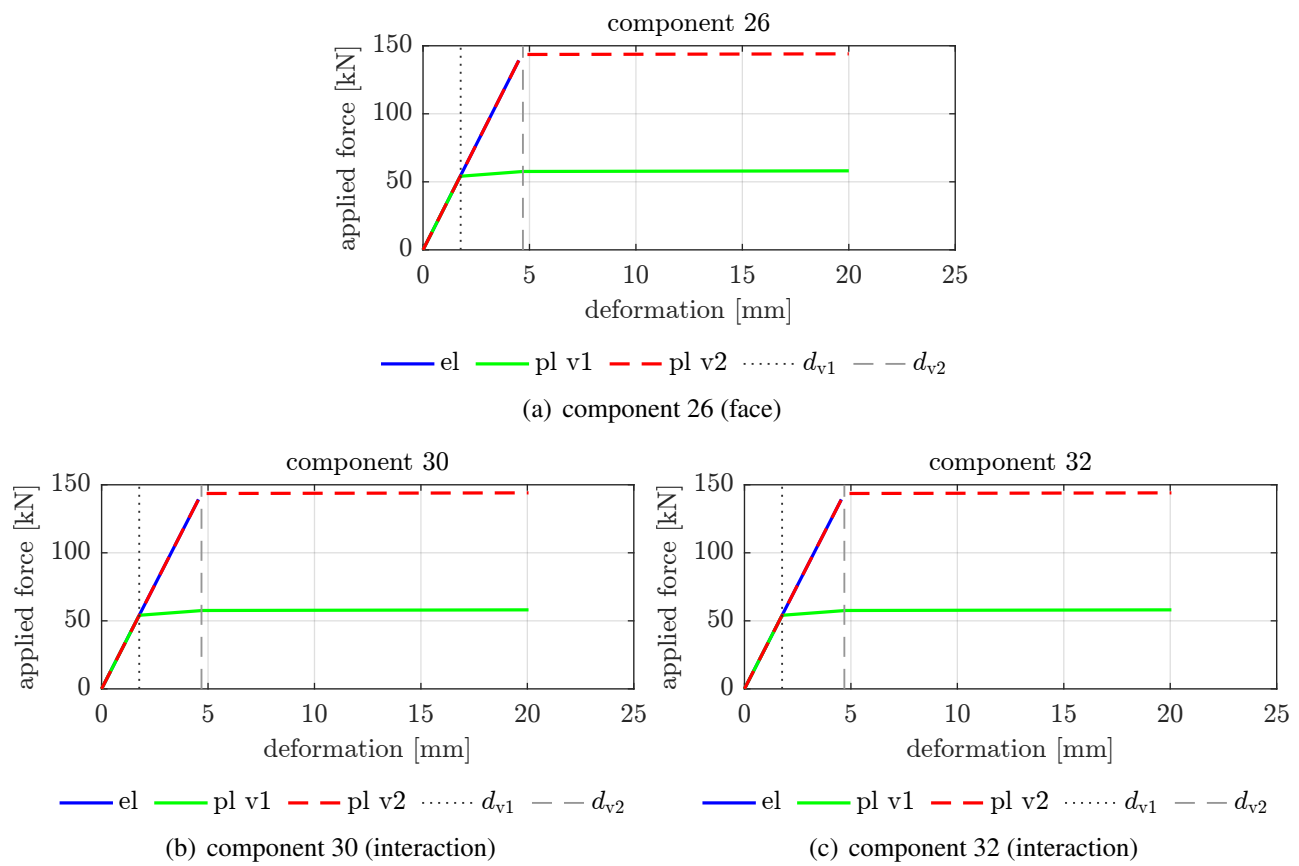


Figure P.4: Force-deformation curves in the tube components under LP02-L2.

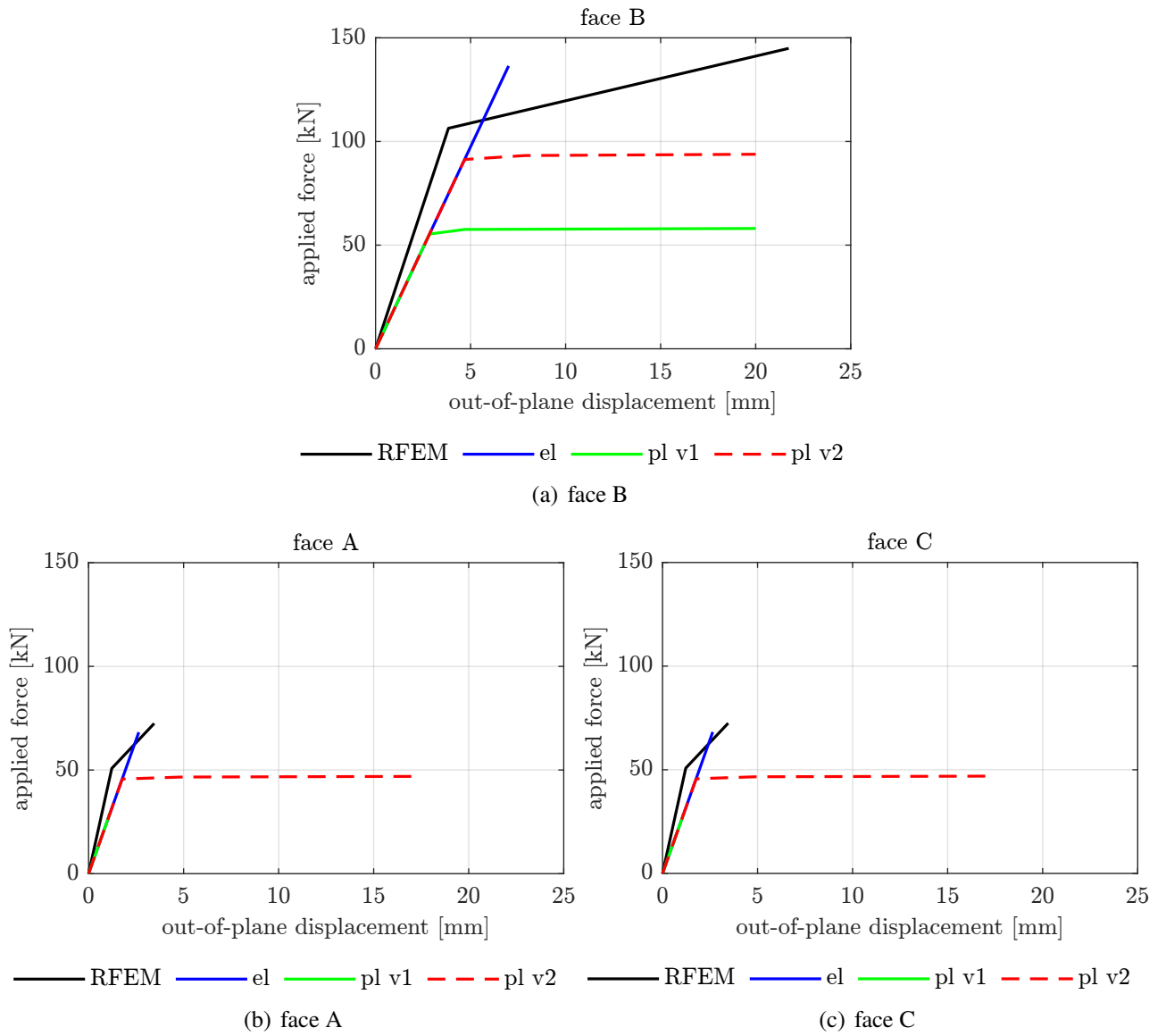


Figure P.5: Force-displacement under LP03-L2.

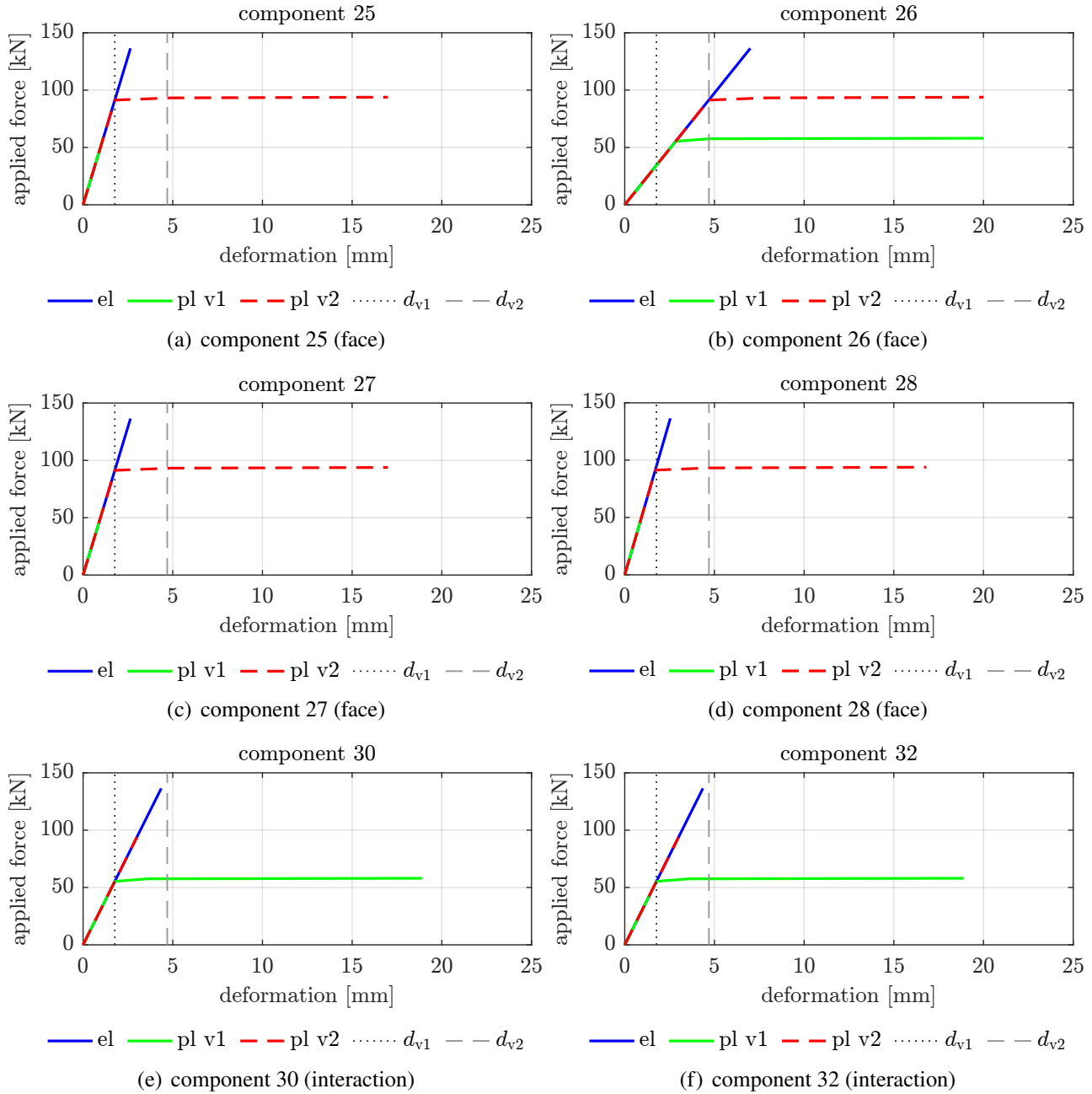


Figure P.6: Force-deformation curves in the tube components under LP03-L2.

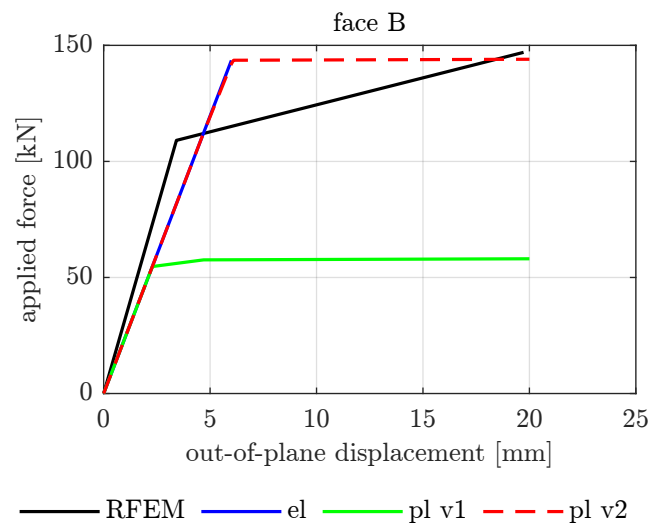


Figure P.7: Force-displacement under LP04-L2.

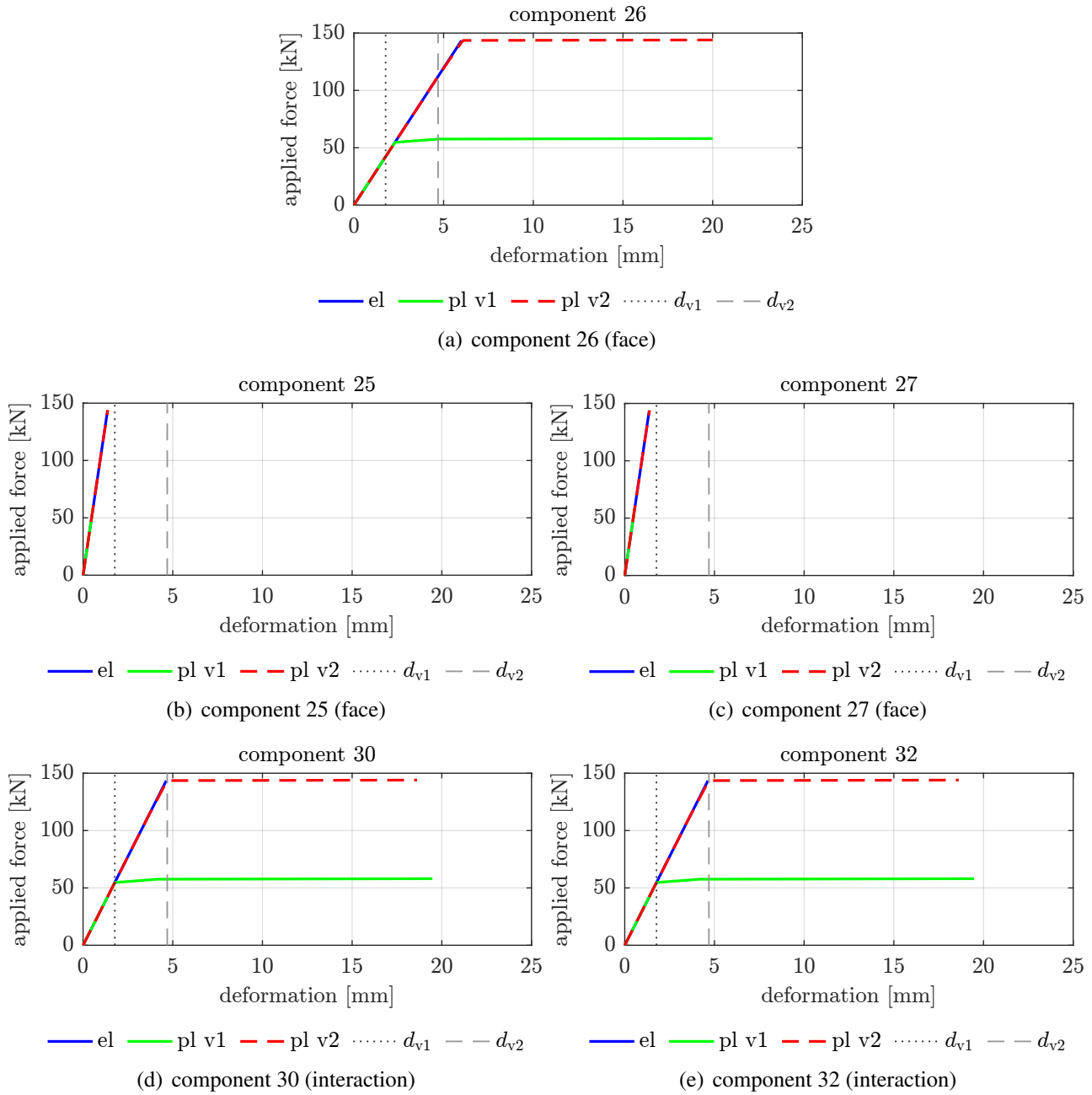


Figure P.8: Force-deformation curves in the tube components under LP04-L2.

Bibliography

- [1] L. Simões da Silva, L. C. Silva, T. Tankova, *et al.*, “Performance of modular hybrid cold-formed/tubular structural system,” *Structures*, vol. 30, no. August 2020, pp. 1006–1019, Apr. 2021. DOI: 10.1016/j.istruc.2021.01.066.
- [2] R. M. Lawson and R. G. Ogden, “Hybrid Systems in Light Steel and Modular Construction,” in *International Conference On Adaptable Building Structures*, Eindhoven, 2006, pp. 252–256.
- [3] J.-P. Jaspart and K. Weynand, *Design of Joints in Steel and Composite Structures*. Weinheim, Germany: Wiley-VCH Verlag GmbH & Co. KGaA, Apr. 2016. DOI: 10.1002/9783433604762.
- [4] C. Dan-Adrian, K. D. Tsavdaridis, D.-A. Corfar, and K. D. Tsavdaridis, “A comprehensive review and classification of inter-module connections for hot-rolled steel modular building systems,” *Journal of Building Engineering*, vol. 50, no. January, p. 104006, Jun. 2022. DOI: 10.1016/j.jobbe.2022.104006.
- [5] European Commission, *INNOvative 3D JOINTS for robust and economic hybrid tubular construction. Project carried out with a financial grant of the Research Programme of the Research Fund for Coal and Steel. Grant Agreement Number 749959*. Research Programme of the Research Fund for Coal and Steel.
- [6] M. Lawson, R. Ogden, and C. Goodier, *Design in Modular Construction*. New York: Taylor & Francis Group, 2014.
- [7] N. Bertram, S. Fuchs, J. Mischke, R. Palter, G. Strube, and J. Woetzel, “Modular construction: From projects to products,” 2019.
- [8] R. M. Lawson, J. Prewer, and P. J. Trebilcock, “Modular Construction using Light Steel Framing : An Architect’s Guide,” *SCI*, 1999.
- [9] E. M. Generalova, V. P. Generalov, and A. A. Kuznetsova, “Modular Buildings in Modern Construction,” *Procedia Engineering*, vol. 153, pp. 167–172, Jan. 2016. DOI: 10.1016/j.proeng.2016.08.098.

- [10] F. E. Boafó, J. T. J. H. Kim, and J. T. J. H. Kim, “Performance of modular prefabricated architecture: Case study-based review and future pathways,” *Sustainability (Switzerland)*, vol. 8, no. 6, pp. 1–16, 2016. DOI: 10.3390/su8060558.
- [11] H. T. Thai, T. Ngo, and B. Uy, “A review on modular construction for high-rise buildings,” *Structures*, vol. 28, no. January, pp. 1265–1290, 2020. DOI: 10.1016/j.istruc.2020.09.070.
- [12] A. W. Lacey, W. Chen, H. Hao, and K. Bi, “Structural response of modular buildings – An overview,” *Journal of Building Engineering*, vol. 16, pp. 45–56, Mar. 2018. DOI: 10.1016/j.jobe.2017.12.008.
- [13] W. Ferdous, Y. Bai, T. D. Ngo, A. Manalo, and P. Mendis, “New advancements, challenges and opportunities of multi-storey modular buildings – A state-of-the-art review,” *Engineering Structures*, vol. 183, pp. 883–893, Mar. 2019. DOI: 10.1016/j.engstruct.2019.01.061.
- [14] J. Packer, “Tubular construction,” *Progress in Structural Engineering and Materials*, vol. 2, pp. 41–49, 2000.
- [15] J. Wardenier, J. Packer, X.-L. Zhao, and A. Ven der Vegte, “Hollow section in structural applications,” Tech. Rep., 2010.
- [16] R. Simões, S. Jordão, J. Diogo, and J. Fernandes, “Development and design of a concealed splice joint configuration between tubular sections,” *Engineering Structures*, vol. 137, pp. 181–193, Apr. 2017. DOI: 10.1016/j.engstruct.2017.01.054.
- [17] N. A. Rahman, “Cold-formed steel stud-plank system for mid-rise construction,” *Proceedings of the Structures Congress and Exposition*, vol. 2006, p. 52, 2006. DOI: 10.1061/40889(201)52.
- [18] R. M. Lawson, “New developments in use of cold formed steel in buildings,” *Construction and Building Materials*, vol. 6, no. 4, pp. 201–204, Jan. 1992. DOI: 10.1016/0950-0618(92)90038-Z.
- [19] L. Gardner, Y. Bu, P. Francis, N. R. Baddoo, K. A. Cashell, and F. McCann, “Elevated temperature material properties of stainless steel reinforcing bar,” *Construction and Building Materials*, vol. 114, pp. 977–997, 2016. DOI: 10.1016/j.conbuildmat.2016.04.009.
- [20] A. Landesmann, D. Camotim, and R. Garcia, “On the strength and DSM design of cold-formed steel web/flange-stiffened lipped channel columns buckling and failing in distortional modes,” *Thin-Walled Structures*, vol. 105, pp. 248–265, 2016. DOI: 10.1016/j.tws.2016.03.023.
- [21] J. Henriques, N. Rosa, H. Gervasio, P. Santos, and L. S. da Silva, “Structural performance of light steel framing panels using screw connections subjected to lateral loading,” *Thin-Walled Structures*, vol. 121, no. January, pp. 67–88, Dec. 2017. DOI: 10.1016/j.tws.2017.09.024.

- [22] P. Sharafi, M. Mortazavi, N. Usefi, K. Kildashti, H. Ronagh, and B. Samali, *Lateral force resisting systems in lightweight steel frames: Recent research advances*, Sep. 2018. DOI: 10.1016/j.tws.2018.04.019.
- [23] B. Schafer, D. Ayhan, J. Leng, *et al.*, “Seismic Response and Engineering of Cold-formed Steel Framed Buildings,” *Structures*, vol. 8, pp. 197–212, Nov. 2016. DOI: 10.1016/j.istruc.2016.05.009.
- [24] EN 1998-1, *Eurocode 8: Design of structures for earthquake resistance - Part 1: General rules, seismic actions and rules for buildings*, 2004. DOI: [Authority : TheEuropeanUnionperRegulation305/2011,Directive98/34/EC,Directive2004/18/EC].
- [25] R. Landolfo, S. Shakeel, and L. Fiorino, “Lightweight steel systems: Proposal and validation of seismic design rules for second generation of Eurocode 8,” *Thin-Walled Structures*, vol. 172, no. November 2021, p. 108 826, Mar. 2022. DOI: 10.1016/j.tws.2021.108826.
- [26] F. S. K. Bijlaard, A. M. G. Coelho, and V. J. D. A. Magalhães, “Innovative joints in steel construction,” *Steel Construction*, vol. 2, no. 4, pp. 243–247, 2009. DOI: 10.1002/stco.200910033.
- [27] J. Schijve, *Fatigue of Structures and Materials*, 2nd Ed. Springer, 2009.
- [28] EN 1993-1-8, *Eurocode 3: Design of steel structures - Part 1-8: Design of joints*, 2005.
- [29] J. Schoof, *Endspurt am Belvedere: Wiens neuer Hauptbahnhof*.
- [30] NZ Wood, *Wynn Williams House | NZ Wood*.
- [31] J. N. J. A. Vambersky, “High-Rise Buildings in the Netherlands : Hybrid Structures and Precast Concrete,” in *October*, vol. 136, 2004, pp. 136–143.
- [32] A. Dall’Asta, G. Leoni, A. Zona, *et al.*, “Innovative hybrid and composite steel-concrete structural solutions for building in seismic area, Final Report, EUR 26932 EN,” EUROPEAN COMMISSION - Directorate-General for Research and Innovation, Tech. Rep., 2015. DOI: <http://dx.doi.org/10.2777/85404>.
- [33] K.-U. Schober and T. Tannert, “Hybrid connections for timber structures,” *European Journal of Wood and Wood Products*, vol. 74, no. 3, pp. 369–377, May 2016. DOI: 10.1007/s00107-016-1024-3.
- [34] C. Loss, M. Piazza, and R. Zandonini, “Connections for steel–timber hybrid prefabricated buildings. Part II: Innovative modular structures,” *Construction and Building Materials*, vol. 122, pp. 796–808, Sep. 2016. DOI: 10.1016/J.CONBUILDMAT.2015.12.001.

- [35] R. E. Smith, *Prefab Architecture: A Guide to Modular Design and Construction*. 2011, p. 304.
- [36] Ž. Bučmys and G. Šaučiuvėnas, “The Behavior of Cold Formed Steel Structure Connections / Šaltai Formuotų Plieninių Konstrukcijų Mazgų Elgsena,” *Engineering Structures and Technologies*, vol. 5, no. 3, pp. 113–122, 2014. doi: 10.3846/2029882x.2013.869416.
- [37] Ž. Bučmys and A. Daniunas, “Component Method in the Strength Evaluation of Cold-formed Steel Joints,” *Procedia Engineering*, vol. 172, pp. 143–148, Jan. 2017. doi: 10.1016/j.proeng.2017.02.036.
- [38] L. Fiorino, V. Macillo, and R. Landolfo, “Experimental characterization of quick mechanical connecting systems for cold-formed steel structures,” *Advances in Structural Engineering*, vol. 20, no. 7, pp. 1098–1110, Jul. 2017. doi: 10.1177/1369433216671318/FORMAT/EPUB.
- [39] M. Zeynalian, A. Shelley, and H. R. Ronagh, “An experimental study into the capacity of cold-formed steel truss connections,” *Journal of Constructional Steel Research*, vol. 127, pp. 176–186, Dec. 2016. doi: 10.1016/J.JCSR.2016.08.001.
- [40] K. Roy, H. H. Lau, T. C. Huon Ting, R. Masood, A. Kumar, and J. B. Lim, “Experiments and finite element modelling of screw pattern of self-drilling screw connections for high strength cold-formed steel,” *Thin-Walled Structures*, vol. 145, p. 106 393, Dec. 2019. doi: 10.1016/j.tws.2019.106393.
- [41] M. Shahini, A. B. Sabbagh, P. Davidson, and R. Mirghaderi, “Development of cold-formed steel moment-resisting connections with bolting friction-slip mechanism for seismic applications,” *Thin-Walled Structures*, vol. 141, pp. 217–231, Aug. 2019. doi: 10.1016/J.TWS.2019.04.011.
- [42] I. Encyclopædia Britannica, *Definition of Plug And Play by Merriam-Webster*. (visited on 10/26/2020).
- [43] Z. Chen, Y. Liu, X. Zhong, and J. Liu, “Rotational stiffness of inter-module connection in mid-rise modular steel buildings,” *Engineering Structures*, vol. 196, p. 109 273, Oct. 2019. doi: 10.1016/j.engstruct.2019.06.009.
- [44] Z. Chen, J. Wang, J. Liu, and Z. Cong, “Tensile and shear performance of rotary inter-module connection for modular steel buildings,” *Journal of Constructional Steel Research*, vol. 175, p. 106 367, Dec. 2020. doi: 10.1016/j.jcsr.2020.106367.
- [45] Y. Liu, Z. Chen, J. Liu, Y. Bai, X. Zhong, and X. Wang, “Lateral stiffness evaluation on corner-supported thin walled modular steel structures,” *Thin-Walled Structures*, vol. 157, p. 106 967, Dec. 2020. doi: 10.1016/j.tws.2020.106967.

- [46] J. Liu, Z. Chen, Y. Liu, Y. Bai, and X. Zhong, "Full-scale corner-supported modular steel structures with vertical inter-module connections under cyclic loading," *Journal of Building Engineering*, vol. 44, p. 103 269, Dec. 2021. DOI: 10.1016/J.JOBE.2021.103269.
- [47] F. Zhao, Y. Yu, S. Lin, M. Man, and F. Ding, "Working mechanism evaluations and simplified models of corner bracket type inter-module connections," *The Structural Design of Tall and Special Buildings*, vol. 30, no. 9, Jun. 2021. DOI: 10.1002/tal.1858.
- [48] A. W. Lacey, W. Chen, H. Hao, K. Bi, and F. J. Tallwin, "Shear behaviour of post-tensioned inter-module connection for modular steel buildings," *Journal of Constructional Steel Research*, vol. 162, Nov. 2019. DOI: 10.1016/j.jcsr.2019.105707.
- [49] X. H. C. He, T. M. Chan, and K. F. Chung, "Effect of inter-module connections on progressive collapse behaviour of MiC structures," *Journal of Constructional Steel Research*, vol. 185, p. 106 823, Oct. 2021. DOI: 10.1016/J.JCSR.2021.106823.
- [50] A. W. Lacey, W. Chen, H. Hao, and K. Bi, "Simplified structural behaviours of post-tensioned inter-module connection for modular buildings," *Journal of Constructional Steel Research*, vol. 175, p. 106 347, Dec. 2020. DOI: 10.1016/J.JCSR.2020.106347.
- [51] A. W. Lacey, W. Chen, H. Hao, and K. Bi, "Lateral behaviour of modular steel building with simplified models of new inter-module connections," *Engineering Structures*, vol. 236, p. 112 103, Jun. 2021. DOI: 10.1016/J.ENGSTRUCT.2021.112103.
- [52] A. W. Lacey, W. Chen, H. Hao, and K. Bi, "New interlocking inter-module connection for modular steel buildings: Experimental and numerical studies," *Engineering Structures*, vol. 198, p. 109 465, Nov. 2019. DOI: 10.1016/J.ENGSTRUCT.2019.109465.
- [53] A. W. Lacey, W. Chen, H. Hao, and K. Bi, "New interlocking inter-module connection for modular steel buildings: Simplified structural behaviours," *Engineering Structures*, vol. 227, p. 111 409, Jan. 2021. DOI: 10.1016/J.ENGSTRUCT.2020.111409.
- [54] S. V. Sendanayake, D. P. Thambiratnam, N. Perera, T. Chan, and S. Aghdamy, "Seismic mitigation of steel modular building structures through innovative inter-modular connections," *Heliyon*, vol. 5, no. 11, e02751, Nov. 2019. DOI: 10.1016/J.HELIYON.2019.E02751.
- [55] S. V. Sendanayake, "Seismic mitigation of steel modular buildings using novel inter-modular connections," Ph.D. dissertation, Queensland University of Technology, 2020. DOI: 10.5204/thesis.eprints.180893.

- [56] S. Sendanayake, D. Thambiratnam, N. Perera, T. Chan, and S. Aghdamy, “Enhancing the lateral performance of modular buildings through innovative inter-modular connections,” *Structures*, vol. 29, pp. 167–184, Feb. 2021. DOI: 10.1016/j.istruc.2020.10.047.
- [57] G. Nadeem, N. A. Safiee, N. Abu Bakar, I. Abd Karim, and N. A. Mohd Nasir, “Finite Element Analysis of Proposed Self-Locking Joint for Modular Steel Structures,” *Applied Sciences*, vol. 11, no. 19, p. 9277, Oct. 2021. DOI: 10.3390/app11199277.
- [58] G. Zhang, L. H. Xu, and Z. X. Li, “Theoretical and parametric studies of a self-centering modular steel structure connection,” *Engineering Structures*, vol. 247, p. 113 146, Nov. 2021. DOI: 10.1016/J.ENGSTRUCT.2021.113146.
- [59] G. Zhang, L. H. Xu, and Z. X. Li, “Development and seismic retrofit of an innovative modular steel structure connection using symmetrical self-centering haunch braces,” *Engineering Structures*, vol. 229, p. 111 671, Feb. 2021. DOI: 10.1016/J.ENGSTRUCT.2020.111671.
- [60] J.-S. Lee, H.-D. Lee, K.-J. Shin, H.-J. Kim, and K.-M. Lee, “Structural Performance Evaluation of Modular Connections Using Developed Blocks,” *International Journal of Steel Structures*, vol. 21, no. 4, pp. 1250–1259, Aug. 2021. DOI: 10.1007/s13296-021-00500-2.
- [61] A. Lytle, K. Saidi, W. Stone, and J. Gross, “Report of the NIST Workshop on Automated Steel Construction,” in *Proceedings of the 19th International Symposium on Automation and Robotics in Construction (ISARC)*, Sep. 2002, pp. 1–7. DOI: 10.22260/ISARC2002/0039.
- [62] F. S. Bijlaard and J. W. Brekelmans, “Plug and play type joints in steel and steel–concrete composite constructions: Development guide and design considerations,” *IES Journal Part A: Civil and Structural Engineering*, vol. 1, no. 4, pp. 237–256, 2008. DOI: 10.1080/19373260802228626.
- [63] A. A. Najafi, “End Plate Connections And Their Influence On Steel And Composite Structures,” Ph.D. dissertation, University of Warwick, 1992.
- [64] EN 1993-1-1, *Eurocode 3: Design of steel structures - Part 1-1: General rules and rules for buildings*, 2005.
- [65] W.-f. Chen, N. Kishi, and M. Komuro, *Semi-rigid Connections Handbook*. J. Ross Publishing, Inc., 2011.
- [66] J. Baker, *First report. steel structures research committee. department of scientific and industrial research*, 1934.
- [67] J. Baker, *Second report. steel structures research committee. department of scientific and industrial research*, 1934.

- [68] J. C. Rathbun, "Elastic properties of riveted connections," *Transactions of the American Society of Civil Engineers*, vol. 101, no. 1, pp. 524–563, 1936.
- [69] J. E. Lothers, "Elastic restraint equations for semi-rigid connections," *Transactions of the American Society of Civil Engineers*, vol. 116, no. 1, pp. 480–494, 1951.
- [70] S. R. Lionberger and W. Weaver Jr, "Dynamic response of frames with nonrigid connections," *Journal of the Engineering Mechanics Division*, vol. 95, no. 1, pp. 95–114, 1969.
- [71] K. M. Romstad and C. V. Subramanian, "Analysis of frames with partial connection rigidity," *Journal of the Structural Division*, vol. 96, no. 11, pp. 2283–2300, 1970.
- [72] T. Tarpy and J. Cardinal, "Behavior of semi-rigid beam-to-column end plate connections," *Joints in structural steelwork*, pp. 2–3, 1981.
- [73] R. Melchers and D. Kaur, "Behaviour of frames with flexible joints," in *Proceedings of 8th Australian Conference Mechanical of Structural Materials*, 1982, pp. 27–1.
- [74] E. Lui and W.-F. Chen, "Analysis and behaviour of flexibly-jointed frames," *Engineering Structures*, vol. 8, no. 2, pp. 107–118, 1986. doi: [https://doi.org/10.1016/0141-0296\(86\)90026-X](https://doi.org/10.1016/0141-0296(86)90026-X).
- [75] R. Zandonini and P. Zanon, "Experimental analysis of end plate connections," *Elsevier Applied Science Publishers Ltd.*, pp. 41–51, 1988.
- [76] P. D. Moncarz and K. H. Gerstle, "Steel frames with nonlinear connections," *Journal of the Structural Division*, vol. 107, no. 8, pp. 1427–1441, 1981.
- [77] Z. Razzaq, "End restraint effect on steel column strength," *Journal of Structural Engineering*, vol. 109, no. 2, pp. 314–334, 1983.
- [78] C. Poggi and R. Zandonini, "Behaviour and strength of steel frames with semi-rigid connections," in *Connection Flexibility and Steel Frames, ASCE Convention*, 1985, pp. 57–76.
- [79] D. Kennedy, "Moment-rotation characteristics of shear connections," *Engineering J, Am Inst Steel Constr*, 1969.
- [80] W. H. Sommer, "Behaviour of welded header plate connections," Ph.D. dissertation, University of Toronto, 1969.
- [81] M. J. Frye and G. A. Morris, "Analysis of Flexibly Connected Steel Frames," *Canadian Journal of Civil Engineering*, vol. 2, no. 3, pp. 280–291, 1975. doi: 10.1139/l76-034.
- [82] A. Picard, Y.-M. Giroux, and P. Brun, "Discussion: Analysis of flexibly connected steel frames," *Canadian Journal of Civil Engineering*, vol. 3, no. 2, pp. 350–352, 1976.

Bibliography

- [83] W. ALTMAN, “Moment-rotation characteristics of semi-rigid steel beam-column connections[final report],” 1982.
- [84] A. V. Goverdhan, “A collection of experimental moment-rotation curves and evaluation of prediction equations for semi-rigid connections,” Ph.D. dissertation, Vanderbilt University, 1983.
- [85] P. Prabha, S. Rekha, V. Marimuthu, M. Saravanan, G. S. Palani, and M. Surendran, “Modified Frye–Morris polynomial model for double web-angle connections,” *International Journal of Advanced Structural Engineering (IJASE)*, vol. 7, no. 3, pp. 295–306, 2015. DOI: 10.1007/s40091-015-0100-y.
- [86] BIS-800, *Code of practice for general construction in steel*, 2007.
- [87] F.-H. Wu, “Semi-rigid connections in steel frames,” Ph.D. dissertation, Purdue University, 1988.
- [88] Y. L. Yee and R. E. Melchers, “Moment-Rotation Curves for Bolted Connections,” *Journal of Structural Engineering*, vol. 112, no. 3, pp. 615–635, Mar. 1986. DOI: 10.1061/(ASCE)0733-9445(1986)112:3(615).
- [89] C. Batho and S. Lash, “Further investigations on beam and stanchions connection, including connections encased in concrete; together with laboratory investigations on a full-scale steel frames”, final report of the steel structures research committee, department of scientific and industrial research,” *His Majesty’s Stationery Office, London*, 1936.
- [90] N. Krishnamurthy, H.-T. Huang, P. K. Jeffrey, and L. K. Avery, “Analytical $m-\theta$ curves for end-plate connections,” *Journal of the Structural Division*, vol. 105, no. 1, pp. 133–145, 1979.
- [91] A. Colson, “Connections incidence on the inelastic behaviour of steel structures,” in *Euromech Colloquium 174*, 1983.
- [92] N. Kishi and W. Chen, “Moment-rotation relation of top and seat angle connections,” *Structural Engineering Report No. CE-STR-87-4, School of Civil Engineering, Purdue Univ., West Lafayette*, 1987.
- [93] N. Kishi, W. Chen, K. Matsuoka, and S. Nomachi, “Moment-rotation of single-double web angle connections,” in *Proceeding of the Workshop on Connections and the Behaviour, Strength and Design of Steel Structures*, 1987.
- [94] R. M. Richard and B. J. Abbott, “Versatile elastic-plastic stress-strain formula,” *Journal of the Engineering Mechanics Division*, vol. 101, no. 4, pp. 511–515, 1975.

- [95] A. Kukreti, T. Murray, and A. Abolmaali, "End-plate connection moment-rotation relationship," *Journal of Constructional Steel Research*, vol. 8, pp. 137–157, 1987. DOI: [https://doi.org/10.1016/0143-974X\(87\)90057-5](https://doi.org/10.1016/0143-974X(87)90057-5).
- [96] Z. Benterkia, "End-plate connections and analysis of semi-rigid steel frames," Ph.D. dissertation, University of Warwick, 1991.
- [97] F. Al-Bermani, B. Li, K. Zhu, and S. Kitipornchai, "Cyclic and seismic response of flexibly jointed frames," *Engineering Structures*, vol. 16, no. 4, pp. 249–255, 1994. DOI: [https://doi.org/10.1016/0141-0296\(94\)90064-7](https://doi.org/10.1016/0141-0296(94)90064-7).
- [98] K. Zhu, F. Al-Bermani, S. Kitipornchai, and B. Li, "Dynamic response of flexibly jointed frames," *Engineering Structures*, vol. 17, no. 8, pp. 575–580, 1995, Dynamic Behaviour of Flexible Joints and Analysis of Flexibly Connected Steel Frames. DOI: [https://doi.org/10.1016/0141-0296\(95\)00008-U](https://doi.org/10.1016/0141-0296(95)00008-U).
- [99] W. Ramberg and W. R. Osgood, "Description of stress-strain curves by three parameters," Washington, Tech. Rep., Jul. 1943.
- [100] K. M. Ang and G. A. Morris, "Analysis of three-dimensional frames with flexible beam-column connections," *Canadian Journal of Civil Engineering*, vol. 11, pp. 245–254, 1984.
- [101] W. Chen and A. Saleeb, "Uniaxial behavior and modeling in plasticity," *Structural Engineering Report No. CE-STR-82-35, School of Civil Engineering, Purdue University*, 1982.
- [102] Y. F. Dafalias and E. P. Popov, "Plastic Internal Variables Formalism of Cyclic Plasticity," *Journal of Applied Mechanics*, vol. 43, no. 4, pp. 645–651, Dec. 1976. DOI: 10.1115/1.3423948.
- [103] N. Cook, "Strength of flexibly-connected steel frames and load histories," Ph.D. dissertation, University of Colorado, Boulder, Colorado, 1983.
- [104] G. Yoshiaki, S. Satsuki, and C. Wai-Fah, "Analysis of critical behavior of semi-rigid frames with or without load history in connections," *International Journal of Solids and Structures*, vol. 27, no. 4, pp. 467–483, 1991. DOI: [https://doi.org/10.1016/0020-7683\(91\)90135-3](https://doi.org/10.1016/0020-7683(91)90135-3).
- [105] Y. Goto, S. Suzuki, and W.-F. Chen, "Stability behaviour of semi-rigid sway frames," *Engineering Structures*, vol. 15, no. 3, pp. 209–219, 1993. DOI: [https://doi.org/10.1016/0141-0296\(93\)90055-9](https://doi.org/10.1016/0141-0296(93)90055-9).
- [106] P. Zoetemeijer, "A Design Method for the Tension Side of Statically Loaded, Bolted Beam-to-Column Connections," 1974. DOI: <http://resolver.tudelft.nl/uuid:f2dff8e5-dd92-4a3c-89db-c4fa945ea759>.

- [107] G. Huber and F. Tschemmerneegg, “Modelling of Beam-to-Column Joints,” *Journal of Constructional Steel Research*, vol. 45, no. 2, pp. 199–216, 1998. DOI: 10.1016/S0143-974X(97)00072-2.
- [108] J. P. Jaspart, “General report: Session on connections,” *Journal of Constructional Steel Research*, vol. 55, no. 1-3, pp. 69–89, 2000. DOI: 10.1016/S0143-974X(99)00078-4.
- [109] F. Tschemmerneegg, A. Tautschnig, H. Klein, C. Braun, and C. Humer, “Zur nachgiebigkeit von rahmenknoten (i.),” *Der Stahlbau*, vol. 56, no. 10, pp. 299–306, 1987.
- [110] K. Weynand, J.-p. Jaspart, and M. Steenhuis, “The stiffness model of revised annex j of eurocode 3,” in *Connections in Steel Structures III*, Elsevier, 1996, pp. 441–452. DOI: 10.1016/B978-008042821-5/50100-0.
- [111] J. Fish and T. Belytschko, *A first course in finite element method*. Wiley, 2011, p. 336.
- [112] S. Bose, G. McNeice, and A. Sherbourne, “Column webs in steel beam-to-column connections part i - formulation and verification,” *Computers & Structures*, vol. 2, no. 1, pp. 253–279, 1972. DOI: [https://doi.org/10.1016/0045-7949\(72\)90030-2](https://doi.org/10.1016/0045-7949(72)90030-2).
- [113] Hibbit, Karlsson, and Sorenson, *Abaqus/cae user’s manual*, Pawtucket, RI, USA, 2000.
- [114] A. Inc., *Ansys user’s guide*, 2008.
- [115] F. McKenna, M. H. Scott, and G. L. Fenves, “Nonlinear Finite-Element Analysis Software Architecture Using Object Composition,” *Journal of Computing in Civil Engineering*, vol. 24, no. 1, pp. 95–107, Jan. 2010. DOI: 10.1061/(ASCE)CP.1943-5487.0000002.
- [116] N. Windows, “Msc/nastran configuration and operations guide,” 1998.
- [117] G. M. Barsan and C. G. Chiorean, “Computer program for large deflection elasto-plastic analysis of semi-rigid steel frameworks,” *Computers and Structures*, vol. 72, no. 6, pp. 699–711, 1999. DOI: 10.1016/S0045-7949(98)00310-1.
- [118] C. G. Chiorean, “A computer method for nonlinear inelastic analysis of 3D composite steel-concrete frame structures,” *Engineering Structures*, vol. 57, pp. 125–152, 2013. DOI: 10.1016/j.engstruct.2013.09.025.
- [119] C. G. Chiorean, “Second-order flexibility-based model for nonlinear inelastic analysis of 3d semi-rigid steel frameworks,” *Engineering Structures*, vol. 136, pp. 547–579, 2017. DOI: <https://doi.org/10.1016/j.engstruct.2017.01.040>.
- [120] J. O. Hallquist *et al.*, “Ls-dyna keyword user’s manual,” *Livermore Software Technology Corporation*, vol. 970, pp. 299–800, 2007.

- [121] C. V. Miculaş, “Nonlinear analysis of steel-concrete composite beams with full and partial shear connection,” Ph.D. dissertation, UPC, Escola Tècnica Superior d’Enginyers de Camins, Canals i Ports de Barcelona, Departament d’Enginyeria de la Construcció, Jun. 2015.
- [122] R. Balc, A. Chira, and N. Chira, “Finite element analysis of beam to column end plate bolted connection,” *Acta Technica Napocensis: Civil Engineering & Architecture*, vol. 55, no. 1, pp. 24–29, 2012.
- [123] S. Jordão, L. Simões Da Silva, and R. Simões, “Behaviour of welded beam-to-column joints with beams of unequal depth,” *Journal of Constructional Steel Research*, vol. 91, pp. 42–59, 2013. doi: 10.1016/j.jcsr.2013.07.023.
- [124] M. Pavlović, Z. Marković, M. Veljković, and D. Bucrossed D Signevac, “Bolted shear connectors vs. headed studs behaviour in push-out tests,” *Journal of Constructional Steel Research*, vol. 88, pp. 134–149, 2013. doi: 10.1016/j.jcsr.2013.05.003.
- [125] S. Jordão, L. Simões da Silva, and R. Simões, “Design formulation analysis for high strength steel welded beam-to-column joints,” *Engineering Structures*, vol. 70, pp. 63–81, Jul. 2014.
- [126] G. S. Prinz, A. Nussbaumer, L. Borges, and S. Khadka, “Experimental testing and simulation of bolted beam-column connections having thick extended endplates and multiple bolts per row,” *Engineering Structures*, vol. 59, pp. 434–447, Feb. 2014. doi: 10.1016/j.engstruct.2013.10.042.
- [127] P. Barata, J. Ribeiro, C. Rigueiro, A. Santiago, and J. P. Rodrigues, “Assessment of the T-stub joint component at ambient and elevated temperatures,” *Fire Safety Journal*, 2014. doi: 10.1016/j.firesaf.2014.08.009.
- [128] M. Latour, G. Rizzano, A. Santiago, and D. S. L. Simoes, “Experimental analysis and mechanical modeling of T-stubs with four bolts per row,” *Journal of Constructional Steel Research*, 2014. doi: 10.1016/j.jcsr.2014.05.004.
- [129] I. C. Muresan and R. Balc, “Finite element analysis of an extended end-plate connection using the t-stub approach,” in *AIP Conference Proceedings*, AIP Publishing LLC, vol. 1648, 2015, p. 850 091.
- [130] R. Rahnavard, A. Hassanipour, and N. Siahpolo, “Analytical study on new types of reduced beam section moment connections affecting cyclic behavior,” *Case Studies in Structural Engineering*, vol. 3, pp. 33–51, 2015. doi: <https://doi.org/10.1016/j.csse.2015.03.001>.

- [131] H. Augusto, L. Simões da Silva, C. Rebelo, and J. M. Castro, “Characterization of web panel components in double-extended bolted end-plate steel joints,” *Journal of Constructional Steel Research*, vol. 116, pp. 271–293, Jan. 2016. DOI: 10.1016/j.jcsr.2015.08.022.
- [132] H. Augusto, “Characterization of the behaviour of partial-strength joints under cyclic and seismic loading conditions,” Ph.D. dissertation, Universidade de Coimbra, 2017.
- [133] H. Ma, S. Ren, and F. Fan, “Experimental and numerical research on a new semi-rigid joint for single-layer reticulated structures,” *Engineering Structures*, vol. 126, pp. 725–738, 2016. DOI: 10.1016/j.engstruct.2016.08.028.
- [134] C. Mathieson, G. C. Clifton, and J. B. Lim, “Novel pin-jointed connection for cold-formed steel trusses,” *Journal of Constructional Steel Research*, vol. 116, pp. 173–182, Jan. 2016. DOI: 10.1016/j.jcsr.2015.08.009.
- [135] P. Krolo, D. Grandić, and M. Bulić, “The Guidelines for Modelling the Preloading Bolts in the Structural Connection Using Finite Element Methods,” *Journal of Computational Engineering*, vol. 2016, pp. 1–8, 2016. DOI: 10.1155/2016/4724312.
- [136] A. Ataei, M. A. Bradford, and X. Liu, “Computational modelling of the moment-rotation relationship for deconstructable flush end plate beam-to-column composite joints,” *Journal of Constructional Steel Research*, vol. 129, pp. 75–92, 2017. DOI: 10.1016/j.jcsr.2016.11.007.
- [137] R. Rahnavard and R. J. Thomas, “Numerical evaluation of the effects of fire on steel connections; part 1: Simulation techniques,” *Case Studies in Thermal Engineering*, vol. 12, pp. 445–453, 2018. DOI: <https://doi.org/10.1016/j.csite.2018.06.003>.
- [138] R. Rahnavard and R. J. Thomas, “Numerical evaluation of the effects of fire on steel connections; part 2: Model results,” *Case Studies in Thermal Engineering*, vol. 13, p. 100 361, 2019. DOI: <https://doi.org/10.1016/j.csite.2018.11.012>.
- [139] A. F. Santos, A. Santiago, M. Latour, G. Rizzano, and L. Simões da Silva, “Response of friction joints under different velocity rates,” *Journal of Constructional Steel Research*, vol. 168, 2020. DOI: 10.1016/j.jcsr.2020.106004.
- [140] A. F. Santos, A. Santiago, M. Latour, and G. Rizzano, “Robustness analysis of steel frames subjected to vehicle collisions,” *Structures*, vol. 25, no. February, pp. 930–942, 2020. DOI: 10.1016/j.istruc.2020.03.043.
- [141] A. F. H. P. d. Santos, “Behaviour of friction joints under impact loads,” Ph.D. dissertation, 2020.

- [142] S. M. Hosseini and R. Rahnavard, “Numerical study of steel rigid collar connection affecting cyclic loading,” *Engineering Structures*, vol. 208, p. 110 314, 2020. DOI: <https://doi.org/10.1016/j.engstruct.2020.110314>.
- [143] E. Elettore, F. Freddi, M. Latour, and G. Rizzano, “Parametric study and finite element analysis of self-centring steel column bases with different structural properties,” *Journal of Constructional Steel Research*, vol. 199, p. 107 628, 2022. DOI: <https://doi.org/10.1016/j.jcsr.2022.107628>.
- [144] T. Tankova, H. Craveiro, L. C. Silva, *et al.*, “Behaviour of plug-and-play joints between RHS columns and CFS trusses,” *Structures*, vol. 41, no. May, pp. 1719–1745, Jul. 2022. DOI: [10.1016/j.istruc.2022.05.099](https://doi.org/10.1016/j.istruc.2022.05.099).
- [145] F. Gentili, R. Costa, and L. Simoes da Silva, “Development of a simplified model for joints in steel structures,” in *9^o Congresso Nacional de Mecânica Experimental*, 2014.
- [146] E. Bayo, J. Gracia, B. Gil, and R. Goñi, “An efficient cruciform element to model semirigid composite connections for frame analysis,” *Journal of Constructional Steel Research*, vol. 72, pp. 97–104, 2012. DOI: [10.1016/j.jcsr.2011.11.006](https://doi.org/10.1016/j.jcsr.2011.11.006).
- [147] E. Bayo, J. M. Cabrero, and B. Gil, “An effective component-based method to model semi-rigid connections for the global analysis of steel and composite structures,” *Engineering Structures*, vol. 28, no. 1, pp. 97–108, 2006. DOI: [10.1016/j.engstruct.2005.08.001](https://doi.org/10.1016/j.engstruct.2005.08.001).
- [148] R. J. Costa, F. Gentili, and L. Simões da Silva, “Simplified model for connections of steel structures in OpenSees,” *Nordic Steel Construction Conference*, no. January, 2015.
- [149] F. Gentili, L. Simões da Silva, S. Oliveira, R. J. T. Costa, and F. Gentili, “Design and analysis of steel structures considering the 3D behaviour of the joints,” Tech. Rep. 2, Jun. 2020, pp. 137–145. DOI: [10.18057/IJASC.2020.16.2.5](https://doi.org/10.18057/IJASC.2020.16.2.5).
- [150] E. Bayo, A. Loureiro, M. Lopez, and L. Simões da Silva, “General component based cruciform finite elements to model 2D steel joints with beams of equal and different depths,” *Engineering Structures*, vol. 152, pp. 698–708, Dec. 2017. DOI: [10.1016/j.engstruct.2017.09.042](https://doi.org/10.1016/j.engstruct.2017.09.042).
- [151] E. Bayo, A. Loureiro, and M. Lopez, “Performance of cruciform finite elements that model 2D steel joints with beams of unequal depth in frame analysis,” *ce/papers*, vol. 1, no. 2-3, pp. 729–738, 2017. DOI: [10.1002/cepa.112](https://doi.org/10.1002/cepa.112).
- [152] Y. Harada and L. Simões da Silva, “Approach to macro-modeling of 3D tubular column-to-beam joint: An extension of component method for joint modelling,” *Connections in Steel Structures VIII*, vol. 1, no. c, pp. 163–172, 2016.

- [153] Y. Harada and L. Simões da Silva, “Three-dimensional macro-modeling of beam-to-rectangular hollow section column joints under cyclic loading. Part 1: Modeling of cyclic out-of-plane behavior of single isolated plate element,” *Journal of Constructional Steel Research*, vol. 162, p. 105 713, 2019. DOI: 10.1016/j.jcsr.2019.105713.
- [154] Y. Harada and L. S. da Silva, “Three-dimensional macro-modeling of beam-to-rectangular hollow section column joints under cyclic loading. Part 2: Modeling of beam-to-column joint by extended component-based approach,” *Journal of Constructional Steel Research*, vol. 162, p. 105 714, Nov. 2019. DOI: 10.1016/j.jcsr.2019.105714.
- [155] L. Costa Neves, “Monotonic and cyclic behaviour of minor axis and tubular joints in steel and steel and concrete composite structures.,” Doctoral dissertation, PhD Thesis (in Portuguese), University of Coimbra, Portugal, 2004.
- [156] EN 1993-1-3, *Eurocode 3: Design of steel structures - Part 1-3: General rules - Supplementary rules for cold formed thin gauge members and sheeting*, 2006.
- [157] B. Stroustrup, *The C++ Programming Language*, 3rd. USA: Addison-Wesley Longman Publishing Co., Inc., 2000.
- [158] F. McKenna, “Object oriented finite element programming frameworks for analysis, algorithms and parallel computing,” Ph.D. dissertation, University of California, Berkeley, 1997, p. 302.
- [159] B. W. Kernighan and D. M. Ritchie, *The C programming language*. 2006.
- [160] E. Akin, *Object-oriented programming via Fortran 90/95*. Cambridge University Press, 2003, vol. 1.
- [161] A. Altoontash, “Simulation and damage models for performance assessment of reinforced concrete beam-column joints,” Ph.D. dissertation, Stanford University, 2004.
- [162] J. K. Ousterhout *et al.*, *Tcl: An embeddable command language*. Citeseer, 1989.
- [163] M. Zhu, F. McKenna, and M. H. Scott, “OpenSeesPy: Python library for the OpenSees finite element framework,” *SoftwareX*, vol. 7, pp. 6–11, Jan. 2018. DOI: 10.1016/j.softx.2017.10.009.
- [164] G. Van Rossum, F. L. Drake, *et al.*, *Python reference manual*. Centrum voor Wiskunde en Informatica Amsterdam, 1995.
- [165] A. Schellenberg, T. Yang, and E. Kohama, *Opensees navigator*, 2005.
- [166] S. Mazzoni, *Buildingtcl/buildingtclviewer*, 2010.
- [167] NextFEM2015, *NextFEM designer user’s manual*. Version 1.7, 2015.

- [168] V. K. Papanikolaou, T. Kartalis-Kaounis, E. Protopapadakis, and T. Papadopoulos, “A new graphical user interface for opensees,” in *1st European conference on OpenSees*, 2017, pp. 73–6.
- [169] M. Petracca, F. Candeloro, and G. Camata, “Stko user manual,” *ASDEA Software Technology: Pescara, Italy*, vol. 551, 2017.
- [170] N. K. Psyrras and A. G. Sextos, “Build-x: Expert system for seismic analysis and assessment of 3d buildings using opensees,” *Advances in Engineering Software*, vol. 116, pp. 23–35, 2018. doi: <https://doi.org/10.1016/j.advengsoft.2017.11.007>.
- [171] P. Mackenzie-Helnwein, P. Arduino, F. McKenna, and T. Sweet, *Nheri-simcenter / pilegrouptool*, version v2.1.0, This work is funded by the National Science Foundation under grant CMMI 1612843, Nov. 2018. doi: 10.5281/zenodo.1478813.
- [172] F. McKenna, *Multiple degrees of freedom application*, version 1.1, The SimCenter is supported by a grant from the National Science Foundation (#1612843), Jan. 2018. doi: 10.5281/zenodo.1410693.
- [173] A. Almutairi, J. Lu, A. Elgamal, and K. Mackie, “Msbridge: Opensees pushover and earthquake analysis of multi-span bridges-user manual,” *SSRP*, vol. 16, no. 05, 2018.
- [174] G. Baltzopoulos, R. Baraschino, I. Iervolino, and D. Vamvatsikos, “Dynamic analysis of single-degree-of-freedom systems (dyanas): A graphical user interface for opensees,” *Engineering Structures*, vol. 177, pp. 395–408, 2018. doi: <https://doi.org/10.1016/j.engstruct.2018.09.078>.
- [175] M. M. Rahman, T. T. Nahar, and D. Kim, “Fevuew: Finite element model (fem) visualization and post-processing tool for opensees,” *SoftwareX*, vol. 15, p. 100751, 2021. doi: <https://doi.org/10.1016/j.softx.2021.100751>.
- [176] S. Mazzoni, *eSEES: a Scripting & Graphical User Interface for OpenSees*. Version v1.0, Oct. 2021.
- [177] A. Shabani and M. Kioumarsi, “Hyperomet: An opensees interface for nonlinear analysis of unreinforced masonry buildings,” *SoftwareX*, vol. 20, p. 101230, 2022. doi: <https://doi.org/10.1016/j.softx.2022.101230>.
- [178] J. Abell, *A simple python module to use gmsh and opensees together in python*. Version v1.0, Dec. 2022.
- [179] J. Guo, A. Ye, X. Wang, and Z. Guan, “Openseespyview: Python programming-based visualization and post-processing tool for openseespy,” *SoftwareX*, vol. 21, p. 101278, 2023. doi: <https://doi.org/10.1016/j.softx.2022.101278>.

- [180] GitHub, *OpenSees: Joint Element Library*.
- [181] L. N. Lowes, N. Mitra, and A. Altoontash, “A Beam-Column Joint Model for Simulating the Earthquake Response of Reinforced Concrete Frames,” Tech. Rep. August, 2003, p. 69.
- [182] C.-Y. Seo, Y.-C. Lin, R. Sause, and J. Ricles, “Development of Analytical Models for 0.6 Scale Self-Centering MRF with Beam Web Friction Devices,” in *6th International Conference for Steel Structures in Seismic Area (STESSA)*, Philadelphia: CRC Press, 2009, pp. 849–854.
- [183] P. Alanjari, B. Asgarian, and N. Salari, “Elastic tubular joint element for modelling of multi-brace, uni-planar tubular connections,” *Ships and Offshore Structures*, vol. 10, no. 4, pp. 404–415, Jul. 2015. DOI: 10.1080/17445302.2014.942077.
- [184] L. N. Lowes and A. Altoontash, “Modeling reinforced-concrete beam-column joints subjected to cyclic loading,” *Journal of Structural Engineering*, vol. 129, no. 12, pp. 1686–1697, 2003. DOI: 10.1061/(ASCE)0733-9445(2003)129:12(1686).
- [185] T. L. Karavasilis, J. Ricles, and C.-Y. Seo, *HybridFEM : A program for dynamic time history analysis of 2D inelastic framed structures and real-time hybrid simulation*. 2010.
- [186] Computers and Structures Incorporated (CSI), *CSI Analysis Reference Manual For SAP2000®, ETABS®, SAFE® and CSiBridge*, Berkley, CA, 2020.
- [187] Autodesk, *Robot Structural Analysis Professional 2021 User’s Guide*, 2020.
- [188] L. Simões da Silva, T. Tankova, H. D. Craveiro, L. C. Silva, R. Simões, and R. Costa, “Innovative 3D joint for steel modular construction,” *ce/papers*, vol. 4, no. 2-4, pp. 958–963, Sep. 2021. DOI: 10.1002/cepa.1384.
- [189] A. Poursadrollah, M. D’Aniello, A. De Martino, and R. Landolfo, “Preliminary study on the seismic performance of hybrid steel structures with truss lightweight girders and plug-and-play connections,” *International Journal*, vol. 37, no. 1-2020, 2020.
- [190] Centre Technique Industriel de la Construction Metallique (CTICM), *Inno3DJoints*, France, 2020.
- [191] European Commission, *INNOvative 3D JOINTS for robust and economic hybrid tubular construction. Deliverable D7.1 Report on new rules for hybrid joints based on the component method*. Research Programme of the Research Fund for Coal and Steel, 2021.
- [192] R. M. Lawson, *Light Steel Modular Construction - Technical Information Sheet ED014*.
- [193] A. Poursadrollah, “Flexural buckling of steel cold-formed hollow profiles in the framework of eurocodes,” Ph.D. dissertation, Università degli Studi di Napoli Federico II, 2021.

- [194] A. Poursadrollah, M. D’Aniello, and R. Landolfo, “Experimental and numerical tests of cold-formed square and rectangular hollow columns,” *Engineering Structures*, vol. 273, no. June, p. 115 095, 2022. DOI: 10.1016/j.engstruct.2022.115095.
- [195] A. Poursadrollah, “Finite element reliability analysis of flexural buckling of cold-formed hollow section members,” in *AIP Conference Proceedings*, AIP Publishing LLC, vol. 2425, 2022, p. 120 015.
- [196] J. Valdez, “Innovative hybrid plug-and-play connections for CFS-tubular modular buildings - Project of Thesis draft (INNO3DJOINTS internal report),” University of Coimbra | ISISE, Tech. Rep., 2018.
- [197] European Commission, *INNOvative 3D JOINTS for robust and economic hybrid tubular construction. Deliverable D4.1 Report on components assembly and on the model leading to the construction of the joint macro finite element*. Research Programme of the Research Fund for Coal and Steel, 2021.
- [198] European Commission, *INNOvative 3D JOINTS for robust and economic hybrid tubular construction. Deliverable D4.2 Report on software tools*. Research Programme of the Research Fund for Coal and Steel, 2021.
- [199] T. M. Nguyen and A. Rodier, “Macro-modelling of 3d tubular column-to-truss beam joints,” *ce/papers*, vol. 4, no. 2-4, pp. 924–928, 2021.
- [200] A. Ghali, A. M. Neville, and T. G. Brown, *Structural Analysis: A unified classical and matrix approach (6th edition)*. CRC Press, 2009. DOI: 10.1201/9781315273006.
- [201] V. D. da Silva, *Mechanics and Strength of Materials*. Berlin, Heidelberg: Springer Berlin Heidelberg, 2006. DOI: 10.1007/3-540-30813-X.
- [202] Microsoft Corporation, *Visual Studio 2019*, 2019.
- [203] H. Matthies and G. Strang, “The solution of nonlinear finite element equations,” *International Journal for Numerical Methods in Engineering*, vol. 14, no. 11, pp. 1613–1626, 1979. DOI: 10.1002/nme.1620141104.
- [204] GitHub, *OpenSees/OpenSees: OpenSees Source Code Repository*.
- [205] T. Togo, “Experimental Study on Mechanical Behavior of Tubular Joints (in Japanese),” Ph.D. dissertation, Osaka University, 1967.
- [206] F. Gomes, “État Limite Ultime de la Résistance de l’âme d’une Colonne dans un Assemblage Semi-rigide d’axe Faible,” Université de Liège, Liège, Tech. Rep., 1990.

Bibliography

- [207] L. Costa Neves and F. Gomes, “Semi-rigid behaviour of beam-to-column minor- axis joints,” in *IABSE Int.Colloquium on Semi-Rigid Structural Connections*, 1996, pp. 207–216.
- [208] “Rotational Stiffness of Rectangular Hollow Sections Composite Joints,” *Journal of Structural Engineering*, vol. 129, no. 4, pp. 487–494, Apr. 2003. doi: 10.1061/(ASCE)0733-9445(2003)129:4(487).
- [209] M. H. Scott, *Algorithmic Limerick*, 2019.
- [210] C. V. Miculaş, *Abqtcphd: An abaqus rsg to build a tubular column with socket faces*. Version v1.0, Mar. 2023.
- [211] C. V. Miculaş. “Abqtcphd: An abaqus rsg to build a tubular column with socket faces.” (Mar. 2023).
- [212] Hibbit, Karlsson, and Sorenson, *Abaqus theory manual*, Pawtucket, RI, USA, 1997.
- [213] J. Packer, J. Wardenier, X.-L. Zhao, A. Ven der Vegte, and Y. Kurobane, “Design guide for rectangular hollow section (RHS) joints under predominantly static lading,” CIDECT, Tech. Rep., 2009.
- [214] CEN/TC250/SC3/WG8 N154 and N155, *Eurocode 3 – Design of steel structures – Part 1-8: Design of joints. Final draft with changes agreed at WG8 meeting in Bucharest*, 2019.
- [215] L. Simões da Silva, “Towards a consistent design approach for steel joints under generalized loading,” *Journal of Constructional Steel Research*, vol. 64, no. 9, pp. 1059–1075, Sep. 2008. doi: 10.1016/j.jcsr.2008.02.017.
- [216] M. Garifullin, S. Pajunen, K. Mela, and M. Heinisuo, “3D component method for welded tubular joints.,” in *Proceedings of the 16th international symposium on tubular structures*, A. Heidarpour and X.-L. Zhao, Eds., Melbourne, Australia: Taylor and Francis Group, 2018.